รายงานวิจัยฉบับสมบูรณ์

การพัฒนาฟิลม์บางของโบรอน-โดปไดมอนด์โดยการแอโนไดซ์

Development of Boron-Doped Diamond Thin Film by Anodization

รศ.ดร.อรวรรณ ชัยลภากุล

31 สิงหาคม 2550

กิตติกรรมประกาศ

ขอขอบคุณ
สำนักงานกองทุนสนับสนุนการวิจัย
จุฬาลงกรณ์มหาวิทยาลัย

สัญญาเลขที่ RSA4780027

รายงานวิจัยฉบับสมบูรณ์

การพัฒนาฟิล์มบางของโบรอน-โดปไดมอนด์โดยการแอโนไดซ์

Development of Boron-Doped Diamond Thin Film by Anodization

รศ.ดร.อรวรรณ ชัยลภากุล

ภาควิชาเคมี คณะวิทยาศาสตร์ จุฬาลงกรณ์มหาวิทยาลัย

สนับสนุนโดยสำนักงานกองทุนสนับสนุนการวิจัย

บทคัดย่อ

รหัสโครงการ RSA4780027

ชื่อโครงการ: การพัฒนาฟิลม์บางของโบรอน-โดปไดมอนด์โดยการแอโนไดซ์

E-mail Address: corawon@chula.ac.th

ระยะเวลาที่ทำการวิจัย: 3 ปี

ในงานวิจัยนี้ได้มุ่งเน้นไปที่การพัฒนาการใช้ฟิล์มบางของโบรอน-โดปไดมอนด์ซึ่งผ่านการดัดแปรผิวหน้าด้วยการแอโนไดซ์และการฝังโลหะนิกเกิลสำหรับการหาปริมาณของสารในกลุ่มเตตร้าไซคลิน โดยทำการศึกษาเคมีไฟฟ้าของสารเตตร้าไซคลินที่ขั้วไฟฟ้าฟิล์มบางของโบรอน-โดปไดมอนด์ซึ่งผ่านการแอโนไดซ์ด้วยไซคลิกโวลแทมเมทรีและโฟลว์อินเจคชัน ซึ่งต่อกับระบบตรวจวัดทางเคมีไฟฟ้า เปรียบเทียบผลการทดลองโดยไซคลิกโวลแทมเมทรีกับขั้วไฟฟ้ากลาสสิคาร์บอนและขั้วไฟฟ้าฟิล์มบางของโบรอน-โดปไดมอนด์ พบว่าขั้วไฟฟ้าฟิล์มบางของโบรอน-โดปไดมอนด์ซึ่งผ่านการแอโนไดซ์จะให้ผลของไซคลิกโวลแทมโมแกรมสำหรับปฏิกิริยาออกซิเดชันของสารเตตร้าไซคลินแบบไม่ผันกลับที่ชัดเจนและให้สัญญาณกระแสไฟฟ้าสูงสุดเมื่อเปรียบเทียบกับขั้วไฟฟ้ากลาสสิคาร์บอนและขั้วไฟฟ้าฟิล์มบางขอโบรอน-โดปไดมอนด์ วิธีดังกล่าวสามารถนำไปประยุกต์ใช้กับการตรวจวัดสารเตตร้าไซคลินในตัวอย่างยาเตรียมได้ จากการศึกษาร้อยละการกลับคืนของสารมาตรฐานที่เติมในตัวอย่าง พบว่าผลการทดลองที่ได้เป็นที่น่าพอใจมีความสอดคล้องกับค่าที่ระบุในฉลาก สำหรับการวิเคราะห์ทางเคมีไฟฟ้าของสารเตตร้าไซคลินด้วยขั้วไฟฟ้าฟิล์มบางของโบรอน-โดปไดมอนด์ซึ่งผ่านการฝังโลหะนิกเกิล เปรียบเทียบผลการทดลองกับขั้วไฟฟ้าฟิล์มบางของโบรอน-โดปไดมอนด์ พบว่าที่ขั้วไฟฟ้าฟิล์มบางของโบรอน-โดปไดมอนด์ซึ่งผ่านการฝังด้วยโลหะนิกเกิลให้ผลของไซคลิกโวลแทมโมแกรมสำหรับปฏิกิริยาออกซิเดชันของสารเตตร้าไซคลินแบบไม่ผันกลับที่ชัดเจนและให้สัญญาณกระแสไฟฟ้าที่สูงกว่า นอกจากนี้ ได้นำขั้วไฟฟ้าฟิล์มบางของโบรอน-โดปไดมอนด์ซึ่งผ่านการฝังโลหะนิกเกิลไปใช้เป็นตัวตรวจวัดในระบบโฟลว์อินเจคชันเพื่อหาปริมาณของสารเตตร้าไซคลินในสารตัวอย่างยาด้วย และในส่วนสุดท้ายแสดงถึงผลที่ได้จากการนำขั้วไฟฟ้าฟิล์มบางของโบรอน-โดปไดมอนด์ซึ่งผ่านการฝังโลหะนิกมาใช้เป็นตัวตรวจวัดสารเตตร้าไซคลินที่ผ่านการแยกจากระบบไฮเปอร์ฟอร์มานซ์ลิควิดโครมาโทกราฟี ภายใต้ภาวะคือทำการแยกด้วยคอลัมน์ C18 ใช้เฟสเคลื่อนที่ที่ประกอบด้วยสารละลายฟอสเฟสบัพเฟอร์ (พีเอช 2.5) และแอซิโทรไนไตร์ ในอัตราส่วน 80:20 และตรวจวัดที่ 1.55 โวลต์ จากการสอบทวนในช่วงความเข้มข้น 0.05-100 พีพีเอ็ม ได้ค่าร้อยละการกลับคืนระหว่าง 83.3 – 102.5 ด้วยค่าเบี่ยงเบนมาตรฐานสัมพัทธ์ต่ำกว่า 10 เปอร์เซ็นต์ จากการนำวิธีนี้ไปใช้สำหรับการหาปริมาณสารเตตร้าไซคลินในสารตัวอย่างกุ้ง พบว่าวิธีที่เสนอนี้เป็นวิธีที่มีความเที่ยง ความแม่น และมีความไวต่อการหารปริมาณเตตร้าไซคลิน

คำสำคัญ: เตตร้าไซคลิน, ฟิล์มบางของโบรอน-โดปไดมอนด์ซึ่งผ่านการแอโนไดซ์, ฟิล์มบางของโบรอน-โดปไดมอนด์ซึ่งผ่านการฝังโลหะนิกเกิล, ไซคลิกโวลแทมเมทรี, โฟลอินเจคชัน, ไฮเปอร์ฟอร์มานลิควิดโครมาโทกราฟี, แอมเพอโรเมทรี

Abstract

Project code: RSA/21/2547

Project Title: Development of Boron-Doped Diamond Thin Film by Anodization

E-mail Address: corawon@chula.ac.th

Project period: 3 years

This research focused on the development of employing the modified boron-doped diamond thin film (BDD) including anodized BDD and Ni-implanted (Ni-DIA) BDD electrodes for the determination of tetracyclines (TCs). The electrochemistry of TCs was studied at an anodized BDD electrode using cyclic voltammetry and flow injection (FI) with electrochemical detector. At anodized BDD electrode, comparative experiments by cyclic voltammetry were performed at polishing glassy carbon (GC) and as-deposited BDD electrodes. The anodized BDD electrode exhibited well-defined irreversible cyclic voltammograms for the oxidation of TCs with the highest current signals compared to the as-deposited BDD and GC electrodes. The proposed method was also applied to determine TCs in pharmaceutical formulations. Recoveries of spiked standard solution were determined. The results obtained were satisfactory with label. For the electrochemical analysis of TCs using Ni-DIA BDD electrode, comparison experiments were carried out using as-deposited BDD electrode. Ni-DIA BDD electrode provided well-resolved oxidation irreversible cyclic voltammograms and the higher current signals when compared to those of as-deposited BDD electrode. Results using Ni-DIA BDD electrode in FI system coupled with amperometric detection were illustrated for the determination of TCs in drug samples. Moreover, in the last part, HPLC with amperometric detection using Ni-DIA electrode was also demonstrated. The chromatography was performed using a commercially available Inertsil C18 column, with the mobile phase being: 80% phosphate buffer (pH 2.5)–20% acetonitrile and detected at 1.55V. The methods were validated over the concentration range 0.05–100 ppm with the overall average recoveries from 83.3 to 102.5% and R.S.D. of less than 10%. The proposed method was further applied to analyze shrimp samples. The results obtained showed that this method is precise, accurate, and sensitive for the determination of TCs.

Keywords: TETRACYCLINES, ANODIZED BORON-DOPED DIAMOND THIN FILM ELECTRODE, Ni-IMPLANTED DIAMOND ELECTRODE, CYCLIC VOLTAMMETRY, FLOW INJECTION SYSTEM, HPLC, AMPEROMETRIC DETECTION

Executive Summary

วัตถุประสงค์

1. ศึกษาลักษณะของขั้วไฟฟ้าฟิล์มบางโบรอนโดปไดมอนด์ที่ได้พัฒนาโดยการแอโนไดซ์และโดยการฝังด้วยโลหะนิกเกิล
2. ศึกษาภาวะที่เหมาะสมสำหรับการใช้งานของขั้วไฟฟ้าฟิล์มบางโบรอนโดปไดมอนด์ที่ผ่านการแอโนไดซ์ และโดยการฝังด้วยโลหะนิกเกิล ตัวอย่างเช่น ผลของ pH สารละลายอิเล็กโทรไลท์ อัตราการสแกน เป็นต้น
3. ประยุกต์ใช้ขั้วไฟฟ้าฟิล์มบางโบรอนโดปไดมอนด์ที่ได้ดัดแปรโดยการแอโนไดซ์และโดยการฝังด้วยโลหะนิกเกิล กับการวิเคราะห์เชิงปริมาณ
4. ตรวจสอบอุปกรณ์ตรวจวัดที่ประกอบจากโบรอนโดปไดมอนด์อิเล็กโทรดที่ผ่านการดัดแปรเข้ากับระบบของไหลและระบบที่มีการแยก หาภาวะที่เหมาะสมในการวิเคราะห์แล้วนำไปทดลองใช้หาปริมาณของสารตัวอย่างจริง

การดำเนินงานวิจัย และผลงานวิจัยที่ได้รับอย่างย่อ ๆ

1. ค้นคว้าข้อมูลและเอกสารที่เกี่ยวข้อง
2. ตรวจสอบสารเตตร้าไซคลิน ใช้ขั้วไฟฟ้าฟิล์มบางโบรอน-โดปไดมอนด์ที่ได้ดัดแปรโดยการแอโนไดซ์ และโดยการฝังด้วยโลหะนิกเกิล ด้วยเทคนิค ไซคลิกโวลแทมเมทรี และแอมเพอโรเมทรี
3. หาภาวะที่เหมาะสมในการวิเคราะห์เตตร้าไซคลิน เพื่อปรับปรุงวิธีการวิเคราะห์ให้สามารถวิเคราะห์ได้ที่ความเข้มข้นต่ำ และเปรียบเทียบสมบัติทางเคมีไฟฟ้าของสารเตตร้าไซคลินเมื่อใช้ขั้วไฟฟ้าฟิล์มบางโบรอน-โดปไดมอนด์ที่ได้ดัดแปรโดยการแอโนไดซ์ ขั้วไฟฟ้าฟิล์มบางโบรอน-โดปไดมอนด์ และขั้วไฟฟ้ากลาสิคาร์บอนโดยใช้เทคนิคไซคลิกโวลแทมเมทรี จากการทดลองพบว่า สารเตตร้าไซคลินสามารถเกิดปฏิกิริยาผันกลับไม่ได้ที่ขั้วไฟฟ้าทั้งสามชนิด แต่ขั้วไฟฟ้าฟิล์มบางโบรอน-โดปไดมอนด์ที่ได้ดัดแปรโดยการแอโนไดซ์ จะให้ค่าสัญญาณของกระแสต่อพื้นหลังที่สูงกว่าขั้วไฟฟ้าฟิล์มบางโบรอน-โดปไดมอนด์และขั้วไฟฟ้ากลาสิคาร์ ค่า pH ที่เหมาะสมที่ให้สัญญาณในการตรวจวัดสูงสุดสำหรับเตตร้าไซคลิน ได้แก่ 2.0 สำหรับการหาภาวะที่เหมาะสมในการวิเคราะห์เตตร้าไซคลินด้วยขั้วไฟฟ้าฟิล์มบางโบรอน-โดปไดมอนด์ที่ได้ดัดแปรโดยการฝังด้วยโลหะนิกเกิล เมื่อเปรียบเทียบสัญญาณที่ได้จากปฏิกิริยาออกซิเดชันเมื่อใช้ขั้วไฟฟ้าฟิล์มบางโบรอน-โดปไดมอนด์ พบว่า ที่ขั้วไฟฟ้าฟิล์มบางโบรอน-โดปไดมอนด์ที่ได้ดัดแปรโดยการฝังด้วยโลหะนิกเกิล ให้สัญญาณที่สูงกว่าที่ค่า pH ของสารละลายเท่ากับ 2.0 เช่นกัน

4. หาภาวะที่เหมาะสมโดยใช้เทคนิคแอมเพอโรเมทรี ร่วมกับการตรวจวัดด้วยระบบโฟลว์อินเจคชันโดยใช้ขั้วไฟฟ้าฟิล์มบางโบรอน-โดปไดมอนด์ที่ได้ดัดแปรโดยการแอโนไดซ์หรือโดยการฝังด้วยโลหะนิกเกิล เป็นขั้วไฟฟ้าทำงาน จากผลการทดลองที่ได้จากขั้วไฟฟ้าฟิล์มบางโบรอน-โดปไดมอนด์ที่ได้ดัดแปรโดยการแอโนไดซ์ พบว่าศักย์ไฟฟ้าที่เหมาะสมในการตรวจวัดสารในกลุ่มเตตร้าไซคลิน ซึ่งประกอบด้วย ได้แก่ 1.50 โวลต์ สำหรับคลอเตตร้าไซคลิน และ 1.60 โวลต์ สำหรับเตตร้าไซคลิน ออกซีไซคลิน และด๊อกซีไซคลิน ตามลำดับ สำหรับผลที่ได้จากเทคนิคโฟลว์อินเจคชันให้ค่าขีดจำกัดต่ำสุดสำหรับสารทั้งสี่ชนิด ในการตรวจวัดที่ 10 นาโนโมลาร์ (S/N ≈ 3) จากผลการทดลอง เตตร้าไซคลิน ให้ช่วงความเข้มข้นที่เป็นเส้นตรงจาก 0.1 ถึง 50 ไมโครโมลาร์ และสำหรับคลอเตตร้าไซคลิน ออกซีไซคลิน และด๊อกซีไซคลิน ให้ช่วงความเข้มข้นที่เป็นเส้นตรงจาก 0.5 ถึง 50 ไมโครโมลาร์ ผลการทดลองที่ได้จากขั้วไฟฟ้าฟิล์มบางโบรอน-โดปไดมอนด์ที่ได้ดัดแปรโดยการฝังโลหะนิกเกิล เมื่อต่อกับระบบโฟลว์อินเจคชัน พบว่า ศักย์ไฟฟ้าที่เหมาะสมในการตรวจวัดสารเตตร้าไซคลิน คือ 1.55 โวลต์ ค่าขีดจำกัดต่ำสุดในการตรวจวัดเท่ากับ 10 นาโนโมลาร์ (S/N ≈ 3) และให้ช่วงความเข้มข้นที่เป็นเส้นตรงจาก 1 ถึง 100 ไมโครโมลาร์ เมื่อนำขั้วไฟฟ้าฟิล์มบางโบรอน-โดปไดมอนด์ที่ได้ดัดแปรโดยการฝังโลหะนิกเกิล มาใช้เป็นตัวตรวจวัดในระบบไฮเปอร์ฟอร์มานส์ลิควิดโครมาโทกราฟี พบว่า ได้ค่าขีดจำกัดต่ำสุดในการตรวจวัดอยู่ในช่วง 0.01 – 0.05 พีพีเอ็ม (S/N ≈ 3) ช่วงความเข้มข้นที่เป็นเส้นตรงจาก 0.05 ถึง 100 พีพีเอ็ม สำหรับเตตร้าไซคลินและคลอเตตร้าไซคลิน และจาก 0.1 ถึง 100 พีพีเอ็ม สำหรับออกซีไซคลินและด๊อกซีไซคลิน ตามลำดับ
5. นำวิธีที่เหมาะสมมาใช้หาปริมาณเตตร้าไซคลินในสารตัวอย่างยา การทดลองใช้เทคนิคการเติมสารมาตรฐานพบว่า ได้ร้อยละของการคืนกลับอยู่ในช่วง 98.40 -101.50 มีความเที่ยง 1.30-3.0 เปอร์เซ็นต์ กรณีที่ใช้ ขั้วไฟฟ้าฟิล์มบางโบรอน-โดปไดมอนด์ที่ได้ดัดแปรโดยการแอโนไดซ์ และค่าร้อยละของการคืนกลับในช่วง 97.22-102.38 ความเที่ยง 2.82 เปอร์เซ็นต์ สำหรับขั้วไฟฟ้าฟิล์มบางโบรอน-โดปไดมอนด์ที่ได้ดัดแปรโดยการฝังด้วยโลหะนิกเกิล สำหรับการหาปริมาณเตตร้าไซคลินในสารตัวอย่างกุ้ง หลังจากที่แยกด้วยระบบไฮเปอร์ฟอร์มานส์ลิควิดโครมาโทกราฟี พบว่า ได้ร้อยละของการคืนกลับอยู่ในช่วง 97.00 -103.70 สำหรับตัวอย่างกุ้งฟาร์ม และร้อยละ 96.5-99.4 สำหรับตัวอย่างกุ้งทะเล จากผลการทดลองพบว่าการใช้เทคนิคแอมเพอโรเมทรีร่วมกับระบบโฟลว์อินเจชันหรือระบบไฮเปอร์ฟอร์มานส์ลิควิดโครมาโทกราฟี ให้ผลการทดลองที่ถูกต้อง มีความสามารถในการทำซ้ำ และให้ช่วงการทำงานที่เป็นเส้นตรงที่กว้าง จึงสามารถนำไปประยุกต์กับการวิเคราะห์ตัวอย่างได้อย่างมีประสิทธิภาพ

INTRODUCTION

Introduction

Currently, the use of synthetic conductive diamond thin films, a new carbon material, is being increasingly reported [1-10]. Diamond is one of the most insulating of insulators; however, boron can be used as a convenient dopant in diamond, at levels all the way from about 10^{16} up to 10^{21} cm^{-3}, with activation energies down to less than one tenth of an electron volt, so that the conductivity can be fine-tuned for a variety of purposes [11]. Therefore, boron-doped diamond (BDD) is one of the most promising new materials for electroanalytical measurements. It has been reported that the BDD electrode possesses electrochemically attractive properties compared to other electrodes, including low and stable voltammetric background currents. The currents for double layer charging are quite small, due to the low number of carriers and the nearly complete lack of porosity. These attributes make the BDD electrode well suited for current-based electrochemical measurements. Other attractive features include the wide working potential window in aqueous electrolyte solution, low adsorption of polar molecules from aqueous solution, long-term response stability, and good activity without any pretreatment [12-15].

Besides the as-deposited BDD electrode, recently, modified diamond surfaces are becoming more and more extensively used. The modification techniques, which include chemical, electrochemical and photochemical techniques, have been reported; these include ways of attaching anything from terminating atoms, such as oxygen, as well as metal particles and metal oxides. From these modification techniques, chemically pretreated by electrochemical oxidation is the simplest technique. The anodized diamond electrodes retain the excellent properties of the as-deposited diamond electrode even though, the electrode surface of anodized diamond electrode is applied by a high anodic potential. Anodized diamond electrodes are suitable for determination of various analytes such as chlorophenol [16], dopamine and uric acid in the presence of ascorbic acid [17] and homocysteine [18]. These anodized

electrodes have exhibited some attractive properties such as excellent stability and high reproducibility.

While some metals, such as platinum is known to oxidize hydrogen peroxide and methanol, as well as nickel is conventionally used for carbohydrates electrochemical detection in alkali solution [19–21]. BDD electrode is found completely inactive for those kinds of catalytic reactions. However, it has been reported that the dispersion of metallic particles within an organic polymer or an inert surface resulted indrastic increase of the catalytic activity and sensitivity of the electrode because the dispersed particles behave like microelectrode arrays [20]. The chemically modified electrodes (CMEs) which are capable of lowering the operational potential required to oxidize scarcely electroactive organic compounds has caught a great deal of interest. Reduced electrode fouling has also been reported. CMEs based on the modification of glassy carbon or graphite rods with various metals (e.g. copper [22-24], cobalt [25], and nickel [20, 21, 26–28]) have shown catalytic activities towards polyhydroxy compounds. These electrodes have been successfully applied to detect carbohydrate [20–22, 25, 26], amino acids [26, 28], sugars [23] and aliphatic alcohol compounds [27] using amperometric detection. Unfortunately, glassy carbon electrode has a major drawback of yielding high background current. These metalmodified diamond electrodes appear to be well suited to overcome such problems. BDD film would be the best choice for the deposition of metal electrocatalysts. The preparation of some metal-modified BDD electrodes for electrochemical analysis by using chemical precipitation and electrochemical deposition method had been reported [19].

Ion implantation into a material can be used to form near surface composites. The method is used to modify the structure of a target-near-surface by bombardment with heavy ions. This method is popular for the preparation of doping semiconductors, such as silicon and gallium arsenide, so it has been of particular interest for the fabrication of ion-implanted diamond. At present, some applications for electrochemical use by metal-implanted conductive BDD electrodes have been reported [29].

Therefore, we are interested in developing a method for the determination of tetracyclines by using anodized BDD electrode the Ni-implanted diamond electrode

as a working electrode for amperometric determination using flow injection system and HPLC system.

Tetracyclines (Figure1) are board spectrum antibiotics for their high activity against nearly all gram-positive and gram-negative bacteria. Tetracycline, chlortetracycline, oxytetracycline and doxycycline are four members of this antibiotic group that are commonly used in food protection animals (including honeybee), because of their board spectrum activity and low production cost. However, use of these drugs has become the serious problem as regard infectious diseases, as they are substances that residue in milk or meat which can be directly toxic or else cause allergic reactions in some hypersensitive individuals in human. Owing their extensive use in infectious diseases therapy, there are several methods used to determine these compounds in pharmaceutical preparations, biological samples and milk samples. Official methods such as microbiological-based techniques can also provide both qualitative and quantitative analysis for tetracyclines [30-32]. These methods available have their characteristic disadvantages: microbiological tests are not only time consuming laborious and expensive but also poor in term of sensitivity and selectivity. Other methods for quantification the amount of tetracyclines were developed based on batch procedures with spectrophotometry [33-34], chemiluminescence [35-38], spectrofluorimetry [39], and electrochemical method [40]. Flow injection system was incorporated with conventional analytical instrument to improve sample throughput and sensitivity that are the requirement to develop approach in pharmaceutical industry. Many detection methods were coupled to a flow injection system such as spectrophotometry [41-42], chemiluminescence [43-44] and electrochemical method [45-47]. Flow injection based on the spectrophotometric detection is described to determine tetracyclines by the monitoring the color product formed by their reaction with 4-aminophenazone and hexacyanoferrate (III). However, this method has a limitation in a concentration range. Under the optimized conditions, tetracyclines were determined in the ranges 1-20 and 20-250 mg L^{-1}. The lowest limit of detection is 0.2 mg L^{-1} for doxycycline [33]. For chemiluminescence using oxidizing agent such as *N*-Bromosuccinimide, is an alternative method but the oxidizing agent is highly toxic and the methods are expensive. The working range for determining is 0.05-3.00 mg L^{-1} for tetracycline, 0.50-5.00 mg L^{-1} for oxytetracycline and 0.50-7.00 mg L^{-1} for doxycycline and

chlortetracycline. The detection limit is 0.0049, 0.40, 0.23, and 0.22 mg L^{-1} for tetracycline, oxytetracycline, doxycycline, and chlortetracycline respectively [35]. Electrochemical techniques such as amperometric and potentiometric detection are good alternative methods that are widely used in the pharmaceutical application because they are easy to operate, fast and inexpensive. The sensitivity of electrochemical method is also higher than the spectrophotometric method such as the detection limit from HPLC-amperometric detection of 0.1-1 mg L^{-1} for tetracycline family [48]. The calibration graph showed linear relationship between 0.1 and 50 mg L^{-1} for tetracycline, oxytetracycline and doxycycline and relationship between 0.5-50 mg L^{-1} for chlortetracycline. Procedures in electroanalysis strongly depend on working electrode materials. Hence, the searching and synthetic the new electrode material is necessary. Thus, for part I, we described to use of the anodized diamond electrode for the determination of tetracyclines using cyclic voltammetry. Glassy carbon (GC) and as-deposited diamond electrodes were also used for comparison. The anodized diamond electrode was exploited as working electrode for amperometric determination of antibiotic drugs, using flow injection system.

Moreover, today the shrimp farming is an important economic section in south-east asian countries, especially Thailand. The most markets of these countries are Japan, the United States and Europe, which have regulations to control quality of imports. The shrimp farming cannot avoid using antibiotics; however, tetracyclines that are the most important ones of antibiotics are generally used in the shrimp farming. The residues of tetracyclines may be found in shrimps and the levels of tetracycline residues may be unacceptable for the international markets. Therefore, the methods of the detection of tetracyclines at low levels are intensively required.

For detecting the tetracycline residues, the microbiological assays, the official methods, are most usually used, but they are complicated, time-consuming and non-specific. Therefore, sensitive and specific analytical methods for identification and quantitation of tetracyclines are required. High performance liquid chromatography (HPLC) is normally used for this purpose.

HPLC is a common method that separates tetracyclines in the reverse-phase mode with a variety of detection methods, such as spectrophotometry [49-50],

fluorometry [51-52], mass spectrometry [53-54] and electrochemistry [55-56]. Among these, the electrochemical method is distinctly attractive owing to its simplicity, no need for derivatization, fast analysis, low cost and high sensitivity. There are several reports utilizing polarography, potentiometry [57] and amperometry [55-56, 58] for the analysis of tetracycline. In 2005, Charoenraks et al. reported the use of high performance liquid chromatography with pulsed amperometric detection at anodized boron-doped diamond thin film electrode for the detection of tetracyclines.

Therefore, in following part, we report the use of Ni-implanted boron-doped diamond thin film electrodes (Ni-DIA) to study the electrochemical oxidation of tetracyclines using cyclic voltammetry. Focus is placed on comparing the results with as-deposited BDD and glassy carbon electrodes. In addition, the performance of the Ni-DIA electrode for the detection of tetracycline was examined by HPLC with amperometric detection for determination of tetracyclines in shrimp.

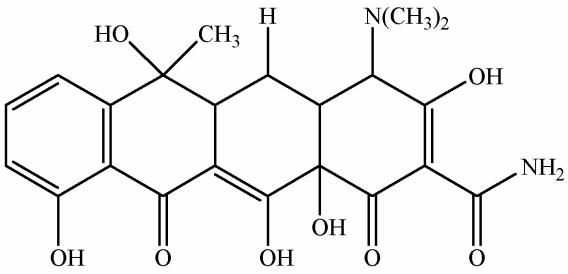

Tetracycline

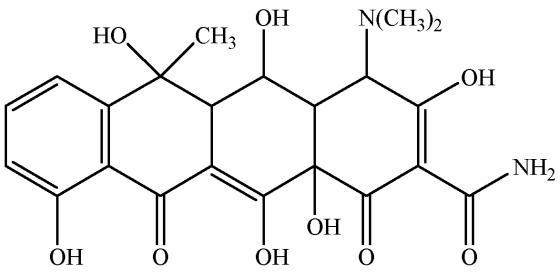

Oxytetracycline

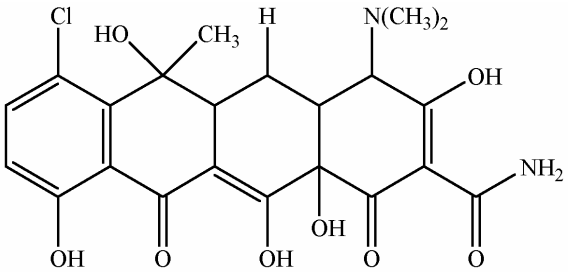

Chlortetracycline

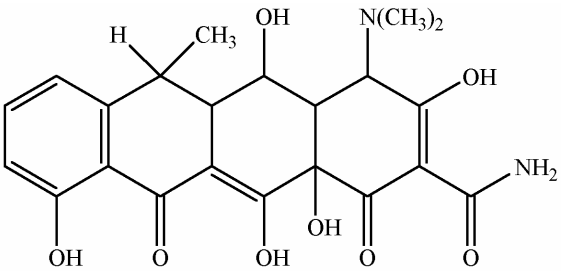

Doxycycline

Figure 1 Structures of 4 tetracyclines

The Objective of Research

The main objective of this research is to develop an analytical method for the determination of tetracyclines at low levels in antibiotic drugs and shrimps. The use of flow injection and high performance liquid chromatography (HPLC) with amperometric detection is proposed.

In the amperometric detection, three electrodes, namely, a BDD electrode, an anodized boron-doped diamond thin film electrode and Ni-implanted boron-doped diamond thin film electrodes (Ni-DIA) are used. In the process of developing the above mentioned method the following specific objectives of the study should therefore be described.

(1) To investigate the oxidation of tetracyclines using cyclic voltammetry at a BDD electrode, an anodized boron-doped diamond thin film electrode and Ni-implanted boron-doped diamond thin film electrodes (Ni-DIA).
(2) To obtain the optimal parameters for ampermetric detection using anodized BDD electrodes under FIA or HPLC system.
(3) To establish the optimal conditions for FIA or HPLC system.
(4) To study the validation of the method.
(5) To compare the developed method to the AOAC Official method.

EXPERIMENTAL

Chemical Reagents

- Tetracycline hydrochloride (Sigma)
- Oxytetracycline hydrochloride (Sigma)
- Chlortetracycline hydrochloride (Sigma)
- Doxycycline hydrochloride (Sigma)
- Potassium dihydrogen orthophosphate (BDH)
- Disodium hydrogen orthophosphate (BDH)
- Phosphoric acid (Merck)
- Diaminetetraacetic acid disodium salt (Fluka)
- Citric acid (J.T.Baker)
- Acetonitrile (HPLC Grade, Merck)
- Methanol (HPLC Grade, Merck))
- 2-Propanol (Analytical Grade, Merck)
- Oxalic acid dihydrate (Merck)

Instruments and Equipments

- An Autolab Potentiostat (PGSTAT 30, Metrohm)
- A Water No. 510 solvent delivery system (Waters Associates Inc, Milford, MA, USA)
- A Rheodyne injection valve, Model 7225 (Altech), with a 20 μl stainless steel injection loop (0.5 mm. i.d.)
- Automated LC system (HP 1100 series from Agilent Technologies, USA.) consisted of auto-sampler, binary pump, on-line degasser, UV-Visible and fluorescence detector
- Milli-Q water system, model Millipore ZMQS5V00Y, (Millipore, USA) (CENTAURA 2, Sanyo)

- Mobile phase filter set included 300 mL glass reservoir, glass membrane holder, 1000 mL flask and metal clip (Millipore, USA)
- Autopipette and tips (Eppendorf, Germany)
- Inertsil-ODS3 C_{18} (5 μm, 4.6 mm × 25 cm, GL Science)
- C18-E cartridges 500 mg, 6 mL, (Phenomenex, USA.).
- A Ag/AgCl electrode (Bioanalytical System Inc.)
- A platinum wire (Bioanalytical System Inc.)
- The as-deposited boron doped-diamond electrode (WD769/1, Purchased from Centre Suisse d' Electronicat de Microtechnique SA (CSEM) and obtained from Associate Prof. Kensuke Honda.
- A polish set of 0.05 and alumina powder slurry (Metrohm)
- A thin layer flow cell (Bioanalytical System Inc.)
- A Teflon cell gasket (Bioanalytical System Inc.)
- Peek tubing (0.25 mm i.d.) and connecting (Upchurch)
- Teflon tubing (1/10 inch i.d., Upchurch)
- A cutting set (Altech)
- A 0.45 μm Nylon membrane filter (Altech)
- A 0.45 μm Nylon membrane syringe filter with polypropylene (Orange Scientific filter)
- A pH meter (Metrohm)
- A sonicator (USA, A006651)
- An analytical balance (Metler, AT 200)
- HPLC vials 2.0 mL with PTFE screw caps (Agilent Technologies, USA)
- Glass containers with Teflon screw cap 25 Ml
- Erlenmeyer flasks 10, 100, and 250 mL
- Separatory funnels 500 mL
- Volumetric flasks 10, 25, 50 and 100 mL
- Beakers 10, 25, 50, 100, 500 and 1,000 mL

Preparation of chemical solutions

❖ Preparation of 0.1 M phosphate buffer solution

13.6 g and 17.6 g of potassium dihydrogen phosphate and disodium hydrogen phosphate dehydrate were dissolved in 1 L of deionized water to make the solution of 0.1 M potassium dihydrogen phosphate buffer and 0.1 M disodium hydrogen phosphate. The recipes of each pH solution were shown in Table 3.1

Table 3.1 Recipes of phosphate buffer preparation.

pH	0.1 M Potassium dihydrogen phosphate (mL)	0.1 M Disodium hydrogen phosphate (mL)
5	99.2	0.8
6	88.9	11.1
7	41.3	58.7
8	3.7	96.3

The 0.1 M of potassium dihydrogen phosphate was adjusted by phosphoric acid to make the range of pH from 2 to 4.

❖ Stock Standard Solutions

Each stock standard solution (1000 μg/mL) of TC, OTC, CTC and DC was prepared daily by weighing 50 mg of each standard into a 50 mL volumetric flask and the volume was adjusted to 50 mL with the mobile phase.

❖ **Working Standard Solutions**

First, the mixture of 4 TCs solutions containing 100 μg/mL was prepared by pipetting 1.0 mL of each standard solution 1000 μg/mL into a 10 mL volumetric flask and the volume was adjusted to 10 mL with mobile phase. Working standard solutions were prepared by diluting the standard mixture solutions 100 μg/mL with mobile phase. All of the solutions were protected from exposure to light and stored in the refrigerator.

❖ **Preparation of Mobile Phase**

The mobile phase for HPLC condition was consisted of acetonitrile and the phosphate buffer solution. The phosphate buffer solution of pH 2.5 was prepared daily by mixing of 0.01 M H_3PO_4 + 0.1 M Na_2HPO_4 (a few drops to adjust the pH). The phosphate buffer was filtered with a 0.45 μm Nylon membrane filter.

❖ **5 Preparation of Na_2EDTA-McIlvaine Buffer**

Na_2EDTA -McIlvaine buffer solution (pH 4) was prepared by dissolving 15 g of disodium hydrogenphosphate dihydrate, 13 g of citric acid monohydrate and 3.72 g of EDTA in deionized water in 1 L volumetric flask.

❖ **Sample Preparation**

- **Drug Analysis**

The pharmaceutical preparations analyzed and the labeled contents (amount present in 1 capsule) were: Tetracycline hydrochloride containing 250 mg tetracycline hydrochloride (TC); Aureomycin containing 250 mg chlortetracycline (CTC); Oxycline containing 250 mg oxytetracycline (OTC); Medomycin containing 100 mg doxycycline (DC). The powder of 20 drug capsules were each weighed so as to obtain the mean capsule weight. An accurately weighed was portion of

homogenized powder corresponding the mean capsule weight was transferred into volumetric flask and dissolved with 0.1 mol l^{-1} phosphate buffer (pH 2), and then shake well. The portion of sample solutions was filtrated through 0.45- μm nylon membrane. The filtrated solutions were further diluted using 0.1 mol L^{-1} phosphate buffer (pH 2) to make the final concentration in the range of 0.96-5.15 μg ml^{-1} within the linear dynamic range. All tetracycline antibiotic solutions were protected form light by covering with aluminum foil and stored at the temperature of 4 ^{0}C in the refrigerator.

- **Shrimp Analysis**

The shells, fins and tails of shrimp were removed and ground in a conventional meat grinder. The ground shrimp were stored at below -10°C until analysis.

2.50±0.05 g of ground shrimp was placed in 25 mL centrifuge tube, 12.5 mL of Na_2EDTA-McIlvaine buffer (pH 4) was added, then the mixture was centrifuged at 3500 rpm for 20 min. The supernatant was loaded into SPE cartridge, previously activated with 10 mL of methanol and 10 mL of Milli-Q water. After sample loading, the SPE cartridge was washed with 10 mL of Milli-Q water and finally tetracyclines were eluted by 10 mL of methanol. The solvent was removed under a nitrogen stream. The residues were diluted in the total volume of 10 mL and the solutions were filtered with a 0.45 μm PTFE filter. Then, 20 μL of aliquot was injected to the HPLC system.

Preparation of Anodized BDD Electrode

An anodized BDD electrode was prepared by treating an as-deposited BDD electrode in 0.1 M KOH solution. The potential was applied between 0 to 2 V versus Ag/AgCl using cyclic voltammetry for 30 min. The anodized BDD electrode was also rinsed with ultrapure water before use.

Preparation of Ni--implanted boron-doped diamond thin film electrodes (Ni-DIA)

The experimental conditions and the apparatus used for the diamond film growth have been described in detail elsewhere. The films were prepared by deposition of the boron-doped polycrystalline diamond than films on highly conductive n-Si (100) substrates by high-pressure microwave plasma-assisted chemical vapor deposition (CVD) system (ASTex Corp., Woburn, MA). The boron source, B2O3, was dissolved in this solvent mixture so that the B/C ratio was approximately 102 ppm. These films were implanted with 750 keV Ni2+ with a dose of 5 x 1014 cm-2 (Tandetron 4117-HC, HVEE). The annealing was performed at 850°C for 10 min in an H2 ambient (80Torr). The nickel-implanted boron-doped diamond electrodes (Ni-DIA) have been prepared in Associate Professor Yasuaki Einaga's laboratory. The presence of Ni particles on BDD surface was con.rmed by XPS and SEM. The experimental conditions and the apparatus used for this characterization have been described in detail elsewhere26. The Ni-DIA electrodes were rinsed with ultra-pure water prior to use.

Cyclic Voltammetric Study

Each of 1 mM of OTC, TC, CTC and DC standard solutions was prepared by weighing 0.0495, 0.0481, 0.0515, and 0.0481 g, respectively and transfering into 100 mL volumetric flask. The phosphate buffer was used for diluting this aliquot to the mask. These solutions were used for the investigation of the oxidation of TCs by cyclic voltammetry at the BDD electrode, the anodized BDD electrode and Ni-implanted boron-doped diamond thin film electrodes (Ni-DIA)

Electrochemical experiment was carried out in the single compartment three-electrode glass cell. The BDD electrode was pressed against a smooth ground joint at the bottom of the cell, isolated by an O-ring vitron (area 0.07 cm^2). Ohmic contact was made by placing the backside of the Si substrate. The GC carbon was used as working electrode for the comparison. The Ag/AgCl with salt bridge and Pt wire were used as reference electrode and counter electrode respectively. The voltammetric measurement was performed with the three types of electrodes using Autolab Potentiostat 100 (Eco-Chemie, The Netherlands).

- **Voltammetric study of TCs**

The 0.5 mM of TCs in 0.1 M potassium dihydrogen phosphate (pH 2) were investigated using BDD electrode by cyclic voltammetry at scan rate 50 mV s^{-1}. Comparison the results using as-deposited BDD and GC electrodes were carried out.

- **The scan rate dependence study**

The 1 mM solution of TCs, experiments were performed at various scan rates including 10, 20, 50, 100, 200 and 300 mV s^{-1} to investigate the adsorption of the analytes on the surface of electrode.

- **pH dependence study**

The 1 mM of the analyte at each pH was measured using anodized BDD electrode by cyclic voltammetry to obtain the optimum pH of the measurement. A scan rate of 50 mV s^{-1} was used. The surface area was 0.28 cm^2. The experiment was carried out in plastic cap cell.

Flow injection with amperometric detection

The flow injection system consisted of a thin layer flow cell (Bioanalytical System, Inc), a 20-µl stainless steel loop of injection port (Rheodyne 7725), a peristaltic pump, and electrochemical detection (Autolab potentiastat 100). The carrier solution (0.1 mol L^{-1} potassium dihydrogen phosphate pH 2) was regulated at the flow rate of 1 ml min^{-1} by measuring the volume of carrier solution in 1 min. The thin layer flow cell consisted of a silicone rubber gasket as a spacer, a Ag/AgCl electrode as the reference electrode and a stainless steel tube as an auxiliary electrode and an outlet of the flow cell. The experiments were performed in a copper faradaic cage to reduce the electronic noise. All experiments were done at room temperature.

HPLC Optimization

A HPLC method equipped with a C_{18} column and phosphate buffer (pH 2.5) and acetonitrile as the mobile phase was used to develop the separation of 4 tetracyclines; i.e. oxyetracycline (OTC), tetracycline (TC), chlortetracycline (CTC) and doxycycline (DC). The injection volume was 20 μL and the detector was Ni-implanted boron-doped diamond thin film electrodes (Ni-DIA). The optimization was determined by vary the mobile phase strength. The separation of tetracyclines was first tested with standard mixture and the condition was later tested with shrimp samples spiked mixed standard.

Calibration and Linearity

Each concentration of the mixed standard TCs solutions at 0.1, 0.5, 1.0, 5.0, 8.0, 10, 25, 50 and 100 mg/L was injected in duplicate. The calibration curves were plotted between the peak areas and the concentrations.

Limit of Detection (LOD) and Limit of Quantitation (LOQ)

The LOD and LOQ were determined by various concentrations under HPLC conditions and optimal PAD parameters. The detection limit (LOD) and quantitation limit (LOQ) are defined as the concentration that provided a current response higher 3 times than the noise ($S/N \geq 3$) and 10 times than the noise ($S/N \geq 10$), respectively.

Precision and Accuracy

For intra-day precision, the repeat of analysis of spiked sample was studied in one day. For inter-day precision, the repeat of analysis of spiked sample was studied on different days. The spiking at level 0.5, 1.0, 5.0 and 10 mg/kg was used in the study and at each level was repeated in triplicate.

Applications

The HPLC-amperometric detection using the Ni-implanted boron-doped diamond thin film electrodes (Ni-DIA) was applied to detect tetracyclines in shrimps. Two types of shrimp that purchased from the local markets were farming-shrimp and sea-shrimp. The developed method was compared to the AOAC Official method (995.09) and Laboratory Center for Food and Agricultural Products Company Limited (LCFA).

AOAC Official Method (995.09)

This method could be used to detect tetracycline, chlortetracycline and oxytetracycline. The column used in this method was the same as in HPLC-EC systems. The HPLC conditions were carried out using the mobile phase of oxalic acid (0.1 M) – methanol – acetonitrile (60:10:30; v/v) on a C_{18} column at a flow rate of 1.0 mL/min at room temperature. The injection volume was 20 μL and the detector was UV-Visible detector at 350 nm.

❖ Preparation of Chemical Solutions

o Preparation of Mobile Phase

First, the oxalic acid solution was prepared by weighing 1.26 g of oxalic acid dihydrate and dissolving into 1 L volumetric flask with Milli-Q water. Then, the mobile phase 600 mL oxalic solution was combined with 300 mL acetonitrile and 100 mL methanol.

o Preparation of McIlvaine buffer-EDTA solution

28.4 g of anhydrous Na_2HPO_4 was dissolved into 1 L volumetric flask and dissolved with deionized water. Then, 21.0 g citric acid was dissolved into another 1 L volumetric flask and dilute to 1 L with deionized water. The mixed solution was the combination of 1 L citric acid solution and 625 mL Na_2HPO_4 solution in 2 L beaker. The mixed solution was adjusted to pH 4.0 by adding 0.1 M

HCl or 0.1 M NaOH. Finally, 60.5 g disodium EDTA dihydrate was dissolved with 1.625 L of mixed solution.

- **Preparation of Methanolic acid**

1.26 g oxalic acid dihydrate was dissolved into 1 L volumetric flask with methanol.

❖ **Sample Preparation**

5.00±0.05 g of sample was placed into 50 mL centrifuge tube, added 20 mL McIlvaine buffer-EDTA solution and blended 30 sec with homogenizer. Then, this tube was centrifuged for 10 min at 2500 rpm and put the supernatant into another 50 mL centrifuge tube. Adding 20 mL McIlvaine buffer-EDTA solution in the first centrifuged tube containing the sample and repeated all steps to obtain the second extraction. Finally, adding 10 mL McIlvaine buffer-EDTA solution in the first centrifuged and repeated all steps. The supernatant from 3 extractions was collected in the second tube, then loaded to the SPE extraction.

SPE cartridges were set, and conditioned with 20 mL methanol and 20 mL Milli-Q water. The supernatant was loaded into SPE cartridge. After sample loading, the SPE cartridge was washed with 10 mL of Milli-Q water and finally tetracyclines were eluted by 6 mL of methanolic oxalic acid. The residues were diluted in the total volume of 10 mL, and the solutions were filtered with a 0.45 μm PTFE filter. Then, 20 μL of aliquot was injected to the HPLC system.

RESULTS AND DISCUSSION

In this chapter, details will be separated into three parts. The first part was the results and discussion from using anodized boron-doped diamond thin film electrode for the determination of tetracycline antibiotic drugs. The results obtained from batch system and flow injection analysis will be presented respectively. For the second part, the working electrode was changed from anodized BDD electrode to Ni-implanted boron-doped diamond thin film electrodes (Ni-DIA) for the analysis of tetracycline using flow injection system and HPLC system. The results obtained were categorized in the same steps as shown in the first part. Additionally, HPLC results will be discussed as well at the end of this part.

Determination of TCs using an anodized BDD electrode

This study focused on the method development of the tetracycline antibiotic determination, based on the electrochemical method using an anodized BDD electrode. The study was separated into 2 parts including cyclic voltammetry and flow injection with amperometric detection. The details of each part were described as the follows.

❖ Investigation of TCs using cyclic voltammetry

o Voltammetric study of TCs

As commonly known, the synthesis of as-deposited BDD electrodes by microwave plasma-assisted chemical vapor deposition is hydrogen-terminated on the diamond surface. The chemical modification can be carried out by anodic polarization or oxygen plasma treatment to change the hydrogen-terminated surface to an oxygen-terminated surface one. In this study, anodic polarization in alkaline solution (0.1 M potassium hydroxide) was used, as described in the experiment chapter. The major type of oxygen functional group is the carbonyl group, which is believed to exist on faces. The highly oriented carbonyl groups

provide a surface dipolar field that could repel a neutral molecule with oxygen-containing functional groups surrounding a central core. On the other hand, the oxygen plasma treatment or thermal oxidation can induce the bridge form of C-O-C on the surface of diamond.

The electrooxidation of four TCs was investigated on as-deposited BDD, GC, and anodized BDD electrodes. Figures 1-4 show cyclic voltammograms of 500 μM of TCs in 0.1 potassium dihydrogen phosphate (pH 2) together with the background voltammograms at the as-deposited BDD, GC, and anodized BDD electrodes. All electrodes provided irreversible cyclic voltammograms. This irreversible behavior suggested that TCs were oxidized, and then reacted rapidly to form a new product. Cyclic voltammetric results of TC, CTC, OTC, and DC at as-deposited BDD, GC, and anodized BDD electrodes are summarized in Table 1. Results showed that the highest current signals were obtained for TC, CTC, OTC, and DC at the anodized BDD electrode and they can be explained in recent work carried out with glutathione on the basis of attractive electrostatic interaction between the negatively charged anodized surface and the positively charged substrates. TCs were fully positively charged in strongly acidic pH, as we used in this experiment. Hence, the positively charged substrates could be attracted to the negative surface of the anodized BDD electrode, which induced the electrooxidation to occur easily. In contrast to as-deposited BDD, the surface is positively charged and non-polar (covered with hydrogen atoms), and the electrostatic interaction was less permitted, which presumably resulted in the ill-defined cyclic voltammagrams.

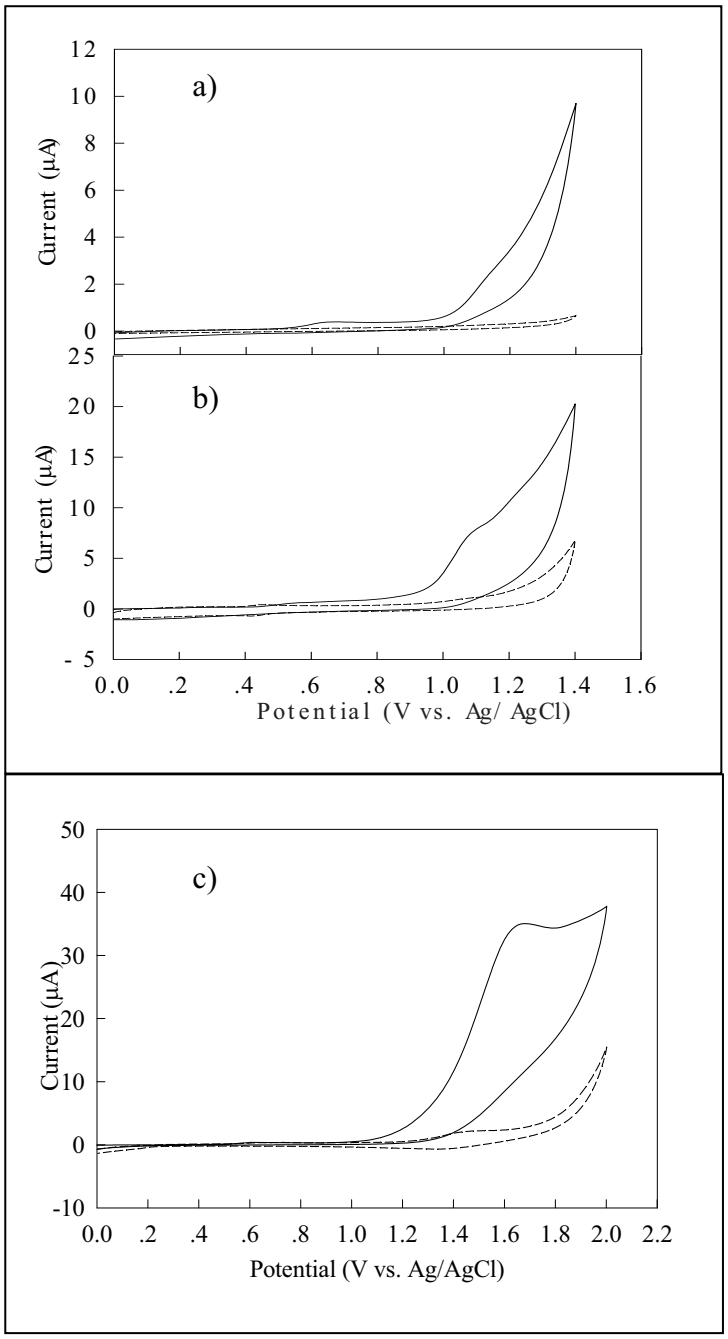

Figure 1 Cyclic voltammograms of 500 μM OTC (solid line) in 0.1 M potassium hydrogen phosphate (pH 2) together with the corresponding background current (dashed line) at a) as-deposited BDD b) GC, and c) anodized BDD electrodes.

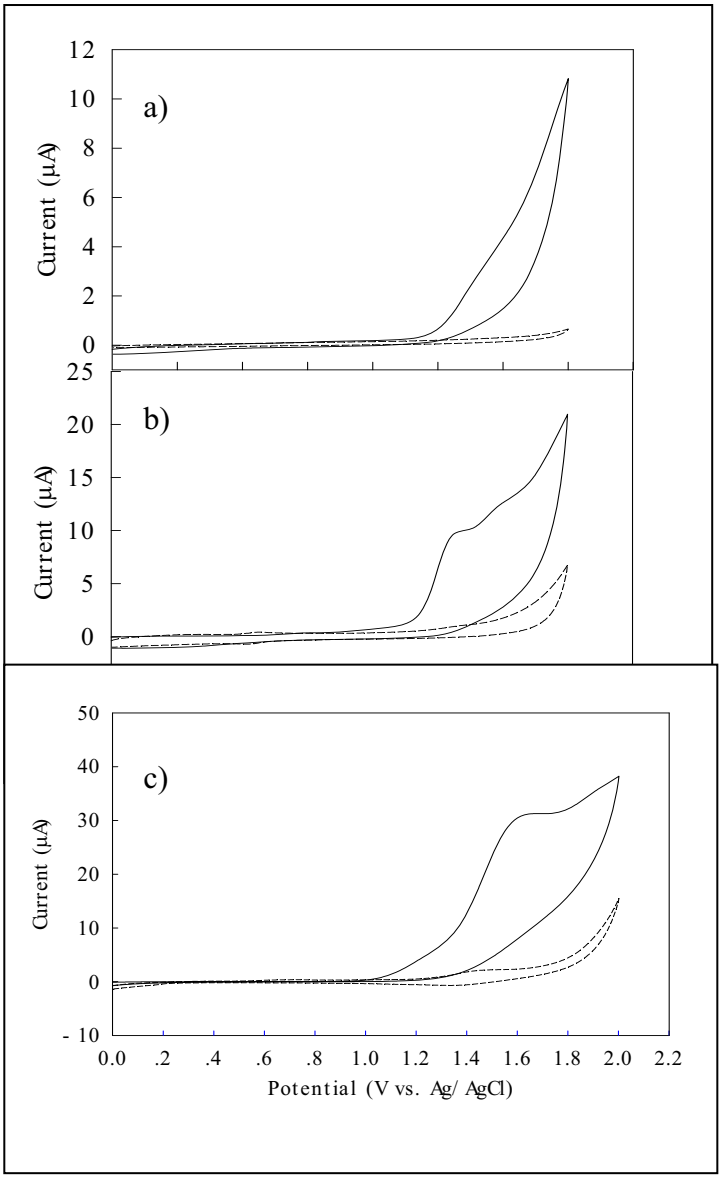

Figure 2 Cyclic voltammograms of 500 μM TC (solid line) in 0.1 M potassium dihydrogen phosphate (pH 2) together with the corresponding background current (dashed line) at a) as-deposited BDD b) GC, and c) anodized BDD electrodes**.**

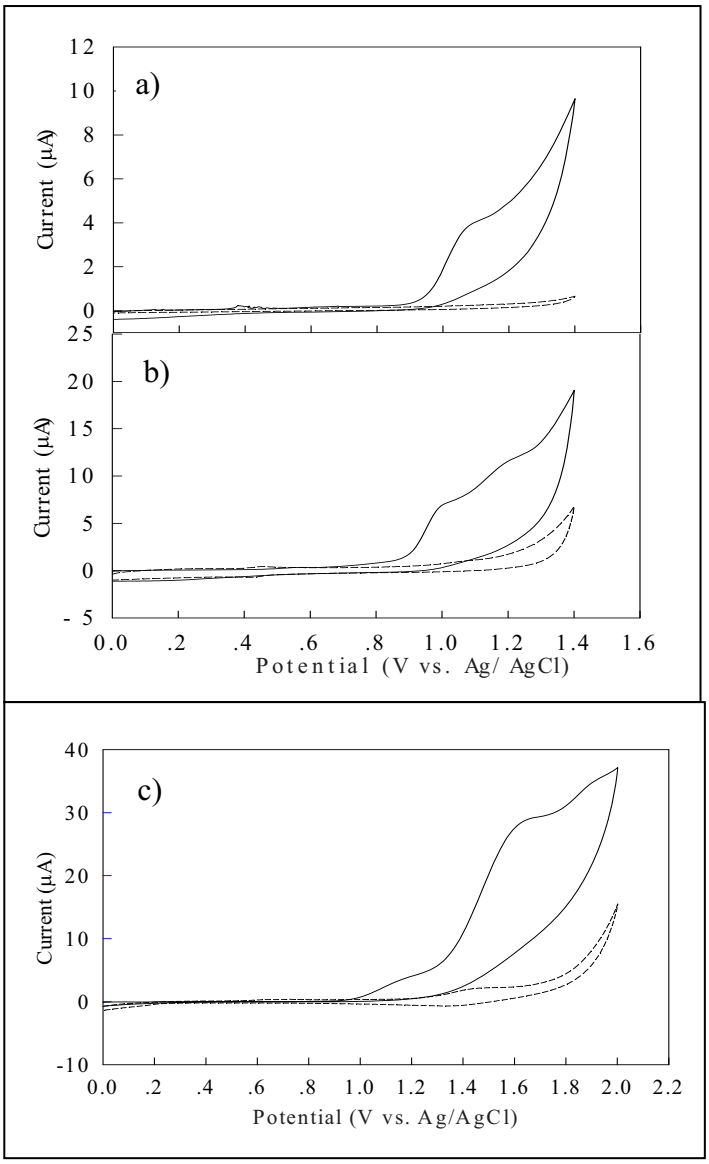

Figure 3 Cyclic voltammograms of 500 µM CTC (solid line) in 0.1 M potassium dihydrogen phosphate (pH 2) together with the corresponding background current (dashed line) at a) as-deposited BDD b) GC, and c) anodized BDD electrodes**.**

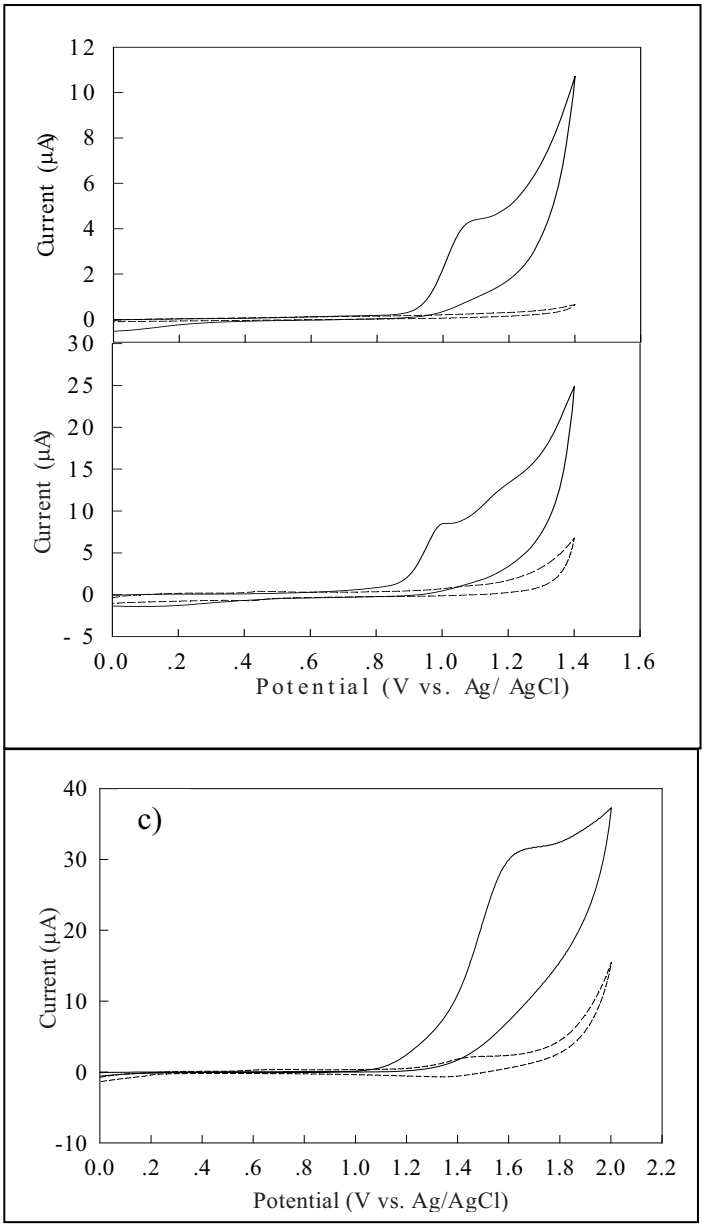

Figure 4 Cyclic voltammograms of 500 μM DC (solid line) in 0.1 M potassium dihydrogen phosphate (pH 2) together with the corresponding background current (dashed line) at a) as-deposited BDD b) GC, and c) anodized BDD electrodes**.**

Table 1 Electrochemical oxidation data obtained from cyclic voltammetry of OTC, TC, CTC, and DC at as-deposited BDD, GC, and anodized BDD electrodes.

Analytes	Concentration (μM)	As-deposited BDD		GC		Anodized BDD	
		E_p (V)	i_p (μA)	E_p (V)	i_p (μA)	E_p (V)	i_p (μA)
OTC	100	1.12	1.21	1.08	2.05	1.59	5.03
	500	1.13	2.02	1.09	6.51	1.69	32.34
TC	100	1.14	1.16	1.08	2.65	1.54	5.20
	500	1.16	3.22	1.06	8.85	1.65	29.88
CTC	100	1.06	1.03	0.99	1.59	1.57	4.67
	500	1.10	3.67	1.02	6.44	1.63	26.10
DC	100	1.04	1.06	0.99	2.95	1.56	4.85
	500	1.07	4.01	1.00	7.77	1.66	28.70

- **pH dependence**

To find the optimum pH for detection of four TCs, the experiments were carried in the pH solution ranged from 2 to 9 at anodized BDD electrode. A plot of pH versus E_p was investigated (Fig. 3.5) with ambiguous results and the expected pK_a was inconsistent with the pK_a value of the dissociation in the literature.

The details concerning the current response and peak potential of TCs at each pH was investigated, as shown in Table 2. In acidic buffer, the well-resolved cyclic voltammograms of tetracyclines were obtained whereas, in neutral and alkaline buffer, ill-defined cyclic voltammograms were obtained. Results for all TCs demonstrated that pH 2 gave the highest current signal.

It can be explained that tetracyclines are derived from a system of four membered rings arranged linearly with characteristic double bonds. They are amphoteric compounds with high polarity and an isoelectric point between 4 and 6. From the reference literature, three portotropic dissociations have been observed for TCs, with pK_1, pK_2, and pK_3 as shown in Table 3.3. In strongly acidic pH, the tetracycline molecules exist as fully protonated from as a singly charged cation. As

proposed in the previous work, the surface of anodized BDD is negatively charged, and the electrostatic interaction between the negatively charged covering of the anodized surface and the positively charged substrates is attractive. Hence, the fully positively charged TCs at pH 2 provided the highest response, and this pH was chosen as the optimum pH for the rest of the experiments.

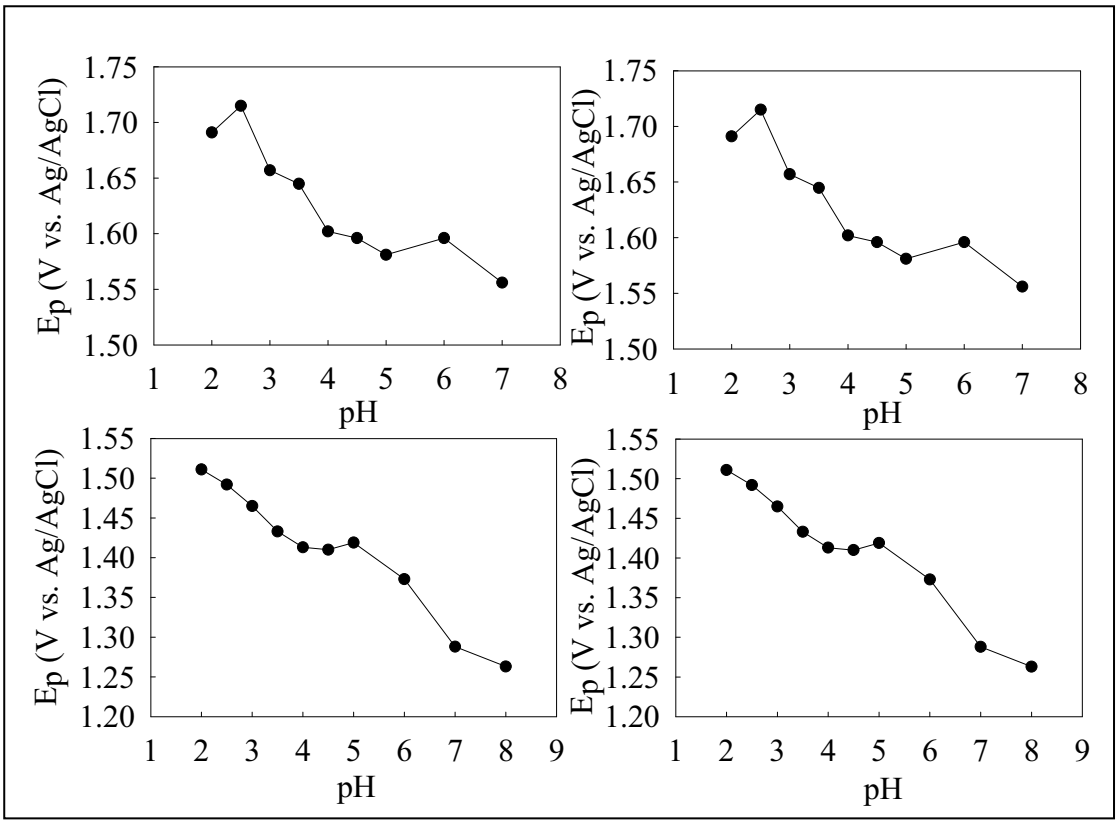

Figure 5 Relationship between the pH and E_p.

Table 2 Electrochemical oxidation data obtained from cyclic voltammetry of 1 mM OTC, TC, CTC, and DC at anodized BDD electrodes.

pH	OTC		TC		CTC		DC	
	E_p (V)	i_p (μA)	E_p (V)	i_p (μA)	E_p (V)	i_p (μA)	E_p (V)	i_p (μA)
2	**1.65**	**170.20**	**1.69**	**161.80**	**1.54**	**242.90**	**1.51**	**191.30**
2.5	1.65	146.60	1.72	130.80	1.57	178.40	1.49	161.50
3	1.61	130.20	1.66	127.80	1.55	173.30	1.47	156.40
3.5	1.60	138.70	1.65	132.50	1.48	154.80	1.43	152.30
4	1.58	142.60	1.60	128.30	1.46	158.70	1.41	155.70
4.5	1.59	138.60	1.60	137.90	1.47	154.10	1.41	149.40
5	1.57	140.80	1.58	137.70	1.46	151.60	1.42	149.00
6	1.58	165.90	1.60	151.60	1.49	178.40	1.37	159.80
7	1.56	163.70	1.56	156.10	1.48	193.50	1.29	169.80
8		-		-	1.38	235.80	1.26	187.60
9		-		-		-		-

Table 3 pK_a values of TCs in aqueous solutions.

Analytes	pK_1	pK_2	pK_3
OTC	3.27	7.32	9.11
TC	3.30	7.68	9.69
CTC	3.30	7.68	9.27
DC	nf*	nf*	nf*

*nf : no reference found

❖ **Determination of TCs using flow injection with amperometric detection**

- **Hydrodynamic voltammetry**

To find the optimum potential, hydrodyanamic voltammetry was carried out. A hydrodynamic voltammogram was obtained from the average of three aliquot injections of the 20 μL of 100 μM TCs solutions in the flow injection system at increasing values of the applied potential from 1.1 to 2.0 V vs. Ag/AgCl in the flow injection system. The carrier solution was 0.1 M potassium dihydrogen phosphate (pH 2). Fig 6a shows the hydrodynamic voltammogram of TCs with the corresponding background current. The hydrodynamic voltammogram of TCs did not exhibit the sigmodial shape of the signal vs. potential probably due to the high oxidation potential of TCs. To obtain the optimum potential, the S/B ratios from Fig 3.6b were calculated at each potential and plot the results versus the potential. The maximum S/B ratio was found at 1.5 V. vs. Ag/AgCl for CTC and 1.6 V vs. Ag/AgCl for TC, OTC, and DC. Hence, this study used these optimum potentials for the quantification experiment in the flow injection system.

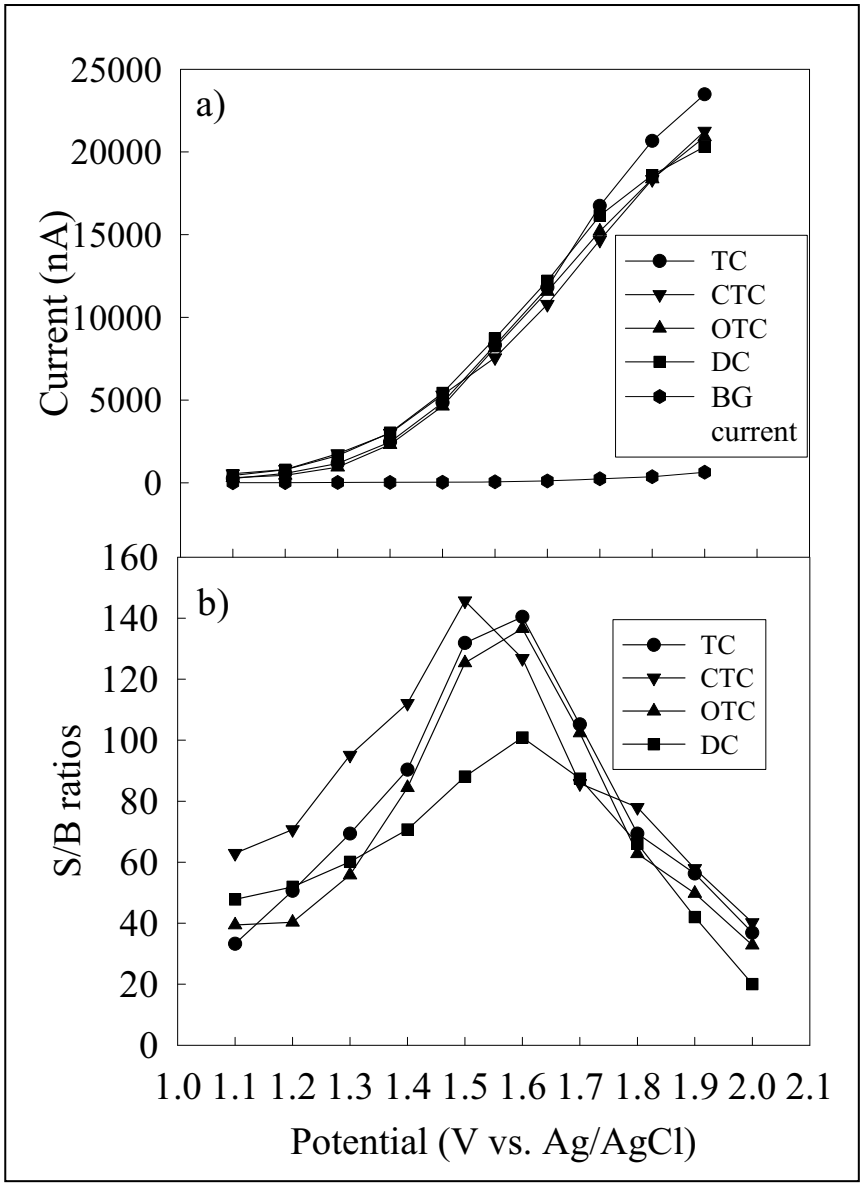

Figure 6 a) Hydrodynamic voltammogram for 100 μM TCs (●) : OTC; (▲):TC; (▼): CTC; and (■):DC in 0.1 M potassium dihydrogen phosphate (pH 2), using 0.1 M potassium dihydrogen phosphate (pH 2) as carrier solution. The flow rate was 1 mL min^{-1}. b) Hydrodynamic voltammogram of signal-to-background ratios.

- **Analytical performance of anodized BDD electrode using the flow injection system**

A series of analytical figures of merit were performed on the proposed method for the quantification of TC, CTC, OTC, and DC.

Linearity and LOD: the calibration curves were constructed separately for each drug in the concentration range of 0.1 to 1000 μM as shown in Fig. 7. Each point of the calibration graph corresponded to the mean value from three replicated injections. The regression analysis parameters for each TC standard solution were summarized such as the linear range and LOD in Table 4. Linear range of the method was about two orders of magnitude range from 0.1-50 for TC and 0.5-50 μM for OTC, CTC, and DC. The LOD defined as the concentration that provided the signal-to-noise ratio of 3 was 10 nM for the four TCs.

Repeatability: to check the repeatability of the proposed method, the experiments were carried out by injecting 10 replicates of the three concentrations (5, 10, 50 μM) of each drug. The peak variability defined as the relative standard deviation (%RSD) was 1.3-1.7, 2.4-3.0, 1.6-3.0, and 1.7-2.7 for TC, CTC, OTC, and DC, respectively.

Stability: the response received from anodized BDD electrodes with amperometric detection was very stable. The flow injection signal obtained by repetitive 100 injections of 50 μM CTC on the anodized diamond provided a peak variation of about 3.4%. Moreover, the anodized BDD electrode could be reactivated in situ by applying a high positive potential (2.6 V vs. Ag/AgCl) during the flow injection measurement. The sample throughput was approximately seventy injections per hour.

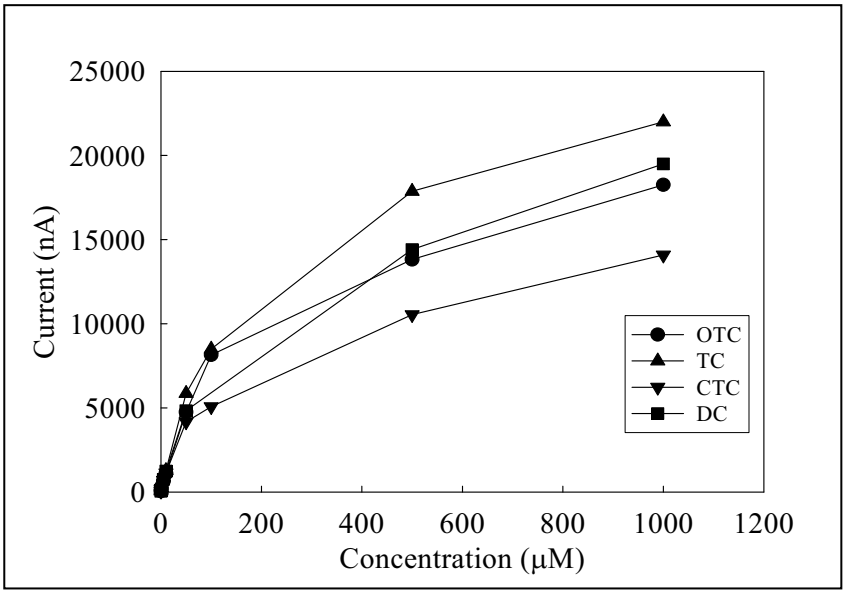

Figure 7 Calibration curves of four TCs (OTC, TC, CTC, and DC) using flow injection system.

Table 4 Regression analysis of parameters, linear range, and LOD for the determination of TCs by FIA with amperometric detection using an anodized BDD electrode (n=2).

Analytes	Linear range (μM)	a	b	r^2	LOD (nM)
TC	0.1-50	110.00±5.96	192.13±4.86	0.9968±0.0006	10
CTC	0.5-50	76.93±3.87	199.72±29.68	0.9969±0.0001	10
OTC	0.5-50	90.23±2.99	165.17±28.86	0.9992±0.0006	10
DC	0.5-50	96.23±3.81	213.73±48.92	0.9966±0.0001	10

[a] $y = ax+b$, where y = current (nA), x = concentration (μM), a = slope (nA μM^{-1})

- **Application**

The proposed method of this study was applied for drug formulations using the standard addition method. The precision of this method was based on the intra-assay and inter-assay. The amounts of each drug were compared with the label contents. The results are summarized in Table 5. There was no significant difference in results between the label contents and those obtained by the proposed method for the intra-assay and inter-assay precision (3 days). To check the accuracy of the method, recoveries of the spiked standard solution were evaluated. The results are summarized in Table 6.

Table 5 Results of TC determination in drug formulations.

Analytes	Intra-assay (n = 2)			Inter-assay (n = 6)		
	Label amount (mg)	Found (mg)	%Found	Label amount (mg)	Found (mg)	%Found
TC	250	249.4±1.7	99.8±0.7	250	246.3±3.2	98.5±1.3
CTC	250	249.7±1.3	99.9±0.5	250	247.3±4.0	98.9±1.6
OTC	250	254.6±2.5	101.9±1.0	250	257.5±3.3	103.0±1.3
DC	100	98.4±1.0	98.4±1.0	100	99.5±1.3	99.5±1.3

Table 6 Recovery studies for the determination of TCs in drug formulations.

Analytes	Intra-assay (n = 2)			Inter-assay (n = 6)		
	Added ($\mu g\ mL^{-1}$)	Found ($\mu g\ mL^{-1}$)	%Recovery	Added ($\mu g\ mL^{-1}$)	Found ($\mu g\ mL^{-1}$)	%Recovery
TC	1.20	1.22±0.01	101.5±0.5	1.20	1.22±0.04	101.5±3.3
	2.40	2.43±0.02	101.4±0.8	2.40	2.41±0.03	100.4±1.3
	3.60	3.56±0.06	98.7±1.6	3.60	3.53±0.09	97.9±2.4
	4.81	4.82±0.05	100.3±1.1	4.81	5.91±0.06	101.0±1.3
CTC	1.29	1.25±0.01	96.9±0.4	1.29	1.26±0.03	97.4±2.7
	2.58	2.55±0.05	98.8±1.9	2.58	2.53±0.04	98.2±1.5
	3.86	3.80±0.00	98.5±0.0	3.86	3.80±0.09	98.6±2.4
	5.15	5.22±0.03	101.4±0.6	5.15	5.22±0.06	101.4±1.2
OTC	1.24	1.19±0.02	95.6±1.2	1.24	1.17±0.06	94.5±4.8
	2.48	2.41±0.07	97.1±2.7	2.48	2.36±0.08	95.1±3.0
	3.73	3.68±0.06	98.7±1.6	3.73	3.73±0.06	100.2±1.6
	4.97	4.98±0.01	100.2±0.2	4.97	5.05±0.08	100.7±1.6
DC	0.96	0.9±0.0	97.5±2.2	0.96	0.92±0.03	94.1±3.7
	1.92	1.86±0.03	96.4±0.0	1.92	1.92±0.06	100.2±2.9
	2.89	2.78±0.08	96.0±2.7	2.89	2.89±0.10	99.9±3.3
	3.85	3.97±0.06	103.2±1.7	3.85	3.87±0.09	100.6±2.3

❖ **Summary**

Anodized BDD electrode has exhibited the attractive feature for the detection of tetracycline antibiotics. Cyclic voltammetric results of tetracycline antibiotics at anodized BDD electrode exhibited a well-resolved peak current response than GC and as-deposited BDD electrode. Flow injection with amperometric detection using anodized BDD electrode also enhanced the sensitivity and improved the detection limit (0.0048 mg L^{-1} for tetracycline and doxycycline, 0.0050 mg L^{-1} for oxycycline and 0.0052 mg L^{-1} for chlortetracycline) of the quantification of tetracycline antibiotics. The remarkably low detection limit obtained from this work showed the superb technique for applying to determine tetracycline antibiotics in biological samples that their common amount was very low. The present method was also overcome the drawback of previous methods based on spectrophotometry and HPLC-amperometry, include simple, fast, low cost, and high sensitivity method. Moreover, the investigated method can be successfully applied to determination tetracyclines in pharmaceutical formulation with the satisfactory results. All tetracycline antibiotics content of the drug were found to be in agreement with the declared amount on the label.

Electroanalysis of Tetracycline Using Nickel-implanted Boron-Doped Diamond Thin Film Electrode Applied to Flow Injection System

❖ **Cyclic voltammetry**

Figures 8 (a) and (b) show cyclic voltammograms for tetracycline oxidation at Ni-DIA and BDD electrodes in 1 mM tetracycline + 0.1 M phosphate buffer (pH 2). The corresponding backgrounds are also shown. The Ni-DIA electrode exhibited a well-defined irreversible oxidation peak at ~1.5 V *versus* Ag/AgCl, whereas the BDD electrode provided a well-defined irreversible oxidation peak at ~1.4 V *versus* Ag/AgCl. Both Ni-DIA and BDD electrodes provided well-defined cyclic voltammograms.

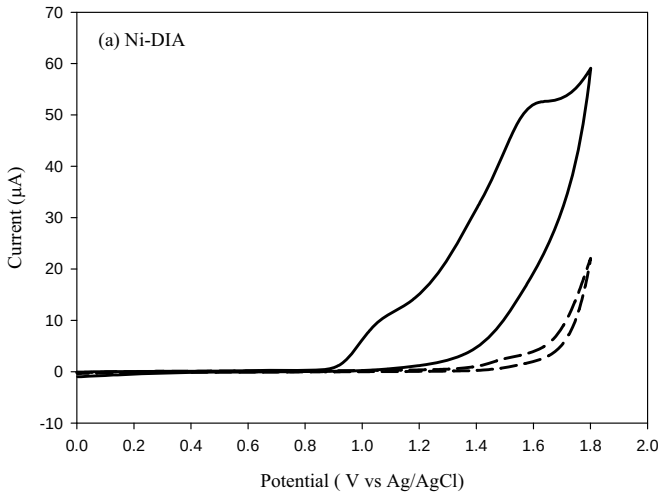

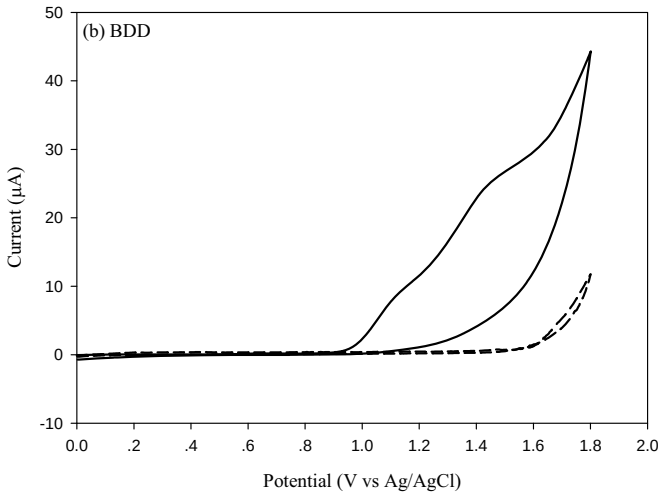

Figure 8 Cyclic voltammograms for 1 mM tetracycline in 0.1 M phosphate buffer (pH 2) at (a) nickel-implanted boron-doped diamond thin film electrode The potential (b) as-deposited boron-doped diamond thin film electrode (solid line). The potential sweep rate was 50 mVs^{-1}. Background voltammograms (0.1 M phosphate buffer, pH 2) are also shown in this Figure (dotted line).

❖ pH dependence study

Table 7 summarizes the electrochemical data obtained from cyclic voltammograms of 1 mM tetracycline hydrochloride oxidation at pH 2, 3, 4, 5, 6, 7, 8, 9, and 10 at the Ni-implanted diamond electrode. The experimental results show that the analyte oxidation peak potential, Ep^{ox} (positive scan) are shifted to more negative values as the pH of the solutions increase. These phenomena may be attributed to the fact that tetracycline hydrochloride was easier to epimerize to the anhydrotetracycline in acidic media or to isotetracycline in basic media. The proposed mechanisms of the epimerization of this compound are shown in Figure 9. In both acidic and alkaline solutions, the epimerization occurred at C-6 hydroxyl group. These occurrences imply that the oxidation process of tetracycline hydrochloride released hydrogen ion into the solution, and the reduction process took up hydrogen ion from the solution. From the electrochemical data displayed in Table 7, the highest oxidation current response at the oxidation peak potential about 1.516 V vs. Ag/AgCl was obtained at the pH 2. Therefore, this pH value was chosen as the optimum pH for the study of tetracycline hydrochloride. The cyclic voltammograms of tetracycline hydrochloride in different pH solutions are shown in Figure 10-12, respectively.

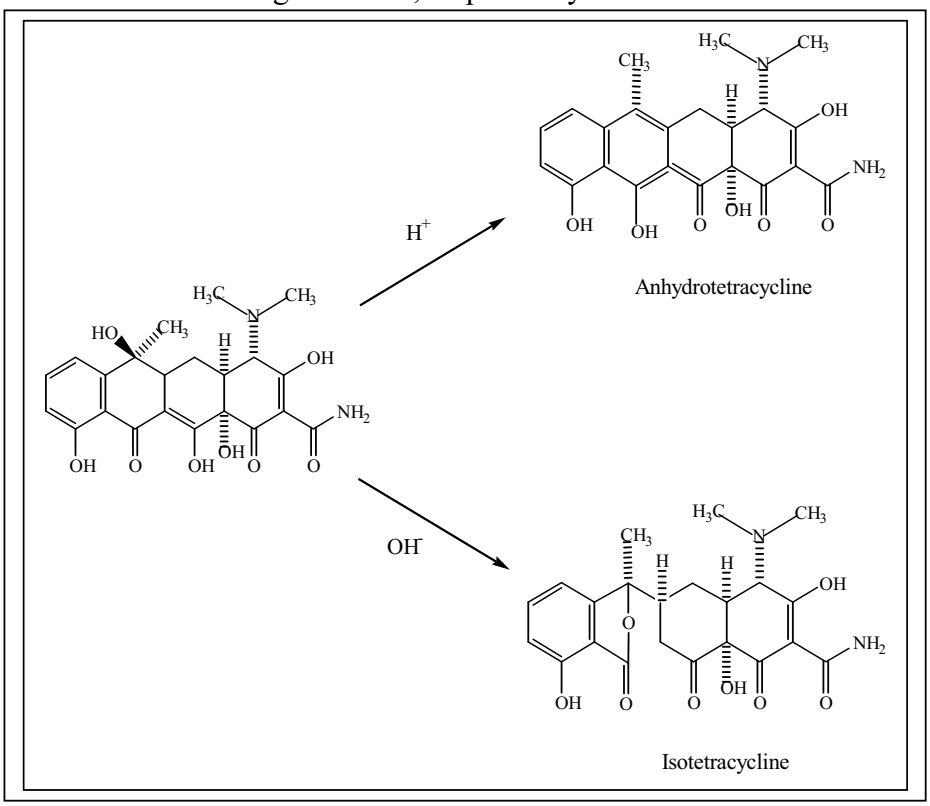

Figure 9 The proposed epimerization mechanism of tetracycline

Table 7 Comparison of electrochemical data obtained from cyclic voltammograms of the 1 mM tetracycline at pH 2, 3, 4, 5, 6, 7, 8, 9, and 10

pH	E_p^{ox} * (V vs. Ag/AgCl)	I_p^{ox} ** (μA)
2	1.516	34.10
3	1.516	28.90
4	1.506	26.30
5	1.511	26.60
6	1.511	30.40
7	1.511	22.30
8	1.516	22.40
9	1.506	19.00
10	1.486	28.80

* Oxidation peak potential of tetracycline

**Oxidation peak current of tetracycline

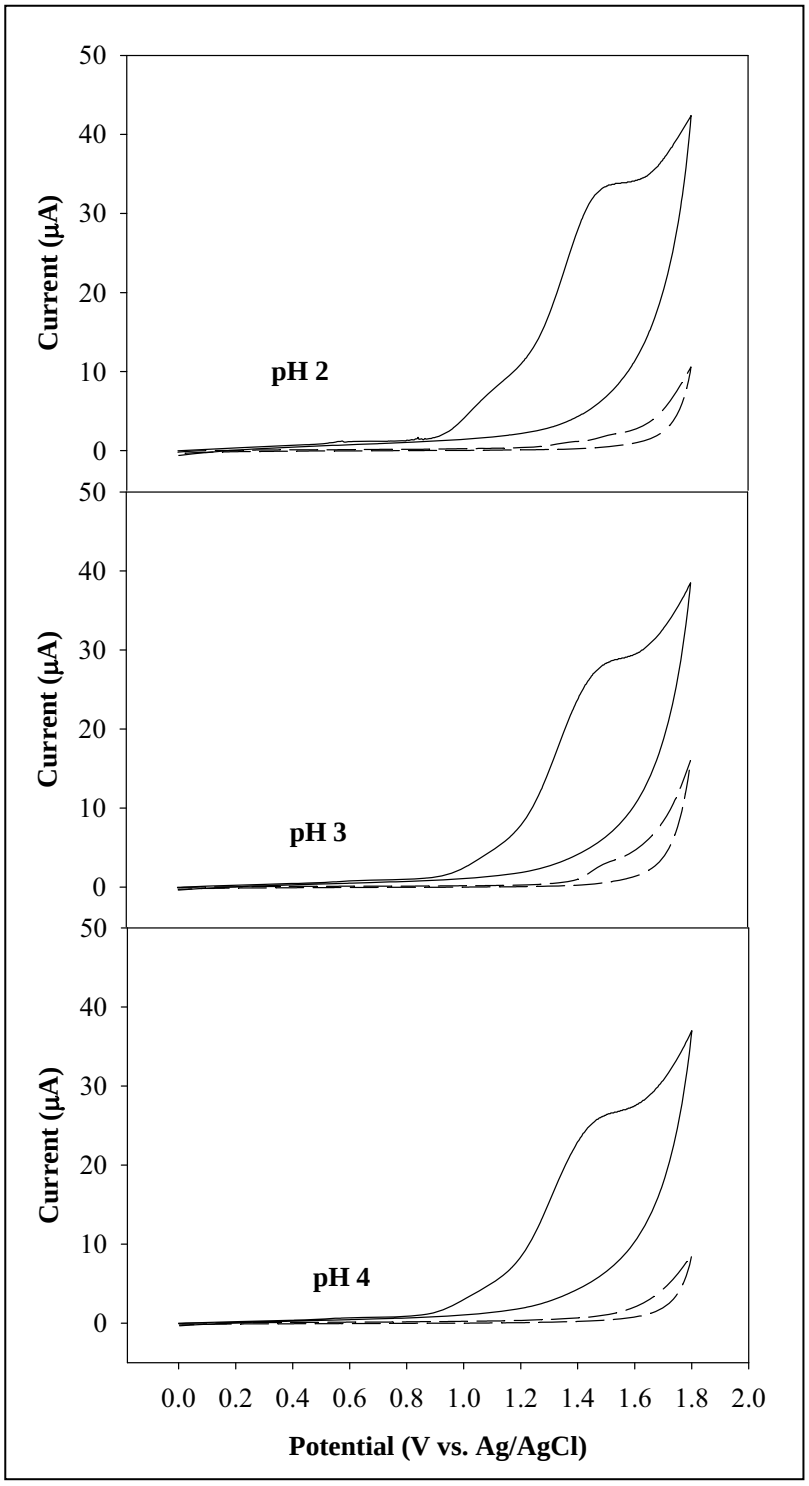

Figure 10 Cyclic voltammogram of 1 mM tetracycline in 0.1 M phosphate buffer (pH 2, 3 and 4) at Ni-implanted diamond electrode (solid line). The scan rate was 50 mV/s^{-1}. Background voltammogram is also shown in this Figure (dash line).

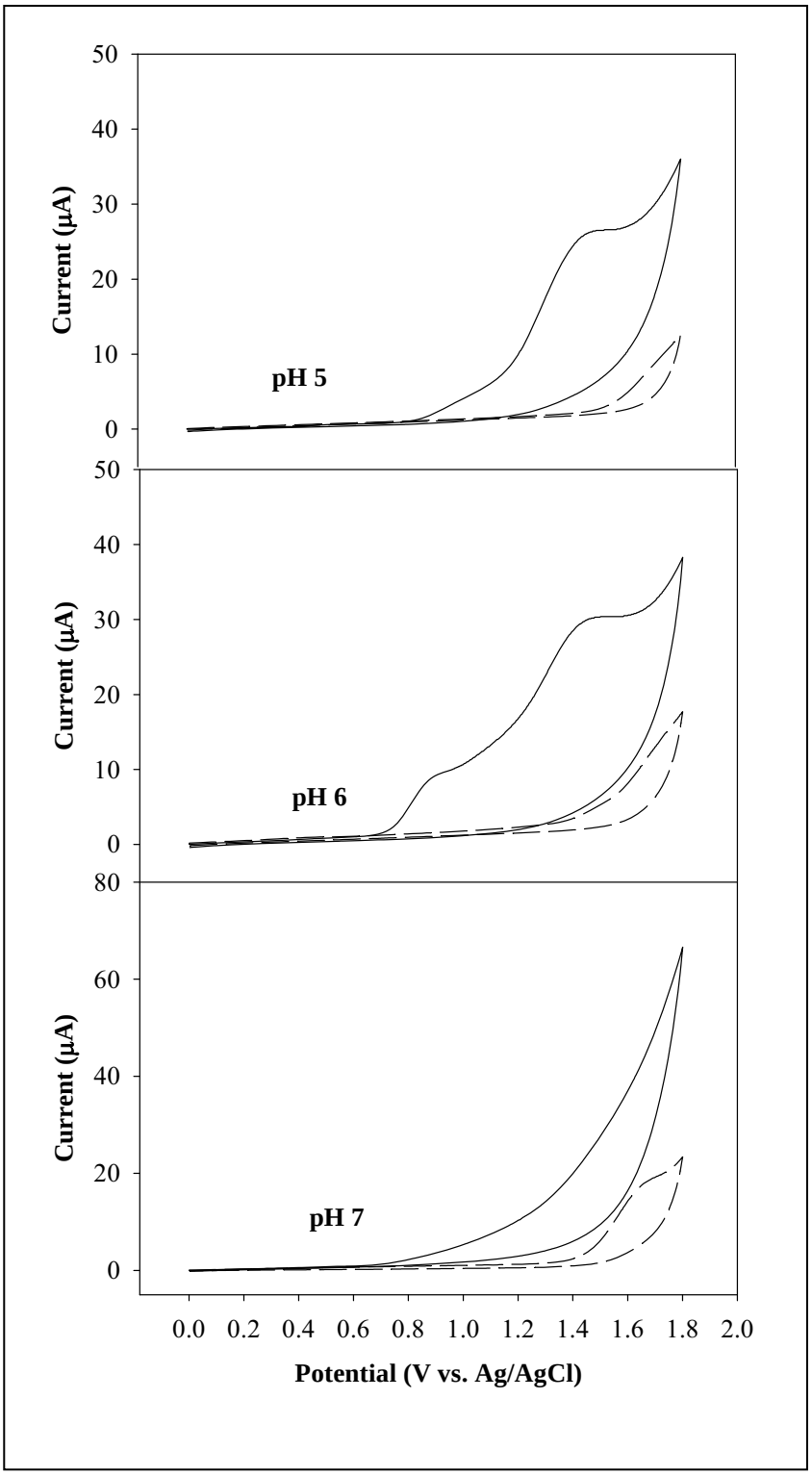

Figure 11 Cyclic voltammogram of 1 mM tetracycline in 0.1 M phosphate buffer (pH 5, 6and 7) at Ni-implanted diamond electrode (solid line). The scan rate was 50 mVs^{-1}. Background voltammogram is also shown in this Figure (dash line).

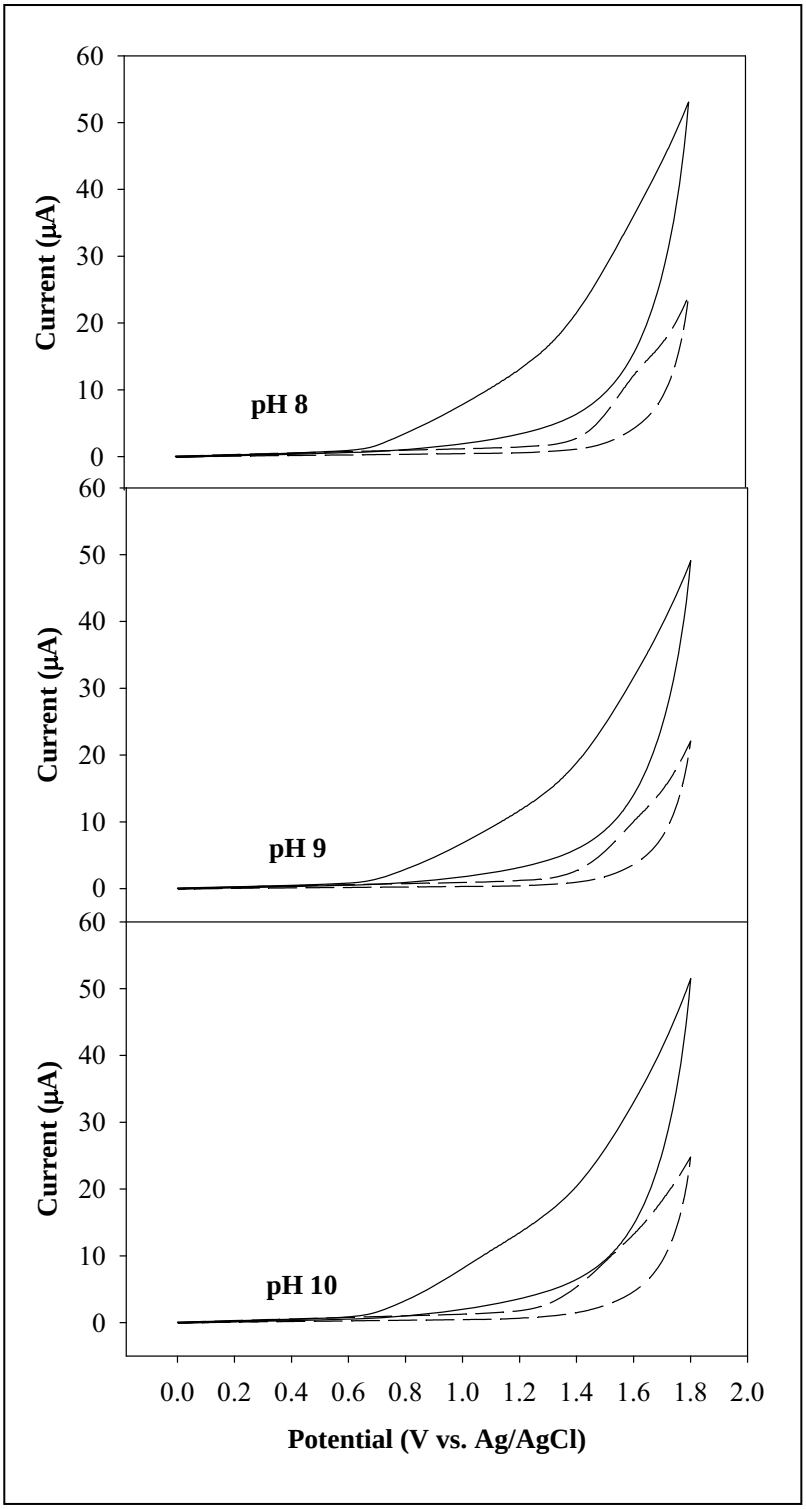

Figure 12 Cyclic voltammogram of 1 mM tetracycline in 0.1 M phosphate buffer (pH 8, 9and 10) at Ni-implanted diamond electrode (solid line). The scan rate was 50 mVs^{-1}. Background voltammogram is also shown in this Figure (dash line).

❖ **Scan rate dependence study**

Figure 13 shows the cyclic voltammetric response of 1 mM tetracycline in 0.1 M phosphate buffer (pH 2) with variation of scan rates from 0.01 to 0.3 Vs^{-1} at the Ni-DIA electrode. The oxidation current varied highly linearly (r^2 > 0.99) with the square root of scan rate ($\upsilon^{0.5}$), as shown in the inset of this figure, indicating semi-infinite linear diffusion of reactant to the electrode surface.

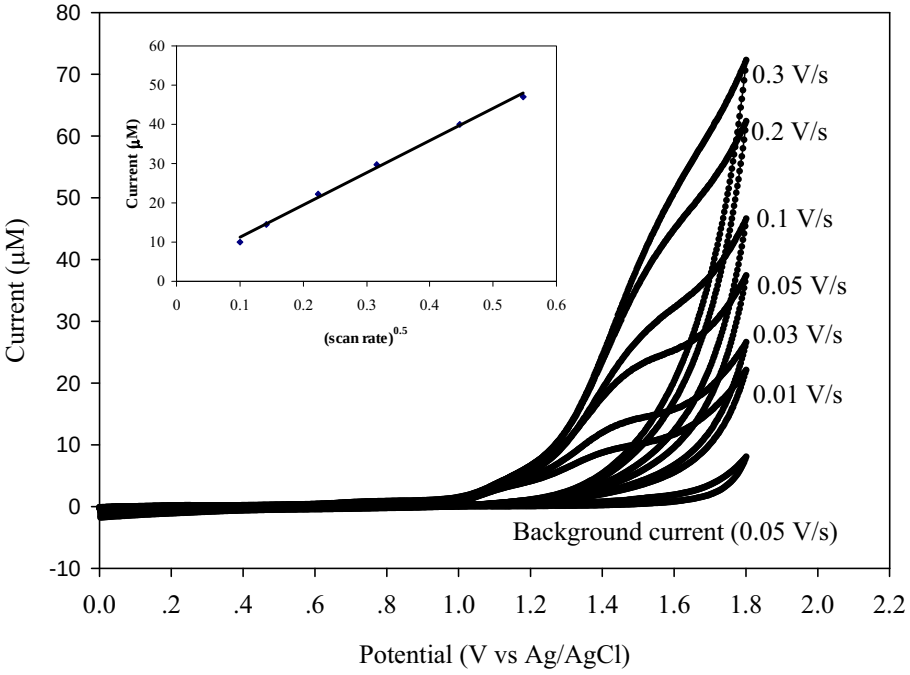

Figure 13 Cyclic voltammograms for 1 mM tetracycline in 0.1 M phosphate buffer (pH 2) at Ni-DIA electrode for a series of sweep rates, area of electrode was 0.07 cm^2. The dependence between peak current (μA) and the square root of the sweep rate appears in the inset.

❖ **Concentration dependence study**

The oxidation peak current was investigated for the concentration range from 0.1 to 3.0 mM of tetracycline at the Ni-DIA. Figure 14 shows the cyclic voltammograms with the concentrations of the tetracycline varied from 0.1 to 3.0

mM. Linear regression analysis of current (μA) *versus* concentration (μM) profile gave a wide linearity from 0.1 to 3.0 mM. (r^2 > 0.99) for the Ni-DIA electrode, as shown in the inset of this Figure.

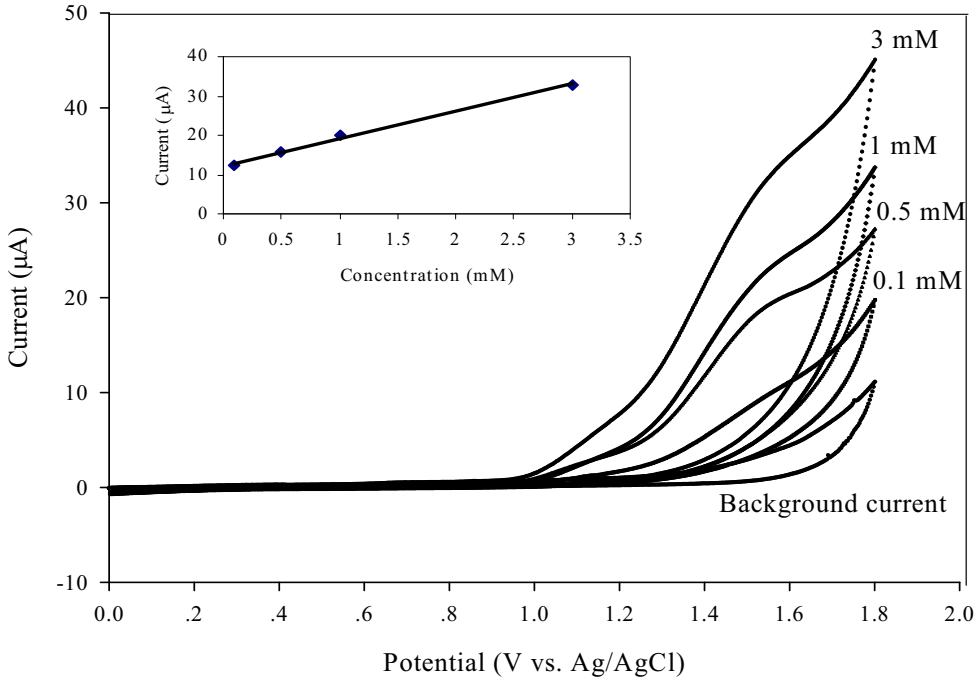

Figure 14 Cyclic Voltammograms for tetracycline in 0.1 M phosphate buffer (pH 2) at Ni-DIA electrode for a series of tetracycline concentrations. The sweep rate was 50 mVs^{-1}; the area of electrode was 0.07 cm^2. The dependence between peak current (μA) and concentrations at the potential of 50 mVs^{-1} appears in the inset.

❖ Flow injection analysis with amperometric detection

o Hydrodynamic voltammetry

Figure 15 (a) shows the hydrodynamic voltammetric *i-E* curves obtained at a Ni-DIA electrode for 20 μL injection of 100 μM of tetracycline in 0.1 M of phosphate buffer (pH 2), using phosphate buffer (pH 2) as the carrier solution. Each datum shows the average of injections. The absolute magnitude of the

background current at each potential is also shown for comparison. Hydrodynamic voltammogram for tetracycline did not produce a sigmodial shape of the signal versus potential. To obtain the maxima potential point, we calculated the S/B ratio from Fig. 3.15 (a) at each potential. Hydrodynamic voltammetric S/B ratio *versus* potential curve was obtained as shown in Fig.15 (b) with the maximum S/B ratio of 1.55 V *versus* Ag/AgCl. Hence, this potential was set as the amperometric potential detection value in flow injection analysis experiments.

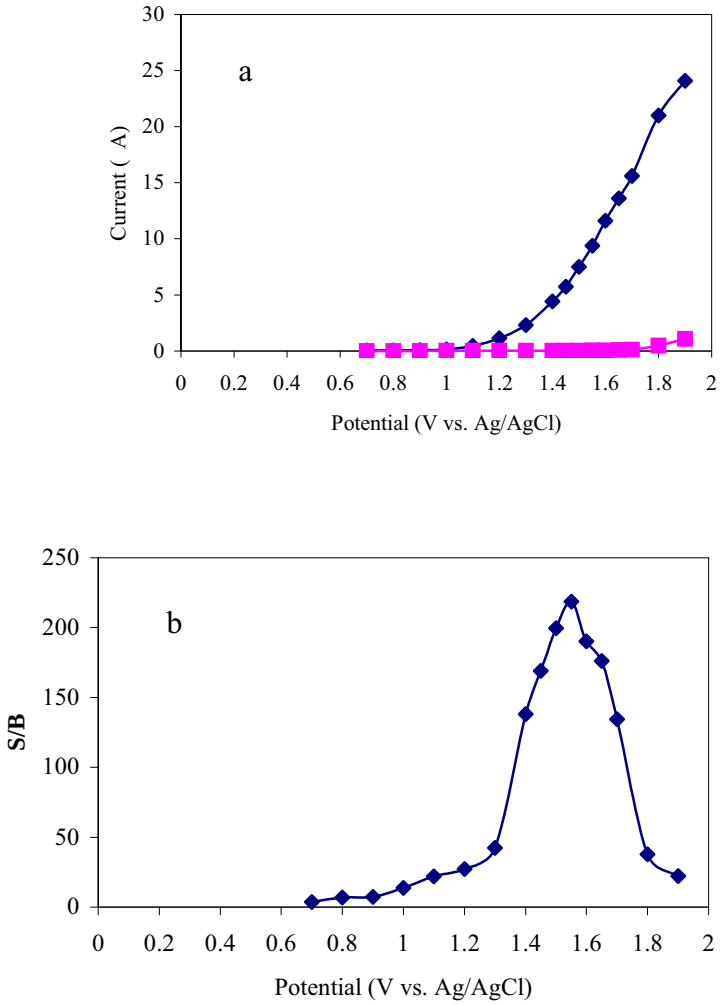

Figure 15 (a) Hydrodynamic voltammograms of (- -) 1 µM of tetracycline in 0.1 M phosphate buffer (pH 2) and (-Δ-) 0.1 M phosphate buffer (pH 2, background current) with four injection of analytes, using 0.1 M phosphate buffer (pH 2) as a carrier solution. (b) Hydrodynamic of signal-to-background ratio. The flow rate was 1 mL min^{-1}.

- **Linear range, detection limit and reproducibility**

A series of repetitive 20 μL injections of tetracycline at a concentration of 1 – 100 μM in 0.1 M phosphate buffer (pH 2) was examined using amperometric potential of 1.55 V *versus* Ag/AgCl. The calibration curve was obtained from three injections of five concentrations of tetracycline (1, 5, 25, 50 and 100 μM). Using a least square-linear regress fit, it was found that slope (sensitivity) was 0.058 μA/mM, intercept was 0.6476 μA and correlation coefficient $r^2 > 0.99$. A linear dynamic range was obtained over two orders of magnitude, from 1 to 100 μM. The limit of detection (LOD) is the concentration of analyte, which provides three times of the ratio of the analyte current to noise signal (S/N ≥ 3). Interestingly, LOD of this proposed method was obtained after five injections of 10 nM tetracycline. The precision of the method was investigated for the standard solution at concentrations of 10 and 25 μg/mL. Ten measurements were made with each concentration on the same day. Results exhibited very good precision with peak variabilites of 2.82%.

- **Drug analysis of tetracycline capsules**

The proposed method for tetracycline was applied to the determination of tetracycline hydrochloride capsules. The precision of the method was obtained on the basis of intra-assay comparisons using standard addition. Recovery results are summarized in Table 8.

The tetracycline content of the drug calculated from this calibration plot (251.03 ± 0.05 mg per tablet, $n = 2$) was found to be in satisfactory agreement with the labeled amount of 250 mg per capsule. There was no significant difference between the labeled contents and those obtained by the proposed method. Recoveries ranged from 97.22 to 102.38%.

Table 8 Recovery of tetracycline capsule sample with amperomatric detection using Ni-DIA electrode applied to flow injection system (n = 2)

Amount of tetracycline tablet sample added/ μg ml^{-1}	Amount of tetracycline tablet sample found/ μg ml^{-1}	Percent of recovery, %
0.36	0.35 ± 0.01	97.22 ± 1.39
0.42	0.43 ± 0.00	102.38 ± 0.00
0.48	0.49 ± 0.01	100.00 ± 1.04
0.54	0.54 ± 0.01	100.00 ± 1.85
0.60	0.61 ± 0.01	101.66 ± 0.83

- **Comparison with other methods**

Table 9 summarizes data obtained from the other methods for determination of tetracycline compared with the proposed method. It was found that using the Ni-DIA electrode with amperometric FIA gave the wide linear dynamic range (two orders of magnitude). Interestingly, the proposed method provided a very low detection limit of 10 nM, because the Ni-DIA electrode exhibited very low background current and noise signals. It also resulted in very high sensitivity. This outstanding performance of the BDD electrode makes it attractive for using as working electrode in FIA system for analysis of tetracycline.

Table 9 Comparison of data for tetracycline determination

Method	Linear dynamic range/μM	Detection limit/ μM	Precision, % RSD	Reference
Flow injection with UV spectrophotometric	1 – 25	0.14	0.7	34
Chemiluminescence	0.2 – 5	0.06	3.2	38
Liquid chromatography with ultraviolet detector	0.104 – 1.350	0.01	1.2	39
Liquid chromatography with coulometric electrode array	0.104 – 2.079	0.04	≤ 4.3	40
Flow injection with pulsed amperometric detection	5 – 600	1.0	3.5	45
Ni-implanted boron-doped diamond thin film electrode applied to flow injection system	1 – 100	0.01	2.8	[a]

[a] This proposed method.

❖ Summary

This is the first use of Ni-DIA electrodes for the electroanalysis of tetracycline. It was found that Ni-DIA electrodes exhibited excellent performance for the oxidative detection of tetracycline. Well-defined voltammograms were obtained

at the Ni-DIA electrode, which exhibited high sensitivity and demonstrated significant advantages over the BDD electrode, because of its superior electrochemical properties. The outstanding capabilities of the Ni-DIA electrode were demonstrated by coupling with FIA. Application of the proposed method for determination of tetracycline in commercially available tablet forms shows that this method is precise, accurate and very sensitive.

Use of nickel implanted boron-doped diamond thin film electrode coupled to HPLC system for the determination of tetracyclines

This part was carried out in the HPLC system. Figure 16 depicts the optimum potential i-E curve obtained at the Ni-implanted diamond electrode for a 20 μl injection of 100 μM of tetracycline mixture standard solution 0.1 M of phosphate buffer (pH 2.5) was used as the carrier solution. Each datum represents the average of two injections. The magnitude of the background current at each potential is also shown in Figure 16. The hydrodynamic voltammogram of tetracycline mixture standard solution at the Ni-implanted diamond electrode exhibited a well-defined sigmodal shape with a half peak potential at about 1.55 V vs. Ag/AgCl. Therefore, this potential was fixed for the amperometric potential detection in HPLC system analysis experiments.

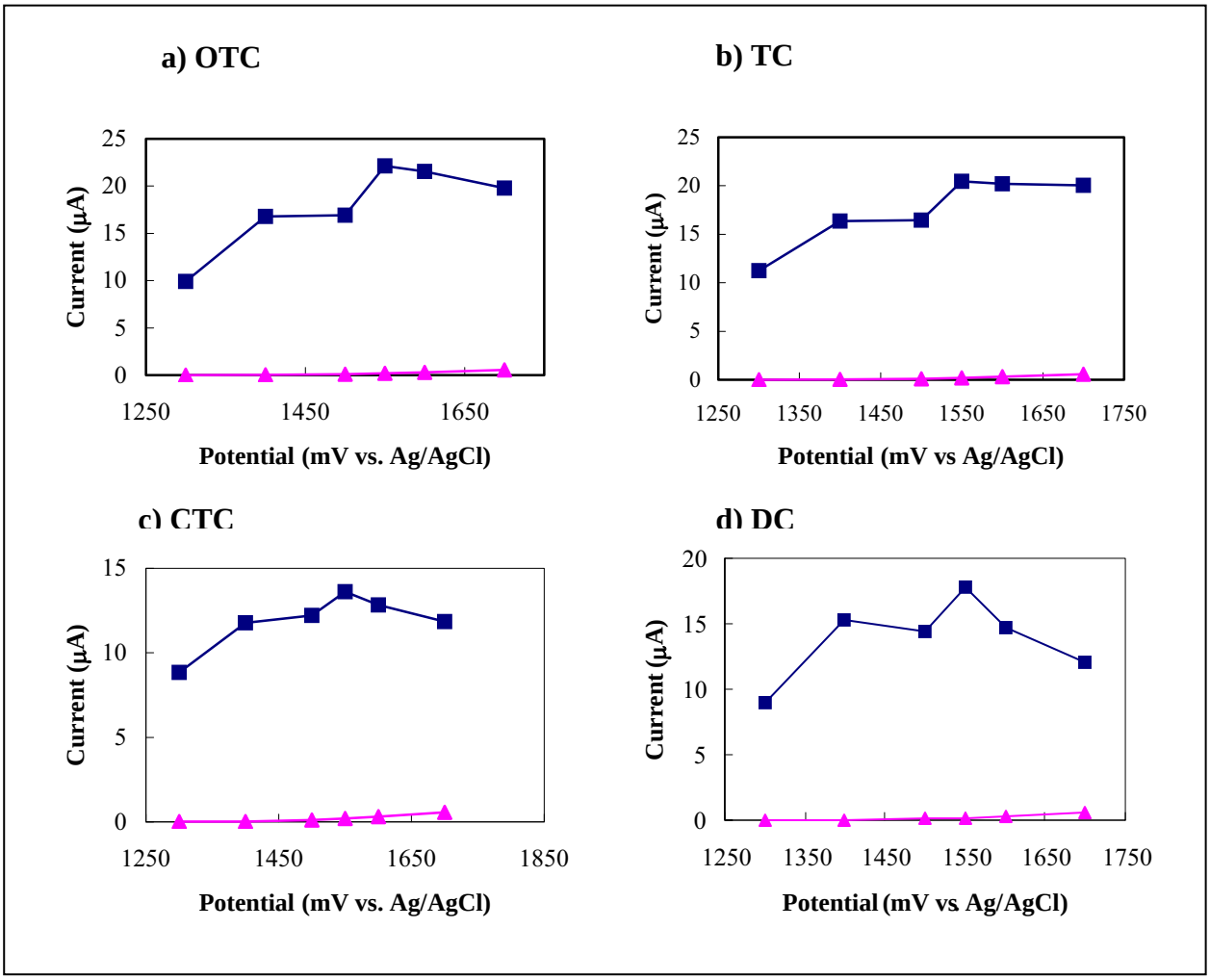

Figure 16 Optimum potential of (- -) 10 ppm of oxytetracycline a), tetracycline b), chlortetracycline c) and doxycycline d) in 0.1 M phosphate buffer (pH 2.5) and (-Δ-) 0.1 M phosphate buffer (pH 2.5, background current) with two injections of analyte. 0.1 M phosphate buffer (pH 2.5) was used as a carrier solution, flow rate 1 ml min^{-1}.

❖ Calibration curve and linear range

The tetracycline mixture standard solutions covering the concentration range of 0.01-100 ppm were analyzed and their peak areas were plotted versus concentration. The regression data are summarized in Table 3.10. Regression plots of the concentration and peak area are shown in Figure 17.

From Table 10, the data of the 10 point calibration curve was acceptable for quantitation because the correlative coefficient (R^2) obtained were between 0.9975 to 0.9996.

Table 10 Linear regression statistics results

Analytes	Linear dynamic range (ppm)	Slope (peak areas units/mg/kg)	Intercept (μA)	R^2
Oxytetracycline	0.05-100	0.0473	0.0562	0.9975
Tetracycline	0.05-100	0.0395	0.0453	0.9977
Chlortetracycline	0.1-100	0.0110	0.0045	0.9990
Doxycycline	0.1-100	0.0111	0.0066	0.9996

The determination of each tetracycline by HPLC can be distinguished by the retention time of 5.97, 7.55, 18.87 and 26.95 min for oxytetracycline hydrochloride, tetracycline, chlortetracycline and doxycycline, respectively.

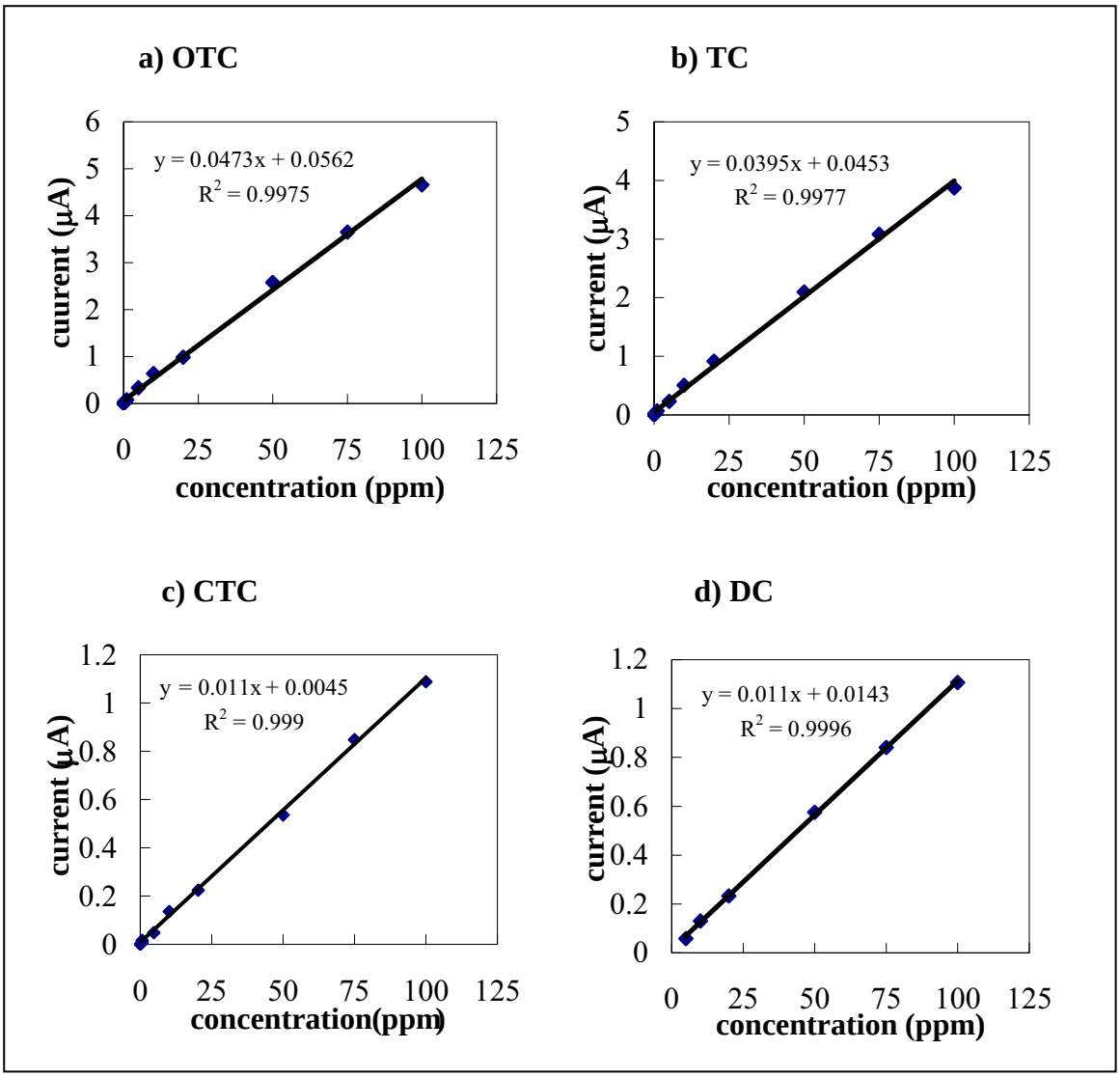

Figure 17 Calibration curve of oxytetracycline a), tetracycline b), chlortetracycline c) and doxycycline d) obtained from HPLC data.

❖ Limit of detection (LOD) and Limit of quantitation (LOQ)

The limit of detection (LOD) and limit of quantitation (LOQ) were defined as the concentration of that yielded the peak area of analyte in matrix standard solutions that signalled significantly different from the peak area of noise equal 3 for LOD and 10 for LOQ of each compound. These are shown in Table 11.

The limit of detection and limit of quantitation of the 4 tetracyclines are in the range of 0.01-0.05 ppm and 0.03-0.17 ppm respectively.

Table 11 The limit of detection and limit of quantitation of analyte in matrix standard solutions.

Analytes	LOD (ppm)	LOQ (ppm)
Oxytetracycline	0.01	0.03
Tetracycline	0.01	0.03
Chlortetracycline	0.05	0.17
Doxycycline	0.05	0.17

- **Precision**

The method for extraction as described in chapter 2 was used to determined %recovery and precision of this method at spiking level of 5 mg/kg for shrimp farming samples and shrimp sea samples.

Table 12-13 displays the intra-day precision of this method at the spiking level of 5 mg/kg for shrimp farming samples and shrimp sea samples respectively.

Table 14-15 illustrates the inter-day precision of the method at the spiking level of 5 mg/kg for shrimp farming samples and shrimp sea samples respectively.

Table 12 Mean of %Recovery of tetracyclines (intra-day precision) at spiking level of 5 mg/kg in Shrimp farming sample (n=3)

Analytes	%Recovery			Mean±SD	%RSD
	1	2	3		
Oxytetracycline	101.4	100.9	100.8	101.1±0.3	0.3
Tetracycline	101.2	101.6	100.5	100.4±1.7	1.7
Chlortetracycline	100.2	99.4	97.0	98.9±1.6	1.6
Doxycycline	101.8	99.9	101.6	101.1±1.0	1.0

Table 13 Mean of %Recovery of tetracyclines (intra-day precision) at spiking level of 5 mg/kg in Shrimp sea sample (n=3)

Analytes	%Recovery			Mean±SD	%RSD
	1	2	3		
Oxytetracycline	107.7	106.4	107.5	107.2±0.7	0.6
Tetracycline	100.9	101.1	101.9	101.3±0.5	0.5
Chlortetracycline	103.0	99.8	98.7	100.5±2.2	2.2
Doxycycline	103.6	99.0	95.9	99.5±3.8	3.8

Table 14 Mean of %Recovery of tetracyclines (inter-day precision) at spiking level of 5 mg/kg in Shrimp farming sample (n=6)

Analytes	%Recovery						Mean±SD	%RSD
	1	2	3	4	5	6		
Oxytetracycline	101.5	101.4	100.9	101.4	100.9	100.8	101.1±0.3	0.3
Tetracycline	101.6	100.5	102.8	101.2	101.6	100.5	101.3±0.8	0.8
Chlortetracycline	100.2	99.4	97.0	99.1	98.2	100.4	99.1±1.2	1.2
Doxycycline	97.2	101.8	99.9	101.6	98.9	101.4	100.1±1.8	1.8

Table 15 Mean of %Recovery of tetracyclines (inter-day precision) at spiking level of 5 mg/kg in Shrimp sea sample (n=6)

Analytes	%Recovery						Mean±SD	%RSD
	1	2	3	4	5	6		
Oxytetracycline	100.3	102.6	101.1	107.7	106.4	107.5	104.3±3.3	3.1
Tetracycline	101.1	100.0	100.9	100.9	101.7	101.9	101.1±0.6	0.6
Chlortetracycline	102.3	99.6	99.6	103.0	99.8	98.7	100.5±1.7	1.7
Doxycycline	93.7	100.3	94.3	103.6	99.0	95.5	97.7±3.8	3.9

3.3.4 Accuracy

From Table 16, %recovery of 4 tetracyclines in Shrimp farming sample at spiking level of 0.5 mg/kg are in the range of 81.6-98.9%, while these of the 1mg/kg, 5 mg/kg and 10 mg/kg spiking levels are in the range of 80.4-99.0%, 87.9-105.0 % and 93.2-109.2%, respectively. And from Table 17, %recovery of 4 tetracyclines in Shrimp sea sample at spiking level of 0.5 mg/kg are in the range of 84.2-109.1%, while these of the 1mg/kg, 5 mg/kg and 10 mg/kg spiking levels are in the range of 72.2-97.4%, 80.3-91.7 % and 93.7-109.1%, respectively. These values agree within the acceptable range set forth by AOAC Regulations of %recovery at 75-125 mg/kg level.

Table 16 Accuracy of extraction method at spiking level of 0.5, 1, 5 and 10 mg/kg for Shrimp farming sample (n=3).

Analytes	Mean of %Recovery			
	Spiking level of 0.5 mg/kg	Spiking level of 1 mg/kg	Spiking level of 5 mg/kg	Spiking level of 10 mg/kg
Oxytetracycline	84.8±3.0	96.8±2.7	102.5±3.4	99.6±1.8
Tetracycline	93.3±5.5	85.9±7.7	96.6±2.4	97.0±5.5
Chlortetracycline	91.48±5.3	94.8±5.9	91.6±5.2	97.9±3.8
Doxycycline	89.2±6.7	88.4±3.0	97.7±5.4	103.7±7.4

Table 17 Accuracy of extraction method at spiking level of 0.5, 1, 5 and 10 mg/kg for Shrimp sea sample.(n=3)

Analytes	Mean of %Recovery			
	Spiking level of 0.5 mg/kg	Spiking level of 1 mg/kg	Spiking level of 5 mg/kg	Spiking level of 10 mg/kg
Oxytetracycline	94.9±1.6	83.3±4.3	86.8±5.0	96.5±2.4
Tetracycline	92.0±1.1	88.4±4.4	89.2±1.2	96.9±4.6
Chlortetracycline	91.8±8.6	91.9±3.0	86.0±8.0	93.3±5.1
Doxycycline	102.0±9.0	96.2±1.7	90.6±0.1	99.4±2.4

3.3.5 AOAC standard method

Standard calibration curve and linear range

The mixed 3 standard tetracyclines solution covering the concentration range of 0.05-10 ppm were measured. The regression data are summarized in Table 18.

From Table 18, the data of the 8 point calibration curve is acceptable for quantitation because the correlative coefficient (R^2) obtained were at 0.9975 to 0.9996.

Table 18 Linear regression statistics results

Analytes	Linear dynamic range (ppm)	Slope(peak areas units/mg/kg)	Intercept	R^2
Oxytetracycline	0.05-10	46.656	3.9474	0.9996
Tetracycline	0.05-10	55.960	4.3590	0.9995
Chlortetracycline	0.10-10	28.108	1.6850	0.9999

- **Limit of detection (LOD) and limit of quantitation (LOQ)**

The limit of detection (LOD) and limit of quantitation (LOQ) were defined as the concentration of that yielded the peak area of analyte in matrix standard solutions that signalled significantly different from the peak area of noise equal 3 for LOD and 10 for LOQ of each compound. These are shown in Table 19

The limit of detection and limit of quantitation of the 3 tetracyclines are in the range of 0.05-0.10 ppm and 0.17-0.33 ppm respectively.

Table 19 The limit of detection and of quantitation of analyte in matrix standard solutions

Analytes	LOD (ppm)	LOQ (ppm)
Oxytetracycline	0.05	0.17
Tetracycline	0.05	0.17
Chlortetracycline	0.10	0.33

- **The result of accuracy**

From Table 20, %recovery of 3 tetracyclines in Shrimp farming sample at spiking level of 0.5 mg/kg are in the range of 72.5-78.6%, while these of the 1mg/kg, 5 mg/kg and 10 mg/kg spiking levels are in the range of 72.6-80.2%, 77.5-82.5% and 80.2-90.2%, respectively. And from Table 3.21, %recovery of 3 tetracyclines in Shrimp sea sample at spiking level of 0.5 mg/kg are in the range of 74.2-80.2%, while these of the 1mg/kg, 5 mg/kg and 10 mg/kg spiking levels are in the range of 76.2-81.2%, 79.3-85.9% and 90.0-92.5%, respectively. This is within the acceptable range set forth by AOAC Regulations %recovery 75-125.

Table 20 Accuracy of extraction method at spiking level of 0.5, 1, 5 and 10 mg/kg for Shrimp farming sample (n=3)

Analytes	Mean of %Recovery			
	Spiking level of 0.5 mg/kg	Spiking level of 1 mg/kg	Spiking level of 5 mg/kg	Spiking level of 10 mg/kg
Oxytetracycline	78.6±6.5	79.0±6.3	82.5±3.2	89.9±3.8
Tetracycline	75.8±8.2	80.2±5.3	80.0±3.5	90.2±2.1
Chlortetracycline	72.56±5.4	72.6±7.7	77.5±4.2	80.2±4.2

Table 21 Accuracy of extraction method at spiking level of 0.5, 1, 5 and 10 mg/kg for Shrimp sea sample.(n=3)

Analytes	Mean of %Recovery			
	Spiking level of 0.5 mg/kg	Spiking level of 1 mg/kg	Spiking level of 5 mg/kg	Spiking level of 10 mg/kg
Oxytetracycline	80.2±5.3	78.4±5.9	85.9±4.5	92.5±3.0
Tetracycline	75.3±7.2	81.2±6.5	82.3±3.7	91.4±2.5
Chlortetracycline	74.2±6.7	76.2±7.0	79.3±4.0	90.0±4.0

Finally results determined tetracyclines in shrimp sample. From Table 3.22-3.23, the comparisons results of 3 methods in 2 shrimp samples at blank sample.

Table 22 Comparisons results of 3 methods in shrimp farming sample

Analyte	Found (mg/kg)		
	HPLC-ECD	AOAC method**	Result for LCFA***
Oxytetracycline	nd*	nd*	nd*
Tetracycline	nd*	nd*	nd*
Chlortetracycline	nd*	nd*	nd*
Doxycycline	nd*	-	-

* Not detected

** AOAC official method 995.09 (Chlortetracycline, Oxytetracycline and Tetracycline in edible animal tissues)

*** Result of Laboratory Center for Food and Agricultural product Co.,Ltd (LCFA)

Table 23 Comparisons results of 3 methods in shrimp sea sample

Analyte	Found (mg/kg)		
	HPLC-ECD	AOAC method**	Result for LCFA***
Oxytetracycline	nd*	nd*	nd*
Tetracycline	nd*	nd*	nd*
Chlortetracycline	nd*	nd*	0.07
Doxycycline	nd*	-	-

* Not detected

** AOAC official method 995.09 (Chlortetracycline, Oxytetracycline and Tetracycline in edible animal tissues)

*** Result of Laboratory Center for Food and Agricultural product Co.,Ltd (LCFA)

❖ Summary

This is the first use of Ni-DIA electrodes for the electroanalysis of tetracyclines. It was found that Ni-DIA electrodes exhibited excellent performance for the oxidative detection of tetracycline.Well-defined voltammograms were obtained at the Ni-DIA electrode, which exhibited high sensitivity and demonstrated significant advantages over the BDD and glassy carbon electrode. The outstanding capabilities of the Ni-DIA electrode were demonstrated by coupling with HPLC. HPLC with amperometry at Ni-DIA electrode has been successfully applied to determine four types of tetracyclines (oxytetracycline, tetracycline, chlortetracycline and doxycycline) in shrimp samples. Experimental detection limit of 0.01–0.05 μg/mL were obtained for four tetracyclines studied. A linear dynamic range from 0.05 to 100 μg/mL was achieved. Application of the proposed method for the determination of tetracycline in shrimp sample shows that this method is precise, accurate and very sensitive.

CONCLUSIONS

In this research, the modified BDD electrodes were used to investigate tetracycline antibiotics. BDD have been widely used as electrode for many electrochemical applications. The superior electrochemical properties were low background current leads to the enhancement of the S/B ratios, wide working potential window in the aqueous solution and slightly adsorption of polar molecules. Moreover, the BDD surfaces covered with hydrogen make this electrode lack of the catalytic property. The modification of BDD surface to change the functional group on the diamond surface can be extended the catalytic capability and enhanced the sensitivity of the electrode. This work was focused on two modification methods (i) anodized BDD electrode and (ii) Ni-implanted diamond electrode for the determination of tetracycline antibiotics in pharmaceutical formulation and shrimp.

The anodized BDD electrode was modified by anodic polarization in the alkaline solution using cyclic voltammetry to make the surface of BDD terminated with oxygen. The obtained anodized BDD electrode was applied to detect tetracycline antibiotics. The electrochemical properties of tetracyclines were investigated using cyclic voltammetry. Comparison results were carried out using glassy carbon and as-deposited BDD electrodes. From the results, all electrodes provided the irreversible cyclic voltammograms. However, the highest current signal was obtained at the anodized BDD electrode. In order to find the optimum pH for the determination of TCs at anodized BDD electrode, the experiments were carried out in the pH solution 2-9. It was found that the pH 2 gave the maximum current signal because the TCs were formed in the fully positive charge that could be attracted to the negatively charged on the anodized BDD surface. The anodized BDD electrode was used as the amperometric detector in the flow injection system. To find the optimum working potential, hydrodynamic voltammetry of TCs were investigated. The results indicated that the optimum potentials were 1.5 V vs. Ag/AgCl for CTC, and 1.6 V vs. Ag/AgCl for TCs, OTC, and DC. The analytical performances of anodized BDD electrode in flow system including the linear range and LOD were investigated. The linear ranges were 0.1–50 μM for TC and 0.5-50 μM for OTC, CTC and DC. The LOD was 10 nM for four TCs. The proposed method was applied to determination TCs in the pharmaceutical formulations. The precision of the method based on the

intra- and inter-day assay were studied. The results were summarized in the Table 3.5 and 3.6.

Ion implantation has been successfully used in doping semiconductors such as silicon and gallium arsenide. In particular, applications of the ion-implanted diamond have recently come to light. In these studies, the electrical conductivity and other physical properties could be controlled by ion-implanting diamond. Flow injection analysis and HPLC electrochemical detection at the Ni-implanted BDD electrode has been accomplish applied to determine TCs in pharmaceutical drugs and shrimps, respectively. The outstanding capabilities of the Ni-DIA electrode were demonstrated by coupling with FIA. Application of the proposed method for determination of tetracycline in commercially available tablet forms shows that this method is precise, accurate and very sensitive.

For the validation of this method, the linear concentration range of TCs was 0.05 to 100 ppm, with correlation coefficient $R^2 > 0.99$. The LOD of this method was in the range of 0.01-0.05 ppm. The recovery of TCs at the spiking level of 0.5 mg/kg, 1.0 mg/kg, 5.0 mg/kg and 10 mg/kg were studied. The recovery was in the range of 83.3-102.0% with RSD < 10%. These results indicated that HPLC electrochemical detection at the Ni-implanted BDD electrode provided high accuracy and precision, respectively.

References

1. Ngamukot, P.; Charoenraks, T.; Chailapakul, O.; Motomizu, S.; Chuanuwatanakul, S. *Analytical Sciences* **2006**, *22*, 111.
2. Treetepvijit, S.; Preechaworapun, A.; Praphairaksit, N.; Chuanuwatanakul, U.; Einaga, Y.; Chailapakul, O. *Talanta* **2006**, *68*, 1329.
3. Lawrence, N. S.; Pagels, M.; Meredith, A.; Jones, T. G. J.; Hall, C. E.; Pickles, C. S. J.; Godfried, H. P.; Banks, C. E.; Compton, R. G.; Jiang, L. *Talanta* **2006**, *69*, 829.
4. Ivandini, T. A.; Rao, T. N.; Fujishima, A.; Einaga, Y. *Analytical Chemistry* **2006**, *78*, 3467.
5. Basu, S.; Kang, W. P.; Davidson, J. L.; Choi, B. K.; Bonds, A. B.; Cliffel, D. E. *Diamond and Related Materials* **2006**, *15*, 269.
6. Peckova, K.; Mocko, V.; Opekar, F.; Swain, G. M.; Zima, J.; Barek, J. *Chemicke Listy* **2006**, *100*, 124.
7. Batchelor-McAuley, C.; Banks, C. E.; Simm, A. O.; Jones, T. G. J.; Compton, R. G. *Analyst* **2006**, *131*, 106.
8. Bouvrette, P.; Hrapovic, S.; Male, K. B.; Luong, J. H. T. *Journal of Chromatography A* **2006**, *1103*, 248.
9. Welch, C. M.; Banks, C. E.; Komorsky-Lovric, S.; Compton, R. G. *Croatica Chemica Acta* **2006**, *79*, 27.
10. Xie, S. T.; Shafer, G.; Wilson, C. G.; Martin, H. B. *Diamond and Related Materials* **2006**, *15*, 225.
11. Xu, J. S.; Granger, M. C.; Chen, Q. Y.; Strojek, J. W.; Lister, T. E.; Swain, G. M. *Analytical Chemistry* **1997**, *69*, A591.

12. Chailapakul, O.; Popa, E.; Tai, H.; Sarada, B. V.; Tryk, D. A.; Fujishima, A. *Electrochemistry Communications* **2000**, *2*, 422.

13. Granger, M. C.; Xu, J. S.; Strojek, J. W.; Swain, G. M. *Analytica Chimica Acta* **1999**, *397*, 145.

14. Wangfuengkanagul, N.; Chailapakul, O. *Talanta* **2002**, *58*, 1213.

15. Swain, G. M.; Anderson, A. B.; Angus, J. C. *MRS Bulletin* **1998**, *23*, 56.

16. C. Terashima, T.N. Rao, B.V. Sarada, D.A. Tryk, A. Fujishima, *Anal. Chem*. **2002**, *74*, 895.

17. E. Popa, Y. Kubota, D.A. Ttyk, A. Fujishima, *Anal. Chem*. **2000**, *72,* 1724.

18. O. Chailapakul, W. Siangproh, B.V. Sarada, C. Terashima, T.N. Rao, D.A. Tyrk, A. Fujishima, *Analyst* **2002**, *127,* 1164.

19. F. Montilla, E. Morallon, I. Duo, C. Comninellis, J.L. Vasquez, *Electrochim. Acta* **2003**, *48*3, 891.

20. I.G. Casella, E. Desimoni, T.R.I. Cataldi, *Anal. Chim. Acta* **1991**, *248*, 117.

21. I.G. Casella, E. Desimoni, A.M. Salvi, *Anal. Chim. Acta* **1991**, 243, 61.

22. S.V. Prabhu, R.P. Baldwin, *Anal. Chem*. **1989**, *61*, 852.

23. S.V. Prabhu, R.P. Baldwin, *Anal. Chem*. **1989**, *61*, 2258.

24. P. Luo, S.V. Prabhu, R.P. Baldwin, *Anal. Chem*. **1990**, *62,* 752.

25. T.R.I. Cataldi, I.G. Casella, E. Desimoni, T. Rotunno, *Anal. Chim. Acta* **1992** , *270* , 161.

26. E. Wang, A. Liu, *J. Electroanal. Chem.* **1991**, *319*, 217.

27. I.G. Casella, T.R.I. Cataldi, A.M. Salvi, E. Desimoni, *Anal. Chem*. **1993**, *65,* 3143.

28. A. Liu, E. Wang, *Anal. Chim. Acta* 1993, *280*, 223.

29. T.A. Ivandini, R. Sato, Y. Makide, A. Fujishima, Y. Einaga, *Diamond Relat.*

Mater. **2004** , *13*, 2003.

30. The United Pharmacopoeia, 21st revision, Easton PA, Mack Printing Company, USP XXI, **1985.**
31. The British Pharmacopeia, HMSO, London **1988**.
32. J. Kurittu, S. Lonnberg, M. Virta, M. Karp, *J. Agri. Food. Chem.* **2000**, *48* 3372.
33. K.M. Emara, H.F. Askal, G.A. Saleh, *Talanta* **1991**, *38*, 1219.
34. U. Saha, A.K. Sen, T.K. Das, S.K. Bhowal, *Talanta* **1990**, *37*, 1193.
35. X.R. Zhang, W.R.G. Baeyens, A. Vandenborre, G. Vanderweken, A.C. Calokerinos, S.G. Schulman, *Analyst* **1995**, *120* , 463.
36. H. Han, Z. He, Y. Zeng, *Anal. Sci.* **1999**, *15,* 467.
37. S. Marczynski, *Biopolymers* **2000**, *57*, 365.
38. A. Pena, L.P. Palilis, C.M. Lino, M.I. Silveira, A.C. Calokerinos, *Anal. Chim. Acta.* **2000**, *405,* 51.
39. S. Croubels, C. V. Peteghem, W. Baeyens, *Analyst* **1994**, *11, 9*2713.
40. S. Sabhawal, K. Kishore, P.N. Moorthy, *J. Pharm. Sci.* **1988**, *77*, 78.
41. R. Karlicek, P. Solich, *Anal. Chim. Acta* **1994**, *285,* 9.
42. S.M. Sultan, F.E.O. Suliman, S. O. Duffuaa, I. I. Abu-Abdoun, *Analyst* **1992**, *117* , 1179.
43. S. A. Halvatzis, M. M. Timotheou-Potamia, A. C. Calokerinos, *Analyst* **1993**, *118* , 633.
44. A. B. Syropoulos, A. C. Calokernos, *Anal. Chim. Acta* **1991**, *255,* 403.
45. C.M. Couta, J.L.F.C. Lima, M. Conceicao, B.S.M. Montenegro, S. Reis, *J. Phram. Biomed. Anal.* **1998**, *18*, 527.
46. H. Ji, E. Wang, *Analyst* **1988,** *113,* 1541.

47. W. Oungpipat, P. Southwellkeely, P.W. Alexander, *Analyst* **1995** , *120* , 1559.

48. A. G. Kazemifard, D. E. Moore, *J. Pharm. Biomed. Anal.* **1997**, *16*, 689.

49. J. Sokol, E. Matisova, *J. Chromatogr. A* **1994**, *669,* 75.

50. J.R. Walsh, L.V. Walker, J.J. Webber, *J. Chromatogr. A* **1992**, *596*, 211.

51. S. Croubels, W. Baeyens, C.V. Peteghem, *Anal. Chim. Acta* **1995** ,*303*,11.

52. D.S. Vienneau, C.G. Kindberg, *J. Pharm. Biomed. Anal.* **1997**, *16*, 111.

53. J. Zhu, D.D. Snow, D.A. Cassada, S.J. Monson, R.F. Spalding, *J. Chromatogr. A* **2001** ,*928*, 177.

54. M. Cherlet, M. Schelkens, S. Croubels, P.D. Backer, *Anal. Chim. Acta* **2003,** *492,* 199.

55. A.G. Kazemifard, D.E. Moore, *J. Pharm. Biomed. Anal.* **1997** ,*16,* 689.

56. S. Palaharn, T. Charoenraks, N. Wangfuengkanagul, K. Grudpan, O. Chailapakul, *Anal. Chim. Acta* **2003**, *499*,191.

57. C.M.C.M. Couto, J.L.F.C. Lima, M. Conceicao, B.S.M. Montenegro, S. Reis, *J. Pharm. Biomed. Anal*. **1998** ,*18*, 527.

58. T. Charoenraks, S. Chuanuwatanakul, K. Honda, Y. Yamaguchi, O. Chailapakul, *Anal. Sci*. **2005**, *212*, 41.

Output

ผลงานวิจัยที่ตีพิมพ์

1. Wangfuengkanagul, N.; Siangproh, W.; Chailapakul, O., Electrochemical analysis of Tetracycline using an Anodized boron-doped diamond thin film electrode. *Talanta* **2004,** 64, (5), 1183-1188.
2. Treetepvijit, S.; Chuanuwatanakul, S.; Einaga Y.; Sato, R and Chailapakul, O Electroanalysis of tetracycline using nickel-implanted boron-doped diamond thin film electrode applied to flow injection system *Analytical Sciences,* **2005**, 21, 531.
3. Kanokporn, B.; Chuanuwatanakul, S.; Wangfuengkanagul, N and Chailapakul, O.; Electroanalysis of lincomycin using boron-doped diamond thin film electrode applied to flow injection system *Sensors and Actuators B: Chemical,* **2005***,108,* 627.
4. Treetepvijit, S.; Preechaworapun, A.; Praphairaksit, N.; Chuanuwatanakul, U.; Einaga Y.; Chailapakul, O Use of nickel implanted boron-doped diamond thin film electrode coupled to HPLC system for the determination of tetracyclines *Talanta* **2006,** 64, (5), 1329-1335.
5. Ngamukot, P.; Charoenraks, T.;Chailapakul, O.; Motomizu, S.; Chuanuwatanakul, S.; Cost-effective flow cell for the determination of malachite green and leucomalachite green at a boron-doped diamond thin-film electrode *Analytical Sciences,* **2006**, *22*, 111.
6. Chailapakul, O.; Siangproh, W.; Tryk, D. A.; Boron-doped diamond-based sensors: A review *Sensor Letters* **2006**, 4 (2), 99-119.

การไปเสนอผลงาน

1. Treetepvijit, S.; Duanchai, W.; Bunnium, R.; Chailapakul, O. “Determination of Hydrogen Peroxide Based on Electrocatalytic Oxidation Using Chrmium(III) Hexacyanoferrate(II) Modified Boron-Doped Diamond Thin Film Electrode” *The 30th Congress on Science and Technology of Thailand,* 19-21 October **2004**, Muang Thong Thani, Bangkok, Thailand

2. Chailapakul, O. ; Treetepvijit, S. “Using Nickel implanted Boron-Doped Diamond Thin Film Electrode Coupled to FIA/HPLC System for the Determination of Tetracyclines” *The 13th International Conference on Flow Injection Analysis,* 24-29 April **2005**. Las Vegas, Nevada US
3. Chailapakul, O. “The use of as-grown and modified boron-doped diamond thin film electrodes for the electroanalysis” *The 11 th Asian Chemical Congress* August, **2005**., Zeoul, Korea
4. Chailapakul, O. “FIA-electrocatalytic determination of hydrogen peroxide at chromium (III) hexacyanoferrate (II) modified boron-doped diamond electrodes” *Pacifichem 2005,* 15 -23 December **2005**, Honolulu, Hawaii, US
5. Chailapakul, O. “Electroanalysis of chloramphenicol at reduction potential using boron-doped diamond thin film electrode applied to a flow injection system” *The 11th International Meeting on Chemical Sensors* , 16-19 July **2006**, University of Brescia, Brescia, Italy.
6. Chailapakul, O. “Boron-Doped Diamond Electrode and its Application to Flow based electroanalysis” 21st Century COE KEIO-LCC International Symposium (*The 9h International Mini-symposium on Diamond Electrochemistry and related Topics*) , 9-10 March **2007**, Keio University Japan.

หนังสือ

1. Chailapakul, O.; Tryk, D. A. and Fujishima, A. In Diamond Electrochemistry Fujishima, A; Einaga. Y.; Rao, T. N. and Tryk, D. A., Ed.; BKC, Tokyo, Japan, 2005, chapter 15, *p 321*
2. Siangproh, W.; Tryk, D. A.; Chailapakul, O. In Recent Advances in Analytical Electrochemistry 2007, Kenneth I. Ozoemena., Ed.; Transworld Research Network: kerala, India, 2007, chapter 6, p.167

Available online at www.sciencedirect.com
SCIENCE DIRECT®
Talanta 64 (2004) 1183–1188
Talanta
www.elsevier.com/locate/talanta

A flow injection method for the analysis of tetracycline antibiotics in pharmaceutical formulations using electrochemical detection at anodized boron-doped diamond thin film electrode

N. Wangfuengkanagul, W. Siangproh, O. Chailapakul*

Department of Chemistry, Faculty of Science, Chulalongkorn University, 254 Phyathai Road, Patumwan, Bangkok 10330, Thailand

Received 1 March 2004; received in revised form 26 April 2004; accepted 26 April 2004
Available online 23 August 2004

Abstract

A method using flow injection (FI) with amperometric detection at anodized boron-doped diamond (BDD) thin films has been developed and applied for the determination of tetracycline antibiotics (tetracycline, chlortetracycline, oxytetracycline and doxycycline). The electrochemical oxidation of the tetracycline antibiotics was studied at various carbon electrodes including glassy carbon (GC), as-deposited BDD and anodized BDD electrodes using cyclic voltammetry. The anodized BDD electrode exhibited well-defined irreversible cyclic voltammograms for the oxidation of tetracycline antibiotics with the highest current signals compared to the as-deposited BDD and glassy carbon electrodes. Low detection limit of 10 nM (signal-to-noise ratio = 3) was achieved for each drug when using flow injection analysis with amperometric detection at anodized BDD electrodes. Linear calibrations were obtained from 0.1 to 50 mM for tetracycline and 0.5–50 mM for chlortetracycline, oxytetracycline and doxycycline. The proposed method has been successfully applied to determine the tetracycline antibiotics in some drug formulations. The results obtained in percent found (99.50–103.01%) were comparable to dose labeled.

Keywords: Tetracycline; Chlortetracycline; Oxytetracycline; Doxycylcine; Flow injection system; Anodized boron-doped diamond thin film electrode

1. Introduction

Tetracyclines are broad spectrum antibiotics for their high activity against nearly all gram-positive and gram-negative bacteria. Tetracycline, chlortetracycline, oxytetracycline and doxycycline are commonly used in food protection animals (including honeybee), because of their board spectrum activity and low production cost. However, tetracycline residues in milk or meat are also toxic and can cause allergic reactions in some hypersensitive individuals in human. Owing to their extensive use in infectious diseases therapy, there have been several analytical methods available for these compounds in pharmaceutical preparations, biological samples and milk samples. Official methods such as microbiological-based techniques can also provide both qualitative and quantitative analysis for tetracyclines [1–3]. These methods have characteristic disadvantages: microbiological tests are not only time consuming, laborious and expensive but also poor in term of sensitivity and selectivity. There are also some batch procedures which employ spectrophotometry [4,5], chemiluminescence [6–9], spectrofluorimetry [10], and electrochemical method [11].

Flow injection (FI) is a well-known tool that offers improvement in most batch methods, especially the high sample throughput. For the tetracyclines, there are some FI methods available with all types of detection such as spectrophotometry [12,13], chemiluminescence [14,15] and electrochemical method [16–18]. The spectrophotometric FI method detections [12,13] for tetracyclines are based on the formation of a color product by their reaction with 4-aminophenazone and hexacyanoferrate(III). However, this method has a limited concentration range. Under the optimized conditions, tetracyclines were determined in the ranges of 1–20 and 20–250 mg L^{-1}. The lowest limit of detection is 0.2 mg L^{-1} for doxycycline [12]. For the chemiluminescence method [14], a highly toxic and expensive agent,

* Corresponding author. Tel.: +66 2 218 7615; fax: +66 2 254 1309.
E-mail address: corawon@chula.ac.th (O. Chailapakul).

0039-9140/$ – see front matter © 2004 Elsevier B.V. All rights reserved.
doi:10.1016/j.talanta.2004.04.032

N-bromosuccinimide is used. The reported working range are 0.05–3.00 mg L^{-1} for tetracycline, 0.50–5.00 mg L^{-1} for oxytetracycline and 0.50–7.00 mg L^{-1} for doxycycline and chlortetracycline.

Electrochemical techniques such as amperometric and potentiometric detection are good alternative methods that are widely used in pharmaceutical applications. The techniques are usually easy to operate, fast and inexpensive. The sensitivity of electrochemical methods is often greater than the spectrophotometric method. For example, the detection limits using HPLC amperometric detection varied from 0.1 to 1 mg L^{-1} for tetracycline family [19].

Procedures in electroanalysis strongly depend on working electrode materials, so the searching and development of new electrode material is necessary. Boron-doped diamond (BDD) thin film electrodes have been emerged as new electrode material in the many fields in electrochemistry, especially in electroanalysis applications [20–29]. The most importance electrochemical properties are: (i) the wide working potential window in aqueous and non-aqueous media; (ii) a stable and low background current, leading to improved signal-to-background and signal-to-noise ratios; (iii) slight adsorption of polar molecules and long term stability of the response, leading to improved resistance to electrode deactivation and fouling. Recently, a diamond electrode has been chemically pretreated by electrochemical oxidation [30–32]. The anodized diamond electrodes retain the excellent properties of the as-deposited diamond electrode even though, the electrode surface of anodized diamond electrode is applied by a high anodic potential. Anodized diamond electrodes are suitable for determination of various analytes such as chlorophenol [30], dopamine and uric acid in the presence of ascorbic acid [31] and homocysteine [32]. These anodized electrodes have exhibited some attractive properties such as excellent stability and high reproducibility. In this present work, the anodized diamond electrode was used for the electrochemical determination of tetracyclines using cyclic voltammetry. Glassy carbon (GC) and as-deposited diamond electrodes were also used for comparison. The anodized diamond electrode was exploited as working electrode for amperometric determination of antibiotic drugs, using flow injection system.

2. Experimental

2.1. Chemicals and reagents

All reagents were analytical reagent grade. All solutions were prepared in ultrapure water. Standards (hydrochloric forms) of tetracycline, chlortetracycline, oxytetracycline and doxycycline were supplied by Sigma Chemical (USA). Potassium dihydrogen phosphate (BDH), disodium hydrogen phosphate, sodium hydroxide (Merck) and phosphoric acid 85% (J.T. Baker) were used to prepare the buffer solution. Phosphate buffer (0.1 M) solutions with pH ranges from 5.0 to 8.0, were prepared by dissolving the appropriate amounts of potassium dihydrogen phosphate and disodium hydrogen phosphate. Phosphoric acid and sodium hydroxide were used to adjust the desired pH that is out of the above range.

The standard tetracycline antibiotics were prepared by dissolving an appropriate amount of the tetracycline antibiotics in the buffer solution. The solutions were prepared daily.

2.2. Electrodes

The as-deposited BDD electrodes used in this work are from Professor Akira Fujishima' s Laboratory. The electrodes were prepared by deposition of the BDD thin films on highly conductive *n*-Si(1 1 1) substrate using the technique of microwave plasma-assisted chemical vapor deposition. Deposition was usually carried out for 10 h to achieve a film thickness of approximately 30 μm. The nominal B/C atomic ratio in the gas phase was 1:100, and the typical boron-doped level in the film was ca. 10^{21} cm^{-3}. The experimental conditions and the apparatus used for the diamond film growth have been described in detail elsewhere [23]. A piece of diamond was rinsed with ultrapure water prior to use for electroanalysis.

Anodized BDD electrode was prepared by treating an as-deposited BDD electrode in 0.1 M KOH solution. The potential was applied between 0 and 2.2 V versus Ag/AgCl using cyclic voltammetry for 30 min. The anodized BDD electrode was also rinsed with ultrapure water before use.

The GC electrode was purchased from Bioanalytical System, Inc. (area 0.07 cm^2). It was pretreated by sequential polishing with 1 and 0.05 μm of alumina/water slurries on felt pads, followed by rinsing with ultrapure water prior to use.

2.3. Cyclic voltammetric investigation

Electrochemical experiments were conducted out in a single compartment three-electrode glass cell. The BDD electrode was pressed against a smooth ground joint at the bottom of the cell, isolated by an *O*-ring vitron (area 0.07 cm^2). Ohmic contact was made by placing the backside of the Si substrate. The GC carbon was used as working electrode for the comparison. The Ag/AgCl with salt bridge and Pt wire were used as reference electrode and counter electrode respectively. The voltammetric measurement was performed with the three types of electrodes using Autolab Potentiostat 100 (Eco-Chemie, The Netherlands).

2.4. Flow injection with amperometric detection

The flow injection system consisted of a thin layer flow cell (Bioanalytical System, Inc), a 20 mL stainless steel loop of injection port (Rheodyne 7725), a peristaltic pump, and

electrochemical detection (Autolab potentiastat 100). The carrier solution (0.1 M potassium dihydrogen phosphate pH 2) was regulated at the flow rate of 1 mL min^{-1} by measuring the volume of carrier solution in 1 min. The thin layer flow cell consisted of a silicone rubber gasket as a spacer, a Ag/AgCl electrode as the reference electrode and a stainless steel tube as an auxiliary electrode and an outlet of the flow cell. The experiments were performed in a copper faradaic cage to reduce the electronic noise. All experiments were done at room temperature.

2.5. Sample preparation

The contents within the pharmaceutical capsule (as described on the label) were: 250 mg tetracycline hydrochloride™ (Tetracycline hydrochloride); 250 mg Aureomycin™ (chlortetracycline); 250 mg Oxycline™ (oxytetracycline); 100 mg Medomycin™ (doxycycline). The powder of twenty capsules of each drug was accurately weighed and homogenized so as to obtain the mean capsule weight. A portion of the homogenized powder corresponding to the mean capsule weight was then transferred into volumetric flask and dissolved in 0.1 M phosphate buffer (pH 2), and then mixed thoroughly. A portion of the sample solutions was filtrated through 0.45 mm nylon membrane. The filtrated solutions were further diluted using 0.1 M phosphate buffer (pH 2) to make the final concentration in the range of 0.96–5.15 mg mL^{-1} within the linear dynamic range. All tetracycline antibiotic solutions were protected from light by covering with aluminum foil and stored at 4 °C.

3. Results and discussion

3.1. Cyclic voltammetry

3.1.1. Voltammetric study

According to Fig. 1, the anodized BDD electrode (Fig. 1c) provided well-resolved irreversible oxidation cyclic voltammogram with the highest current responses in comparison to the as-deposited BDD and the glassy carbon electrodes, Fig. 1a and b respectively. These electrodes produced oxidative waves at +1.0 V versus Ag/AgCl, however the as-deposited BDD electrode produced no voltammetric peak shape in contrast to the results at the anodized BDD electrode. The results obtained from the other antibiotics, i.e., chlortetracycline, oxytetracycline and doxycycline were analogous to the results shown for tetracycline in Fig. 1. These results can be rationalized as follows. The surface of the BDD, after the anodizing treatment, is partly covered with oxygen atoms [30–32]. In acidic condition, all the tetracycline are positively charged. This therefore encourage electrostatic interaction between the negatively charged BDD anodized surface and the analytes. In contrast, the as-deposited BDD, the surface is non-polar (covered with hydrogen atoms), and therefore the electrostatic interaction

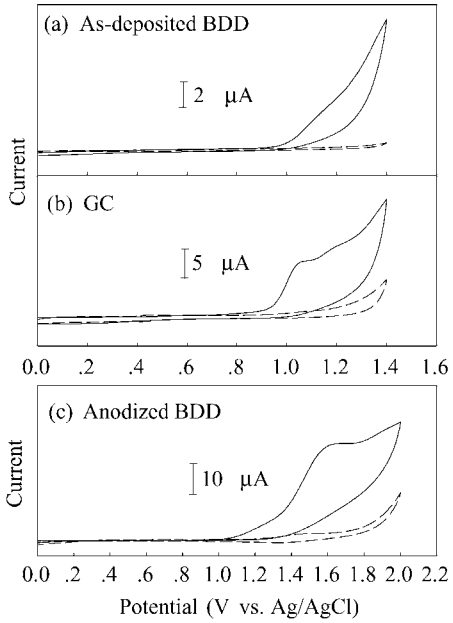

Fig. 1. Cyclic voltammetric results of 500 μM tetracycline (solid line) in 0.1 M potassium dihydrogen phosphate (pH 2) with the corresponding background current (dashed line) at: (a) as-deposited BDD; (b) glassy carbon; and (c) anodized BDD electrodes.

is less permitted. This may be the reason for the ill-defined peak current, in Fig. 1a, for example.

3.1.2. pH dependence

The effect of pH was investigated from pH 2–9 for all four compounds using anodized BDD electrode. A plot of pH versus Ep has been investigated. It was found that results were ambiguous, and the expected pK was inconsistant with the pK value of the dissociation in the literature.

For quantitative purposes, the information concerning about the current response was also investigated. It was found that in acidic buffer, tetracyclines provided the well-defined oxidative responses cyclic voltammograms. However, in neutral and alkaline buffer, ill-defined voltammetric waves were obtained. The current response decreased with increasing the pH. Results for all, the antibiotics demonstrated that pH 2 gave the highest current signal (Fig. 2). Therefore, pH 2 was chosen as the optimal pH for the rest of experiments.

It can be explained that tetracyclines are derived from a system of four membered rings arranged linearly with characteristic double bonds. They are amphoteric compounds with high polarity, and an isoelectric point between 4 and 6. From the literature [33,34], three dissociations have been observed for tetracyclines, with $pK_1 = 3.3$, $pK_2 = 7.5$ and $pK_3 = 9.4$. In strongly acidic pH, the tetracycline molecule exists in its fully protonated form as a singly charged cation. As proposed [30–32], the surface of anodized BDD electrode covered with the negative charge, electrostatically attracts the positive tetracycline. Hence, at pH 2 the positively charged tetracycline provided the highest response.

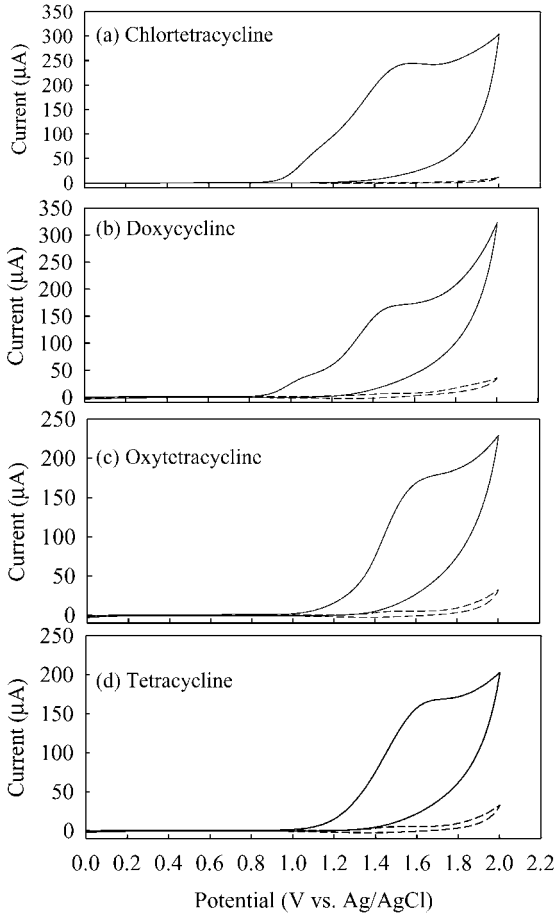

Fig. 2. Cyclic voltammograms at anodized BDD electrode vs. Ag/AgCl in 500 μM chlortetracycline, doxycycline, oxytetracycline, and tetracycline in 0.1 M phosphate buffer pH 2 (solid lines) and 0.1 M phosphate buffer pH 2 (dashed lines). The scan rate was 50 mV s^{-1}; area of electrode, 0.07 cm^2.

Moreover, the anodized diamond surface can be recovered by in situ reactivation (applying a high positive potential 2.6 V versus Ag/AgCl) during the flow injection measurement [30].

3.1.3. Scan rate dependence

The scan rate dependence study was carried out by varying the scan rate ranging from 0.01 to 0.3 V s^{-1}. From the result, we found for all four compounds, that the relationship between current and square root of scan rate was linear with the correlation coefficient of approximately 0.99 (data not shown). The results indicated that the oxidation currents are controlled by the diffusion of tetracyclines in the interfacial reaction zone.

3.2. Flow injection with amperometric detection

3.2.1. Hydrodynamic voltammetry

Hydrodynamic voltammogram was obtained from the average of three injections at aliquot of 20 μL of 100 mM tetracycline antibiotic solutions in the flow injection system. In this case the applied potential was gradually increased from 1.1 to 2.0 V versus Ag/AgCl. The carrier solution was 0.1 M potassium dihydrogen phosphates (pH 2). Fig. 3a shows the hydrodynamic voltammogram of tetracycline antibiotics with the corresponding background currents. The hydrodynamic voltammogram of tetracycline antibiotics did not exhibit the sigmoidal shape of the signal versus potential probably due to the high oxidation potential of tetracycline. To obtain the optimum potential, we calculated the S/B ratios from the results in Fig. 3a at each potential and plotted the ratios versus potentials (Fig. 3b). The maximum S/B ratio was found at 1.5 V (versus Ag/AgCl) for chlortetracycline and at 1.6 V (versus Ag/AgCl) for tetracycline, oxytetracycline and doxycycline. Hence, these optimum potentials were used for the quantification experiments in amperometric flow injection.

3.2.2. Analytical performance of the FI system at anodized BDD electrode

A series of analytical features were performed on the proposed method for the quantification of tetracycline, chlortetracycline, oxytetracycline and doxycycline. Calibration parameters and the linear ranges for all the drugs are summarized in Table 1. The limit of detection (3S/N) was 10 nM for all compounds. To obtain the repeatability, 10 replicates of injections were carried out at three concentrations (5, 10, 50 mM). The peak variability defined as the relative standard deviation (R.S.D. %), were found to be 1.3–1.7 (for tetracycline hydrochloride), 2.4–3.0 for chlortetracycline, 1.6–3.0

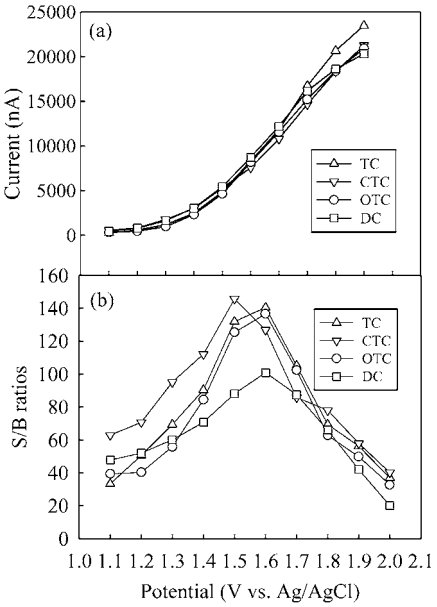

Fig. 3. Hydrodynamic voltammetric results for 100 μM tetracycline antibiotics. (a) (△): tetracycline, TC; (▽): chlortetracycline, CTC; (○): oxytetracycline, OTC; and (□): doxycycline, DC in 0.1 M potassium dihydrogen phosphate (pH 2), using 0.1 M potassium dihydrogen phosphate (pH 2) as carrier solution. The flow rate was 1 mL min^{-1}. (b) Hydrodynamic voltammogram of signal-to-background ratios.

Table 1
Regression parameters and linear range for the determination of tetracycline antibiotics by flow injection with amperometric detection using anodized boron-doped diamond electrode ($n = 2$)

Analytes	Linear range (μM)	a	b	r^2
Tetracycline	0.1–50	110.0 ± 5.9	192.1 ± 5.0	0.997
Chlotetracycine	0.5–50	76.9 ± 3.9	199.7 ± 29.7	0.997
Oxytetracycline	0.5–50	90.2 ± 3.0	165.2 ± 28.9	0.999
Doxytetracycline	0.5–50	96.2 ± 3.8	213.7 ± 48.9	0.997

$ay = ax + b$, where y: current (nA); x: concentration (μM); a: slope (nA/μM); b: intercept (nA).

Table 2
Determination of tetracycline antibiotics in drug formulations ($n = 2$)

Drug formulations	Label amount (mg)	Found (mg)	Found (%)
Tetracycline	250	249.4 ± 1.7	99.8 ± 0.7
Aureomycine	250	249.7 ± 1.3	99.87 ± 0.5
Oxycline	250	254.6 ± 2.5	101.85 ± 1.0
Medeomycin	100	98.4 ± 1.0	98.4 ± 1.0

for oxytetracycline and 1.7–2.7 for doxycycline. The stability of the amperometric response using flow injection at the anodized BDD electrode was obtained by conducting 100 repetitive injections of 50 mM chlortetracycline. It was observed that the peak variation was about 3.4%. The throughput of sample is approximately seventy injections per hour.

3.2.3. Application

Our method was applied for determination of each compound in four drug formulations using the standard addition method. The results are presented in Table 2. The percentages of recovery indicate that the amounts are comparable between the labeled quantity and the value obtained from the proposed method.

4. Conclusion

Anodized treatment has significantly improved the analytical performance of the BDD thin film for the analysis of tetracycline drugs. Current signal of the anodized BDD electrode is greater than the current signal of the glassy carbon electrode. It was observed from the cyclic voltammetric study that pH strongly influenced the current response of the voltammograms with pH 2 being selected for the method development, since the highest current was obtained with a well-defined voltammetric signal.

Amperometric detections of four compounds, i.e., tetracycline, chlortetracycline, oxytetracycline and doxycycline was employed in the method development, using flow injection. The developed method has been successfully applied to determine four types of tetracyclines in various pharmaceutical formulations. The tetracycline antibiotics content of the drug was found to be in excellent agreement with the declared amount on the label.

Acknowledgements

This research was supported by the Thailand Research Fund through the Royal Golden Jubilee Ph.D. Program (Grant No. PHD/0209/2544) and Methee Vijai Grant, the Ratchadaphisek Somphot Endowment Grant and TJTTP-OECF. Special thanks are extended to Professor A. Fujishima (The University of Tokyo) for the BDD electrodes used in this research. The authors also would like to thank Dr. Nathan Lawrence (New Mexico State University) for editing the manuscript.

References

[1] The United Pharmacopoeia, 21st revision, Easton PA, Mack Printing Company, USP XXI, 1985
[2] The British Pharmacopeia, HMSO, London, 1988
[3] J. Kurittu, S. Lonnberg, M. Virta, M. Karp, J. Agric. Food. Chem. 48 (2000) 3372.
[4] K.M. Emara, H.F. Askal, G.A. Saleh, Talanta 38 (1991) 1219.
[5] U. Saha, A.K. Sen, T.K. Das, S.K. Bhowal, Talanta 37 (1990) 1193.
[6] X.R. Zhang, W.R.G. Baeyens, A. Vandenborre, G. Vanderweken, A.C. Calokerinos, S.G. Schulman, Analyst 120 (1995) 463.
[7] H. Han, Z. He, Y. Zeng, Anal. Sci. 15 (1999) 467.
[8] S. Marczynski, Biopolymers 57 (2000) 365.
[9] A. Pena, L.P. Palilis, C.M. Lino, M.I. Silveira, A.C. Calokerinos, Anal. Chim. Acta 405 (2000) 51.
[10] S. Croubels, C.V. Peteghem, W. Baeyens, Analyst 119 (1994) 2713.
[11] S. Sabhawal, K. Kishore, P.N. Moorthy, J. Pharm. Sci. 77 (1988) 78.
[12] R. Karlicek, P. Solich, Anal. Chim. Acta 285 (1994) 9.
[13] S.M. Sultan, F.E.O. Suliman, S.O. Duffuaa, I.I. Abu-Abdoun, Analyst 117 (1992) 1179.
[14] S.A. Halvatzis, M.M. Timotheou-Potamia, A.C. Calokerinos, Analyst 118 (1993) 633.
[15] A.B. Syropoulos, A.C. Calokernos, Anal. Chim. Acta 255 (1991) 403.
[16] C.M.C.M. Couta, J.L.F.C. Lima, M. Conceicao, B.S.M. Montenegro, S. Reis, J. Phram. Biomed. Anal. 18 (1998) 527.
[17] H. Ji, E. Wang, Analyst 113 (1988) 1541.
[18] W. Oungpipat, P. Southwellkeely, P.W. Alexander, Analyst 120 (1995) 1559.
[19] A.G. Kazemifard, D.E. Moore, J. Pharm. Biomed. Anal. 16 (1997) 689.
[20] N. Spataru, B.V. Sarada, E. Popa, D.A. Tryk, A. Fujishima, Anal. Chem. 73 (2001) 514.
[21] J. Xu, G.M. Swain, Anal. Chem. 70 (1998) 1502.
[22] M.D. Koppang, M. Witek, J. Blau, G.M. Swain, Anal. Chem. 71 (1999) 1188.
[23] B.V. Sarada, T.N. Rao, D.A. Tryk, A. Fujishima, Anal. Chem. 72 (2000) 1632.
[24] N. Wangfuengkanagul, O. Chailapakul, J. Pharm. Biomed. Anal. 28 (2002) 841.
[25] N. Wangfuengkanagul, O. Chailapakul, Talanta 58 (2002) 1213.
[26] T.N. Rao, B.V. Sarada, D.A. Tryk, A. Fujishima, J. Electroanal. Chem. 491 (2000) 175.
[27] M.C. Granger, J. Xu, J.W. Strojek, G.M. Swain, Anal. Chim. Acta 397 (1999) 145.
[28] T.A. Ivandini, B.V. Sarada, C. Terashima, T.N. Rao, D.A. Tryk, H. Ishiguro, Y. Kubota, A. Fujishima, J. Electroanal. Chem. 521 (2002) 117.

[29] T.N. Rao, B.H. Loo, B.V. Sarada, C. Terashima, A. Fujishima, Anal.Chem. 74 (2002) 1578.
[30] C. Terashima, T.N. Rao, B.V. Sarada, D.A. Tryk, A. Fujishima, Anal. Chem. 74 (2002) 895.
[31] E. Popa, Y. Kubota, D.A. Ttyk, A. Fujishima, Anal. Chem. 72 (2000) 1724.
[32] O. Chailapakul, W. Siangproh, B.V. Sarada, C. Terashima, T.N. Rao, D.A. Tyrk, A. Fujishima, Analyst 127 (2002) 1164.
[33] X. Ding, S. Mou, J. Chromtogr. A 897 (2000) 205.
[34] J.H. Knox, J. Jurand, J. Chromatogr. 186 (1979) 763.

Available online at www.sciencedirect.com
SCIENCE DIRECT®
Sensors and Actuators B 108 (2005) 627–632
SENSORS AND ACTUATORS B CHEMICAL
www.elsevier.com/locate/snb

Electroanalysis of lincomycin using boron-doped diamond thin film electrode applied to flow injection system

Kanokporn Boonsong, Suchada Chuanuwatanakul, Nattakarn Wangfuengkanagul, Orawon Chailapakul *

Department of Chemistry, Faculty of science, Chulalongkorn University, 254 Phyathai Road, Patumwan, Bangkok 10330, Thailand

Received 12 July 2004; received in revised form 20 December 2004; accepted 23 December 2004
Available online 9 February 2005

Abstract

The electroanalysis of lincomycin was investigated using boron-doped diamond thin film (BDD) electrodes. First, the electrochemistry of lincomycin was studied by cyclic voltammetry as a function of pH of the solution, scan rate and the concentration of lincomycin. Comparison experiments were carried out using glassy carbon electrode. Boron-doped diamond thin film electrode provided well-resolved oxidation irreversible cyclic voltammogram. It was found that the peak position was 1.2 V (versus Ag/AgCl reference electrode). Second, the amperometric detection with BDD electrode was coupled with the flow injection analysis for the determination of lincomycin. The linear range of 0.5–125 μM and the detection limit of 0.02 μM were obtained. The percent recovery was shown in a range of 96–103. This purposed method was also applied to a drug formulation sample. It was found that the results (293 mg mL^{-1}) were comparable to those labeled (300 mg mL^{-1}).

Keywords: Lincomycin; Boron-doped diamond thin film electrode; Cyclic voltammetry; Flow injection with amperometric detection

1. Introduction

Boron-doped diamond thin film electrode is very attractive for many potential applications due to its outstanding properties [1]. The number of researches in electroanalysis is progressively increasing every year. A great deal of properties are very low and stable voltammetric background current [2], wide potential window in aqueous electrolyte solutions (2.5–3 V) [3], slight adsorption of polar organic molecules, high resistance to deactivation and good activity toward some redox analytes without any conventional pretreatment [4].

Lincomycin is a medium spectrum antibiotic produced by *Streptomyces lincolnensis*. Lincomycin inhibits the growth mainly of Gram-positive bacteria. It is used in both human and veterinary medicine. Common impurities in lincomycin bulk drug are lincomycin B and 7-epilincomycin, which are formed during biosynthesis.

Several methods proposed for the determination of lincomycin, including microbiological assay methods [5], which have originally been used, are non-specific and less accurate. Alternative analytical methods were used for lincomycin including chemical assay, thin layer chromatography or paper chromatography, and isotachophoresis [6]. These methods also lack specificity and lincomycin cannot be differentiated from lincomycin B or 7-epilincomycin. Gas chromatographic technique has been introduced [7,8], it requires elaborate extraction and derivatization steps and is not selective for 7-epilincomycin. Liquid chromatography (LC) methods have also been described for quantitative determination of lincomycin [9,10]. One of the important limitations of LC techniques is the fact that lincomycin lacks sufficient UV absorption so a pre- or post-column derivation procedure is normally required. Therefore, these methods increase cost and complication of analysis. Electrochemical techniques are alternative methods for the lincomycin determination because they are simple, fast and low cost. The electrochemical detection of lincomycin has been reported using gold [11,12] as the working electrode. Nevertheless,

* Corresponding author. Tel.: +66 2218 7615; fax: +66 2254 1309.
E-mail address: corawon@chula.ac.th (O. Chailapakul).

0925-4005/$ – see front matter © 2005 Elsevier B.V. All rights reserved.
doi:10.1016/j.snb.2004.12.087

the severe detection conditions can damage the electrode and cause fluctuating background current and the electrode itself can be easily suffered from electrode fouling. Capillary zone electrophoresis with amperometric detection was recently described for the determination of lincomycin and lincomycin B in bulk drug and pharmaceutical formulations using copper disk [13] and copper microparticle-modified carbon fiber microarray electrodes [14]. Boron-doped diamond thin film electrodes can be used to eliminate these problems without any pretreatments because of the stable surface morphologies and the surface carbon atoms terminated by hydrogen. Thus, the BDD surface is relatively non-polar, very stable and suffers less adsorption of polar molecules, as reported by Xu et al. [4]. Because of these attractive properties, boron-doped diamond thin film was used to study several electroanalytical application [15–18].

Alternative automatic procedure based on flow injection technique has been widely suggested, since it enables reduced analysis time. Moreover, it can provide reproducible and accurate results. Flow injection with amperometric detection using a boron-doped diamond thin film electrode has been reported for the determination of some organic compounds such as histamine and serotonin [2], polyamine [19] and sulfa drugs [20].

In this propose, we report the use of the boron-doped diamond thin film electrode to study lincomycin using cyclic voltammetry compared with the glassy electrode. Hydrodynamic voltammetry and flow injection analysis with amperometric detection was also used to determine lincomycin in the standard chemical form and commercial available.

2. Experimental

2.1. Chemical and reagents

All chemicals were analytical grade and used without further purification. All solutions were prepared using deionized water. Phosphate buffers (pH 2.5–9), 0.1 M, were prepared from 0.1 M of potassium dihydrogen phosphate (Merck) and 0.1 M disodium hydrogen phosphate (BDH). Phosphate buffer (pH 2.5) was prepared from 0.1 M potassium dihydrogen phosphate and pH was adjusted with orthophosphoric acid (85%, Carlo Erba). Phosphate buffer (pH 9.0), 0.1 M, was prepared from 0.1 M of potassium dihydrogen phosphate and 0.1 M disodium hydrogen phosphate and the pH was adjusted with 0.1 M sodium hydroxide (Merck) solution.

The standard lincomycin hydrochloride (Fluka) solution was freshly prepared in 0.1 M phosphate buffer.

2.2. Electrode

The BDD electrode was grown on Si(1 0 0) substrate (obtained from Professor A. Fujishima) using microwave assisted chemical vaporization. It was rinsed with ultrapure water prior to use.

The glassy carbon (GC) electrode was purchased from Bioanalytical System, Inc. (area 0.07 cm^2). It was pretreated by sequential polishing with 1 and 0.05 μm of alumina/water slurries on felt pads, followed by rinsing with ultrapure water prior to use.

2.3. Cyclic voltammetry

Electrochemical measurements were recorded using an Autolab Potentiostat 100 (Metrohm, Switzerland) with a standard three-electrode configuration. The BDD electrode was pressed against a smooth ground joint at the bottom of the cell isolated by an O-ring (area 0.07 cm^2) and served as the working electrode. Ohmic contact was made by placing the backside of the Si substrate on a brass plate. A GC electrode was also used as a working electrode in the comparison study with the BDD electrode. A platinum wire and an Ag/AgCl electrode with a salt bridge were used as the counter and reference electrodes, respectively. Cyclic voltammetry was used to probe the electrochemical reaction. The electrochemical measurements were housed in a Faradaic cage to reduce electronic noise. All experiments were done at a room temperature.

2.4. Flow injection analysis with amperometric detection

The FIA system consisted of a thin layer flow cell (Bioanalytical System, Inc.), an injection port (Rheodyne 7725) with a 20 μL injection loop, a peristaltic pump (Ismatec), and an electrochemical detector (PG100). The carrier stream, 0.1 mol L^{-1} phosphate buffer (pH 7), was regulated by a reagent delivery module at a flow rate of 1 mL min^{-1}. A pulse dampener was used in series to reduce the pulsation introducing by the alternation of the roller of the peristaltic pump. The thin layer flow cell consisted of a silicone gasket as a spacer, Ag/AgCl as the reference electrode, stainless steel tube as an auxiliary electrode and outlet. The experiments were performed in a copper Faradaic cage to reduced electrical noise. A hydrodynamic voltammogram was obtained before the amperometric determination was performed. The peak current after each injection was recorded, together with the corresponding background current. These data were plotted as a function of applied potential to obtain hydrodynamic voltammograms. The amperometric measurements were carried out at the potential giving a maximum signal-to-background (S/B) ratio in the hydrodynamic voltammograms.

2.5. Sample preparation

A volume of 2 mL of real sample (LINCON injection) was transferred to a 100 ml volumetric flask and was diluted with 0.1 M of phosphate buffer pH 7. An aliquot of this initial solution was diluted again with appropriated volume of 0.1 M of phosphate buffer pH 7 to yield a final concentration of 6 μg mL^{-1}. In all cases it was assumed that the actual

content of the syrup corresponds to that reported by the manufacturing laboratories.

3. Results and discussion

3.1. Cyclic voltammetry

Fig. 1(a) and (b) shows typical cyclic voltammetric *i–E* curves for 0.1 M of lincomycin with the corresponding background voltammogram of 0.1 M phosphate buffer (pH 7) at BDD and GC electrodes. Both of the BDD and GC electrodes exhibited well-defined peak currents, however the BDD electrode gave well-resolved irreversible peak and higher current signal than the one obtained from using glassy carbon electrode at the same electrode area.

3.1.1. pH effect

The effect of the buffer pH was investigated from pH 2.5 to 9. At buffer between pH 7 and 9 changing of buffer pH effects the oxidation peak potential. It was found that increasing the buffer pH, decrease the oxidation peak potential, probably due to the more facile oxidation of the thiol group of lincomycin in the alkaline medium. In addition the buffer also affected the peak current of the cyclic voltammogram. At the BDD electrode, lincomycin provides the highest S/B in phosphate buffer at pH 7. Therefore, we used this pH for the next experiments.

3.1.2. Scan rate dependence study

Fig. 2 shows the cyclic voltammetric response of 1 mM lincomycin in 0.1 M phosphate buffer pH 7 with variation of the scan rate from 0.02 to 0.3 V s^{-1} at the BDD electrode. The oxidation current varies highly linearity ($r > 0.99$) with the square root of the scan rate, $\nu^{1/2}$, as shown in the inset of this figure. The results indicate that the electrochemical reaction is a diffusion controlled process.

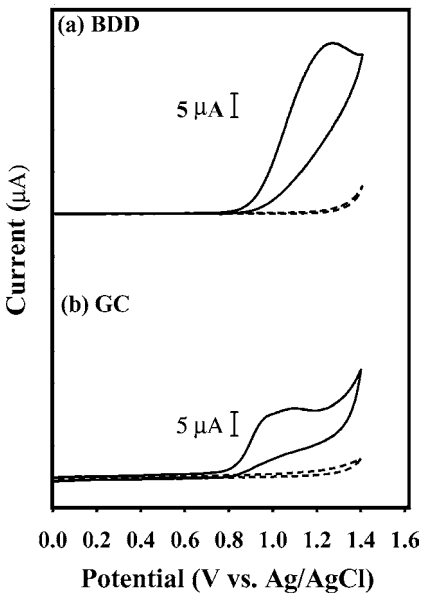

Fig. 1. Cyclic voltammograms for 1 mM lincomycin in 0.1 M phosphate buffer pH 7 (a) at boron-doped diamond thin film and (b) GC electrodes (solid line). Background voltammograms were also shown in this figure (dash line) (scan rate 50 mV s^{-1}).

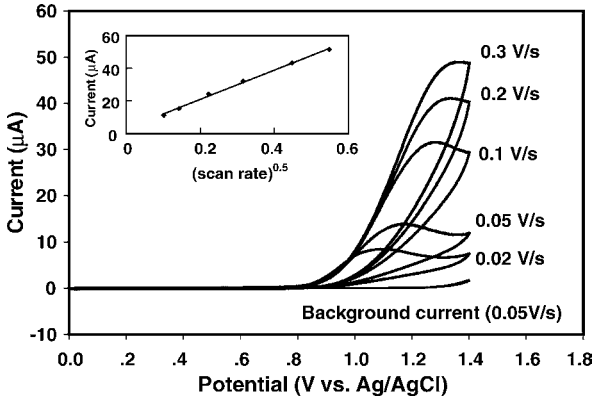

Fig. 2. Cyclic voltammogram for 1 mM lincomycin in 0.1 M phosphate buffer (pH 7) at BDD electrode for a series of sweep rates; area of electrode, 0.07 cm^2. The dependence between peak current (μA) and square root of sweep rate appears in the inset.

3.1.3. Concentration dependence study

The oxidation peak current was measured at the BDD electrode for the lincomycin concentration range from 0.01 to 10 mM in 0.1 M phosphate buffer (pH 7) at sweep rate 50 mV s^{-1}. Based on a series from 0.02 to 0.63 mM, a linear regression statistical analysis of peak current (μA) versus concentration (mM) was obtained, linearly proportional in the range 0.02–0.63 mM ($r > 0.99$, data shown in Fig. 3) The GC electrode provides no linear regression relationship between the oxidation current and the concentration. This may be due to the electrode fouling. At a concentration as low as 0.04 mM and above, a well defined peak with the S/B ratios > 3 was

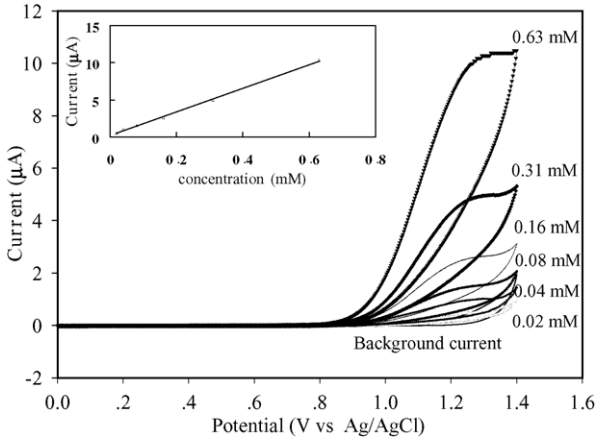

Fig. 3. Cyclic voltammogram for lincomycin in 0.1 M phosphate buffer (pH 7) at BDD electrode for a series of lincomycin concentrations. The sweep rate was 50 mV s^{-1}; area electrode, 0.07 cm^2. The dependence between peak current (μA) and concentration at the sweep rate of 50 mV s^{-1} appears in the inset.

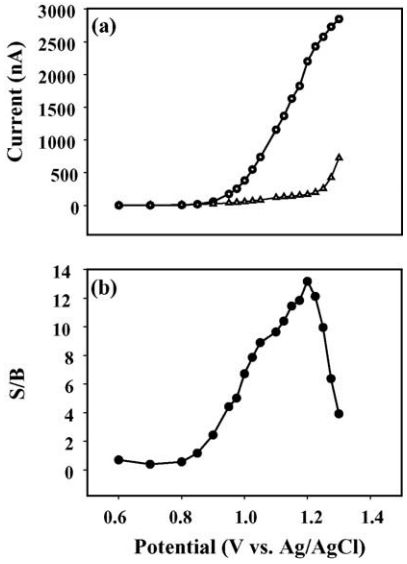

Fig. 4. (a) Hydrodynamic voltammogram of (-△-) 0.1 M phosphate buffer (pH 7, background current) and (-◯-) 0.1 mM of lincomycin in 0.1 M phosphate buffer (pH 7) with four injections of analysis, using 0.1 M phosphate buffer (pH 7) as a carrier solution. (b) Hydrodynamic of signal-to-background ratio. The flow rate was 1 ml min^{-1}.

obtained at the BDD electrode while the GC electrode provided this S/B value at the concentration of 0.5 mM due to its high background current.

3.2. Flow injection with amperometric detection

3.2.1. Hydrodynamic voltammetry

To obtain the optimal potential for amperometric detection in flow injection analysis, the hydrodynamic behavior of lincomycin was studied. Fig. 4 shows a hydrodynamic voltammetric *i–E* curve obtained at the BDD electrode for 20 μL injections of 0.1 mM lincomycin in 0.1 M phosphate buffer (pH 7) as the carrier solutions. Each datum represents the average of four injections. The absolute magnitude of the background current at each potential is also shown for comparison. The S/B ratios were calculated from the Fig. 4(a) at each potential to obtain the maximum potential point. Therefore, the hydrodynamic voltammetric S/B ratios versus potential curve are shown in Fig. 4(b) with the maximum S/B ratio at 1.2 V. Hence, this potential was set as the amperometric potential detection in flow injection analysis experiments. Therefore, this potential was selected for quantitative amperometric detection in flow injection analysis experiments.

3.2.2. Linear range, detection limit and reproducibility

Fig. 5 shows a series of repetitive 20 μL injection of lincomycin in 0.1 M phosphate buffer pH 7 at the detection potential of 1.2 V versus Ag/AgCl. Well-defined signals without peak tailing were obtained at all concentration from 10 nM to 2.5 mM. The current signal increased linearly with the increasing of concentration from 0.5 to 125 μM. The

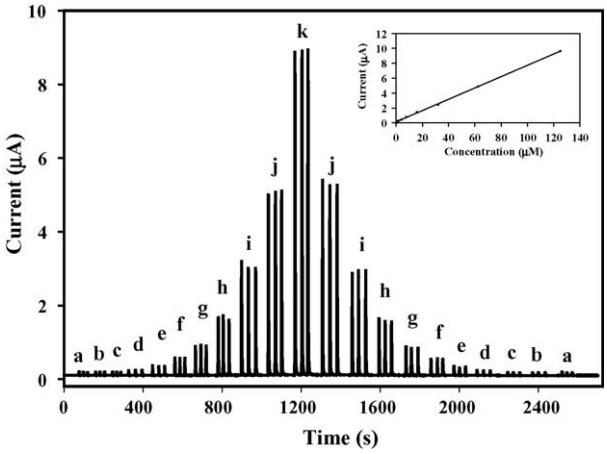

Fig. 5. Flow injection with amperometric detection results for various concentrations of lincomycin in 0.1 M phosphate buffer pH 7 (a) 0.25 μM, (b) 0.5 μM, (c) 1.0 μM, (d) 2.0 μM, (e) 4.0 μM, (f) 8.0 μM, (g) 16 μM, (h) 32 μM, (i) 62.5 μM, (j) 125 μM. Inset is the standard lincomycin calibration graph.

sensitivity of this method, which is the slope of the relation plot between the current and the concentration over the linear range, was 61.1–82.5 nA μM^{-1}. Interesting, the detection limit with S/N > 3 were obtained at the concentration as low as 20 nM of lincomycin. The reproducibility of the response was also examined. A peak variability of 2.04% was found during a course of 50 injections of 100 μM lincomycin, indicating the high stability of the BDD electrode.

3.3. Quantitative determination of lincomycin

Lincomycin in pharmaceuticals sample (LINCON injection) was determined using BDD electrode by the method of the calibration curve. The results were obtained were shown in Fig. 6. Linear least square calibration curve provided a slope of 95.4 nA μM^{-1} (sensitivity) and correlation coefficient of 0.9998. Accuracy and recovery were obtained from using real sample of lincomycin solution and standard addition method. Three concentrations of added solution (0, 1.25, 2.50 μg mL^{-1}) were chosen. Results obtain from 10 injections gave 1.2–2.0% of relative standard deviation (R.S.D.). The recoveries of the added lincomycin are summarized in Table 1. Relative error compared with the claimed amount was lower than 4%.

Table 1
Recovery of lincomycin sample with amperometric detection using diamond electrode applied to flow injection system ($n = 2$)

Amount of lincomycin sample added (mg mL^{-1})	Amount of lincomycin sample found (mg mL^{-1})	Percent of recovery (%)
1.25	1.21 ± 0.02	96.32 ± 2.4
2.50	2.58 ± 0.02	103.1 ± 3.3

Table 2
Comparison of electroanalytical data for determination of lincomycin

Method	Electrode	Linear dynamic range (μmol L^{-1})	Detection limit (μmol L^{-1})	Precision (%R.S.D.)	Ref.
Capillary electrophoresis	Carbon fiber microdisk array electrode	40–2000	6.7	5.9	[14]
Liquid chromatography with pulsed electrochemical detection	Gold electrode	0.3–1.9	–	1.1	[11]
Amperometry applied to flow injection analysis	Diamond thin film electrode	0.5–125	0.02	1.2	[a]

(–) No report.
[a] This proposed method.

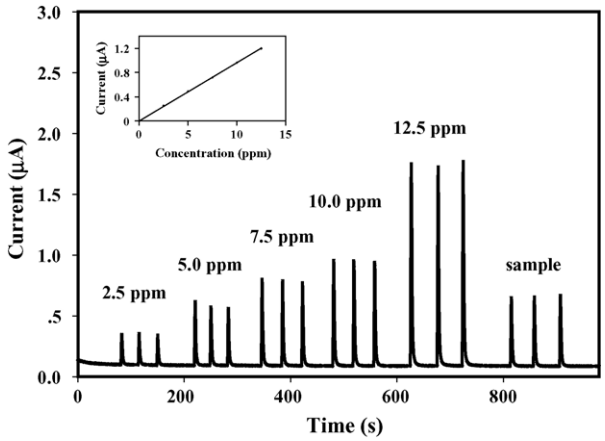

Fig. 6. Flow injection with amperometric detection results for lincomycin hydrochloride standard solution and lincomycin hydrochloride in commercially available solutions and calibration graph at the applied potential of 1.2 V vs. Ag/AgCl in 0.1 M phosphate buffer (pH 7).

3.4. Comparison with other methods

Table 2 summarizes the electroanalytical method for lincomycin from this study compared with other methods. It can be observed that using the BDD electrode with flow injection with amperometric detection provides a significant low detection limit (20 nM), high sensitivity and reproducible response without pretreatment or modification of the electrode, there is no fouling at the BDD electrode and the background current is also very low. Moreover the use of the BDD electrode applied to flow injection with amperometric detection is simple, rapid, and provides high sample throughput.

4. Conclusions

This is the first use of BDD thin film electrodes for the electroanalysis of lincomycin. It was found that the BDD electrodes exhibited excellent performance for the oxidative detection of lincomycin. Well-defined voltammograms were obtained at the BDD electrode, which exhibited high sensitivity, and demonstrated significant advantage over the GC electrode. The use of BDD electrode is simple because no chemical modification is required. Cleaning of the electrode is also not necessary due to the long-term stability of the BDD electrode response. Flow injection analysis with amperometric detection using BDD electrode provides a linear range from 0.25 to 125 μM and remarkably low detection limit (20 nM). The results indicate that lincomycin can be detected amperometrically without derivatization or use of a pulse waveform. BDD electrode is able to achieve a highly stable and sensitive response. Detection of lincomycin in commercially available solution forms shows that this method is precise, accurate, and very sensitive.

Acknowledgements

Acknowledgment is made to the Thailand Research Fund and the Ratchadaphisek Somphot Grant for the financial support.

References

[1] J. Xu, M.C. Granger, Q. Chen, J.W. Strojek, T.E. Lister, G.M. Swain, Boron-doped diamond thin-film electrode, Anal. Chem. 69 (1997) 591A–597A.
[2] B.V. Sarada, T.N. Rao, D.A. Tryk, A. Fujishima, Electrochemical oxidation of histamine and serotonin at highly boron-doped diamond electrodes, Anal. Chem. 72 (2000) 1632–1638.
[3] G.M. Swain, R. Ramesham, The electrochemical activity of boron-doped polycrystalline diamond thin-film electrodes, Anal. Chem. 65 (1993) 345–351.
[4] J. Xu, Q. Chen, G.M. Swain, Anthraquinonedisulfonate electrochemistry: a comparison of glassy carbon, hydrogenated glassy carbon, highly oriented pyrolytic graphite, and diamond electrodes, Anal. Chem. 70 (1998) 3146–3154.
[5] A.R. Barbiers, A.W. Neff, Screening and confirmatory methods for determining lincomycin residues in animal tissues, J. Assoc. Off. Anal. Chem. 59 (1976) 849–854.
[6] H. Klein, R. Teichmann, Isotachophoretic assay of aminoglycosides and lincomycins in pharmaceuticals, J. Chromatogr. 250 (1978) 152–156.
[7] W. Luo, B. Yin, C.Y.W. Ang, L. Rushing, H.C. Thompson Jr., Determination of lincomycin residues in salmon tissues by gas chromtography with nitrogen–phosphorus detection, J. Chromatogr. B 687 (1996) 405–411.
[8] M. Margosis, Analysis of antibiotics by gas chromatography: I. Lincomycin, J. Chromatogr. A 37 (1968) 46–54.
[9] J.A. Orwa, F. Bosmans, S. Depuydt, E. Roets, J. Hoogmartens, Liquid chromatographic method for separation of lincomycin from its related substances, J. Chromatogr. A 829 (1998) 161–166.
[10] P.A. Asmus, J.B. Landis, C.L. Vila, Liquid chromatographic determination of lincomycin in fermentation beers, J. Chromatogr. A 264 (1983) 241–248.

[11] J. Szunyog, E. Adams, K. Liekens, E. Roets, J. Hoogmartens, Analysis of a formulation containing lincomycin and spectinomycin by liquid chromatography with pulsed electrochemical detection, J. Pharm. Biomed. Anal. 29 (2002) 213–220.
[12] W.R. LaCourse, C.O. Dasenbrock, Pulsed electrochemical detection of sulfur- containing antibiotics following high performance liquid chromatography, J. Pharm. Biomed. Anal. 19 (1999) 239–252.
[13] F. Xiaoming, L. Xialfeng, Y. Jiannong, F. Yuzhi, Determination of lincomycin and lincomycin B in bulk drug and pharmaceutical formulations by capillary zone electrophoresis with amperometric detection, Anal. Lett. 29 (1996) 1975–1984.
[14] W.C. Yang, A.M. Yu, H.Y. Chen, Applications of a copper microparticle-modified carbon fiber microdisk array electrode for the simultaneous determination of aminoglycoside antibiotics by capillary electrophoresis, J. Chromatogr. A 905 (2001) 309–318.
[15] O. Chailapakul, E. Popa, H. Tai, B.V. Sarada, D.A. Tryk, A. Fujishima, The electrooxidation of organic acids at boron-doped diamond electrodes, Electrochem. Commun. 2 (2000) 422–426.
[16] O. Chailapakul, P. Aksaharanandana, T. Frelink, Y. Einaga, A. Fujishima, The electrooxidation of sulfur-containing compounds at boron-doped diamond electrode, Sens. Actuat. B 80 (2001) 193–201.
[17] T.N. Rao, I. Yagi, T. Miwa, D.A. Tryk, A. Fujishima, Electrochemical oxidation of NADH at highly boron-doped diamond electrodes, Anal. Chem. 71 (1999) 2506–2511.
[18] T. Yano, D.A. Tryk, K. Hashimoto, A. Fujishima, Electrochemical behavior of highly conductive boron-doped diamond electrodes for oxygen reduction in alkaline solution, J. Electrochem. Soc. 145 (1998) 1870–1876.
[19] M.D. Koppang, M. Witek, J. Blau, G.M. Swain, Electrochemical oxidation of polyamines at diamond thin-film electrodes, Anal. Chem. 71 (1999) 1188–1195.
[20] T.N. Rao, B.V. Sarada, D.A. Tryk, A. Fujishima, Electroanalytical study of sulfa drugs at diamond electrodes and their determination by HPLC with amperometric detection, J. Electroanal. Chem. 491 (2000) 175–181.

Biographies

Kanokporn Boonsong received her BSc in Analytical Chemistry from Rajamangala Institute of Technology in 1999. She has been a Lecturer at Rajamangala Institute of Technology since 1999. Now, she is a doctoral course student of the Department of Chemistry, Chulalongkorn University.

Suchada Chuanuwatanakul received her BSc and MSc degrees in Analytical Chemistry from Chulalongkorn University, Thailand, in 1978 and 1981, respectively. She is currently an Assistant Professor at the Department of Chemistry, Faculty of Science, Chulalongkorn University, Thailand. Her research activity is focused on diamond sensors and food chemistry.

Nattakarn Wangfuengkanagul received her BSc in industrial chemistry in 1999 from King Mongkut ‘s Institute of Technology Ladkrabang and MSc in 2002 from Chulalongkorn University. Presently, she has received the Royal Golden Jubilee scholarship from Thailand Research Fund for her PhD in Analytical Chemistry at Chulalongkorn University since 2002.

Orawon Chailapakul is an Associate Professor at Department of Chemistry, Faculty of Science, Chulalongkorn University. She received her BSc in Chemistry from Mahidol University in 1982, MSc from Chulalongkorn University in 1987, and PhD from The University of New Mexico in 1994. Her research interest includes development of biosensors and diamond sensors. She is now the member of Materials Chemistry and Catalysis Research Unit and Sensor Research Unit.

Available online at www.sciencedirect.com
SCIENCE DIRECT
Talanta 68 (2006) 1329–1335
Talanta
www.elsevier.com/locate/talanta

Use of nickel implanted boron-doped diamond thin film electrode coupled to HPLC system for the determination of tetracyclines☆

Surudee Treetepvijit[a], Anchana Preechaworapun[a], Narong Praphairaksit[a], Suchada Chuanuwatanakul[a], Yasuaki Einaga[b], Orawon Chailapakul[a,*]

[a] *Materials Chemistry and Catalysis Research Unit, Department of Chemistry, Faculty of Science, Chulalongkorn University, Patumwan, Bangkok 10330, Thailand*
[b] *Department of Chemistry, Faculty of Science and Technology, Keio University, 3-14-1 Hiyoshi, Yokohama, Kanagawa 223-8522, Japan*

Received 24 May 2005; received in revised form 24 July 2005; accepted 24 July 2005
Available online 25 August 2005

Abstract

The electrochemical analysis of tetracyclines was investigated using nickel-implanted boron-doped diamond thin film electrode (Ni-DIA) by cyclic voltammetry and high performance liquid chromatographic with amperometry. Cyclic voltammetry was used to study the electrochemical oxidation of tetracyclines. Comparison experiments were carried out utilizing as-deposited BDD and glassy carbon electrodes. Ni-DIA electrode provided well-resolved oxidative irreversible cyclic voltammograms and the highest current signals among the electrode studied. High performance liquid chromatography (HPLC) with amperometric detection was also studied. The chromatography was performed using a commercially available Inertsil C18 column, with the mobile phase being: 80% phosphate buffer (pH 2.5)–20% acetonitrile and detected at 1.55 V. The methods were validated over the concentration range 0.05–100 ppm with the overall average recoveries from 83.3 to 102.5% and R.S.D. of less than 10%. The proposed method was further applied to analyse shrimp samples.

Keywords: Tetracyclines; Nickel-implanted boron-doped diamond; Cyclic voltammetry; Flow injection system; HPLC; Amperometric detection

1. Introduction

Conductive boron-doped diamond electrodes (BDD) have attracted tremendous interest for various electrochemical applications, including electroanalysis [1], electrosynthesis [2] and electrochemical treatment of wastewater [3]. BDD electrodes have recently attracted a great deal of attention due to their superior properties, which are significantly different from those of other conventional electrodes, e.g. glassy carbon or platinum electrode materials [4,5]. The growing popularity of this boron-doped diamond electrode in analytical applications over its conventional counterparts lies mainly on its various attractive features, such as very low and stable voltammetric background currents, wide working potential window in aqueous solutions, high resistance to deactivation via fouling, insensitivity to dissolved oxygen and long-term response stability [6–8].

While some metals, such as platinum is known to oxidize hydrogen peroxide and methanol, as well as nickel is conventionally used for carbohydrates electrochemical detection in alkali solution [9–11]. BDD electrode is found completely inactive for those kinds of catalytic reactions. However, it has been reported that the dispersion of metallic particles within an organic polymer or an inert surface resulted in drastic increase of the catalytic activity and sensitivity of the electrode because the dispersed particles behave like microelectrode arrays [10]. The chemically modified electrodes (CMEs) which are capable of lowering the operational potential required to oxidize scarcely electroactive organic compounds has caught a great deal of interest. Reduced electrode fouling has also been reported. CMEs based on the modification of glassy carbon or graphite rods with various metals (e.g.

☆ Presented at the 13th International Conference on Flow Injection Analysis, April 24–29, 2005, Las Vegas, Nevada, and erroneously omitted from Talanta 62(2) 2005.

* Corresponding author. Tel.: +662 2187615; fax: +662 2541309.
E-mail address: corawon@chula.ac.th (O. Chailapakul).

0039-9140/$ – see front matter © 2005 Elsevier B.V. All rights reserved.
doi:10.1016/j.talanta.2005.07.047

copper [12–14], cobalt [15], and nickel [10,11,16–18]) have shown catalytic activities towards polyhydroxy compounds. These electrodes have been successfully applied to detect carbohydrate [10–12,15,16], amino acids [16,18], sugars [13] and aliphatic alcohol compounds [17] using amperometric detection. Unfortunately, glassy carbon electrode has a major drawback of yielding high background current. These metal-modified diamond electrodes appear to be well suited to overcome such problems. BDD film would be the best choice for the deposition of metal electrocatalysts.

The preparation of some metal-modified BDD electrodes for electrochemical analysis by using chemical precipitation and electrochemical deposition method had been reported [9].

Ion implantation into a material can be used to form near surface composites. The method is used to modify the structure of a target-near-surface by bombardment with heavy ions. This method is popular for the preparation of doping semiconductors, such as silicon and gallium arsenide, so it has been of particular interest for the fabrication of ion-implanted diamond. At present, some applications for electrochemical use by metal-implanted conductive BDD electrodes have been reported [19]. Therefore, we are interested in developing a method for the determination of tetracyclines by using the Ni-implanted diamond electrode.

Many antibiotics are widely used in veterinary for preventing and treating diseases as well as for promoting growth in food producing animals. These antibiotics are, for example, aminoglycosides, β-lactams, chloramphenicol, tetracyclines, macrolides, sulphonamides, quinolines, and nitrofurans. Tetracycline is one of the most important antibiotics utilizing in the industry and thus it is of particular interested. Tetracycline is a broad-spectrum antibiotic, such as tetracycline (TC), chlortetracycline (CTC), doxycycline (DC) and oxytetracycline (OTC). These compounds are commonly used in human pathologies as well as in veterinary medicine, animal nutrition and feed additives for cattle growth. It is used to treat many different infections, such as respiratory tract infections, urethritis and severe acne. It also plays a major role in the treatment of multidrug resistant malaria. Adverse effects in these subtances include gastrointestinal disturbances, renal dysfunction, hepatotoxicity, raised intracranial pressure and skin infections, such as rosacea and perioral dermatitis. Tetracyclines are widely used in diary cattle, poultry and shrimp.

The percentage of total worldwide shrimp consumption produced by farming increased from less than 2% in 1980 to more than 26% in 1989 [20]. In recognition of the steadily increasing amount of shrimp produced by aquaculture (rising from∼100 million lbs worldwide in 1979 to 1600 million lbs in 1999), oxytetracycline (OTC) is widely known to be one of the most common antibiotics used in shrimp aquaculture, particularly in countries other than the US. Therefore, shrimps were chosen as the test subject in this study.

Numerous methods have been reported for the determination of tetracyclines in various samples, such as milk [21], shrimp [22], animal feed [23,24], animal tissues [25,26] and pharmaceutical formulations [27,28] based on thin-layer chromatography, capillary electrophoresis [29], and high performance liquid chromatography (HPLC). HPLC is a common method that separates tetracyclines in the reverse-phase mode with a variety of detection methods, such as spectrophotometry [25,26], fluorometry [30,31], mass spectrometry [32,33] and electrochemistry [27,28].

Among these, the electrochemical method is distinctly attractive owing to its simplicity, no need for derivatization, fast analysis, low cost and high sensitivity. There are several reports utilizing polarography, potentiometry [34] and amperometry [27,28,35] for the analysis of tetracycline. In 2005, Charoenraks et al. reported the use of high performance liquid chromatography with pulsed amperometric detection at anodized boron-doped diamond thin film electrode for the detection of tetracyclines.

In this present work, we report the use of Ni-implanted boron-doped diamond thin film electrodes (Ni-DIA) to study the electrochemical oxidation of tetracyclines using cyclic voltammetry. Focus is placed on comparing the results with as-deposited BDD and glassy carbon electrodes. In addition, the performance of the Ni-DIA electrode for the detection of tetracycline was examined by HPLC with amperometric detection for determination of tetracyclines in shrimp.

2. Experimental

2.1. Chemicals and reagents

Tetracycline-HCl (TC), oxytetracycline-HCl (OTC), chlorteteacycline-HCl (CTC), and doxycycline-HCl (DTC) were available from Sigma–Aldrich. Acetonitrile and methanol (Merck) were of HPLC grade. Disodium hydrogenphosphate (BDH), citric acid monohydrate (J.T. Baker), ethylenediaminetetraacetic acid disodium salt dehydrate (Fluka), and phosphoric acid (Merck) were of analytical grade. Distilled water was purified in a Milli-Q system (Millipore, Bedford, MA, USA). Soild-phase extraction (SPE) C-18E cartridges (500 mg, 6 mL) were obtained from Phenomenex (USA).

Phosphate buffer solution of pH 2.5 were prepared from 0.01 M H_3PO_4 and adjusted to 2.5 by adding drop-wise 0.1 M Na_2HPO_4. The mobile phase for the HPLC condition consisted of 20% acetonitrile in 0.01 M phosphate buffer (pH 2.5).

Na_2EDTA–McIlvaine buffer solution (pH 4) was prepared by dissolving 15 g of disodium hydrogen phosphate dihydrate, 13 g of citric acid monohydrate and 3.72 g of EDTA in water and diluting to 1 L.

Stock standard solutions of tetracycline, oxytetracycline, chlortetracycline, and doxycycline were prepared by dissolving 10 mg of each compound in 10 mL of mobile phase to obtain a final concentration of 1000 μg/mL. Working standard solutions were prepared by diluting the stock solution

with the mobile phase. All of the solutions were protected from exposure to light and stored in a refrigerator.

2.2. Sample preparation procedure

Sea and farming shrimp were purchased locally. The shells and tails of shrimp were removed and ground in a conventional meat grinder. The homogenate was degassed overnight and kept in frozen until use. A 2.50 g shrimp samples were placed in 15 mL capped centrifuge tubes, 12.5 mL of Na_2EDTA–McIlvaine buffer (pH 4) was added to each tube portion and blended for 30 s with a homogenizer. The resulting homogenates were shaken for 10 min on a flatbed shaker at high speed. The tube was removed from the shaker and centrifuged for 30 min at 3500 radian per second. The supernatant was loaded into a SPE cartridge, previously activated with 10 mL of methanol and 10 mL of Milli-Q water. After sample loading, the SPE cartridge was washed with 10 mL of Milli-Q water, and finally tetracyclines were eluted by 10 mL of methanol. The solvent was removed under room temperature. The residues were filtered with a 0.45 μm PTFE filter. The solutions were analysed by HPLC.

2.3. Electrode

Highly boron-doped diamond electrode was deposited on Si (100) wafers in microwave plasma-assisted chemical vapor deposition (MPCVD) system (ASTeX Corp., Woburn, MA). A mixture of acetone and methanol in the ratio of 9:1 (v/v) was used as the carbon source. B_2O_3, used as the boron source, was dissolved in the acetone–methanol solution at B/C atomic ratio of 1:100. These films were implanted with 750 keV Ni^{2+} with a dose of 5×10^{14} cm^{-2} (Tandetron 4117-HC, HVEE). Annealing process was performed at 850 °C for 10 min in an H_2 ambient (80 Torr). It was reported that surface morphology and color change after implantation were not observed, a SEM image of the BDD surface after implantation showed the presence of small holes [19]. The presence of metal particles could not be seen, because the particle size is very small as well as the metal position is deeply inside the holes due to the high energy of the bombardment in implantation process.

The nickel-implanted boron-doped diamond electrodes have been prepared in Associate Professor Yasuaki Einaga's laboratory. The Ni-DIA electrodes were rinsed with ultrapure water prior to use.

2.4. Voltammetry

Electrochemical measurements were recorded using an Autolab Potentiostat 30 (Metrohm, Switzerland) with a standard three-electrode configuration. The planar working Ni-DIA or BDD electrode was pressed against a smooth ground joint at the bottom of the cell, isolated by an o-ring (area 0.07 cm^2). Placing the backside of the Si substrate on a brass plate made ohmic contact. For comparison, the as-deposited BDD electrode was used. A platinum wire was used as the auxiliary electrode and Ag/AgCl in KCl (sat'd) was used as the reference. Cyclic voltammetry was used to study the electrochemical reaction. The electrochemical measurements were housed in a Faradaic cage to reduce electronic noise. All experiments were performed at room temperature.

2.5. LC system and conditions

The LC system consisted of a thin layer flow cell (GL Science), an injection port (Rheodyne No. 7125) with a 20 μL injection loop and a pump (Water Model 510 solvent delivery system, Waters Associates Inc., Milford, MA, USA). The column was ODS-3 Inertsil C18, 5 μM 4.6 mm × 250 mm i.d. (GL Science Inc.). The electrochemical detector was applied using a computer controlled potentiostat (Autolab PGSTAT 30, Metrohm, Switzerland). Separations were carried out under isocratic conditions using a mobile phase of 0.01 M phosphate buffer (pH 2.5)–acetonitrile (80:20, v/v). The flow rate was 1 mL/min. The thin layer flow cell consisted of a silicone gasket as a spacer, the Ag/AgCl in 3 M in NaCl as the reference electrode, and a stainless steel tube as the auxiliary electrode and outlet. The experiments were performed in a copper faradaic cage to reduce electrical noise.

3. Results and discussion

3.1. Cyclic voltammetry

Fig. 1(a–d) shows the cyclic voltammograms obtained for 1 mM tetracycline hydrochloride, 1 mM chlortetracycline, 1 mM doxycycline and 1 mM oxytetracycline + 0.1 M phosphate buffer (pH 2) at Ni-DIA electrode, as-deposited diamond electrode and glassy carbon electrode. The corresponding backgrounds are also shown. A well-defined irreversible cyclic voltammograms were obtained at the Ni-DIA electrode and diamond electrode while an ill-defined irreversible cyclic voltammograms was obtained at the glassy carbon electrode for all analytes. The electrochemical data obtained from cyclic voltammograms of these solutions at the mentioned electrodes is shown in Table 1. It was found that the Ni-DIA electrode provided the highest S/B ratios for tetracycline, chlortetracycline, doxycycline and oxytetracycline among the three electrodes studied. We have also carried out the experiments using pure nickel electrode for the comparison with the Ni-DIA electrode. It was found that no any response obtained for the determination of tetracycline antibiotics when using pure nickel electrode.

3.2. Liquid chromatography with amperometric detection

In general, because tetracyclines are analyzed by reversed phase HPLC, the seperation in this experiment was then per-

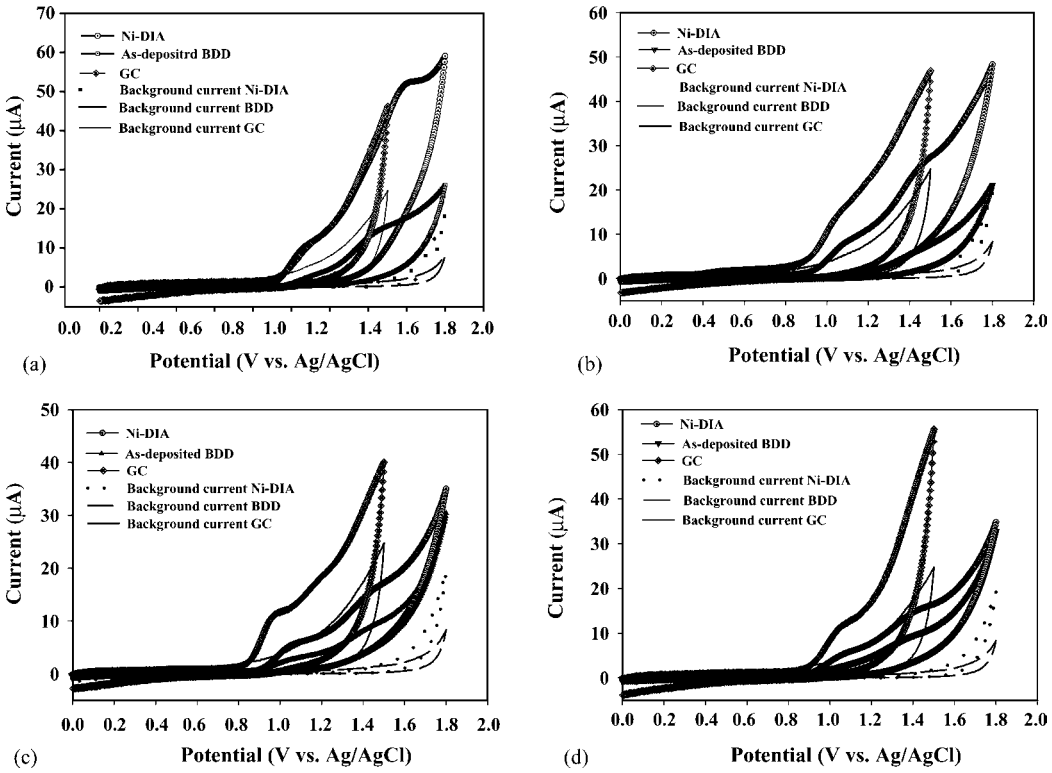

Fig. 1. Cyclic voltammograms for (a) tetracycline, (b) oxytetracycline, (c) chlortetracycline, and (d) doxycycline in 0.1 M phosphate buffer (pH 2) at Ni-DIA, as-deposited diamond and glassy carbon electrodes. The scan rate was 50 mVs^{-1}. Background voltammogram (0.1 M phosphate buffer, pH 2) is also shown in this figure.

formed using a C-18 column. The pH of the mobile phase was selected to be 2.5 so as to reduce the formation of isometric analogues. This pH also gave a well-defined and high signal of cyclic voltammograms of tetracycline oxidation. In this experiment, the phosphate buffer was chosen because it provided low background currents. No reaction between buffer and tetracyclines was observed over the potential range of interest. Therefore, phosphate buffer (0.01 M, pH 2.5) was used to separate tetracyclines, and significantly prolonged the retention time in the presence of 20% acetonitrile. The chromatograms of a standard solution of tetracyclines are presented in Fig. 2. The orders of elution were oxytetracycline,

Table 1
The electrochemical data of 1 mM tetracycline, 1 mM chlortetracycline, 1 mM doxycycline and 1 mM oxytetracycline at Ni-DIA electrode, as-deposited diamond electrode and glassy carbon electrode

Analytes	Electrode	E_p^{oxa}(V)	I_p^{oxb}(μA)	S/B^c
Tetracycline	Ni-DIA	1.501	20.90	12.06
	BDD	1.501	17.00	11.56
	GC	1.178	7.10	1.42
Chlortetracycline	Ni-DIA	1.501	17.30	9.61
	BDD	1.438	9.00	6.12
	GC	0.975	7.80	1.56
Doxycycline	Ni-DIA	1.501	16.60	9.22
	BDD	1.477	10.60	7.21
	GC	1.059	7.00	1.40
Oxytetracycline	Ni-DIA	1.511	27.90	15.50
	BDD	1.506	7.80	5.31
	GC	1.064	9.90	1.98

[a] Oxidation peak potential.
[b] Oxidation peak current.
[c] calculated from I_p^{ox}/background current.

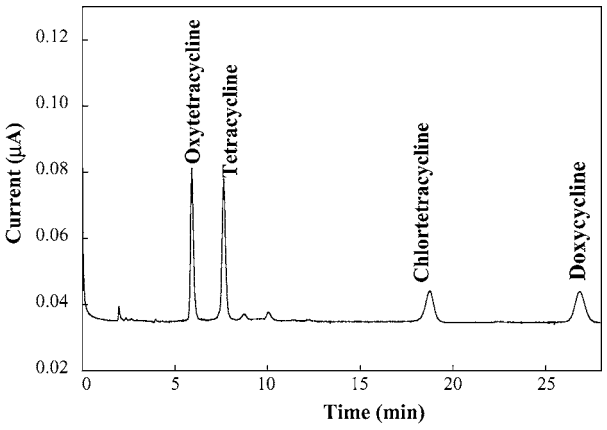

Fig. 2. Chromatogram of 1 ppm a standard mixture seperated on ODS Inertsil C18 column (5 μM 4.6 × 250 mm i.d.) using a mobile phase of phosphate buffer (0.01 M, pH 2.5)–acetonitrile (80:20). The injection volume was 20 μL, and the flow rate was 1 mL/min.

Table 2
Calibration characteristics of oxyteracycline, tetracycline, chlortetracycline and doxycycline for the proposed method at the Ni-DIA electrode

Analytes	Linear dynamic range ($\mu g\,mL^{-1}$)	Slope (peak areas units/mg/kg)	Intercept (μA)	R^2	Limit of detection ($\mu g\,mL^{-1}$)
Oxytetracycline	0.05–100	0.0473	0.0562	0.9975	0.01
Tetracycline	0.05–100	0.0395	0.0453	0.9977	0.01
Chlortetracycline	0.1–100	0.0110	0.0045	0.9990	0.05
Doxycycline	0.1–100	0.0111	0.0066	0.9996	0.05

Table 3
Recoveries of tetracyclines in shrimp farming samples using the HPLC with amperometry method at the Ni-implanted electrode ($n = 3$)

Analyte	Mean of %recovery ($x \pm$ S.D.)			
	Spiking level of 0.5 mg kg^{-1}	Spiking level of 1 mg kg^{-1}	Spiking level of 5 mg kg^{-1}	Spiking level of 10 mg kg^{-1}
Oxytetracycline	84.8 ± 3.0	96.8 ± 2.7	102.5 ± 3.4	99.6 ± 1.8
Tetracycline	93.3 ± 5.5	85.9 ± 7.7	96.6 ± 2.4	97.0 ± 5.5
Chlortetracycline	91.48 ± 5.3	94.8 ± 5.9	91.6 ± 5.2	97.9 ± 3.8
Doxycycline	89.2 ± 6.7	88.4 ± 3.0	97.7 ± 5.4	103.7 ± 7.4

Table 4
Recoveries of tetracyclines in shrimp sea samples using the HPLC with amperometry method at the Ni-DIA electrode ($n = 3$)

Analyte	Mean of %recovery ($x \pm$ SD)			
	Spiking level of 0.5 mg/kg	Spiking level of 1 mg/kg	Spiking level of 5 mg/kg	Spiking level of 10 mg/kg
Oxytetracycline	94.9 ± 1.6	83.3 ± 4.3	86.8 ± 5.0	96.5 ± 2.4
Tetracycline	92.0 ± 1.1	88.4 ± 4.4	89.2 ± 1.2	96.9 ± 4.6
Chlortetracycline	91.8 ± 8.6	91.9 ± 3.0	86.0 ± 8.0	93.3 ± 5.1
Doxycycline	102.0 ± 9.0	96.2 ± 1.7	90.6 ± 0.1	99.4 ± 2.4

tetracycline, chlortetracycline and doxycycline, respectively. To complete the separation of tetracyclines, approximately 27 min are required.

3.3. Optimum potential for HPLC

Fig. 3 depicts the optimum potential *i–E* curve obtained at the Ni-DIA electrode for a 20 μl injection of 100 μM of tetracyclines mixture standard solution. 0.01 M of phosphate buffer (pH 2.5) was used as the carrier solution. Each datum represents an average of two injections. The magnitude of the background current at each potential is also shown for comparison. The optimum potential of tetracyclines mixture standard solution at the Ni-DIA electrode exhibited a well-defined sigmodal shape with a half peak potential at about 1.55 V versus Ag/AgCl. Therefore, this potential was fixed for the amperometric potential detection in HPLC system analysis experiments.

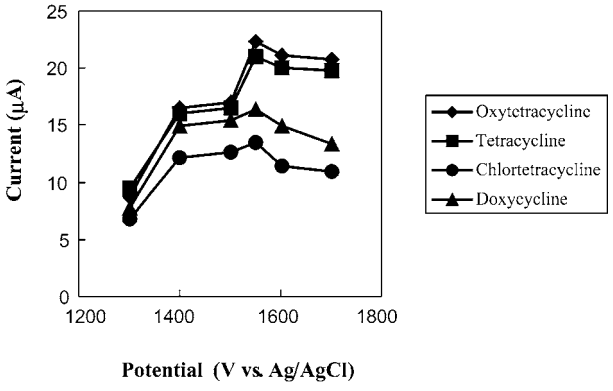

Fig. 3. Optimum potential of 10 ppm of tetracyclines in 0.01 M phosphate buffer (pH 2.5). 0.1 M phosphate buffer (pH 2.5) was used as a carrier solution, flow rate 1 ml min^{-1}.

3.4. Linearity and detection limit

The tetracycline mixture standard solutions covering the concentration range of 0.01–100 $\mu g\,mL^{-1}$ were analyzed and their peak areas were plotted versus concentration. The calibration characteristics of oxytetracycline, tetracycline, chlortetracycline and doxycycline at the Ni-DIA electrode are given in Table 2.

3.5. Recoveries

The average recoveries of tetracyclines from shrimp farming and shrimp sea sample at four different spiking levels (0.5, 1, 5 and 10 μg/mL each compound) are summarized in Tables 3 and 4. It can be observed from the chromatogram

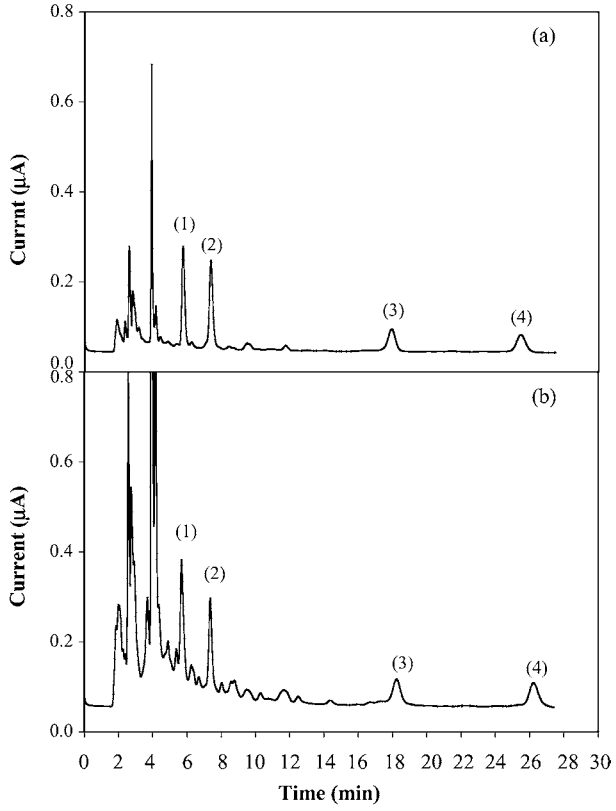

Fig. 4. HPLC chromatograms of (a) shrimp farming sample and (b) shrimp sea sample spiking with 5 μg/mL each of (1) oxytetracycline, (2) tetracycline, (3) chlortetracycline, and (4) doxycycline at the Ni-implanted diamond electrode. The other conditions are the same as in Fig. 2.

(Fig. 4) that the peaks due to the other components did not interfere with those of tetracyclines.

4. Conclusions

This is the first use of Ni-DIA electrodes for the electroanalysis of tetracyclines. It was found that Ni-DIA electrodes exhibited excellent performance for the oxidative detection of tetracycline. Well-defined voltammograms were obtained at the Ni-DIA electrode, which exhibited high sensitivity and demonstrated significant advantages over the BDD and glassy carbon electrode. The outstanding capabilities of the Ni-DIA electrode were demonstrated by coupling with HPLC. HPLC with amperometry at Ni-DIA electrode has been successfully applied to determine four types of tetracyclines (oxytetracycline, tetracycline, chlortetracycline and doxycycline) in shrimp samples. Experimental detection limit of 0.01–0.05 μg/mL were obtained for four tetracyclines studied. A linear dynamic range from 0.05 to 100 μg/mL was achieved. Application of the proposed method for the determination of tetracycline in shrimp sample shows that this method is precise, accurate and very sensitive.

Acknowledgements

The authors would like to thank The Thailand Research Fund, Ratchadaphisek Somphot Grant and Chulalongkorn University. Special thanks are extended to Associate Professor Yasuki Einaga (Keio University) for providing the Ni-DIA electrodes used in this research

References

[1] M.C. Granger, G.M. Swain, J. Electrochem. Soc. 146 (1999) 12.
[2] F. Okino, H. Shibata, S. Kawasaki, Electrochem. Solid-State Lett. 2 (1999) 382.
[3] M. Fryda, D. Herrmann, L. Schater, et al., New Diamond Frontier Carbon Technol. 9 (1999) 229.
[4] D. Sopchak, B. Miller, Y. Avyigal, R. Kalish, J. Electroanal. Chem. 538–539 (2002) 39.
[5] T.A. Ivandini, B.V. Sarada, C. Terashima, T.N. Rao, D.A. Tryk, H. Ishiguro, Y. Kubota, A. Fujishima, J. Chromatogr. B 791 (2003) 63.
[6] O. Chailapakul, P. Aksharanandana, T. Frelink, Y. Einaga, A. Fujishima, Sens. Actuators B 80 (2001) 193.
[7] N. Wangfuengkanagul, O. Chailapakul, J. Pharm. Biomed. Anal. 28 (2002) 841.
[8] M.C. Granger, J. Xu, J.W. Strojek, G.M. Swain, Anal. Chim. Acta 397 (1999) 145.
[9] F. Montilla, E. Morallon, I. Duo, C. Comninellis, J.L. Vasquez, Electrochim. Acta 48 (2003) 3891.
[10] I.G. Casella, E. Desimoni, T.R.I. Cataldi, Anal. Chim. Acta 248 (1991) 117.
[11] I.G. Casella, E. Desimoni, A.M. Salvi, Anal. Chim. Acta 243 (1991) 61.
[12] S.V. Prabhu, R.P. Baldwin, Anal. Chem. 61 (1989) 852.
[13] S.V. Prabhu, R.P. Baldwin, Anal. Chem. 61 (1989) 2258.
[14] P. Luo, S.V. Prabhu, R.P. Baldwin, Anal. Chem. 62 (1990) 752.
[15] T.R.I. Cataldi, I.G. Casella, E. Desimoni, T. Rotunno, Anal. Chim. Acta 270 (1992) 161.
[16] E. Wang, A. Liu, J. Electroanal. Chem. 319 (1991) 217.
[17] I.G. Casella, T.R.I. Cataldi, A.M. Salvi, E. Desimoni, Anal. Chem. 65 (1993) 3143.
[18] A. Liu, E. Wang, Anal. Chim. Acta 280 (1993) 223.
[19] T.A. Ivandini, R. Sato, Y. Makide, A. Fujishima, Y. Einaga, Diamond Relat. Mater. 13 (2004) 2003.
[20] A.W. Fast, Marine Shrimp Aquaculture: Principles and Practices, Elsevier, New York, 1992.
[21] F.J. Schenck, P.S. Callery, J. Chromatogr. A 812 (1998) 99.
[22] M.C. Carson, M.A. Ngoh, S.W. Hadley, J. Chromatogr. B 712 (1998) 113.
[23] A.D. Cooper, G.W.F. Stubbings, M. Kelly, J.A. Tarbin, W.H.H. Farrington, G. Shearer, J. Chromatogr. A 812 (1998) 321.
[24] W. Naidong, S. Hua, E. Roets, J. Hoogmartens, J. Pharm. Biomed. Anal. 33 (2003) 85.
[25] J. Sokol, E. Matisova, J. Chromatogr. A 669 (1994) 75.
[26] J.R. Walsh, L.V. Walker, J.J. Webber, J. Chromatogr. A 596 (1992) 211.
[27] A.G. Kazemifard, D.E. Moore, J. Pharm. Biomed. Anal. 16 (1997) 689.
[28] S. Palaharn, T. Charoenraks, N. Wangfuengkanagul, K. Grudpan, O. Chailapakul, Anal. Chim. Acta 499 (2003) 191.
[29] J. Tjornelund, S.H. Hansen, J. Chromatogr. A 779 (1997) 235.
[30] S. Croubels, W. Baeyens, C.V. Peteghem, Anal. Chim. Acta 303 (1995) 11.

[31] D.S. Vienneau, C.G. Kindberg, J. Pharm. Biomed. Anal. 16 (1997) 111.
[32] J. Zhu, D.D. Snow, D.A. Cassada, S.J. Monson, R.F. Spalding, J. Chromatogr. A 928 (2001) 177.
[33] M. Cherlet, M. Schelkens, S. Croubels, P.D. Backer, Anal. Chim. Acta 492 (2003) 199.
[34] C.M.C.M. Couto, J.L.F.C. Lima, M. Conceicao, B.S.M. Montenegro, S. Reis, J. Pharm. Biomed. Anal. 18 (1998) 527.
[35] T. Charoenraks, S. Chuanuwatanakul, K. Honda, Y. Yamaguchi, O. Chailapakul, Anal. Sci. 21 (2005) 241.

SENSOR LETTERS

www.aspbs.com/sensorlett

VOLUME 4
NUMBER 2
JUNE 2006

53–213 (2006)
ISSN 1546-198X
EISSN 1546-1971

Manuscript Submission

Submit your manuscript electronically as a PDF or MS Word file to the Editor-in-Chief, Professor Craig A. Grimes, or one of the Regional Editors.

SENSOR LETTERS

www.aspbs.com/sensorlett

VOLUME 4
NUMBER 2
JUNE 2006

53–213 (2006)
ISSN 1546-198X
EISSN 1546-1971

ON THE COVER: The cover image shows the fluorescence spectra of PBA and myristic acid layers chemisorbed onto nanoporous alumina, from "Fluorescence Behavior of Pyrene-1-Butylic Acid Chemisorption Layer onto Nano-Porous Anodic Oxidized Aluminum with Myristic Acid Layer for Optical Oxygen Sensing," *Yuki Fujiwara and Yutaka Amao*, pp. 139–143 of this issue.

REVIEWS

GENERAL RESEARCH ARTICLES

FOREWORD

RESEARCH ARTICLES

SENSOR LETTERS

www.aspbs.com/sensorlett

Editor-in-Chief:

Professor Craig A. Grimes
Department of Electrical Engineering
The Pennsylvania State University
University Park, PA 16802, USA
Tel.: (814) 865-9142
Fax: (814) 865-2326
E-mail: cgrimes@engr.psu.edu

FOR SUBSCRIPTION

SENSOR LETTERS
American Scientific Publishers
25650 North Lewis Way
Stevenson Ranch, CA 91381-1439, USA
Tel.: (661) 254-0807
Fax: (661) 254-1207
E-mail: order@aspbs.com

Aims and Scope:

The growing interest and activity in the field of sensor technologies requires a forum for rapid dissemination of important results: *Sensor Letters* is that forum. *Sensor Letters* offers scientists, engineers and medical experts timely, peer-reviewed research on sensor science and technology of the highest quality. *Sensor Letters* publishes original rapid communications, full papers and timely state-of-the-art reviews encompassing the fundamental and applied research on sensor science and technology in all fields of science, engineering, and medicine. Highest priority will be given to short communications reporting important new scientific and technological findings. Authors receive these benefits:

Research Topics Covered:

Innovative sensing concepts, Cell and tissue-based sensors, Chemical, biological and physical sensors, Sensor networks and systems, Sensor system integration, Advanced sensing materials, Sensor architectures, Self-cleaning sensors, One-shot disposable sensors, Biotoxin sensors, Data fusion of sensor arrays, Sensor fabrication, packaging, testing and reliability, Sensor instrumentation, Electronic interfaces and data processing, Sensor signal processing electronics, Sensor applications and uses, Optical, acoustic, mechanical, thermal, electromagnetic, electrochemical and radiation sensors, Environmental sensors, Fiber optic sensors, Sonar sensors, Flow sensors, Analytical μ-systems, lab-on-a-chip, Sensor neural networks, Sensor telemetry, Measurement compensation and calibration, Electronic-nose sensors, Nanosensors, Computational and theoretical aspects of sensors, Fabrication techniques, Characterization, Spectroscopy, and much more.

Instructions for Authors:

Please visit the journal Web site (http://www.aspbs.com/sensorlett) or see the instructions in each issue of the journal. Authors should follow the instructions when submitting their manuscripts.

Manuscript Submission:

Submit your manuscript electronically. Send an electronic file in a PDF or Word format to Editor-in-Chief Professor Craig A. Grimes at the above address. Please see "Instructions for Authors" for submitting manuscripts.

Books for Review:

Publications should be sent to the Editorial Office: Sensor Letters, American Scientific Publishers, 25650 North Lewis Way, Stevenson Ranch, CA 91381-1439, USA; Tel.: (661) 254-0807; Fax: (661) 254-1207; Email: sensor@aspbs.com. Readers are encouraged to send books that may be of interest to other readers of *Sensor Letters*.

Referee's Report:

Please submit Reviewer's Reports on the *Sensor Letters* home page.

Annual Subscription Rates (Print Edition) for 2006:

Volume 4, 2006, 4 issues
Personal: US$ 200 (USA)/US$ 300 (Foreign)
Institutional: US$ 690 (USA)/US$ 790 (Foreign)
Postage and handling charges add $50 for USA, $100 for foreign.
The publisher reserves the right to refuse nonqualified subscriptions.

Web Edition:

Sensor Letters is available to subscribers via the internet. For institutional subscriptions to the Web Edition or site licensing, please contact publisher.

Subscription Orders, Advertising, Renewals and Reprints:

For quotes, and other details, contact: American Scientific Publishers
Tel.: (661) 254-0807 Fax: (661) 254-1207
E-mail: order@aspbs.com, sensor@aspbs.com

Honorable Claim Period:

Claims for issues not received will be honored only if submitted within 90 days of the issue date for subscribers in North America or 180 days for all other subscribers. Send your written request to American Scientific Publishers.

Digital Object Identifier (DOI):

The DOI identification system for digital media has been designed to provide persistent and reliable identification of digital objects. Information on the DOI and its governing body, the International DOI Foundation, can be found at http://www.doi.org. The DOI appears in the lower right of the first page of each article.

SENSOR LETTERS
Vol. 4, 53–98, 2006

REVIEW

Carbon Materials for Chemical Sensors: A Review

Jerzy P. Łukaszewicz

Faculty of Chemistry, Nicholas Copernicus University ul. Gagarina 7, 87-100 Torun, Poland

(Received: 2 October 2004. Accepted: 6 February 2006)

This paper reviews application of different carbon materials, including graphite, polycrystalline carbon, carbon black, and carbon nanotubes, to the construction of chemical sensors. Basic chemical properties of carbons are presented as well as selected synthesis methods. Different ways of carbon surface functionalization are considered in relation to chemical sensing properties.

Keywords: Carbon, Chemical Functionalization, Carbon Black, Nanotubes, Fullerenes, Sensor, Sensing.

CONTENTS

1. INTRODUCTION

Chemical sensors have become one of the most important branches of contemporary science and technology. Recently there is growing interest in application of fullerenes and carbon nanotubes in chemical sensors. However, the term "carbon" or "carbonaceous material" is not limited to fullerenes and nanotubes but also applicable to carbon black, glassy carbon, or active carbon. The aim of this paper is to review the basic types of carbon-based materials, selected methods of carbon preparation, and the most recent announcements on application of carbon to chemical sensing. We intend to show how the chemical properties of the carbon surface can be controlled, and how the properties influence possible application of carbons to the construction of chemical sensors.

*Corresponding author; E-mail: lukaszju@chem.uni.torun.pl

Carbon is an element mostly known as a basic component of organic molecules. However, elemental carbon may also be found in the nature, e.g., graphite and diamond. The term carbon is often extended to numerous synthetic materials that are characteristic because of their high carbon content. The synthetic materials usually called "carbon" should be rather named "carbonaceous materials" because:
(1) Often they are not pure, i.e., they contain considerable amounts of other elements such as oxygen, nitrogen, metal ions, etc.
(2) Their chemical and crystallographic structure differs from elemental carbon, e.g., diamond and graphite; very often so called "carbons" are amorphous materials with minor traces of graphite.

However, the term "carbon" is traditionally used in science since it is convenient in use. Therefore the general term "carbon" will be in use in this review keeping in mind the above mentioned qualifications.

Carbons are often artificially synthesized in a laboratory or on an industrial scale, with the fabrication route influencing their chemical and physical properties which in turn determine their field of application. One may propose a rough classification of carbonaceous materials with reference to the most common applications:
(1) Carbon as a construction material: Carbon fibres as reinforcement in composites, mechanically, and thermally stable bearings, artificial joints and other elements implanted in human bodies, chemically resistant laboratory ware, etc.
(2) Carbon for electrochemical applications (electrodes for industrial application, electrodes in the sources of electric power: Metal-gas batteries, lithium batteries, fuel cells etc.).

(3) Carbon as a material with chemically active surface: Carbon adsorbents for the removal of impurities form gases and liquids in military, industry and at home.
(4) Carbon as an absorber for storage of gases like hydrogen and methane.
(5) Carbon as a catalyst or support for a catalyst.

The above listed major fields of carbon application rely to the specific mechanical, electrical, and chemical properties. One may find in the literature many different materials of various properties all referred to as carbons; the broad terminology prevents definition of materials with well-defined and stable chemical and physical properties.

1.1. Basic Types of Carbon and the Methods of Their Preparation

1.1.1. Polycrystalline Carbons

The much differentiated properties and applications of carbons result from the selection of raw materials and methods of carbon production. Many of the technically applicable carbons are obtained by a thermal decomposition of carbon-rich organic substances. There are many possibilities in selecting a raw material but it is quite rare that one obtains the same carbon material from different precursors. Usually the raw material significantly influences the final properties of the carbon. Raw materials for carbon fabrication can be divided in to two general categories, natural carbon-rich substances, and synthetic organic materials. To the first group of materials one may account: Different types of wood, nut shell (coconut), fruit stones (plums, olives, apricot), black coal, brown coal, peat, cellulose-rich substances, sugar, and other carbohydrates, selected hydrocarbons (sucrose), selected proteins (e.g., animal blood). The second group of precursors consists of temperature degradable synthetic polymers: Polyvinyl chloride, poly(vinilydene chloride), poly(styrene), poly(acrylonitrile), etc., Some of them are thermosetting polymers and resins (poly(furfuryl alcohol), epoxy resins, rubber, bakelite, phenol based resins), which easily can be carbonised to active carbon. Any successful transformation of commonly used polymers (polyethylene, polypropylene, polyesters etc.,) into technically applicable carbons may help to solve ecological problems by the partial elimination of poorly degradable polymers from the environment. However, these polymers usually transform into volatile products upon heat-treatment at elevated temperatures. Brown coal often yields macroporous and mesoporous active carbons while from black coal and anthracite one often obtains microporous active carbon. Commercially available active carbons from brown coal are not stable from a mechanical point of view. Anthracite is an attractive raw material used in the production of molecular sieves.

The mentioned carbon-rich raw materials undergo thermal decomposition during the necessary heat-treatment (carbonisation). In the first step, the chemical structure of the organic raw material decomposes, i.e., the original system of chemical bonds vanishes. This process is usually accompanied by more or less intensive evolution of volatile products such as H_2O, HCl, NH_3, HCOH, CO_2, CO, aliphatic, and aromatic hydrocarbons, etc. Usually, the most dramatic changes occur between 150–400 °C. The nature of volatile products depends on the chemical nature of the raw material. In some cases (polyethylene, some polyesters), the carbonised substance yields almost only volatile products. It happens despite the very high carbon content in such materials. The raw solid obtained just after the completion of the most spectacular stage of thermal decomposition (temperature range 150–400 °C) is often called coke or raw coke. At this stage, the obtained solid mainly consists of carbon atoms randomly bonded to each other and some residual foreign atoms (e.g., oxygen, nitrogen, sulphur, phosphor). There are many unsaturated bonds and defects in the material. Coke is a chaotic mixture of carbon atoms that may form bonds using sp, sp^2, and sp^3 hybrid orbitals.

The second stage in the thermal decomposition of organic solids occurs above 400–500 °C. At this stage one observes the re-arrangement of the chaotic system of carbon–carbon and carbon–hetero atom bonds and the formation of regions of specifically oriented carbon atoms, i.e., small graphite layers that later can be stuck one over another. Thus, small domains of graphite start to grow in the amorphous carbon phase. The changes in the structure of a heat-treated carbon-rich organic material may be summarized in Figure 1.[1]

Dr. Jerzy P. Lukaszewicz has been working in the field of chemistry since 1977 when he was employed at Nicholas Copernicus University. His attention is currently focused on the synthesis of new materials for different purposes: adsorbents, catalysts, chemically sensitive materials. His expertise covers in particular fabrication of semiconductor carbon films, carbon-based molecular sieves and carbon-based electrode materials containing nano-sized particles of metals and metal oxides. He pays special attention to the characterization of carbon surfaces by instrumental methods. SEM, AFM, FT-IR, UV-VIS, HREELS, XPS, DTA-DTG-TG, TPD-TPR, and gas adsorption. He has got Ph.D. in chemistry in 1983. Since that time he was mainly employed as a post-doc fellow.

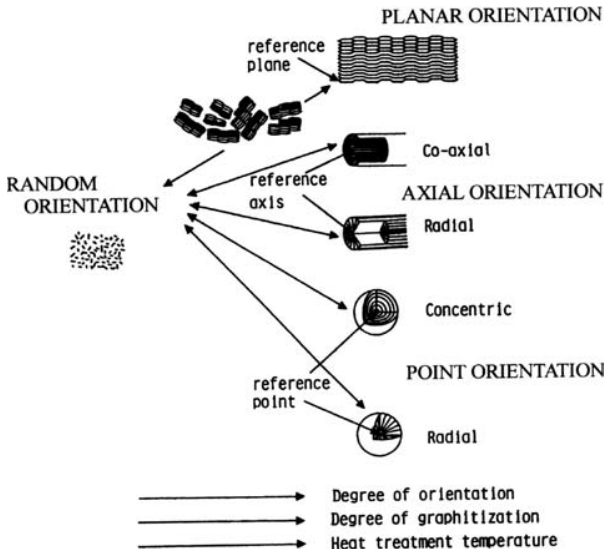

Fig. 1. Changes of the degree of orientation and the degree of graphitisation of heat-treated carbons. Reprinted with permission from [1], M. Inagaki, New carbons. *Control of structure and functions* **(2000)**, p. 11. © 2000, Elsevier.

The structure of most carbons obtained by thermal decomposition of organic species is described as turbostratic[2] (Fig. 2). The turbostratic structure consists of numerous small and randomly oriented graphite domains (crystallites) suspended in amorphous carbon phase. Carbons of turbostratic structure are mainly obtained at relatively low temperatures up to 1000–1300 °C.

There is a possibility to transform carbons of turbostratic structure into pure graphite. The longer the carbonisation duration and the higher the temperature the bigger are the graphite crystallites. Their growth upon increasing temperature and heat-treatment duration often leads to the formation of pure graphite. In such a case, the whole process is called graphitisation. The process of graphite formation from disordered carbon atoms is accompanied by the elimination of foreign atoms from the heat-treated carbon material. Finally, at elevated temperatures of ca. 3000 °C one may obtain pure carbon in graphitic form. The mentioned process of carbon structure re-arrangement and purification usually negatively affects specific surface properties of carbons since defects and foreign atoms are usually active in adsorption and catalysis over the surface of carbons obtained by pyrolysis.

Chemical changes occurring upon heat-treatment have been widely investigated for different raw materials. Thermal degradation of polyvinyl alcohol (PVAl)[3] may be used to illustrate typical processes associated to the transformation from the polymer to coke and carbon. It also means the transformation from a liner polymer (non-conducting) to an aromatic structure (conducting graphene sheets). Figure 3 shows that degradation of PVAl begins with elimination of water along linear polymeric chains. The process is intensive up to 300 °C when it

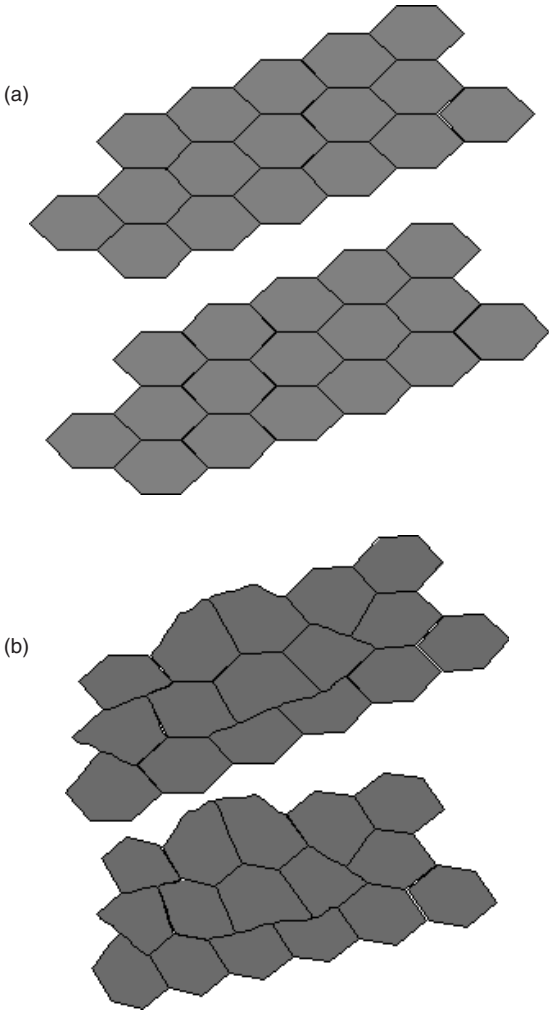

Fig. 2. Graphitic an turbostratic structure of graphene layers in graphite (a) and polycrystalline carbon (b).

seems to stop. At this stage, the material consists of polymer chains with numerous double bonds. Further heating above 300 °C leads to cyclisation (Deals-Alder mechanism or intermolecular mechanism) and aromatisation (elimination of H_2). This is a spectacular example illustrating how linear polymer chains transform into aromatic structures and finally into graphite layers. The variety of carbon materials that may be obtained as a terminate stage of various organic compounds is presented in Figure 4.[4]

Carbonisation of organic matter also yields turbostratic carbons. It means that despite a completely different chemical structure of the raw material (comparing to PVAl), the thermal decomposition leads finally to aromatisation, i.e., a system of condensed aromatic rings. On the way to the final stage, (carbon) the basic components of wood (cellulose, chemicelluloses, and lignin) undergo several processes like depolymerization, dehydratation, hydrolysis, oxidation, decarboxylation, and transglycosylation. In the case of wood, one observes the evolution of acetic acid

REVIEW

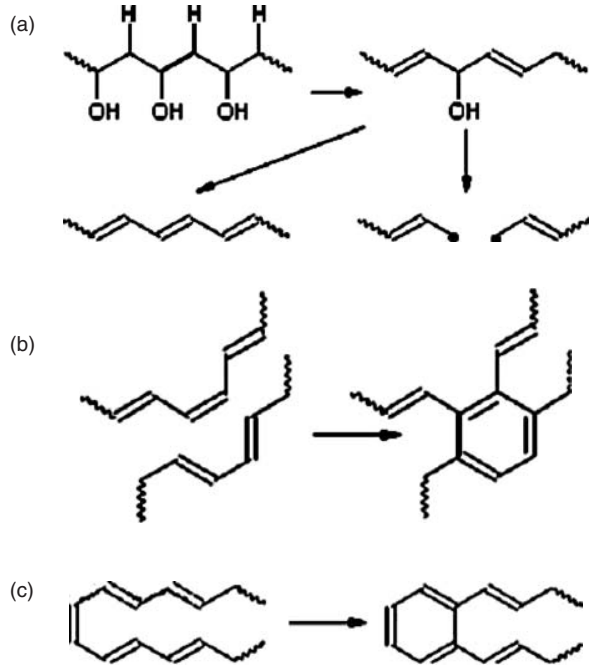

Fig. 3. Thermal degradation of poly(vinyl alcohol). (a) Chain-stripping—elimination of H_2O, (b) Intermolecular cyclisation (Diels-Alder reaction), and (c) Intermolecular cyclisation.

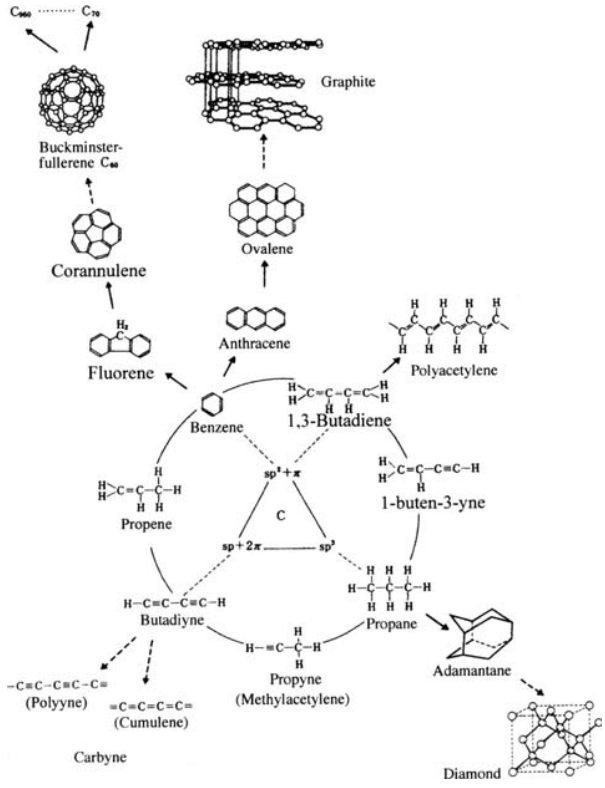

Fig. 4. Enormous organic compounds based on carbon-carbon bonds using sp^3, sp^2, and sp hybrid orbitals and inorganic materials as their extension. Reprinted with permission from [4], M. Inagaki, New carbons. *Control of Structure and Functions*, Elsevier, Amsterdam **(2000)**, p. 9. © 2000, Elsevier.

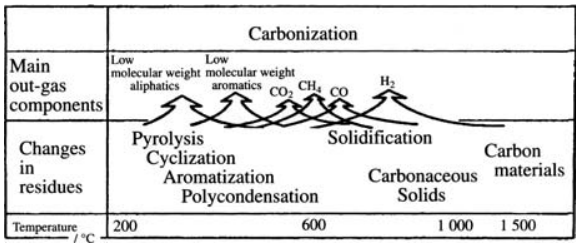

Fig. 5. General scheme of out-gas components and changes in residues with carbonisation. Reprinted with permission from [5], M. Inagaki, New carbons. *Control of Structure and Functions*, Elsevier, Amsterdam **(2000)**, p. 124. © 2000, Elsevier.

(decomposition of cellulose and chemicelluloses) and phenols (degradation of lignin) beside the usual volatiles: Water, carbon monoxide, carbon dioxide, and aliphatic hydrocarbons. All possible processes occurring during heat treatment of organic solids are summarized[5] in Figure 5 where they are placed on a temperature scale.

Spray pyrolysis is a method that may be very useful in the preparation of carbons needing only liquid precursors. This requirement results from the merit of the method: The substance must be transformed into the form of small drops. The drops of precursor move (powered by a stream of gas applied in atomizer) towards a hot solid substrate (or to a hot environment). The temperature of the substrate is usually kept at the level enabling thermal decomposition of the substance. The liquid drops, in contact with hot substrate, may undergo a variety of processes at a given temperature. The result is that preparation of carbon requires rapid solidification of the liquid precursor. Solidification may result from different phenomena depending on the nature of the raw material used. In the case of some monomers, one observes polycondensation, or polymerisation of the monomer being sprayed in pure or diluted form. Furfuryl alcohol is a typical example; the monomer polycondensates yielding a solid thermosetting resin. The resin is not stable at elevated temperatures (above 300 °C) and decomposes giving a black coke. A similar effect can be achieved by the application of polymer solutions or dispersions. A typical example is a solution of polystyrene (in organic solvents), water solution of polyvinyl alcohol (PVAl) or water dispersion of polyvinyl acetate (PVAc). In the case of the mentioned polymers, solvent or dispersing liquid evaporates from the drops of precursor. After the removal of liquid, one gets a layer of polymer on a hot substrate. Sometimes due to polymer transformation into volatile products (PVAc and PVAl) the raw coke phase grows very slowly on the substrate.

At this stage, the deposited film cannot be treated as a film of carbon. It is only a film of partially decomposed polymer or any other raw material due to the low substrate temperature, usually 200–300 °C. Such a temperature is high enough to decompose the raw material but much to low to initiate aromatisation. On the other had, it is not

possible to lift the temperature of substrate considerably above 300 °C if spray pyrolysis is performed at room conditions, i.e., when oxygen from air has an access to the film. Coke is a burnable solid that easily ignites itself in contact with air provided the temperature is high enough. Therefore, spray pyrolysis does not yield carbon materials directly. Usually, the raw product of pyrolysis (a film of coke) needs an additional heat-treatment to become a carbon material containing microcrystallites of graphite. This means heating of raw coke in a furnace without oxygen. The temperature of carbonisation and its duration depend on the desired properties (electric and surface), which the final product should exhibit. The presence of a solid substrate is inevitable when one intends to prepare a coke or carbon film. It is possible to spray liquid precursor to a wide chamber where temperature is high enough to cause the rapid evaporation of dispersing liquid and/or begin solidification (polymerisation, crystallization, etc.) of the dispersed matter. In such a case, one gets the solid in form of fine powder.

Another chemical method to carbon fabrication is the thermal decomposition of carbon-rich gaseous substances in conditions required by the method called Chemical Vapour Deposition (CVD). The standard CVD method is sometimes combined with physical techniques like radio frequency sputtering. One can obtain carbons by other methods that are more physical in character, for example evaporation of carbon particles from a solid sample of carbon (or graphite) in vacuum. Evaporation of carbon phase may result from the application of high temperature or the formation of plasma by means of an applied electromagnetic field. Evaporated carbon particles condense (on a substrate) in form of a thin carbon film.

Pyrolysis of carbon-rich substances uses combustible gases (methane, propane, acetylene), a gaseous oxidant (oxygen pure or from air) and a burner to ignite the flame. Such a flame has two different zones called: Oxidizing zone and reductive zone. In the reductive zone, combustion of the applied burnable gas is incomplete. This part of the flame contains products of partially oxidized gaseous fuel. A sudden insertion of a cool solid object can additionally reduce the temperature of the reductive zone. In these conditions, combustion of some hydrocarbons yields element carbon as one of the products. The gases flowing through the burner can be saturated with vapours of organic liquids (aliphatic hydrocarbons, aromatic hydrocarbons, and their derivatives with hetero atoms, etc.) or inorganic ones (gases, vapours, atomised solutions). In such a case, the formed carbon particles contain residuals of the substances added to the flame. It is well known that the flame over benzene may be the source of carbon black. It is enough to put a cold object into the flame to get its surface covered with a carbon black film. It consists of small particles and part of it is easily removable by rubbing. Therefore, the mechanical stability of such obtained carbon films is unsatisfactory regarding the requirements usually expected from the materials applied in chemical sensors.

In some cases, the carbon material applied for the construction of a chemical sensor is in fact a kind of carbon black. The reports dealing with carbon black usually pay little attention to the surface properties of carbon black. Frequently carbon black is treated like a chemical reagent of known formula and properties that always behave in the same manner. However carbon black properties, in common with other types of carbon materials, is sensitive to surface chemical treatment, as will be discussed.

1.1.2. Glassy Carbon, Carbon Black, Fullerenes, Nanotubes

Relatively new members of the "carbon family" such as nanotubes, fullerenes, and glassy carbon are currently the focus of considerable investigation. Glassy carbon can be obtained by the thermal decomposition of resins as phenol-formaldehyde and poly(furfuryl alcohol). The resins should be thermosetting providing the specific form of carbon called 'glassy,' with properties that include high hardness, low gas transparency, high chemical, and thermal stability. In chemical sensing glassy carbon usually is employed for fabrication of sensing electrodes.

The family of carbon nanotubes (CNTs) consist of two basic types of the tubes: Single-walled (SWCNTs) and multi-walled (MWCNTs). There are three methods of CNT fabrication: Arc-discharge (gas or liquid environment), decomposition of hydrocarbons over a metal/metal oxide catalyst, and laser ablation. The synthesis of nanotubes is a separate branch of carbon science and technology and more detailed information may be found in extended reviews.[6] The report of Rao and co-workers, as well as other reviews, present the conditions favourable for the synthesis of SWCNTs or MWCNTs. CNTs are of a great interest for sensor applications. The current report devotes a large part of the text to chemical sensing applications of CNTs.

1.2. Chemical Functionalisation of Carbon Surfaces

1.2.1. Oxygen-, Nitrogen-, Sulphur-Containing Functionalities

Carbonised organic matter (coke, char) mostly consists of carbon atoms bonded to each other by hybridised orbitals (sp^3, sp^2, or sp). Non-carbon atoms, i.e., heteroatoms, are usually implanted in the system of carbon–carbon bonds. It is probable that heteroatoms are not uniformly distributed between the surface and the bulk since the carbon matrix retains some heteroatoms from the raw material. The adsorbed molecules often react with carbon atoms at the surface yielding so called surface functional groups. The process is particularly important in the case of oxygen. Therefore, one has to expect the presence of O-containing

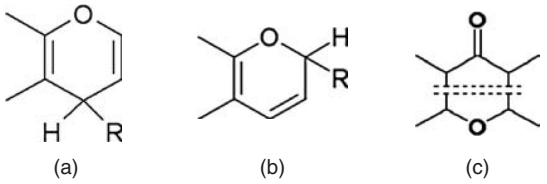

Fig. 6. The structure of oxygen functional groups of base properties. Reprinted with permission from [7], V. A. Garten and D. E. Weiss, *Australian J. Chem.* 10, 309 **(1957)**. © 1957, CSIRO Publ.

surface functional groups in most samples of carbon if it was stored for long in air. Heteroatoms in bulk carbon trace the chemical nature of the precursor while heteroatoms at the surface may be regarded as the witness of the carbon sample history. The process of carbon self-oxidation (low temperature) has been investigated extensively; see Figure 6.[7] The most reactive spots in the carbon matrix are: Broken bonds at carbon atoms, edge carbon atoms in aromatic rings and triple bonds between carbon atoms.

The mechanism of basic self-oxidation is valid for relatively low temperatures, up to 150 °C. Carbons with such groups on the surface adsorb acids from solution. Basic properties of the groups may differ from case to case since the groups are strongly influenced by π-electrons from the system of aromatic (graphitic) rings to which the groups are bonded or incorporated. The proposed growth mechanism assumes the evolution of CO_2. It means in practice a slow, low temperature burning of carbon. This statement may be confirmed by the well-known phenomenon of self-ignition of some carbon-rich substances like black coal. Basic groups can be also created at elevated temperatures (usually above 800–900 °C) if carbon is in contact with limited amounts of oxygen.

Carbon surfaces are oxidized when in contact with oxygen at intermediate temperatures (150–800 °C). Thus, simple heating of a carbon sample in air above 300 °C may dramatically change the chemical structure of its surface. Moreover, oxygen atoms may react with carbon atoms when they are subjected to the action of other oxidising agents in gas (ozone) or in liquid phase (wet chemistry oxidants like $Cr_2O_7^{2-}$, ClO_4^-, ClO^-, H_2O_2, HNO_3, NO_3^-). Wet oxidation is limited by the boiling point of water, which is the major component of the oxidising mixtures. To be effective, wet oxidation should be performed at 50–90 °C. Both treatments i.e., oxidation by O_2 at intermediate temperatures and wet oxidation in a warm solution create so-called acidic O-containing surface functional groups. Researchers have investigated a number of structures including: Carbonyl (quinone type), carboxyl, phenolic hydroxyl, carboxylic anhydride, and lactone (normal and fluoresceine type, see Fig. 7).[8]

The acidic nature of the various structures may be experimentally tested in simple reactions with basic solutions. Boehm and other researches[9] established a set of standard base solutions to determine the acidity of a sample. These

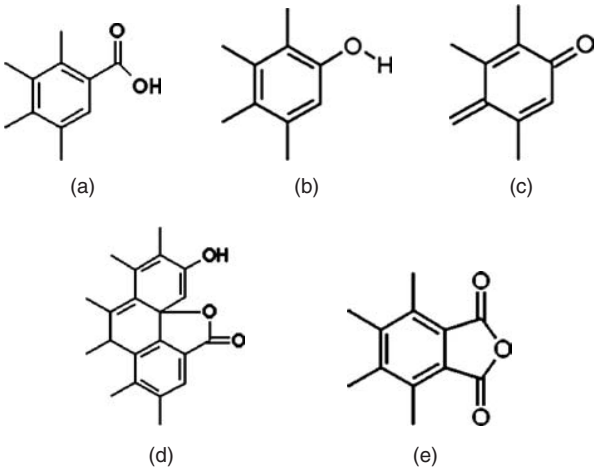

Fig. 7. The structure of acidic oxygen-based functionalities on carbon surface. Reprinted with permission from [8], J. S. Mattson and H. B. Mark, Jr., *Activated Carbon*, M. Dekker, New York **(1971)**.

are solutions of $NaHCO_3$, Na_2CO_3, NaOH, and C_2H_5ONa. The reagents neutralize surface functional groups of different acidity in a relatively selective way: $NaHCO_3$—carboxylic, Na_2CO_3—carboxylic, and lactone, NaOH—carboxylic, lactone, and phenolic, C_2H_5ONa—carboxylic, lactone, phenolic, and carbonyl. The results of acid-base titration enable determination of surface functional groups of a certain type. Beside that simple chemical method, a large number of advanced instrumental methods (FT-IR, XPS, NMR, EPR, TPD, thermogravimetry, electrochemical methods etc.,) can be applied for carbon surface characterization. One can also use additional reagents designed to react exclusively with a certain type of surface functional groups. Acetilation, methylation, reaction with hydroxylamine, $LiAlH_4$, diazomethane are in common use for this purpose. The reaction of surface groups with the reagents transforms the groups into new organic structures, which are detectable by means of chemical and instrumental methods. Regarding the differentiated electron structure of particular carbon atoms at the surface (radicals, broken bonds, interaction with π-electrons etc.,) and oxidising conditions (type of oxidant, phase of reaction, temperature etc.,) one may expect a variety of surface structures called as O-containing surface functional groups. Laszlo et al.[10] elaborated a diagram (Fig. 8) that additionally includes possible positions of radicals and electron pairs.

Oxygen is not the only element that is present in the bulk and surface carbon. Nitrogen is often responsible for specific (basic) surface properties of carbons due to the presence of N-containing surface functional groups. Nitrogen can be introduced to carbon matrix in two ways: As a residual element from a nitrogen-rich precursor or due to the secondary treatment of carbon with a nitrogen containing reagent like NH_3 at elevated temperatures above 1000 K. As mentioned above, oxygen

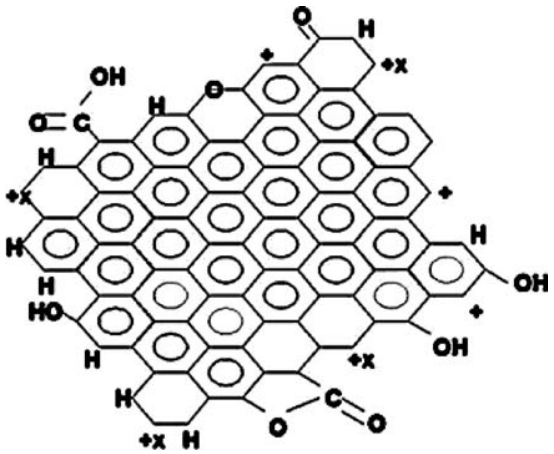

Fig. 8. Graphene bonded to different oxygen containing functional groups. Unpaired σ and localized π electrons marked as x+ and +, respectively. The graph follows the idea of Ref. [10], K. Laszlo et al., *Anal. Sci.* 17, i1741 **(2001)**. © 2001.

from air reacts with carbon atoms at the surface even at room temperature. Atmospheric nitrogen is an inert gas if brought to contact with the bare carbon surface at low temperatures. However, an oxidized carbon surface reacts with NH_3 even at room temperature yielding mainly ammonium salts—ONH_4 (reaction with hydroxyl—OH groups) and less amide—$CONH_2$ and imide—CO-NH-CO- derivatives. Carbonyl C═O groups react as shown in Figure 9.[11] Biniak et al.[12] investigated NH_3-modified carbons by means of several instrumental (XPS, FTIR, TPD-MS, mercury porosimetry) and chemical (acid-base titration) methods. The results are consistent with the above statements.

Nitrogen due to its electron structure is able to enter aromatic (graphitic) rings being built in the carbon matrix. That can happen if one treats a carbon surface (even not oxidized) with NH_3 at temperatures above 600 °C. The action of NH_3 changes also physical properties of carbons like developing their pore structure.

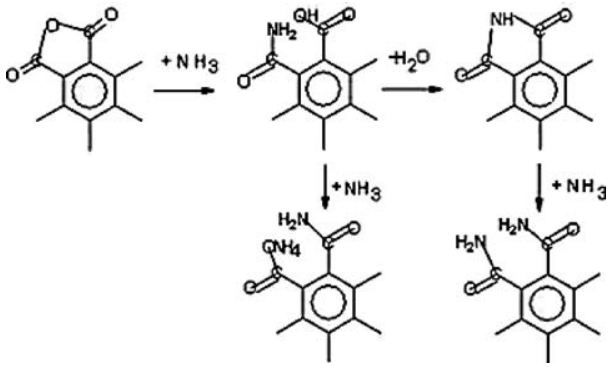

Fig. 9. The reaction pathway for the oxygen functional groups and ammonia according to the concept presented in Ref. [11], H. Jankowska et al., Adsorpcja jonów na weglu aktywnym (in Polish), PWN, Warsaw **(1991)**, p. 88.

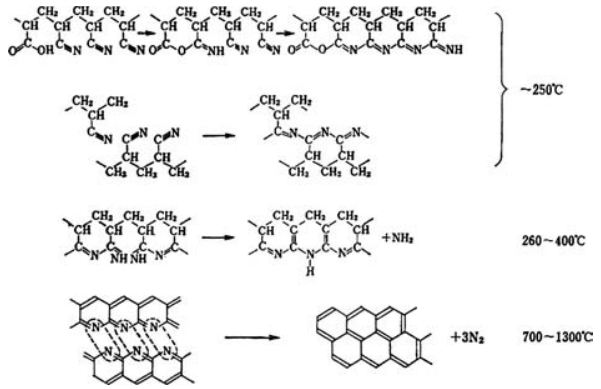

Fig. 10. Changes in the molecular structure of PAN at high temperatures. Reprinted with permission from [13], M. Inagaki, New Carbons. *Control of Structure and Functions*, Elsevier, Amsterdam **(2000)**, p. 88. © 2000, Elsevier.

Carbonisation of N-rich substances like some polymers poly(acrylonitryle—PAN and poly(imide)) yields carbons containing aromatic rings like in the case of poly(vinyl alcohol) or cellulose. Figure 10 presents the idealized mechanism of chain-to-ring transformation emphasizing the presence of nitrogen atoms.[13] Nitrogen atoms contained in the nitrogen surface functional groups exhibit nucleophilic properties that influence some catalytic reactions.

Contrary to O-containing and N-containing functional groups on the carbon surface, there are few papers published on S-containing functional groups. S-containing surface species are thermally stable and hardly decompose below 500 °C. Element sulphur cannot be extracted from S-containing carbons by means of aniline or CS_2. Beside residual sulphur atoms from carbonised precursor S-atoms can be introduced to carbons by heating of mixed carbon and sulphur particles above 100 °C or by reaction with vapour of sulphur. Moreover, one observed the transfer of sulphur from CS_2 vapours to carbon surface when the substances were in contact at elevated temperature. The action of strong oxidants in liquid phase removes sulphur as H_2SO_4 however some residual (oxidized) forms of sulphur remain on the carbon surface. Sulphur can be present on the carbon surface as sulfonic functional groups, SO_3H. The groups are polar and hydrophilic exhibiting strong acidic properties. One may also find papers describing methods for immobilisation of fluorine, chlorine, bromine, and iodine atoms on the carbon surface. The methods are usually based on the high chemical reactivity of these elements. Direct contact with the elements (gases or vapours) at elevated temperatures almost always causes direct reaction with carbon.

1.2.2. Ion Exchange

Some carbons exhibit a unique ability for the adsorption and durable bonding of ions (particularly cations). This

property may be utilized in two general ways:
(1) Application of carbons for purification of liquids from dangerous impurities like heavy metal cations.
(2) Controlled deposition of metal cations on the carbon surface to prepare chemically active materials, where implanted metal atoms (ionised or not) play the role of catalytic centres.

Accumulation of ions on a carbon surface may result from its exchange properties that are similar to the exchange properties of minerals (clays, zeolites) and polymer ion exchangers: The ions being exchanged must have the same type of electric charge, and the total electric charge taken by ions leaving the exchanger must be equal to the total electric charge brought by ions adsorbed from solution.

In the case of carbons, one has to specify sulfonic, carboxylic, and phenolic surface functional groups as possible centres of ion exchange. The groups are polar, easily dissociate in water and release proton H^+. In this way, cations from solution can take the empty places. One can prepare a carbon having such polar functional groups following some methods previously described. The content of metal in carbons subjected to ion exchange may be very different. Szymański et al.[14] prepared carbons modified by ion exchange of Zn^{2+}, Ni^{2+}, and Na^+ containing from 0.0278 mol/kg C to 0.654‘mol/kg C of these cations. In another paper,[15] one reported the introduction of metal cations like Mn^{2+}, Pb^{2+}, Cu^{2+}, Al^{2+}, Cr^{3+}, K^+ but the metal content was similar to that of Szymanski and co-workers.[14] One report specifies Fe^{3+} ion exchange on oxidised carbons with 9.2% atomic content of iron on the carbon surface.[16] The concentration of the ion exchange groups on carbons is often similar to the resin-based ion exchangers. Metal cations bearing more than a single positive elementary charge should interact with 2, 3, or 4 polar groups on carbon surface to keep electric neutrality of the adsorbent. It is not possible if the number of polar groups is too small within certain regions. In such a case the electric neutrality of the system is provided by the immobilisation of anions from solution in the adsorbed layer. Therefore, one should expect the presence of anions (sometimes undesired) when one tries to immobilize metal cations on the carbon surface.

In the case of carbons an additional bonding effect may appear due to mobile π-electrons that are present in the partly graphitised carbon matrix. Metal cations are bonded directly at carbon surface (without any assistance of functional groups) by the formation of coordination complexes where π-electrons from graphite rings play the role of ligands. The capability for such non-ionic immobilisation of metal cations is a specific property of carbons and does not occur in the case of mineral, polymer, and bio exchangers.

Since the adsorption of metal cations on carbons is a complex phenomenon, the affinity of the carbon surface to a particular cation depends on many factors. These factors may be divided into two basic categories: factors related to cation properties (electronic configuration, polarizability), and factors resulting from the conditions of ion exchange (concentration of metal cations, pH of the solution, advancement of ion exchange). Jankowska et al.[11] summarized the known experimental data and suggested that the affinity of metal cations to the oxidised carbon surface increases in the following order: $NH_4^+ < Na^+ < Rb^+ < Cs^+ < Mg^{2+} < Ca^{2+} < Ba^{2+} < Mn^{2+} < Co^{2+} < Sr^{2+} < Zn^{2+} < Fe^{2+} < Ni^{2+} < Pb^{2+} < Al^{3+} < La^{3+} < Y^{3+} < Cr^{3+} < Be^{2+} < Cu^{2+} < Fe^{3+}$. Since the metal cations adsorbed on carbon surface are under the influence of π-electrons their oxidation number can be changed. The change of oxidation state is particularly probable when the introduction of metal cations appears in the carbon bulk. Upon carbonisation, the metal cations are immobilised in the solidified organic precursor and later in the carbon matrix. The reductive influence of π-electrons is so effective that the implanted metal cation are reduced to lower oxidation states. Lukaszewicz[17] found experimental evidences that even cations of alkali metal are reduced to neutral atoms if they are implanted in the carbon matrix. Additional heating of carbons with deposited metal cation in an inert gas atmosphere causes reduction on metal cations to a metallic state. Wang and Lu[18] reported that after deposition of Ni^{2+} ions by immersing of carbon particles in water solution of $Ni(NO_3)_2 \cdot 6H_2O$ and its subsequent thermal treatment at 500 °C in N_2 part of nickel atoms was reduced to metallic state (XRD measurements). Molina-Sabio et al.[19] observed the reduction of copper and chromium ions upon the influence of carbon matrix. Metal cations on a carbon surface often act as active centres catalysing some chemical reactions. This function of deposited metal atoms is particularly important regarding possible sensor applications. Many semiconductor sensor materials are non-stoichiometric. In the case of tin dioxide, the non-stoichiometric character consists in the presence of domains where tin ions are reduced to lower oxidation states including Sn^0. Other modifications of SnO_2—based sensing materials consist in the introduction of metal particles (Pd, Pt, etc.).

Deposited metal cations on a carbon surface can be reduced to element metal atoms by a secondary chemical treatment like heating in a stream of hydrogen. In this manner, one can drive two basic effects:
(1) Reduction of O-containing surface species, and
(2) reduction of the deposited cations to its elemental form.

Numerous papers have been published on metal cation deposition on carbon surface and the influence of the cations on catalytic properties of so modified materials. The reactions that are catalysed by carbon having metal ions/atoms on its surface are listed in Table I. Other catalytic reactions involving metal particles deposited on carbon were reviewed by Auer.[20] Some of these reactions might be applied for the construction of a chemical sensor

Table I. Chemical reactions catalysed by means of carbons containing metal cations and/or atoms.

Carbon	Metal	Catalysed reaction	Phase
From poly(furfuryl alcohol)	Zn^{2+}, Ni^{2+}	Dehydration and dehydrogenation of n-butan-2	Gas
	Oxygen-containing functionalities	Dehydration of 2-methylpropan-2-ol	Gas
	Ni^{2+} oxygen-containing functionalities	Methane reforming with CO_2	Gas
	Fe^{3+} oxygen- and nitrogen-containing functionalities	NO_x reduction	Gas
	oxygen-and nitrogen-containing functionalities	NO_2 reduction	Gas
	oxygen- and nitrogen-containing functionalities	O_2 reduction	solution
Graphite single layers	metallic Pt	Oxidation of H_2	Gas
active carbon	oxygen-containing functionalities	Oxidation of H_2S	Gas

but we have found no reports in the literature that such an idea has been realised. Catalytic removal of SO_x by means of a carbon-supported catalyst is a good example of a potentially useful reaction. Mochida et al.[21] presented the mechanism of H_2SO_4 formation from adsorbed SO_2 molecules. The presence of H_2SO_4 molecules should considerably influence electric conductivity of the whole system (carbon surface under the influence of SO_2) since the molecules of sulphuric acid dissociate and contribute to charge transfer through the sample, see Figure 11.

1.2.3. Intercalation Compounds

Intercalation compounds are a specific group of carbon-based substances. Intercalation consists in the insertion of heteroatoms, ions, or molecules between the layers of graphite by an appropriate chemical treatment.

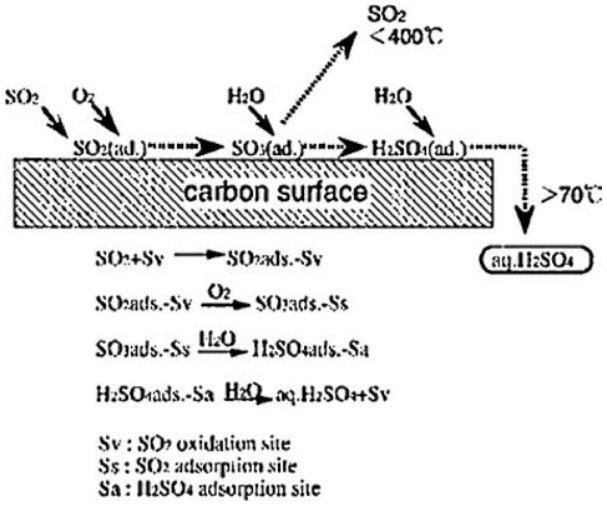

Fig. 11. The mechanism of SO_2 removal over the carbon surface. Reprinted with permission from [21], I. Mochida et al., *Carbon* 38, 227 (2000). © 2000, Elsevier.

The insertion is a result of one of three basic methods:
(1) Intercalation by the action of intercalate vapour at elevated temperatures.
(2) Intercalation by direct reaction between graphite and the intercalate at elevated temperature.
(3) Intercalation by the action of dissolved intercalate (wet method).

Frequently, the proportion between carbon atoms and the number of inserted heteroatoms or molecules is constant. In such a case, the whole system is treated as a stoichiometric compound. The formulas like KC_8, KC_{24}, or $(CF)_n$ are in frequent use. Intercalates and graphite layers can exchange electric charges between them. Inagaki [1]reviewed several examples of such transfer classifying numerous intercalates as donors (Li, Na, K, Rb, Cs, Ca, Sr, Ba, and other metals), acceptors (F, Br, ICl, IBe, IF_5, $FeCl_3$, $NiCl_2$, $AlCl_3$, AsF_5, SbF_5, CrO_3), and intercalates incorporated by coordination bonding. Parallel insertion of two kinds of intercalates is also possible. Intercalation compounds exhibit several unique properties enabling particular functions. One may obtain highly conductive materials, electrode materials (including lithium batteries), catalysts and adsorbents for gas storage. In addition, simple aliphatic hydrocarbons (methane, ethane, propane, *n*-butane, *n*-pentane, etc.) can be accumulated by some intercalation compounds. The process of hydrocarbon adsorption proceeds at elevated temperatures from 90 to 350 °C and is reversible. This property might be applied to mass-sensitive chemical sensing devices.

1.3. Chemical Functionalization of Carbon Nanotubes

Fuctionalization is one of the most important steps in the fabrication of carbon materials for chemical sensors. The specific surface composition of carbons determines phenomena such as adsorption and catalysis, which are essential for the successful detection of chemical

substances. The observed progress in the application of carbon nanotubes to chemical sensing is in part based on some chemical manipulations run on this kind of carbon. One may assume that the further steps in this domain of science will rely on chemical manipulations since the application of bare CNTs seems to be quite limited.

1.3.1. Oxidation of CNTs

The oxidation of CNTs seems to be one of the most important chemical manipulations to be performed on the tubes. Except diamond, the remaining carbon allotropes are characteristic because of the presence (sometimes very limited) of conjugated aromatic rings. Therefore, aromatic rings-containing carbons are predestined to react with electrophilic substances like oxygen, chlorine, fluorine, and free radicals. Carbon in form of SWCNTs or MWCNTs becomes rather easy oxidized in "wet" chemistry processes such as HNO_3 treatment in the presence of H_2SO_4. Kuznetsova and co-workers[22] reported that such treated SWCNTs can incorporate up to 6.7% wt of oxygen, which they assigned to the existence of surface functional groups of carboxyl (–COOH), carbonyl (C═O) and ether (C–O–C) structure at the tube edge. These groups were thermally stable up to 600 °C. Oxygen-containing species were also present at the defect sites like in other carbon materials. The functionalities were removable by an appropriate heat-treatment; heating to 800 °C led to the release of low mass products like CO, CO_2, CH_4, and H_2,[23] with the thermal desorption opening the terminal openings to enhance access to the CNT interior.

Room temperature adsorption of oxygen on CNTs was reported by Collins and co-workers.[24] The report implied the application of the discovered phenomena to the construction of an oxygen sensitive resistor. One found a reversible decrease of electric resistance of SWCNTs-based resistor when it was exposed to a cyclic change from air to vacuum at room temperature (Fig. 12). The results were explained on the same principles as in the case of NO_2 and NH_3 adsorption on *p*-semiconductor SWCNTs. Thus, oxygen was treated as an electrophilic medium. The longer (and frequent) was the exposure to oxygen the more difficult was the recovery of the starting value of CNTs resistance at room temperature. Heat-treatment in vacuum at 110–150 °C led to the expected renewal of the starting properties of CNTs. That indicated the tendency to a slowly proceeding chemisorption of oxygen. The resistance-based observations were supported by the changes of thermoelectric power. The first investigated samples were *p*-type semiconductors but they changed dramatically after an intensive oxidation of SWCNTs. After the treatment, the samples behaved like apparent metallic conductors.

A question may arise how to determine the acidity of CNTs containing oxygen functionalities. Hu et al.[25] investigated acid-base properties of SWCNTs of that kind. The

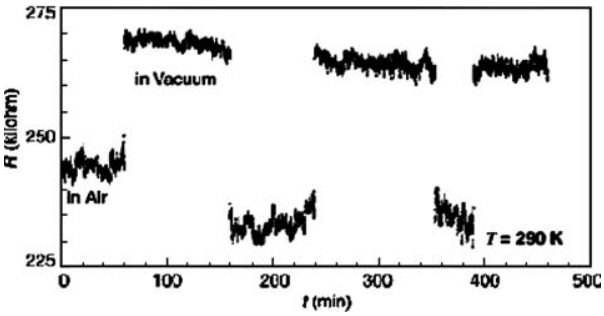

Fig. 12. Sensitivity of the electrical resistance *R* of SWCNT to gas exposure at a temperature (*T*) of 290 K. The nanotube resistance switched by 10 to 15% as the chamber surrounding the sample was alternately flooded with air or evacuated. Identical results were obtained if pure dry oxygen was used rather than air, indicating that oxygen was the source of the effect. Likewise, changing the chamber purge gas between oxygen and any inert gas resulted in similar stepwise changes in *R*. Reprinted with permission from [24], P. G. Collins et al., *Science* 287, 1801 (**2000**). © 2000, AAAS.

method was based on the assumption that the standard method of Bohem, applied widely for other carbon materials, was also applicable to CNTs. Thus, authors employed NaOH and $NaHCO_3$ solutions to determine the total acidity of oxidised sites (NaOH titration) and the content of –COOH groups ($NaHCO_3$ titration). It was found that commercially available SWCNTs contained up to 3% acidic sites that responded to the titration with NaOH. Moreover, almost the whole acidity could be ascribed to –COOH groups. Thus, the acid-base behaviour of oxygen functionalities on CNTs did not differ much from analogous groups on other carbon materials.

The action of fluorine leads to direct reaction between F and C atoms in CNTs. Lee et al.[26] tried to functionalise SWCNTs by treating them with fluorine (direct action on bare tubes). The temperature of the treatment was set at 150–300 °C. At the latter temperature the F/C ratio reached the value of 0.65. XPS investigations revealed a subsequent reduction of the number of sp^2 hybridized carbon atoms. The effect was attributed to the carbon atoms at the ends of the tubes. Extended fluorination led to the formation of $–CF_2$- and $–CF_3$ groups due to breaking of carbon–carbon bonds. The electric conductance of fluorinated SWCNTs decreased substantially which was ascribed to an electron transfer from the tubes to fluorine atoms. Fluorination positively influenced the solubility of CNTs in alcohols and other solvents.

1.3.2. Metallization and Deposition of Metal Oxides

Metal cluster modified CNTs are of interest for chemical sensing since some metals (as well as their oxides) are regarded as catalyst for many reactions potentially to be employed in sensor operation. Deposition of metal particles on the walls of CNTs and filling them with metal particles or wires were one of the most important problems

solved by groups working on novel carbon materials. Metal or metal oxide introduction to CNTs can be divided into two general categories: insertion and encapsulation. Insertion is when the modifying substance is immobilised inside (or outside) already exiting CNTs. Encapsulation is the process in which CNTs either grow around modifying particles or are synthesised parallel with crystallization of modifiers. Several methods have been announced so far; Chen and co-workers[27] reported a successful application of three basic approaches to solving the problem, so called:
(1) one-step,
(2) two-step, and
(3) two-step by means of metal complexes.

The one-step method of insertion consists of heating MWCNTs in a mixed solution of HNO_3 (azeotropic solution ca. 68% wt) and a metal nitrate. Nitric acid due to its oxidative properties opened the tubes by cup removal at the ends of MWCNTs. Beside that, the action of nitric acid removed some impurities from CNTs like amorphous carbon particles and catalyst residuals. Parallel to the process of MWCNTs "decapitation," ions from the dissolved metal nitrate could penetrate the inner space of CNTs and crystallize after drying. Then, one needed to reflux the excess reactants with water. Subsequent calcination at 400–500 °C of such treated samples in an inert gas atmosphere transformed the deposited metal nitrates into corresponding metal oxides (Fig. 13). At this stage, such treated tubes were in fact metal oxide-modified CNTs and the whole process could be terminated if one intended to synthesise that kind of modified CNTs. A further reduction of oxide-modified CNTs was possible upon hydrogen treatment at 400–500 °C. In this way, metal oxide particles were reduced to metal particles. The one-step insertion was also helpful for filling CNTs with complex oxides like perovskite-type oxides (Table II). That was possible provided the primary modifying solution contained (beside concentrated nitric acid) a stoichiometric mixture of appropriate metal nitrates (dissolved). Heat treatment in an inert gas atmosphere led to crystallization of the complex oxides.

The two-step method of insertion was applicable for filling CNTs with materials (or their derivatives) that were not soluble in water or were not resistant to the action of water vapour, oxygen, carbon dioxide, and HNO_3. The merit of the two-step method consisted in the separation of tube opening from the filling of CNTs with modifying chemicals. Thus, the combined opening and purifying of CNTs by concentrated HNO_3 was the first step. The oxidative treatment of HNO_3 created oxygen functionalities (mostly –COOH and –OH) at the open ends of CNTs. The functionalities blocked the entrance to the interior of the MWCNTs. Therefore the groups often had to be removed by a heat treatment in a stream of inert gas or in vacuum (900–1000 °C) in which the groups were removed and the species like CO_2, CO, H_2O evolved. Such cleaned

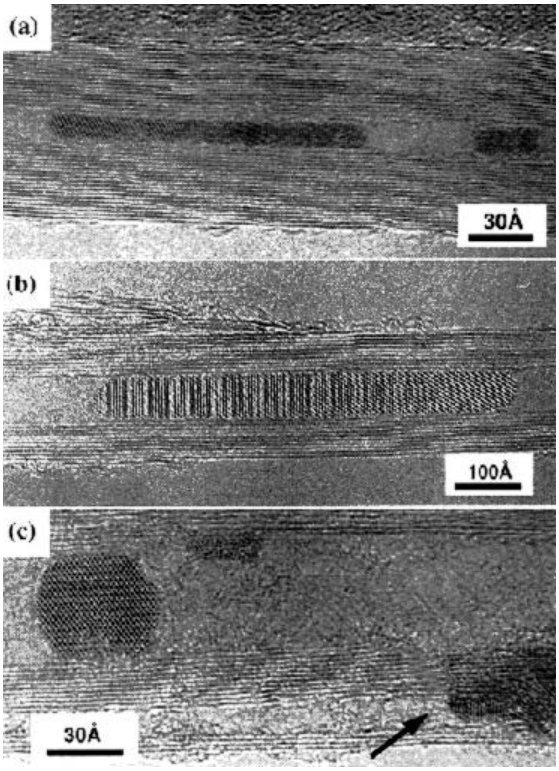

Fig. 13. (a) Nanotube filled with nickel material; the observed fringes of 2.4 ± 0.05 Å correspond to the distance between the (111) planes in NiO. (b) Encapsulated single crystal of Sm_2O_3 with two sets of metal fringes seen inside a carbon nanotube. The Sm_2O_3 lattice fringes 90° to the nanotube wall correspond to the (400) lattice planes of Sm_2O_3. (c) Nanotube containing cavity intercalated crystalline Nd_2O_3 (in the bore of the nanotube) and intralayer intercalated Nd_2O_3 (arrowed). Reprinted with permission from [27], Y. K. Chen et al., *J. Mater. Chem.* 7, 545 **(1997)**. © 1997, Royal Society of Chemistry.

Table II. The list of encapsulated metal and metal oxide particles.

Encapsulated or inserted substance	Starting materials
La_2O_3	$La(NO_3)_3\ 6H_2O$
Pr_2O_3	$Pr(NO_3)_3\ 6H_2O$
CeO_2	$Ce(NO_3)_3\ 6H_2O$
Y_2O_3	$Y(NO_3)_3\ 5H_2O$
Nd_2O_3	$Nd(NO_3)_3\ xH_2O$
Sm_2O_3	$Sm(NO_3)_3\ 6H_2O$
$FeBiO_3$	$Fe(NO_3)_3\ 9H_2O + Bi(NO_3)_3\ 5H_2O$
UO_{2-x}	$UO_2(NO_3)_2\ 6H_2O$
NiO	$Ni(NO_3)_2\ 6H_2O$
MoO_3	MoO_3
MoO_2	MoO_3
ZrO_2	$ZrCl_4$
ZrO_2	$ZrO(NO_3)_2\ xH_2O$
Re	$KReO_4$
Pd	$Pd(NO_3)_2$
Ag	$AgNO_3$
AuCl	$5AuCl_3$
Au	$AuCl_3$
CdO	$Cd(NO_3)_2\ 4H_2O$
CsS	$CdO + H_2S$

Source: Reprinted with permission from [27], Y. K. Chen et al. *J. Mater. Chem.* 7, 545 **(1997)**. © (2005), Royal Society of Chemistry.

CNTs could be brought to contact with the filling substances since there were no geometric and chemical (possible reaction with O-containing functionalities) obstacles. The filling substance could be applied in molten state. The filling could be followed by the measures described in the case of the one-step method, i.e., calcination or calcination with subsequent reduction to achieve metal oxide particles or metal particles respectively.

There was a substantial difference in the form of the modifying substances after their introduction to CNTs, which was dependent on the form of filling substance. The application of solutions resulted in the formation of small (1–5 nm) metal and metal oxide particles while molten modifiers often produced long, continuous metal and metal oxide crystals (wires). Rao et al.[28] also obtained metal wires in SWCNTs by the contact of the tubes with molten salts and subsequent reduction with oxygen. Surface tension of molten modifiers is the main obstacle hindering the process of modifier infiltration when the surface tension is too high. If high surface tension of a molten modifier excluded its application in the way described above, other metal insertion could be employed in the second step. After opening and the removal of O-type functionalities, CNTs were subjected to the penetration by metal complexes in solution. Subsequent calcination or calcination followed by reduction transformed the introduced complexes in metal and metal oxides as formerly mentioned. In general, the above described methods result in the filling of the interior of CNTs with desired species. In some cases on observed the penetration of the interlayer spaces in MWCNTs and subsequent bulge of the materials i.e., the inter lattice distance increased from 0.34 nm to 2 nm.

Liu and co-workers[29] synthesised CNTs decorated with well-dispersed Co particles. The CNTs were obtained by the method of C_2H_2 (in N_2) decomposition over Co catalyst first deposited onto a SiO_2 substrate. Such obtained MWCNTs were treated with a concentrated solution of HNO_3, rinsed and then subjected to impregnation with $Co(NO_3)_2$. The sample was calcinated at 480 °C and reduced with H_2 at 420 °C. Apparently, the route was similar to the two-step method of internal metallization of CNTs described previously but there was one significant difference. There was no step in which the oxygen containing functionalities (certainly present after the HNO_3 treatment) were removed. Thus, the functionalities remained. As in the case of polycrystalline carbons the –COOH and –OH groups are capable for ion exchange. The same groups may be expected at the open ends of oxidized CNTs or defect sites. Liu and co-workers found in TEM investigations that the synthesised MWCNTs and later oxidized tubes had numerous defects at the walls (Figs. 14 and 15).

Some reports suggest[30] the formation of metal particles started from the open end of CNTs and proceeded towards the central part of the tubes. The results obtained

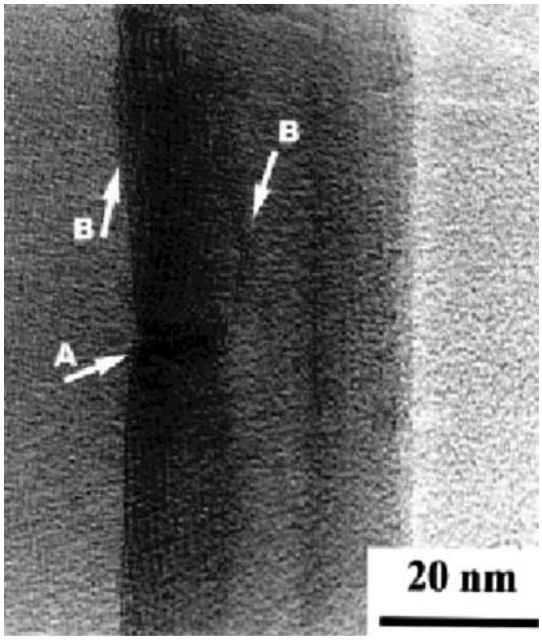

Fig. 14. HRTEM image of a CVD-grown carbon nanotube with defects. Arrow A points out a topological defect and arrows B indicate incomplete graphitic layers. Reprinted with permission from [29], Zong-Jian Liu et al., *Phys. Chem. Chem. Phys.* 3, 2518 (**2001**). © 2001, Royal Society of Chemistry.

by Satishkumar et al.[31] are consistent in full with the above conclusion. The authors achieved a perfect distribution of metal particles (Au, Ag, and Pt) deposited on the oxidized (HNO_3 treatment) SWCNTs by simultaneous reflux with NHO_3 and $HAuCl_4$ (or H_2PtCl_6, $AgNO_3$), and subsequent reflux first with HNO_3 and then with $HAuCl_4$ (or H_2PtCl_6, $AgNO_3$). In this case (MWCNTs), the metal particles were situated outside the tubes. It is to remember that the result reported for SWCNTs claimed an internal metallization of the tubes. It might be a result of different internal diameter of the MWCNTs and SWCNTs. Probably the wider was the tube the easier was metal insertion in the cavity of CNTs. The second method produced also small Au particles but much more uniformly scattered along the tube (Fig. 17). Another method involved the admission of ethylene glycol to the Pt-, Au-, and Ag-containing solution. The yield of metal particles was higher since ethylene glycol acted as a reductor (Fig. 18). The deposited Pt particles were small and of uniform size (ca. 2 nm). Chen and co-workers[27] proved that other species could be deposited in the cavities of CNTs. They transformed the encapsulated metal oxides not only in element metals (reduction by the hydrogen treatment described) but it was possible to change them in metal sulphides under the action of H_2S. For instance, one got CdS by the transformation of CdO.

Metal and their derivatives can be introduced in the CNTs cavity by encapsulation achieved by a modification of the standard arc discharge method of CNTs synthesis. The modification consists in the introduction of metals or

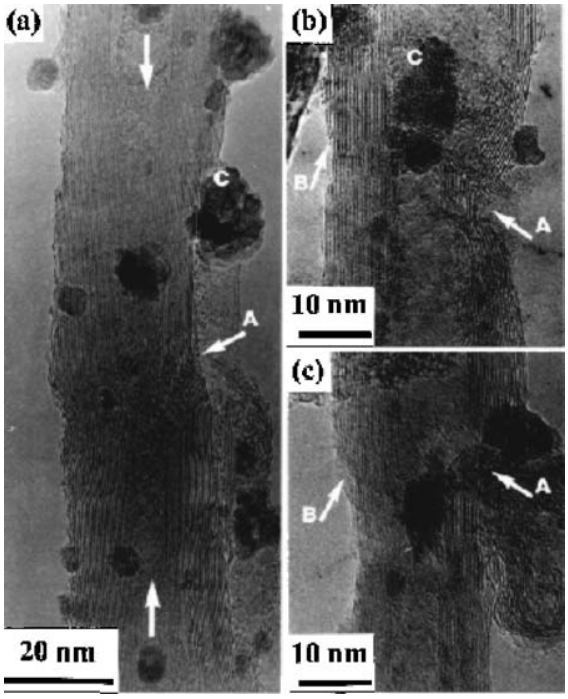

Fig. 15. HRTEM images of Co-deposited carbon nanotubes oxidized by nitric acid. Arrows A indicate the corroded regions and arrows B indicate the open edges of graphitic sheets. (a) A nanotube with its internal diameter decreasing from both the ends along the nanotube axis indicated by two arrows in the middle of the nanotube. (b) Both outer and inner walls of nanotubes after being attacked by nitric acid. (c) A thinned nanotube with a hole in the right side wall. Reprinted with permission from [29], Zong-Jian Liu et al., *Phys. Chem. Chem. Phys.* 3, 2518 **(2001)**. © 2001, Royal Society of Chemistry.

metal derivatives to graphite electrodes, which are employed for lighting the arc. The vaporized electrode (anode) material contains carbon and metal atoms that later can deposit in form of metal filled CNTs. Moreover, the formation of metal carbides also occurs. This method of CNTs metallization seems to be less controllable and less flexible than the presented wet chemistry methods.

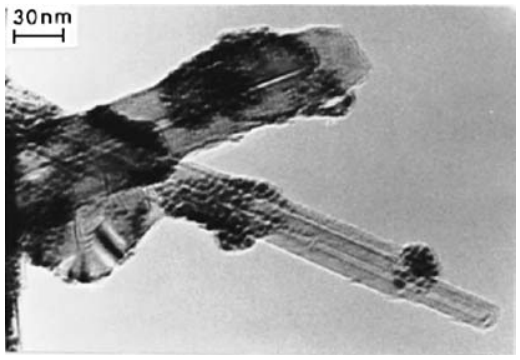

Fig. 16. A TEM image of pristine nanotubes with agglomerated gold particles. Reprinted with permission from [31], B. C. Satishkumar et al., *J. Phys. D: Appl. Phys.* 29, 3173 **(1996)**. © 1996, Institute of Physics IOP Publishing Ltd.

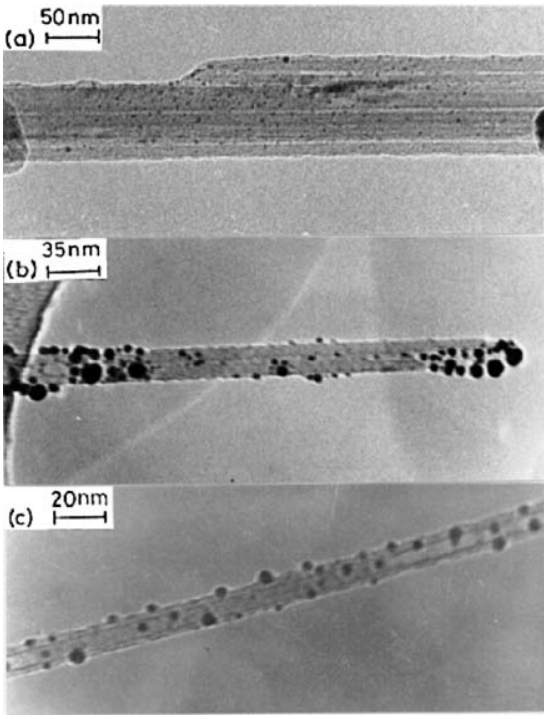

Fig. 17. TEM images of nanotubes decorated by Au nanoparticles; decoration carried out (a) by refluxing with $HAuCl_4$ and HNO_3, (b) by refluxing acid treated nanotubes with $HAuCl_4$ and THPC and (c) by the same procedure as (b) except with mild sonication. Reprinted with permission from [31], B. C. Satishkumar et al., *J. Phys. D: Appl. Phys.* 29, 3173 **(1996)**. © 1996, Institute of Physics IOP Publishing Ltd.

The arc encapsulation of metal was described by Sloan and co-workers.[32] According to numerous quoted literature announcements almost half the elements in the Periodic Table have been introduced into CNTs by the

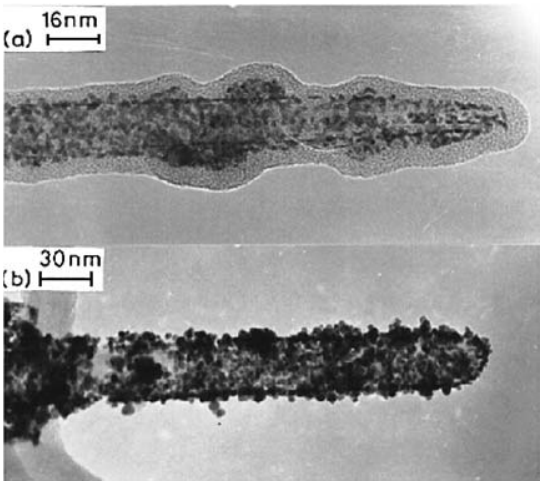

Fig. 18. TEM images of nanotubes decorated by Pt nanoparticles: Decoration carried out (a) by refluxing with H_2PtCl_6 and HNO_3 and (b) by refluxing with H_2PtCl_6 and ethylene glycol. Reprinted with permission from [31], B. C. Satishkumar et al., *J. Phys. D: Appl. Phys.* 29, 3173 **(1996)**. © 1996, Institute of Physics IOP Publishing Ltd.

method: Lanthanides, the first row of transition metals, the platinum group, the main group elements (see references in the review paper).

Metallization of CNTs often occurs during pyrolysis. Bladh and Rohmund[33] fabricated SWCNTs by the catalytic decomposition of a mixture of gases on iron catalyst particles (1000–1100 °C). The mixture consisted of CO, C_2H_2, and H_2. Carbon monoxide was additionally saturated with $Fe(CO)_5$ to the concentration of few ppm. The obtained SWCNTs were characteristic because of iron particles that were encapsulated in the tubes and covered by several graphite layers. The insertion of metal particles into the tubes hinders their direct contact with environment. Therefore, their influence on sensing processes may be questionable. The addition of hydrogen to the gas mixture increased the yield of CNTs due to the reaction: $CO + H_2 \rightarrow H_2O + C$, that supported the standard reaction responsible for the growth of CNTs: $CO + CO \rightarrow C + CO_2$.

Chen and co-workers[34] investigated alkali metal-modified MWCNTs. The nanotubes were obtained by a standard method of catalytic decomposition of methane. The investigated CNTs were then purified from catalyst residuals. After that, the tubes were subjected to the modification with Li and K atoms. The metals were inserted by a solid-state reaction between the nanotubes and lithium (or potassium)-containing compounds like carbonates and nitrates. The basic physical properties of the modified MWCNTs were as follows: Specific surface area ca. 130 m^2/g, density below 1 g/cm^3 (lithium doped). The Li/C and K/C atomic ratios were close to 1/15. Such CNTs were subsequently heated and cooled down to room temperate in H_2 stream. One noticed outstanding hydrogen uptake reaching 20% wt (Li-MWCNTs) and 14% wt (K-MWCNTs) at hydrogen pressure of 1 atm. Comparative samples of Li- and K-modified graphite exhibited a considerable lower affinity to hydrogen i.e., only 35–70% of the H_2-uptake recorded for the modified CNTs. Authors additionally investigated the mechanism of hydrogen adsorption with particular attention to the role of inserted lithium and potassium atoms. It was found basing on FTIR investigations that Li–H bonding preceded the formation of C–H bonds. The dissociative adsorption of H_2 molecules was assumed as the first stage flowed by a spill over of hydrogen atoms. This step was followed by the reaction of atomic hydrogen with carbon atoms in MNCNTs. Thus, lithium atoms were considered as catalytic sites for the formation of atomic hydrogen (in adsorbed form). XRD investigations revealed the formation of CH_x due to the reaction between hydrogen atoms and carbon atoms. It was shown that alkali metals significantly increase the adsorption of hydrogen on modified CNTs. The phenomenon might be applied in mass sensitive devices, however the presented way of hydrogen capture needed elevated temperatures (ca. 500 °C). Such a high temperature is not acceptable by the mentioned mass-sensitive devices as well as the long saturation time (1–2 hours). Fortunately, the K-modified materials could adsorb hydrogen at room temperature. The formation of carbon–hydrogen species on the surface of CNTs may modulate the electric properties of the tubes. That might be a good foundation to employ such modified CNTs as chemiresitors sensitive to hydrogen. Thus, the modification by alkali metals yields interesting material, which has been not intensively explored in sensor research.

Metal oxides can be deposited not only inside CNTs but can cover the walls of the tubes, too. Han and Zettl[35] reported a simple room temperature rout to the functionalization of SWCNTs by covering them with 3–6 nm thick layer of SnO_2. The method is based on the oxidation of Sn^{2+} ions first adsorbed on the walls of the tubes from the solution of $SnCl_2$. The mechanism of SnO_2 formation on the tubes was supposed to be based on the process: $2SnCl_2 + 2H_2O + O_2 \rightarrow 2SnO_2$ 4HCl. Surprisingly the procedure did not need any calcinations at elevated temperature and simple drying in air at room temperature was enough for the formation of oxide coating (Fig. 19).

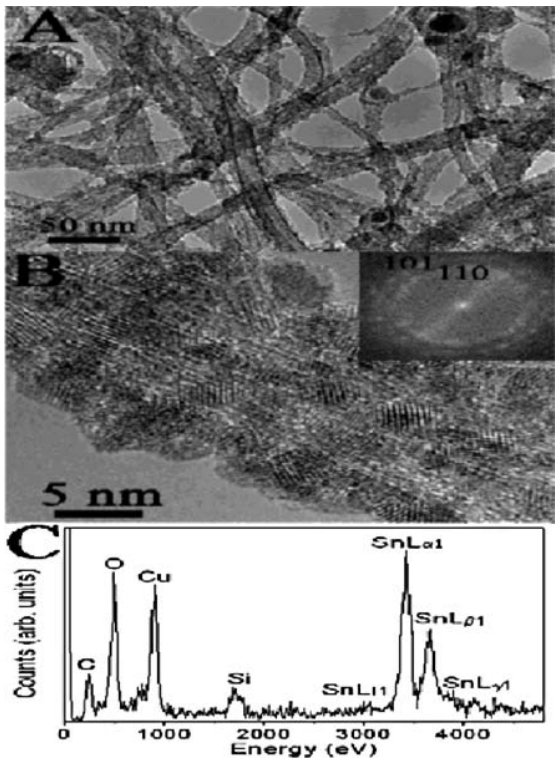

Fig. 19. (A) Low-resolution TEM image of fully coated SWCNTs. (B) High-resolution TEM image of a SWCNT bundle fully coated with SnO_2. The inset is the corresponding FFT diffraction pattern. The three polycrystalline rings correspond to crystal faces of (110), (101), and (200) of tetragonal SnO_2. (C) Typical EDS spectrum of SnO_2-coated SWCNTs. The atomic ratio of O to Sn is near 2. Reprinted with permission from [35], Wei-Qiang Han and A. Zettl, *Nano Lett.* 3, 681 **(2003)**. © 2003, American Chemical Society.

1.3.3. Other Chemical Manipulations

Chemical manipulation of CNTs are not limited to oxidation, metallization, and the deposition of metal oxides. There is long list of other manipulations that are usually performed aiming at better affinity of the tubes to selected substances like water and organic solvents. As will be discussed, the sensing performance of CNTs depend strongly even on non-covalent functionalization.

In the extended report of Seo and co-workers[36] one can find a description of several chemical and physical manipulations of CNTs. Beside widely presented methods for inorganic coating of CNTs (inorganic coating with derivatives of Al–, Ti–, Mg–, and Si– by means of metallorganic and inorganic reactants), one can learn of sidewall covalent alkylation of the tubes that exhibit two basic properties: High affinity towards non-polar organic solvent which eases any further manipulation in such solvents, and susceptibility of the attached alkyl or aryl chains to further chemical modifications. This opens the way for tailoring of basic chemical and physical properties of the modified CNTs. For example, Lim and co-workers[37] elaborated a route to functionalise SWCNTs in which thionyl groups are introduced at the end of the tubes later employed to attach noble metal particles due to the strong affinity of organic thionyl derivatives to metals (Fig. 20). In some other experiments it was shown that –SH groups were isolated from CNTs by long alkyl chains.[38] The phenomenon of CNTs immobilisation on metal surfaces is potentially important for manufacturing of chemical sensors in particular for fabrication of selective electrodes.

Even the alignment of CNTs may be regarded as a kind of functionalization affecting the surface properties of CNTs. Qikun et al.[39] ran amperometric studies on H_2 storage on CNTs obtained by various methods. One investigated CNTs obtained by the arc discharge method, CVD method (C_2H_2 decomposition on an iron catalyst on a Si substrate) and catalytic decomposition of Fe(II) phthalocyanine (self-catalysed decomposition). The results obtained for H_2 adsorption (room temperature, atmospheric pressure) revealed a slow but intensive hydrogen adsorption on the CNTs fabricated by the later method. The maximum hydrogen storage capacity exceeded 8% by weight. Authors quoted reference[40] where one investigated the influence of CNTs alignment on the hydrogen uptake and stated that high hydrogen storage capacity occurred preferable on well-aligned CNTs. In such a case, strong Van der Waals interactions between the tubes positively influenced the adsorption of hydrogen. The adsorption of hydrogen, as concluded from the run of hydrogen uptake curves (Fig. 21) was dependent on the layer structure of the examined MWCNTs.

Sometimes functionalization is used to ease further manipulations with CNTs. Star and co-workers[41] described a route for fabrication of hydrophilic CNTs without any covalent functionalization. Such a non-covalent functionalization does not impair the original properties of CNTs. They adapted the idea originally proposed for the functionalization of fullerenes with cyclodextrines. The method involved sonication of a dispersion containing starch-iodine complex and SWCNTs. The merit of the synthesis consisted in the displacement of I_2 (placed inside a left-handed helix of amylose) by SWCNTs as depicted in Figure 22. The amylose molecules wrap around the tubes allowing stable dispersion of SWCNTs in water. The process seems to be selective to CNTs. Moreover, Star and co-workers showed that the process was reversible and the SWCNTs-amylose complex was destroyed by the hydrolytic action of an enzyme (amyloglucosidase from Rhizopus mold, see Fig. 23).

Zhao et al.[42] proposed another route to functionalise SWCNTs by the attachment of polymer chains to carboxylic groups at the open ends. The process was based on the application of oxalyl chloride to transform –COOH groups into reactive acyl chlorides. The derivatized groups served to anchor polymer chains of poly(m-aminobenzene sulfonic acid)—PABS (Fig. 24). In this way the hydrophobic virgin SWCNTs were changed into a hydrophilic solid due to the polar groups ($-SO_3H$) occurring along the attached chains. The new hydrophilic properties were very helpful for dispersing CNTs in water and other polar solvents. PABS is only one of many possible modifying polymers. According to Zhao and co-workers, the following polymers can be bonded to CNTs, see Table III. An interesting feature of oxygen functionalised CNTs was reported by Sano and co-workers.[43] The oxygen containing functionalities (particularly –COOH groups) at the ends of SWCNTs were forced to condensate that led to the formation of CNT-based rings as presented in Figures 25 and 26. Dicyclohexylcarbodiimide (DCC) was the reagent used to close the CNT-ring by easing the condensation of –COOH and –OH groups. It was also found that the length of SWCNTs prior to the formation of ring had a crucial influence of the process, i.e., if the SWCNTs were shorter than 1 μm only few rings formed. So far, no report has appeared on the application of such cyclic CNTs to chemical sensing where only surface effects may contribute to sensing mechanism and the influence of inner space is excluded.

1.4. Porosity of Carbons

Porosity is an important factor in sensor research since it may positively or negatively influence the sensing properties of a material. Using the term "porosity" in the review one should concentrate on so called open pores, i.e., vacancies in a solid material that are open to environment. Internal vacancies exist in solids but they are of secondary importance. Pores directly influence the adsorption abilities of a solid. Dubinin and other researchers[44] proved that molecules in pores are subjected to much

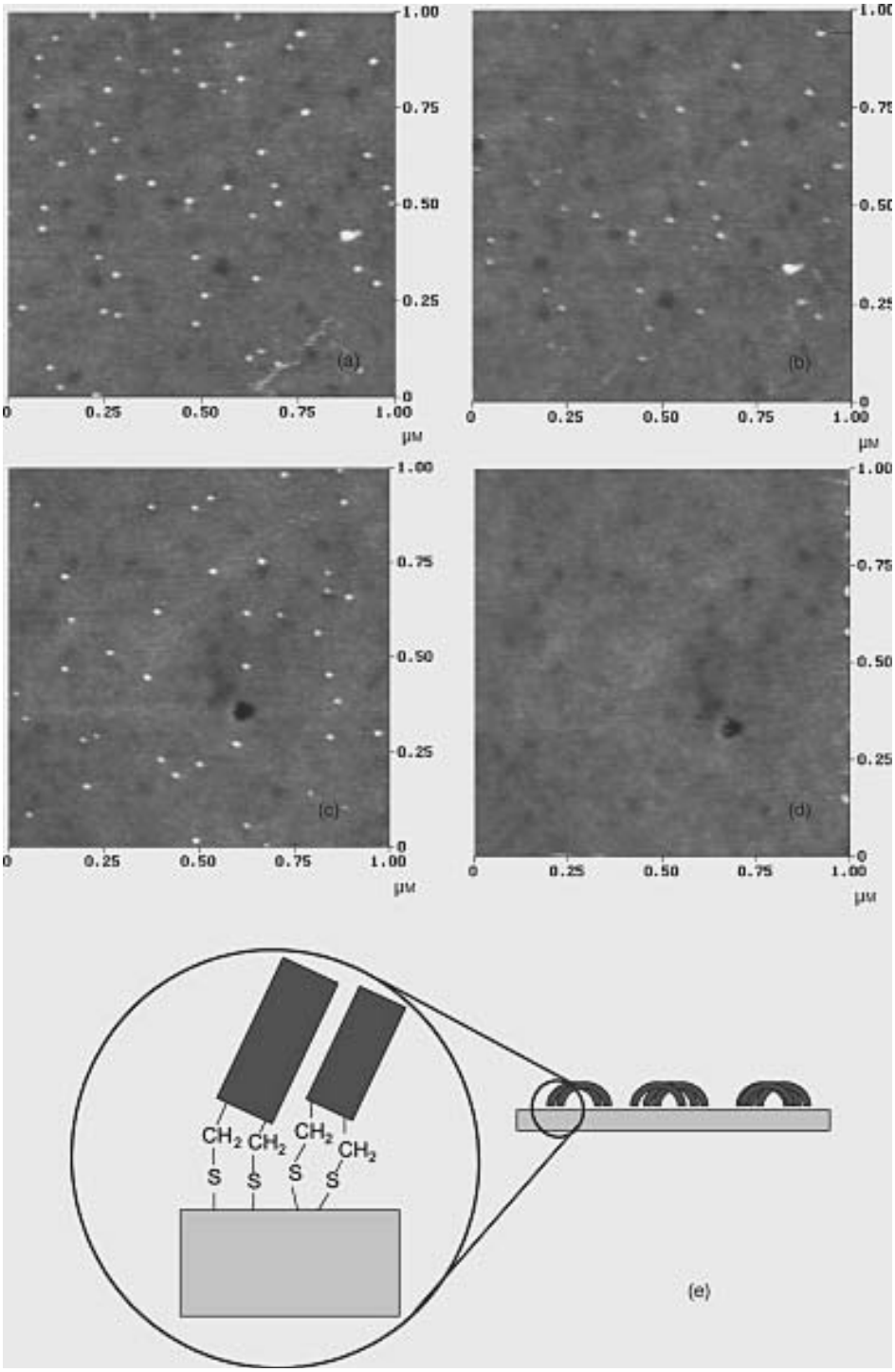

Fig. 20. The AFM images of thiolated CNTs on a gold surface, obtained by a scanning force of (a) 1 nN and (b) 2 nN in the contact mode. The substrate was a silicon wafer coated by a 9 nm thick gold layer, with a 1 nm thick titanium layer in between. The peak-to-valley roughness of the gold surface was within 1 nm. Reduction in the number of the CNTs in (b) reflects their removal from the viewing area by a larger scanning force. The images (c) and (d) were obtained in another region, with a scanning force of 1 and 5 nN, respectively, in the contact mode. The CNTs are seen to be readily removed in (d) by a scanning force of 5 nN. (e) A schematic representation of the vertical view image of (a). The thiolated CNT has thiol groups at both ends, which bind to the gold surface. The flexible tube body of SWNT allows the CNT to conform its geometry for maximum binding energy at the expense of the bending energy. The result is a "bow-type" bundle of the thiolated CNTs. Reprinted with permission from [37], Jong Kuk Lim et al., *Synth. Meter.* 139, 521 **(2003)**. © 2003, Elsevier.

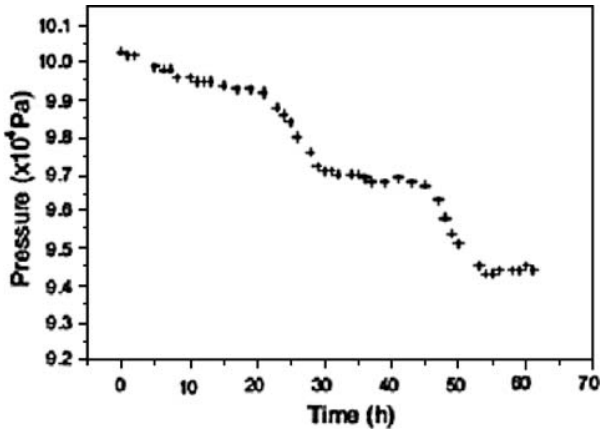

Fig. 21. Uptake of H_2 for sample 3. The plot shows obvious descending steps of the pressure. Reprinted with permission from [39], W. Qikun et al., *Int. J. Hyd. En.* 27, 497 **(2002)**. © 2002, Elsevier.

stronger attraction forces compared to adsorption on a flat surface. The intensive attractive forces are often described as an adsorption potential of pores. The last statement is particularly important in the case of small pores. IUPAC established limits regarding the terms micropore (diameter below 2 nm), mesopore (diameter between 2 and 50 nm) and macropore (diameter above 50 nm). Regarding the sensor related applications open porosity may be the factor supporting sensing properties of the active material applied. For example, the presence of pores increases adsorption of detected molecules from gas or liquid phase. In this way, substances present around a porous material get concentrated on its surface (in pores) much more intensively than on a nonporous solid. On the other hand, immobilization of detected molecules particularly inside micropores is often an irreversible effect at the temperature at which the molecules are adsorbed. Often desorption from micropores must be forced by heating the porous solid.

The importance of porosity in determining the performance characteristics of an adsorbing material was proven by Varghese et al.[45] They studied the effect of pore size and uniformity on the sensing performance of nanoporous alumina films towards water vapour. The porous alumina films were fabricated by anodic oxidation of aluminum film in water solutions of oxalic and sulfuric acid. The pore size was ranging from 2.6 to 60 nm. During extensive sensitivity studies one disclosed that smaller pore size expanded the sensing range (relative humidity RH). The sensitivity of the porous sensors increased in the range of low RH values. The operating range of the sensors could be adjusted to particular needs by the selection of appropriate pore structure of the sensors. The paper points out the importance pore-based effects in sensing phenomena particularly if the adsorbed substance exhibits the tendency to capillary condensation.

Carbon porosity seems to be a natural property regarding the mechanism of graphite formation (nano- and

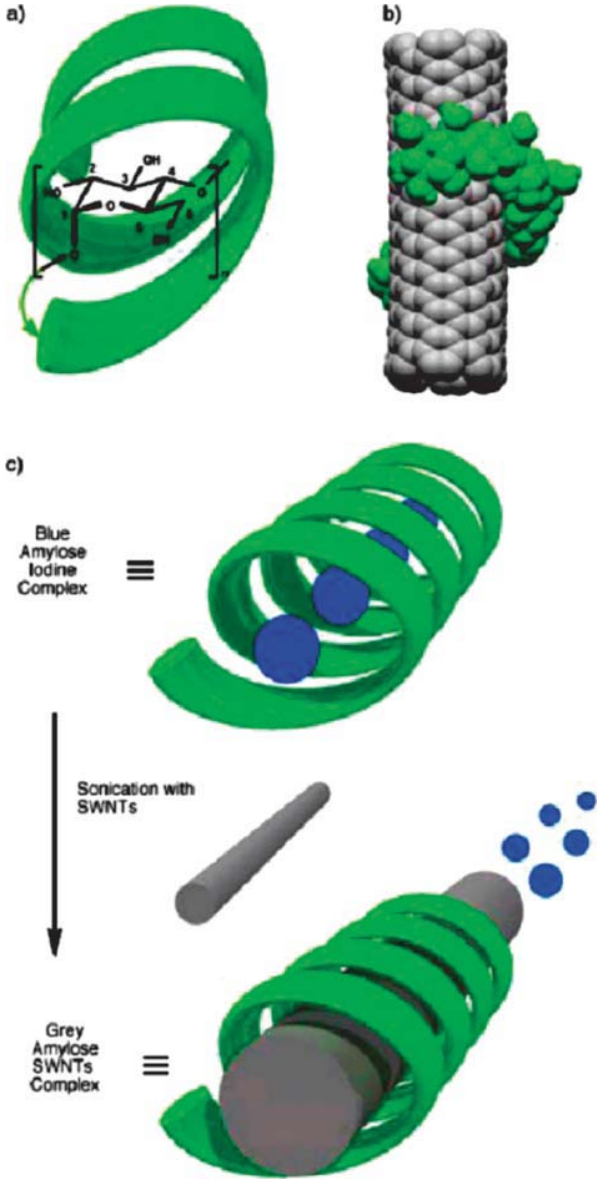

Fig. 22. (a) Schematic representation of the left-handed helix adopted by amylose when it complexes with small molecules. One α-1,4-linked ρ-glucopyranose residue, with its numbering system is overlaid on the helix. (b) Space-filling representation of the result of computer modelling (molecular mechanics and molecular dynamics simulations using the solvation model for water) between a short (6,6)-SWCNT and maltooctaose. (c) Schematic representation of the ™pea-shooting type of mechanism whereby carbon nanotubes displace iodine molecules from the amylose helix. Reprinted with permission from [41], A. Star et al., *Angew. Chem. Int. Ed.* 41, 2508 **(2002)**. © 2002, Wiley-VCH.

microcrystallites) during the carbonisation of some carbon-rich substances. The process of graphite formation is accompanied by an intensive emission of gases and vapours. Mass loss of a heat-treated sample sometimes exceeds 90% of the initial mass, with the atoms involved in the molecules of emitted gases leaving vacancies in the solid. The subsequent aromatisation causes the shrinkage

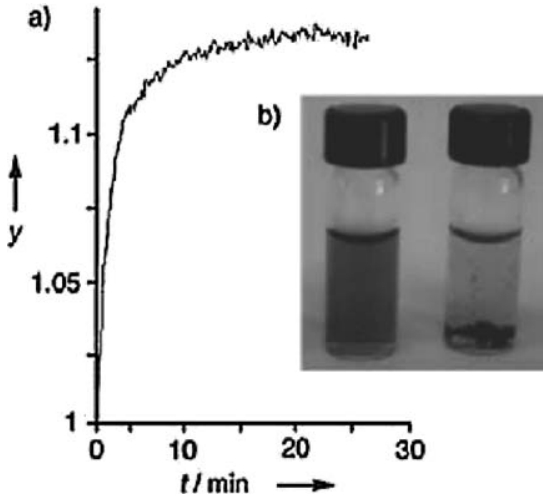

Fig. 23. Enzymatic hydrolysis of the starch-SWNT complex. (a) Changes (y is the refraction in arbitrary units) in light scattering upon addition of amyloglucosidase and (b) a photograph of vials containing the complex before (left) and after (right) addition of the enzyme. Reprinted with permission from [41], A. Star et al., *Angew. Chem. Int. Ed.* 41, 2508 **(2002)**. © (2002), Wiley-VCH.

of some domains in the carbonised material. One assumes the pores in carbon to be slit-type pores.[46] Simplified picture of pores in polycrystalline carbons is presented in the diagram below (Fig. 27).

The porosity of carbons obtained by a direct carbonisation of a selected precursor is often limited. So-called activation is necessary to increase the specific surface area of carbons and to develop their pore structure. There are several classic activation methods like activation by means of gases (and vapours) and activation by the impregnation of precursor. Activation by means of gas consists in the application of gases and vapours causing oxidation and gasification of atoms on carbon matrix. For this method, one may apply O_2, H_2O (steam), and CO_2 at elevated temperatures.

Impregnation of a carbon-rich precursor (or mixing) with substances like $ZnCl_2$, H_3PO_4, NaOH, Na_2CO_3, and Na_2SO_4 can facilitate pore formation.[47] The action of the impregnants consists in their dehydration properties.

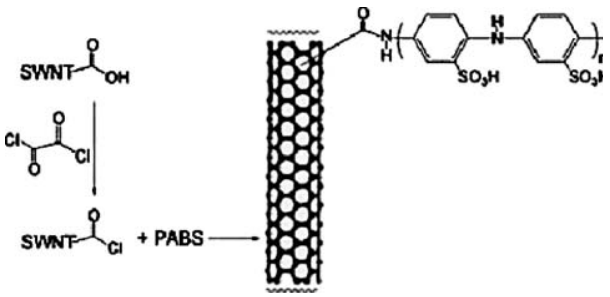

Fig. 24. Reaction of SWCNTs with PABS. Reprinted with permission from [42], B. Zhao et al., *Adv. Fuct. Mat.* 14, 71 **(2004)**. © 2004, Wiley-VCH.

Table III. Polymers attachable to CNTs.

Polymer
Poly(vinyl pyrolidone)—PVP
Poly(styrene sulfonate)—PSS
Poly(m-phenylenevinylidene)–PmPV
Poly(pyrrole)—Ppy
Poly(p-phenylenebenzobisulfonate)—PBO
Poly(vinyl acetate –co-vinyl alcohol)

Source: Reprinted with permission from [42], B. Zhao et al., *Funct. Mat.* 14, 71 **(2004)**. © (2004), Wiley-VCH.

The agents can help to hydrolyse some components of organic substances, e.g., wood. The residuals of the activators should be rinsed with water leaving pores. Means of alkaline activators, particularly NaOH or KOH, reduce the temperature needed to carbonise organic substances. The bases act as oxidants transferring atoms from carbon matrix to the gas phase. One may tailor the pore structure of carbons by the polymer blending method proposed by Ozaki et al.[48] and shown on the below diagram (Fig. 28). The merit of the method is the blending of two kinds of polymer and subsequent carbonisation of the mixture. One of the polymers is a "high carbon yield polymer" (sometimes called a carbonising polymer) that evolves low amounts of volatile products. The second polymer is a "low carbon yield polymer" that is characteristic because of high emission of volatile by-products (sometimes called pyrolyzing polymer). The last one decomposes almost totally and vanishes from the product of carbonisation. The product consists of residuals of the carbonising polymer with empty spaces, i.e., pores left by volatilised polymer. Micropores exist in the carbon matrix formed from carbonising polymer while mesopores are in fact the vacancies left by the decomposed pyrolyzing polymer.

Another way to develop a porous structure in carbon is means of sol–gel technique to obtain carbon-rich foams and carbonise them later. Tamon[49] proposed the way leading to the formation of a polymer aqua gel as presented in Figure 29. Another original method is a template

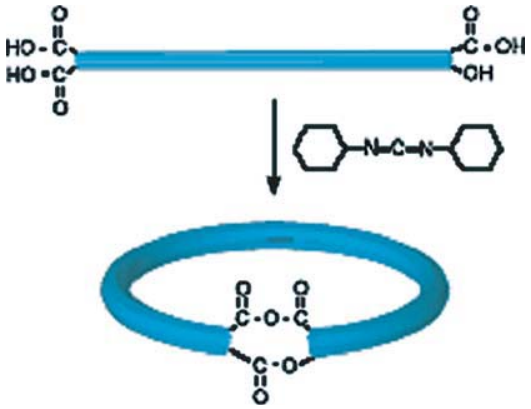

Fig. 25. A possible scheme for the ring-closure reaction with DCC. Reprinted with permission from [43], M. Sano et al., *Science* 293, 1299 **(2002)**. © 2002, AAAS.

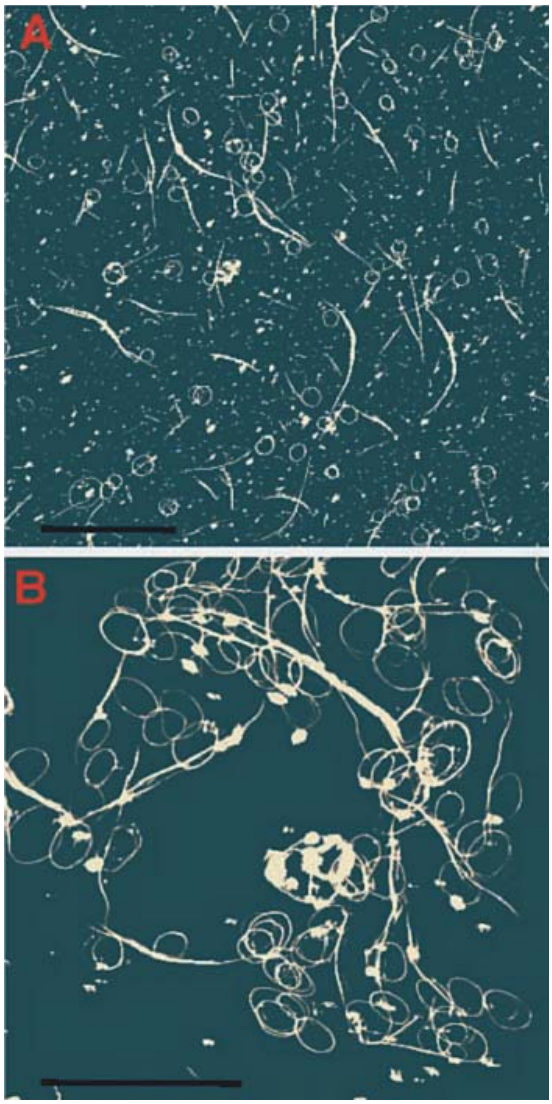

Fig. 26. AFM images of carbon nanotube rings cast on mica. (A) A reaction mixture without any purification. Each ring is dispersed well and is not a part of a long tube. Scale bar, 5 mm. (B) A reaction mixture after washing and filtering through 0.8-mm Tefon Filer. Rings appear to stick to each other after these processes. Scalebar, 2 mm. Reprinted with permission from [43], M. Sano et al., *Science* 293, 1299 (**2002**). © 2002, AAAS.

carbonisation. The merit of the method is the introduction of a liquid organic precursor (pure or in solution) into an inorganic material having accessible vacancies of nanomeytric dimensions. The liquid precursor penetrates the inorganic template and later both components (organic and inorganic) are subjected to a heat-treatment. Then, the inorganic template may be removed by a selected chemical treatment. Kyotami[50] carbonised polymers in the space between lamellae of a clay. Beside different types of clay, the application of porous silica has been also reported.[51] This methods yields meso- and microporous carbons of high specific surface area. Microporous solids can play the role of a selective membrane that is permeable for

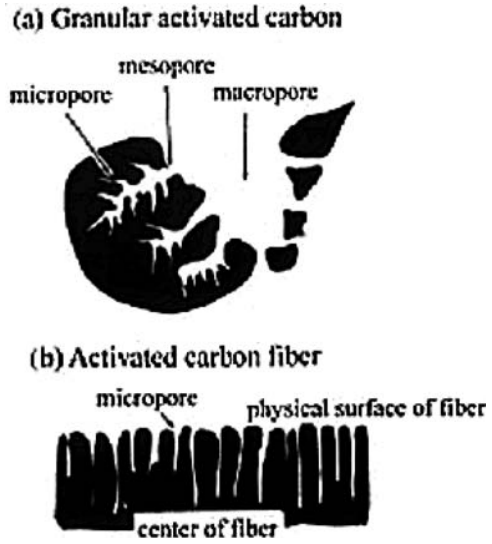

Fig. 27. Pores in granular carbon materials (a) and in carbon fibres (b). Reprinted with permission from [1], M. Inagaki, New Carbons. *Control of structure and functions* (**2000**). © 2000, Elsevier.

atoms and molecules of an appropriate size and shape. Carbons, if properly prepared exhibit excellent molecular sieving properties. That may be important for some chemical sensors if the problem of cross-sensitivity to undesired molecules occurs.

1.5. Electric Properties of Carbons

From the above-presented phenomena, it is obvious that the heat-treatment conditions must affect the electrical properties of carbons. Usually amorphous carbon is a bad electric current conductor while graphite is a very good

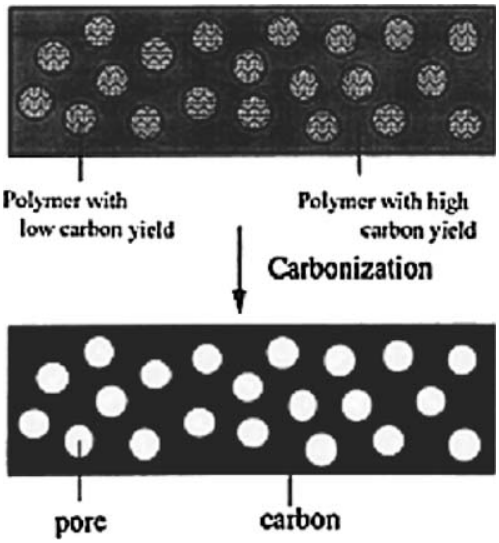

Fig. 28. Visualisation of blending method for developing of carbon porosity. Reprinted with permission from [48], J. Ozaki et al., *Carbon* 35, 1997, 1031 (**1997**). © 1997, Elsevier.

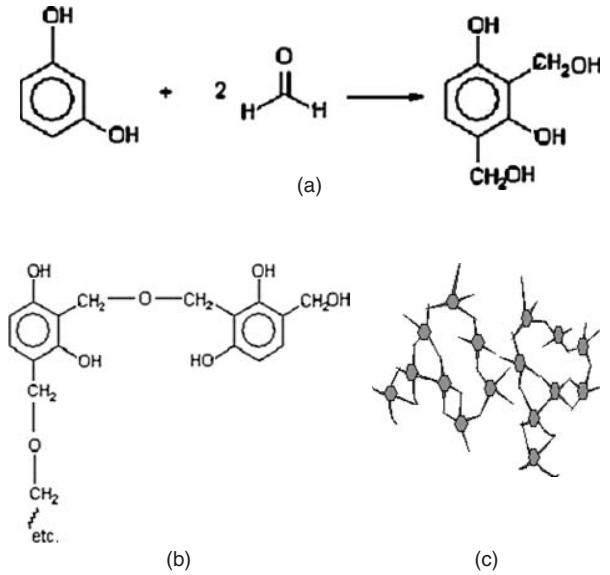

Fig. 29. Formation of organic aqua-gel as a preliminary step to carbon synthesis by sol–gel method as proposed by Tammon.

one when this parameter is measured parallel to graphite planes. Real samples of polycrystalline carbon are a mixture of these two forms of carbon and behave like typical semiconductors. The changes in electronic structure of pyrolyric carbons are summarized in the Mrozowski[52] diagram. The resistivity of pyrolytic carbons decreases dramatically upon increasing temperature of carbonisation.[53] Heat-treatment of CNTs also modifies their electric properties and one may even expect the transformation from *p*-semiconductor to metallic behaviour. Hence it is possible to adjust the electrical properties of carbons for specific applications. Coming from the same raw material one may obtain an insulator, a semiconductor of different energy gap, and an excellent (almost metallic) conductor. No other material offers so much freedom in tailoring of its electrical properties.[54–55] Beside the possibilities offered by heat treatment, carbon materials may be subjected to all modification resulting from doping with foreign atoms.

2. APPLICATION OF CARBONS TO CHEMICAL SENSORS

As mentioned above, carbons may play very differentiated roles in the construction and operation of chemical sensors. In the case of semiconductor chemical sensors, two basic actions must occur to ensure detection of selected species in the gas or liquid phase:

(1) adsorption of detected species on the surface of semiconductor, and

(2) specific interaction of adsorbed-detected species with current carriers in the solid semiconductor.

This phenomenon may proceed by capture or release of current carries by adsorbed species, and through surface reactions between detected species and other molecules as in catalytic oxidation of combustible gases and vapours.

2.1. Carbon Nanotubes as Chemiresistors

The earliest papers announcing successful applications of CNTs to the construction of chemically sensitive devices were published almost ten years ago. Among the works, the paper of Kong, Franklin co-workers[56] is frequently quoted as pioneer one. They investigated *p*-type SWCNTs as chemiresitor sensor for NO_2 and NH_3 detection in air or argon. The obtained results were attributed to the behaviour of single tubes. The CNTs-containing sensors exhibited substantial increase or decrease of electric conductivity upon exposure to the gases. The detected molecules were different regarding their electron affinity. NO_2 was treated as an electron acceptor while electron donor properties were ascribed to NH_3. Thus, one could expect the capture of electron or holes respectively. Since holes were the majority current carriers, their localization (NH_3 adsorption) resulted in an increase of electric resistance. On the contrary, the capture of electrons (NO_2 adsorption) caused the expected decrease of resistance. The examined SWCNTs reacted eagerly with the gases and the response times were short (the order of the of seconds). The ease of adsorption complex formation influenced negatively the time of recovery of the initial resistance, usually reaching the level of hours. Metallic SWCNTs exhibited smaller changes of electric resistance in the same experimental conditions, attributed to the high concentration of current carriers. Metallic SWCNTs exhibited, on the contrary to *p*-semiconductor SWCNTs, a reverse direction of electric resistance change upon adsorption of the gases. Thus, NO_2 adsorption increased the resistance while NH_3 adsorption was responsible for a decreased resistance. The observed behaviour of CNTs obeyed the general rules describing the transfer of charges during adsorption of electron donors or acceptor on semiconductors and metals. As it will be seen, often a peculiar influence of gas adsorption (including NH_3 and NO_2) on the conductance of CNTs has been reported. It particularly deals with the direction of the observed changes of electric resistance, which are not consistent with the general rules and with the results of Kong and Franklin. In most cases, the disagreement is caused by the complex nature of the examined samples. Therefore, one cannot exclude some interparticle-phenomena or an influence of non-CNTs components of hybrid materials.

More recently, Valentini et al.[57,58] investigated the influence of a high temperature exposure to oxygen on the sensing properties of CNTs towards NO_2. The study revealed that intensive oxidation of CNTs at 650 °C causes a dramatic change in the conduction properties of the tubes, with a conversion from a *p*-type semiconductor to metallic. The electric conductivity conversion influenced negatively

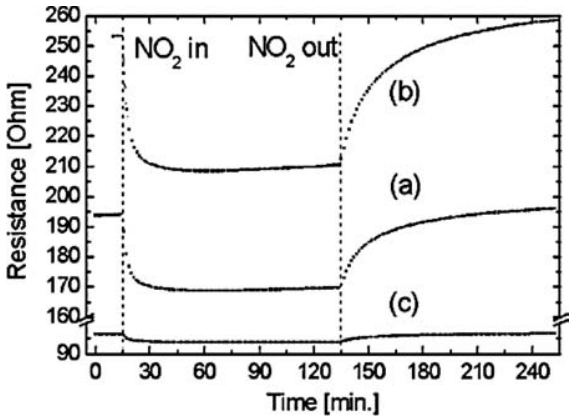

Fig. 30. Resistance changes at an operating temperature of 165 °C in the presence of 100 ppb NO_2 of: (a) As deposited CNTs film after the first thermal treatment; (b) as deposited CNTs film after the second thermal treatment, and (c) CNTs film annealed in air at 650 °C. Reprinted with permission from [56, 57], L. Valentini et al., *Thin Solid Films* 436, 95 **(2003)**. © 2003, Elsevier.

the sensitivity of CNTs towards NO_2. Metallic CNTs (multiwalled, 40–50 nm thick) exhibited rather low sensitivity but still their resistance decreased upon NO_2 adsorption. On the contrary, a gentle heat-treatment at intermediate temperatures (up to 300 °C) helped to develop better sensitivity (Fig. 30).[57, 58] It is suggested that this positive effect resulted from the purification of the as deposited CNTs while defective sites responsible for NO_2 adsorption were still present. The purification consisted in the removal of some graphite particles co-deposited during the growth of CNTs. The high temperature annealing in air (XPS investigations) resulted in the oxidation of nickel cups (residuals of catalyst) to NiO while the carbon atoms were not significantly oxidized. NO_2-sensitivity tests were run at the optimised temperature of 165 °C.

The influence of the catalyst geometry on the growth of CNTs and their electrical response to NO_2 within the range 10–100 ppb have been described.[59] In the study, one compared the sensing properties of two sensors fabricated based on MWCNTs grown on the catalyst layer of different thickness 3 and 5 nm. The thin layer of catalyst led to randomly oriented MWCNTs with diameter of 20–30 nm while the growth on the thick-layer catalyst initiated the formation of uniform MWCNTs but of much wider diameter (Fig. 31).

Compared to oriented MWCNT arrays, randomly oriented nanotubes exhibited relatively high electric resistance, which decreased sharply upon the increase of temperature. The random orientation of MWCNTs resulted in a high sensitivity of such fabricated sensors to the chemical signal of 10–100 ppb of NO_2 in the stream of air. Unfortunately, a drift of base electric resistance was noticed in the case of randomly oriented CNTs, which increased upon increasing number of gas exposures (Fig. 32).

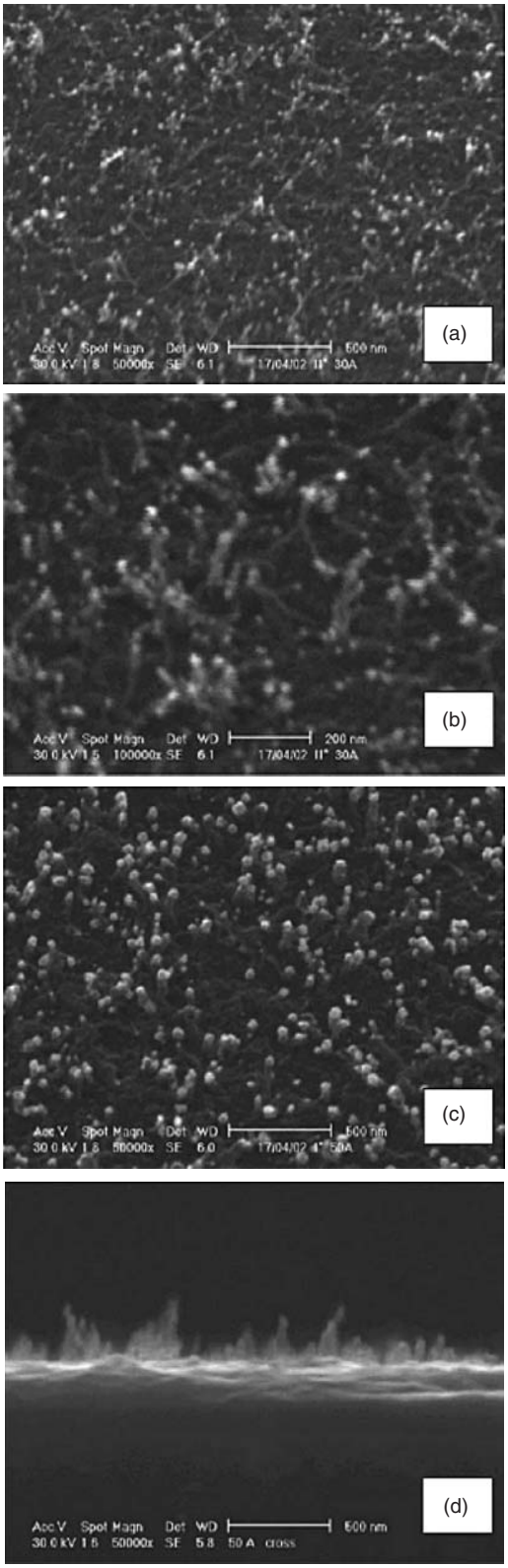

Fig. 31. SEM photograph of CNTs. Top view for sensor A (a) (b), and sensor B (c) cross section for sensor B (d). Reprinted with permission from [59], C. Cantalini et al., *Sens. Actuators B* 93, 333, **(2003)**. © 2003, Elsevier.

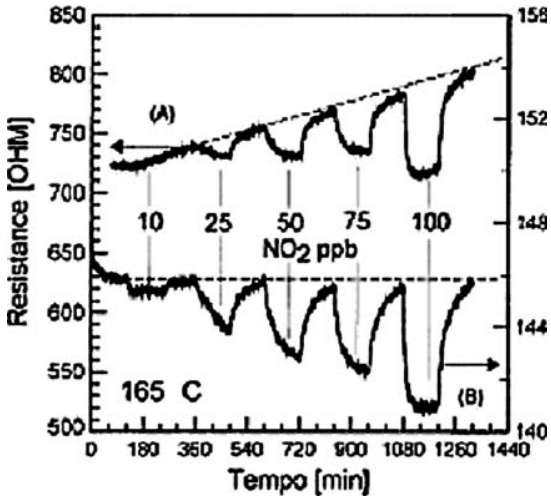

Fig. 32. Dynamic sensor response at 165 °C operating temperature and NO_2 concentrations ranging from 10 to 100 ppb in dry air carrier gas of sensor A and sensor B. Reprinted with permission from [59], C. Cantalini et al., *Sens. Actuators B* 93, 333, (**2003**). © 2003, Elsevier.

The sensors employing well-developed MWCNTs (grown on a thick film of Ni) were less sensitive to NO_2 but reacted faster and gave reversible responses at 165 °C. The behaviour of not-aligned CNTs in the presence of NO_2 was explained basing on the presence of well-developed agglomeration pores and high surface area of CNTs. Thus, the reported work indicates how many factors (physical, chemical, and geometrical) can influence the final sensing profile of the tested CNTs. Li and co-workers[60] investigated a CNT-based chemical sensor for the detection of NO_2 and nitrotoluene vapours. The sensor consisted of SWCNTs deposited on a substrate with interdigitated electrodes. The tubes were synthesised using nickel catalyst, which had to be removed by a standard purification method. Such obtained tubes exhibited extremely high surface area above 1500 m^2/g. The deposition method yielded an ohmic contact between the electrodes and the sensing material made of randomly oriented SWCNTs. No binder was applied and CNTs were only dispersed in dimethylformamide (DMF) and drop-deposited on the sensor background. Authors decided about the use of DMF hoping to debundle CNTs due to the formation of a separation layer of DMF molecules around each individual carbon tube. The initial resistance of the sensing element depended on the number of adhered CNTs, which was controlled by counting the number of dispersion drops set on the substrate. The examined SWCNTs-based sensors responded to the presence of NO_2 within the concentration range 6–100 ppm. The sensors reduced their electric resistance, which effect was qualitatively identical with the result reported by other researchers. There were two distinct drawbacks to the sensors, Figure 33, long recovery and the constant drift of base resistance (a continuous decrease). Li and co-workers proposed to eliminate (or reduce) the negative phenomena by means

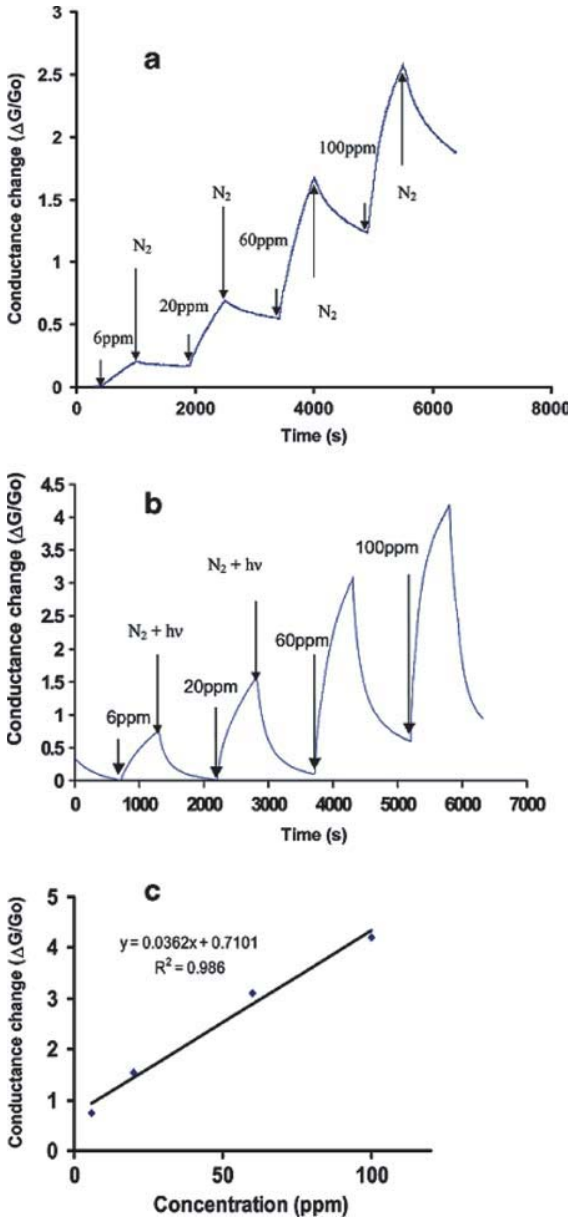

Fig. 33. Representative sensor response for NO_2. Various concentrations of the sample gas and the pure gas injections are shown by arrows. The sample gas is NO_2 in a 400 cm^3/min nitrogen flow at room temperature. Ultrapure nitrogen is used for dilution and purging. (a) Without UV light in the recovery. (b) With UV light for sensor recovery. The UV illumination and N_2 purging start simultaneously. (c) Calibration curve obtained from (b). Reprinted with permission from [60], J. Li et al., *Nano Lett.* 3, 929 (**2003**). © 2003, American Chemical Society.

of UV irradiation during the recovery cycle. That measure reduced the baseline drift and accelerated the recovery to 10 minutes. In the case of nitrotoluene, the response, and recovery proceeded faster while the magnitude of the resistance changes was smaller. In both cases the sensors response was linear versus the gas (vapour concentration) up to 100–150 ppm level. The difference in the response magnitude was explained assuming a

weak bonding (and minor charge transfer) of nitrotoluene to CNTs that resulted from repellent forces between CNTs and aromatic ring in the adsorbate molecules. Additionally, one investigated the influence of benzene and acetone vapours on the resistance of the SWCNTs-based sensors. The extrapolation of the linear sensing characteristic led them to calculate lowest detection limits for both substance which values were 44 ppb for NO_2 and 262 ppb for nitrobenzene. The response to other vapours of different nature like acetone (polar solvent) and benzene (non-polar solvent) were mentioned. The sensitivity to acetone molecules was assumed due to the electron withdrawal from SWCNTs by the interaction with the C=O group. The response to non-polar molecules was a unique finding since hydrocarbon (benzene) adsorption on CNTs was commonly recognized as a minute-charge transfer phenomenon. In such a case, the observed variations of SWCNTs resistance resulted from intertube modulation, i.e., the influence of benzene molecules on the tube-to-tube transport of current carriers. The last phenomenon may be regarded as analogous to the change of interparticle potential barriers in widely investigated (and applied) polycrystalline SnO_2-based chemical sensors for combustible gas detection.

Zhao and co-workers[61] presented a theoretical study on non-covalent functionalization of CNTs by aromatic molecules. The study considered (density functional theory) the interaction between CNTs and selected organic molecules like benzene, cycloheksane, 2,3-dichloro-5,6-dicyyano1,4-bezoquinone (DDQ). Non-covalent functionalization became interesting since it was considered as non-deteriorating for physical and chemical properties of CNTs. Such a functionalization is (in general) considered a reversible process, which can lead to chemical sensing applications. Zhao et al. showed that the adsorption of organic molecules resulted in coupling of π-electrons of adsorbate (if they had such ones) and of adsorbent CNTs. Benzene and cyclohexane were found to be weak electron donors. In general, the theoretical study proved that electronic properties of CNTs were under control by adsorption of organic species, see Figure 34.

The success of SWCNTs application to the detection of NO_2 resulted in theoretical studies describing gas adsorption. Won-Leung Yim[62] investigated the phenomenon by means of the density functional theory. One found that interaction between NO_2 molecule and flat graphene sheets was different from the interaction with rolled up ones. The tensions exiting on the bended spots reduced the stabilization effects of conjugated π-bonds in aromatic rings. That increased the reactivity of the atoms placed in such spots especially in the closing cups at the ends of CNTs. Therefore, the action of NO_2 led to the chemisorption of the molecules at the more reactive sites in SWCNTs. On the contrary, physical adsorption of NO_2 predominated at the walls of CNTs where the state of carbon atoms

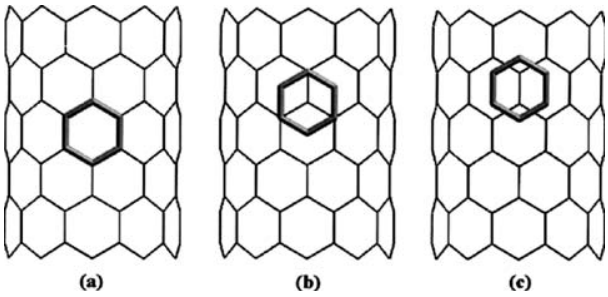

Fig. 34. Three possible sites (a) top, (b) stack, (c) bridge for adsorption of a six-membered ring molecule on a SWCNT. The hydrogen or other atoms on the six-membered ring are not plotted for a clearer visualization. The bridge site is found to be the most favorable. Reprinted with permission from [61], J. Zhao et al., *Appl. Phys. Lett.* 82, 3746 (**2003**). © 2003, American Institute of Physics.

could be described as less reactive. The chemisorption of NO_2 was considered as a direct addition to C=C bonds. The process of chemical bonding of NO_2 was found to be exothermic and hardly reversible while the weak (physical) adsorption was slightly endothermic and therefore reversible. The results may be consistent with the practical observation done during the exposure of SWCNTs to the action of NO_2.

The concept of a novel sensor material was presented by Wei and co-workers.[63] Commercially available SWCNTs were mixed with SnO_2 aiming at the utilization of very well known and widely employed sensing properties of thin (IV) oxide. The composite (containing CNTs) was prepared by the admission a bundle of SWCNTs to the solution of Sn(OOCCH (C_2H_5) C_4H_9), homogenisation and spin coating on a Al_2O_3 substrate with golden electrodes. The sensors were then heat-treated at 500 °C in air. The most important feature of the novel material and sensor was the low operation temperature. The sensor could detect NO_2 in air and nitrogen at room temperature. The observed changes of electric resistance upon the adsorption of NO_2 were completely reversible without any additional cleaning measures like heating or UV irradiation. The sensing characteristics of the sensor, i.e., relative resistance versus NO_2 concentration, were linear up to 1000 ppm. Thus, the presence of SWCNTs in the sensing composite (even in a small amount) caused a spectacular sensitivity increase of the composite sensors with an excellent recovery of the initial electric properties. SEM investigations revealed that SWCNTs were embedded in the SnO_2 matrix, from which Wei and co-workers assumed the existence of two depletion regions in the hybrid SWCNTs/SnO_2 fibres. The material had a fibrillose structure and a cross section of a bundle of the fibres is depicted in Figure 35. The first depletion layer (Fig. 36) existed on the surface of SnO_2 coating. The surface reaction of NO_2 that led to the formation of NO^- may be represented by: $NO_{2(gas)} + O^-_{(SnO_2)} \rightarrow NO^-_{(ads)} + O_{2(gas)}$. The second depletion layer existed near the SnO_2/SWCNTs

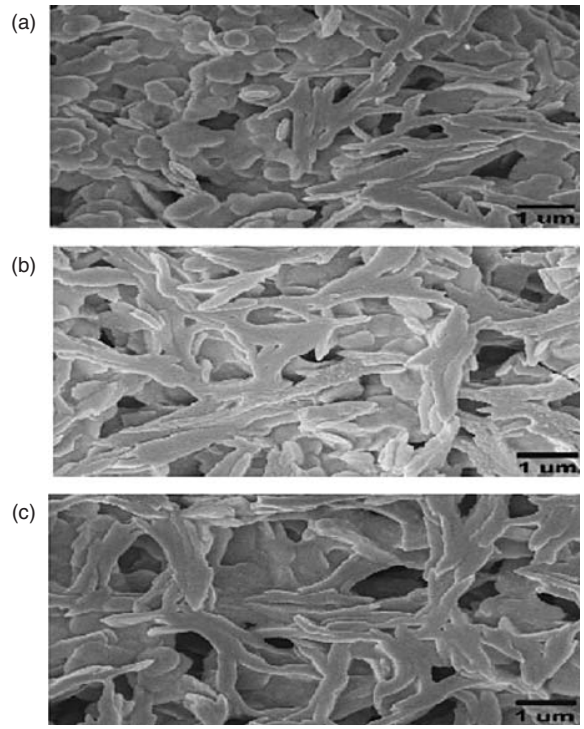

Fig. 35. FE-SEM micrographs of (a) SnO_2 (blank), (b) hybrid SWCNTs/SnO_2 A sensor, and (c) hybrid SWCNTs/SnO_2 B sensor. Reprinted with permission from [63], B. Y. Wei et al., *Sens. Actuators B* 101, 81 **(2004)**. © 2004, Elsevier.

interface. The adsorption of NO_2 molecules proceeded also at that sensitive interface since the sample was porous. Thus, the concentration of electrons in SnO_2 was strongly affected by the depletion layers, which depth increased upon the contact with NO_2. Therefore, the resistance of the hybrid material increased during sensing of NO_2. In the

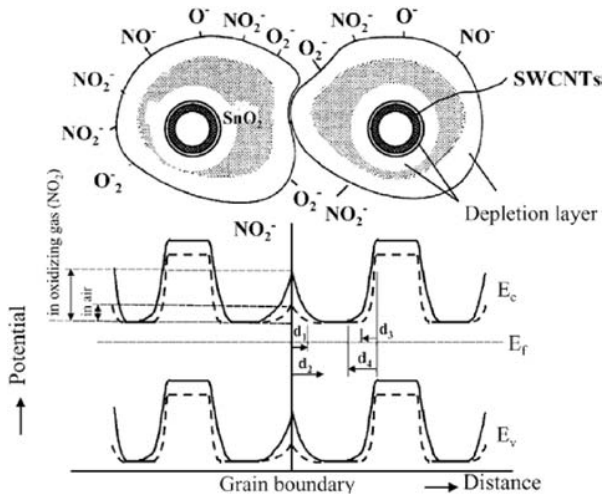

Fig. 36. Model of a potential barrier to electronic conduction at grain boundary for hybrid SWCNTs/SnO_2 sensors. Reprinted with permission from [63], B. Y. Wei et al., *Sens. Actuators B* 101, 81 **(2004)**. © 2004, Elsevier.

case of pure SWCNTs (*p*-semiconductor), the adsorption caused a decrease of electric resistance due to immobilisation of electrons i.e., the minority current carriers. The presented hybrid sensors and the model of its operation assume that the real sensing material was tin (IV) oxide while SWCNTs were only an amplifying substance. It is certainly a novel role ascribed to CNTs in chemical sensing.

Inorganic coatings may be replaced by organic wrapping. An and co-workers[64] embedded SWCNTs in poly (pyrrole) preparing a composite material that was sensitive to NO_2 at room temperature. The hybrid material was fabricated by *in situ* polymerisation of pyrrole mixed with SWCNTs on top of a solid substrate with evaporated electrodes (cyclic drop-wise deposition); the polymer uniformly wrapped the SWCNTs (Fig. 37). The tubes were cross-linked due to the sticking influence of the polymer. In addition, the polymer coating increased the surface area of the nano-composite, which was 3-fold bigger than that of the polymer alone. However, it is not clear how the presence of the polymer influenced the access of gases to the CNTs. The sensitivity of the poly(pyrrole)-SWCNTs composite-based sensors was much enhanced than the sensitivity of a sensor fabricated from SWCNTs only. The adsorption of NO_2 caused an increase of electric resistance of the whole composite. The result was in contrast to other studies on NO_2 adsorption on SWCNTs (described above) without any coating. In these studies NO_2 molecules being in fact radicals, reduced the resistance of *p*-type SWCNTs due to the formation of adsorption complexes, in which electrons from *p*-semiconductor CNTs were immobilized. The peculiar behaviour of the composite (if compared to the reaction of SWCNTs alone) was ascribed to the presence of metallic SWCNTs (beside the semiconductor ones) in the bundle of CNTs that were used for fabrication of the composite sensors. According to the authors, the sample consisted of metallic and semiconductor CNTs and the metallic ones dominated the conduction through the composite material. Authors also assumed that the polymer was modified during polymerisation due to the presence of iron (III) chloride and sodium p-toluene sulfonate (polymer dopant) in an excess amount. Thus, the poly(pyrrole) binder also behaves as an electronic conductor. Although, the sensor was sensitive to NO_2 at room temperature its practical application was affected by a long-term recovery probably caused by NO_2 chemisorption on defected sites on CNTs. It has to be pointed out that the sensing composite became stable and sensitive after annealing at 400 °C for 30 minutes.

Electrical phenomena occurring in solution may be employed to fabricate CNT containing gas sensors. Suehiro and co-workers[65] used dielectrophoresis (DEP) for entrapping of MWCNTs (first dispersed in ethanol) on a selected spot between the interdigitated electrodes. The positive dielectrophoresis force directed the dispersed

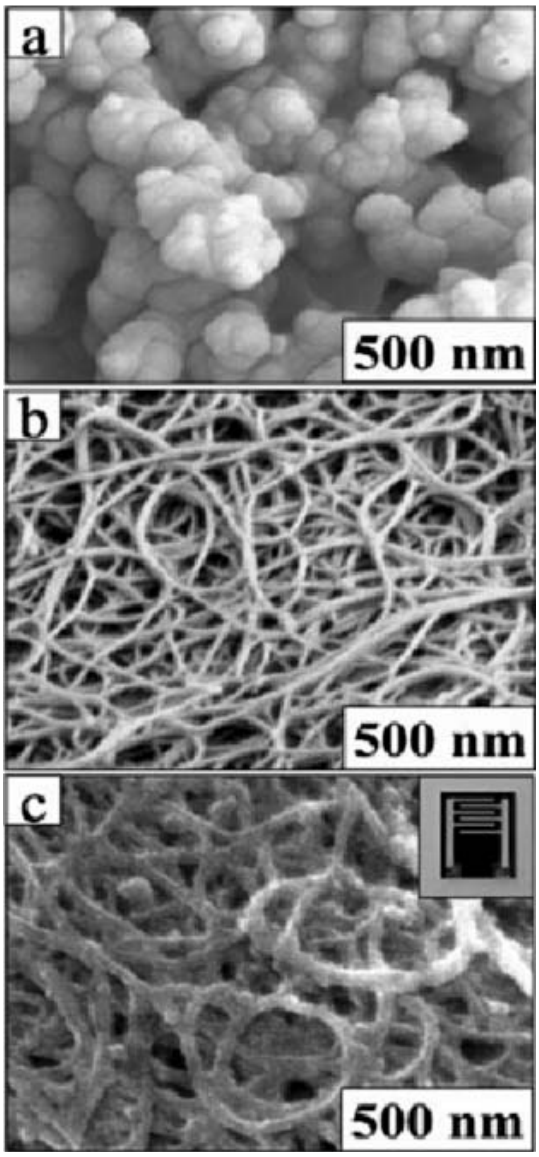

Fig. 37. FE-SEM images of (a) the PPy formed by chemical polymerisation without SWCNTs, (b) the purified SWCNT bundles with a diameter of about 20 nm, and (c) PPy nanocomposite formed by *in situ* chemical polymerisation. Reprinted with permission from [64], K. H. An et al., *Adv. Mater.* 16, 1005 **(2004)**. © 2005, Wiley-VCH Verlag.

MWCNTs towards the region of high intensity of electric field. During dielectrophoresis polarized molecules started to move to a selected spot. Figure 38 shows the schematic diagram of the experimental set-up. The electrodes had a castle-wall pattern in order to create the regions of differentiated intensity of electric field. CNTs were constantly fed to the electrode region where they were entrapped under the influence of AC voltage of 100 kHz and 10 V amplitude. The AC voltage was additionally employed for measuring of the impedance of the sensing layer. After 3 hours, the trapped MWCNTs formed a relatively thick film of randomly oriented CNTs

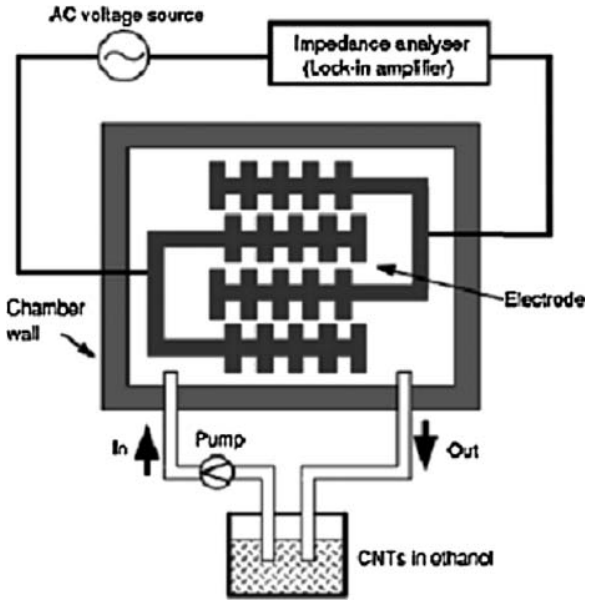

Fig. 38. Schematic diagram of the experimental set-up for MWCNT gas sensor fabrication on a microelectrode using DEP. Reprinted with permission from [65], J. Suehiro et al., *J. Phys. D: Appl. Phys.* 36, L109 **(2003)**. © 2003, Institute of Physics IOP Publishing Ltd.

(Fig. 39). Impedance measurements were employed for the simultaneous observation of the sample's conductance and capacitance during the adsorption of NH_3 (100 ppm at 30 °C). One noticed a reversible decrease of the conductance of the deposited MWCNTs while the capacitance of the CNTs-layer grew. The results are qualitatively consistent with the achievements reported in other studies provided the investigated MWCNTs were *p*-semiconductors. The response of the sensor was linear to the increasing concentration of ammonia in the range up to 10 ppm, beyond which the response diminished.

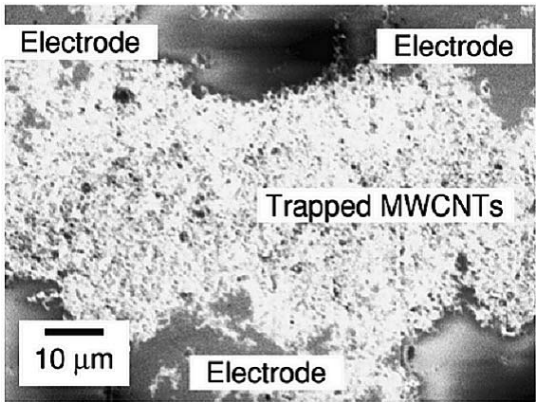

Fig. 39. SEM images of the DEP collection process of MWCNTs on a castellated microelectrode. The amplitude and frequency of the electrode energizing potential were 10 V (peak-to-peak) and 100 kHz, respectively. After 3 h of the DEP process (high magnification). Reprinted with permission from [65], J. Suehiro et al., *J. Phys. D: Appl. Phys.* 36, L109 **(2003)**. © 2003, Institute of Physics IOP Publishing Ltd.

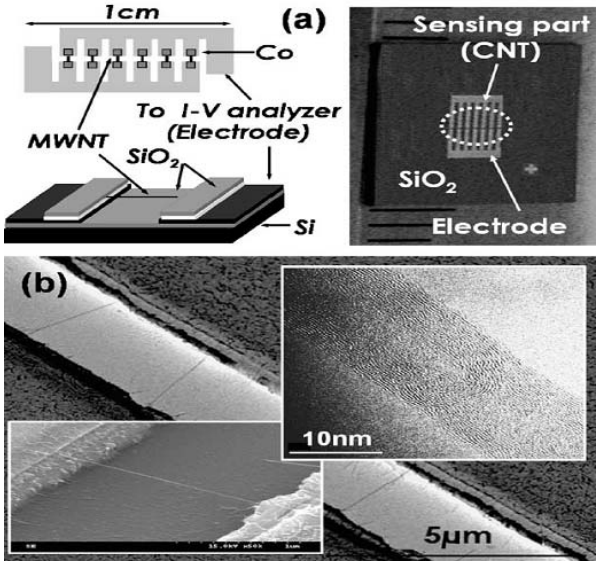

Fig. 40. (a) Photograph of completed MWCNTs based chemical sensor (b) SEM image of aligned CNTs resting on SiO_2 surface after directed growth. The CNTs show clear alignment in the direction of the electric field. The insert shows TEM image of laterally grown CNTs. Reprinted with permission from [66], Yoon-Taek Jang et al., *Sens. Actuators B* 99, 118 **(2004)**. © 2004, Elsevier.

More recently, Jang and co-workers[66] fabricated an ammonia sensor based on laterally grown MWCNTs. The tubes were grown from C_2H_4 by its thermal decomposition between interdigitated electrodes made of nobium. The metal electrodes worked as catalytic sites for the lateral grown of CNTs. The synthesis was additionally accelerated by 3 V bias voltage set across the electrodes. Such obtained tubes were straight MWCNTs that bridged the electrodes as presented in Figure 40. The electrical nature of the CNTs was not homogenous but a combination of metallic and *p*-semiconductor tubes. Since the electric resistance of metallic CNTs do not change significantly upon gas adsorption, all the observed changes were ascribed to *p*-semiconductor CNTs. Oxygen adsorption caused a decrease of electric resistance of the CNTs that was explained as the action of an electron acceptor on minority current carries in a *p*-type semiconductor. On the contrary, electron-donating gas NH_3 caused a reverse phenomenon, i.e., an increase of the electric resistance of the CNTs. The orientation of the tubes suggests that all measured electric effects are results of the adsorbate-CNTs interactions (chemical and physical). The technique proposed by Jang and co-workers seems an excellent approach for fundamental research on CNT gas adsorption.

Valentini and co-workers[67] ran pioneer studies on CH_4 detection by MWCNTs grown on a Ni catalyst. The study was focused on the direct adsorption of both gases on CNTs and the role of Ni catalyst remaining was not considered in detail. Authors proposed the mechanism of charge transfer in the CH_4-CHTs adsorption complexes. After outgassing

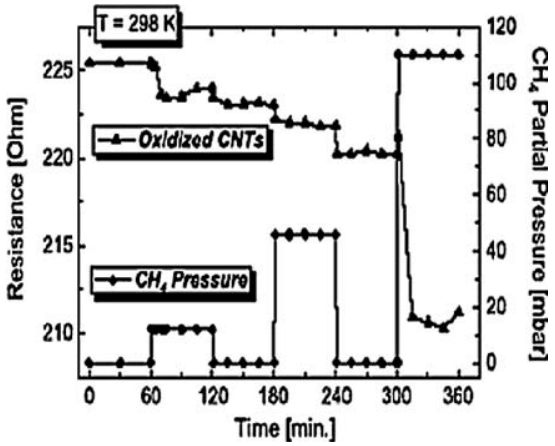

Fig. 41. Dynamic gas response of oxidized CNT films at an operating temperature of 298 K and CH4 partial pressures ranging from 12–110 mbar. Reprinted with permission from [67], L. Valentini et al., *Mat. Sci. Eng. C* 24, 527 **(2004)**. © 2004, Elsevier.

in vacuum, the examined MWCNTs behaved like typical *p*-semiconductors. Methane molecules, being in fact a reducing substance, acted as a donor of electrons. Thus, the adsorption of methane on "clean" CNTs resulted in the capture of holes, increasing the resistance. In another experiment, the CNTs were additionally oxidized before the experiments with methane. The oxidation of CNTs resulted in an increased resistance of CNTs. However, the subsequent adsorption of methane on the oxidised CNTs yielded surprising results, i.e., one observed a decrease of sensor's electric resistance (Fig. 41), the opposite of that obtained for non-oxidized samples. The explanation of the phenomenon based on a formerly published theoretical simulation[68] assumed the presence of oxygen compressed all the holes of semiconductor CNTs. Therefore, oxidized CNTs became an extrinsitic *n*-semiconductor and the adsorption of electron-donators as methane had to decrease the resistance of metallic CNTs. The study announced that the *p*-semiconductor to *n*-semiconductor transition of CNTs is possible not only by heating at elevated temperatures but also on a chemical way, i.e., by oxygen functionalization of CNTs. Moreover, one calculated that methane adsorbs physically on the CNT surface via a minute electron transfer to CNTs (0.027 electron per molecule).

The problem of CH_4 detection in air at room temperature was investigated by Lu and co-workers.[69] The CNTs used in that study differed significantly from those applied in other investigations. It is quite a common practice that CNTs for chemical sensor manufacturing are in a "raw" state. Many employ them "as grown" or at least oxidized. Sometimes one does not realize that often performed purification of CNTs means in fact oxidation of them since the purifying treatment involves the usage of strong oxidants. Thus, Lu and co-workers made a step ahead performing a more complex chemical manipulation. SWCNTs were subjected to metallization by sputtering of Pd particle onto the powder of CNTs. Then the sample was

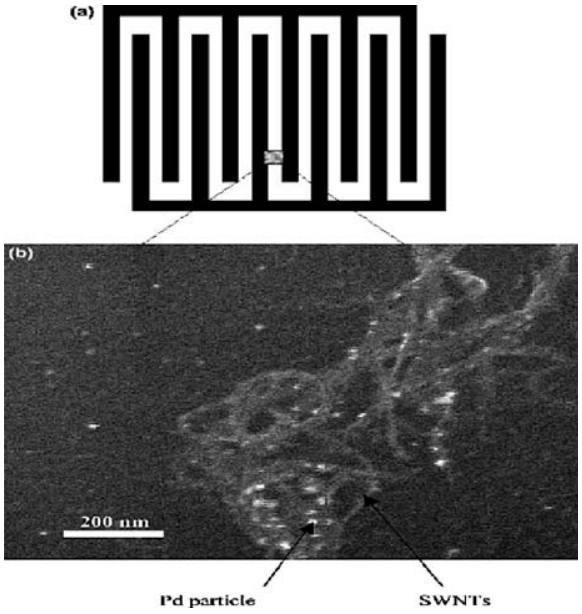

Fig. 42. (a) The interdigitated fingers use a finger width of 10 μm and a gap distance of 8 μm. (b) The scanning electron microscopic (SEM) image of Pd loaded SWCNT bundles dispersed on the interdigitated fingers. The bright spots are Pd particles with measured average size of 10 nm. Reprinted with permission from [69], Y. Lu et al., *Chem. Phys. Lett.* 391, 344 **(2004)**. © 2004, Elsevier.

carefully mixed. The Pd content by weight was close to 1%. The Pd/SWCNTs mixture was dispersed and successively drop-deposited onto a substrate with two interdigitated electrodes as presented in Figure 42. The fabrication procedure provided that the particles of Pd were small (ca. 10 nm in diameter) and well dispersed among the bundle of SWCNTs. The operation of the sensor was tested towards 0–100 ppm of methane in air at temperatures ranging from 25 to 150 °C. The resistance of the Pd-SWCNTs-containing resistors was tested upon the contact with CH_4 when 1 V bias voltage was set on the electrodes. A sensing mechanism was proposed to explain the observed resistance changes. As depicted in Figure 43. Pd particles were expected to donate electrons to adsorbed CH_4 molecules, which became charged negatively. Thus, the Pd particle was charged positively against the surface of a carbon tube. Therefore, Pd particles could restore the transferred electrons by attracting the electrons from CNTs. According to authors, the semiconductor SWCNTs were loosing minority current carriers, i.e., electrons. Thus, the conductance of CNTs had to increase as observed in practice. There was a problem with the renewal of the base resistance after exposure to pure air. The baseline was hard to recover suggesting that some durable adsorption complexes had to appear. Therefore, one applied UV irradiation to return to the starting resistance. The UV irradiation caused a significant increase of sensor's resistance probably due to deterioration of numerous surface species existing on Pd particles and CNTs.

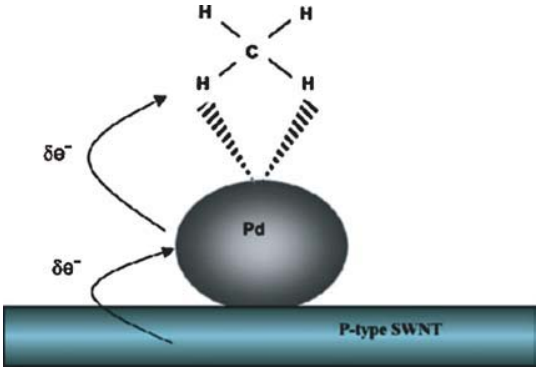

Fig. 43. The proposed sensing mechanism for room temperature methane detection using Pd-SWCNT sensors. Pd tends to form weakly bound complex Pd-(CH_4) at room temperature. When loaded on a SWCNT, the SWCNT can facilitate the formation of the complex by transfer charge to methane. As a result, *p*-typed SWCNT gains more holes as carriers for increased conductance. Reprinted with permission from [69], Y. Lu et al., *Chem. Phys. Lett.* 391, 344 **(2004)**. © 2004, Elsevier.

Novak and co-workers[70] fabricated a CNTs-based transistor and showed that the device was sensitive to many substances (ammonia, xylene vapour, and hexane vapour). Additionally, they investigated the sensitivity towards DMMP vapours (dimethyl methylphosphate) in the region of sub-ppm concentrations. The test using DMMP is one of pioneer works regarding the properties of the substance, which is a simulant for the nerve agent Sarin. The sensor design was equivalent to a chemically sensitive transistor (Fig. 44). It was achieved by the direct growth of SWCNTs onto a SiO_2 layer covering a Si substrate that

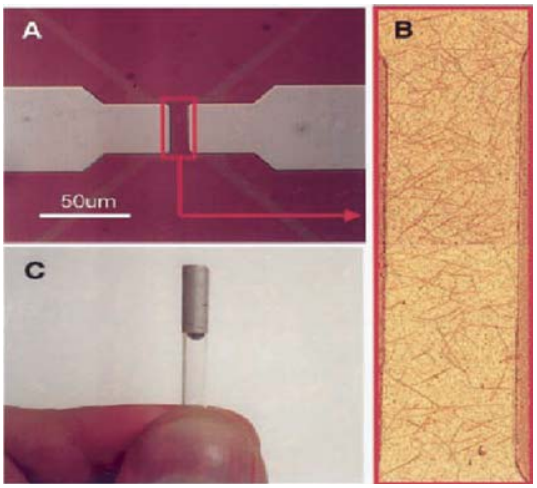

Fig. 44. (a) Optical micrograph of a SWCNT device. Ti contacts were evaporated on top of a SWCNT film grown on thermal SiO_2. The source/drain channel dimensions are 10×30 μm^2. The Si substrate serves as a back gate. (b) Representative AFM image of a SWCNT network that shows multiple conduction pathways via interconnected CNTs. (c) Optical micrograph of a SWCNT flow-cell chemiresistor sensor made from 1/8 in. outer diameter quartz tubing. Reprinted with permission from [70], J. P. Novak et al., *Appl. Phys. Lett.* 83, 4026 **(2003)**. © 2003, American Institute of Physics.

REVIEW

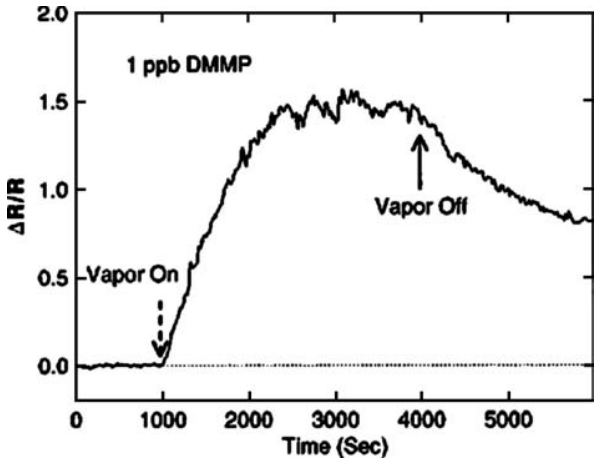

Fig. 45. Relative change in resistance versus time for a chemiresistive flow-cell exposed to a 1 ppb concentration of DMMP. Reprinted with permission from [70], J. P. Novak et al., *Appl. Phys. Lett.* 83, 4026 **(2003)**. © 2003, American Institute of Physics.

served as a back gate while two electrodes were working as drain and source. Moreover, one designed chemiresistor flow cells, in which the inner surface of a quartz tube served as a background for *in situ* growth (over and iron catalyst) of CNTs. The ends of the SWCNTs were then metallised to create electric contacts for end-to-end resistance measurements (Fig. 45). The deposited network of CNTs behaved like *p*-type semiconductor. According to the authors, the application of the SWCNTs-network made the sensors more stable than the devices employing single CNTs. The adsorption of DMMP (a strong electron donor) on the *p*-semiconductor CNTs resulted in a substantial increase of their electric resistance. It was attributed to the donor interaction of a DMMP molecule on the majority current carries in SWCNTs i.e., the capture of holes was expected due to the transfer of a negative charge from adsrobate to CNTs. It was also discovered that setting of a positive potential at the back gate (Si-background) was necessary to offset the negative charge induced in CNTs by the bonded DMMP molecules. The interaction between the negative charge on the phosphate oxygen atoms (in DMMP) and CNTs helps to explain the observed electric effects. The positive bias at the gate electrode was very helpful for the recovery of the starting resistance of the CNTs-based transistor. Simple recovery attempts by the exposure to pure air were not successful since the removal of residual DMMP molecules lasted for hours, however positive bias at the back gate shortened the recovery process. The sensors exhibited no response to some contaminants, such as vapours of water and hexane. Novak and co-workers presented another spectacular effect achieved by the application of a strong hydrogen-bonding polymer as pre-filter which differentiated the response of sensor to specific substances.

Cui and co-workers[71] reported a side wall osmylation of SWCNTs, i.e., immobilisation of an osmium tetraoxide

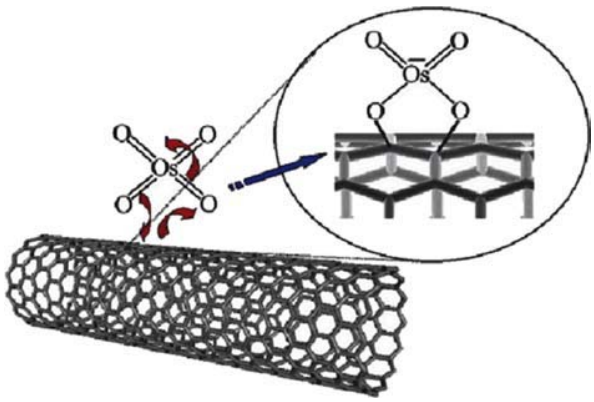

Fig. 46. Reaction scheme illustrating the cycloaddition of osmium tetroxide (OsO_4) to the sidewall of a Single-Walled Carbon Nanotube (SWCNT) leading to an osmyl ester of a 5-membered ring structure. Arrows indicate the flow of electrons during bond formation. Reprinted with permission from [71], J. Cui et al., *Nano Lett.* 3, 613 **(2003)**. © 2003, American Chemical Society.

on the tubes. The reaction was performed by cycloaddition of OsO_4 to double bonds in the rolled graphene sheets as presented in Figure 46. The sidewall functionalization of SWCNTs was achieved in the gas phase in the presence of oxygen. UV irradiation was necessary to initiate the reaction. The osmylation decreased the conductance of the SWCNTs by several orders of magnitude. The process of osmylation was found to be a reversible phenomenon, in which the simultaneous action of three factors caused the effect of enhanced sensitivity. That were: The presence of OsO_4, the presence of O_2 and UV irradiation (Fig. 47). When the action of one of them was terminated the process of osmylation was frozen (the lack of UV) or reversed (no contact with OsO_4). No reaction with O_2 was noticed

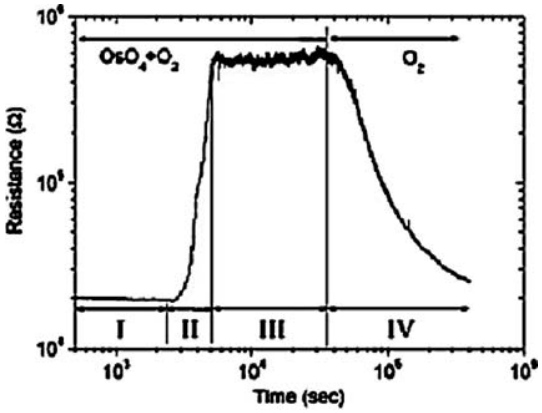

Fig. 47. Two-terminal resistance of the metallic SWCNT measured *in situ* for different gas-phase compositions. Regions I and II correspond to the tube in the $OsO_4 + O_2$ atmosphere without and with UV light irradiation (254 nm), respectively. Within region III, no UV light was used. After the removal of OsO_4, the sample was again irradiated with UV light, this time in a pure O_2 atmosphere (region IV). Reprinted with permission from [71], J. Cui et al., *Nano Lett.* 3, 613 **(2003)**. © 2003, American Chemical Society.

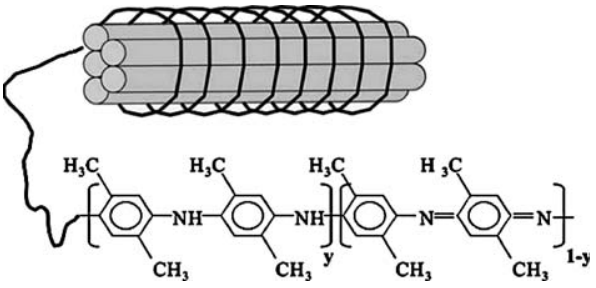

Fig. 48. Schematic of PDMA conducting polymer wrapped up around MWCNTs. Reprinted with permission from [72], V. Bavastrello et al., *Sens. Actuators B* 98, 247 **(2004)**. © 2004, Elsevier.

even if the treated sample was under UV irradiation. The experiment showed that some sidewall functionalisations could be reversible and might be employed for chemical sensing as in the case of volatile metal oxide (OsO_4).

Another non-conventional CNTs- based sensor was presented by Bavastrello et al.[72] They synthesized a nanocomposite consisting of poly(2,5-dimethylaniline) and MWCNTs. The authors suggested an interaction between the component that was characteristic because of chains of the conducting polymer (PDMA) wrapped around packages of aligned MWCNTs as it is depicted in Figure 48. The material was obtained in a multi-step procedure and was sensitive to the presence of acidic vapour like HCl. The adsorption of HCl strongly influenced the equilibrium between the doped and undoped form of the polymer. The doping-undoping transition affected electric conductivity of the investigated nanocomposite. In this study, the polymer was recognized to fulfill two roles: adsorption of the detected acidic vapours, and change its electrical properties upon adsorption of HCl.

2.2. Carbon Nanotubes as Sensitive Electrode Material

Carbon nanotubes have been investigated as a material for the construction of selective electrodes. Electrodes interact not only with the molecules of detected substances but can react with the solvent (in most cases water) particularly at high or low pH. Therefore electrode manufacturing that ensures long-term stability in liquid solutions is challenging task. The following section is focused on the preparation of carbon-based electrodes with particular emphasis on applications. Generally, carbon based electrodes can be fabricated in one of the following basic forms:

(1) A complex system consisting of a conductive background covered by a sensing carbon layer by means of a chemical glue or hardening agent.

(2) A complex system consisting of a conductive foundation being in contact with a powder of carbon materials (active carbon, carbon black, carbon nanotubes, graphite etc.).

(3) Monolithic carbon electrodes prepared in form of a rod or film where no separate carbon-based layer exists.

(4) Soft or solid carbon electrode consisting of small carbon particles assembled by means of an inert media (oil, polymer etc.).

Thus, in some electrodes one can expect two phases: a passive part that is responsible for charge transfer (carbon-based conductor, metal or conducting polymer) and an active carbon phase that is responsible for the electrode processes. Despite the role ascribed to carbon materials, all such electrodes are usually called carbon-electrodes with a little regard if the carbon component is passive or active.

Carbon in any of the mentioned forms can be applied as-prepared or in a chemically modified form, i.e., by means of some additional chemical treatments like oxidation, reduction, metallization, deposition of chemically active substances (or mixing with). In addition, the form of the active carbon phase can be very different and one may use active carbon, carbon black, graphite, fullerenes, or carbon nanotubes. Writing a complete survey on the application of carbon-based electrodes for chemical sensing seems to be quite a complicated matter due to the variety of possible electrode constructions, chemical treatments, and forms of carbon. Therefore, we present only selected problems with respect to electrode design and application.

Generally, CNT-containing electrodes may utilize them in form of a loose powder or as a solid deposit where single tubes are constrained by means of an inert substance. Gavalas et al.[73] immobilized MWCNTs (obtained by decomposition of methane over a dispersed iron catalyst) using the sol–gel method. Since the conventional sol–gel pathways like hydrolysis of a silane precursor require extreme pH conditions, Gavalas et al.[73] elaborated a modified method to avoid undesired reactions of CNTs in alkaline solution. The method relied on the application of sodium silicate solution (of strong base reaction) but it was stepwise neutralized by an acidic ion-exchange resin, HCl solution, and finally stabilized by a phosphate buffer containing a biologically active substance, the enzyme L-Aminoacid Oxidase (L-AAOx). At this stage, MWCNTs were added and the whole mixture was left until gelation. The resulting homogenous CNTs-based composites were packed into a Teflon tube affixed with a metal contact. Such fabricated electrodes were tested for the determination of the concentration of an amino acid (L-Phenylalanine). The overall electrode reaction was expressed by: L-Amino-Acid $+ H_2O + O_2 \rightarrow$ (L-AAOx) 2-Oxo-Acid $+ NH_3 + H_2O_2$. The H_2O_2 molecules underwent electrocatalytic oxidation on the MWCNTs yielding current when the sensing electrode was included into an amperometric experimental set-up and the potential of $+800$ mV versus Ag/AgCl electrode. Thus, one ascribed an active role to CNTs assuming their catalytic activity in

oxidation of hydrogen peroxide. Moreover, CNTs incorporated in the composite were responsible for current conduction within the electrode what was summarized in the expression "CNTs facilitated fast electron transfer."

Another approach to CNT-immobilisation was elaborated by Sotiropoulu et al.,[74] who worked on novel carbon materials for the construction of amperometric sensors for glucose detection. The background idea for the reported study was the combination of positive features of fullerenes and porous glassy carbon. Glassy carbon is a good candidate for electrode fabrication since it is mechanically stable, chemically resistant, effective current conductor. Fullerenes and CNTs offer unique electric and catalytic properties (frequently investigated and understood in part only) that have been utilized for the fabrication of chemically sensitive materials. Both materials i.e., porous glassy carbon and fullerenes are able to accommodate biologically active substances like proteins (particularly enzymes). The authors reported that the application of porous glassy carbon electrode loaded with fullerenes and glucose oxidase resulted in an enhanced electrode performance. Glucose detection in solution and oxidation of hydrogen peroxide were the test reactions to evaluate the performance of the electrodes. One attributed the immobilization of the enzyme to the properties of glassy carbon particularly to the presence of mezopores and to the presence of oxygen-containing surface functional groups. The sensitivity of the electrodes to the detection of dissolved glucose increased with the fullerene amount packed in the glassy carbon background.

Two basic factors rule the process of organic molecule immobilisation on carbons, geometrical (pore structure), and chemical (surface functionalization). The presence of micropores and mezopores means the existence of spaces on the carbon surface where the adsorption potential is high since the attraction forces cumulate inside the pores. The non-specific adsorption forces resulting from the curvature of the solid surface can be supported by specific interaction resulting from the existence of surface functional groups (also in the pores). Thus, the groups of various chemical compositions (containing oxygen, nitrogen, hydrogen, sulphur, etc.,) contribute significantly to the complex adsorption forces. Contrary to other porous materials, pores in carbon are slit-like ones what ease the adsorption of large molecules of organic substances. Moreover, all carbons are good electric current conductors and can work as an excellent mediator for processes involving charge transfer. The carbon matrix transmits electrical signals like electron capture (or release) to the encapsulated molecules (like enzymes) what would by extremely difficult in the case of insulating matrices.

Using water-based solutions of PTFE and MWCNTs Weinecke et al.[75] fabricated membrane-electrodes exhibiting an increased electrode sensitivity for gas sensor application. The composite electrode material was prepared by

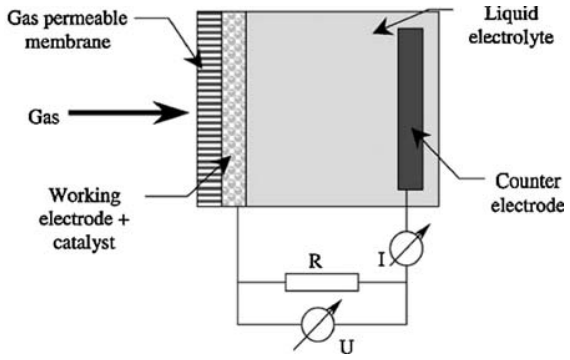

Fig. 49. Schematic presentation of an amperometric gas sensor with two electrodes. Reprinted with permission from [75], M. Wienecke et al., *Synth. Met.* 138, 165 **(2003)**. © 2003, Elsevier.

mixing water-based PTFE solution with MWCNTs aiming at the target CNTs concentration from 0.5 to 10% wt. The mixture was filtrated through a PTFE membrane and the whole material was sintered for 15 minutes at 150–300 °C. Metal particles were deposited by immersing of CNTs containing membranes in a solution of $AgNO_3$ and $SnCl_2$. Sintering and the presence of CNTs with metal particles provided low electrical resistance of the whole electrode. The membrane was in contact with gas and with liquid electrolyte in which a counter electrode was immersed. One could measure the current intensity and its changes versus the concentration of traced gas being in contact with the membrane-electrode (Fig. 49). The PTFE matrix was responsible for gas molecule separation, while the CNTs and metal particles ensured electrode conductivity and acted as an active catalyst. The membrane-electrode geometry helped to upgrade sensitivity from ppm to ppb level.

Male et al.[76] describe an electrode consisting of a glassy carbon conducting support covered by SWCNTs on which Cu particles were present (Fig. 50). The metal particles were deposited via the chemical reduction of cupper dodecyl sulphate ($Cu(DS)_2$). The cyclic voltammetry and TEM images confirmed that Cu particles were in contact with the glassy carbon background through SWCNTs. The electrodes were examined for the determination of glucose concentration in water up to 250 μM. The electrodes worked in an amperometric mode (+0.65 V put on the sensing electrode versus Ag/AgCl reference) and exhibited four-fold increase in the sensitivity when compared to a bare Cu disk electrode. One assumed a synergistic effect in the Cu-SWCNTs system that resulted in an enhanced sensitivity of the electrodes. Authors claimed that the reproducibility within a series of electrodes consisting of 30 elements was 5.7% at 100 μM glucose concentration. Additionally, some experiments were performed using monosacharides like galactose, arabinose, xylose, fructose, and mannose (similar current response as for glucose) and disaccharides maltose, lactose, sucrose, trehalose (reduced current response than for monosacharides). The presence of SWCNTs in the composite sensing layer improved

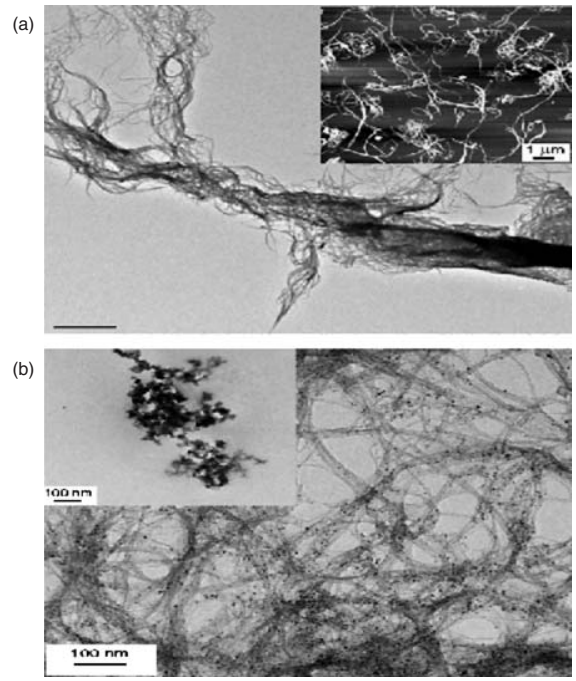

Fig. 50. (a) TEM micrograph of untreated SWCNTs dissolved in 0.5% Nafion, inset: AFM tapping-mode height image (size: 10 μm × 10 μm, data scale: 100 nm) of SWCNTs. (b) TEM micrograph of SWCNT in the presence of Cu nanoparticles, inset: TEM micrograph of Cu nanoparticles in the presence of Nafion. Reprinted with permission from [76], K. B. Male et al., *Anal. Chim. Acta* 516, 35 **(2004)**. © 2004, Elsevier.

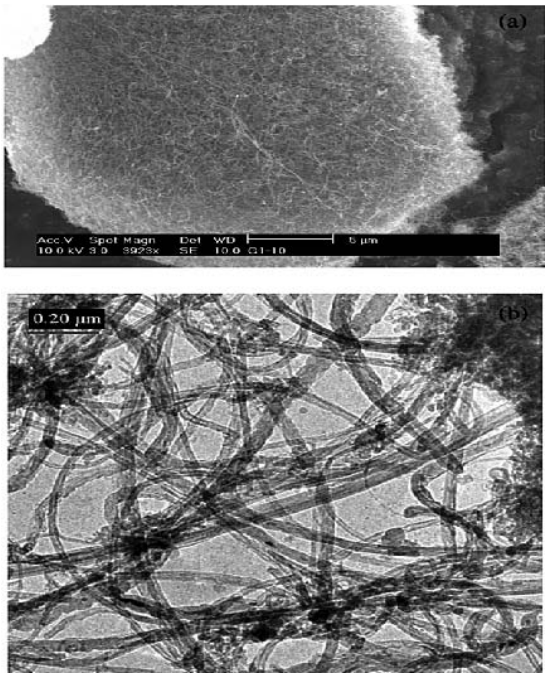

Fig. 51. STM (a) and TEM (b) images of carbon nanotubes used to fabricate the CNTPME. Reprinted with permission from [78], Y. D. Zhao et al., *Micromech. J.* 75, 189 **(2003)**. © 2003, Elsevier.

the selectivity of such electrodes to glucose when some test were performed to find out the influence of selected electroactive interferents (typical blood components like uric acid, ascorbic acid, acetaminophen) on the electrode performance.

Wu et al.[77] examined another way of fabrication of a CNTs-containing electrode, which later was tested as an amperometric sensor for indole-3-acetic acid (IAA), that is a substance known to regulate some basic biological processes like division, elongation, and differentiation of cell. MWCNTs were stuck on a glassy carbon background by means of hydrophobic surfactant dihexadecyl hydrogen phosphate (DHP) that was added to water dispersion of CNTs. After water evaporation the hydrophobic surfactant physically bonded a layer of randomly oriented CNTs to the surface of glassy carbon. The electrode with the CNTs layer was stable and its response to a fixed concentration of IAA was reproducible even after 36 measurements. The electrode resisted cyclic voltammetry tests at pH = 2. The presence of the MWCNTs layer significantly enhanced the current corresponding to oxidation of IAA compared to the behaviour of a bare glassy carbon electrode. The sensor found an application to the determination of IAA in plant leaves and the results were comparable with the results obtained by HPLC. From the experimental section of the paper one may assume that MWCNTs (synthesized by a catalytic pyrolysis) were cut, decapitated, and partially oxidized by HNO_3 treatment lasting for 10 hours.

Zhao et al.[78] applied CNTs as a sensing material for fabrication of sensing electrodes. The CNTs were not immobilised and were utilized as a powder for the electrooxidation and electroreduction of nitrite. The CNTs were prepared by catalytic chemical vapour decomposition of methane over Co/MgO catalyst. Such obtained CNTs were placed in a cavity first etched in a Pt microelectrode (Fig. 51). The sensing electrode was a part of a standard three-electrode cell (CNTs/Pt–Pt-Ag/AgCl). The test reactions were electro-oxidation and electro-reduction of nitrite that were found to be either 2-electron oxidation: $HNO_2 + H_2O \rightarrow NO_3^- + 3H^+ + 2e$ or 1-electron reduction. Reduction of nitrite was selected to detect its concentration since that helped to avoid the interference of other ions at high oxidation potential (above +0.7 V). One observed the change of limiting current and noticed short response times (ca. 10 s) when +0.3 V potential was established on the sensing electrode. The logarithm of limiting current (nitrite reduction on CNTs) was linearly growing with the growth of logarithm of the nitrite concentration in solution with the detection limit of 8 μM. The study demonstrated the catalytic properties of CNTs and an easy way how to fabricate a sensitive electrode without any binder.

He et al.[79] also investigated MWCNTs for the fabrication of a powder microelectrode. A Pt disk electrode was applied to ensure a good electric contact with the powder of MWCNTs (catalytic decomposition of methane over Ni/Mg catalyst). In this study, MWCNTs were subjected to

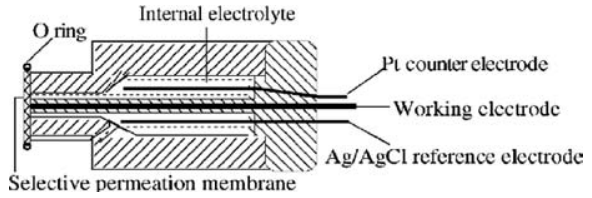

Fig. 52. Scheme of the CO gas sensor. Reprinted with permission from [79], J. B. He et al., *Sens. Actuators B* 99, 1 **(2004)**. © 2004, Elsevier.

a chemical pre-treatment consisting of backing at 550 °C (30 minutes) and a subsequent action of concentrated solutions of $HClO_4$ and HNO_3. In this way, the CNTs were purified, open at the ends and oxidized. The investigated CO gas sensor was a construction resembling the standard Clark electrode (Fig. 52). MWCNTs were stuck on a Pt rod in a small cavity. Additionally, the sensitive material was separated from the solution by a selective permeation membrane made of poly(ethylene). The response of the electrode was investigated towards CO concentration at constant potential of +0.7 V versus the Ag/AgCl reference electrode. The linear relationship of current versus the concentration of CO (in N_2 stream) was found for the range from 0.6 to 52 μg/ml. Comparative studies with the application of a bare Pt electrode confirmed the leading role of MWCNTs in oxidation of CO to CO_2. Overvoltage decreased for MWCNTs since some active oxygen containing species like $-OH_{ads}$ were easily generated and bonded to the surface of the tubes. The novel solution presented in this study consisted in the application of a selective membrane to solve the problem of selectivity.

Liu and Hu[80] constructed an electrochemical sensor for the detection of NO_2^- by means of MWCNTs encapsulated in a cavity that was etched at the tip of Pt disk. This concept, i.e., a direct utilization of CNTs powder placed on a Pt support, is similar to that it the previously mentioned studies however the MWCNTs were oxidised *in situ* by anodic polarization of the sensing electrode (+1.4 V vs. SCE) for 80 minutes in 0.05 M H_2SO_4. Assuming the behaviour of CNTs to be similar to glassy carbon, Liu, and Hu expected to create quinone type functionalities on the surface of the tubes. Anodically oxidized MWCNTs were shorter than before the treatment (proven by TEM investigations), and probably open at the ends since the energy needed to decapitate the tubes was lower than that one necessary for cutting. The oxidized MWCNTs were soaked in 5 mM $Os(bpy)_3^{+2}$ to adsorb these ions and modify the catalytic properties of the tubes towards the reduction of NO_2^-. They discovered that the adsorption of $Os(bpy)_3^{+2}$ catalyst on non-oxidized CNTs was weak and the osmium catalyst was easy to leach in water. The adsorption of the ions after anodic oxidation was more durable. The careful analysis of the $Os(bpy)_3^{+2}$ reduction peak led to the conclusion that the $Os(bpy)_3^{+2}$/MWCNT ratio is close to 1 suggesting that the ions were adsorbed at the open ends of the tubes.

The synthesis of CNTs created new opportunities for the construction of biosensors for the detection of biologically active molecules like DNA or proteins. The application of bare CNTs, however successful as presented above, is not the only possibility. A step ahead can be done provided one subjects CNTs to chemical manipulations. The detection of DNA is often based on the known ability of pairing interaction. The process of pairing of DNA chains is highly selective. Some attempts have been made towards the immobilization of single DNA molecules on various backgrounds. He and Dai[81] proposed a novel method of DNA immobilization on aligned SWCNTs. The problem of DNA attachment is not simple since the use of aligned CNTs in many chemical manipulations led to the destruction of the parallel alignment of the tubes. The novel method proposed by He and Dai[80] consisted of the synthesis of aligned SWCNTs on a gold support (thermal decomposition of iron (II) phthalocyanine) by acetic acid plasma treatment. In this way the CNTs preserved their alignment and underwent carboxylic functionalization at the ends in the same time. That step was followed by grafting single-strand DNA due to amide formation between −COOH groups and amino group at the 5′-phosphate end in the presence of [1-(3-dimethylaminopropyl)-3-ethylcarbodiimide hydrochloride] as it is depicted in Figure 53. Complementary DNA (cDNA) marked with ferrocenecarboxalehyde was used as for hybridization with the immobilized DNA stands. Thus, double strand DNA helices were formed on the aligned carbon nanotube electrode. The DNA helices grew not only at the ends of CNTs but also at the walls. Cyclic voltammetry studies let to observe a long-range electron

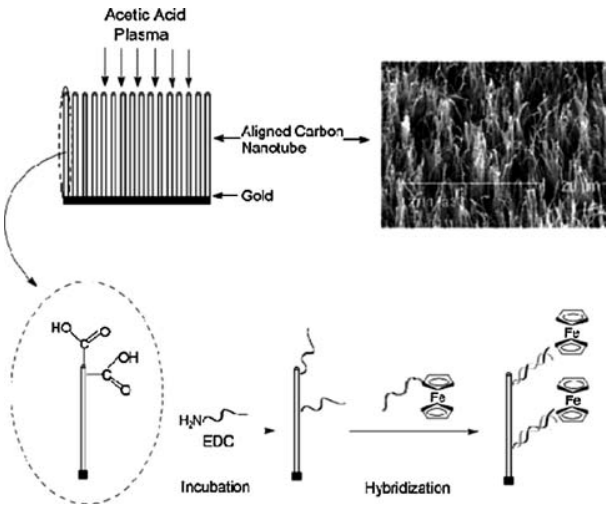

Fig. 53. A schematic illustration of the aligned nanotube–DNA electrochemical sensor. The upper right SEM image shows the aligned carbon nanotubes after having been transferred onto a gold foil. For reasons of clarity, only one of the many carboxyl groups is shown at the nanotube tip and wall, respectively. Reprinted with permission from [81], P. He and L. Dai, *Chem. Commun.* 3, 348 **(2004)**. © 2004, Royal Society of Chemistry.

transfer from the ferrocene marked DNA to the CNTs-electrode via the DNA duplex. Additionally, a strong oxidation peak of ferrocene was observed at the potential +0.29 V. Side effects like non-specific DNA paring and physical adsorption of marked DNA chains on CNTs-electrode could be neglected.

Ye and co-workers[82] proposed another analytically important functionalization of CNTs-based electrodes aiming at the fabrication of electrodes sensitive to dissolved oxygen. They assumed that hemin (iron (III) protoporphyrin) being a centre of heme-proteins like hemoglobin could act as an effective catalyst for dioxygen and hydrogen peroxide reduction. One may add that hemoglobin molecule contains a structure resembling hemin molecule. The central iron atom is capable (in hemoglobin) of reversible adsorption of molecular oxygen and CO_2. The important difference between the two substances consists in the oxidation state of iron, which is (III) in hemin and (II) in hemoglobin. The method of MWCNTs synthesis (pyrolysis of organic substances) provided that the tubes with diameter of 80–120 nm were long (ca. 10 μm) and well aligned (Fig. 54). One applied Ta plate covered with a thin layer of Co particles, with diameters ranging from 8 to 50 nm. The metal support with grown MWCNTs was stuck by means of Ag paste on the tip of a glassy carbon rod that was separated from the solution by a Teflon coating.

The hemin-fuctionalization consisted in the immersing of a bare MWCNTs-electrode in the hemin solution

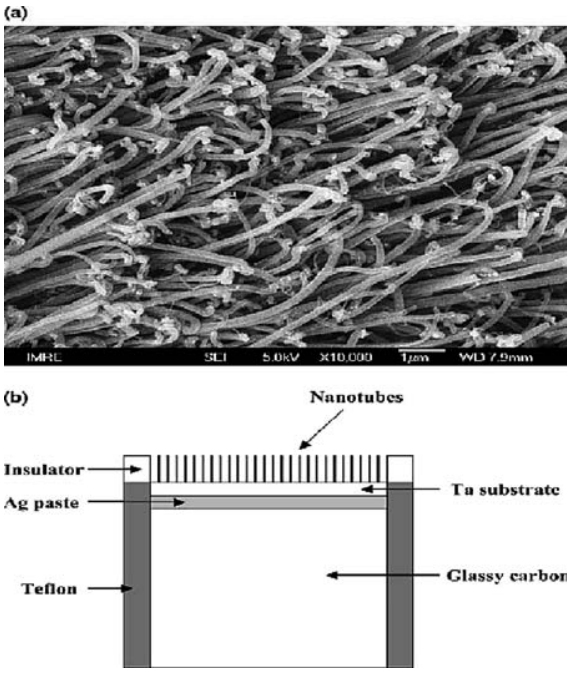

Fig. 54. (a) Scanning electron microscopy (SEM) images of the well-aligned MWCNTs. (b) Schematic of details showing the cross section of the MWCNT electrode. Reprinted with permission from [82], J. S. Ye et al., *J. Electroanal. Chem.* 562, 241 **(2004)**. © 2004, Elsevier.

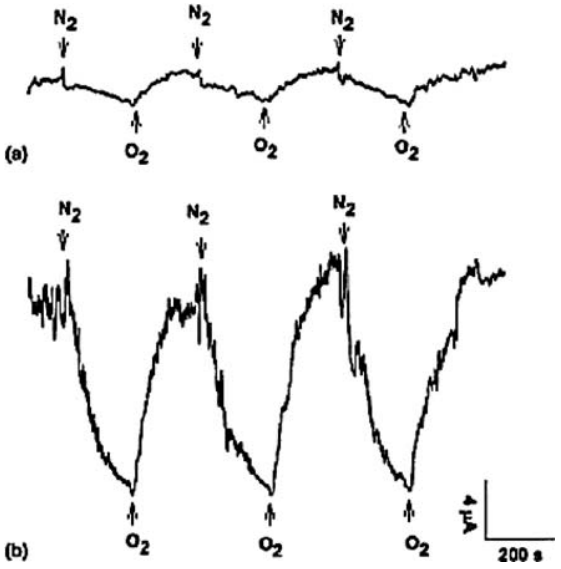

Fig. 55. Amperometric response of oxygen reduction in pH 7.4 PBS to the bubbling of N_2 or O_2 gas at either (a) the MWCNT electrode or (b) the hemin-modified MWCNT electrode. Applied potential: 0 V. Reprinted with permission from [82], J. S. Ye et al., *J. Electroanal. Chem.* 562, 241 **(2004)**. © 2004, Elsevier.

in 0.03 M KOH. Authors suggested that the performed functionalization was non-covalent and proceeded due to π-π interactions in the hemin—MWCNTs system. As-grown and hemin-modified MWCNTs electrodes were subjected to the influence of oxygen dissolved in a phosphate buffer (pH = 7.4). Hemin-modified MWCNTs electrodes gave three peaks corresponding to the reduction of O_2 at −0.087, −0.182, and −0.290 V versus Ag/AgCl (3 M KCl) reference electrode. The recorded reductive current was 4 times higher than for electrodes without hemin (Fig. 55). The influence of oxygen concentration on the electrode current was tested in a phosphate buffer solution when the hemin-modified and non-modified amperometric sensors were exposed to the bubbling N_2 and O_2. One observed a reversible increase of reducing current (at 0 potential) upon switching to pure oxygen. The recorded increase of current for the hemin-modified electrode was sevenfold greater than for the non-modified electrode.

2.3. Mass-Sensitive Devices Incorporating CNTS

Mass sensitive devices can be also constructed employing CNTs. Their operation requires only the adsorption of detected species and charge transfer is not necessary for sensor operation. The signal generated by the mass sensitive devices (a shift of resonant frequency) is usually caused by extremely small amounts of adsorbed species.

Ono et al.[83] reported the construction of a mass sensitive device for H_2 detection in air, which was designed by employing CNTs as sensitive material. CNTs are an attractive candidate for sensing materials because of known

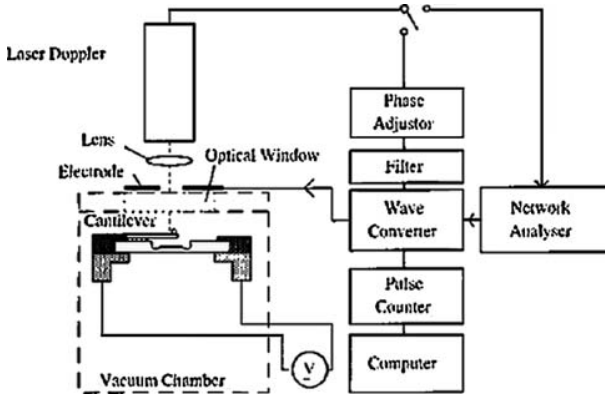

Fig. 56. Experimental set-up of the vibration measurement system. Reprinted with permission from [83], T. Ono et al., *Rev. Sci. Instrum.* 74, 1240 **(2003)**. © 2003, American Institute of Physics.

CNTs capability to the reversible hydrogen storage. In the study, thin (170 nm) cantilevers were used a resonant element for the deposition of 10^{-12}–10^{-13} g of CNTs. The CNTs were synthesised by a hot-filament CVD method using H_2/C_2H_2 and iron catalyst. The CNTs were of 2–8 nm diameter. A bundle of separately synthesised CNTs was trapped by mechanical manipulation with a sharp tip and the end of silicon cantilever as in Figure 56. The bundle needed to be cleaned from adsorbed species by heating up to 1000 °C in nitrogen. The cantilever was brought to oscillate due to electrostatic forces. Both the mass of CNTs and the amount of adsorbed hydrogen were calculated from the observed changes of the resonant frequency of the cantilever. The device exhibited an extreme mass sensitivity of 5×10^{-18} g with a 2–3 Hz drift per day atop the basic signal of ca. 100 kHz. One has to notice that bare CNTs can reversibly and effectively adsorb molecular hydrogen. Nevertheless, the results show that the device is quite far from a practical application.

Wei and co-workers[84] tried to detect CO, NO_2, H_2, and N_2 in air at the operation temperatures from 25 to 200 °C. It was discovered that temperatures above 100 °C upgraded the sensitivity of such sensors. The sensors' response noticed for lower temperatures were significantly less spectacular. Surprisingly, the adsorption of the investigated gases increased the resonant frequency of CNTs-coated crystals. In usual cases, quartz crystal microbalance sensing devices generate a decrease of its resonant frequency during detection. Due to the unexpected frequency increase, authors assumed that the sensing mechanism was more complex and based on the weight lost instead of increase. The given explanation implied the adsorption of oxygen prior to the adsorption of detected gases. It seems to be probably since the elevated temperature of operation (the best results were achieved at 200 °C) has to ease the oxidation of CNTs. The adsorbed oxygen molecules were later competing with detected molecules for occupation of the same adsorption sites. Thus, the detection mechanism should be seen as a mass change (parallel desorption and adsorption) resulting from gas exchange in adsorption complexes, or change in coating elasticity.

SAW sensors are another class of gas sensitive devices that can employ CNTs as a sensing material. Penza and co-workers[85] demonstrated that such a sensor reacted to the change in concentration of selected volatile organic liquids. For this purpose, MWCNTs and SWCNTs were applied. CNTs were deposited as a sensing layer onto a substrate by means of spray-painting method. The tubes were dispersed in ethanol or toluene and overlayed without any binder. Their adherence to the background and the mechanical stability of the oscillators was provided by coverage the substrate with a thin SiO_2 film (sputtered). The sensor design (Figs. 57, 58) is an example how

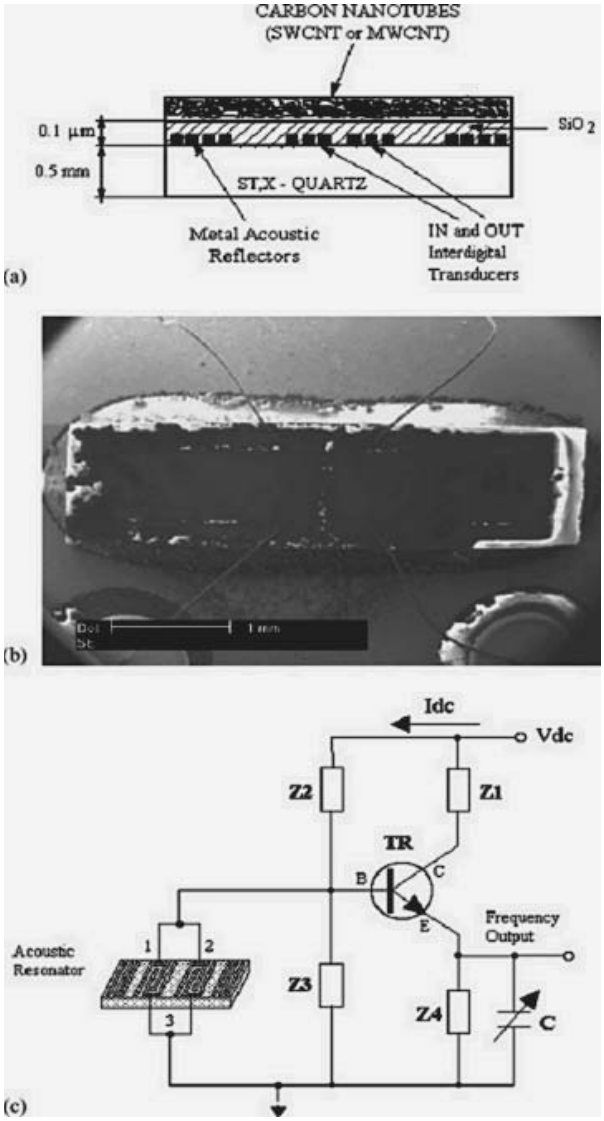

Fig. 57. (a) Cross-sectional view of the SAW sensor coated by carbon nanotubes; (b) top view SEM image of the SAW sensor coated by carbon nanotubes in a TO-39 open case; (c) scheme of SAW sensor oscillator with RF amplifier. Reprinted with permission from [85], M. Penza et al., *Sens. Actuators B* 100, 47 **(2004)**. © 2004, Elsevier.

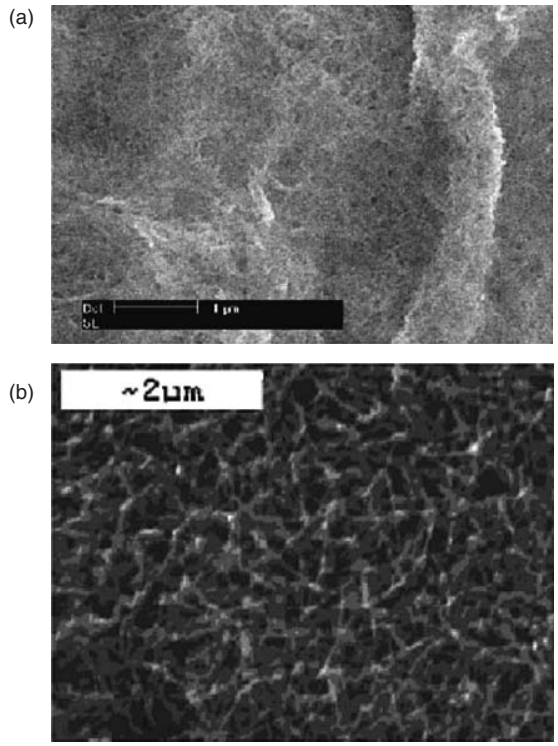

Fig. 58. SEM image of (a) SWCNTs and (b) MWCNTs coatings sprayed onto SAW quartz substrate. Reprinted with permission from [85], M. Penza et al., *Sens. Actuators B* 100, 47 **(2004)**. © 2004, Elsevier.

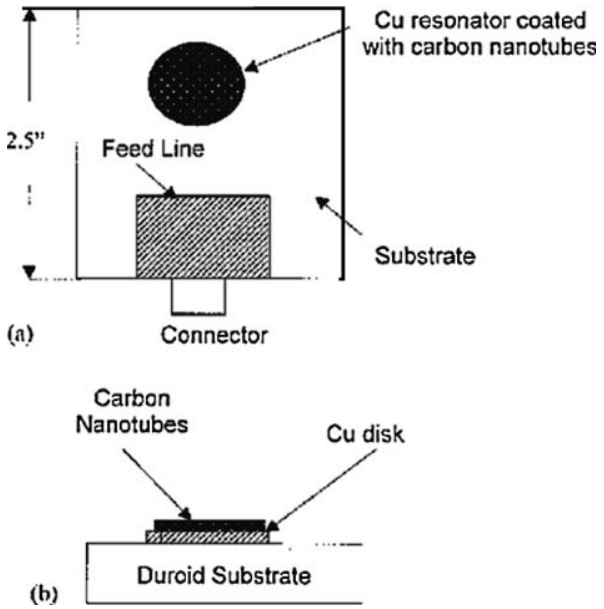

Fig. 59. (a) Schematic of the resonator sensor used in this study. The shaded regions represent copper metal on which the nanotube coating is applied. (b) Cross-sectional view of the resonator sensor. Reprinted with permission from [86], S. Chopra et al., *Appl. Phys. Lett.* 80, 4632 **(2002)**. © 2002, American Institute of Physics.

the nanotubes can be immobilized without any particular binder yielding a coherent layer. The SAW sensors exhibited a substantial downshift of the oscillation frequency due to adsorption of organic molecules. It has to be noticed that the adsorption of several organic species (vapours of ethanol, ethylacetate, and toluene) modulated the resonant frequency at room temperature. The lowest detection limit of ca. 1.3 ppm was achieved for toluene vapours that were interacting with SWCNTs deposited from the toluene dispersion and for ethanol vapour interacting with SWCNTs deposited from the ethanol dispersion. The tests were performed for the concentration range from single ppm to ca. 200 ppm (ethyl acetate) or to ca. 100 ppm (ethanol and toluene). The highest sensitivity was achieved for the substances that were also used for the preparation of CNTs dispersions. It was suggested that the phenomenon resulted from the presence of the solvent residuals on the surface of the CNTs. Thus, the detection was easier since the adsorbate and adsorbent surface had a high affinity to each other. Moreover, it was proven that oxygen chemisorbed first on CNTs helped to retain quite durably some ethanol molecules on the surface due the formation of hydrogen bonds. On the contrary, the chemisorbed oxygen promoted only weak attraction of non-polar solvents like toluene that was used for the dispersion of CNTs. The CNTs deposited from toluene dispersion did not retain toluene molecules as strongly as ethanol molecules were attracted by the oxidised carbon surface. It is reasonable that one may consider the contact of organic liquids (from a dispersion of CNTs) as a kind of a non-covalent functionalization of CNTs. The example points out the key role of CNTs functionalization and their surface state in design of chemical sensors containing the CNTs.

Chopra et al.[86] described a sensing device based on the downshift in resonant frequency of circular electromagnetic resonator as depicted in Figure 59. CNTs were stuck onto a copper resonator by means of a conductive epoxy resin. The resonant frequency of the sensing element was determined by the properties of dielectric materials, i.e., Duroid board and CNTs interacting with electromagnetic field generated by a RF transmitter. CNTs were supposed to change their dielectric properties upon adsorption of gases and vapours as it was presented by means of NH_3. Authors suggested that NH_3 molecules, when interacted with carbon atoms in CNTs, created surface charges leading to variations of the dielectric constant value. Thus, the phenomenon was based on the ability of adsorbed molecules towards the charge transfer to and from CNTs. The detection of NH_3 consisted in the continuous monitoring of the frequency downshift of the resonator by means of a remote antenna. Thus, the detection system did not need any direct electric connection between the sensitive element and the electronic device transmitting and receiving electromagnetic waves. This principle of operation enables a remote detection of chemical substance inside packages or other isolated spaces. In the study, one employed SWCNTs and MWCNTs as adsorbing material. The frequency shifts noticed for the NH_3 adsorption on

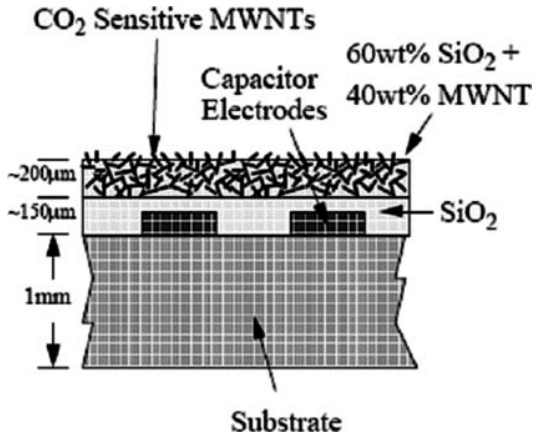

Fig. 60. Cross sectional view of the interdigital capacitor. An electrically insulating 150 μm hick SiO_2 layer is first applied to protect the sensor, followed by a 200 μm MWNT-SiO_2 gas sensing layer. Reprinted with permission from [87], K. G. Ong and C. A. Grimes, *Sensors* 1, 193 (**2001**). © 2001, MDPI Publ.

SWCNTs were ranging from 0.5 to 6 MHz when ammonia concentration changed from ca. 100 to 1400 ppm (base frequency 4 GHz).

The advantages remote-query sensing systems were utilized by Ong and Grimes[87] to trace CO_2 in isolated spaces; the resonator is depicted in Figure 60. The sensor structure has a certain capacitance (C) and inductance (L), which interact with electromagnetic signals using the resonant frequency ascribed to the resonators. The LC sensors did not need to be connected to any power supply. It provided a long and wireless operation of such sensors even if they were placed in a quite remote area. The fabricated sensors consisted of two electrodes deposited onto a substrate. The whole assembly was first covered with a layer of SiO_2 and then by a mixture of SiO_2 and MWCNTs (3 : 2 ratio). SiO_2 played the binding role for CNTs. The sensor's response was detected by measuring the impedance spectrum of a remote antenna that monitored the LC sensors. The analysis of the antenna impedance let to calculate the value of complex permittivity of the sensing material i.e., CNTs incorporated in the sensing layer. The phenomenon was ascribed to the interactions between the electron pairs in CO_2 molecules and CNTs. Authors found that complex permittivity of MWCNTs decreased upon the exposure to pure CO_2 due to higher adsorption rate of CO_2 on MWCNTs than for other competitive gases like N_2. Although not proven in the experimental way, the last assumption is fully justified since nitrogen is a poorly adsorbing gas at room temperatures despite the nature of adsorbing solid. Nitrogen adsorption increases significantly at liquid nitrogen temperature what is conventionally employed for the determination of pore structure of solids. The sensor's response to the changes of CO_2 concentration was fast (ca. 50 seconds) in adsorption and desorption cycle. No sensing hysteresis was noticed. A limited cross sensitivity occurred towards water vapour but the problem was solved by the construction of a sensor array employing additional sensors: SiO_2-coated and uncoated one. The last two sensors did not respond to CO_2. Therefore, the complex response of the array was possible to resolve aiming at the elimination of water vapour influence on the CO_2 readings. The MWCNTs used in the study were synthesised by thermal decomposition of ferrocene dissolved in xylene under Ar/H_2 atmosphere. Such obtained CNTs were dispersed in liquide SiO_2 solution and dropped onto the substrate forming a porous, 200 μm thick coverage.

Varghese and co workers[88] performed comparative studies on the application of MWCTs to the detection of humidity, carbon dioxide, carbon monoxide, and ammonia. Two different kinds of sensors we examined. The first category of sensors had structure identical as the sensor depicted in Figure 60. The sensing layer contained MWCNTs mixed with a silica-based binder. A pair of interdigital electrodes let to treat the sensor as gas sensitive capacitor. The second type of sensors had a different structure. A serpentine path of SiO_2 was created by photolithography on the surface of silicon plate (ca. 1.7 cm $\times$ 1.7 cm) first oxidized at elevated temperature. Then, the substrate with etched serpentine of SiO_2 served as a background for MWCNTs deposition from gas phase (pyrolysis of ferrocene and xylene, Ar/H_2 atmosphere, 750 °C). In those conditions one observed the growth of MWCNTs only on the surface of SiO_2 serpentine which length was close to 45 cm. No deposition of carbon tubes was observed on the Si surface between the SiO_2 serpentine. This kind of sensor was treated as a resistor-type chemical sensor. Impedance analyzer let to collect impedance data resulting from the exposure of both types of sensors to the above mentioned gases and water vapour. The measures total impedance of both sensors was deconvoluted by means of appropriate theoretical models. In this way, one could determine equivalent circuits consisting of several capacitances and resistances. The impedance of the capacitor-type sensor increased significantly upon the increase of humidity. The resistances of resistor-type sensors increased upon water vapour adsorption but the growth was rather minor. The presence of ammonia, carbon monoxide, and carbon dioxide increased the resistance of the sensors, too. The gases are considered as electron donors. Thus, the electrons may localize holes in *p*-type MWCNTs incorporated in the sensors. The authors indicated that the sensing performance of the sensors was strongly affected the composition of sensing layer. Both type of sensors did react to the presence of oxygen but it was associated to the instant and durable adsorption of oxygen after exposure of the tubes to air. It could not be desorbed by the performed vacuum treatment at 100 °C. One assumed that ammonia molecules replaced pre-adsorbed oxygen causing irreversible changes of electric properties of the tubes and sensors incorporating MWCNTs. A similar capacitor-type sensor was reported by Ong, Zeng, and Grimes.[89] The sensor exhibited reversible changes of complex permittivity

(dermined by relative permittivity and conductivity of the sensing layer) upon adsorption of oxygen and carbon dioxide. The adsorption of ammonia caused reversible and irreversible effects. When the sensors were cycled between nitrogen and oxygen one observed an increase of conductivity of MWCNTs due to electron localization of the *p*-type tubes. Also in this study it was confirmed that NH_3 and CO_2 were acting as donors of electrons that could localize majority current carriers. The difference between the above described studies consisted mainly in the response of the sensors to oxygen.

2.4. Other CNT Chemical Sensors

Wong and co-workers[90] fabricated a quite complex structure in a four-step procedure: sputtering deposition of a thin palladium film (catalyst for growing CNTs) on a highly conductive *n*-type silicon plate, growing of MWCNTs on the metallized *n*-Si surface by means of microvawe plasma enhanced CVD from CH_4/H_2 mixture, short annealing for better adhesion of CNTs to the silicon plate (900 °C in argon), sputtering deposition of a thin Pd-layer on the top of CNTs. The fabricated structure is presented in Figures 61 and 62. The whole device had the structure equivalent to a Schottky-diode Pd/CNTs/n^+-Si, in which the Pd/CNTs interface was an ohmic one while the diode junction existed at the CNTs/n^+-Si interface. The recorded *I–V* curves were shaped as for typical metal-semiconductor diodes. The device was sensitive to molecular hydrogen at room temperature. The run of *I–V* curves was dependent on the presence of hydrogen. Generally, the adsorption of H_2 increased the potential barrier at the sensitive interface. Pd served as a catalyst for dissotiative adsorption of hydrogen. Hydrogen atoms penetrated the outer Pd-layer reaching the sensitive interface. The atoms

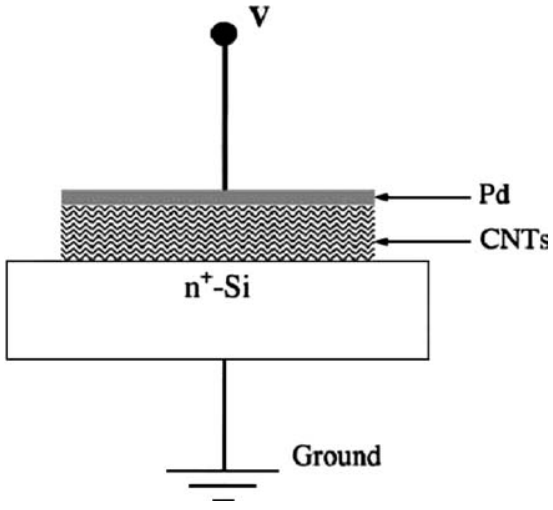

Fig. 61. Schematic diagram of the experimental setup of the CNTs-based gas sensor. Reprinted with permission from [90], Y. M. Wong et al., *Sens. Actuators B* 93, 327 **(2003)**. © 2005, Elsevier.

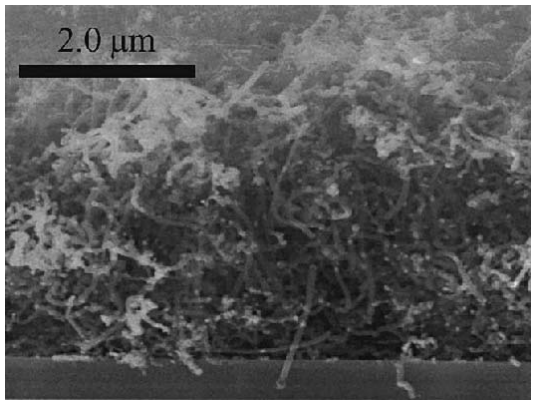

Fig. 62. SEM micrograph of the carbon nanotubes grown by MPECVD. Reprinted with permission from [90], Y. M. Wong et al., *Sens. Actuators B* 93, 327 **(2003)**. © 2003, Elsevier.

introduced dipoles at the interface. The induced voltage increased the potential barrier the Pd/CNTs interface. At elevated temperature of 170 °C the device lost its diode character since all the contacts became ohmic. Room operation and reversible response to hydrogen gas were the most important features of the described diode-type sensing devices.

Chen et al.[91] described non-covalent functionalization of CNTs for highly specific electronic biosensors that were sensitive to proteins. SWCNTs worked as platforms for the non-specific deposition of proteins. Protein sensitive devices were prepared by *in situ* synthesis of interconnected SWCNTs on a quartz substrate covered by an iron catalyst. The layer of SWCNTs behaved as a typical *p*-type semiconductor that bridged two metal electrodes. AFM and QCM studies revealed that 1 hour contact of CNTs with 10–50 nM buffered solution of a protein (streptavidin—SA, avidin, staphylococcal protein A-SpA, α-glucosidase-GCD, human IgG, BSA) resulted in a non-covalent attachment of some proteins due to hydrophobic interaction (Fig. 63). Non-specific bonding was found to be irreversible. Table IV indicates whether the mentioned proteins can be attached to as grown and modified CNTs. It is clear that pre-adsorption of some mentioned surfactants prevented the non-covalent bonding of some proteins that might be utilized for a selective adsorption of the desired proteins. The conductance of the inter-electrode layer of CNTs was gated by the voltages created by a Pt electrode immersed in a buffer solution above the sensitive area of the device (Fig. 64). The adsorption of protein molecules caused a significant shift in the conductance of CNTs layer versus gate voltage characteristics. Therefore, the whole device could be regarded as a FET device sensitive to protein adsorption. All adsorbed protein caused a decrease in conductance of the sensitive layer of as-grown CNTs. Authors expected a further progress in the application of such biosensitive devices basing on the synthesis of nanotube micro-arrays capable to detect a number of

REVIEW

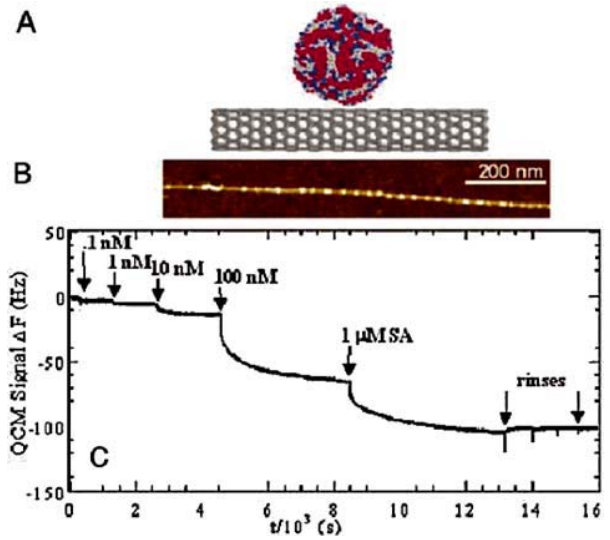

Fig. 63. Proteins tend to bind nonspecifically onto as-grown carbon nanotubes. (A) Schematic illustration of globular protein adsorption onto a nanotube. (B) An AFM image showing protein A (bright dot-like structures decorating the line-like nanotube) nonspecifically adsorbed on a nanotube. We have also observed a certain degree of NSB of proteins on regions of the (SiO_2) substrate free of nanotubes (data not shown). (C) QCM data (frequency shift Df vs. time t) revealing NSB of SA onto nanotubes at increasing protein concentrations. The NSB is irreversible upon rinsing. Reprinted with permission from [91], J. R. Chen et al., *PNAS* 100, 4984 (**2003**). © 2003, National Academy of Sciences.

Table IV. Selective bonding of proteins due to the pretreatment with some surfactants.

Nanotubes	SA	Avidin	BSA	GCD	SpA
As grown	Y	Y	Y	Y	Y
Tween 20-treated	N	N	N	N	N
Pluronic P103-tretaed	N	N	N	N	N
Triton X-100-treated	N	Y	Y	Y	N
Dextran-treated	Y	Y	Y	Y	Y

Source: Reprinted with permission from [91], R. J. Chen et al., *PNAS* 100, 4984 (**2003**). © (2003), National Academy of Sciences.

various proteins. The device would not need any labeling of proteins since the problem of selectivity could be solved by an appropriate pre-treatment with carefully selected surfactants.

Electric phenomena occurring in CNTs that might be induced by gas or vapour adsorption are not limited to the changes in electrical resistance. Sumanasekera and co-workers[92] investigated the influence of various gases and vapours on the thermoelectric power (TEP) generated in SWCNTs-based materials. The authors found that the thermoelectric power generated in CNTs was very sensitive to adsorption of gas even if the gas was inert. Thus, variation of TEP were observed upon the adsorption of oxygen, hydrogen, nitrogen, helium, methanol, ethanol, buthanol, benzene 1,3-cyclohexadiene, cyclohexane, and cyclohexene. A correlation between the number

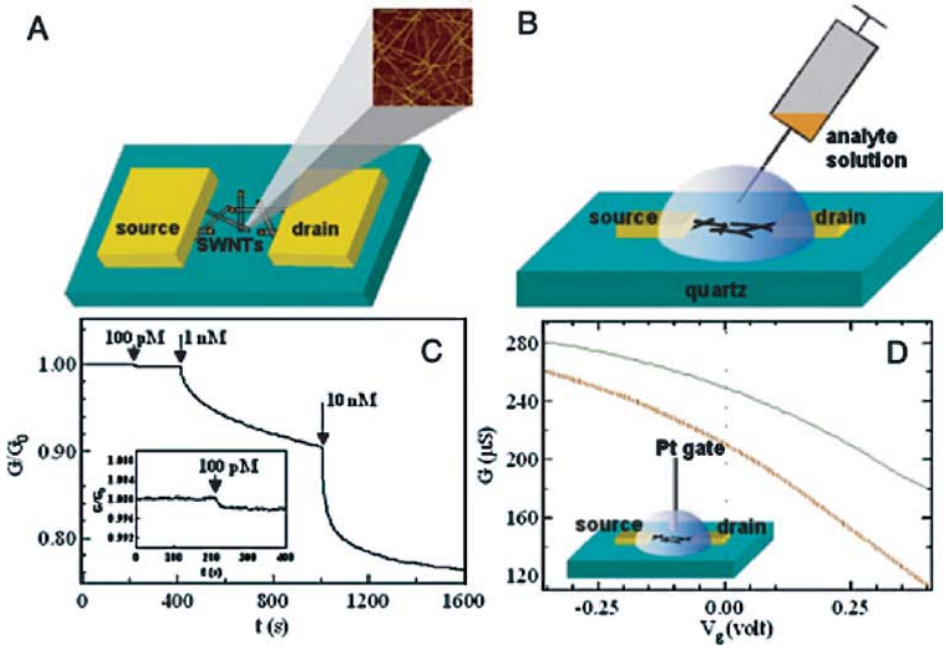

Fig. 64. Carbon nanotubes as electronic devices for sensing in aqueous solutions. (A) Schematic views of the electronic sensing device consisting of interconnected nanotubes bridging two metal electrode pads. An AFM image of a portion of the nanotube network (0.5 mm on a side) is shown. (B) Schematic setup for sensing in solution. (C) Conductance (G) evolution of a device for electronic monitoring of SA adsorption on nanotubes. The conductance is normalized by the initial conductance G_0. (*Inset*) Sensitivity to a 100-pM protein solution is shown. (D) Electrical conductance (G) versus gate voltage (V_g) for a device in a 10-mM phosphate buffer solution. The gate voltage is applied through a Pt electrode immersed in the solution (*Inset*). The green (solid) and orange (broken) curves are the G–V_g characteristics for the device before and after SA binding, respectively. The shift in the two curves suggests a change in the charge environment of the nanotubes. Reprinted with permission from [91], J. R. Chen et al., *PNAS* 100, 4984 (**2003**). © 2003, National Academy of Sciences.

of π-electrons in the organic rings (if a molecule contained such ones) and the magnitude of the registered TEP changes was found. The higher the number of π-electrons the more dramatic (larger) was the change of the TEP.

2.5. Electrodes and Chemiresitors

The physical properties of carbon pastes can differ significantly from the properties of solid carbon materials like glassy carbon, polycrystalline carbon, etc. Carbon pastes are soft substances that can be spread over a selected spot. The pastes are often self-sticking and do not need any other binder to stay on a covered spot. One may use different carbon powders or powdered carbons (grinded graphite, grinded active carbon, carbon black, CNTs, fullerenes) for fabrication of carbon pastes. Carbon pastes can be obtained by mixing of carbons in powdered form with a liquid component providing adhesion between the carbon particles and plasticity of the mixture. If the liquid component can harden upon polymerisation or evaporation of a solvent, such a carbon paste becomes a conductive solid preserving properties typical for carbons (good conductivity, chemical composition of the surface, porosity, and high surface area). The pastes before hardening can be mixed with other substances that can react more selectively with detected substances offering application to the construction of chemical and biological sensors. Often the sensitisation of a carbon paste by the admission of active substances like enzymes is much more easier and effective that the deposition of such substances on solid carbons like glassy carbon electrodes. There are many reports in the literature announcements on chemical sensors and biosensors fabricated by means of a carbon paste. Many of them do not consider the role nor pedigree of the carbon particles, with little attention paid to their chemical properties.

A recent report concerns the electrochemical reduction and oxidation of nucleic acids at carbon-based electrodes.[93] The electrodes exhibited the ability for interfacial accumulation of DNA or RNA molecules. Fabricating the carbon paste electrodes one utilized the possibility of mixing the paste with an appropriate reagent enhancing catalytic properties (oxidation/reduction) of bare carbon particles. As comparative samples one applied non-modified carbon electrodes believing that carbon particle also possessed natural ability to run elctrocatalytic processes. The addition of an organo-ruthenium catalyst upgraded significantly the sensing properties of the modified electrodes if comparing them to the behaviour of non-modified carbon-paste electrodes. The test reaction was electrocatalytic guanine oxidation of single-strand DNA in a cyclic voltammetry experimental set up. The carbon paste was prepared from graphite powder (not chemically characterized), mineral oil, and organo-ruthenium catalyst ($Ru(Bpy)_3^{2+}$). The electrodes worked in the three-electrode amperometric regime. Easy renewal of the surface was one the most important features of the bulk-modified electrodes. Ruthenium-modified electrodes exhibited a substantial current enhancement, which was related to the catalytic guanine oxidation of single-strand DNA molecules at +0.9 V potential. Calibration plots (electrode current vs. concentration) for the detection of single-strand DNA were linear up to 50 ppm. The study is a good example of an ordinary practice that assumes that carbon particles (graphite powder) plays only the role of electric conductor.

In the similar, way one can prepare enzyme-modified carbon electrodes. In such cases the electrodes are prepared by admission of dissolved enzyme like alcohol dehydrogenase.[94] Such electrodes were tested for measuring alcohol content in some food products like wine, sake, beers, and soy sauce. The obtained results were comparable with results obtained by widely approved methods. Authors modified the applied enzyme with poly(ethylene glycol) aiming at improving electrode lifetime. The successful usage of the electrodes needed mediators that were non-soluble in water. Authors pointed out that the short lifetime of the enzyme-containing electrodes could be the biggest drawback of them since many components of carbon pastes were water soluble and leached out from the sensing material. They also proved that a successful design of such electrodes required numerous components that had to be selected according to the needs of active organic species (alcohol dehydrogenase).

The ongoing drive for miniature biosensors turn the attention towards the application of carbon fibres and CNTs. Ge and co-workers[95] presented a series of micro-scale modifications by means of scanning electrochemical microscope. According to authors, microbiosensors often suffer from the imperfect immobilization of enzymes. Amination can follow the pathway starting from the attachment of nitrophenol (reduction of diazonim salts), and subsequent reduction to aminophenyl functional groups. Enzymes can be covalently bonded using biotin-avidin chemistry. The amine groups acted as anchors for some organic molecules like enzymes (glucose oxidase). Small dimensions of carbon fibres and precise chemical/instrumental methods allow the fabrication micro-enzymatic electrodes that are capable to direct investigation of biological objects.

The way in which carbon pastes are manufactured provides much space for manipulation like changing the proportions between carbon, hardening agent and chemically sensitive substance. That allows fabrication of carbon paste-based materials that can exhibit a wide spectrum of sensing properties changing gradually according to the relative compositions. Such a manipulation is hard to achieve in the case of other carbon-based materials where the implantation of an active component is not easy to control. The mentioned advantages of carbon pastes fit the needs of sensor arrays. It is a key point in the fabrication of sensor arrays that each single sensor differs from the other sensitive elements in the array, which is relatively easily

achieved with carbon pastes. Moreover, carbon paste-based sensitive materials being self-sticking and self-hardening, are ideal candidates for the deposition of active covers or layers on the substrates like plates, rods, or wires. The sensing materials prepared from a carbon paste mixed with an active (sensitive) substance can be considered as relatively homogenous. Thus, the bulk and the surface of such a material exhibit the same chemical properties. The sensing element surface (particularly electrodes) undergoes mechanical and chemical deterioration caused by some undesired by-reactions occurring when the sensors are in operation or stored for long. Bulk homogeneity of carbon paste-based sensors provide an unique opportunity to renew the original state of the surface by a gentle abrasion. Such a possibility does not exist in the case of sensitive electrodes that are not homogenous like glassy carbon electrodes covered by a thin layer of a sensitive material. Diffusion-based side effects that can occur in thick layers of carbon paste seem to be the main shortcoming of the application carbon pastes for chemical sensor design.

Sensor arrays fabricated by means of carbon black often rely on the phenomenon of polymer swelling upon adsorption of organic vapours. The phenomenon of swelling influences the geometry of the sensing composite layer and changes the contacts between carbon black particles. This affects the transduction of electric current through the swelled sensor. The presented principle of operation requires a careful selection of polymers to suite the properties of the detected species. In such a case the preparation of the composite material consists in mixing of carbon black particles with a dissolved polymer until a homogenous paste is obtained. Then the paste can be deposited on a desired substrate by spraying, spin coating, screen-printing, dip coating, etc.

Zee and Judy[96] investigated arrays of chemiresitors prepared from a carbon black-polymer composite to identify several organic vapours. The authors tried to find a way to prepare the composite-base sensors of possibly identical amount of sensing material between the electrodes. The problem was solved by a "well" design of each sensor as it is presented in the following pictures (Figs. 65, 66). The deposited film of composite after the evaporation of solvent excess had always a comparable geometry. Six polymers were applied for the array fabrication, with the reproducibility of samples' geometry and their sensing properties ensured by the injecting of dissolved composite into the "wells." Additionally, it was proven that the size of "wells" did not affect the obtained results. It indicated that the way of composite film deposition provided high homogeneity of the sensing films.

Lonergan and co-workers[97] reported an application of 17 polymers for the preparation of a carbon paste containing carbon black (see Table V). All the polymers were non-conductive in the pure form but became conductive

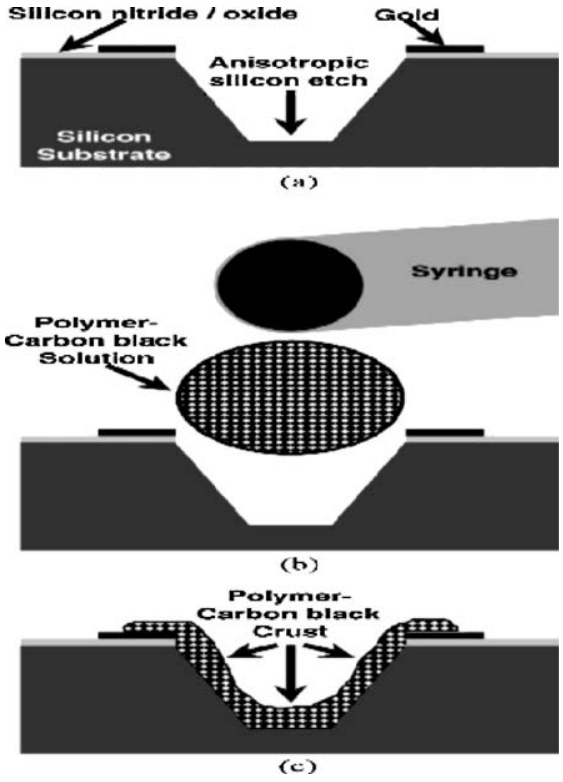

Fig. 65. Fabrication of the gas sensor using bulk-micromachining techniques: (a) anisotropically etched "well" into a silicon wafer with patterned silicon nitride/oxide insulation and gold metallization; (b) polymer-carbon black solution deposited into the "well" with a syringe, and (c) crust of polymer-carbon black film remains after drying. Reprinted with permission from [96], F. Zee and J. W. Judy, *Sens. Actuators B* 72, 120 **(2001)**. © 2001, Elsevier.

after the admission of carbon particles. The sensor array was exposed to the action of various vapours. The response of the array let them distinguish between a variety of substances (Fig. 67). The exposure to the mixed vapour of ethanol and methanol gave pathways between the responses to pure vapours of the alcohols. The response (increase of electric resistance of the sensors) was linear versus the concentration of organic vapours.

Uniform distribution of carbon black particle in carbon pastes, especially in these that were intensively diluted before use, is a serious problem. Dickson and Goddman[98] indicated that carbon black particles got restructured upon evaporation of solvent during drying of carbon pastes. The particles tended to accumulate at the edges of the drop forming a so called "coffee ring." After drying, the edge-accumulated carbon black particles formed highly conductive pathways between electrodes, which were not sensitive to the adsorption of detected species. A special electrode geometry was designed to overcome this problem. Sensor electrodes in a single chemiresitor had a concentric structure consisting of an inner ring-electrode and an outer square-ring electrode (135 micron on side) as it is shown on Figure 68 and Figure 69. The exterior part of

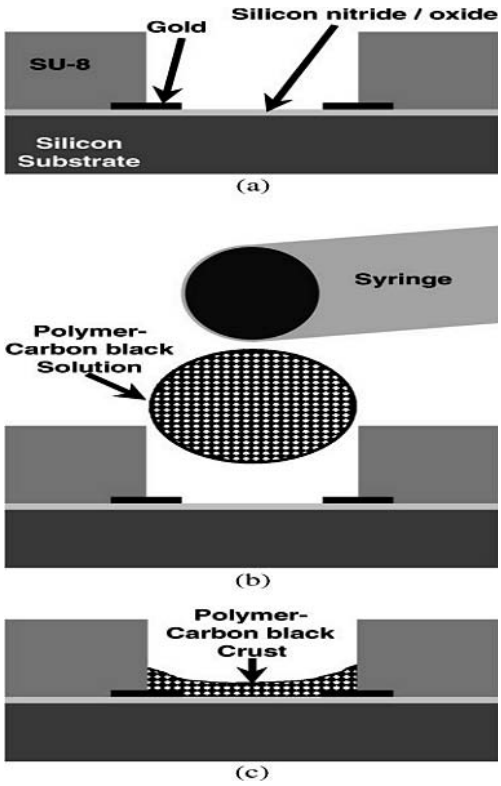

Fig. 66. Fabrication of the gas sensor using surface-micromachining techniques: (a) Patterned silicon nitride/oxide insulation, gold metallization and SU-8 photoresist to form "well" on silicon substrate; (b) polymer-carbon black solution deposited into the "well" with a syringe and (c) crust of polymer-carbon black film remains after drying. Reprinted with permission from [96], F. Zee and J. W. Judy, *Sens. Actuators B* 72, 120 **(2001)**. © 2001, Elsevier.

the sensors was common to all sensors. Thus, the conductors were shared among all the sensors and aggregation of carbon black particles at that spots decreased the contact resistance between the sensing material and the outer electrodes. According to authors, it helped to change carbon black agglomeration at the edges "from a problem to a benefit." The sensor array was successfully employed for the detection of some organic vapours (toluene, THF, acetone, methanol, octanol).

Some of the already reviewed papers were characteristic because the carbon black particles were considered as playing a secondary and rather passive role in the chemical sensing. This ignored the adsorption of the vapours on carbon black particles in the composite. However it is well known that carbon blacks exhibit high affinity towards organic vapours. The affinity of organic vapour towards carbon black, as well as towards other kinds of carbon, strongly depends on the chemical composition of the carbon surface. The variety of surface treatments and their resulting chemical properties of their surface suggests that the application of carbon black-based pastes or composites for sensing purposes should consider the fact that carbon blacks are different and are

Table V. Polymers applied for the fabrication of sensors array.

Sensor no.	Polymer
1	Poly(4-vinyl phenol)
2	Poly(styrene-*co*-allyl alcohol), 5.7% hydroxyl
3	Poly(α-methylstyrene)
4	Poly(vinyl chloride-*co*-vinyl acetate), 10% vinyl acetate
5	Poly(vinyl acetate)
6	Poly(*N*-vinylpyrrolidone)
7	Poly(carbonate bisphenol A)
8	Poly(styrene)
9	Poly(styrene-*co*-maleic anhydride0), 50% styrene
10	Poly(sulfone)
11	Poly(methyl methacrylate)
12	Poly(methyl vinyl ether-*co*-maleic anhydride), 50% maleic anhydride
13	Poly(vinyl butyral)
14	Poly(vinylidene chloride-*co*-acrylonitrile), 80% vinylidene chloride
15	Poly(caprolactone)
16	Poly(ethylene-*co*-vinyl acetate), 80% ethylene
17	Poly(ethylene oxide)

Source: Reprinted with permission from [97], M. C. Lonergan et al., *Chem. Mater.* 8, 2298 **(1996)**. © (1996), American Chemical Society.

not inert solids especially during adsorption of organic vapours. Fortunately, several studies were performed that considered the presence of carbon black surface functional groups and their role in the fabrication and application of such carbon black-polymer composites for chemical sensing. Tsubokawa and co-workers[99] applied the existence of surface functional groups on carbon black particles for the initiation of polymerisation of a selected polymer. Polymer chains were grafted by a direct condensation of carboxyl groups on the carbon black surface with terminal hydroxyl groups in polymer chains by means of a condensing agent. Hydroxyl groups were originally present on the carbon surface and were quantitatively characterized. In this way one obtained carbon black grafted with poly(ε-caprolactone)—PCL, poly(ethylehe glycol)—PEG and poly(ethylene adipate)—PEA. Grafting of carbon black particles provided good affinity of the modified particles to the same polymers utilized later as binding polymer for the preparation of sensing composites. It helped to prepare homogenous mixtures of the modified carbon black, the dissolved polymers and some amounts of THF. After mixing, the paste was deposited on solid substrates (with screen-printed interdigitated electrodes) forming after solvent evaporation a chemically sensitive resistor ready for use. The sensors exhibited rapid and reversible responses to the presence of organic contaminants added to hexane, which was selected as a basic solvent for tests. As expected, the polymers applied as binders for grafted carbon black particles swelled upon the contact with chloroform, trichloroethane and ethyl alcohol but the behaviour of the samples was significantly differentiated. The type of grafting polymer played an important role. Composites containing PCL-grafted carbon black (also PCL as binding polymer) swelled easily in hexane containing 10% vol. of

REVIEW

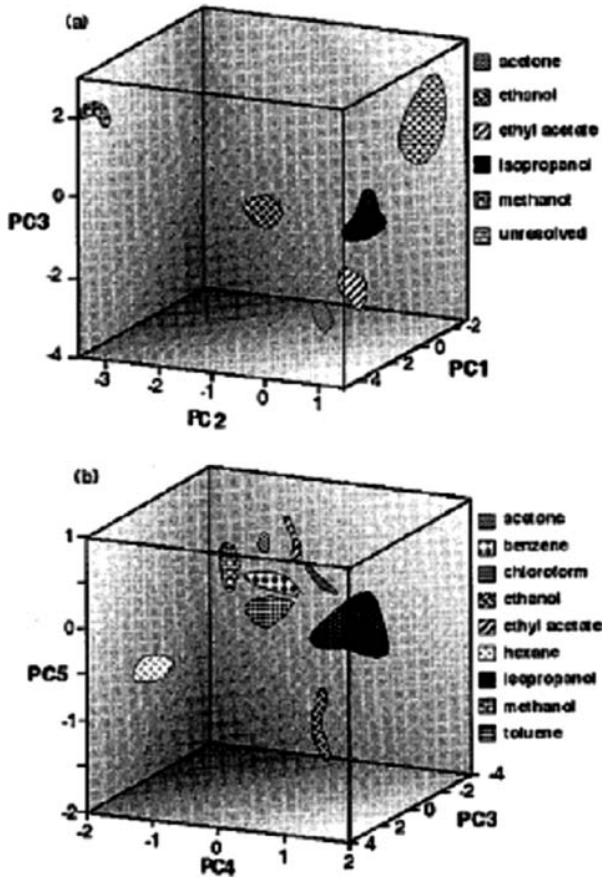

Fig. 67. Results from the exposure of the 17-element array to nine solvents as represented in (a) the first three dimensions of principal component space and (b) the third, fourth, and fifth dimensions of principal component space. These five principal components contain over 98% of the total variance in the data. Reprinted with permission from [97], M. C. Lonergan et al., *Chem. Mater.* 8, 2298 **(1996)**. © 1996, American Chemical Society.

chloroform at 20 °C, while samples that contained non-grafted carbon particles did not exhibit such a dramatic reaction. PCL-grafted carbon black/PCL composites were also sensitive to trichloroethane and ethanol dissolved in hexane (10% vol.). The logarithm of sensors' resistance (PCL-grafted carbon black/PCL) increased spectacularly in the linear mode versus the concentration of chloroform in hexane (test range 0–12%). Other investigations revealed that chloroform adsorbed by composites upon the contact with 10% solution of $CHCl_3$ was readily released after rinsing with pure hexane. Moreover, grafting with PEG changed the carbon black surface from a hydrophobic to hydrophilic one. PCL- and PEA-grafted carbon black particles were still hydrophobic. In other studies authors claimed that PEI- and PEG-grafted carbon black responded significantly (the change of electric resistance) to the contact with water and alcohol vapours which reacted (high affinity) with the grafted chains.

The study clearly shows that the chemical state of carbon black particles can play a key role in the enhancement

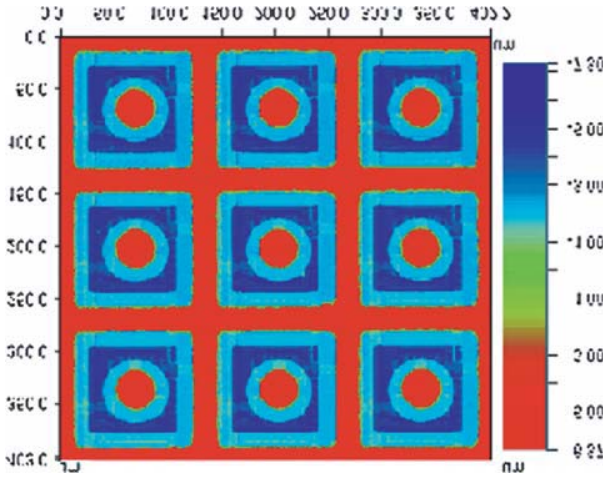

Fig. 68. Profilometry of a 3×3 section of array after the post-fabrication processing. The plating is approximated 10 microns high, and each sensor is 135 microns on a side. The internal contact is connected to the switch transistor, while the common perimeter contact is ground. Reprinted with permission from [98], J. A. Dickinson and R. M. Goodman, *IEEE International Symposium of Circuits and Systems* (*ISCAS'2000*), Geneva **(2000)**, p. 341. © 2000, IEEE.

or depressing of sensing properties of carbon black-polymer composites. However, the role of binding polymer cannot be neglected. Authors ascribed specific sensing properties of some composites to the phenomena occurring in polymer upon the contact with organic solvents like the change of crystalline structure of the polymers. The modelling of carbon black surface properties was also helpful in successful preparation of the composites. The problem of the influence of the carbon surface

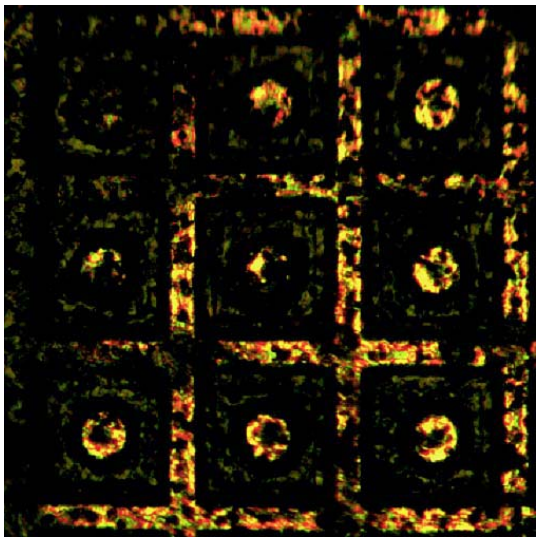

Fig. 69. Sensor material deposited on a plated chip. The active circuitry is located underneath each sensor. Reprinted with permission from [98], J. A. Dickinson and R. M. Goodman, *IEEE International Symposium of Circuits and Systems* (*ISCAS'2000*), Geneva **(2000)**, p. 341. © 2000, IEEE.

quality on the performance of enzyme modifies carbon black-based electrodes was investigated by Razumiene et al.[100] Their electrodes were fabricated from a series of home synthesised carbon blacks. The carbon black surface properties were modified by means of HNO_3, Br_2 + Fe, N_2H_2 2HCl, and H_2O_2. The treatment influenced the type and quantity of surface functional groups: carboxylic, lactone, and hydroxyl which concentration was estimated using the standard method of Boehm. Carbon black for electrode manufacturing was additionally modified by immobilisation of aldehyde dehydrogenase (ADH) and glucose dehydrogenase (GDH). The synthesis of carbon black was a complex process consisting of 11 technological operations including delamination of graphite structures, tailoring of surface properties, and particle size. The enzyme layers were additionally protected by the deposition of a permeable terylene film. Such electrodes were examined as amperometric sensors working in the three-electrode mode for the detection of ethanol and glucose dissolved in water (a flow-through experimental cell). It was proven that sensitivity and stability of the sensors were improved by increasing of the concentration of oxygen-containing surface functional groups. The authors ascribed the enhancement of sensing properties to the better contact between the carbon black particles and enzyme molecules. The close connection of both components resulted from the intermolecular binding forces that were more intensive when the polarity of carbon surface became a fact. Thus, the unique achievement of the study is showing the importance of the surface quality of carbon black particles applied for the fabrication of enzyme electrodes. According to the paper, carbon particles can play a complex role not limited to current conduction. The contacts between carbon black particles and enzyme molecules seem to be crucial for charge transfer during the electrode reactions. Therefore, the concentration and quality of the surface functionalities must influence the sensing properties of the electrodes.

Matthews et al.[101] reported the application of a composite consisting of carbon black with attached chains of poly(alkyl acrylate). The polymer-modified carbon black particles in solution were sprayed (after dilution) over an array of 42 pairs of electrodes of different size. In this way, one could investigate the influence of electrode size on the sensing performance towards toluene vapours (100, 500, 1000 ppm). The response magnitude, fundamental noise and signal-to-noise ratio of each sensor were considered as function of geometry of electrodes. No important influence of the geometrical factor on the mentioned sensing parameters was noticed. It suggested that carbon black-polymer composites were a homogenous resistive material suitable for fabrication of toluene vapour sensor of different size. Authors modified carbon black to increase its affinity to organic solvents aiming at easy paste preparation and improved sensitivity of the sensors.

Chen and McCreery[102] announced a detailed report on the role of surface oxygen species on glassy carbon electrodes in immobilisation of several organic substances. Surface modification of glassy carbon included oxidation (and oxygen removal), derivatization of surface oxides and adsorption of various organic substances. Some of the deposited substances were capable to specific interactions with surface functionalities while other ones were adsorbed in a non-specific form. Many of them like methylene blue were capable to form durable monolayers just by the adsorption from solution. One investigated several complex redox systems observing electron transfer kinetics. It was found, among other cases, that electron transfer to a particular redox system was dependent on oxygen-containing surface functionalities. The smaller the O/C ratio in the surface region the slower was the charge transfer. A negative influence on the charge transfer was noticed if a non-specific monolayer was adsorbed and if surface oxides were derivatized i.e., chemically transformed in other species. The chemical state of glassy carbon electrodes is depicted in Figure 70.

Graphite, which is highly conductive material, can find an application to chemical sensing not only as an electrode material. Miremadi and Colbow[103] constructed a hydrogen sensor basing on thin layer of graphite obtained be a two-step method. The first step started from intercalation of Li atoms into the pores and among graphite layers of graphite sample. The intercalation of Li atoms into graphite was run in two ways. Direct intercalation consisted in the action of Li vapours on carbon in vacuum while the second pathway was a "wet" chemical reaction (immersion of graphite samples in a hexane solution of *n*-bythyl lithium). The subsequent immersion of intercalated graphite samples in water (the second step) resulted in evolution of hydrogen due to the reaction: $2Li + 2H_2O \rightarrow 2LiOH + H_2$. The pressure of evolved hydrogen acted as a separation force causing the exfoliation of single graphite layers. The exfoliated graphite sheets were stuck on a solid substrate (glass or alumina) upon sintering above 300 °C. The obtained graphite films were highly resistive and their electric resistance depended strongly on the sintering temperature. Some reactive sites existed in the films and were connected with immobilized Pt (or Pd) particles that served as adsorption centres for molecular hydrogen and oxygen. The adsorption of hydrogen led to its dissociation and the release of electrons: $H_{2(gas)} + 2Pt^0 \leftrightarrow 2Pt{:}H \rightarrow 2Pt^0 + 2H^+ + 2e$.

Since the adsorption of hydrogen on Pt particles was a chemical process, it was accompanied by the formation of H^+ ions and the transfer of electrons from hydrogen to Pt. The fabricated graphite-based sensors exhibited good sensitivity to the chemical signal consisting of 300 ppm of hydrogen in air at 110 °C. The relation between sensors sensitivity and the concentration of H_2 in air was linear up to 300 ppm. Other reductive gases as CO, CH_4,

propane, alcohol vapours, and H_2S did not interfere the measurements of H_2 concentration probably since the temperature of operation was too low for the reduction of the mentioned species. The changes of electric conductance of the film upon hydrogen adsorption were significant since there was no inert "bulk" in the adsorbing film. In such conditions, the depth of surface zone of increased conductivity was comparable with the thickness of the whole film.

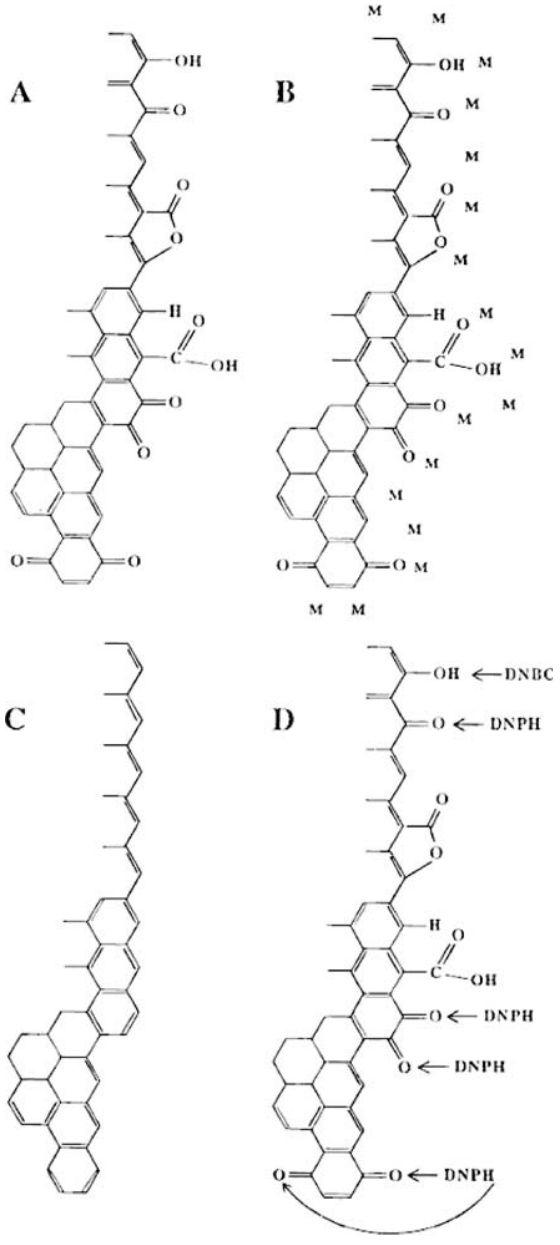

Fig. 70. Normally polished and desired GC surfaces: (A) normally polished GC surface, (B) GC surface covered by a monolayer absorber, (C) oxide-free GC surface, and (D) GC surface on which carbonyl and hydroxyl groups are derivatized. Reprinted with permission from [102], P. Chen and R. L. McCreery, *Anal. Chem.* 68, 3958 **(1996)**. © 1996, American Chemical Society.

3. CONCLUSIONS

Chemical sensors are of great importance for improved medical care, control of industrial processes, and ensuring environmental safety to name but a few applications. We review the field of chemical sensors based on the use of carbon-based materials; selected methods of carbon preparation are considered, as well as the most recent announcements on application of carbon to chemical sensing. We review how the chemical properties of the carbon surface can be controlled, and how these properties influence the application of carbon materials to the construction and use of chemical sensors. This paper reviews application of different carbon materials, including graphite, polycrystalline carbon, carbon black, and carbon nanotubes, to the construction of chemical sensors. Basic chemical properties of carbons are presented as well as selected synthesis methods. Different ways of carbon surface functionalization are considered in relation to chemical sensing properties.

Acknowledgments: The review was prepared based primarily on a grant by the Rector of Nicholas Copernicus University of Torun (Poland).

References and Notes

1. M. Inagak, New Carbons. *Control of Structure and Functions*, Elsevier, Amsterdam **(2000)**, p. 11.
2. J. C. Bokros, Chemistry and Physics of Carbon, edited by P. L. Walker, Jr., M. Dekker, New York **(1969)**, Vol. 5.
3. J. W. Gilman, D. L. Vander Hart, and T. Kashiwagi, Material and Test for Hazard Prevention, American Chemical Society. ACS Symposium Series 599, Thermal Decomposition Chemistry of Poly(vinyl alcohol), Washington **(1994)**.
4. M. Inagaki, New Carbons. *Control of Structure and Functions* Elsevier, Amsterdam **(2000)**, p. 9.
5. M. Inagaki, New Carbons. *Control of Structure and Functions* Elsevier, Amsterdam **(2000)**, p. 124.
6. C. N. R. Rao, B. C. Satishkumar, A. Govindaraj, and M. Nath, *Chem. Phys. Chem.* 2, 78 **(2002)**.
7. V. A. Garten and D. E. Weiss, *Australian J. Chem.* 10, 309 **(1957)**.
8. J. S. Mattson and H. B. Mark, Jr., Activated Carbon, M. Dekker, New York **(1971)**.
9. H. P. Boehm, *Adv. in Catalysis* 16, 179 **(1966)**.
10. K. Laszlo, K. Josepovits, and E. Tombacz, *Anal. Sci.* 17, i1741 **(2001)**.
11. H. Jankowska, A. Swiatkowski, L. Starostin, and J. Ławrinienko-Omiecynska, Adsorpcja jonów na weglu aktywnym (in Polish), PWN, Warsaw **(1991)**, p. 88.
12. S. Biniak, G. Szymanski, J. Siedlewski, and A. Swiatkowski, *Carbon* 35, 1799 **(1997)**.
13. M. Inagaki, New Carbons. *Control of Structure and Functions*, Elsevier, Amsterdam **(2000)**, p. 88.
14. G. Szymanski and G. Rychlicki, *Carbon* 29, 489 **(1991)**.
15. G. Szymanski and G. Rychlicki, *React. Kinet. Catal. Lett.* 43, 475 **(1991)**.
16. G. Szymanski, T. Grzybek, and H. Papp, *Catal. Today*, (in print).
17. J. P. Lukaszewicz, *J. Mater. Sci.* 32, 6063 **(1997)**.
18. S. Wang and G. Q. Lu, *Carbon* 36, 283 **(1998)**.
19. M. Molina-Sabio, F. Rodriguez-Reiniso, F. Caturla, and M. J. Selles, *Carbon* 34, 457 **(1996)**.
20. E. Auer, A. Freund, J. Pietsch, and T. Tacke, *Appl. Catalysis A: General* 173, 259 **(1998)**.

21. I. Mochida, Y. Korai, M. Shirahama, S. Kawano, T. Hada, Y. Seo, M. Yosikawa, and A. Yasutake, *Carbon* 38, 227 **(2000)**.
22. A. Kuznetsova, I. Popova, J. T. Yates, Jr., M. J. Bronikowski, Ch. B. Huffman, J. Liu, R. E. Smalley, H. H. Hwu, and J. G. Chen, *J. Am. Chem. Soc.* 123, 10699 **(2001)**.
23. A. Kuznetsova, J. T. Yates, Jr., J. Liu, and R. E. Smalley, *J. Chem. Phys.* 112, 9590 **(2000)**.
24. P. G. Collins, K. Bradley, M. Ishigami, and A. Zettl, *Science* 287, 1801 **(2000)**.
25. H. Hu, P. Bohowmik, B. Zhao, M. A. Hamon, M. E. Itkis, and R. C. Haddon, *Chem. Pys. Lett.* 345, 25 **(2001)**.
26. Y. S. Lee, T. H. Cho, B. K. Lee, J. S. Rho, K. H. An, and Y. H. Lee, *J. Fluor. Chem.* 120, 99 **(2003)**.
27. Y. K. Chen, A. Chu, J. Cook, M. L. H. Green, P. J. F. Harris, R. Heesom, M. Humphries, J. Sloan, S. C. Tsang, and J. F. C. Turner, *J. Mat. Chem.* 7, 545 **(1997)**.
28. C. N. R. Rao, G. U. Kulkarni, A. Govindaraj, B. C. Satishkumar, and P. J. Thomas, *Pure Appl. Chem.* 72, 21 **(2000)**.
29. Z. J. Liu, Z. Y. Yuan, W. Zhou, L. M. Peng, and Z. Xu, *Phys. Chem. Chem. Phys.* 3, 2518 **(2001)**.
30. P. M. Ajayan and Ijima, *Nature* 361, 333 **(1993)**.
31. B. C. Satishkumar, E. M. Vogl, A. Govindaraj, and C. N. R. Rao, *J. Phys. D: Appl. Phys.* 29, 3173 **(1996)**.
32. J. Sloan, J. Cook, M. L. H. Green, J. L. Hutchinson, and R. Tenne, *J. Mater. Chem.* 7, 1089 **(1997)**.
33. K. Bladh, L. K. L. Falk, and F. Rohmund, *Appl. Phys. A* 70, 317 **(2000)**.
34. P. Chen, X. Wu, J. Lin, and K. L. Tan, *Science* 285, 5424 **(1999)**.
35. W. Q. Han and A. Zettl, *Nano Lett.* 3, 681 **(2003)**.
36. J. W. Seo, E. Couteau, P. Umek, K. Hernadi, P. Marcoux, B. Lukic, C. Miko, M. Milas, R. Gaal, and L. Forro, *New J. Phys.* 5, 120.1 **(2003)**.
37. J. K. Lim, W. S. Yun, M. Yoon, S. K. Lee, C. H. Kim, K. Kim, and S. K. Kim, *Synth. Mater.* 139, 521 **(2003)**.
38. J. Liu, A. G. Rinzler, H. J. Dai, J. H. Hafner, R. K. Bradley, P. J. Boul, A. Lu, T. Iverson, K. Shelimov, C. B. Huffman, F. R. Macias, Y. S. Shon, T. R. Lee, D. T. Colbert, and R. E. Smalley, *Science* 280, 1253 **(1998)**.
39. W. Qikun, Z. Changchun, L. Weihua, and W. Ting, *Int. J. Hydr. Chem.* 27, 497 **(2002)**.
40. Y. Q. Wang, *J. Phys. Chem. B* 1999, 103, 4809 **(1999)**.
41. A. Star, D. W. Steuerman, J. R. Heath, and J. F. Stoddart, *Angew. Chem. Int. Ed.* 41, 2508 **(2002)**.
42. B. Zhao, H. Hu, and C. Haddon, *Adv. Funct. Mater.* 14, 71 **(2004)**.
43. M. Sano, A. Kamini, J. Okamura, and S. Shinkai, *Science* 293, 1299 **(2002)**.
44. M. M. Dubinin, Progress in Surface Membrane Science, Academic Press, New York **(1975)**.
45. O. K. Varghese, D. Gong, M. Paulose, K. G. Ong, C. A. Grimes, and E. C. Dickey, *J. Mater. Res.* 17, 1162 **(2002)**.
46. M. Inagaki, New Carbons. *Control of Structure and Functions* Elsevier, Amsterdam **(2000)**, p. 130.
47. H. Teng, T. S. Yeh, and L. Y. Hsu, *Carbon* 36, 1387 **(1998)**.
48. J. Ozaki, N. Endo, W. Ohizomi, K. Igarashi, M. Nakahara, A. Oya, S. Yoshida, and T. Iizuka, *Carbon* 35, 1031 **(1997)**.
49. A. Tamon, Personal communication to Kyotami.
50. T. Kyotami, N. Sonobe, and A. Tomita, *Nature* 331, 331 **(1988)**.
51. J. H. Knox and M. T. Gilbert, Preparation of Porous Carbon US Patent 4,263,268 **(1981)**.
52. S. Mrozowski, *J. Chem. Phys.* 21, 492 **(1953)**.
53. T. Koyama and M. Endo, *Jpn. J. Appl. Phys.* 13, 1175 **(1974)**.
54. K. Tsukagoshi, E. Watanabe, I Yagi, N. Yoneya, and Y. Aoyagi, *New J. Phys.* 6, 2 **(2004)**.
55. R. Saito, G. Dresselhaus, and M. S. Dresselhaus, Physical Properties of Carbon Nanotubes, Imperial College Press, London **(1998)**.
56. F. Kong and N. R. Franklin, *Science* 287, 622 **(2000)**.
57. L. Valentini, L. Lozzi, C. Cantalini, I. Armentano, J. M. Kenny, L. Ottaviano, and S. Santucchi, *Thin Solid Films* 436, 95 **(2003)**.
58. L. Valentini, C. Cantalini, L. Lozzi, I. Armentano, J. M. Kenny, and S. Santucchi, *Mater. Sci Engin.* C23, 523 **(2003)**.
59. C. Cantalini, L. Valentini, L. Lozzi, I. Armentano, J. M. Kenny, and S. Santucci, *Sens. Actuators B* 93, 333 **(2003)**.
60. J. Li, Y. Lu, Q. Ye, M. Cinke, J. Han, and M. Meyyappan, *Nano Lett.* 3, 929 **(2003)**.
61. J. Zhao and J. P. Lu, *Appl. Phys. Lett.* 82, 3746 **(2003)**.
62. W. L. Yim, X. G. Gong, and Z. F. Liu, *J. Phys. Chem B* 107, 9363 **(2003)**.
63. B. Y. Wei, M. C. Hsu, P. G. Su, H. M. Lin, R. J. Wu, and H. J. Lai, *Sens. Actuators B* 101, 81 **(2004)**.
64. K. H. An, S. Y. Jeong, H. R. Hwang, and Y. H. Lee, *Adv. Mater.* 16, 1005 **(2004)**.
65. J. Suehiro, G. Zhou, and M. Hara, *J. Phys. D: Appl. Phys.* 36, L109 **(2003)**.
66. Y. T. Jang, S. I. Moon, J. H. Ahn, Y. H. Lee, and B. K. Ju, *Sens. Actuators B* 99, 118 **(2004)**.
67. L. Valentini, I. Armentano, L. Lozzi, S. Santucchi, and J. M. Kenny, *Mater. Sci. Engin. C* 24, 527 **(2004)**.
68. M. Grujicic, G. Cao, and R. Singh, *Appl. Surf Sci.* 211, 166 **(2003)**.
69. Y. Lu, J. Li, J. Han, H. T. Hg, C. Binder, C. Partridge, and M. Meyyappan, *Chem. Phys. Lett.* 391, 344 **(2004)**.
70. J. P. Novak, E. S. Snow, E. J. Houser, D. Park, J. L. Stepnowski, and R. A. McGill, *Appl. Phys. Lett.* 83, 4026 **(2003)**.
71. J. Cui, M. Burghard, and K. Kern, *Nano Lett.* 3, 613 **(2003)**.
72. V. Bavastrello, E. Stura, S. Carrara, V. Erokhin, and C. Nicolini, *Sens. Actuators B* 98, 247 **(2004)**.
73. V. G. Gavalas, S. A. Law, J. C. Ball, R. Andrews, and L. G. Bachas, *Anal. Biochem.* 329, 247 **(2004)**.
74. S. Sotiropoulu, V. G. Gavalas, V. Vamvakaki, and N. A. Chaniotakis, *Biosens. Bioelectron.* 18, 211 **(2003)**.
75. M. Weinecke, M. C. Bunescu, M. Pietrzak, K. Deistung, and P. Fedtke, *Synth. Met.* 138, 165 **(2003)**.
76. K. B. Male, S. Hrapovic, Y. Liu, D. Wang, and J. H. T. Luong, *Anal. Chim. Acta* 516, 35 **(2004)**.
77. K. Wu, Y. Sun, and S. Hu, *Sens. Actuators B* 96, 658 **(2003)**.
78. Y. D. Zhao, W. D. Zhang, Q. M. Luo, and S. F. Y. Li, *Micromech. J.* 75, 189 **(2003)**.
79. J. B. He, C. L. Chen, and J. H. Lui, *Sens. Actuators B* 99, 1 **(2004)**.
80. P. Liu and J. Hu, *Sens. Actuators B* 84, 194 **(2002)**.
81. P. He and L. Dai, *Chem. Comm.* 348 **(2004)**.
82. J. S. Ye, Y. Wen, W. D. Zhang, H. F. Cui, L. M. Gan, G. Q. Xu, and F. S. Sheu, *J. Electroanal. Chem.* 562, 241 **(2004)**.
83. T. Ono, X. Li, and H. Miyashita, *Rev. Sci. Instrum.* 74, 1240 **(2003)**.
84. B. Y. Wei, C. S. Lin, and H. M. Lin, *Sens. Mater.* 15, 177 **(2003)**.
85. M. Penza, F. Antolini, and M. V. Antisari, *Sens. Actuators B* 100, 47 **(2004)**.
86. S. Chopra, A. Pham, J. Gaillard, A. Parker, and A. M. Rao, *Appl. Phys. Lett.* 80, 4632 **(2002)**.
87. K. G. Ong and C. Grimmes, *Sensors* 1, 193 **(2001)**.
88. O. K. Varghese, P. D. Kichambre, D. Gong, K. G. Ong, E. C. Dickey, and C. A. Grimes, *Sens. Actuators B* 81, 32 **(2001)**.
89. K. G. Ong, K. Zeng, and C. A. Grimes, *IEEE Sens. J.* 2, 82 **(2002)**.
90. Y. M. Wong, W. P. Kang, J. L. Davidson, A. Wisitsora-at, and K. L. Soh, *Sens. Actuators B* 93, 327 **(2003)**.
91. J. R. Chen, S. Bangsaruntip, K. A. Drouvalakis, N. W. S. Kam, M. Shim, Y. Li, W. Kim, P. J. Utz, and H. Dai, *PNAS* 100, 4984 **(2003)**.
92. G. U. Sumanasekera, B. K. Pradham, C. K. Adu, H. E. Romero, H. C. Foley, and P. C. Eklund, *Mol. Cryst. Liq. Cryst.* 387, 255 **(2002)**.
93. N. A. El-Maali and J. Wang, *Sens. Actuators B* 76, 211 **(2001)**.

94. Q. Yao, S. Yabuki, and F. Mitzutani, *Sens. Actuators B* 65, 147 **(2000)**.
95. F. Ge, R. C. Tenent, and D. O. Wipf, *Anal. Sci.* 17, 27 **(2001)**.
96. F. Zee and J. W. Judy, *Sens. Actuators B* 72, 120 **(2001)**.
97. M. C. Lonergan, E. Severin, B. J. Doleman, S. A. Beaber, R. H. Grubb, and N. S. Lewis, *Chem. Mater.* 8, 2298 **(1996)**.
98. J. A. Dickinson and R. M. Goodman, *IEEE International Symposium of Circuits and Systems* (*ISCAS'2000*), Geneva **(2000)**, p. 341.
99. N. Tsubokawa, M. Tsuchida, J. Chen, and Y. Nakazawa, *Sens. Actuators B* 79, 92 **(2001)**.
100. J. Razumiene, V. Gureviciene, V. Laurinavicius, and J. V. Grazulevicius, *Sens. Actuators B* 78, 243 **(2001)**.
101. B. Matthews, J. Li, S. Sunshine, L. Lerner, and J. W. Judy, *IEEE Sensor. J.* 2, 160 **(2002)**.
102. P. Chen and R. L. McCreery, *Anal. Chem.* 68, 3958 **(1996)**.
103. B. K. Miremadi and K. Colbow, *Sens. Actuators B* 46, 30 **(1998)**.

SENSOR LETTERS
Vol. 4, 99–119, 2006

REVIEW

Boron-Doped Diamond-Based Sensors: A Review

Orawon Chailapakul[1], Weena Siangproh[2], and Donald A. Tryk*, †

[1] Sensor Research Unit, Department of Chemistry, Faculty of Science, Chulalongkorn University, Bangkok 10330, Thailand
[2] Department of Chemistry, Faculty of Science, Srinakharinwirot University, Bangkok, Thailand

(Received: 13 January 2005. Accepted: 30 January 2006)

Electrically conductive, boron-doped diamond (BDD) films, prepared by means of chemical vapor deposition, have been studied intensively just over the past ten years as electrode materials for electrochemistry. During this time, it has become apparent that BDD films are in many ways ideal for high-sensitivity analytical measurements of a wide variety of inorganic and organic species, opening the door to a host of sensor applications. The techniques for preparing micro-scale and nano-scale electrodes have also been developed, which will further widen the sensor possibilities. Preparation and characterization techniques, as well as recent developments in specific inorganic and organic determinations, are reviewed.

Keywords: Boron-Doped Diamond, Electrochemistry, Diamond Electrodes, Amperometric Sensors.

CONTENTS

1. INTRODUCTION

Electrochemical sensors are electrical sensors that usually involve an interface between a solid or liquid electronically conducting phase (the electrode) and a solid or liquid ionically conducting phase (the electrolyte).[1–6] The types of electrical measurements that can be made include potential, current, charge, capacitance, conductance, and impedance. In the present review, we will focus on current-based measurements at solid electrodes in liquid electrolytes.

In the case of current-based electrochemical measurements, there is usually an electron transfer (ET) process that can occur at a discrete potential.[7] Often, the latter can be related, albeit indirectly at times, to the standard potential for the ET that involves the species of interest. This aspect can provide some chemical information, as in the oxidative (anodic) stripping of mixtures of metals deposited on the electrode. In many cases, however, this aspect is not important, as in the non-specific oxidation of organic compounds that have already been separated chromatographically or electrophoretically.

In current-based measurements, the electrode itself should interfere as little as possible with the measurement. There are several sources of current that can be traced to the electrode; these include

(1) oxidation and reduction of the solvent;

(2) oxidation and reduction of the electrolyte ions;

(3) adsorption of ions on the electrode surface accompanied by ET;

(4) bulk oxidation or reduction of the electrode material; and

(5) charging and discharging of the electrochemical double layer at the solid-liquid interface.

All of these sources are more or less electrode material-dependent. For example, platinum is highly catalytic for oxidation and reduction processes involving water as a solvent (type 1), processes involving hydrogen and hydroxide adsorption (type 3), a near-surface oxidation process that occurs at highly positive potentials (type 4), and double-layer charging (type 5). In fact, the intrinsic electrochemistry of platinum in aqueous solution has been intensively studied (see, e.g., the work of Clavilier and coworkers.[8]) In a second, contrasting example, glassy carbon and pyrolytic

*Corresponding author; E-mail: tryk@comp.metro-u.ac.jp
†Present Address: Department of Applied Chemistry, Metropolitan University, Minami-Ohsawa, Hachiohji, Tokyo 192-0397, Japan.

graphite have little catalytic activity for type 1 reactions involving water, little activity for type 3 processes,[9] but they can undergo progressive type 4 oxidation of the surface.[10] In addition, due to the slightly porous nature of the material, the current for type 5 (double layer charging) can be relatively large.

Recently, electrically conductive films of boron-doped chemical vapor-deposited (CVD) diamond have gained popularity in a variety of electrochemical applications, in large part due to the fact that the electrode-based currents are relatively small.[11–15] In fact, for very high quality films, the currents can be orders of magnitude smaller than those for other types of electrode materials.[16] The catalytic activity for water oxidation/reduction (type 1) is very small.[17] The ability to undergo hydrogen adsorption (type 3) is small. The ability to undergo covalent attachment of hydroxyl or carbonyl oxygen is significant at highly positive potentials, but it appears that the surface is not progressively oxidized (type 4), as in the case of sp^2-type carbons and graphites but stops after the modification of the top layer of carbon atoms.[18] The currents for double layer charging (type 5) are quite small, due to the low number of carriers and the nearly complete lack of porosity. These attributes make conductive diamond well suited for current-based electrochemical measurements. Recently, the use of diamond as an electrode material in electrochemistry has been extensively reviewed.[19]

In the next section, we shall briefly review the preparation and characterization of conductive diamond films, principally of the boron-doped type. In the subsequent two sections, we shall review the use of diamond film electrodes as electrochemical sensors for inorganic species and organic species, respectively.

2. PREPARATION AND CHARACTERIZATION

2.1. Preparation and Availability of Conductive Diamond Films by CVD Processes

There are several possible methods for preparing CVD diamond films, which have been reviewed recently.[20]

Orawon Chailapakul is an Associate Professor in the Department of Chemistry, Faculty of Science, Chulalongkorn University. She received her B.Sc. in Chemistry from Mahidol University in 1982, the M.Sc. from Chulalongkorn University in 1987, and the Ph.D. from the University of New Mexico in 1994. Presently, she is a member of the Materials Chemistry and Catalysis Research Unit and the Sensor Research Unit. Her research interests include diamond electrochemistry, chemical sensors and biosensors, labs-on-a-chip, and nanomaterials and their applications in food and environmental science.

Weena Siangproh received her Bachelor of Science (Chemistry) from Srinakharinwirot University in 1998. She is a Lecturer in the Department of Chemistry, Faculty of Science, Srinakharinwirot University, Thailand. At present, she is pursuing her doctoral research, supported by The Thailand Research Fund through the Royal Golden Jubilee Ph. D. Program, at the Department of Chemistry, Faculty of Science, Chulalongkorn University, Thailand, under the direction of Associate Professor Orawon Chailapakul. Her research interests include diamond electrochemistry, microchip capillary electrophoresis, and nanomaterials and their applications in electroanalysis.

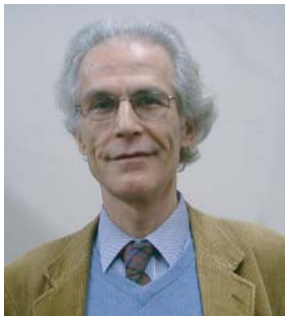

Donald A. Tryk graduated from the University of Florida in 1969 with a Bachelor of Science in Chemistry and from the University of New Mexico in 1980 with a Doctorate in Chemistry. From there, he went on to Case Western Reserve University, where he was a Senior Research Associate in the Chemistry Department until 1995. He was at the University of Tokyo as a Research Associate and Special Associate Professor in the group of Professor Akira Fujishima until 2001. He was then a Visiting Professor, first at Tokyo Metropolitan University in the Department of Applied Chemistry, in the group of Professor Haruo Inoue, then in 2003 at the University of Puerto Rio, and then again, in 2005, at Tokyo Metropolitan University. His research interests include analytical electrochemistry, electrocatalysis, photoelectrochemistry, and photocatalysis. He is particularly interested in the use of diamond as an electrode material, as well as the development of biomimetic electrocatalysts for redox reactions such as those involving dioxygen, dihydrogen, and carbon dioxide.

The principal methods are hot-filament CVD,[21] microwave plasma CVD,[22] radio-frequency plasma CVD[23] and arc-jet.[24] The hot filament and microwave methods have been used extensively to prepare boron-doped films. Boron can be introduced in any of several forms, e.g., solids that are placed in the CVD chamber, including boron metal,[25] boron nitride and boron-containing ceramics,[26] gases introduced into the chamber, including diborane[27] or trimethylborane,[28] or as a compound dissolved in a spray of liquid droplets, e.g., boron oxide, dissolved in a mixture of methanol and acetone entrained in the hydrogen feed gas.[29] Films can be prepared in one of several possible particle sizes, depending upon the growth conditions, ranging from microcrystalline (MCD), with crystallites typically in the 1–10 μm range[30] to nanocrystalline (NCD), with particles in the range below 1 μm,[27,31] down to ultra-nanocrystalline (UNDC), with particles in the range down to 1 nm.[32,33] There are several commercial suppliers of boron-doped MCD films, including Element Six (UK), Condias (Germany), Sumitomo (Japan) and sp3 Diamond Technologies (USA).

The most commonly used form of conductive diamond that has been used for analytical purposes is the boron-doped MCD CVD film, which we will refer to simply as boron-doped diamond (BDD). Films typically exhibit a somewhat random arrangement of crystal grains that are on the order of 1–10 μm in diameter (Fig. 1). The microcrystals usually present either a rectangular (100) or a triangular (111) face on the polycrystalline surface. These faces are known to incorporate boron from the gas phase at different rates during the growth process, with the (111) faces taking up a higher concentration.[34] This leads to a situation in which the ET process may be carried predominantly by the more highly doped (111) faces,[35] which can lead to electrochemical behavior that tends toward that of a microelectrode array, i.e., sigmoidal voltammograms at slow potential sweep rates.[36,37]

The microcrystalline surface can also be polished to a high degree of smoothness by combined chemical-mechanical techniques, for example. Not much work has been published on the electrochemical behavior of these polished surfaces, although some results have appeared as part of articles that have dealt with nanotextured surfaces.[38] In most cases, the analytical techniques that have been reported do not involve the need to mechanically polish the electrode surface. The range of possible applications will probably be greater if polished films are available. However, NCD and UNDC films are also highly smooth as deposited and circumvent the polishing process.

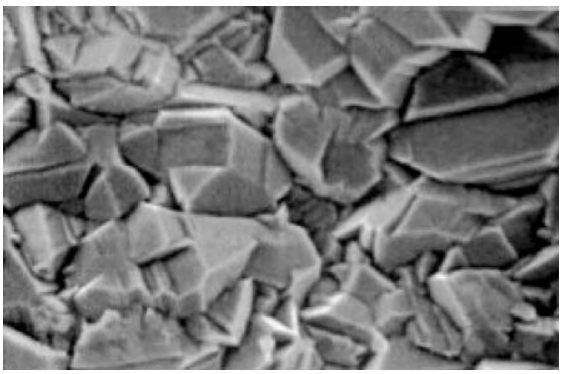

Fig. 1. Scanning electron micrograph of a microcrystalline, boron-doped CVD diamond film.

One of the attractive attributes of diamond films is that they have little tendency to adsorb species from solution and consequently there is little buildup of films,[39] so that there is not a strong incentive to physically polish the electrode. Any films that adhere can usually be removed by maintaining a positive, oxidizing potential for a few seconds to minutes.[40]

Another type of diamond surface that can be used in sensor devices is the non-doped, hydrogen-terminated film. This type of surface possesses surface conductivity that can be used as the basis for a conductimetric sensor directly in the gas phase[41,42] or in liquid solution phase, either as an electrode in a simple electrochemical measurement or with a fabricated metal-semiconductor field-effect transistor (MESFET), as described in a later section. Non-doped CVD films can be used after suitable preparation, which can involve treatment in strong acid to remove non-diamond carbon, followed by a brief rehydrogenation in a pure hydrogen plasma (see, e.g., Refs. [43–45]). Even non-doped synthetic and natural single crystals can be hydrogenated by placing them in a CVD chamber and treating them in a hydrogen-containing plasma.[45,46] The hydrogenation step converts the oxygen termination, which is typical for the acid-treated surface, as well as for polished diamond, to hydrogen termination. Some authors have argued that this type of procedure also introduces hydrogen into a thin region just below the surface, in a layer that could be on the order of a few nanometers[43,47] up to several hundred nanometers,[46,48–50] in which the hydrogen acts as a *p*-type dopant. Others have argued that the surface termination by itself is sufficient to impart conductivity.[45,51,52] Differences in the various types of pretreatments no doubt lead to differences in the resulting depth distribution or lack thereof. The subject of surface conductivity will be discussed later in terms of the types of specific sensors.

Another dopant that can be used to produce conductive films is sulfur, with *n*-type conduction. Sulfur is usually thought to be a deep donor, i.e., one that has an activation energy that is too large for room-temperature conductivity, but, after some initial controversy,[53–55] it has become recognized recently that it can be a shallow donor, i.e., a room-temperature conductor,[51,56–58] perhaps due to the formation of sulfur-hydrogen[59] or sulfur-vacancy pairs.[56] Thus far, sulfur-doped diamond films have not been used for electrochemistry, with the exception of one report,[60]

but there is preliminary work on its use in the surface conductance mode as a sensor (see later).

Modified diamond surfaces are becoming more and more extensively used recently. The modification techniques, which include chemical, electrochemical, and photochemical techniques, have been reviewed recently;[61] these include ways of attaching anything from terminating atoms, such as oxygen,[62–64] chlorine,[65,66] nitrogen,[65,66] or fluorine,[67–69] all the way to proteins[70] and DNA strands,[71–73] as well as metal particles[74–77] and metal oxides.[78–82] New ones are continually being reported. Some of the specific modified surfaces will be mentioned later in the context of the analytical methods.

2.2. Characterization of Conductive Diamond Films

2.2.1. Microscopy

The quality of microcrystalline CVD films is conveniently assessed with SEM, to ensure that the crystallinity is good. For example, in Figure 1, the presence of various types of crystalline morphologies can be seen. Typically, the (111)-type grains are darker, which correlates with the previously mentioned tendency of this grain type to incorporate higher levels of boron; the (100)-type grains are lighter. This produces a characteristic pattern of light and dark areas. SEM is also a good technique with which to examine the surface after the deposition of metal particles.[74–76,83]

2.2.2. Raman Spectroscopy

Raman is an essential characterization technique: one of the routine ways Raman is used is to gauge the presence of sp^2 carbon, which shows up typically as a very broad peak centered at ca. 1600 cm^{-1}, while diamond itself has a highly characteristic peak, due to the principal phonon mode, at very close to 1332 cm^{-1} Refs. [84–86]. This peak is extremely intense for highly crystalline diamond. The presence of a high concentration of boron as a dopant leads to an increase in a broad peak at ca. 1200 cm^{-1}. This peak is thought to be due to the presence of either very small crystalline domains of diamond or disordered diamond,[84] either of which could result from the perturbation of the structure by the boron dopant atoms.

2.2.3. X-Ray Photoelectron Spectroscopy

The surface termination of the diamond film, whether hydrogen or oxygen, can affect the electrochemical properties greatly.[62–64,87–90] This can be established through the use of x-ray photoelectron spectroscopy (XPS). The O 1s/C 1s peak area ratio typically reaches a maximum of 0.10 to 0.15 with increased time of oxidizing treatment, for example, electrochemical oxidation.[64] This may correspond approximately to a monolayer coverage with oxygen-containing functional groups. It is possible to attain higher O/C ratios with oxygen plasma treatment, but this type of aggressive treatment may lead to surface damage, e.g., graphitization,[18] similar to the type of damage observed even with bombardment with light ions such as D^+ and He^+ Refs. [18, 91]. XPS is a useful technique for the examination of chemically modified diamond surfaces, particularly if the modifier contains characteristic elements, e.g., N, Si[18] or F.[92]

3. DETECTION AT BORON-DOPED DIAMOND ELECTRODES

3.1. Detection of Inorganic Species

The use of BDD films for the detection of inorganic species makes particular use of the extremely wide potential range. Such films have been used as working electrodes to detect various kinds of metals, including Pb, Cd, Cu, Ag, and Hg, typically with the use of anodic stripping voltammetry (ASV). Cations such as Ce^{3+} and anions such as nitrite and azide were also investigated. In the context of such analyses, new methods, including abrasive anodic stripping voltammetry, as well as ultrasonic activation (sonoelectroanalysis) and microwave activation, have also been introduced.

3.1.1. Detection of Ionic Species and Dissolved Gases

Because of the extended potential range in the positive direction, the cyclic voltammetric response of Ce^{3+} ions in aqueous sulfuric acid, nitric acid, and perchloric acid solutions was investigated at highly doped BDD electrodes.[93] The concentration dependence was studied voltammetrically, as shown in Figure 2. The diffusion coefficients and electron transfer kinetic parameters can be conveniently determined in a way that is not possible with other types

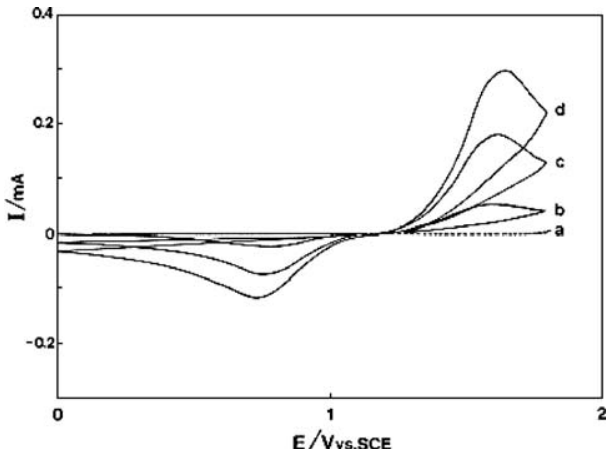

Fig. 2. Cyclic voltammograms in 0.1 M H_2SO_4 at a BDD electrode for various $Ce_2(SO_4)_3$ concentrations: (a) 0 mM, (b) 1 mM, (c) 3 mM, and (d) 5 mM; potential sweep rate, 10 mV s^{-1}; temperature, 25 °C.

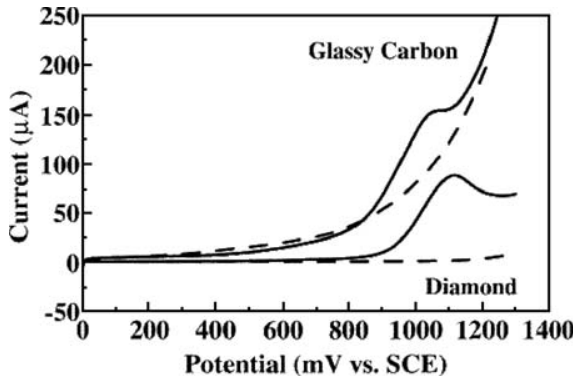

Fig. 3. Linear sweep voltammetric $i-E$ curves for freshly polished glassy carbon and a diamond thin film (D803961) in 1 mM NaN_3/0.1 M phosphate buffer, pH 7.2. The total and background currents are shown for both electrodes; sweep rate, 100 mV s^{-1}.

of electrodes, due to the interference of the background current. It was concluded that highly doped BDD is an excellent electrode material for the electrochemical analysis of species with highly positive redox potentials in aqueous solutions.

The azide anion dissolved in aqueous media was determined by Xu et al. with high-quality BDD thin-film electrodes.[94] The linear sweep, differential pulse voltammetric technique was employed to study the reaction at neutral pH as a function of the potential sweep rate, analyte concentration, and electrolyte composition. Figure 3 shows linear sweep voltammetric current-potential curves for glassy carbon (GC) and BDD in 1 mM NaN_3/0.1 M phosphate buffer (pH 7.2). A peak-shaped oxidation response was observed for both electrodes, but the background currents, upon which the Faradaic response is measured, were dramatically different. The background current for the GC electrode was significantly larger than that for BDD, with the difference at 1200 mV being a factor of approximately 200.

The lower background current for diamond at the potential for azide oxidation is a great advantage in its electroanalysis. Furthermore, when a BDD-based detector is coupled with a hydrodynamic system such as that for flow-injection analysis (FIA) or high-performance liquid chromatography, in the amperometric mode, it can be used to detect azide with very high sensitivity. This idea will be discussed in greater detail in the section on organic species. Thus, BDD can serve as an analytically useful sensor for the detection of azide anion and exhibits superior performance characteristics compared with GC.

The detection of sulfide through the electrocatalytic oxidation of ferrocyanide to ferricyanide at a BDD electrode with the use of both cyclic voltammetry and chronoamperometry was reported by the Compton group.[95] The analytical utility has been compared with that of other common electrode substrates (Pt, Au, glassy carbon). The high oxidation potential for the direct oxidation of sulfide at a BDD electrode allows clear resolution of the ferrocyanide and sulfide oxidation waves, with the result being a clearly distinguishable analytical signal at the oxidation peak potential for ferrocyanide. This procedure was used to determine the % recovery of a sulfide spike in a sewage effluent ($102 \pm 4.5\%$).

The surface conductivity phenomenon has been used to develop sensors for ionic species in solution, including the chloride ion by the Kawarada group,[96,97] and the hydrogen ion (pH) by Garrido et al.,[98] both with the use of MESFET devices. For the chloride ion response, the authors developed essentially an electrostatic model, in which the chloride ion attracts the majority carrier holes to the surface, creating higher surface conductivity. Increasingly negative drain-source currents at given drain-source voltages are observed for increasing chloride concentrations. In contrast, for the pH sensor, the authors report *decreasingly* negative drain-source currents for increasing hydrogen ion concentrations (decreasing pH values), again at given drain-source voltages, because the positively charged hydrogen ions repel the holes away from the surface. It is interesting to note that the chloride response requires a hydrogen-terminated surface, whereas the hydrogen ion response requires a partially oxygenated surface (via ozone treatment).

Not only can cations and anions be detected at BDD electrodes but also gases such as nitrogen oxides (NO and NO_2) dissolved in aqueous solution can be detected voltammetrically.[99] The voltammetric curves exhibit well-defined anodic peaks, with a response that is superior to that obtained with GC electrodes. In addition, it was found that the anodic voltammetric peak for the oxidation of the nitrite anion is well defined and suitable for analytical applications. The conclusion was that BDD is promising for the detection of these nitrogenous species.

The surface conductivity effect can also be used to detect species in the gas phase, with the conductivity being measured by use of a two-point probe technique. Ri et al. studied this effect in a series of papers.[41,100,101] In their first paper, they examined the effects of acidic vapors (HCl) and basic vapors (NH_3) and found that the former increased the conductivity, whereas the latter decreased it.[101] Their model was essentially the same as that discussed above, i.e., electrostatic attraction or repulsion of holes from the surface. In their second paper, they examined a set of oxidizing gases (NO_2, HCl, and O_3), finding increased conductivity, and a reducing gas (NH_3), which decreased the conductivity.[41] Here, the model is more complicated, because it is considered to involve electron transfer; for example, NO_2 is reduced to NO_2^- at the surface, whereupon it acts electrostatically to attract holes to the surface. In a third paper, the authors support their model with Hall effect measurements of the carrier concentrations in the presence of NO_2 and NH_3.[100]

In recent work by Gonzalez et al., a similar effect has been studied with oxygen gas dissolved in aqueous

solution.[102] This work is based on the suggestion by Chakrapani et al. that oxygen should be an oxidizing species,[42] in the same sense as used by Ri et al. above.[41, 100] Indeed, it was found that dissolved oxygen leads to higher electrochemical currents for hydrogen evolution for non-doped (*p*-type) films, whereas it leads to lower currents for sulfur-doped (*n*-type) films. The proposed mechanism involves the reduction of O_2 to the superoxide radical anion $O_2^{\cdot-}$, which can then electrostatically attract the majority carrier holes toward the surface of *p*-type non-doped films, whereas it repels the electrons in sulfur-doped *n*-type films. When the carriers are close to the electrode surface, they are more easily transferred to the protons in solution, and thus the hydrogen evolution current increases. Clearly, when the carriers are further from the surface, ET is more difficult, and the current is smaller. The possible relationship of these results to the surface conductivity effect and the "transfer-doping model" of Ristein et al.[51, 52] has not been entirely established.

3.1.2. Chemically Modified Diamond Electrodes

The chemical modification of the BDD surface can provide enhanced sensitivity and selectivity for the detection of various species. Several approaches for modification have been developed thus far; these include surface oxidation, attachment of organic functional groups, attachment of biomolecules and the deposition of metal or metal oxide particles. These approaches have been reviewed recently.[61] These modified surfaces have been used more extensively for the analysis of organic and biochemical compounds, but some have also been used for inorganic species.

For example, hydrous iridium oxide (IrO_x) electrodeposition has been used for the modification of the BDD surface to selectively detect peroxide.[103] The electrodeposition technique allows the amount deposited to be precisely controlled, and thus highly reproducible electrochemical behavior can be achieved. The detection limit for H_2O_2 was ca. 10 times lower than that for bulk platinum electrodes. It was also found that IrO_x/BDD electrodes exhibit excellent, highly stable pH response over a wide pH range. The idea of using iridium oxide-modified BDD was also later taken up by the Compton group, for the trace analysis of As(III).[82]

3.1.3. Trace Metal Detection

The Fujishima group was the first to utilize unmodified BDD films for the electrochemical detection of trace concentrations of lead dissolved in aqueous solution by differential pulse anodic stripping voltammetry (DP-ASV).[104] Thus, this was one of the earliest, most successful examples of anodic stripping analysis of metals carried out without benefit of mercury. The stripping peak current was observed to increase linearly with increasing lead concentration, as shown in Figure 4. Lead concentrations down to

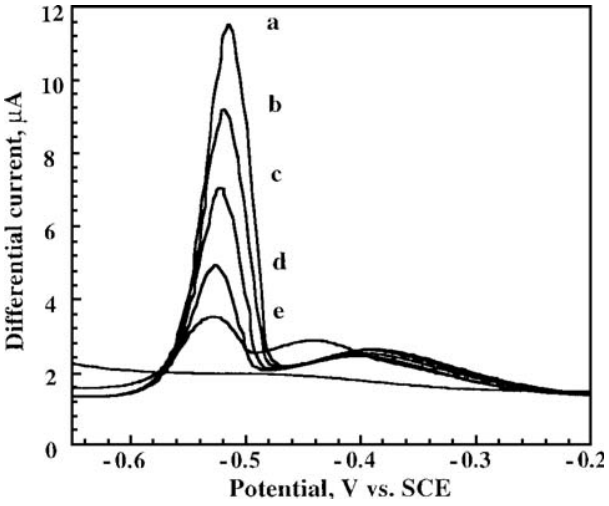

Fig. 4. DPASV for $Pb(NO_3)_2$ in 0.1 M KCl (pH 1), obtained for a highly doped diamond electrode after holding the potential at −1.0 V versus SCE for 2 min. The concentrations were (a) 2×10^{-6} M; (b) 1.6×10^{-6} M; (c) 1.2×10^{-6} M; (d) 8×10^{-7} M; (e) 4×10^{-7} M; and (f) background. The sweep rate was 20 mV s^{-1}, the pulse amplitude was 100 mV, and the sampling time was 10 ms.

4×10^{-9} M were detected. It should be noted that Goeting et al. had already examined lead deposition on BDD, but the concentrations used were higher, and the particles were probably larger, so that the stripping was not quantitative, due to possible problems with adhesion or poor electronic contact.[25] In the work of Manivannan et al., the stripping was found to be quantitative, probably because the particles were small enough to avoid problems with adhesion or contact.

The Compton group also found that boron-doped diamond can be used for mercury-free lead detection, but they used a slightly different approach, in which they anodically deposited the lead as lead dioxide and then cathodically stripped by reducing the PbO_2 to soluble Pb^{2+} Ref. [105]. These workers also used ultrasonic enhancement of the mass transport in order to achieve lower detection limits, as discussed later. The same group also developed a method for the detection of lead in blood using a bismuth film-modified BDD electrode.[106]

The Compton group examined the simultaneous detection of lead and copper in solution using ASV with BDD electrodes.[107] Peaks due to Cu and Pb were identified, and interactions between the two metals were studied. The results indicated that this technique could be used for the independent detection of Cu and Pb via conventional standard addition procedures. The Fujishima group also examined the problem of the simultaneous detection of two metals in solution, first with Pb and Cd[108] and then with Pb and Cu.[109] These workers also concluded that it is straightforward to simultaneously quantify two metals if the interactions are specifically taken into account. Foord et al. have also recently examined the interactions between Pb and Ag in detail.[110]

Interestingly, BDD electrodes were also used for the detection of mercury itself. Linear behavior was obtained in the mercury concentration range from 10^{-10} to 10^{-9} M with the use of the co-deposition of a small amount of gold, which was purposely added to the analyte solution in order to enhance the deposition of Hg.[111] Thus, the ASV technique, which makes use of bare polycrystalline diamond electrodes, shows great promise for the analysis of trace toxic metals.

3.1.4. Abrasive Stripping Voltammetry

The Fujishima group developed a novel approach for the electrochemical "fingerprinting" of a wide range of materials using abrasive stripping voltammetry (AbrSV) at BDD electrodes.[112] The rough, microcrystalline BDD surface was used to abrade the surfaces of metals and alloys, and small particles of the material were found to adhere to the electrode. These were then analyzed with anodic stripping. The abrasive stripping voltammetry of Pb and Fe samples and of a brass alloy sample was investigated.

The Compton group also investigated metal samples containing silver and tin using abrasive stripping voltammetry at BDD electrodes.[113] The mechanical and electrical contact of the abraded particles was dependent on the contact force used during the abrasion. Silver was found to be yield useful analytical results from the ASV measurements, but tin was found to be less reproducible.

3.1.5. Ultrasonic and Microwave Enhancement

The use of ultrasonic agitation of the analyte solution with BDD electrodes (sonoanalysis) is an interesting new approach to the enhancement of mass transport. As already mentioned, it has been used for the determination of lead via cathodic stripping.[105] It has also been used for the determination of silver, with the use of both cathodic and anodic stripping.[114] It was found that, after deposition of metallic silver on the bare BDD electrode surface under ultrasonic agitation, anodic stripping square-wave voltammetry could be used for the sensitive analysis of silver ions. The detection limit for Ag^+ was 10^{-9} M with a deposition time of 300 s.

The same group also determined Pb^{2+} using another novel technique, i.e., microwave activation.[115] The detection of Pb^{2+} in a 0.1 M HNO_3 solution was strongly enhanced by microwave activation of the deposition and stripping processes at the BDD electrode. The anodic stripping was carried out with square wave voltammetry. Pb concentrations in a water sediment sample were also measured; the results agreed well with those of two other independent analytical techniques, ICP mass spectroscopy and sono-cathodic stripping voltammetry.

3.2. Detection of Organic Compounds

BDD electrodes provide a very attractive means of measuring inorganic species; in many cases, these undergo reversible electron transfer. In addition, they can be used to measure a great variety of organic compounds; as well shall see, these can undergo either reversible or, in many cases, due to the complexity of the processes, irreversible electrochemical reactions. Many specific examples have been reported, and those published through 2003 have been summarized in earlier review articles.[11, 116–122] In the present review, we highlight some important developments and review more recent work.

3.2.1. Voltammetry, Flow Injection Analysis and Related Techniques

This section can be separated into separate topics based on the type of heteroatom contained in the organic compound: nitrogen, sulfur, and others, including oxygen and halogens.

3.2.1.1. Detection of Nitrogen-Containing Compounds Cyclic voltammetry was first used to examine the electron transfer reactions of organic redox-active analytes such as dopamine (DA) at BDD electrodes. In an early paper, the effect of surface pretreatment was studied at as-deposited and chemically oxidized diamond thin-film electrodes.[123] The measurement of the background current response and capacitance of interfaces formed at as-deposited polycrystalline BDD thin-film electrodes in contact with aqueous electrolytes was also performed.

In order to enhance the selectivity for dopamine detection in the presence of ascorbic acid (AA), cyclic voltammetric and chronoamperometric measurements were carried out at anodically treated BDD surfaces in alkaline solution.[11, 89, 117] These treatments resulted in the incorporation of substantial amounts of oxygen on the surface and substantial shifting in the positive direction for the peak potential for AA oxidation, as shown in Figure 5. Linear

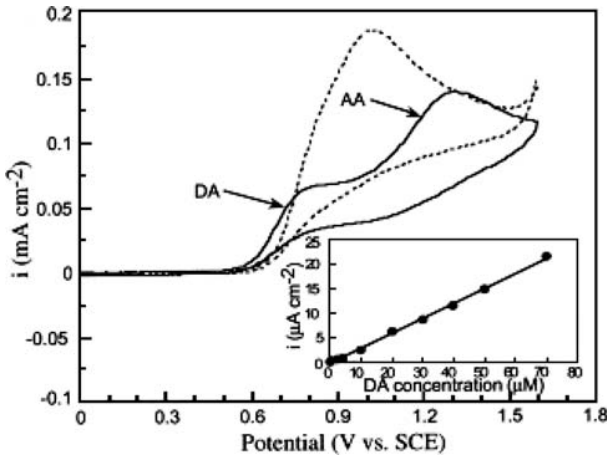

Fig. 5. Cyclic voltammograms for a mixture of 0.1 mM dopamine and 1 mM ascorbic acid in 0.1 M $HClO_4$ at untreated (dashed line) and treated diamond electrodes; sweep rate, 100 mV s^{-1}. Inset shows the calibration curve for dopamine in the presence of 1 mM ascorbic acid. Reprinted with permission from [11], T. N. Rao and A. Fujishima, *Dia. Rel. Mater.* 9, 384 (**2000**). © 2000, Elsevier Science.

calibration curves were obtained for both a higher concentration range (1–70 μM DA, 1 mM AA) and a lower range (0.1–1 μM DA, 0.1 mM AA), respectively. The detection limit appears to be on the order of 50 nM, which is among the lowest values reported.

To increase the sensitivity and efficiently eliminate interferences, highly boron-doped diamond microfiber electrodes (BDDMF) modified with highly oxidized polypyrrole were successfully fabricated and used as microsensors for the detection of dopamine in the presence of AA.[124] The limit of detection (signal/noise ratio, S/N = 3) for dopamine was 0.1 nM, which is one order of magnitude lower than that observed for carbon microfiber electrodes (CMFE), and a linear dynamic range was obtained from 0.5 nM to 100 μM ($r^2 = 0.997$). The amperometric response for 0.5 nM dopamine showed high stability, with a relative standard deviation (RSD) of 5.4% ($n = 5$). Highly reproducible results were obtained with an RSD of 6.2% for 10 measurements for 1 nM DA obtained over a 10-h period.

FIA with diamond thin-film detectors was employed to detect amines such as ethylamine, and ethylenediamine by the Swain group.[125] These redox reactions were studied by cyclic voltammetry, hydrodynamic voltammetry, and FIA with electrochemical detection (FIA-EC) at a BDD electrode. These workers proposed that the oxidation reactions involve the anodic transfer of an oxygen from H_2O. The cyclic voltammetry and FIA results for ethylamine are shown in Figure 6.

The oxidation of polyamines such as putrescine, cadaverine, spermine, and spermidine was investigated at polycrystalline BDD thin-film electrodes with the use of cyclic voltammetry and FIA with amperometric detection.[26] Well-resolved oxidation waves with respect to the background signal were observed. The mechanism proposed involved oxygen transfer from reactive OH radicals electrogenerated at non-diamond carbon impurity sites. The results showed that the BDD electrode can be used to effectively detect

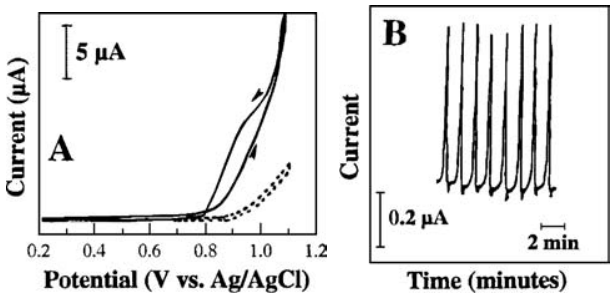

Fig. 6. (A) Cyclic voltammetric $i - E$ curves (background and total current) for a diamond film (D72696) in 1 mM ethylamine + 0.1 M $NaClO_4$/0.01 M carbonate buffer, pH 10; sweep rate, 20 mV s^{-1}. (B) FIA-EC results for a diamond film (D120795) using 20-μL injections of 0.25 mM ethylamine in 0.1 M carbonate buffer, pH 10. The mobile phase was 0.1 M carbonate buffer, pH 10, at a flow rate of 0.5 mL min^{-1}. Reprinted with permission from [125], S. Jolley et al., *Anal. Chem.* 69, 4099 (**1997**). © 1997, American Chemical Society.

polyamines with a detection limit of approximately 1 μM (S/N $\geq$ 3) and a linear dynamic range from 10^{-3} to 10^{-6} M ($r^2 > 0.97$).

The FIA-EC results for cadaverine (CAD), putrescine (PUT), spermine (SPM) and spermidine (SPMD) were reported with particular emphasis on the electrode response variability and stability.[126] Hydrodynamic voltammograms for these amine compounds are shown in Figure 7. A linear dynamic range from 1.0 μM to 1.0 mM and a detection limit of 1.0 μM (S/N $\geq$ 3) were found for CAD, PUT, and SPMD. For SPM, a linear dynamic range from 0.32 μM to 1.0 mM and a detection limit of 0.32 μM were observed. The improvement was achieved by introducing a 3–6-min delay period between injections; thereby, a response variability, as low as 2–4%, was observed. The extension of these results to include a chromatographic separation stage is straightforward, for example, with the use of a simple reverse-phase column.

The electrochemical detection of chlorpromazine and catecholamines was studied with high quality polycrystalline, hydrogen-terminated BDD thin films (3–6 μm thick).[127] Some preliminary results obtained in the amperometric detection mode, coupled with FIA and liquid chromatography (LC), were presented. BDD exhibited superior detector performance; for example, the detection limit (S/N = 3) for chlorpromazine at BDD was 4 nM, and the response variability was 0.3%, while for a GC electrode, the detection limit was 40 nM, and the response variability was 1%.

An important biogenic nitrogen-containing compound, nicotinamide adenine dinucleotide (NADH), was studied at as-deposited BDD electrodes with cyclic voltammetry, amperometry, and the rotating disk electrode technique in neutral pH solution. NADH is an important cofactor in a large number of dehydrogenase-based reactions. With GC and other types of electrodes, reproducible results cannot be obtained for this compound due to the strong adsorption of NAD^+, the principal oxidation product. However, with BDD, highly reproducible, stable, sensitive cyclic voltammograms were obtained for NADH oxidation. The amperometric results for NADH for the BDD electrode at 0.58 V in the nM concentration range are shown in Figure 8. After each injection of an aliquot of NADH stock solution, which caused a concentration step of 10 nM, a sharp rise in the current was observed. A linear calibration plot was obtained up to 500 nM. The results indicate that BDD is an attractive electrode material for use in sensors based on enzyme-catalyzed reactions involving NADH as a cofactor.[128–130]

Histamine (HI) and serotonin (5-hydroxytryptamine (5-HT)) are important biogenic amines that act as chemical messengers. Histamine is also present in many food products. The electrochemical detection of serotonin and histamine was investigated for the first time at BDD thin film electrodes by use of voltammetry and FIA

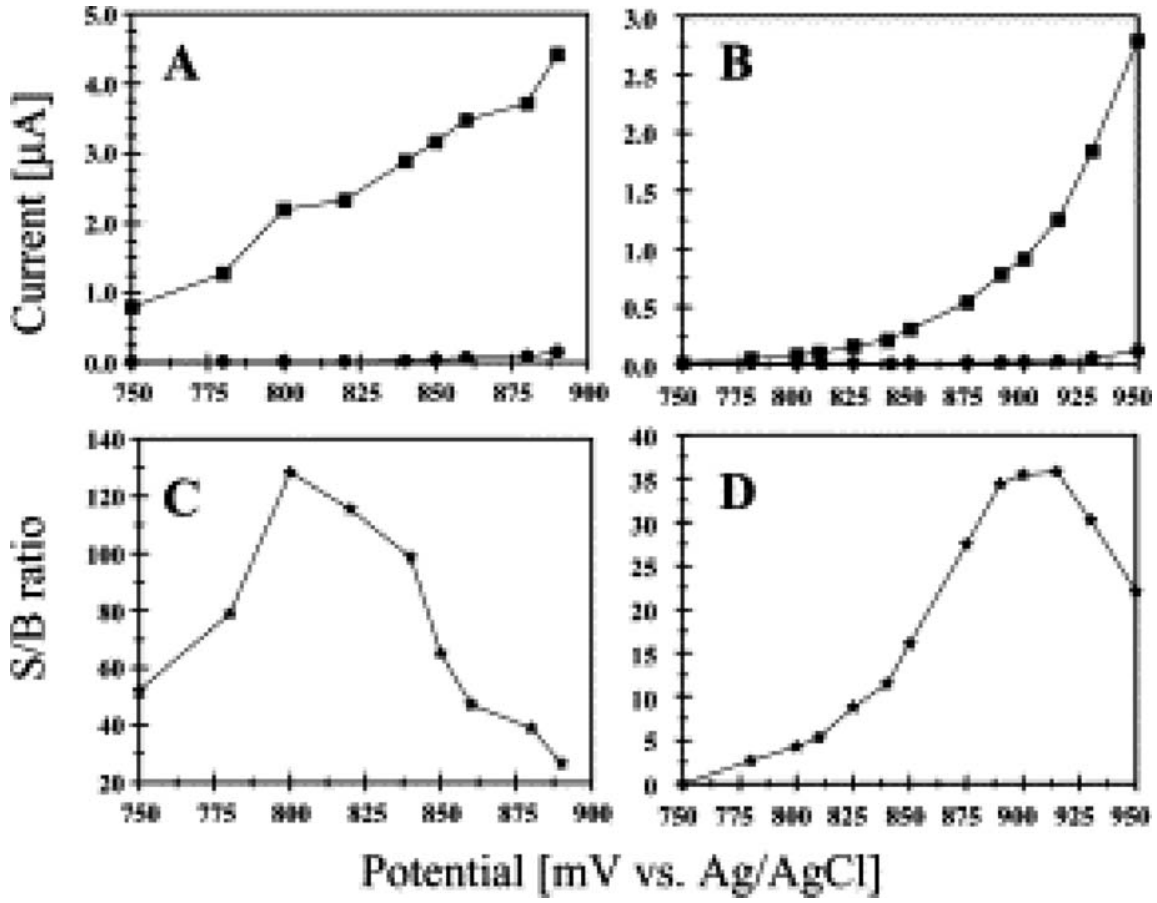

Fig. 7. Hydrodynamic voltammetric $i-E$ curves for 20-μL injections of (A) 1.0 mM SPMD; and (B) 1.0 mM CAD. The carrier solution was in 0.1 M $NaClO_4 + 0.01$ M carbonate buffer, CBpH10. The total current responses are shown as (•) and the background current responses as ( ). Plots of the S/B ratio versus the applied potential are shown for (C) SPMD; and (D) CAD. Working electrodes: unused 0.50% C/H films. The S/B ratio was calculated as $I_{tot} - I_{bkg}/I_{bkg}$; flow rate, 1.0 mL min^{-1}. Reprinted with permission from [126], M. A. Witek and G. M. Swain, *Anal. Chim. Acta* 440, 119 (**2001**). © 2001, Elsevier Science.

with amperometric detection . In comparison to the GC electrode, it was found that BDD provides very low background currents and a low tendency to adsorb the oxidative products on the electrode surface. Figure 9 shows linear sweep voltammograms for 100 μM HI together with the corresponding background voltammograms in 0.1 M phosphate buffer (pH 7) at the GC and BDD electrodes. At the GC electrode, the oxidation of HI occurred at ~1.2 V versus SCE. A rapid increase in the current at this potential was also observed in the background voltammogram due to oxygen evolution and carbon oxidation. For this reason, the voltammogram was ill defined. In the case of the diamond electrode, a very well defined oxidation peak at 1.40 V versus SCE was observed. The voltammetric signal-to-background ratios (S/B) obtained at diamond were one order of magnitude higher than those obtained for GC electrodes at and above histamine concentrations of 100 μM. A linear dynamic range of 3–4 orders of magnitude and a detection limit of 1 μM were observed in the voltammetric measurements. Well-defined sweep rate-dependent voltammograms were also obtained for 5-HT. A detection limit of 0.5 μM (S/N = 13.8) for HI was obtained by use of the FIA technique with the BDD electrode. A very low detection limit (10 nM) was obtained for 5-HT on BDD by the same method. A detection limit of 10 nM (0.2 pmol) was obtained for the FIA technique, indicating that BDD is a stable and sensitive electrode for 5-HT determination.[131, 132]

Selective voltammetric and amperometric detection of uric acid (UA) in the presence of high concentrations of AA was reported for oxidized diamond film electrodes by differential pulse voltammetry and chronoamperometry. A differential pulse (DP) voltammogram obtained for 50 μM UA in the present of AA at electrochemically treated diamond electrodes is shown in Figure 10. The chronoamperometric results show linear calibration curves obtained for UA over the concentration range up to 1×10^{-6} M in 0.1 M $HClO_4$ solution, A statistical analysis of the calibration curve yielded a detection limit of 1.5×10^{-8} M (S/N = 3). The possibility of practical use is shown by the direct measurement of UA in human urine and serum with no electrode pretreatment.[88]

REVIEW

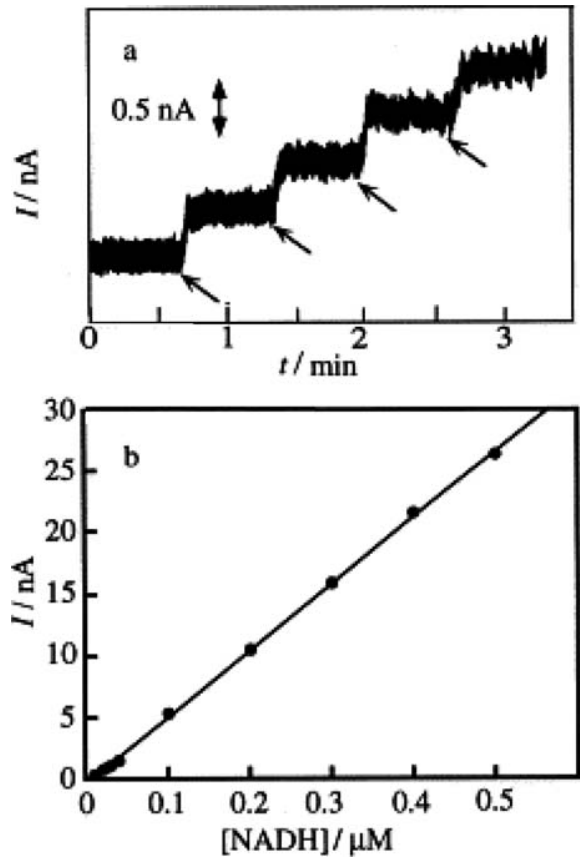

Fig. 8. (a) Amperometric response of a diamond electrode to NADH additions in a stirred solution containing 0.1 M phosphate buffer (pH 7.0) at an applied potential of 0.58 V versus SCE (each addition increased the concentration by 10 nM). (b) Calibration plot. Reprinted with permission from [128], A. Fujishima et al., *J. Electroanal. Chem.* 473, 179 (**1999**). © 1999, Elsevier Science.

Several tricyclic antidepressant drugs (tricyclic antidepressants or TCAs), imipramine, desipramine, clomipramine, amitriptyline, nortriptyline, and doxepin, were

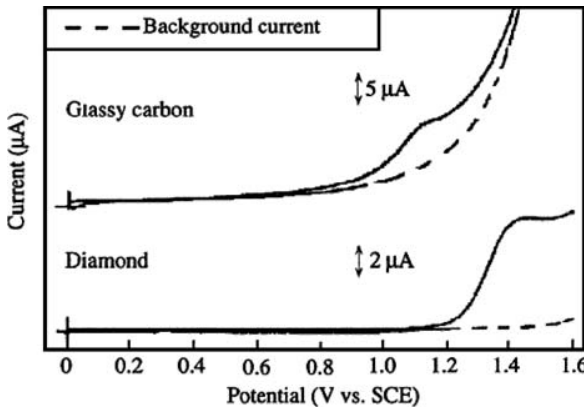

Fig. 9. Linear sweep voltammograms for 100 μM histamine in 0.1 M phosphate buffer (pH 7). (1) GC electrode (0.196 cm^2); (2) diamond electrode (0.189 cm^2). The potential sweep rate was 100 mV s^{-1}. Reprinted with permission from [132], B. V. Sarada et al., *Anal. Chem.* 72, 1632 (**2000**). © 2000, American Chemical Society.

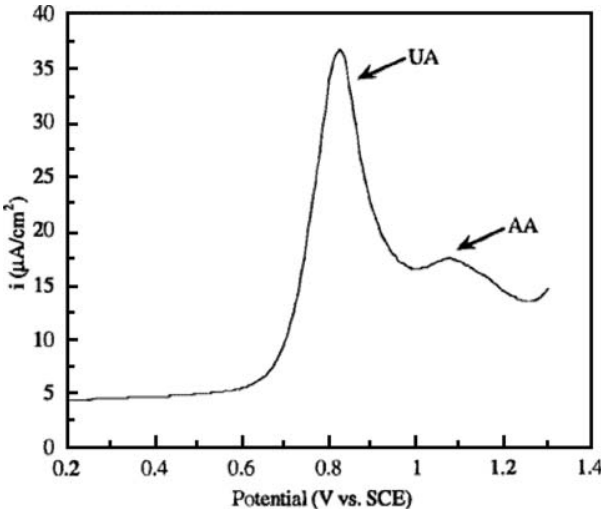

Fig. 10. Differential pulse voltammogram for a mixture of 50 μM UA and 0.25 mM AA at an oxidized diamond electrode in 0.1 M $HClO_4$ solution; sweep rate, 20 mV s^{-1}; pulse amplitude, 50 mV; pulse width, 50 ms; repetition time, 500 ms. Reprinted with permission from [88], E. Popa et al., *Anal. Chem.* 72, 1724 (**2000**). © 2000, American Chemical Society.

reported to be electrochemically detectable by cyclic voltammetry, FIA and HPLC with BDD electrodes.[133] These compounds belong to one of the largest groups of drugs for the treatment of psychiatric disorders such as depression. The function of these drugs is thought to involve blocking the uptake of norepinephrine at nerve endings in the central nervous system. For this group of drugs, distinct ranges of optimal plasma concentration for therapy are required. The therapeutic concentration range for most TCAs is approximately from 280 to 850 nM, while toxic effects can occur when plasma concentrations exceed 1.4 μM. It was found that using FIA-EC, at an operation potential of 0.85 V versus Ag/AgCl, BDD exhibited a background current of 7 nA with rapid stabilization (15 min), in contrast to the case of GC, which appeared to stabilize only after 1 h. Linear calibration curves were from 0.05 to 100 μM. The limits of detection (S/N = 3) were 3 nM for imipramine and desipramine, 0.5 nM for clomiprarmine, 163 nM amitriptyline, 1080 nM for nortriptyline and 92 nM for doxepin. The amperometric response (Fig. 11) obtained for a BDD electrode for 20-μL injections of 100 μM imipramine gave reproducible peaks, with a peak variability of ~3% ($n = 18$), which suggests a lack of adsorption of oxidation products on the electrode surface.

Reproducible results over several days of analysis were obtained. Moreover, this approach has been applied for determinations in plasma samples for imipramine and desipramine. The results demonstrate the promise of the use of BDD as an amperometric detector in HPLC for the analysis of these types of compounds.

Nitrogen-containing pesticides such as *N*-methylcarbamate pesticides (carbaryl, carbofuran, methyl 2-benzimidazolecarbamate, bendiocarb) were electrochemically

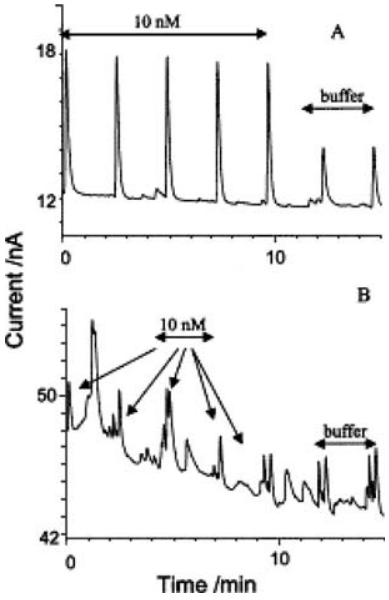

Fig. 11. FIA-ED results for 20-μL injections of: (A) 10 nM imipramine at a BDD electrode and (B) 10 nM imipramine at a GC electrode. The mobile phase was 0.1 M phosphate buffer pH 6.9; the flow rate was 1 mL min^{-1}. Reprinted with permission from [133], T. A. Ivandini et al., *J. Electroanal. Chem.* 521, 117 **(2002)**. © 2002, Elsevier Science.

detected at BDD thin-film electrodes after LC separation. Two kinds of detection methods were adopted in this study. First was a direct detection of the underivatized pesticides carried out at an operating potential of 1.45 V versus Ag/AgCl. The results provided detection limits of 5–20 ng mL^{-1} (or 5–20 ppb) with S/N = 2, due to the low background current and wide potential window of the diamond electrode. In the second method, the pesticide samples were prepared by alkaline hydrolysis in a separate step prior to injection in order to produce the phenolic derivatives. The latter, which oxidized at lower potentials (approximately 0.9 V vs. Ag/AgCl), gave very low detection limits and improved drastically the sensitivity. On-line reactivation of the diamond electrode surface was shown to be possible by an anodic treatment of the electrode at +3 V for 30 min in case of electrode fouling, which may occur after prolonged use. Such treatment can damage GC, Kel-graf (Kel-F resin plus graphite) and metal electrodes, while the diamond electrode is stable. These results suggest that the BDD electrode is better than other, previously used electrodes for the highly sensitive, stable detection of carbamate pesticides.[134] Figure 12A shows the hydrodynamic voltammograms at the diamond electrode for carbaryl, carbofuran, and bendiocarb after the prehydrolysis step. The mobile phase used was a solution of 0.01 M $NaClO_4$ in acetic acid/water/acetonitrile, 0.5%:59.5%:40%. The background current did not rise in the potential region where the phenolic derivatives of three pesticides underwent oxidation. The derivative of carbaryl, 1-naphthol, oxidized much earlier than those of carbofuran and bendiocarb. The potential for the amperometric detection was set at

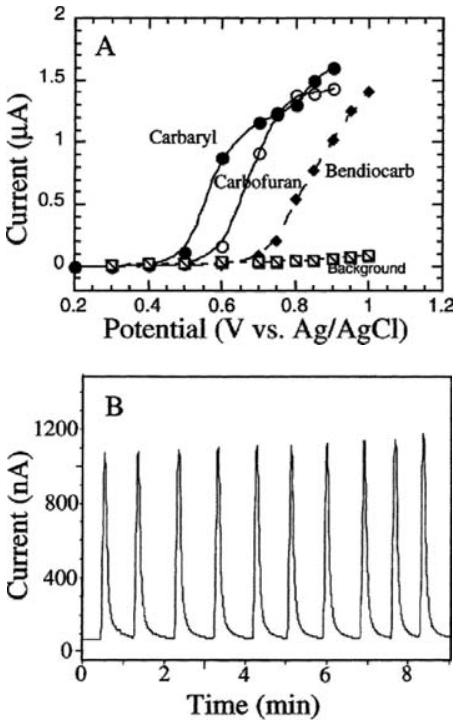

Fig. 12. (A) Hydrodynamic voltammograms for phenolic derivatives of 50 μM carbamates at diamond electrode. The injection volume was 20 μL. (B) FIA-ED results for diamond electrode using 20-μL injections of 50 μM prehydrolyzed carbaryl; applied potential, 0.9 V versus Ag/AgCl. The mobile phase was a mixture of acetic acid/water/acetonitrile, 0.5:59.5:40; the flow rate was 1 mL min^{-1}. Reprinted with permission from [134], T. N. Rao et al., *Anal. Chem.* 74, 1578 **(2002)**. © 2002, American Chemical Society.

0.9 V versus Ag/AgCl, where the derivatives of all three pesticides gave current responses. Figure 12B shows the amperometric response for repetitive 20-μL injections of 50 μM prehydrolyzed carbaryl. As expected, the response was very stable, with a RSD of 2.5% for 10 injections.

The electrochemical oxidation of other important nitrogen-containing compounds such as xanthine and its naturally occurring *N*-methyl derivatives, theophylline, theobromine, and caffeine was also investigated[135] Caffeine and theophylline are methylxanthine derivatives that are widely distributed in plant products and beverages. Theophylline and caffeine have been widely used for the treatment of asthmatic manifestations, neonatal apnea and bronchial spasms. Therefore, it is very important to determine accurately the content of these compounds in foods and pharmaceutical preparations. The effects of pH, concentration and potential sweep rate on the voltammetric response were thoroughly examined. It was found that BDD exhibits excellent behavior, in terms of very well defined, reproducible oxidation peaks, for xanthine, theophylline, theobromine, and caffeine determination. The results enabled BBD electrode to be used as the electrochemical sensor to detect the investigated compounds, within a concentration range of 1 to 400 μM

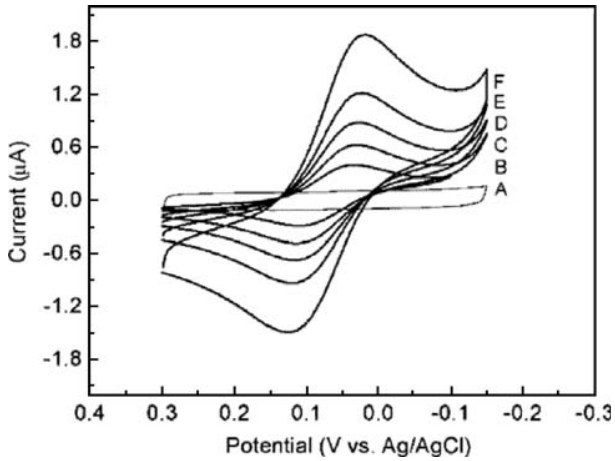

Fig. 13. (A) Background CV at 20 mV s^{-1} for a 20 mM NaCl aqueous solution and (B-F) CVs for 200 μM horse heart cytochrome *c* in 20 mM NaCl, 1 mM Tris HCl pH 7 buffer at different scan rates: (B) 2 mV s^{-1}, (C) 5 mV s^{-1}, (D) mV s^{-1}, (E) 20 mV s^{-1}, and (F) 50 mV s^{-1}; electrode area, 0.2 cm^2. Reprinted with permission from [136], S. Haymond et al., *J. Am. Chem. Soc.* 124, 10634 (**2002**). © 2002, American Chemical Society.

for theophylline, theobromine and caffeine, and of 1 to 100 μM for xanthine. Results obtained for caffeine detection in real samples of commercially available products, without separation from the matrix were promising for quantitative studies.

Figure 13 shows a series of cyclic voltammetric curves for 200 μM horse heart cytochrome *c* in 1 mM Tris HCl buffer (pH 7) containing 20 mM NaCl at a nanocrystalline BDD electrode at various potential sweep rates from 2 to 50 mV s^{-1}.[136] A well-defined, quasi-reversible voltammetric response, characteristic of a diffusion-controlled reaction, was observed in the potential range of 0.3 to −0.2 V. The peak currents varied linearly with the concentration, as shown in Figure 14 and importantly, there was no

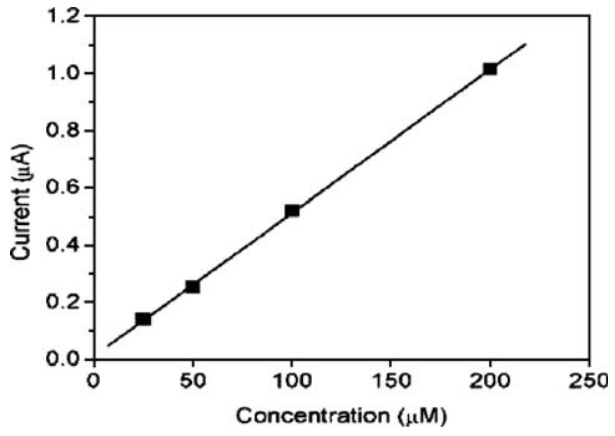

Fig. 14. Plot of cathodic peak current versus cytochrome *c* concentration from 25 to 200 μM at 10 mV s^{-1}; linear regression coefficient, 0.9995; slope, 5.03×10^{-3} μA μM^{-1}. Reprinted with permission from [136], S. Haymond et al., *J. Am. Chem. Soc.* 124, 10634 (**2002**). © 2002, American Chemical Society.

electrode fouling. The results are interesting from the standpoint of the interactions between the diamond surface and cytochrome *c* and their influence on the ET kinetics.

BDD electrodes were used to study the electrochemical analysis of nucleic acids in aqueous solution by Prado et al.[137] The advantages of this electrode material included reproducibility and small background currents observed at very positive potentials. From other work of this group, it is clear that BDD is quite robust under extreme conditions, including ultrasound, so that such conditions could also be used in future applications. tRNA, single and double stranded DNA and 2′-deoxyguanosine 5′-monophosphate (dGMP) were studied, and well defined peaks were observed in all cases and were assigned to the oxidation of deoxyguanosine monophosphate.

BDD is a most useful electrode material with which to examine the electrochemical oxidation of underivatized-nucleic acids in terms of single-stranded and double-stranded DNA. Cyclic voltammetry and square wave voltammetry were used to study the oxidation reactions and to detect DNA without derivatization or hydrolysis steps.[138] Linear calibration results showed linearity of oxidation current with concentrations in the range of 0.1–8 μg mL^{-1} for both guanine and adenine residues at as-deposited BDD. Detection limits (S/N = 3) of 3.7 and 10 ng mL^{-1} for adenine and guanine residues in single-stranded DNA, respectively, and 5.2 and 10 ng mL^{-1} for adenine and guanine residues in double-stranded DNA, respectively, were observed. The results also show the promise of using the oxidation peak current for the adenine moiety for the direct detection of nucleic acids.

The determination of aminonaphthalenes and aminobiphenyls by liquid chromatography with amperometric detection on BDD film electrodes was reported.[139] The noise, background current, signal stability, linearity of the calibration curve and detection limits obtained for the GC electrode were compared with the parameters obtained at the BDD electrode. The calibration curves were linear in the whole range 10^{-7}–10^{-4} mol L^{-1}, and the sensitivity was higher for the GC electrode. The signals for these analytes were reproducible and stable for at least 8 h for both electrode materials. The detection limits for aminonaphthalene and aminobiphenyl were at least a factor of five lower for the BDD electrode due to the lower noise and background current.

The detection of leucine-enkephalinamide (LEA) and its metabolites, tyrosine (T), tyrosyl-alanine (TA), tyrosyl-alanine-glycine (TAG) and leucine-enkephalin (LE) was reported at the BDD electrode with the use of cyclic voltammetry, FIA, and gradient LC with amperometric detection.[140] At BDD electrodes, well-defined and highly reproducible cyclic voltammograms were obtained with S/B ratios 5–10 times higher than those observed for GC electrodes. The analytical peaks of LC for LEA and its metabolites were well resolved. No deactivation of the

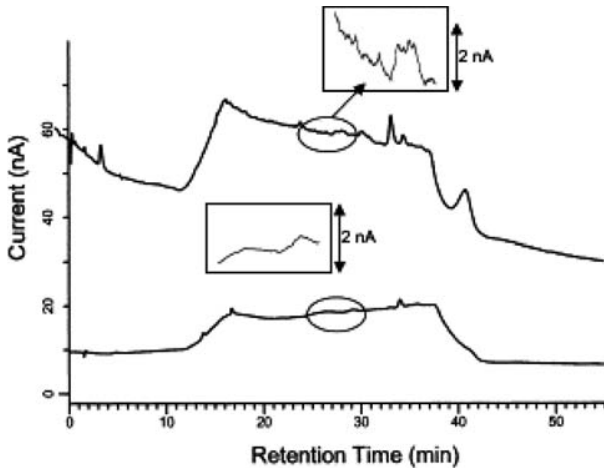

Fig. 15. Baseline obtained at BDD and GC electrodes with gradient elution using an Inertsil ODS-3 column. Operating potentials were 1.2 and 0.9 V versus Ag/AgCl for BDD and GC electrodes, respectively; the flow-rate was 1 mL min^{-1}. Reprinted with permission from [140], T. A. Ivandini et al., *J. Chromatogr. B* 791, 63 **(2003)**. © 2003, Elsevier Science.

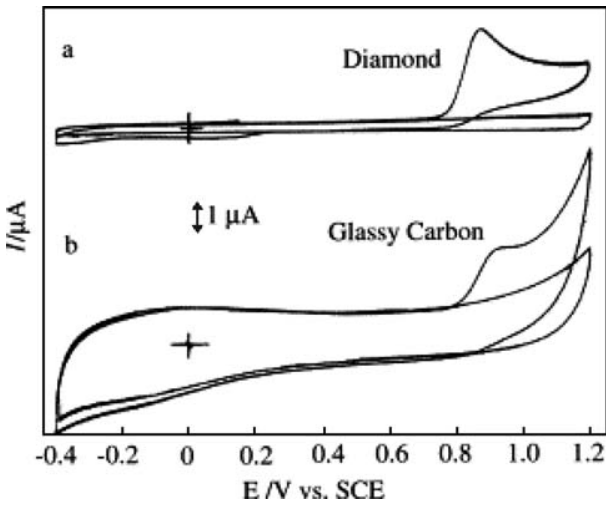

Fig. 16. Cyclic voltammograms for 50 μM sulfadiazine in 0.1 M phosphate buffer (pH 7.1) at (a) diamond electrode (area, 0.12 cm^2) and (b) GC electrode (area, 0.07 cm^2) The sweep rate was 100 mV s^{-1}. Background voltammograms are also shown in the figure. Reprinted with permission from [161], T. N. Rao et al., *J. Electroanal. Chem.* 491, 175 **(2000)**. © 2000, Elsevier Science.

BDD electrodes was found after several experiments with standard as well as plasma samples, indicating high stability of the electrode. The calibration curves were linear over a wide range from 0.06 to 30 μM with regression coefficients of 0.999 for all compounds. The limits of detection obtained based on a S/N ratio of 3 were 3, 2.2, 2.7, 20, and 11 nM for T, TA, TAG, LE, and LEA, respectively. In this work, it was reported that high stability and no fouling were observed with the BDD electrode during analysis, whereas for the GC electrode, the baseline current continuously decreased during the analysis, as shown in Figure 15. The results show the promising use of conducting diamond as an amperometric detector in gradient LC, especially for the analysis of enkephalinamide and its metabolites.

3.2.1.2. Detection of Sulfur-Containing Compounds Sulfa drugs were investigated at diamond electrodes, and their determination by HPLC with amperometric detection was described for the first time by Rao et al. For example, Figure 16 shows the cyclic voltammograms for 50 μM sulfadiazine together with the corresponding background voltammograms in 0.1 M phosphate buffer (pH 7.1) at BDD and GC electrodes. Highly reproducible and well-defined cyclic voltammograms were obtained not only sulfadiazine but also for the other two drugs, sulfamerazine and sulfamethazine, with a S/B ratio of a factor of ten greater than that obtained at two types of freshly polished GC electrodes. With the use of amperometry coupled with an FIA system, BDD exhibited a highly reproducible amperometric response, with a peak variation of approximately 5%. A detection limit of 50 nM and a linear dynamic range of three orders of magnitude were obtained. An important observation in this study was that BDD yields a well-defined chromatogram with a flat baseline (background current), unlike the other two types of GC electrodes, as shown in the Figure 17.

The electrooxidation L-cysteine was first examined at BDD and GC electrodes by use of cyclic voltammetry.[141]

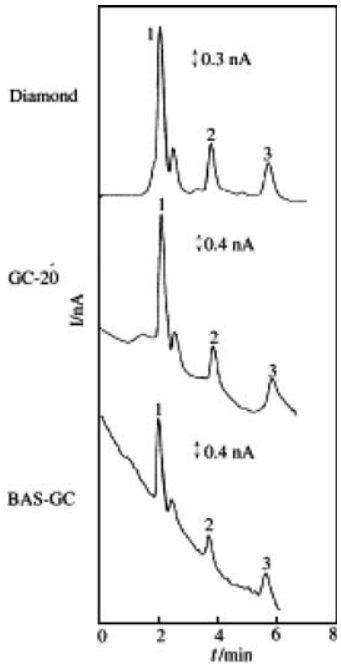

Fig. 17. Chromatograms of a standard mixture containing 100 nM concentrations of (1) sulfadiazine, (2) sulfamerazine and (3) sulfamethazine at diamond and GC electrodes. The mobile phase was 85% 0.1 M phosphate buffer (pH 7.1) + 15% methanol (v/v). The injection volume was 20 μL, and the flow rate was 1 mL min^{-1}. Reprinted with permission from [161], T. N. Rao et al., *J. Electroanal. Chem.* 491, 175 **(2000)**. © 2000, Elsevier Science.

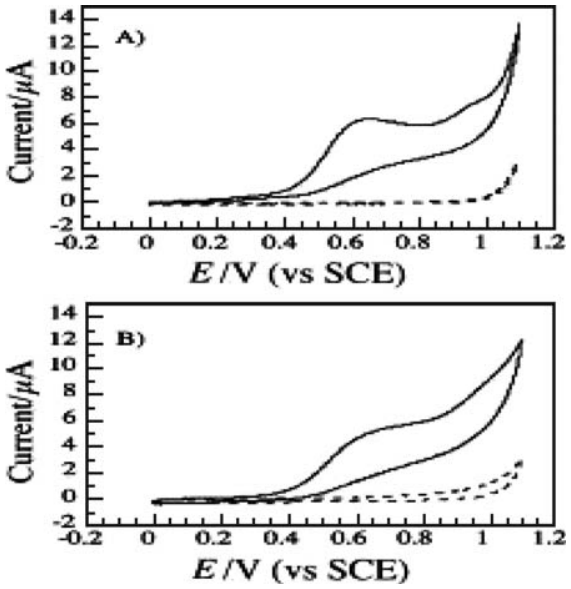

Fig. 18. Cyclic voltammograms for (A) boron-doped diamond and (B) glassy carbon electrodes in L-cysteine + 0.5 M $KHCO_3$ (solid lines) and 0.5 M $KHCO_3$ (dashed lines); potential sweep rate, 20 mV s^{-1}; electrode area, 0.07 cm^2. Reprinted with permission from [141], O. Chailapakul et al., *Electrochem. Commun.* 2, 422 **(2000)**. © 2000, Elsevier Science.

Well-defined, irreversible peaks were obtained for the oxidation of cysteine, as shown in Figure 18. This preliminary study showed that BDD has better sensitivity than GC. The mechanism oxidation reaction of L-cysteine (CySH) was also studied in alkaline media.[142] The results of the voltammetric and polarization measurements showed that the overall CySH oxidation reaction at BDD electrodes was controlled by the initial electrochemical step, i.e., the oxidation of the CyS^- electroactive species. In contrast, under the same conditions, the reaction at GC electrodes was controlled by the desorption of the reaction products. It was found that BDD exhibits excellent behavior for CySH detection.

Interestingly, Nekrassova et al. developed a voltammetric method, using the BDD electrode, for the study of the homogeneous oxidation mechanism of cysteine by aqueous ferricyanide.[143] It was shown that, on the BDD electrode, unlike other electrodes, e.g., platinum, the voltammetric responses of the ferrocyanide and the cysteine were distinctly different, with the ferrocyanide oxidizing at a lower potential, so that the kinetics could be examined via voltammetric methods. Cyclic voltammetry with the BDD electrode was used to show that an electron transfer followed by a chemical reaction (EC' mechanism) occurs, and the appropriate rate constants were determined. Both the protonated and de-protonated forms of cysteine underwent oxidation by ferricyanide. The cyclic voltammetric results obtained with a conventional electrode configuration also agreed well with those obtained with a channel flow cell. The latter was found to provide a simple means of controlling the hydrodynamics at BDD electrodes.

The electrooxidation of homocysteine, glutathione (GSH), 2-mercapto ethanesulfonic acid and cephalexin at BDD and GC electrodes was investigated for the first time by cyclic voltammetry.[144] This preliminary voltammetric study showed that BDD had better sensitivity than GC, as shown in Figure 19. The concentration dependence was studied and indicated the promise of using BDD electrodes for quantitative determination. All of the compounds displayed recognizable oxidation peaks with the BDD electrode at millimolar concentration levels. The scan rate dependence of GSH was examined. It was found that there was negligible adsorption on the surface of the BDD electrode for low concentrations.

At anodized (electrochemically oxidized) BDD electrodes, highly reproducible, well-defined cyclic voltammograms for homocysteine oxidation were obtained in acidic media, while as-deposited BDD did not provide a detectable signal.[145] In alkaline media, however, oxidation peaks were obtained at both as-deposited and anodized electrodes. In the flow system, BDD exhibited a highly reproducible amperometric response, with a peak variation less than 2%. An extremely low detection limit (1 nM) was obtained at 1.6 V versus Ag/AgCl. Homocysteine was also determined in a standard mixture with aminothiols and disulfide compounds with isocratic reverse-phase HPLC with amperometric detection at BDD electrodes. The detection limit was 1 pmol, and the linear dynamic range was three orders of magnitude.

Anodized BDD was also used for the first time to detect disulfides in aqueous acidic media.[146, 147] Cyclic voltammetric signals for 1 mM glutathione disulfide (GSSG) were observed at 1.39 and 1.84 V versus SCE; these values were less positive than those for as-deposited BDD and GC electrodes. It was proposed that an attractive electrostatic interaction between the anodically oxidized diamond surface and the positively charged GSSG caused a positive shift in the peak potential in acidic media. Electrolysis results showed that the oxidation reaction mechanism for glutathione (GSH) and GSSG involves oxygen transfer. Following separation by LC, the determination of both GSH and GSSG in whole rat blood (Fig. 20) was achieved at a constant potential (1.50 V versus Ag/AgCl), and the limits of detection for GSH and GSSG were found to be 1.4 nM (0.028 pmol) and 1.9 nM (0.037 pmol), with a linear dynamic range up to 0.25 mM. These detection limits were much lower than those reported for Bi-PbO_2 electrodes or for LC-mass spectrometry and were comparable with those for enzymatic assay for real samples.

The electrochemically initiated catalytic oxidation of 5-thio-2-nitrobenzoic acid (TNBA) by thiols was examined at a BDD electrode with chronoamperometry.[148] This method provided the basis for the detection of a range of biologically relevant thiols. The method was shown to be capable of measuring total thiol concentration, since the sensitivities of the standard addition plots are independent of the individual thiols. Detection limits of 5.7 μM,

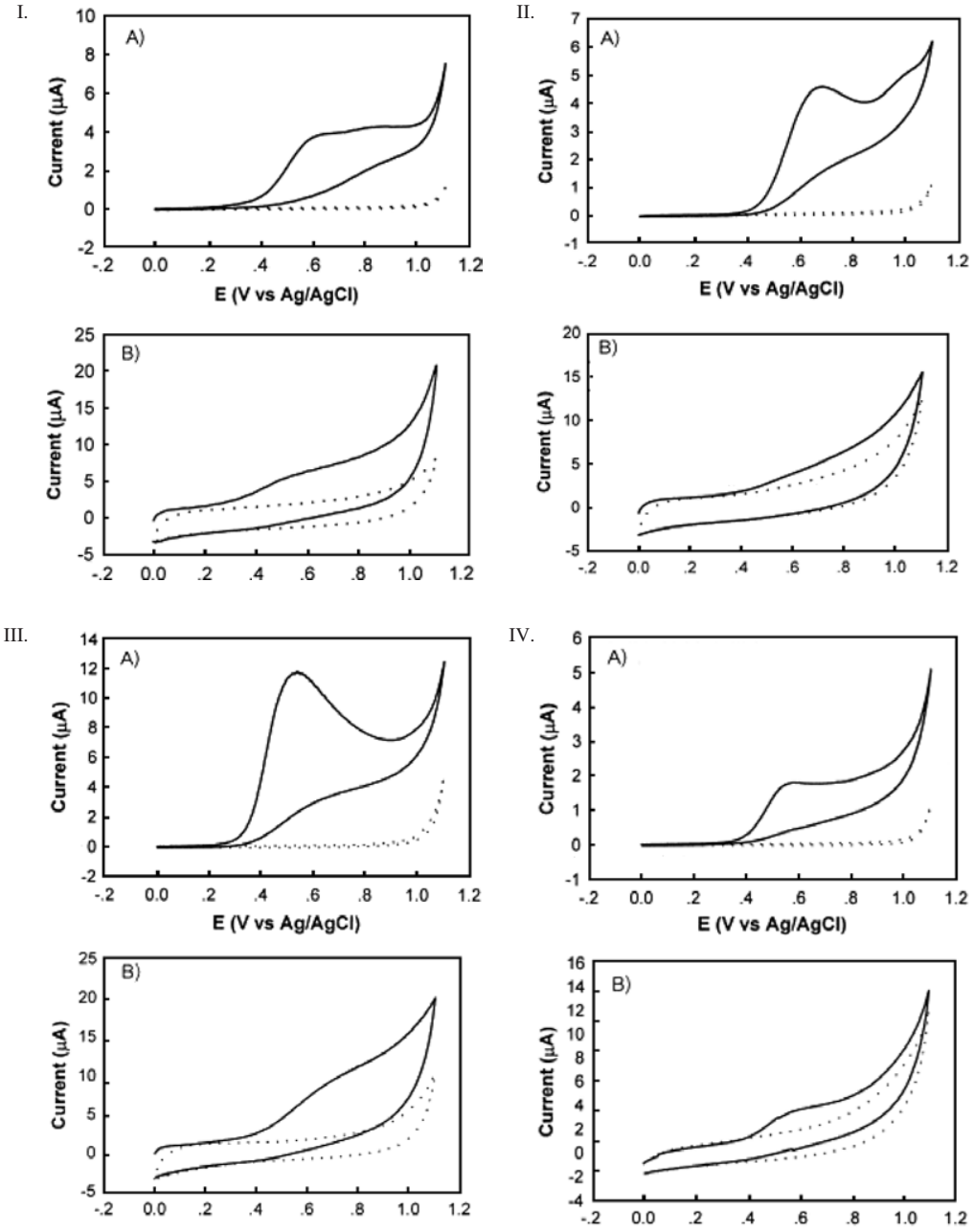

Fig. 19. Cyclic voltammograms for I. homocysteine, II 0.67 mM glutathione, III 1.0 mM 2-mercapto ethanesulfonic acid, IV. 10.0 mM cephalexin (A) BDD electrode and (B) GC electrode versus Ag/AgCl in 0.1 M carbonate buffer (pH 9.2) in the presence (solid lines) and absence (dotted lines) of analytes; sweep rate, 50 mV s^{-1}; area of electrode, 0.07 cm^2.

4.4 μM, and 5.8 μM for the detection of cysteine, homocysteine, and glutathione, respectively, were obtained.

D-penicillamine, a thiol drug, was detected for the first time at a BDD-based electrode with cyclic voltammetry for a range of concentrations and pH.[149] The results were compared with those for a GC electrode. The BDD electrode exhibited a well resolved, irreversible oxidation voltammetric peak, but the GC electrode exhibited an ill defined response. The BDD electrode provided a linear dynamic range from 0.5 to 10 mM and a detection limit of 25 μM (S/B = 3) in the voltammetric measurements. In addition, penicillamine was studied by hydrodynamic voltammetry and FIA with amperometric detection at the BDD electrode. The FIA results indicated a linear dynamic range from 0.5 to 50 μM and a detection limit of 10 nM (S/N approximately 4). The proposed method was applied to the determination of D-penicillamine in dosage form (capsules); the results obtained in the recovery study (255 $\pm$ 2.50 mg per tablet) were in agreement with the nominal values (250 mg per tablet).

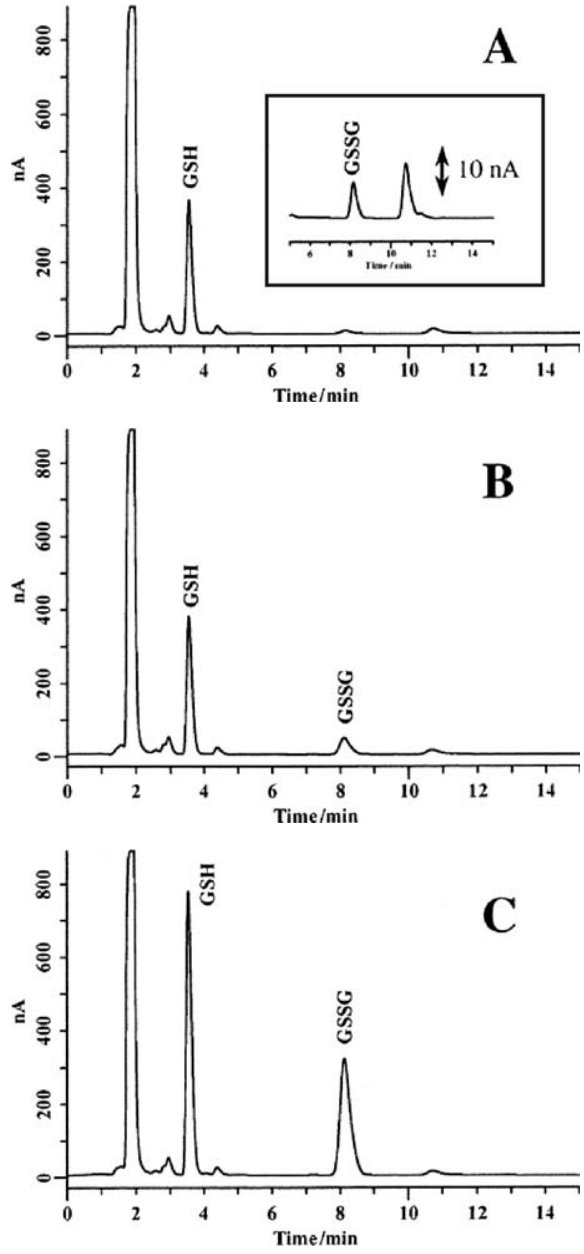

Fig. 20. Chromatograms of rat whole blood (1:80 dilution) showing peaks for GSH and GSSG. (A) No addition of standard GSH and GSG, (B) 82.5 μM each, and (C) 825 μM each of GSH and GSSG was added prior to deproteinization. Separation column: Inertsil ODS-3 (4.6-mm i.d. × 75 mm, dp = 3 μm); mobile phase, MeCN/0.1% TFA = 2/98; temperature, 25 °C; flow rate, 0.7 mL min^{-1}; injection volume, 20 μL. Anodically oxidized (AO) diamond was prepared by applying a potential of 1.50 V versus Ag/AgCl. Reprinted with permission from [146], C. Terashima et al., *Anal. Chem.* 75, 1564 (**2003**). © 2003, American Chemical Society.

A quantitative study of tiopronin, a drug used to prevent kidney stones, was carried out with BDD electrodes with cyclic voltammetry and FIA coupled with amperometry.[150] At the diamond electrode, it was found that tiopronin provided highly reproducible and well-defined cyclic voltammograms, with a peak potential of +0.8 V versus Ag/AgCl. In contrast, tiopronin gave ill-defined cyclic voltammograms at the GC electrode. Linearity at the BDD film electrode was observed over a range of 0.05–10 mmol L^{-1}, with a detection limit of 50 μmol L^{-1} (S/B $\geq$ 3). In addition, the amperometric hydrodynamic voltammetry with FIA with the BDD was studied. A detection potential of +0.8 V was chosen, at which tiopronin exhibited the highest S/B ratios. The FIA results showed the low detection limit of 10 nmol L^{-1} (S/N = 3) and a linear dynamic range of 0.5–50 μmol L^{-1}. This method was applied to the determination of tiopronin in a pharmaceutical formulation. With the use of the standard addition technique, the recoveries obtained were 96.5–108.3%, and the RSD values were 1.10–1.62% (n = 10).

Several techniques, including cyclic voltammetry, hydrodynamic voltammetry and FIA with amperometric detection, were used with the BDD electrode to study the electroanalysis of captopril in phosphate buffer (pH = 9). Catopril is a drug that is used to treat hypertension, congestive heart disease and diabetic kidney disease. Cyclic voltammetry was used to study the reaction as a function of analyte concentration. The results were compared with those obtained with a GC electrode under the same conditions. Captopril undergoes an irreversible reaction at both electrodes. However, the BDD electrode provided a highly reproducible, well-resolved cyclic voltammogram and a higher S/B ratio compared with GC. A linear range from 50 μM to 3 mM and a detection limit of 25 μM (S/B $\approx$ 3) were obtained from the BDD electrode with cyclic voltammetry. The potential sweep rate (υ) dependence for the captopril oxidation peak currents for 1 mM captopril was linear with $\upsilon^{1/2}$, within the range of 0.01 to 0.3 V s^{-1}, which indicates that the oxidation current was diffusion-controlled, with negligible adsorption on the BDD surface. The FIA measurements for the BDD electrode in the concentration range from 0.5 to 100 μM exhibited a linear dynamic range and the very low detection limit of 10 nM (S/N $\approx$ 3). In addition, the determination of captopril in commercial tablets by FIA with amperometric detection at BDD electrodes was also carried out. The results showed good precision (1.21–2.15%).[151]

3.2.1.3. Detection of Other Heteroatomic Compounds The detection of anthraquinone-2,6-disulfonate (2,6-AQDS) at GC, hydrogenated glassy carbon (HGC), the basal plane of highly oriented pyrolytic graphite (HOPG), and BDD electrodes was investigated by use of cyclic voltammetry and chronocoulometry.[152] Quantitative determination of the surface coverage and qualitative assessment of the physisorption strength of 2,6-AQDS adsorption on each of these electrode surfaces were carried out. The diamond and HGC surfaces were nonpolar and hydrogen terminated. The polar 2,6-AQDS did not adsorb on these surfaces, and the electrochemical process was diffusion-controlled. In contrast, the GC and HOPG surfaces were polar, with a significant coverage of carbon-oxygen functionalities. 2,6-AQDS adsorbed strongly on both of these

surfaces at high coverage, and the electrochemical behavior was typical for an adsorbed layer. The initial adsorbed layer could not be completely removed by rinsing, which indicated strong physisorption. The results demonstrated that BDD electrodes are more difficult to foul by polar molecules, in comparison to GC, which is beneficial for a reproducible response.

An ultrasonically facilitated BDD electrochemical technique was developed to analyze the priority pollutant 4-chlorophenol by Saterlay et al.[153] The electroanalysis of this compound is hampered by the formation of a polymeric film on the electrode surface. The combination of ultrasound with the highly robust BDD electrode facilitated the measurement of 4-chlorophenol in aqueous solution. The surface film was removable due its ultrasonic breakup. The ultrasonic field also yielded an enhanced oxidation current signal due to more efficient mass transport of 4-chlorophenol. A detection limit of 1 μM and a linear range of 1–300 μM were reported; this range is useful for environmental measurements.

The detection of chlorophenols (CP) in aqueous solution was also examined with a hydrodynamic channel flow cell and a BDD electrode by Prado et al.154 Due to the film formation problem mentioned above, the use of the channel flow cell was proposed. The results showed linear ranges up to 20 μM. Thus, this technique is useful for environmental applications. Laser ablation voltammetry with a Nd:YAG laser indicated that there was negligible adsorption of oxidation products. The similarity of the sensitivities for 4-chlorophenol, 2-chlorophenol, phenol, 2,4-dichlorophenol, and 4-chloro-3-methylphenol makes it possible to measure a summed total CP concentration, presumably with a simplified separation stage. No interferences were observed for nitrite or sulfite.

In the same year, Terashima et al. reported a detailed study of the electrochemical oxidation of CPs at anodically pretreated BDD electrodes and their determination by HPLC with amperometric detection.[40] The anodization of as-deposited boron-doped polycrystalline diamond thin-film electrodes enabled the CPs to be determined stably over a wide concentration range. The oxidative behavior was compared for ordinary GC, as-deposited BDD, and anodized BDD by cyclic voltammetry and FIA with amperometric detection. At anodized BDD electrodes, reproducible, well-defined cyclic voltammetric peaks were obtained, even at CP concentrations as high as 5 mM, due to the lack of adsorption of oxidation products on the surface. After prolonged use, there was partial deactivation of the BDD surface due to filming, but the electrode was able to be reactivated *in situ* by applying a highly oxidizing potential (2.64 V vs. SCE) for 4 min; this treatment is effective in removing the polymeric film, due to the action of electrogenerated hydroxyl radicals. With FIA, the anodized BDD electrode exhibited excellent stability, with a response variability of 2.3% ($n = 100$), for the oxidation of a high concentration (5 mM) of chlorophenol. In contrast, GC exhibited a response variability of 39.1%. After 100 injections, the relative peak intensity for BDD decreased by 10%, compared to 70% for GC. The detection limit obtained in the FIA mode for 2,4-dichlorophenol was found to be 20 nM (S/N = 3), with a linear dynamic range up to 100 μM. By use of a column-switching technique, which enabled on-line preconcentration , the, detection limit was lowered to 0.4 nM (S/N = 3). With this technique, anodized BDD electrodes were also used for the analysis of CPs in a real sample, specifically, drainwater condensed from the flue gas of a waste incinerator.

The BDD thin film electrode was used to determine acetaminophen in phosphate buffer solution (pH 8) with cyclic voltammetry, hydrodynamic voltammetry, and FIA with amperometric detection.[155] Cyclic voltammetry was used to study the reaction as a function of analyte concentration. The BDD electrode exhibited a linear dynamic range from 0.1 to 8 mM and a detection limit of 10 μM (S/B $\approx$ 3) for the voltammetric measurement. The FIA results indicated a linear dynamic range from 0.5 to 50 μM and a detection limit of 10 nM (S/N $\approx$ 4). Acetaminophen was also measured for syrup samples. The reported recoveries (24.68 ± 0.26 mg mL^{-1}) were comparable to the nominal value of 24 mg mL^{-1}.

Metal-modified diamond electrodes have interesting characteristics in terms of the catalysis of multi-step electrochemical reactions, which can be quite sluggish on unmodified diamond. For example, the oxidation of alcohols and carbohydrates is quite difficult without a metal catalyst but becomes feasible with the addition of small amounts of metals. For example, nickel and copper were used to modify BDD, and the resulting electrodes yielded well-defined, reproducible voltammmetric peaks for the oxidation of 1 mM glucose in alkaline media.[156] These electrodes exhibited excellent electrochemical stability, with low background current for at least one week in an FIA system, indicating good adhesion of the metal clusters to the diamond surface. These results indicate the promising use of nickel- and copper-modified BDD electrodes for the detection of carbohydrates.

A new type of metal-modified BDD surface involves the use of ion implantation; specifically, nickel-implanted BDD electrodes (Ni-DIA) were prepared in order to examine their usefulness for carbohydrate detection. This type of electrode produced well-defined, reproducible voltammograms for the oxidation of 1 mM glucose in alkaline media. The electrode exhibited excellent electrochemical stability, with low background current, even after ultrasonic treatment, which indicated strong bonding of nickel with diamond. These results suggest that ion implantation of metals into BDD electrodes might show promise for the detection of carbohydrates and perhaps amino acids.

Due to the insensitivity of the unmodified BDD surface for the oxidation of alcohols, it is possible to measure a variety of analytes in alcohol solutions without interference. Additional benefits are the lack of electrode

deactivation from fouling and the ability to withstand highly positive electrochemical potentials. For example, the detection of ascorbic acid (AA) was carried out in an ethanol-water mixed solution (0.1 M $NaClO_4$) with a BDD electrode.[157] During FIA of AA in this solution, there was little interference from ethanol oxidation, in contrast to the behavior of a Pt electrode. Moreover, the detection limit for AA observed was lower than that for a GC electrode, because BDD exhibited lower background current, background noise, and lower injection noise. These findings suggest that BDD electrodes may be applied in the detection of other redox-active impurities and added substances in alcohol or alcohol-water solutions, such as chlorophyll, nicotinamide, caffeine, riboflavin, and dl-alpha-tocopherol.

The use of enzyme modification of diamond, as already mentioned, is a highly promising approach to the preparation of analytical electrodes with special selectivity. It was reported that tyrosinase-modified BDD electrodes can be used for the determination of phenol derivatives.[158] BDD electrodes were modified covalently with tyrosinase by the introduction of hydroxyl groups onto the surface and were then treated with (3-aminopropyl)triethoxysilane and finally coated with a tyrosinase film cross-linked with glutaraldehyde. These electrodes were designed for the determination of estrogenic phenol derivatives. The amperometric response of these modified electrodes was measured for bisphenol-A and 17-β-estradiol at -0.3 V versus Ag/AgCl. Interference from dioxygen reduction was nearly negligible. These electrodes were used in an FIA system, and the detection limit for bisphenol-A was found to be 10^{-6} M.

3.2.2. Detection Based on Other Techniques

Shin et al. reported the application of diamond microelectrodes for end-column electrochemical detection in capillary electrophoresis (CE). Diamond microline electrodes were fabricated from BDD thin films (exposed surface area, 300×50 μm), and their analytical performance as CE detectors was evaluated in a laboratory-made CE apparatus. The CE-ED system exhibited high separation efficiency for several catecholamines, including dopamine (DA), norepinephrine (NE), and epinephrine (E). The analytical performance was excellent, e.g., 155,000 theoretical plates for DA. The detection limits were quite low (approximately 20 nM for E at S/N = 3), and current response was highly reproducible for ten repetitive injections of mixtures containing DA, NE, and E (each 50 μM), with relative standard deviations of approximately 5%.

The performance of the BDD electrochemical detector for CE was also evaluated in the detection of CPs. When compared to the carbon fiber microelectrode, the BDD electrode exhibited lower detection limits in an end-column CE detection, as a result of the very low noise levels and high reproducibility. In addition, there was no need for electrode polishing, because analyte fouling was negligible; this makes the analysis significantly more convenient and also leads to higher stability.

Cvacka et al. also studied the use of BDD microelectrodes for CD with electrochemical detection.[159] The microelectrodes were prepared by coating thin films of CVD polycrystalline BDD on electrochemically sharpened platinum wires (76, 25, and 10-μm diameter. The BDD-coated wires were then attached to copper wires. These microelectrodes were characterized by scanning electron microscopy, Raman spectroscopy, and cyclic voltammetry. They exhibited low, stable background currents and voltammetric behavior typical of microelectrodes, i.e., sigmoidal curves for $Ru(NH_3)_6^{3+/2+}$ and $Fe(CN)_6^{3-/4-}$ at low potential sweep rates. The microelectrodes were fabricated by sealing in polypropylene pipet tips. Dopamine, catechol, and ascorbic acid were used to evaluate the performance of the CE-EC system in 10 mM phosphate buffer, pH 6.0, run buffer, and a 30-cm-long fused-silica capillary (75-μm I.D.). The background current ($\sim$100 pA) and noise ($\sim$3 pA) were measured at various detection potentials and were found to be quite stable. Reproducible separation (elution time) and detection (peak current or area) of dopamine, catechol, and ascorbic acid were observed with response precisions of 4.1% or less. Calibration curves constructed from the peak area were linear over 4 orders of magnitude, up to a concentration between 0.1 and 1 mM. Mass limits of detection for dopamine and catechol were 1.7 and 2.6 fmol, respectively (S/N = 3). The separation efficiency was 33,000, 56,000, and 98,000 plates/m for dopamine, catechol, and ascorbic acid, respectively. In addition, the separation and detection of 1- and 2-naphthol in 160 mM borate buffer, pH 9.2, was investigated. Separation of these two analytes was achieved with efficiencies of 118,000 and 126,000 plates/m, respectively.

Wang et al. discussed the advantages of a diamond electrode detector for a micromachined capillary electrophoresis (CE) system.[160] A chemically vapor-deposited BDD film band (0.3×6.0 mm) electrode was used for end-column amperometric detection. The performance of the BDD electrode detector was superior to that for a commonly used thick-film carbon detector. BDD provided enhanced sensitivity, lower noise levels, and sharper peaks for several groups of important analytes (nitroaromatic explosives, organophosphate nerve agents, phenols). The advantages of the BDD-based CE detector included the superior S/B ratios and the much higher resistance to surface fouling. The enhanced stability was evidenced by the RSD of 0.8% for 60 repetitive measurements of 5 ppm 2,4,6-trinitrotoluene (compared to an RSD value of 10.8% at the thick-film carbon electrode). A linear response was obtained for the explosives 1,3-dinitrobenzene and 2,4-dinitrotoluene over the 200–1400 ppb range, with detection limits of 70 and 110 ppb, respectively. BDD is thus quite a promising electrode material for electrochemical detection in CE and micromachined flow systems.

4. CONCLUDING REMARKS

Based on its range of superior characteristics for sensitive electroanalytical measurements, BDD as an electrode material and electrochemical sensor material may constitute one of the more important developments in this area in recent years. In addition, the range of possible analytes is great, as demonstrated in the present review. As the availability of high quality BDD samples becomes greater, there will doubtless be increasing numbers of applications. The ability to chemically tailor the surface with various species, including metals, functional molecules, oligonucleotides and enzymes, continues to grow as well, which further support the development of new applications.

Acknowledgments: The authors would like to acknowledge the Thailand Research Fund, the Rachadapiseksompot Endowment and the National Research Council of Thailand (NRCT) through the Nanopolymer Project (kor-sor-sor 52/2547). The authors would also like to thank Professor Akira Fujishima, Kanagawa Academy of Science and Technology, and his group at the University of Tokyo, for their encouragement and guidance, and to the Ministry of Education, Culture, Sports, Science, and Technology (MEXT) of Japan for support.

References and Notes

1. J. Wang, *Analytical Electrochemistry* Wiley-VCH, New York **(2000)**.
2. D. Diamond (Ed.), Principles of Chemical and Biological Sensors, Chemical Analysis: A Seried of Monographs on Analytical Chemistry and its Applications, Wiley-Interscience, New York **(1998)**, Vol. 150.
3. B. R. Eggins, Chemical Sensors and Biosensors, John Wiley and Sons, New York **(2002)**.
4. G. S. Wilson (Ed.), Bioelectrochemistry, Encyclopedia of Electrochemistry, Wiley-VCH, New York **(2002)**, Vol. 9.
5. R.-I. Stefan, J. F. V. Staden, and H. Y. Aboul-Enein, Electrochemical Sensors in Bioanalysis, Marcel Dekker, New York **(2001)**.
6. C. M. A. Brett, *Pure Appl. Chem.* 73, 1969 **(2001)**.
7. A. J. Bard and L. R. Faulkner, Electrochemical Methods: Fundamentals and Applications, Wiley, New York **(2000)**.
8. J. Clavilier, D. Armand, S. G. Sun, and M. Petit, *J. Electroanal. Chem.* 205, 267 **(1986)**.
9. M. S. Hossain, D. Tryk, and E. Yeager, *Electrochim. Acta* 34, 1733 **(1989)**.
10. K. Kinoshita, Carbon: Electrochemical and Physicochemical Properties, John Wiley and Sons, New York **(1988)**.
11. T. N. Rao and A. Fujishima, *Dia. Rel. Mater.* 9, 384 **(2000)**.
12. Y. Einaga, R. Sato, H. Olivia, D. Shin, T. A. Ivandini, and A. Fujishima, *Electrochim. Acta* 49, 3989 **(2004)**.
13. A. E. Fischer, Y. Show, and G. M. Swain, *Anal. Chem.* 76, 2553 **(2004)**.
14. M. C. Granger, M. Witek, J. Xu, J. Wang, M. Hupert, A. Hanks, M. D. Koppang, J. E. Butler, G. Lucazeau, M. Mermoux, J. W. Strojek, and G. M. Swain, *Anal. Chem.* 72, 3793 **(2000)**.
15. A. Fujishima, C. Terashima, K. Honda, B. V. Sarada, and T. N. Rao, *New Diamond Frontier Technol.* 12, 73 **(2002)**.
16. T. Kondo, Y. Einaga, B. V. Sarada, T. N. Rao, D. A. Tryk, and A. Fujishima, *J. Electrochem. Soc.* 149, E179 **(2002)**.
17. N. Vinokur, B. Miller, Y. Avyigal, and R. Kalish, *J. Electrochem. Soc.* 143, L238 **(1996)**.
18. T. Kondo, K. Honda, D. A. Tryk, and A. Fujishima, *J. Electrochem. Soc.* 152, E18 **(2005)**.
19. A. Fujishima, Y. Einaga, T. N. Rao, and D. A. Tryk (Eds.), Diamond Electrochemistry, BKC, Inc. (Tokyo), Elsevier (Amsterdam) **(2005)**.
20. T. A. Ivandini, Y. Einaga, K. Honda, and A. Fujishima, Diamond Electrochemistry, edited by A. Fujishima, Y. Einaga, T. N. Rao, and D. A. Tryk, BKC, Inc., (Tokyo), Elsevier (Amsterdam) **(2005)**, p. 11.
21. A. Argoita, C. S. Kovach, and J. C. Angus, Handbook of Industrial Diamond and Diamond Films, edited by M. A. Prelas, G. Popovici, and L. K. Bigelow, Marcel Dekker, Inc., New York **(1998)**, p. 797.
22. P. K. Bachmann, Handbook of Industrial Diamond and Diamond Films, edited by M. A. Prelas, G. Popovici, and L. K. Bigelow, Marcel Dekker, Inc., New York **(1998)**, p. 821.
23. S. L. Girshick, Handbook of Industrial Diamond and Diamond Films, edited by M. A. Prelas, G. Popovici, and L. K. Bigelow, Marcel Dekker, Inc., New York **(1998)**, p. 851.
24. M. A. Cappelli, Handbook of Industrial Diamond and Diamond Films, edited by M. A. Prelas, G. Popovici, and L. K. Bigelow, Marcel Dekker, New York **(1998)**, p. 865.
25. C. H. Goeting, F. Jones, J. S. Foord, J. C. Eklund, F. Marken, R. G. Compton, P. R. Chalker, and C. Johnston, *J. Electroanal. Chem.* 442, 207 **(1998)**.
26. M. D. Koppang, M. Witek, J. Blau, and G. M. Swain, *Anal. Chem.* 71, 1188 **(1999)**.
27. Y. Show, M. A. Witek, P. Sonthalia, and G. M. Swain, *Chem. Mater.* 15, 879 **(2003)**.
28. N. Mizuochi, H. Watanabe, J. Isoya, H. Okushi, and S. Yamasaki, *Diamond Rel. Mater.* 13, 765 **(2004)**.
29. K. Okano, H. Naruki, Y. Akiba, T. Kurosu, M. Iida, Y. Hirose, and T. Nakamura, *Jpn. J. Appl. Phys.* 6, 1066 **(1989)**.
30. R. S. Clausing, Handbook of Industrial Diamond and Diamond Films, edited by M. A. Prelas, G. Popovici, and L. K. Bigelow, Marcel Dekker, New York **(1998)**, p. 19.
31. J. Philip, P. Hess, T. Feygelson, J. E. Butler, S. Chattopadhyay, K. H. Chen, and L. C. Chen, *J. Appl. Phys.* 93, 2164 **(2003)**.
32. J. Birrell, J. E. Gerbi, O. Auciello, J. M. Gibson, D. M. Gruen, and J. A. Carlisle, *J. Appl. Phys.* 93, 5606 **(2003)**.
33. J.-Y. Raty and G. Galli, *Nature Mater.* 2, 792 **(2003)**.
34. T. Kolber, K. Piplits, R. Haubner, and H. Hutter, *Fres. J. Anal. Chem.* 365, 636 **(1999)**.
35. K. Honda, T. Noda, M. Yoshimura, K. Nakagawa, and A. Fujishima, *J. Phys. Chem. B* 108, 16117 **(2004)**.
36. D. Becker and K. Juettner, *J. Appl. Electrochem.* 33, 959 **(2003)**.
37. K. B. Holt, A. J. Bard, Y. Show, and G. M. Swain, *J. Phys. Chem. B* 108, 15117 **(2004)**.
38. K. Honda, T. N. Rao, D. A. Tryk, M. Watanabe, K. Yasui, and H. Masuda, *J. Electrochem. Soc.* 147, 659 **(1999)**.
39. D. Shin, D. A. Tryk, A. Fujishima, A. Merkoci, and J. Wang, *Electroanalysis* 17, 305 **(2005)**.
40. C. Terashima, T. N. Rao, B. V. Sarada, D. A. Tryk, and A. Fujishima, *Anal. Chem.* 74, 895 **(2002)**.
41. S. G. Ri, T. Ishikawa, S. Tanaka, T. Kimura, Y. Akiba, and M. Iida, *Jpn. J. Appl. Phys.* 36, 2057 **(1997)**.
42. V. Chakrapani, S. C. Eaton, A. B. Anderson, M. Tabib-Azar, and J. C. Angus, *Electrochem. Solid-State Lett.* 8, E4 **(2005)**.
43. K. Tsugawa, H. Umezawa, and H. Kawarada, *Jpn. J. Appl. Phys.* 40, 3101 **(2001)**.
44. O. A. Williams and R. B. Jackman, *J. Appl. Phys.* 96, 3742 **(2004)**.
45. C. E. Nebel, C. Sauerer, F. Ertl, M. Stutzmann, C. F. O. Graeff, P. Bergonzo, O. A. Williams, and R. Jackman, *Appl. Phys. Lett.* 79, 4541 **(2001)**.
46. T. Maki, S. Shikama, M. Komori, Y. Sakaguchi, K. Sakuta, and T. Kobayashi, *Jpn. J. Appl. Phys.* 31, L1446 **(1992)**.

47. N. Jiang and T. Ito, *J. Appl. Phys.* 85, 8267 (**1999**).
48. K. Hayashi, H. Watanabe, S. Yamanaka, T. Sekiguchi, H. Okushi, and K. Kajimura, *Diamond Rel. Mater.* 6, 303 (**1997**).
49. K. Hayashi, S. Yamanaka, H. Watanabe, T. Sekiguchi, H. Okushi, and K. Kajimura, *J. Cryst. Growth* 183, 338 (**1998**).
50. J. Chevallier, D. Ballutaud, B. Theys, F. Jomard, A. Deneuville, E. Gheeraert, and F. Pruvost, *Phys. Stat. Solid. A* 172, 73 (**1999**).
51. J. Ristein, M. Riedel, and L. Ley, *J. Electrochem. Soc.* E315 (**2004**).
52. F. Maier, M. Riedel, B. Mantel, J. Ristein, and L. Ley, *Phys. Rev. Lett.* 85, 3472 (**2000**).
53. R. Kalish, A. Reznik, C. Uzan-Saguy, and C. Cytermann, *Appl. Phys. Lett.* 76, 757 (**2000**).
54. M. Nishitani-Gamo, E. Yasu, C. Xiao, Y. Kikuchi, K. Ushizawa, I. Sakaguchi, T. Suzuki, and T. Ando, *Diamond Rel. Mater.* 9, 941 (**2000**).
55. S. C. Eaton, A. B. Anderson, J. C. Angus, Y. E. Evstefeeva, and Y. V. Pleskov, *Diamond Rel. Mater.* 12, 1627 (**2003**).
56. R. Kalish, C. Uzan-Saguy, R. Walker, and S. Prawer, *J. Appl. Phys.* 94, 3923 (**2003**).
57. S. Gupta, B. R. Weiner, and G. Morell, *Appl. Phys. Lett.* 83, 491 (**2003**).
58. K. Nakazawa, M. Tachiki, H. Kawarada, A. Kawamura, K. Horiuchi, and T. Ishikura, *Appl. Phys. Lett.* 82, 2074 (**2003**).
59. T. Nishimatsu, H. Katayama-Yoshida, and N. Orita, *Physica B* 302–303, 149 (**2001**).
60. S. C. Eaton, Y. E. Evsteeva, J. C. Angus, A. B. Anderson, and Y. V. Pleskov, *Russ. J. Electrochem.* 39, 170 (**2003**).
61. D. A. Tryk, T. Kondo, and A. Fujishima, Diamond Electrochemistry, edited by A. Fujishima, Y. Einaga, T. N. Rao, and D. A. Tryk, BKC, Inc., (Tokyo), Elsevier, (Amsterdam) (**2005**), p. 174.
62. H. Notsu, T. Fukazawa, T. Tatsuma, D. A. Tryk, and A. Fujishima, *Electrochem. Solid State Lett.* 4, H1 (**2001**).
63. H. Notsu, I. Yagi, T. Tatsuma, D. A. Tryk, and A. Fujishima, *J. Electroanal. Chem.* 492, 31 (**2000**).
64. H. Notsu, I. Yagi, T. Tatsuma, D. A. Tryk, and A. Fujishima, *Electrochem. Solid-State Lett.* 2, 522 (**1999**).
65. K. I. Sotowa, T. Amamoto, A. Sobana, K. Kusakabe, and T. Imato, *Diamond Rel. Mater.* 13, 145 (**2004**).
66. J. B. Miller and D. W. Brown, *Langmuir* 12, 5809 (**1996**).
67. S. Ferro and A. DeBattisti, *J. Phys. Chem. B* 107, 7567 (**2003**).
68. S. Ferro and A. DeBattisti, *Anal. Chem.* 75, 7040 (**2003**).
69. A. Freedman and C. D. Stinespring, *Appl. Phys. Lett.* 57, 1194 (**1990**).
70. A. Hartl, E. Schmich, J. Garrido, J. Hernando, S. Catharino, S. Walter, P. Feulner, A. Kromka, D. Steinmuller, and M. Stutzmann, *Nature Mater.* 3, 736 (**2004**).
71. W. Yang, J. E. Butler, J. N. Russell, Jr., and R. J. Hamers, *Langmuir* 20, 6778 (**2004**).
72. W. Yang, O. Auciello, J. E. Butler, W. Cai, J. A. Carlisle, J. E. Gerbi, D. M. Gruen, T. Knickerbocker, T. L. Lasseter, J. John N. Russell, L. M. Smith, and R. J. Hamers, *Nature Mater.* 1, 253 (**2002**).
73. T. Knickerbocker, T. Strother, M. P. Schwartz, J. N. Russell, Jr., J. Butler, L. M. Smith, and R. J. Hamers, *Langmuir* 19, 1938 (**2003**).
74. J.-S. Gao, T. Arunagiri, J.-J. Chen, P. Goodwill, O. Chyan, J. Perez, and D. Golden, *Chem. Mater.* 12, 3495 (**2000**).
75. D. Roy, Z. H. Barber, and T. W. Clyne, *J. Appl. Phys.* 91, 6085 (**2002**).
76. J. Wang and G. M. Swain, *Electrochem. Solid-State Lett.* 5, E4 (**2002**).
77. F. Montilla, E. Morallon, I. Duo, C. Comninellis, and J. L. Vazquez, *Electrochim. Acta* 48, 3891 (**2003**).
78. K. J. McKenzie, D. Asogan, and F. Marken, *Electrochem. Commun.* 4, 820 (**2002**).
79. S. Ferro and A. DeBattisti, *J. Phys. Chem. B* 106, 2249 (**2002**).
80. A. DeBattisti, S. Ferro, and M. D. Colle, *J. Phys. Chem. B* 105, 1679 (**2001**).
81. N. Spataru, C. Terashima, K. Tokuhiro, I. Sutanto, D. A. Tryk, S.-M. Park, and A. Fujishima, *J. Electrochem. Soc.* 150, E337 (**2003**).
82. A. Salimi, M. E. Hyde, C. E. Banks, and R. G. Compton, *Analyst* 129, 9 (**2004**).
83. I. González-González, D. A. Tryk, and C. R. Cabrera, *Diamond Rel. Mater.* 15, 275 (**2006**).
84. A. M. Zaitsev, Handbook of Industrial Diamond and Diamond Films, edited by M. A. Prelas, G. Popovici, and L. K. Bigelow, Marcel Dekker, New York (**1998**), p. 227.
85. K. M. Rutledge and K. K. Gleason, Handbook of Industrial Diamond and Diamond Films, edited by M. A. Prelas, G. Popovici, and L. K. Bigelow, Marcel Dekker, New York (**1998**), p. 413.
86. D. S. Knight and W. B. White, *J. Mater. Res.* 4, 385 (**1989**).
87. T. Kondo, D. A. Tryk, and A. Fujishima, *Electrochim. Acta* 48, 2739 (**2003**).
88. E. Popa, Y. Kubota, D. A. Tryk, and A. Fujishima, *Anal. Chem.* 72, 1724 (**2000**).
89. E. Popa, H. Notsu, T. Miwa, D. A. Tryk, and A. Fujishima, *Electrochem. Solid State Lett.* 2, 49 (**1999**).
90. I. Yagi, K. Tsunozaki, D. A. Tryk, and A. Fujishima, *Electrochem. Solid-State Lett.* 9, 457 (**1999**).
91. K. Niwase, Y. Kakimoto, I. Tanaka, and T. Tanabe, *Nucl. Instrum. Meth. Phys. Res. B* 91, 78 (**1994**).
92. R. J. Hamers, J. E. Butler, T. Lasseter, B. M. Nichols, J. N. R. Jr., K.-Y. Tse, and W. Yang, *Diamond Rel. Mater.* 14, 661 (**2005**).
93. Y. Maeda, K. Sato, R. Ramaraj, T. N. Rao, D. A. Tryk, and A. Fujishima, *Electrochim. Acta* 44, 3441 (**1999**).
94. J. Z. Xu and G. M. Swain, *Anal. Chem.* 70, 1502 (**1998**).
95. N. S. Lawrence, M. Thompson, C. Prado, L. Jiang, T. G. J. Jones, and R. G. Compton, *Electroanalysis* 14, 499 (**2002**).
96. T. Sakai, Y. Araki, H. Kanazawa, H. Umezawa, M. Tachiki, and H. Kawarada, *Jpn. J. Appl. Phys.* 41, 2595 (**2002**).
97. K.-S. Song, T. Sakai, H. Kanazawa, Y. Araki, H. Umezawa, M. Tachiki, and H. Kawarada, *Biosens. Bioelectron.* 19, 137 (**2003**).
98. J. A. Garrido, A. Härtl, S. Kuch, M. Stutzmann, O. A. Williams, and R. B. Jackmann, *Appl. Phys. Lett.* 86, 073504 (**2005**).
99. N. Spataru, T. N. Rao, D. A. Tryk, and A. Fujishima, *J. Electrochem. Soc.* 148, E112 (**2001**).
100. S. G. Ri, K. Tashiro, S. Tanaka, T. Fujisawa, H. Kimura, T. Kurosu, and M. Iida, *Jpn. J. Appl. Phys.* 38, 3492 (**1999**).
101. S. G. Ri, T. Mizumasa, Y. Akiba, Y. Hirose, T. Kurosu, and M. Iida, *Jpn. J. Appl. Phys.* 34, 5550 (**1995**).
102. I. González-González, J. De Jesús, D. A. Tryk, G. Morell, and C. R. Cabrera, *Diamond Rel. Mater.* 15, 221 (**2006**).
103. C. Terashima, T. N. Rao, B. V. Sarada, N. Spataru, and A. Fujishima, *J. Electroanal. Chem.* 544, 65 (**2003**).
104. A. Manivannan, D. A. Tryk, and A. Fujishima, *Electrochem. Solid State Lett.* 2, 455 (**1999**).
105. A. J. Saterlay, C. Agra-Gutierrez, M. P. Taylor, F. Marken, and R. G. Compton, *Electroanalysis* 11, 1083 (**1999**).
106. J. Kruusma, C. E. Banks, and R. G. Compton, *Anal. Bioanal. Chem.* 379, 700 (**2004**).
107. C. Prado, S. J. Wilkins, F. Marken, and R. G. Compton, *Electroanalysis* 14, 262 (**2002**).
108. A. Manivannan, R. Kawasaki, D. A. Tryk, and A. Fujishima, *Electrochim. Acta* 49, 3313 (**2004**).
109. D. Dragoe, N. Spataru, R. Kawasaki, A. Manivannan, T. Spataru, D. A. Tryk, and A. Fujishima, *Electrochim. Acta* 51, 2437 (**2006**).
110. J. S. Foord, K. Eaton, W. Hao, and A. Crossley, *Phys. Chem. Chem. Phys.* 7, 2787 (**2005**).
111. A. Manivannan, M. S. Seehra, D. A. Tryk, and A. Fujishima, *Anal. Lett.* 35, 355 (**2002**).

112. A. Manivannan, D. A. Tryk, and A. Fujishima, *Chem. Lett.* 851 (**1999**).
113. A. Chatterjee, R. Wiltshire, K. B. Holt, R. G. Compton, J. S. Foord, and F. Marken, *Diamond Rel. Mater.* 11, 646 (**2002**).
114. A. J. Saterlay, S. J. Wilkins, C. H. Goeting, J. S. Foord, R. G. Compton, and F. Marken, *J. Solid State Electrochem.* 4, 383 (**2000**).
115. Y.-C. Tsai, B. A. Coles, K. Holt, J. S. Foord, and F. Marken, *Electroanalysis* 13, 831 (**2001**).
116. T. N. Rao, T. A. Ivandini, C. Terashima, B. V. Sarada, and A. Fujishima, *New Diamond Frontier Carbon Technol.* 13, 79 (**2003**).
117. H. Notsu, I. Yagi, and A. Fujishima, *Electrochemistry* 67, 389 (**1999**).
118. A. Fujishima and T. N. Rao, *Diamond Rel. Mater.* 10, 1799 (**2001**).
119. R. G. Compton, J. S. Foord, and F. Marken, *Electroanalysis* 15, 1349 (**2003**).
120. J. Xu, M. C. Granger, Q. Chen, J. W. Strojek, T. E. Lister, and G. M. Swain, *Anal. Chem.* 69, 591A (**1997**).
121. A. Fujishima, T. N. Rao, and D. A. Tryk, *Electrochim. Acta* 45, 4683 (**2000**).
122. G. M. Swain, A. B. Anderson, and J. C. Angus, *MRS Bull.* 56 (**1998**).
123. S. Alehashem, F. Chambers, J. W. Strojek, and G. M. Swain, *Anal. Chem.* 67, 2812 (**1995**).
124. H. Olivia, B. Sarada, D. Shin, T. Rao, and A. Fujishima, *Analyst* 127, 1572 (**2002**).
125. S. Jolley, M. Koppang, T. Jackson, and G. M. Swain, *Anal. Chem.* 69, 4099 (**1997**).
126. M. A. Witek and G. M. Swain, *Anal. Chim. Acta* 440, 119 (**2001**).
127. M. C. Granger, J. S. Xu, J. W. Strojek, and G. M. Swain, *Anal. Chim. Acta* 397, 145 (**1999**).
128. A. Fujishima, T. N. Rao, E. Popa, B. V. Sarada, I. Yagi, and D. A. Tryk, *J. Electroanal. Chem.* 473, 179 (**1999**).
129. B. V. Sarada, T. N. Rao, D. A. Tryk, and A. Fujishima, *New Diamond Frontier Carbon Technol.* 9, 365 (**1999**).
130. T. N. Rao, I. Yagi, T. Miwa, D. A. Tryk, and A. Fujishima, *Anal. Chem.* 71, 2506 (**1999**).
131. B. V. Sarada, T. N. Rao, D. A. Tryk, and A. Fujishima, *Chem. Lett.* 1213 (**1999**).
132. B. V. Sarada, T. N. Rao, D. A. Tryk, and A. Fujishima, *Anal. Chem.* 72, 1632 (**2000**).
133. T. A. Ivandini, B. V. Sarada, C. Terashima, T. N. Rao, D. A. Tryk, H. Ishiguro, Y. Kubota, and A. Fujishima, *J. Electroanal. Chem.* 521, 117 (**2002**).
134. T. N. Rao, B. H. Loo, B. V. Sarada, C. Terashima, and A. Fujishima, *Anal. Chem.* 74, 1578 (**2002**).
135. N. Spataru, B. V. Sarada, D. A. Tryk, and A. Fujishima, *Electroanalysis* 14, 721 (**2002**).
136. S. Haymond, G. T. Babcock, and G. M. Swain, *J. Am. Chem. Soc.* 124, 10634 (**2002**).
137. C. Prado, G. Flechsig, P. Grundler, J. Foord, F. Markenc, and R. Compton, *Analyst* 127, 329 (**2002**).
138. T. Ivandini, B. Sarada, T. Rao, and A. Fujishima, *Analyst* 128, 924 (**2003**).
139. J. Cvacka, G. M. Swain, J. Barek, and J. Zima, *Chemicke Listy* 96, 33 (**2002**).
140. T. A. Ivandini, B. V. Sarada, C. Terashima, T. N. Rao, D. A. Tryk, H. Ishiguro, Y. Kubota, and A. Fujishima, *J. Chromatogr. B* 791, 63 (**2003**).
141. O. Chailapakul, E. Popa, H. Tai, B. V. Sarada, D. A. Tryk, and A. Fujishima, *Electrochem. Commun.* 2, 422 (**2000**).
142. N. Spataru, B. V. Sarada, E. Popa, D. A. Tryk, and A. Fujishima, *Anal. Chem.* 73, 514 (**2001**).
143. O. Nekrassova, G. D. Allen, N. S. Lawrence, L. Jiang, T. J. Jones, and R. G. Compton, *Electroanalysis* 14, 1464 (**2002**).
144. O. Chailapakul, P. Aksharanandana, T. Frelink, Y. Einaga, and A. Fujishima, *Sens. Actuators B: Chem.* 80, 193 (**2001**).
145. O. Chailapakul, W. Siangproh, B. V. Sarada, C. Terashima, T. N. Rao, D. A. Tryk, and A. Fujishima, *Analyst* 127, 1164 (**2002**).
146. C. Terashima, T. N. Rao, B. V. Sarada, Y. Kubota, and A. Fujishima, *Anal. Chem.* 75, 1564 (**2003**).
147. C. Terashima, T. N. Rao, B. V. Sarada, and A. Fujishima, *Chem. Lett.* 32, 136 (**2003**).
148. O. Nekrassova, N. S. Lawrence, and R. G. Compton, *Electroanalysis* 15, 1655 (**2003**).
149. N. Wangfuengkanagul and O. Chailapakul, *Talanta* 58, 1213 (**2002**).
150. W. Siangproh, N. Wangfuengkanagul, and O. Chailapakul, *Anal. Chim. Acta* 499, 183 (**2003**).
151. W. Siangproh, P. Ngamukot, and O. Chailapakul, *Sens. Actuators B: Chem.* 91, 60 (**2003**).
152. J. Xu, Q. Chen, and G. M. Swain, *Anal. Chem.* 70, 3146 (**1998**).
153. A. J. Saterlay and J. S. Foord, *Electroanalysis* 13, 1065 (**2001**).
154. C. Prado, G. G. Murcott, F. Marken, J. S. Foord, and R. G. Compton, *Electroanalysis* 14, 975 (**2002**).
155. N. Wangfuengkanagul and O. Chailapakul, *J. Pharm. Biomed. Anal.* 28, 841 (**2002**).
156. R. Uchikado, T. N. Rao, D. A. Tryk, and A. Fujishima, *Chem. Lett.* 144 (**2001**).
157. M. Komatsu and A. Fujishima, *Bull. Chem. Soc. Japan* 76, 927 (**2003**).
158. H. Notsu, T. Tatsuma, and A. Fujishima, *J. Electroanal. Chem.* 523, 86 (**2002**).
159. J. Cvacka, V. Quaiserova, J. Park, Y. Show, A. Muck, and G. Swain, *Anal. Chem.* 75, 2678 (**2003**).
160. J. Wang, G. Chen, M. P. Chatrathi, A. Fujishima, D. A. Tryk, and D. Shin, *Anal. Chem.* 75, 935 (**2003**).
161. T. N. Rao, B. V. Sarada, D. A. Tryk, and A. Fujishima, *J. Electroanal. Chem.* 491, 175 (**2000**).

SENSOR LETTERS
Vol. 4, 120–128, 2006

RESEARCH ARTICLE

A Transcutaneous Hydrogen Sensor: From Design to Application

Oomman K. Varghese[1,*], Xiping Yang[2], James Kendig[3], Maggie Paulose[2], Kefeng Zeng[2], Charles Palmer[3], Keat Ghee Ong[2], and Craig A. Grimes[1]

[1] *Department of Electrical Engineering, Department of Materials Science and Engineering, The Pennsylvania State University, 217 Materials Research Laboratory, University Park, PA 16802, USA*
[2] *Sentechbiomed Corporation, 200 Innovation Boulevard, State College, PA 16803, USA*
[3] *Penn State Milton S. Hershey Medical Center, Division of Newborn Medicine, 500 University Drive, Hershey, PA 17033, USA*

(Received: 4 April 2006. Accepted: 10 May 2006)

A transcutaneous hydrogen gas sensor of unprecedented sensitivity was fabricated and applied as a diagnostic tool for determining lactose intolerance due to lactase deficiency. The sensor, based on the use of highly-ordered titania nanotube arrays made by anodization of a 250 μm thick titanium foil, shows a change in electrical resistance of 8.7 orders of magnitude when cycled between air and nitrogen containing 1000 ppm of hydrogen. The sensor is completely reversible with a response time of about 30 seconds. Lactose intolerance tests were conducted at the Pediatric Gastroenterology Clinic of the Penn State Children's Hospital, where the transcutaneous hydrogen gas concentration from lactose intolerant patients was monitored and compared to hydrogen levels in exhaled breath. Results indicate a direct correlation between the transcutaneous and exhaled-breath hydrogen gas concentrations.

Keywords: Titania Nanotubes, Transcutaneous, Hydrogen, Lactose Intolerance, Sensor, Gas.

1. INTRODUCTION

Nano-structured metal oxides fabricated via anodization have been increasingly applied as gas sensors in recent years due to their remarkable gas-sensing properties which include large sensitivity, fast response time, controllable selectivity, and low hysteresis and drift. Varghese and coworkers,[1] for example, incorporated nanoporous alumina onto a surface acoustic wave device for the precise detection of ammonia gas. Lately considerable attention has been paid to the application of highly-ordered titania nanotube arrays[2–8] to measurement of hydrogen gas concentrations, achieved by monitoring the changes in electrical resistance of the nanotube-array sensors in response to hydrogen. Such hydrogen sensors have been incorporated into a sentinel wireless hydrogen sensor network for possible application in neonatal intensive care units.[9] In this work we focus on the optimization and application of the nanotube-array sensors for measurement of transcutaneous hydrogen levels.

Transcutaneous gas monitoring has been used as a means for diagnosing disease, as well as monitoring treatment effectiveness. For example, transcutaneous carbon dioxide is routinely monitored for bronchopulmonary dysplasia, apnea, upper airway obstruction, mechanical ventilation, and respiratory problems associated with hypercapnia.[10] Transcutaneous carbon dioxide is also routinely used in neonatal intensive care units[11,12] or in the preclinical detection of pneumothorax.[13] However, to our knowledge, there has been no effort on using transcutaneous hydrogen gas for diagnosing diseases. As far as we know, this is the first work to use measurement of transcutaneous hydrogen concentrations for detection of lactose intolerance,[14,15] and beyond that can be viewed as an enabling technology that might have a variety of useful clinical applications.

Lactose intolerance is caused by the inability to digest significant amounts of lactose, a major sugar in milk, due to the lack of enzyme lactase produced by the cells in the small intestine.[16] The function of lactase is to break down milk sugar into glucose and galactose, which are then absorbed into the bloodstream. Failure to digest

*Corresponding author; E-mail: dkv3@psu.edu

 1546-198X/2006/4/120/009 doi:10.1166/sl.2006.022

lactose into glucose and galactose causes the person to feel uncomfortable after consuming milk products, exhibiting symptoms such as nausea, cramps, bloating, gas, and diarrhea. Symptoms begin about 30 s to 2 hours after eating or drinking foods containing lactose. Currently, lactose intolerance is diagnosed with the Lactose Tolerance Test,[17, 18] where a patient's blood samples are taken over a 2-hour period to measure the blood glucose levels after lactose consumption to indicate how well the body is able to digest lactose. Alternatively, the Hydrogen Breath Test[14] can be performed to measure the amount of hydrogen present in the patient's breath since undigested lactose in the colon is fermented by bacteria and produces various gases including hydrogen, that is absorbed from the intestines, carried through the bloodstream to the lungs where it is exhaled. As indicated by the enabling work of Gerlach,[19] we hypothesize that a portion of hydrogen in the bloodstream releases through the skin, thus allowing hydrogen detection with a noninvasive, transcutaneous hydrogen sensor.

Our hydrogen sensor is based on the use of highly-ordered titania nanotube arrays, made by anodization of a Ti foil.[6, 20, 21] Micron-length un-doped titania nanotube-arrays exhibit an unprecedented variation in electrical resistance of up to ≈8.7 orders of magnitude, at room temperature, when exposed to alternating atmospheres of nitrogen containing 1000 ppm hydrogen and air.[8] The highly sensitive room, or skin, temperature operation of the sensor is critical for transcutaneous operation without risk of damaging the adjacent skin. The 8.7 orders of magnitude change in response to 1000 ppm hydrogen of the sensor represents the largest known change in electrical properties of any material, to any gas, at any temperature. The dramatic change in resistance is believed to be due to the highly active surface states on the nanoscale walls of the tubes, high surface area of the nanotube architecture, and the well-ordered geometry allowing for hydrogen-sensitive tube-to-tube electrical connections.[6, 8, 22]

The sensor response is characterized by measuring the change in its resistance through electrical contacts. Using a mask, platinum circular electrode pads (500 μm diameter, 100 nm thick, 1 mm edge-to-edge spacing) are sputter-coated onto the nanotube-array samples. Gold wire (1 mil), used for making electrical connections between the material and the measurement electronics, is bonded onto the platinum pads with a Mech-El-907 ultrasonic wire bonder. We have developed a robust electronic interface suitable for handing sensor resistances from 50 GΩ to the metallic range.

Since metal oxides, or indeed most materials, to some extent respond to a variety of environmental parameters, i.e., demonstrate unwanted cross-sensitivities, it is necessary to use other sensors, and cross-correlate the responses of these different sensors to obtain an absolute measurement of the target gas from within a complex environment. Therefore, we incorporated a humidity-temperature sensor along with the hydrogen sensor. The packaged sensor array is displayed in Figure 1. The hydrogen sensor and humidity-temperature sensor are secured in a white teflon housing, which screws onto the adhesive-backed ring that is applied to the skin of the patient undergoing the test.

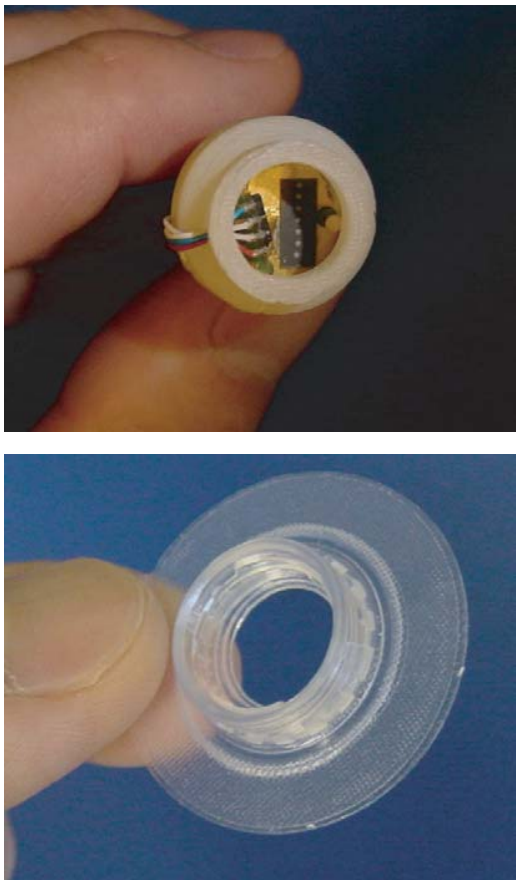

Fig. 1. (a) Packaging of our sensors comprised of a hydrogen sensor and a humidity-temperature sensor. The connector twists onto the adhesive-backed ring. (b) Vent holes (not visible) on the side prevent the accumulation of water vapor and gases in the housing.

2. SYSTEM IMPLEMENTATION

2.1. Fabrication of Titania Nanotube Array by Anodization

Figure 2 illustrates the anodization process; the target metal, in this case titanium, is used as the anode in an electrochemical cell with a platinum cathode. Upon application of a voltage potential across the terminals there is field-enhanced oxidation of the metal. While there is both field-enhanced oxidation of the metal, and field-enhanced dissolution of the oxide, the electric field at the bottom of the pore at the metal-oxide interface is much higher than that at the wall, hence the metal will be consumed at a higher rate near the bottom of the pore allowing continuous growth of the pore depth.

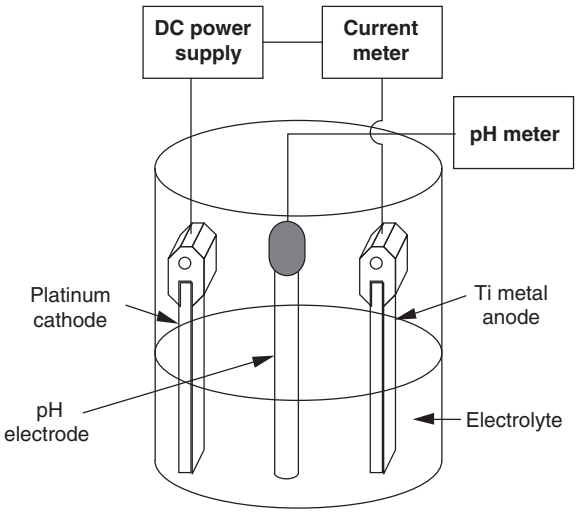

Fig. 2. Anodization setup comprising a glass beaker, some chemicals, and a dc power supply.

Titania nanotube arrays fabricated by anodic oxidation of titanium thick-film foils and thin films in hydrofluoric acid (pH 4.0) containing potassium fluoride, sodium hydrogen sulfate monohydrate, and sodium citrate tribasic dehydrate arrays were reported[20, 21] having lengths up to 400 nm and pore diameters from 22 nm to 90 nm depending on the anodization voltage. The structure consists of adjacent, parallel-oriented nanotubes separated from the un-anodized titanium foil by a thin oxide layer (barrier layer), the initial thickness of which is approximately equal to the nanotube pore radius. Nanotube-arrays of length 200 nm and pore diameter 22 nm coated with a thin palladium layer showed a resistance variation of about five orders in magnitude on exposure to 1000 ppm hydrogen at 290 °C.[22] However device performance was limited by the very low thickness of the array structure, which provided a low resistance path for the current to flow between the platinum-film electrodes on the nanotube surface and the underlying titanium metal layer. Furthermore, it is difficult to make electrical connections to this material, accomplished by wire bonding, since the wire bonder head would commonly break through the barrier layer to the underlying metal resulting in an electrical short.

We have improved the anodization process to fabricate nanotube-array architectures with lengths up to 6.5 μm using a KF or NaF electrolyte, pore diameters from 22 nm to 110 nm, and wall thicknesses from 9 nm to 34 nm. Our ability to control nanotube-array dimensions has enabled our ability to meaningfully test the gas sensing properties of the nanotube arrays. More importantly, these highly stable nano-structures withstand the mechanical handling necessary to transform them from materials to sensors. Figure 3 shows a FESEM image of a hydrogen responsive titania nanotube array sample made by anodization of titanium in a KF-containing electrolyte. The length of the nanotube array is dependent upon the pH, with higher

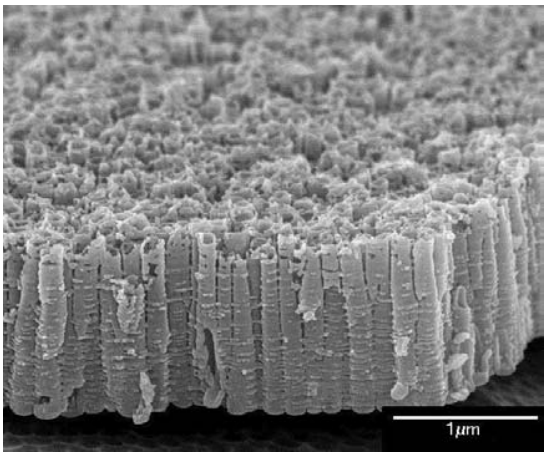

Fig. 3. FESEM images of illustrative TiO_2 nanotube-array grown in a KF based electrolyte of pH 3 using 25 V.

pH values that remain acidic resulting in longer nanotubes. The wall thickness is dependent upon the anodization bath temperature, and the pore diameter is a function of the anodization voltage. At a particular pH value, the pore size and length of the tube increase with the increase in voltage. For example, a 10 V anodization in pH 1.1 results in a nanotube array of 350 nm length and 30 nm pore diameter. A 25 V anodization in pH 5.0 results in a nanotube array of 6.5 μm length, with a 110 nm pore diameter. The longest nanotube array we have achieved to date is 25 μm.

Nanotube-arrays were prepared by anodization of 250 μm-thick titanium foil (99.7% Aldrich, Milwaukee, WI) samples in an electrolyte containing 1 M sodium hydrogen sulfate monohydrate, 0.1 M potassium flouride (ACS reagent 99% Alfa Aesar, Ward Hill, MA) and 0.2 M sodium citrate tribasic dihydrate (ACS reagent 99% Aldrich). Electrolyte pH was adjusted by the addition of sodium hydroxide (97% Aldrich). Nanotube lengths varied from 380 nm to 6.5 μm and pore diameters from 30 nm to 110 nm as dependent on the electrolyte pH (1.11 to 5) and the anodization potential (10–25 V). The samples, upon anodization, are amorphous demonstrating essentially no gas sensing properties. The samples were annealed at 480 °C for 6 hours for crystallization[21] to achieve suitable gas sensing properties.

2.2. Sensor Fabrication

To transform the nanotube-arrays into gas sensors it is necessary to achieve electrical contact with the material, so that the resistance or impedance of the material can be measured as a function of gas ambient. This is accomplished by depositing, through a mask, metal contacts onto the material of interest: Platinum circular electrodes (500 μm diameter, 100 nm thick, 1 mm edge-to-edge spacing) onto the top of the nanotube-array samples. Increasing the electrode separation increases the baseline resistance but does not affect sensitivity. Upon depositing

the electrodes, gold wires (1 mil) were bonded onto the pads with a Mech-El -907 ultrasonic wire bonder. We noticed that with short nanotubes, i.e., approximately 200 nm long, the nanotubes easily broke during the wire bonding stage. However, this problem was averted by making longer nanotube arrays using a KF or NaF electrolyte. These longer nanotube arrays demonstrated greater gas sensitivities, and were also mechanically more robust hence they could be easily connected to the outside world.

A further complicating factor is that the baseline resistance of metal oxide materials can be well over 100 GΩ, an impedance so large that it is virtually impossible to make interface electronics. We found that a post-anodization acid rinse could be used to controllably reduce the thickness of the oxide barrier layer between the nanotubular region and the underlying metal substrate, thus lowering the baseline resistance of the sensor.

2.3. Fabrication of the Sensor Reader

We have developed a robust electronic interface suitable for handling sensor resistances from 50 GΩ to the metallic range. Figure 4 shows a block diagram of the sensor interface electronics. For sensor measurement, a constant current I is applied to the sensor and the resulting dc voltage V is measured. The sensor resistance R is then calculated by $R = V/I$. In order to track the sensor resistance over a wide range (from 0 to 50 GΩ), the microcontroller is programmed to precisely and automatically tune the dc current value as well as the amplifier gain for optimal measurement accuracy. The measured data, including resistance of the hydrogen sensor, humidity, and temperature (the output of these two sensors is a microprocessor compatible voltage) are sent to a PC for storage and processing. Figure 5 shows the transcutaneous hydrogen measurement system.

Figure 6 shows the schematic diagram of the circuit that measures the resistance of the hydrogen sensor. A voltage generation circuit, which uses an ADR380 voltage reference chip (from Analog Devices), is designed to generate two accurate voltages: 2.048 V and 0.2048 V. The two voltages are selectable by an analog switch MAX4526

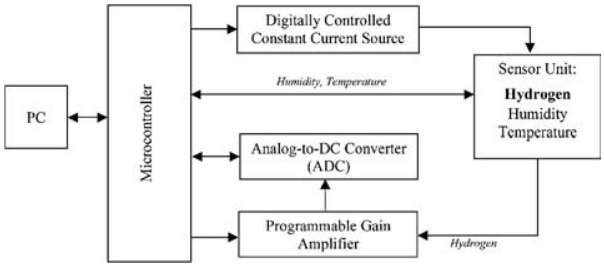

Fig. 4. Block diagram of the sensor interface electronics. The system generates a constant current to the hydrogen sensor, and measures the resulting voltage to determine the resistance. The response of a humidity-temperature sensor is also measured.

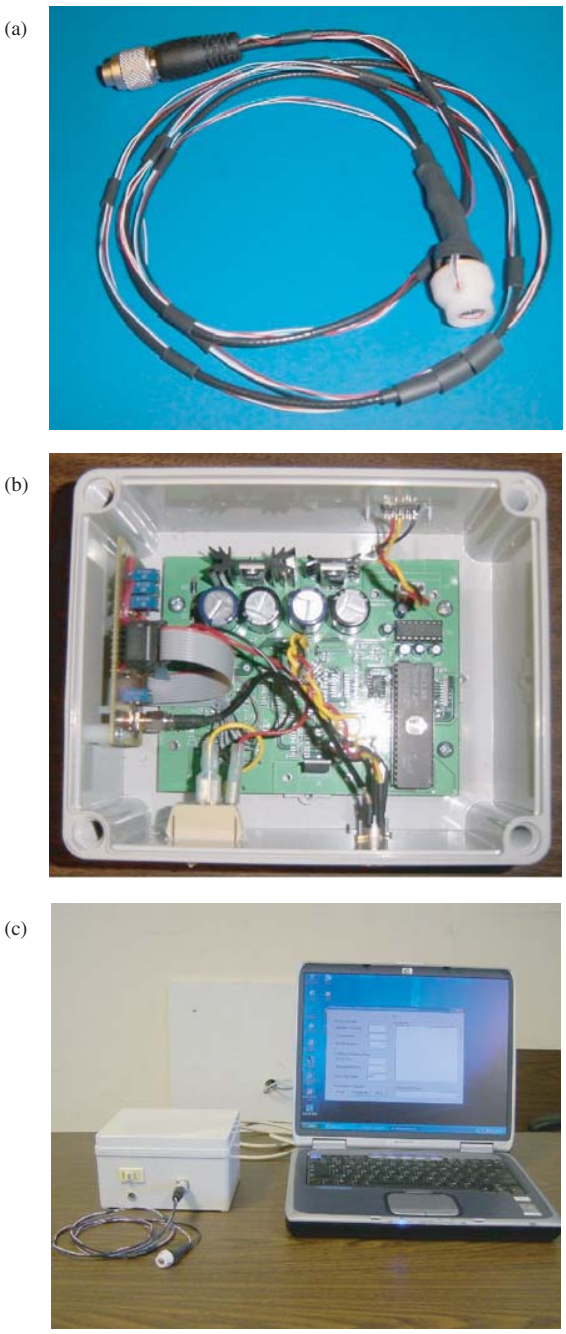

Fig. 5. (a) Packaged sensor with cable connecting sensor to electronics. (b) Internal view of sensor electronics. (c) The sensor, electronics box, and computer interface for data display.

(from Maxim/Dallas Semiconductor). The selected reference voltage is fed to a constant current generation circuit, which uses an analog switch MAX4666 (from Maxim/Dallas Semiconductor) to select the desired constant current value. With the combination of the two analog switches, the circuit can generate four digitally controlled current values: 2.048×10^{-6} A, 2.048×10^{-7} A, 2.048×10^{-9} A, and 2.048×10^{-10} A. The constant current source of a selected value is applied to the sensor under

RESEARCH ARTICLE

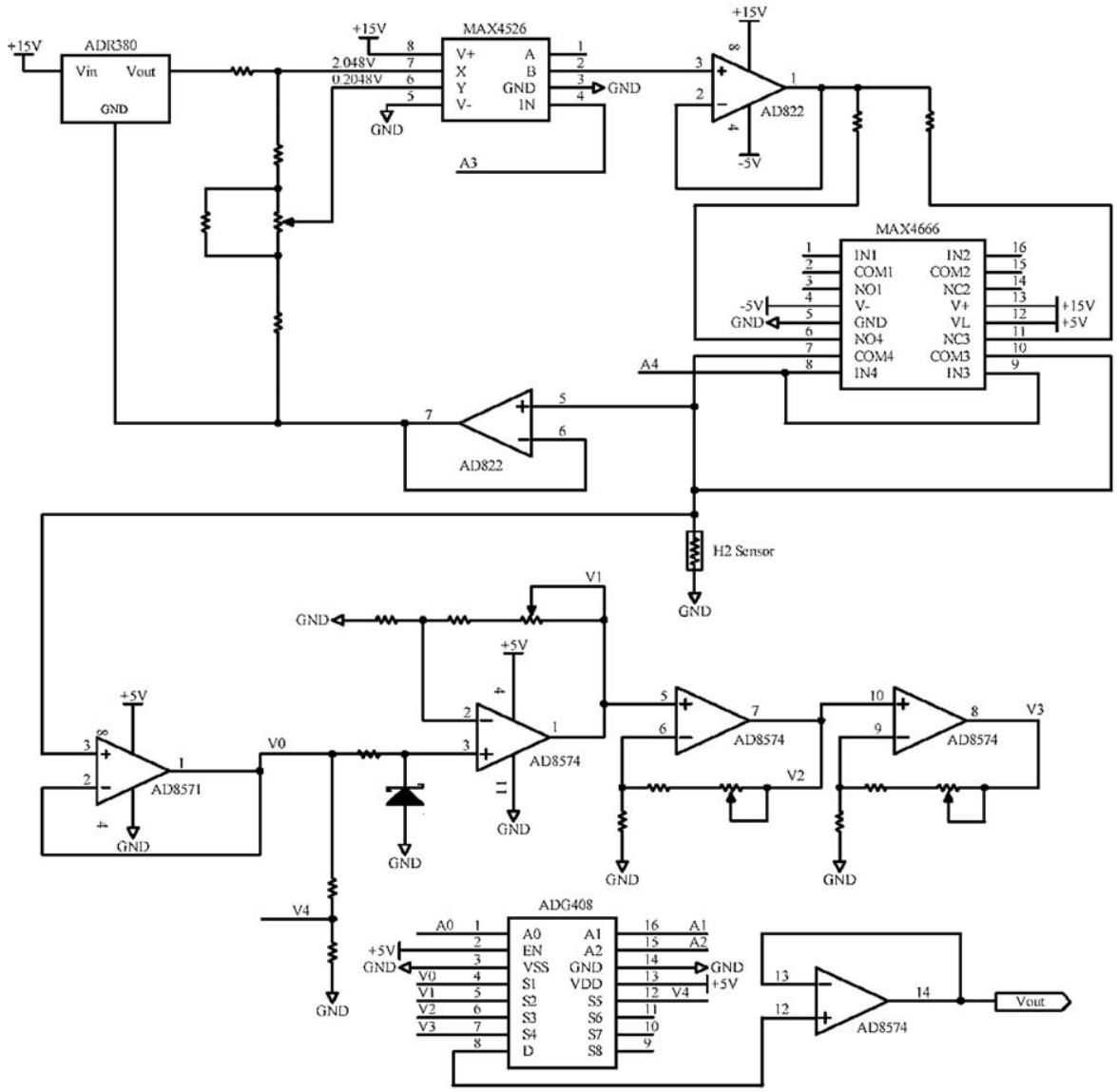

Fig. 6. Schematic diagram of the circuit for measuring the resistance of the hydrogen sensor.

measurement, and the sensor voltage is amplified by an amplifier bank consisting of five op-amps, with five voltage gains of 0.5, 1, 10, 100, and 1000 selectable by an analog multiplexer ADG408. The amplified voltage is sent to an ADC converter AD7817, which is part of the back-end microcontroller control circuit (not shown in the figure). A Dallas Microcircuits multiplexer chip is used to sequence between the difference sensors, with a Visual Basic interface allowing the user to input desired parameters.

The hydrogen sensor is packaged with a humidity/temperature sensor into a single sensor housing so that hydrogen, relative humidity, and temperature can be simultaneously monitored. The humidity sensor, SHT15 from Sensorian Inc., uses a two-wire serial interface to directly send measurements to the microcontroller, which are then processed and sent to a PC for storage.

3. RESULTS AND DISCUSSION

3.1. Hydrogen Sensitivity

The behavior of the nanotube samples in the presence of different gases was tested in a sealed Plexiglas chamber of 110 cm^3 volume. Titania, an n-type semiconductor, decreases its resistance in the presence of reducing gases and hence gas sensitivity S is defined as:[23]

$$S = \frac{G_{gas} - G_{air}}{G_{air}} \approx \frac{G_{gas}}{G_{air}} \quad \text{when} \quad G_{air} \ll G_{gas} \qquad (1)$$

where G_{air} and G_{gas} are, respectively, the conductance of the nanotubes in air and the test gas.

The greatest hydrogen sensitivities are achieved with the 30 nm pore diameter samples fabricated at 10 V,

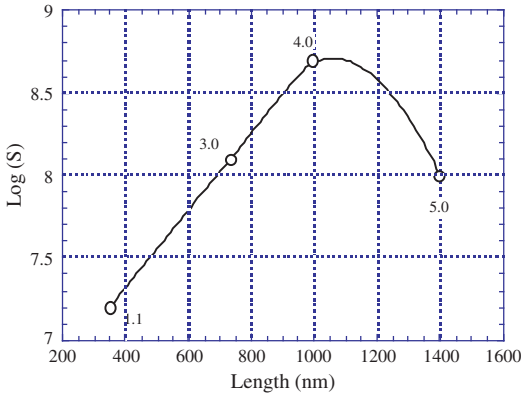

Fig. 7. The sensitivity of the hydrogen sensor depends on the length of the nanotubes. The pH of the electrolyte is listed for each sample.

Consequently the majority of our discussion is focused on these samples. Figure 7 plots the maximum room temperature hydrogen sensitivity, log(S), of the 30 nm pore diameter nanotube arrays in response to 1000 ppm hydrogen, as a function of length, which in turn is determined by electrolyte pH. We note that maximum hydrogen sensitivity was achieved with a 480 °C annealing that crystallizes the initially amorphous nanotube array samples. It can be seen from the figure that the highest resistance variation, 8.7 orders of magnitude was obtained for nanotube samples prepared using electrolyte pH 4.0 (length ∼1 μm, pore diameter ∼30 nm and wall thickness ∼13 nm). To the best of our knowledge, this is the largest change in electrical resistance of any material, to any gas, at any temperature. Sensitivity S is not greatly influenced by nanotube length; for the 10 V samples a sensitivity shift of 7 orders to 8.7 orders is found with an increase in length from 380 nm to 1 μm. It was found that 6 μm long samples (25 V, pH 5.0) showed less sensitivity, with significantly longer response/recovery times due to the time required for hydrogen to diffuse inside the long pores.

We make note that a test chamber capable of accurately flowing less than, approximately, 10 ppm of any gas is a difficult challenge requiring considerable resources. Consequently, we are not able to directly measure the low-level sensitivity of the sensor. The lower limit of our test chamber is approximately 20 ppm, at which we see 7.2 orders of magnitude variation in electrical resistance to 20 ppm hydrogen. The response of the sensor is linear to, approximately, 1000 ppm when it begins to demonstrate a non-linear response.

Figure 8 shows the variation in hydrogen sensitivity of the 10 V samples as a function of electrolyte pH. The response/recovery time (duration for the signal to change to 90% of its final value) of the sensor increases from 30 s to 200 s when the electrolyte pH increases from 1.13 to 4.5 due to the increase in tube length. There is no observable difference in the response time (air-to-hydrogen) and recovery time (hydrogen-to-air). The typical response of

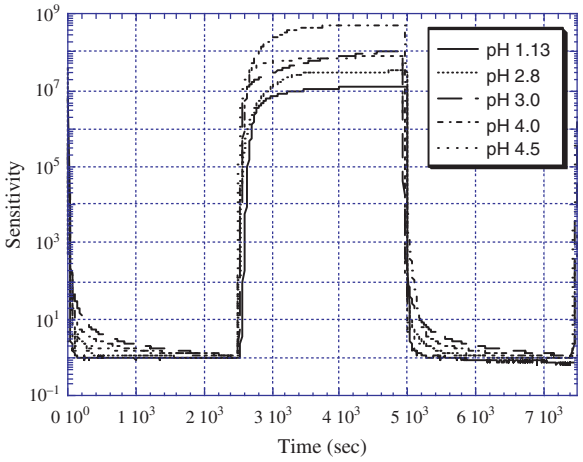

Fig. 8. Variation in hydrogen sensitivity S of 30 nm pore diameter nanotube-array samples as a function of electrolyte pH.

a pH 4.0 sample on repetitive switching of the ambient atmosphere between air and 1000 ppm hydrogen in nitrogen is shown in Figure 9. On exposure to hydrogen a rapid reduction in resistance from several hundred Giga-Ohms to a few hundred Ohms is observed; there is no indication of measurement hysteresis.

3.2. Cross Interference and Calibration

To determine which parameters affect the resistance of the hydrogen sensor, we placed the sensor inside the test chamber and varied the test environment (humidity, a variety of interfering gases, temperature) observing the change, if any, in the sensor resistance.

Temperature: As shown in Figure 10, temperature has a large impact on the resistance of the hydrogen sensor. Nevertheless, in practice the operating temperature of the

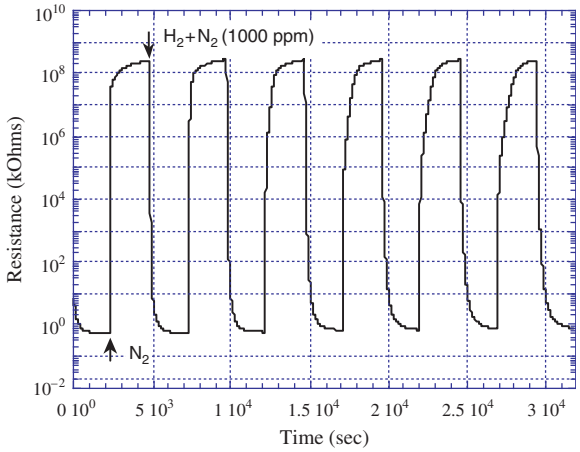

Fig. 9. Room temperature resistance variation of a nanotube-array sample prepared in a pH 4.0 electrolyte using 10 V (30 nm pore diameter), annealed at 480 °C, alternately exposed to air and 1000 ppm hydrogen in nitrogen.

RESEARCH ARTICLE

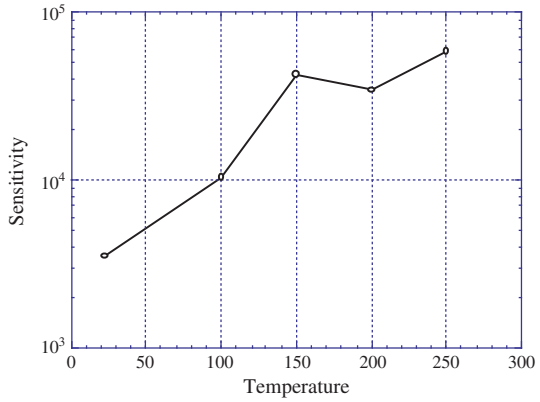

Fig. 10. The sensitivity of a 200 nm long nanotube-array hydrogen sensor increases with temperature.

transcutaneous sensor is near or at body temperature. As indicated in Figure 10, the change in the sensor sensitivity is only ≈0.08 order of magnitude (from 3800 to 4600) from 25° to 37 °C. As a result, although the temperature of the hydrogen sensor was also measured during the experiments, no calibration was performed.

Humidity: Figure 11 plots the change in sensor sensitivity (at 1000 ppm hydrogen) as a function of relative humidity. Between relative humidity of 3% and 56%, the sensitivity of the hydrogen sensor varies from 2.5×10^8 to 7×10^4, a change of more than 3 orders of magnitude. Therefore to ensure measurement integrity, we always measured the humidity level inside the sensor package, and used the humidity readings for calibration.

Oxygen: The addition of oxygen into the test environment reduces the sensitivity of the sensor as indicated in Figure 12. However, results show that the difference in the sensor sensitivity is only about 1 order of magnitude between zero (a pure nitrogen environment) and 20% of oxygen (atmospheric condition). As a result, variations in oxygen concentration do not represent a significant cross-sensitivity to the measurement since the hydrogen sensor

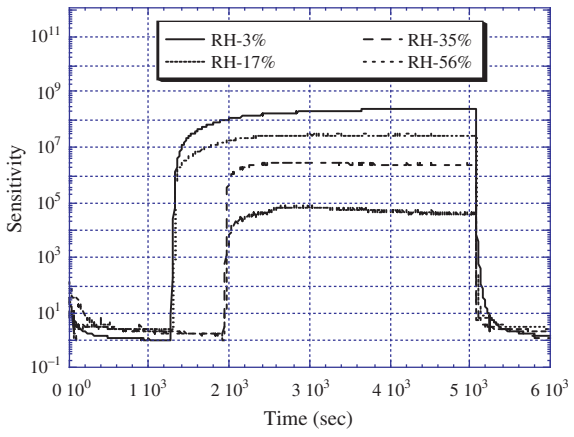

Fig. 11. The sensitivity of the hydrogen sensor reduces with increasing humidity.

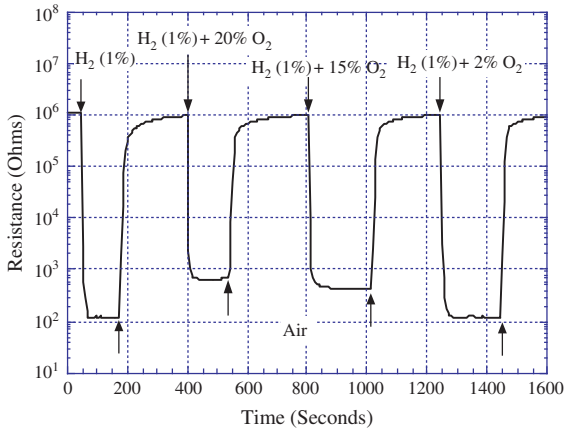

Fig. 12. The sensitivity of the hydrogen sensor reduces with increasing oxygen concentration.

was usually exposed to a near-atmospheric condition, with vent holes in the sensor housing allowing for the free flow-through of gases.

Carbon Dioxide: Figure 13 plots the resistance of the hydrogen sensor when it was switched from a pure nitrogen environment and nitrogen with 10% of CO_2. As clearly indicated in the plot, there is no difference between these two environments. This is expected because carbon dioxide is neither a strong reducing gas nor a strong oxidizing gas.

Carbon Monoxide: Figure 14 plots the change in the sensitivity when the sensor is exposed to 1000 ppm of carbon monoxide. Results show the sensitivity of the sensor to be approximately two orders or magnitude when exposed to 1000 ppm CO. Consequently, the material might usefully serve as a carbon monoxide sensor, however for this application CO cross-sensitivity is not a concern since it is highly unlikely for gas to be released by a patient.

Methane: Figure 14 plots the sensitivity of the sensor when it was exposed to 1000 ppm of methane. Results

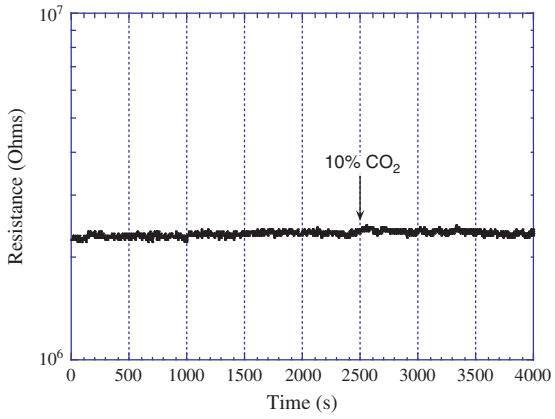

Fig. 13. Carbon dioxide has no effect on the sensor. The sensor was in a pure nitrogen atmosphere with 1000 ppm hydrogen. Ten percent of CO_2 was introduced at 2500 seconds.

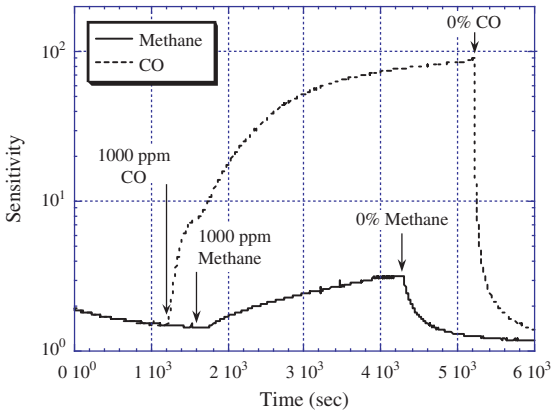

Fig. 14. The introduction of 1000 ppm carbon monoxide causes the sensor sensitivity to increase for about two orders of magnitude, while methane only changes the sensor sensitivity by half order of magnitude.

show that 1000 ppm of methane causes a change in electrical resistance of about a half order of magnitude, much smaller than the effect of hydrogen.

Upon evaluating the performance of the hydrogen sensor against various gases and operating conditions, we have concluded that for transcutaneous hydrogen measurement, the only significant potentially interfering parameter for our test application is humidity, hence we have generated a calibration lookup table to compensate for its effect. Before use, the resistance of the same sensor was measured as a function of humidity and hydrogen concentration, and the results were stored in a database. When taking a measurement, the operating software first obtained the humidity and hydrogen sensor measurements (resistance) from the microcontroller. It then determined the closest humidity and resistance values by going through the lookup table, and found the corresponding hydrogen concentration. The calibrated hydrogen concentration was printed on the screen of the PC in real time.

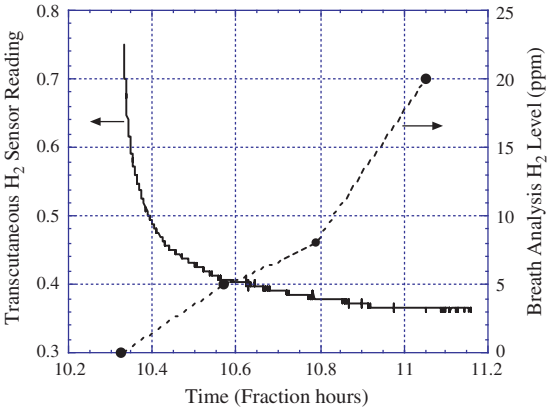

Fig. 15. Measurement of transcutaneous hydrogen concentrations using the described sensor (y-axis on LHS), and exhaled breath hydrogen levels (y-axis on RHS) measured by a gas chromatograph from a lactose intolerant adult volunteer.

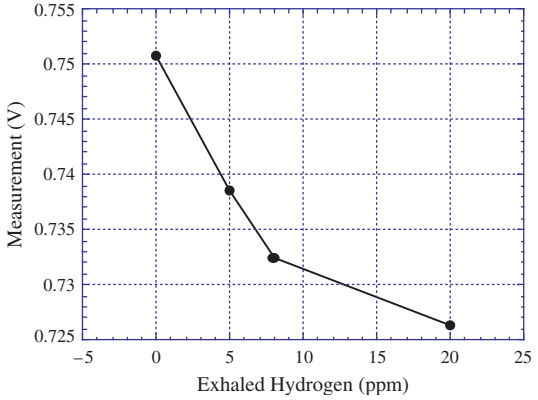

Fig. 16. Correlation between the response of the transcutaneous hydrogen sensor and exhaled hydrogen concentration.

3.3. Transcutaneous Hydrogen and Lactose Intolerance

Our transcutaneous hydrogen sensor was evaluated in the Pediatric Gastroenterology Clinic of the Penn State Children's Hospital with the full approval of the Institutional Research Subjects Review Board. The transcutaneous hydrogen sensor was placed on the forearm of children and adult volunteers who were referred for breath hydrogen testing for the evaluation and diagnosis of possible lactose intolerance due to lactase deficiency. In these patients the sensor has documented the transcutaneous excretion of hydrogen. Moreover in those patients with documented lactose intolerance, there is a good correlation between the transcutaneous sensor readings and the exhaled breath hydrogen levels as measured by the commercial gas chromatography Quintron instrument. We have studied 14 patients, some of whom had no detectable transcutaneous hydrogen excretion or detectable levels of exhaled breath hydrogen. Negative results in some patients have helped to reassure us that the novel hydrogen sensor is not responding to some volatile molecule that might be excreted through the skin. Figure 15 shows illustrative measurement of transcutaneous hydrogen levels using the described transcutaneous sensor, note the sensor measurement is continuous in operation, and the hydrogen levels (ppm) in exhaled breath as measured using a gas chromatograph, from a lactose intolerant adult volunteer who drank a small sample of milk. Figure 16 shows the decrease in the sensor measurement, which indicates an increase in transcutaneous hydrogen, coincides with an increase in exhaled breath hydrogen concentration.

4. CONCLUSIONS

We describe the fabrication, and systematic integration, of a hydrogen sensor based on the use of titania nanotube-arrays and its application to measurement of transcutaneous hydrogen levels. The titania nanotube array sensor shows an unprecedented sensitivity of 8.7 orders

RESEARCH ARTICLE

of magnitude when cycled between air and nitrogen containing 1000 ppm of hydrogen. Experimental results show the sensor is relatively insensitive to other gases such as oxygen, carbon dioxide, and methane. This sensor is significantly affected by changes in humidity, consequently we generated a calibration lookup table to ensure accurate hydrogen sensor operation over a range of humidity levels. By measuring the transcutaneous hydrogen concentration of a lactose intolerant patient, we have demonstrated a good correlation between the transcutaneous sensor reading and the exhaled breath hydrogen level using a commercially available gas chromatograph.

In addition to lactose intolerance, the transcutaneous hydrogen sensor can also be applied to other diseases such as necrotizing enterocolitis (NEC), a devastating disease of uncertain etiology and pathogenesis that causes high levels of mortality and morbidity in about 10% of preterm infants in neonatal intensive care units throughout the world.[24] Almost 20 years ago, several investigators[25, 26] demonstrated that elevated levels of exhaled breath hydrogen gas precede the onset of the clinical and radiographic signs of NEC. From a practical standpoint, it is very difficult to measure gas levels in exhaled breath of preterm infants because of their small tidal volumes and rapid respiratory rates. In neonatal intensive care units, the use of endotracheal tubes, nasal CPAP systems and nasal cannula flow systems are all barriers to the successful collection of undiluted end expiratory gas samples for gas analysis. Therefore, we expect transcutaneous measurement of hydrogen gas in preterm infants has the potential to facilitate the early identification and treatment of cases of NEC. This would permit the early withdrawal of enteral feeds and the early initiation of systemic antibiotics and supportive therapy with fluids, pressors, and blood products. In addition to saving lives, NEC mortality rate is about 35%, the early detection of NEC may also significantly reduce hospital costs, which according to an analysis published in 2002[27] is $95 million per year in the US.

Acknowledgments: O. K. Varghese and C. A. Grimes wish to thank the National Science Foundation, grant CTS-0518269 for support of their efforts associated with this project. X. Yang, M. Paulose, K. Zeng, and K. G. Ong wish to thank the National Institutes of Health, grant 1 R43 HD04233-01, for support of their efforts associated with this project. J. Kendig, C. Palmer, and C. A. Grimes wish to thank a Commonwealth of PA grant, affiliated with the Tobacco fund settlement, for additional financial assistance for this project.

References and Notes

1. O. K. Varghese, D. Gong, W. R. Dreschel, K. G. Ong, and C. A. Grimes, *Sens. Actuators B* 94, 27 **(2003)**.
2. O. K. Varghese and C. A. Grimes, *J. Nanosci. Nanotechnol.* 3, 277 **(2003)**.
3. O. K. Varghese, D. Gong, M. Paulose, K. G. Ong, and C. A. Grimes, *Sens. Actuators B*, 93, 338 **(2003)**.
4. G. K. Mor, O. K. Varghese, M. Paulose, and C. A. Grimes, *Sens. Lett.* 1, 42 **(2003)**.
5. O. K. Varghese, G. K. Mor, C. A. Grimes, M. Paulose, and N. Mukherjee, *J. Nanosci. Nanotechnol.* 4, 733 **(2004)**.
6. Q. Cai, M. Paulose, O. K. Varghese, and C. A. Grimes, *J. Mater. Res.* 20, 230 **(2005)**; G. K. Mor, K. Shankar, M. Paulose, O. K. Varghese, and C. A. Grimes, *Nano Lett.* 5, 191 **(2005)**.
7. G. K. Mor, O. K. Varghese, M. Paulose, K. G. Ong, and C. A. Grimes, *Thin Solid Films* 496, 42 **(2006)**.
8. M. Paulose, O. K. Varghese, G. K. Mor, C. A. Grimes, and K. G. Ong, *Nanotechnology* 17, 398 **(2006)**.
9. C. A. Grimes, K. G. Ong, O. K. Varghese, X. Yang, G. Mor, E. C. Dickey, C. Ruan, M. V. Pishko, J. W. Kendig, and A. J. Mason. *Sensors* 3, 69 **(2003)**.
10. J. Capovilla, C. VanCouwenberghe, and W. A. Miller, *Critical Care Nursing Quarterly* 23, 79 **(2000)**.
11. B. G. Carter, D. Wiwczaruk, M. Hochmann, A. Osborne, and R. Henning, *Anaesthesia and Intensive Care* 29 260 **(2001)**.
12. J. D. Tobias, W. R. Wilson, and D. J. Meyer, *Anesthesia and Analgesia* 88, 531 **(1999)**.
13. N. McIntosh, J. C. Becher, S. Cunningham, B. Stenson, I. A. Laing, A. J. Lon, and P. Badger, *Pediatric Research* 48, 408 **(2000)**.
14. D. E. Hammerschmidt, *Journal of Laboratory and Clinical Medicine* 144, 279 **(2004)**.
15. M. Pimentel, Y. Kong, and S. Park, *Am. J. Gastroenterology* 98, 2700 **(2003)**.
16. A. C. Adam, M. Rubio-Texeira, and J. Polaina, *Critical Reviews in Food Science and Nutrition* 44, 553 **(2004)**.
17. D. M. Goldberg, *Clinical Biochemistry* 20, 63 **(1987)**.
18. L. T. Cavalli-Sforza, P. Menozzi, and A. Strata, *Int. J. Bio-Medical Computing* 14, 31 **(1983)**.
19. P. Gerlach, *Arch. Anat. Physiol.* 431 **(1851)**.
20. D. Gong, C. A. Grimes, O. K. Varghese, W. Hu, R. S. Singh, Z. Chen, and E. C. Dickey, *J. Mater. Res., Rapid Commun.* 16, 3331 **(2001)**.
21. O. K. Varghese, M. Paulouse, D. Gong, C. A. Grimes, and E. C. Dickey. *J. Mater. Res.* 18, 156 **(2003)**.
22. O. K. Varghese, M. Paulose, K. G. Ong, E. C. Dickey, and C. A. Grimes, *Adv. Mater.* 15, 624 **(2003)**.
23. O. K. Varghese, D. Gong, M. Paulose, C. A. Grimes, and E. C. Dickey, *J. Mater. Res.* 17, 1162 **(2002)**.
24. J. A. Bisquera, T. R. Cooper, and C. L. Berseth, *Pediatrics* 109, 423 **(2002)**.
25. R. R. Engel and N. L. Virnig, *Pediatric Research* 7, 292A **(1973)**.
26. G. Godoy, C. Truss, J. Philips, M. Young, K. Coffman, and G. Cassady, *Pediatric Research* 20, 348A **(1986)**.
27. W. I. H. Garstin and V. E. Boston, *Pediatric Research* 22, 208 **(1987)**.

SENSOR LETTERS
Vol. 4, 129–134, 2006

Sensorial System to Detect Chloroform in Water

Eduarda R. Carvalho[1], Nelson Consolin Filho[1], Alessandra Firmino[1,2], O. N. Oliveira, Jr.[2], Luiz Henrique C. Mattoso[1], and Ladislau Martin-Neto[1,*]

[1] *Embrapa Instrumentação Agropecuária, P.O. Box 741, 13560-970, São Carlos-SP, Brazil*
[2] *Universidade de São Paulo, PPG Interunidades em Ciências e Engenharia de Materiais, São Carlos-SP, Brazil*

(Received: 5 April 2006. Accepted: 19 April 2006)

RESEARCH ARTICLE

A sensor system adapted to detect chloroform, a potentially carcinogenic compound, in water was fabricated and tested. Interdigitated gold-coated microelectrodes were covered with various conducting polymers, single, or mixed, under several different conditions, and the resulting sensors characterized and tested on the analyte in question. Polymer films were laid down by a self-assembly technique and their impedance was analyzed over a range of frequencies from 1 Hz to 1 MHz. For practical reasons, the capacitance was also measured, at a fixed frequency of 1000 Hz, which allowed data-acquisition to be simplified. Some of the systems tested were able to detect chloroform in water and to distinguish different concentrations, the detection limit being of the order of 0.01 mg L^{-1}. These results demonstrate the sensitivity of conducting polymers and show that they can be used in the fabrication and assembly of a sensor system capable of detecting by-products of water disinfection, such as chloroform, that exhibit carcinogenic properties.

Keywords: Sensors, Conducting Polymers, Drinking Water, Carcinogenic By-Products, Chloroform.

1. INTRODUCTION

Chlorinated water contains a large number of by-products, formed during the chlorination of organic matter and just a fraction of these have been tested for carcinogenicity in animal experiments.[1] The main focus has been on compounds and classes of compounds produced in greater quantities during chlorination.[1]

The classes of by-products on which most research is done are trihalomethanes, halogenated acetic acids, and chlorinated furanones (CHFs).[1] However, the carcinogenicity of the majority of the by-products has not been tested, even in laboratory tests with animals. Among the trihalomethanes, chloroform has been investigated most intensively, owing to its well-known carcinogenic properties, established in the laboratory in various tests on animals. The International Agency for Research on Cancer (IARC) has described the evidence from animal experiments for the carcinogenicity of chloroform as "sufficient" and classified this by-product as potentially very carcinogenic to humans.[1–2] The long-term effects of its carcinogenicity are chiefly related to damage to the liver, kidneys, and heart. Chloroform provoked tumor formation is strongly associated with cytotoxicity and excessive proliferation of tissue regenerative cells, considered a determining factor in carcinogenicity.[1] Concentrations of chloroform of the order of 2 mg L^{-1} give positive results in bioassays for cancer development.[3]

The general population is exposed to chloroform by ingesting water and food, inhaling contaminated air, and possibly through dermal contact with chloroform-containing water. Drinking water levels as high as 311 mg L^{-1} have been reported in public water supplies.[4] Measurements of chloroform in drinking water ranged from 0.022 to 0.068 mg L^{-1} also has been found.[5]

Thus, in light of the impact of such products on the environment and public health, it is important to research methods of detecting them in water–treatment plants. The growing demand for measures to protect the environment and the elaboration of new directives in this respect have had a very great impact on the development of novel materials, instruments, and sensing devices for the detection and measurement of by-products of disinfection.

The detection of individual substances by means of specific sensors is one of the most active fields in current research and development, owing to its great relevance to a variety of technological applications. The main features required in any sensor are high sensitivity, stability, and selectivity. The control and testing of the quality of air, soil,

*Corresponding author; E-mail: martin@cnpdia.embrapa.br

or water calls for sensors that detect particular molecules in small amounts in a complex mixture; thus, the detection needs to be specific and selective, as well as sensitive. However, currently available commercial sensors made from inorganic semiconductors like tin oxide, while inexpensive, possess very little selectivity. For this reason, new kinds of sensor are being explored[6] and, among these, conducting polymers are attracting a lot of interest.[7] Extensive work has been done in nose and tongue sensors[8–10] aimed at controlling pollutants in the environment and at monitoring the quality of foodstuffs. Most of the devices are based on electrical changes induced by bulk absorption or surface adsorption of molecules in conducting polimeric films.[11]

Conducting polymers stand out as excellent candidate materials for use in chemical and electrochemical sensors, both as sensitive components and as electrodeposited films. Owing to their intrinsic conducting properties, they can be made to sense given chemical species by employing diverse electrochemical techniques. Moreover, one-step electrosynthesis allows an adherent film of polymer to be made on the surface of electrodes (enabling microelectrodes to be built), with chosen anions included in the doping matrix.[12]

Chemical sensors are a viable solution to the problem of the high cost of devices used at present in the detection of by-products and water-quality monitoring. A chemical sensor can be defined as a device that, when exposed to a given type of substance (the analyte), transforms characteristic chemical information, such as polarity, stereochemical form, concentration and so on, to an analytical signal that can be measured, such as electrical resistance, current, potential difference, and frequency.[13]

Over the last few decades, many articles have been published referring to the use of electronic noses and, more recently, tongues.[14] In this context, therefore, a system of various sensory units, modified with natural and conducting polymers, has been tested for the detection and estimation of potentially carcinogenic compounds such as chloroform.

2. EXPERIMENTAL DETAILS

2.1. Conducting and Natural Polymers

The polymers used were: Polyaniline (PANI), poly(o-ethoxyaniline) (POEA), humic substances (HS), sulphonate lignine (SL), and mixtures of these. Polymers PANI and POEA were synthesized as described in Refs. [15–16] and polymer SL was obtained from Melbar S.A.

The POEA chemically synthesized using ammonium peroxydisulfate in solution of 1.0 mol L^{-1} HCl at 0 °C. The humic substances (HS) were isolated from a water sample collected in River João Pereira. This river is a tributary of the River Itapanhaú, located downstream-upstream. The River Itapanhaú is located in an environmentally protected area near the city of Bertioga, in the south coast of São Paulo state/Brazil.[17] The extraction and the fractioning were made according to the International Society of Humic Substances,[18] as well as recommendations made by Malcolm.[19] The HS solutions were prepared in the concentrations of 5, 10, and 30 mg L^{-1}. All the aqueous solutions of POEA, SL, and HS were prepared using ultra pure water from a Milli-Q system (MilliPore®). The pH adjustment of the solutions was made adding amounts of 0.1 M of HCl or 0.1 M of NH_4OH.

2.2. Chloroform Sample

A chloroform sample (PA) with the following characteristics obtained from Supelco was used: 1000 concentration mg (pure); purity degree (99.90%). From the pure solution, a stock solution of 10 mg L^{-1} was prepared. From the stock solution were prepared different solutions in the concentrations of 0.05 mg L^{-1} to 8.0 mg L^{-1}, for the analysis and pH (s) of the solutions were adjusted to 5.0 which coincides with the value presented for the stock solution.

2.3. Experimental Details

The specifications of deposition of polymers in each sensor and films for formation of the sensorial system are presented in Table I.

The conducting polymers based fine films (PANI and POEA) and natural polymers (HS and SL) were manufactured by the Self-Assembly (SA) technique, through monolayers (e.g., only POEA), bilayers (e.g., a layer of POEA over SL—POEA/SL) or complexed mixtures (e.g., solutions of same concentration together- PANI+HS) over solid substrate (interdigitated microelectrodes of gold deposited on glass).[20–23]

In SA technique, the number of deposited layers and the time of deposition of polymers, in the microelectrodes, were effected as follows:

(1) monolayer/3min (POEA and SL);
(2) monolayer/5min (PANI and HS);
(3) complexed mixture/3min (POEA+SL and POEA+HS) and
(4) bilayer/3min (POEA/SL, HS/POEA, PANI/SL).

Table I. Sensing units used in sensor system to analyze the chloroform.

Sensing Unit	Type of Material
S1	no film
S2	POEA
S3	POEA/SL
S4	POEA+SL
S5	SL
S6	HS/POEA
S7	POEA+HS
S8	PANI
S9	HS
S10	PANI/SL

The experiments were conducted at pH 5.0 using POEA, HS, and SL in the concentration of 1×10^{-3} mol L^{-1} and settling time 3 and 5 minutes in aqueous solution. As PANI is insoluble in aqueous medium, this was dissolved in NMP (N-Methyl-2-Pyrrolidone) in the concentration of 1×10^{-3} mol L^{-1}.

The limit of detection (DL) of the system was determined according to the following equation: DL = K.SB/S, where S = sensitivity of the method, SB = shunting line standard of the measures of the white, and K = constant numerical (value recommended for the IUPAC, $K = 3$).[24] The DL is defined as the lowest amount of analyte that can be detected with a trustworthiness level statistics.

The interdigitated gold microelectrodes (without film) were manufactured through the photolythographic method. The characteristics of these interdigitated microelectrodes are: gold microelectrodes containing 50 pairs of digits, each containing 10 μm wide, 10 μm of spacing between the microelectrodes and 0.1 μm thick of the deposited gold layer. Ten sensors were prepared per this technique, and an analysis system was mounted, according to Figure 1. Then the films containing polymers (POEA, PANI, HS, and SL) were deposited. The device used in the data acquisition was an impedance analyzer Solartron SI 1260 installed on a microcomputer. The amplitude of the input signal was 50 mV, with the scanning at intervals of 1 Hz to 1 MHz. The data treatment was made by analyses on the main components (PCA), along with software MATLAB

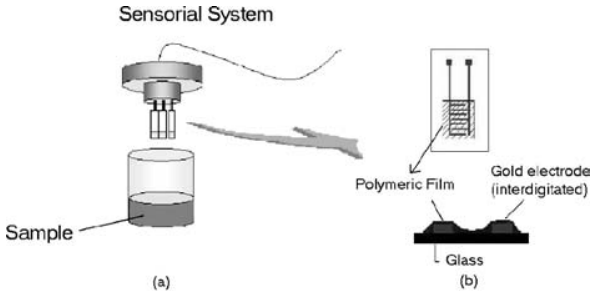

Fig. 1. Diagram illustrating the sensorial system.

version 5.2. The PCA analysis is a mathematical manipulation of the data matrix, in order to reduce its original dimensionality and it is founded on the correlation between the variables.[25]

3. RESULTS AND DISCUSSION

The frequency response for the various sensorial units in the different test conditions and solutions, are presented in the chart in Figure 2. For better visualization the extremes of the chloroform concentrations were chosen. In Figure 2(a) response obtained for solution in the presence of 0.1 mg L^{-1} of chloroform and in Figure 2(b) for 8.0 mg L^{-1}.

It was observed that the capacitance decreases with the increase of the frequency at an almost constant value

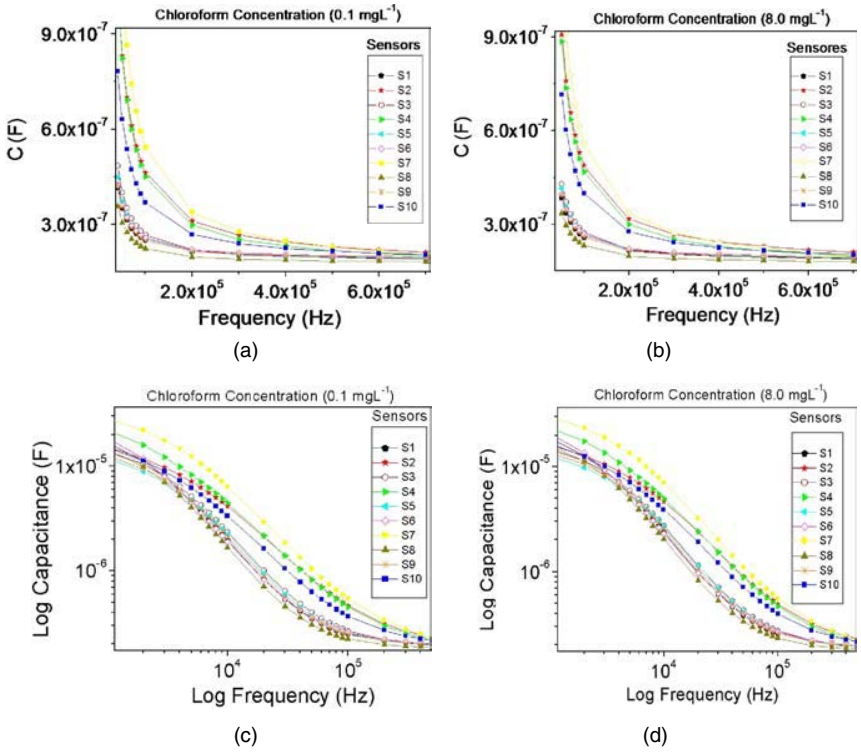

Fig. 2. Capacitance versus frequency: in (a) 0.1 mg L^{-1} of chloroform; (b) 8.0 mg L^{-1} of chloroform; (c) capacitance in function of frequency log for 0.1 mg L^{-1} of chloroform; (d) capacitance in function of frequency log of the frequency for 8.0 mg L^{-1} of chloroform.

RESEARCH ARTICLE

(ranging 10^{-7} F). Similar results were observed for all test solutions, i.e., a general decrease of the capacitance with the increase of the frequency, and an increase of the capacitance with the increase of the concentration of the solutions.

In Figures 2(c) and (d) the data relative to the dependence of the capacitance with the frequency log are presented, for the chloroform solutions in the concentrations of 0.1 mg L^{-1} and 8.0 mg L^{-1}, respectively. With the frequency log, a separation of the lines relative to the each sensor is observed. Each electrode has a specific electric response for the solutions and supplies a distinct signal for the different chloroform concentrations. Consequently, the evaluated disposition of the sensors can be used to detect substances with different properties.

The capacitance measurement can be obtained by selecting a specific frequency (e.g., 10^3 Hz), which simplifies the acquisition of data and, for practical purposes, it facilitates the application. Figure 3 shows to a chart of the capacitance obtained for each sensorial unit at 10^3 Hz, for which, the variations in the measurements better reflect the difference in charge and conductance storage of several films.

The relative sensitivity of the sensorial units is modified, when the chloroform concentration is increased in the solution. That is observed in Figure 3, where for a fixed frequency of 10^3 (Hz), an increase of the capacitance is observed, with the increase of the chloroform concentration in the 0.1 mg L^{-1} solution for 8.0 mg L^{-1}.

However, as conducting and natural polymers were deposited in the sensorial units, in different architectures and concentrations, the selectivity and the response of each sensor regarding the increase in the value of the capacitance, with the increase of the chloroform concentration, was better observed for specific sensorial units. As seen in Figure 3, sensorial units 4 and 7, which represent depositions: POEA complex with SL and, POEA complex with HS respectively, presented better response, that is, higher capacitance value, as to concentration increase and chloroform detection in the solution.

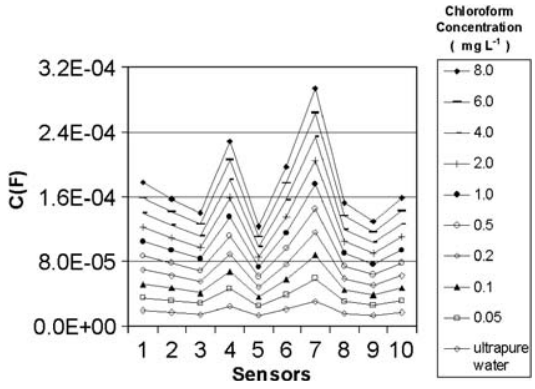

Fig. 3. Capacitance measurements at 10^3 Hz, obtained for chloroform solutions with different concentrations.

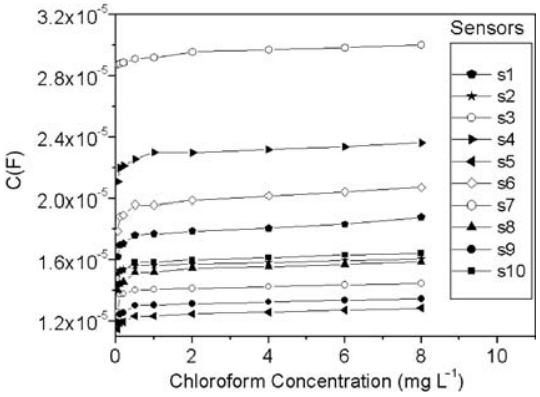

Fig. 4. Analytical curves plotted for the determination of the detection limit.

The analytical curves plotted to determine the detection limit are shown in Figure 4. From the analytical curves the Detection Limits (DL) were obtained for each microelectrode (interval from 0 to 2.0 mg L^{-1}), which are shown in Table II. The limit of detection (DL) was calculated by the equation: $DL = 3 \cdot SD/B$ where SD is the standard deviation average values of the reference sample (in absence of chloroform) and B is the slope of the straight line (analytical curve) obtained, respectively.

Figure 5 shows a bar chart, where we have a better visualization of the detection limits for each microelectrode. As shown in Figure 5, microelectrode 7 was the one that presented the best detection limit, (0.010 mg L^{-1}) followed by microelectrode 4 (0.012 mg L^{-1}). The worst detection limit was 0.190 mg L^{-1}, observed for microelectrode 8. This difference between the microelectrodes is related with the molecular structure of each film.

Microelectrode 7, is made up of a layer of a complexed mixture of POEA and HS. It has been shown that in the interaction between HS and POEA, the HS induces a dopage of the POEA by protonation. In the complex POEA+HS, the carboxylic groups and phenolic acid groups of the HS induce a primary dopage by protonation of imine groups of the POEA.[26]

The presence of HS in the complex with POEA, possibly contributes for a better interaction with chloroform, since the presence of aromatic groups in the HS, which are strongly reactive substrate in substitution and oxidation reactions, favoring this interaction. Substitution and oxidation reactions are typical in the aquatic chlorination, and contribute for the formation of organochlorinated compounds.[27]

In the case of microelectrode 4, the chemical groups contained in the POEA (–NH=) are linked with the SL by electrostatic attraction that involves the interaction between the ionized groups of the poliions and substratum, as well as by interaction by hydrogen linking, that can occur both for doped POEA, and for the non-doped POEA, between the groups $-NH =$ of the POEA and groups HSO_3^- of the SL.[26]

Table II. Results obtained from the analytical curves.

Linear Equation: Y = A + BX						
Sensors	A	Slope B	R	Standard deviation (SD)	Detection limit (DL) mg L^{-1}	Detection limit-Err (yEr±)
S1	1.68346×10^{-5}	6.03999×10^{-7}	0.94	4.86×10^{-9}	0.020	5.000×10^{-3}
S2	1.53323×10^{-5}	3.56633×10^{-7}	0.90	4.86×10^{-9}	0.040	1.000×10^{-2}
S3	1.37611×10^{-5}	3.43776×10^{-7}	0.90	4.86×10^{-9}	0.042	2.000×10^{-2}
S4	2.19418×10^{-5}	1.16592×10^{-6}	0.95	4.86×10^{-9}	0.012	5.000×10^{-4}
S5	1.19043×10^{-5}	4.94898×10^{-7}	0.90	4.86×10^{-9}	0.030	5.000×10^{-3}
S6	1.89754×10^{-5}	5.09950×10^{-7}	0.95	4.86×10^{-9}	0.028	1.000×10^{-2}
S7	2.87201×10^{-5}	1.39798×10^{-6}	0.99	4.86×10^{-9}	0.010	1.000×10^{-3}
S8	1.29905×10^{-5}	7.75714×10^{-8}	0.98	4.86×10^{-9}	0.190	1.350×10^{-1}
S9	1.50660×10^{-5}	1.88286×10^{-7}	0.96	4.86×10^{-9}	0.077	2.50×10^{-3}
S10	1.53830×10^{-5}	3.72347×10^{-7}	0.95	4.86×10^{-9}	0.040	5.90×10^{-2}

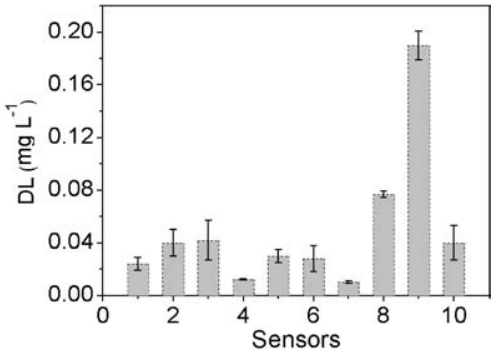

Fig. 5. Detection limits versus modified sensors.

Possibly these groups present both in the SL, and in the POEA, link more strongly to the chloroform and due to this the microelectrode 4 also presented good detection limit. In the case of microelectrode 8, that had the worst detection limit, we saw that the PANI dissolved in NMP (*N*-Methyl-2-Pyrrolidone) does not interact so strongly with chloroform. This is probably associated with the fact that this polymer is insoluble in some solvents[28] which would possibly be contributing to a lesser interaction with chloroform in aqueous medium.

With the application of the PCA, it was possible to notice a clear separation between the different types of polymer deposition and conditions, on the interdigitated microelectrodes, as in Figure 6. It was observed the formation of three (3) distinct groupings. In grouping I, are the sensors that presented the best results for the detection limit, with values below 0.02 mg L^{-1}. In grouping II, the sensors that presented an intermediate band (above 0.02 mg L^{-1} and below 0.05 mg L^{-1}). In grouping III, are the sensors that presented the worst values for the DL, with values above 0.10 mg L^{-1}. Sensor S1 corresponds to the reference microelectrode, that is, without film.

Plotting the score factors on the same PC1-PC2 plan (Fig. 6), we can observe excellent discrimination between the sensors. The sensors present good stability, reproducing the results in more than one measure and, they were able to discriminate the different chloroform concentrations present in the samples.

The samples with different chloroform concentrations were also evaluated using the 10 sensors and the

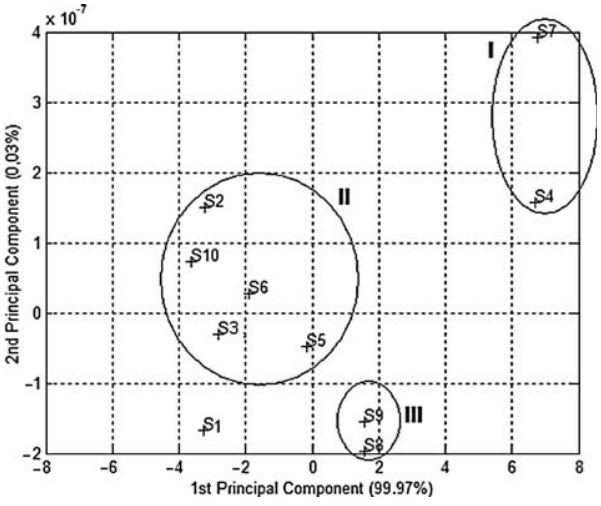

Fig. 6. PCA obtained for the sensors relative to the different polymeric complexes deposited over the interdigited microelectrodes.

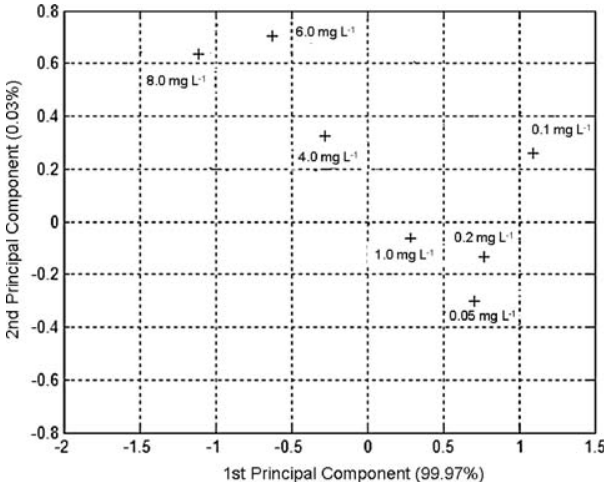

Fig. 7. PCA obtained for the different chloroform concentrations, relative to the different polymeric complexes deposited over the interdigitated microelectrodes.

impedance results also analyzed by PCA (Fig. 7). The sensorial system was able to differentiate the samples, due to their different compositions, which interact in different forms with the polymeric films, producing different impedance values in each sensor, as was previously observed in Figure 3.

The PCA analysis showed that to the values for first and second component represents about 100% of the total variance (PC1 = 99.97%; PC2 = 0.03%) of the observations. These results suggest that the sensors respond in a selective form, when in contact with chloroform, with practically 100% reliability.

4. CONCLUSIONS

A sensorial system using interdigitated microelectrodes and nanostructured conducting polymers allowed a statistical discrimination in the determination and detection of carcinogen compounds as chloroform, a by-product generated from water disinfection processes, in public supply systems. The polymeric films interacted distinctly with the compound present in the water. The use of this system for the evaluation of the water quality shows itself as a potential tool, making it possible, according to the database generated, in a selective way, the implementation of an on-line monitoring system.

Acknowledgments: The authors acknowledge the financial support from Conselho Nacional de Desenvolvimento Científico e Tecnológico (CNPq—Proc. 150042/2004-3, Proc. 302935/2004-3, CT-HIDRO: 550188/2002-9), Fundação de Amparo à Pesquisa do Estado de São Paulo (FAPESP—Proc. 02/07724-0) and Embrapa Instrumentação Agropecuária.

References and Notes

1. H. Komulainen, *Toxicology* 198, 239 **(2004)**.
2. International Agency for Research on Cance 73, 131 **(1999)**.
3. J. Fawell, *Food and Chemical Toxicology* 38, 91 **(2000)**.
4. http://www.atsdr.cdc.gov/toxprofiles/tp6-c5.pdf.
5. Agency for Toxic Substances and Disease Registry (ATSDR). Toxicological Profile for Chloroform. Public Health Service, U.S. Department of Health and Human Services, Atlanta, GA **(1997)**.
6. A. Barraud, *Vaccum* 41, 1624 **(1990)**.
7. J. N. Barisci, C. Conn, and G. G. Wallage, *Trends in Polymer Science* 4, 307 **(1996)**.
8. H. Toko, *Biosen. Bioelectron.* 13, 701 **(1998)**.
9. A. Riul, Jr., D. S. dos Santos, K. Wohnrath, R. Di Tommazo, A. C. P. L. F. Carvalho, F. J. Fonseca, O. N. Oliveira, Jr., D. M. Taylor, and L. H. C. Mattoso, *Langmuir* 18, 239 **(2002)**.
10. A. Riul, Jr., A. M. Gallardo Soto, S. V. Mello, S. Bone, D. M. Taylor, and L. H. C. Mattoso, *Synthetic Metals* 132, 109 **(2003)**.
11. C. J. L. Constantino, P. A. Antunes, E. C. Venâncio, N. Consolin, F. J. Fonseca, L. H. C. Mattoso, R. F. Aroca, O. N. Oliveira, Jr., and A. Rail, Jr., *Sens. Lett.* 2, 95 **(2004)**.
12. J. Janata, Principles of Chemical Sensors, Plenum Press, New York **(1989)**.
13. R. W. Cattrall, Chemical Sensors, Oxford University Press **(1997)**.
14. D. Anil K., D. C. Stone, and M. Thompson, *Int. Journal of Food Science and Technology* 39, 587 **(2004)**.
15. W. J. Zhang, J. Feng, A. G. MacDiarmid, and A. J. Epstein, *Synth. Met.* 84, 119 **(1997)**.
16. L. H. C. Mattoso, S. K. Manohar, A. G MacDiarmid, and A. J. Epstein, *J. Polym. Sci. Part A: Polym. Chem.* 33, 1227 **(1995)**.
17. E. R. Carvalho, L. Martin-Neto, D. M. B. P. Milori, J. C. Rocha, and A. H. Rosa, *J. Braz. Chem. Soc.* 15, 421 **(2005)**.
18. G. R. Aiken, Humic Substances in Soil, Sediment and Water, edited by John Wiley and Sons, New York **(1985)**.
19. R. L. Malcolm, Humic Substances in the Aquatic and Terrestrial Environment, edited by Springer-Verlag, Berlin **(1989)**.
20. W. Kern, *Semicond. Int* 94, **(1984)**.
21. L. G. Paterno, L. H. C. Mattoso, and O. N. Oliveira, Jr., *Quim. Nova* 24, 228 **(2001)**.
22. L. G. Paterno and L. H. C. Mattoso, *Polymer* 42, 5239 **(2001)**.
23. C. J. L. Constantino and O. N. Oliveira, Jr., *Colloids Surf. B: Biointerfaces* 23, 257 **(2002)**.
24. E. B. J. Rupp, *Agricult. Food Chem.* 40, 2016 **(1992)**.
25. S. Wold, *Chemom. Intell. Lab. Sys.* 2, 37 **(1987)**.
26. E. C. Venâncio, N. C. Filho, C. J. L. Constantino, L. Martin-Neto, and L. H. C. Mattoso, *J. Braz. Chem. Soc.* 16, 24 **(2005)**.
27. I. V. Dianova, N. A. Sinikova, and A. T. Lebedev, International Meeting of the International Humic Substances Society, 10th (Toulouse-França) Proceedings Toulouse **(2000)**, pp. 1039–1042.
28. M. G. Han, K. S. Cho, S. G. O. H, and S. S. Im, *Synth. Met.* 126, 53 **(2002)**.

SENSOR LETTERS
Vol. 4, 135–138, 2006

Comparison of ZnO/64° $LiNbO_3$ and ZnO/36° $LiTaO_3$ Surface Acoustic Wave Devices for Sensing Applications

K. Kalantar-Zadeh[1,*], D. A. Powell[1], A. Z. Sadek[1], W. Wlodarski[1], Q. B. Yang[2], and Y. X. Li[2]

[1] *School of Electrical and Computer Engineering, RMIT University, Melbourne, Australia*
[2] *State key Laboratory of High Performance Ceramics and Superfine Structures, Shanghai Institutes of Ceramics, Shanghai 200050, China*

(Received: 9 April 2006. Accepted: 19 April 2006)

The performance of ZnO/64°-YX $LiNbO_3$ and ZnO/36°-YX $LiTaO_3$ layered SAW structures was compared in terms of mass sensitivity and acoustic wave velocity. It was found that the ZnO/64° $LiNbO_3$ structure has a few distinct advantages over ZnO/36° $LiTaO_3$. For ZnO/64° $LiNbO_3$, the mass sensitivity is ~2.5 times larger. Additionally, the optimum thickness of the ZnO guiding layer is approximately half that of the ZnO/36° $LiTaO_3$ structure, which reduces the cost of fabrication.

Keywords: 64° $LiNbO_3$, 36° $LiTaO_3$, ZnO, Layered SAW, Mass Sensing.

RESEARCH ARTICLE

1. INTRODUCTION

Layered Surface Acoustic Wave (SAW) devices are of great interest for physical, chemical, and biochemical sensing applications. Their high mass sensitivity, robustness, ease of immobilization of bio-components on the active surface and low fabrication cost make them attractive for these applications. In this work, devices with different ZnO thicknesses were fabricated both on 64° $LiNbO_3$ and 36° $LiTaO_3$ substrates and their performance was compared. The most commonly utilised piezoelectric material orientations which allow the propagation of shear waves are 90° rotated ST-quartz, 64°-YX $LiNbO_3$, and 36°-YX $LiTaO_3$.[1–4] As a result, they are suitable for sensing applications in liquid media.

By depositing a wave guiding layer onto such substrates, mass sensitivity can be increased as the acoustic energy is more confined towards the surface. Layered SAW sensors for liquid media applications using SiO_2 on 90° rotated ST-quartz have been intensively studied.[5,6] SiO_2 on 36° YX-$LiTaO_3$ layered structure is another SAW structure that offers potential for liquid sensing applications.[7,8] However, such devices have lower sensitivity than devices based on ST cut quartz.

It has been shown that replacing the SiO_2 layer with ZnO, which is a piezoelectric material, results in considerable improvement of mass sensitivity.[9–11] Shoji et al.[10,11] showed that deposition of ZnO layer on $LiNbO_3$ or $LiTaO_3$ results in an improved electromechanical coupling coefficient (K^2). The authors[1] have conducted a comprehensive study regarding the sensitivity of ZnO/36° $LiTaO_3$ and found that maximum K^2 of 0.075 at thickness of $h/\lambda_0 = 0.05$ and maximum mass sensitivity of -70 cm^2/g. Chu et al.[12] investigated on the dependence of ZnO film on the sensitivity of love mode sensor in ZnO/90° rotated ST-cut quartz structure and found that the devices which are unheated during sputtering have higher sensitivity than those which are heated. They also found that the sensitivity of ZnO/90° rotated ST-cut quartz structure is higher than the SiO_2/90° rotated ST-cut quartz structure. Jian et al.[2] investigated the preferred orientation of ZnO films deposited onto a 64° $LiNbO_3$ substrate to apply as a liquid sensor. Zhang et al.[13] investigated a ZnO nanotip guiding layer grown by metal-organic chemical vapor deposition on the 128° Y-cut $LiNbO_3$ for biosensing applications. They claimed that the ZnO nanotip array enhanced DNA immobilization due to its large surface to volume ratio.

In this paper, the performance of the ZnO/36°-YX $LiTaO_3$ and ZnO/64°-YX $LiNbO_3$ SAW devices for sensing applications will be compared.

2. SENSOR FABRICATION

The sensor consists of a two-port resonator with 38 electrode pairs in input and output inter-digital transducers (IDTs), 160 electrodes in each reflective array, 700 μm

*Corresponding author; E-mail: kourosh@kalantar.org

Fig. 1. A typical sensor showing two identical resonators.

aperture width and a periodicity of 40 μm. A two-port resonator structure was chosen over a delay line as its higher phase slope increases oscillation stability. The IDTs and reflectors were formed by patterning an 80 nm Au layer. The Au layer was deposited upon 20 nm Ti for improved adhesion to the substrate. The ZnO guiding layer was deposited by RF magnetron sputtering. The sputtering gas was 40% O_2 in Ar at 1×10^{-2} Torr, substrate temperature was 220 °C, giving a deposition rate of $\sim$1.2 μm/hour. The ZnO thin film was employed as the acoustic wave-guiding layer on both the 64° $LiNbO_3$ and 36° $LiTaO_3$ substrates, with thickness ranging from 0 to 8 μm. Figure 1 shows a $LiTaO_3$ sensor before deposition of the ZnO.

3. MATERIAL ANALYSIS

ZnO films were micro-characterised using the X-Ray Diffraction (XRD) and Scanning Electron Microscopy (SEM) methods. It was observed from the XRD patterns (Fig. 2), that the ZnO thin film grows on $LiNbO_3$ and $LiTaO_3$ substrate with *c*-axis alignment normal and parallel to the surface, respectively.[10] For $LiNbO_3$, the strong (002) peak indicates that the *c*-axis orientation is normal to the substrate. The small peak which appears at 72.6° corresponds to the (004) plane. However, for $LiTaO_3$ the (110) peak indicates that the *c*-axis lies in the plane of the substrate. A smaller (102) peak is also present, but it is much smaller than the (110) peak.

It can be seen from the SEM micrographs (Fig. 3) that the formation of ZnO crystallites differs on $LiNbO_3$ and $LiTaO_3$ (Fig. 2), as does the corresponding crystal orientation, being (002) and (110), respectively as confirmed by XRD.

4. ACOUSTIC WAVE PROPERTIES

The acoustic wave propagation velocity within the structures and their mass sensitivity were studied. The

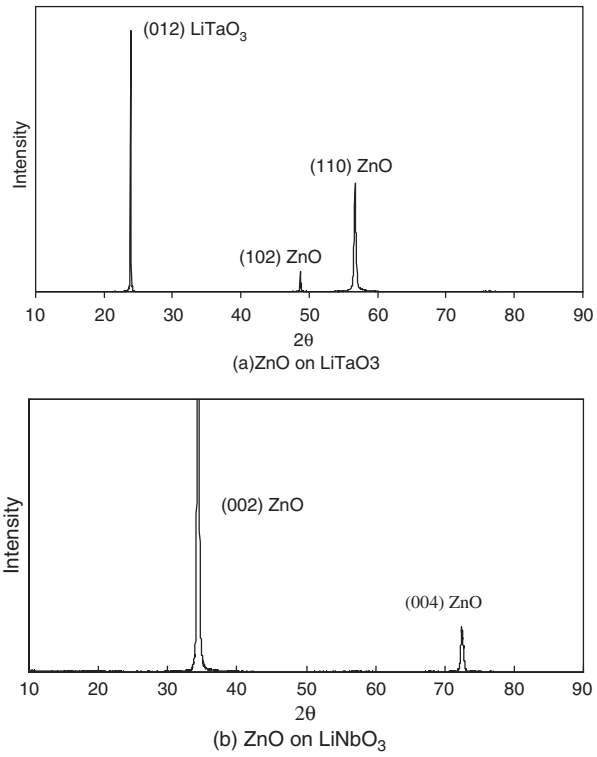

Fig. 2. XRD patterns.

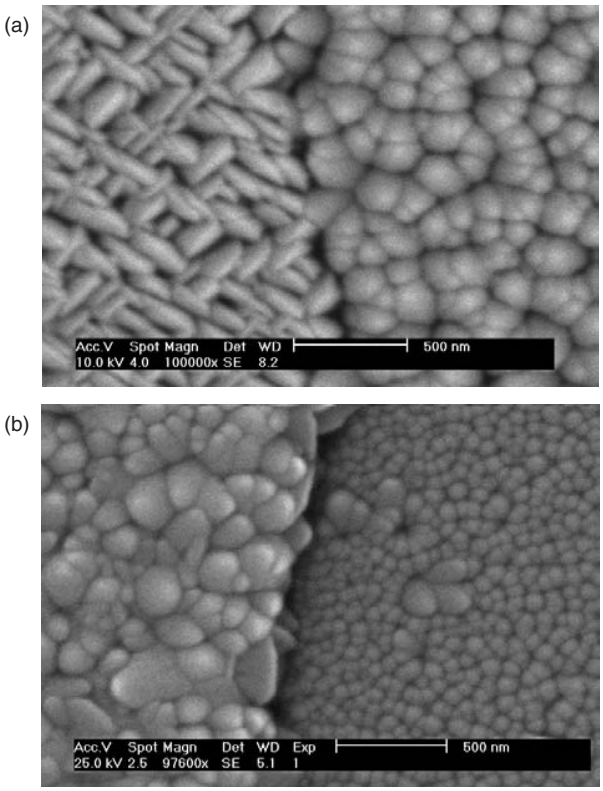

Fig. 3. (a) ZnO growth on bare $LiTaO_3$ (left) and gold (right), (b) ZnO growth on aluminium (left) and bare $LiNbO_3$ (right).

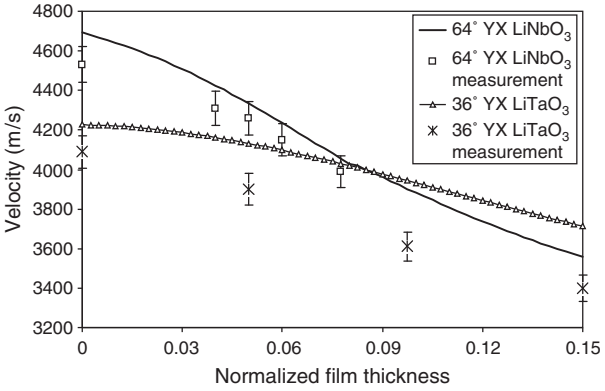

Fig. 4. Acoustic wave propagation velocity versus normalized layer thickness.

theoretical values were calculated using a numerical search technique.[1, 14] A determinant scan was performed in order to find the phase velocity which satisfies the boundary conditions.[15, 16] Theoretical values for propagation velocity are in good agreement with the measured values (Fig. 4). As can be observed, the change in the propagation velocity with the addition of the ZnO layer is much larger for the ZnO/64° $LiNbO_3$ structure than for the ZnO/36° $LiTaO_3$ structure. Each point is the average of three measurements. The deviation of the measurements from the average was less than 2%. The velocity shift with increasing layer thickness is correlated to the mass sensitivity, since the mass sensitivity is influenced by the group velocity, which relates to the change in group velocity with layer thickness.[5]

Theoretical and measured values for mass sensitivity for these two structures are shown in Figure 5. Theoretical values for mass sensitivity were obtained by calculating the phase velocity before and after addition of a perturbing mass layer. Measured values were obtained by spin coating a polymer with a thickness of 0.25 μm onto the active area of the sensors. Each point is the average of three measurements. The deviation of the measurements from the average was less than 15%. It can be seen that

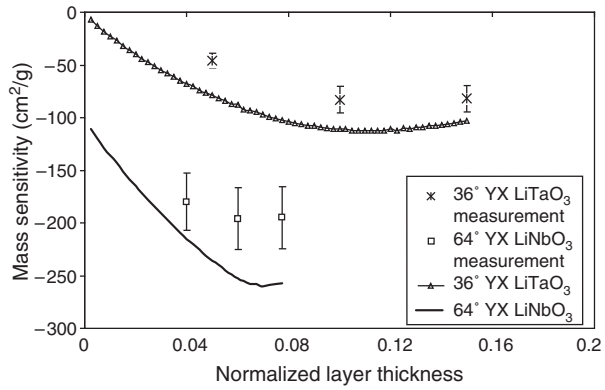

Fig. 5. Mass sensitivity versus the normalized layer thickness.

mass sensitivity reaches a maximum when the normalized layer thickness is 0.07 of the wavelength for the ZnO/64° $LiNbO_3$ structure and when it is 0.12 of the wavelength for the ZnO/36° $LiTaO_3$ structure. The ZnO/64° $LiNbO_3$ device's mass sensitivity of approximately 250 cm^2/g is larger than that of the ZnO/36° $LiTaO_3$ device, which is approximately 100 cm^2/g. Mass sensitivity measurements are in a good agreement with the calculations.

The authors have previously shown that the differing orientations of ZnO which occur on free and metallised regions of the SAW device result in different values for propagation velocity, mass sensitivity and electromechanical coupling coefficient.[1] Additionally, the authors have also shown[15, 16] that the crystal structure of sensitive layers have significant effect on the magnitude of the response of layered SAW devices for gas sensing applications. It is believed that the difference of ZnO crystal structures deposited on various surfaces causes the deviation from the calculated magnitude for mass sensitivities.

5. CONCLUSIONS

The performance of ZnO/$LiTaO_3$ and ZnO/$LiNbO_3$ were compared and for each structure, the ZnO thickness of maximum mass sensitivity was both theoretically and experimentally obtained. For a device operating at approximately 100 MHz the ZnO/64° $LiNbO_3$ structure reaches a maximum mass sensitivity of 250 cm^2/g when the normalized layer thickness is 0.07 of the wavelength. Such a structure is an excellent candidate for the fabrication of micro-mass sensors with numerous applications in immunosensing.

Acknowledgment: Authors would like to thank CRC (cooperative Research Centre) for Micro-technology, Australia, for the financial support.

References and Notes

1. D. A. Powell, K. Kalantar-Zadeh, and W. Wlodarski, *Sens. Actuators A* 115, 456 (**2004**).
2. S.-J. Jian, S.-Y. Chu, T. Y. Huang, and W. Water, *J. Vacuum Sci. Technol. A* 22, 2424 (**2004**).
3. K. Kalantar-Zadeh, W. Wlodarski, Y. Y. Chen, B. N. Fry, and K. Galatsis, *Sens. Actuators B*, 91, 143 (**2003**).
4. K. Kalantar-Zadeh, W. Wlodarski, Y. Y. Chen, B. N. Fry, and K. Galatsis, *Sens. Actuators B* 91, 303 (**2003**).
5. G. Kovacs, G. W. Lubking, M. J. Vellekoop, and A. Venema, *Proc. IEEE Ultrason. Symp.* 281 (**1992**).
6. J. Du, G. L. Harding, A. F. Collings, and P. R. Dencher, *Sens. Actuators A* 60, 54 (**1997**).
7. F. Herrmann and M. Weihnacht, *IEEE Trans. Ultrason. Ferroelec. Freq. Contr.* 48, 268 (**2001**).
8. J. Freudenberg, M. von Schickfus, and S. Hunklinger, *Sens. Actuators B* 76, 147 (**2001**).
9. K. Kalantar-Zadeh, A. Trinchi, W. Wlodarski, and A. Holland, *Sens. Actuators A* 100, 135 (**2002**).
10. K. Nakamura, T. Shoji, and H. B. Kang, *Proc. Int. Symp. App. Ferroelec.* 467 (**2000**).

RESEARCH ARTICLE

11. T. Shoji, K. Nakamura, and D. Yamazaki, *Proc. IEEE Ultrason. Symp.* 215 **(2001)**.
12. S.-Y. Chu, W. Water, and J.-T. Liaw, *Ultrasonics* 41, 133 **(2003)**.
13. Z. Zhang, N. W. Emanetoglu, G. Saraf, Y. M. Chen, P. Wu, J. Zhong, Y. C. Lu, J. Q. Chen, O. Mirochnitchenko, and M. Inouye, *IEEE Trans. Ultrason. Ferroelec. Freq. Contr.* 53, 786 **(2006)**.
14. D. A. Powell, K. Kalantar-Zadeh, and W. Wlodarski, *Proc. IEEE Ultrason. Symp.* 146 **(2003)**.
15. K. Kalantar-Zadeh, D. A. Powell, S. Ippolito, and W. Wlodarski, *Proc. IEEE Ultrason. Symp.* 191 **(2004)**.
16. D. A. Powell, K. Kalantar-Zadeh, S. Ippolito, and W. Wlodarski, *Sens. Lett.* 3, 66 **(2005)**.

SENSOR LETTERS
Vol. 4, 139–143, 2006

Fluorescence Behavior of Pyrene-1-Butylic Acid Chemisorption Layer onto Nano-Porous Anodic Oxidized Aluminum with Myristic Acid Layer for Optical Oxygen Sensing

Yuki Fujiwara and Yutaka Amao*

Department of Applied Chemistry, Oita University, Dannoharu, Oita 8701192, Japan

(Received: 10 February 2006. Accepted: 13 February 2006)

The fluorescence behavior of pyrene-1-butylic acid (PBA) chemisorption layer onto nano-porous anodic oxidized aluminum with a myristic acid layer was investigated and its device was applied as a fluorescence oxygen sensing material. When the ratio of [myristic acid]/[PBA] onto anodic oxidized aluminum plate increased, the fluorescence intensity due to monomer emission increased and the intensity due to excimer emission decreased. These results show that the polarity of the microenvironment around PBA molecules increased by chemisorption of myristic acid and the excimer formation between PBA molecules was suppressed by the myristic acid layer onto nano-porous anodic oxidized aluminum plate. Both of fluorescence attributed to monomer and excimer were quenched by oxygen. The I_0/I_{100} values, where I_0 and I_{100} represent the detected fluorescence intensities from a substrate exposed to 100% argon and 100% oxygen, respectively, in monomer emission increased with increasing the ratio of myristic acid to PBA. In contrast, the I_0/I_{100} values in excimer emission decreased with increasing the ratio of myristic acid to PBA. The PBA onto anodic oxidation of aluminum plates with myristic acid layer obey the modified Stern-Volmer equation and the Stern-Volmer constant, K_{SV} at 376 nm attributed to monomer and 461 nm attributed to excimer increased and decreased with increasing the ratio of myristic acid to PBA.

Keywords: Optical Oxygen Sensing, Pyrene, Nano-Porous Anodic Oxidized Aluminum, Fluorescence.

RESEARCH ARTICLE

1. INTRODUCTION

Ultrathin films such as chemisorption layer, self-assembled monolayer, Langmuir-Blogett (LB) film and layer by layer film have been used for development of molecular devices.[1–3] Among the these techniques, chemisorption layer technique has attracted considerable attention. Chemisorption layers are formed using spontaneous binding between a mercapto group and a noble metal (e.g., Au, Ag, or Pt)[1,4,5] or between a carboxyl group and a metal oxide (e.g., Al_2O_3, Fe_2O_3, or TiO_2).[6,7] The chemisorption technique is very convenient and so is widely used for optical and optoelectronic devices. Recently, a variety of devices and sensors based on luminescence quenching of organic dyes, polycyclic aromatic hydrocarbons (PAHs) such as pyrene or decacyclene immobilized in an oxygen permeable polymer (e.g., silicone polymer and polystyrene) were developed to measure oxygen concentration.[8–11] Since organic dye molecules directly interact with polymer molecules, the properties of sensing films depend strongly on the properties of polymer matrices. To improve these problems, layer of organic dye molecules directly chemisorbed onto substrate without polymer matrices are useful for oxygen sensing devices of no interaction. As the sensing dye molecules are arranged on the solid surface directly using chemisorption layer technique, a highly sensitive device for oxygen sensing will be obtained by using chemisorption layers.

Among PAHs, pyrene and its derivatives display strong fluorescence with high quantum yield and long lifetime.[12] Among pyrene derivatives, pyrene molecules with a carboxyl group are suitable for optical oxygen sensing devices using chemisorption layer because of the formation of a stable layer onto anodic oxidized aluminum and carboxyl

*Corresponding author; E-mail: amao@cc.oita-u.ac.jp

group of pyrene carboxylic acid. We previously reported the properties of optical oxygen sensor using various pyrene carboxylic acid modified onto anodic oxidized aluminum and improvement of oxygen sensitivity of pyrene carboxylic acid modified onto anodic oxidized aluminum by co-adsorption of hydrocarbon layer such as perfluorocarboxylic acid.[13–16] Moreover the fine structures of fluorescence spectrum of pyrene are strongly dependent on its microenvironment. Thus, the pyrene and pyrene derivatives also have been used to investigate the microenvironment of the fluorescent molecule.[17–20] There are two processes in the fluorescence mode of pyrene and pyrene derivatives. One is the emission attributed to monomer of pyrene molecules and the other is attributed to excimer formation of pyrene molecules. The both fluorescence mode depend on the microenvironment of pyrene molecules. The excimer formation of pyrene will be controlled by the co-chemisorbed hydrocarbon with a long alkyl chain such as myristic acid, because the hydrocarbon with a long alkyl chain layer makes a hydrophobic environment around pyrene molecules.

In this work we describe the fluorescence behavior of pyrene-1-butylic acid (PBA) chemisorption layer onto nano-porous anodic oxidized aluminum with myristic acid layer and its application as a fluorescence oxygen sensing material.

2. EXPERIMENTAL DETAILS

2.1. Materials

Pyrene-1-butylic acid (PBA) was obtained from Tokyo Kasei Inc (Tokyo, Japan). Myristic acid was obtained from Wako Pure Chemicals. (Osaka, Japan). Other materials were of the highest grade available obtained from Wako Pure Chemicals (Osaka, Japan).

2.2. Preparation of the Anodic Oxidation of Aluminum Plate

The aluminum plate (1.2 × 4 cm) was washed with 0.5 mol dm^{-3} NaOH aqueous solution for 2 min and then was electrically oxidized in H_2SO_4 solution. The aluminum plate was anodized galvanostatically in a thermostated with stirred bath of 1.0 mol dm^{-3} H_2SO_4 at a temperature of 10 °C for 30 min, a current density of 15 mA cm^{-2}. The applied potential was 20 V. After oxidation, the plate was washed with 0.3 mol dm^{-3} H_3PO_4 solution for 10 min. The anodic oxidized aluminum plates were dried in vacuum at 80 °C for 5 h and stored in vacuum prior to use. By using this method, the depth of pore of anodic oxidized aluminum prepared was 1.5 μm. The anodic oxidized aluminum is nano-porus structure as shown in Figure 1. As the surface of anodic oxidized aluminum plates were observed using scanning electron microscope (SEM), the mean diameter and the surface area of a pore of anodic oxidized aluminum prepared was estimated to be 30 nm and 7.1×10^{12} cm^2. The surface area of one anodic oxidized aluminum pore prepared is c.a. 1.4×10^{-9} cm^2. Thus, the total area of pore of anodic oxidized aluminum per 1 cm^2 is estimated to be c.a. 197 cm^2.

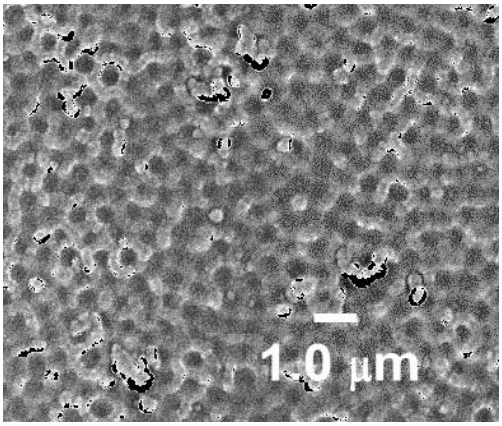

Fig. 1. Scanning electron microscope image of the surface of anodic oxidation of aluminum plate.

2.3. Preparation of PBA and Myristic Acid Chemisorption Layer

Anodic oxidized aluminum plate was dipped into methanol solution with different molar composition ratios of PBA to myristic acid at room temperature for 10 min. After dipping, the plate was washed with water and methanol several times. PBA and myristic acid physically adsorbed onto anodic oxidized aluminum plate were removed by ultrasonication and then dried under vacuum overnight. The PBA concentration was fixed to 0.1 mmol dm^{-3}. The molar composition ratios of PBA to myristic acid were changed 0 to 10. The amount of PBA chemisorbed onto anodic oxidized aluminum plate was determined using a spectrophotometer (Multispec-1500 Shimadzu) according to previous reported method.[21]

2.4. Spectroscopic Measurement

Steady state fluorescence spectra and excitation spectra of the PBA and myristic acid layers were measured using a Shimadzu RF5300-PC fluorescence spectrometer with a 150 W xenon lamp as an excitation light source. Excitation and emission bandpasses were 5.0 nm.

2.5. Characterization of Oxygen Sensor Using PBA and Myristic Acid Chemisorption Layer

The sample substrates were mounted at 45° angle in the quartz cell, for steady state fluorescence experiments, to minimize light scatter from the sample and substrate. Different oxygen standards (in the range 0–100%) in a gas stream were produced by controlling the flow rates of oxygen and argon gases entering a mixing chamber. The total pressure was maintained at 760 Torr. All the experiments

were carried out at room temperature. Oxygen sensing properties of PBA and myristic acid chemisorption layer were characterized by Stern-Volmer quenching constant, K_{SV}, obtained from following equation.

$$I_0/I = 1 + K_{SV}[O_2] \quad (1)$$

where I_0, I and $[O_2]$ are fluorescence intensities in the absence and in the presence of oxygen and oxygen concentrations, respectively. K_{SV} was obtained from a linear plot of (I_0/I)-1 versus $[O_2]$.

3. RESULTS AND DISCUSSION

3.1. Fluorescence Behavior of PBA onto Anodic Oxidation of Aluminum Plate with Myristic Acid Layer

PBA and myristic acid co-chemisorbed layer onto the anodic oxidized aluminum plate showed fluorescence at 376, 396 (attributed to monomer emission) and 474 nm (attributed to excimer emission) when excited at 340 nm under argon saturated condition as shown in Figure 2. The spectra (1), (2), and (3) showed the 0, 2, and 10 of [myristic acid]/[PBA] value, respectively. When the [myristic acid]/[PBA] value increased, the fluorescence intensities at 376 and 396 nm attributed to monomer emission increased and the intensity at 474 nm attributed to excimer emission decreased. As the fine structure of fluorescence spectrum of pyrene derivatives is affected by the polarity of its microenvironment, pyrene derivatives have been used as an indicator for studies on the microenvironment. The enhancement of 0–0 symmetry forbidden band (A) of pyrene molecules in polar media is induced by a decreasing symmetry due to either dipole-dipole interaction with the medium molecules. Thus, the ratio of the fluorescence intensity (B)/(A) is an indicator of the polarity of the microenvironment around pyrene molecules and the higher ratio indicates a less polar environment. Two typical peaks attributed monomer emission, 376 (A) and 396 nm (B) were obtained in the fluorescence spectra of PBA and myristic acid co-chemisorbed layer onto the anodic oxidized aluminum plate. Figure 3 shows the relationship between the ratio of the fluorescence intensity (B)/(A) and the [myristic acid]/[PBA] value. The ratio of (B)/(A) decreased with increasing the [myristic acid]/[PBA] value. Thus, the polarity of the microenvironment around PBA molecules increased by co-chemisorption of myristic acid and the excimer formation between PBA molecules was suppressed by the myristic acid layer onto nano-porous anodic oxidized aluminum plate. In all cases of PBA onto anodic oxidation of aluminum plate with myristic acid layer, the amount of chemisorbed PBA onto anodic oxidation of aluminum plate was estimated to be c.a. 10^{-9} mol cm^{-2} according to the previous reported method.[21] Since the area of PBA molecule is estimated to be c.a. 0.2 nm^2, the area PBA occupied onto 1 cm^2 of anodic oxidation of aluminum plate approximately is 1.2 cm^2. On the other hand, the total area of pore of anodic oxidized aluminum per 1 cm^2 is estimated to be c.a. 197 cm^2. Thus, the PBA and myristic acid layer chemisorbed onto anodic oxidation of aluminum plate will be formed the monolayer as shown in Figure 4.

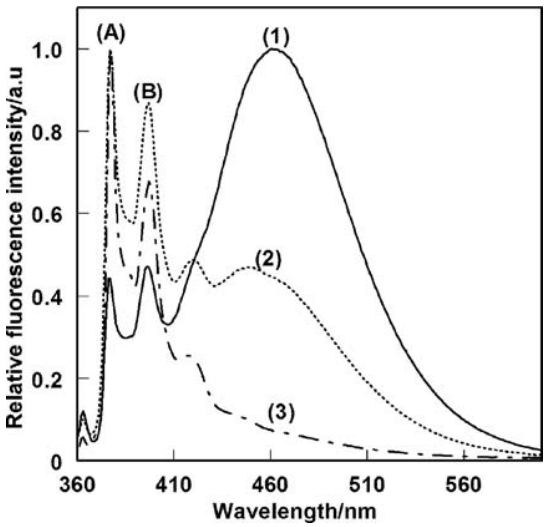

Fig. 2. Fluorescence spectra of PBA and myristic acid chemisorbed layer onto the anodic oxidized aluminum plate under argon saturated condition. The excitation wavelength was 340 nm. The spectra (1), (2), and (3) showed the 0, 2, and 10 of [myristic acid]/[PBA] value, respectively. A: Monomer, B: Excimer emission.

3.2. Oxygen-Induced Fluorescence Spectrum Change of PBA onto Anodic Oxidation of Aluminum Plate with Myristic Acid Layer

Figure 5 shows the fluorescence spectrum change of PBA onto anodic oxidation of aluminum plate with myristic

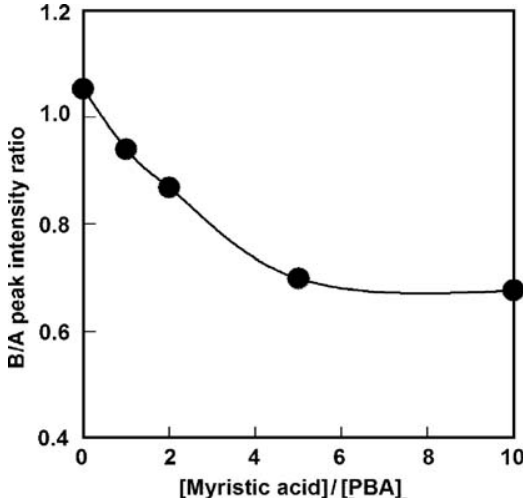

Fig. 3. Peak intensity ratio (B/A) dependent on the different molar composition ratios of myristic acid to PBA onto the anodic oxidized aluminum plate.

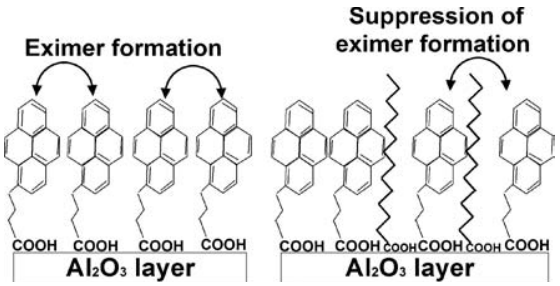

Fig. 4. Schematic representation of PBA and myristic acid layers onto anodic oxidation of aluminum plate.

acid layer by oxygen. The spectra (a) and (b) showed the 0 and 10 of [myristic acid]/[PBA] value, respectively. Both of fluorescence at 376, 396 (attributed to monomer emission) and 474 nm (attributed to excimer emission) were quenched by oxygen. For all cases of molar composition ratio of myristic acid to PBA, both of fluorescence at 376, 396, and 474 nm also were quenched by oxygen. The ratio I_0/I_{100}, where I_0 and I_{100} represent the detected fluorescence intensities from a substrate exposed to 100% argon and 100% oxygen, respectively, is used as an indicator of the sensitivity of the sensing film. In general, a sensor with I_0/I_{100} of more than 3.0 was a suitable oxygen-sensing device.[22] The I_0/I_{100} values of chemisorption layers with different molar composition ratios of PBA to myristic acid were summarized in Table I. The I_0/I_{100} values in monomer emission at 376 nm increased with increasing the ratio of myristic acid to PBA. In contrast, the I_0/I_{100} values in excimer emission at 461 nm decreased with increasing the ratio of myristic acid to PBA.

3.3. Oxygen Sensing Properties of PBA onto Anodic Oxidation of Aluminum Plate with Myristic Acid Layer

Stern-Volmer plot of the relationships between the fluorescence intensities of PBA and myristic acid chemisorbed layer and oxygen concentrations. The plots show nonlinear curve. Demas et al. reported a multi-site model in which the oxygen sensing film has some different oxygen-accessible sites.[23] According to this model, each site has

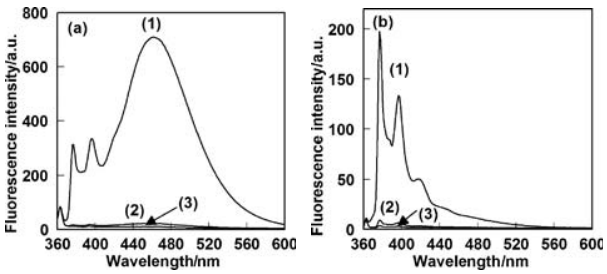

Fig. 5. Oxygen-induced fluorescence spectrum change of PBA onto anodic oxidation of aluminum plate with myristic acid layer. The excitation wavelength was 340 nm. The spectra (a) and (b) showed the 0, and 10 of [myristic acid]/[PBA] value, respectively, [O_2]: (1) 0, (2) 20, and (3) 100%.

Table I. The I_0/I_{100} values chemisorption layers with different molar composition ratios of myristic acid to PBA.

	I_0/I_{100}	
[Myristic acid]/[PBA]	376 nm	461 nm
0	27.9	73.4
1	37.7	47.2
2	56.6	39.6
5	60.0	11.9
10	62.6	9.6

its own individual characteristic-quenching constant. As the observed fluorescence intensity is the sum of emission from different oxygen-accessible sites with their own characteristic quenching constants, the Stern-Volmer relationship is given by

$$I_0/I = [\Sigma(f_n/(1+K_{SVn}[O_2]))]^{-1} \quad (2)$$

where n is an integer. f_n is the fractional contribution to each oxygen accessible site, and K_{SVn} is the quenching constant for each site. Assuming that there are k accessible (and n-k non-accessible) molecules with the same K_{SV}, one can then express equation (2) can be expressed as

$$\frac{I_0}{(I_0-I)} = \frac{1}{(fK_{SV}[O_2])} + \frac{1}{f} \quad (3)$$

where $f = \Sigma f_i$. This is the maximum mole fraction of pyrene molecules that are accessible to oxygen. If only a single class of pyrene molecules with the same accessibility to oxygen is present, $1/f$ in Eq. (3) should be 1. Figure 6 shows the modified Stern-Volmer plots for PBA and myristic acid chemisorbed layer plotted using Eq. (3). Figures 6(a) and (b) indicate the Stern-Volmer plot of monomer emission at 376 nm and excimer emission at 461 nm, respectively. The plot of $I_0/(I_0-I)$ against $1/[O_2]$ showed good linearity, which enhanced compared with the plot of I_0/I against oxygen concentrations. In order to obtain the f value, the regression line is extrapolated to $1/[O_2] = 0$. The value of f indicates the oxygen quenching mole fraction of the PBA molecule and $f = 1$ means that

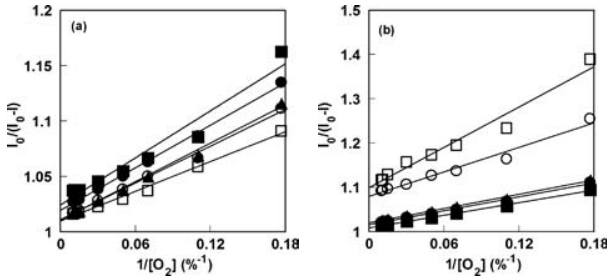

Fig. 6. Modified Stern-Volmer plots for PBA and myristic acid chemisorption layer onto anodic oxidation of aluminum plate monitored at (a) 376 nm and (b) 461 nm. The excitation wavelength was 340 nm. [myristic acid]/[PBA]=0 (closed circle), 1 (closed square), 2 (closed triangle), 5 (open circle), and 10 (open square).

Table II. The K_{SV} values chemisorption layers with different molar composition ratios of myristic acid to PBA.

	K_{SV}/%	
[Myristic acid]/[PBA]	376 nm	461 nm
0	1.4	2.3
1	1.6	2.0
2	1.8	1.8
5	1.9	1.2
10	2.1	0.84

all excited PBA molecules are quenched equally by oxygen. For all cases of molar composition ratio of myristic acid to PBA, both of f values at 376 and 474 nm were nearly to 1.0. The K_{SV} values of chemisorption layers with different molar composition ratios of PBA acid and myristic acid are summarized in Table II. The K_{SV} values at 376 nm due to monomer increased with increasing the ratio of myristic acid to PBA. In contrast, the K_{SV} values at 461 due to excimer nm decreased with increasing the ratio of myristic acid to PBA.

4. CONCLUSION

In this work we describe the fluorescence behavior of pyrene-1-butylic acid (PBA) chemisorption layer onto nano-porous anodic oxidized aluminum with myristic acid layer and its application as a fluorescence oxygen sensing material. When the [myristic acid]/[PBA] value increased, the fluorescence intensity due to monomer emission increased and the intensity due to excimer emission decreased. From the PBA fluorescence shape onto nano-porous anodic oxidized aluminum plate with myristic acid layer, the polarity of the microenvironment around PBA molecules increased by co-chemisorption of myristic acid and the excimer formation between PBA molecules was suppressed by the myristic acid layer onto nano-porous anodic oxidized aluminum plate. For all cases of molar composition ratio of myristic acid to PBA, both of fluorescence at 376, 396, and 474 nm also were quenched by oxygen. The I_0/I_{100} values in monomer emission increased with increasing the ratio of myristic acid to PBA. In contrast, the I_0/I_{100} values in excimer emission decreased with increasing the ratio of myristic acid to PBA. The oxygen sensing properties of PBA onto anodic oxidation of aluminum plate with myristic acid layer was investigated using Stern-Volmer theory. The PBA onto anodic oxidation of aluminum plates with myristic acid layer obey the modified Stern-Volmer equation. The K_{SV} values at monomer emission increased with increasing the ratio of myristic acid to PBA. On the other hand, the K_{SV} values at excimer emission decreased with increasing the ratio of myristic acid to PBA.

Acknowledgments: This work is partially supported by "Molecular Sensors for Aero-Thermodynamic Research (MOSAIC)," the Special Coordination Funds from the Ministry of Education, Culture, Sports, Science, and Technology Agency.

References and Notes

1. A. Ulman, An Introduction to Ultrathin Organic Films: From Langmuir-Blodgett to Self-Assembly, Academic Press, New York (**1991**).
2. G. Decher, J. D. Hong, and J. Schmitt, *Thin Solid Films* 210/211, 831 (**1992**).
3. P. Bertrand, A. Jonas, A. Laschewsky, and R. Legras, *Macromol. Rapid Commun.* 21, 319 (**2000**).
4. R. G. Nuzzo, F. A. Fusco, and D. L. Allara, *J. Am. Chem. Soc.* 109, 2358 (**1987**).
5. P. E. Laibinis and G. M. Whitesides, *J. Am. Chem. Soc.* 114, 1990 (**1992**).
6. K. D. Dobson and A. J. McQuillan, *Spectrochim. Acta A* 55, 1395 (**1999**).
7. K. D. Dobson and A. J. McQuillan, *Spectrochim. Acta A* 56, 557 (**2000**).
8. T. M. Freeman and W. R. Seitz, *Anal. Chem.* 53, 98 (**1981**).
9. T. Ishiji and M. Kaneko, *Analyst* 120, 1633 (**1995**).
10. A. Sharma and O. S. Wolfbeis, *Appl. Spect.* 42, 1009 (**1988**).
11. E. D. Lee, T. C. Werner, and R. Seitz, *Anal. Chem.* 59, 279 (**1987**).
12. E. Mohyi, J. Abu-Zeid, R. Lopez, P. Martinez, J. C. Acevedo, and R. Groff, *Chem. Phys. Lett.* 46, 558 (**1977**).
13. Y. Fujiwara and Y. Amao, *Sens Actuators B* 85, 175 (**2002**).
14. Y. Fujiwara and Y. Amao, *Sens Actuators B* 89, 59 (**2003**).
15. Y. Fujiwara and Y. Amao, *Sens Actuators B* 99, 130 (**2004**).
16. Y. Fujiwara and Y. Amao, *Sensor Lett.* 2, 232 (**2004**).
17. T. Ishiji, K. Kudo, and M. Kaneko, *Sens. Actuators* 22, 205 (**1994**).
18. E. Blatt, A. Launikonis, A. W. H. Mau, and W. H. F. Sasse, *Aust. J. Chem.* 40, 1 (**1987**).
19. K. Rajeshwar and M. Kaneko, *Langmuir* 5, 255 (**1989**).
20. K. Kalyanasundaram and J. K. Thomas, *J. Am. Chem. Soc.* 99, 2039 (**1977**).
21. A. Saeki, H. Sakai, K. Kamogawa, Y. Kondo, N. Yoshino, H. Uchiyama, J. H. Harwell, and M. Abe, *Langmuir* 16, 9991 (**2000**).
22. B. D. MacCraith, C. M. McDonagh, G. O'Keeffe, E. T. Keyes, J. G. Vos, B. O'Kelly, and J. F. McGilp, *Analyst* 118, 385 (**1993**).
23. J. N. Demas, B. A. DeGraff, and W. Xu, *Anal. Chem.* 67, 1377 (**1995**).

SENSOR LETTERS
Vol. 4, 144–154, 2006

RESEARCH ARTICLE

Superoxide Sensors

Takehiro Miyasaka[1,*], Kosuke Endo[2], Seiichi Mochizuki[3], and Kiyotaka Sakai[4]

[1] *Department of Cardiovascular Physiology, Okayama University Graduate School of Medicine, Dentistry, and Pharmaceutical Sciences, Okayama 700-8558, Japan*
[2] *Department of Physiology, Kawasaki Medical School, Okayama 701-0192, Japan*
[3] *Department of Medical Engineering, Kawasaki Medical School, Okayama 701-0192, Japan*
[4] *Department of Chemical Engineering, Faculty of Science and Engineering, Waseda University, Tokyo 169-8555, Japan*

(Received: 19 June 2005. Accepted: 19 July 2005)

The reactive oxygen species (ROS) have important physiological and protective roles in the maintenance of living systems. However, excessive production of ROS can impact cellular homeostasis and lead to oxidative stress. Superoxide has high reactivity acting as a reductant and an oxidant. Because of the pathophysiological roles of superoxide several methods for its detection have been developed. Spectrophotometric assay is nonspecific for superoxide, which limits its use. Chemiluminescent methods have been used frequently for vascular tissue samples because they are more sensitive than other conventional methods. Fluorescence-based assays have also been widely used in cultured cells and vascular tissues. Electron spin resonance (ESR) spectroscopy, also known as electron paramagnetic resonance (EPR), quantitatively measures superoxide concentration but is less suitable for its *in vivo* detection. Electrochemical sensors based on cytochrome c reduction or superoxide dismutase (SOD) enzymatic reaction have been developed for real-time monitoring, but lack adequate performance for *in vivo* superoxide measurement. Newly developed SOD-immobilized superoxide sensors reportedly have satisfactory performance for *in vitro* measurement. In this paper, we review superoxide measurement methods from the early spectrophotometric assays to the third generation of electrochemical sensors.

Keywords: Superoxide, Superoxide Dismutase, Superoxide Sensor, Electrochemical Sensor, Oxidative Stress.

1. INTRODUCTION

The use of oxygen in respiration has had a long and venerable prehistory; eukaryotes and prokaryotes first utilized oxygen perhaps as long ago as 2 billion years. The rapid and varied oxidation reactions make oxygen a very useful molecule in catabolic, and anabolic or biosynthetic pathways. However, oxygen is highly reactive and the resulting oxidative damage makes it toxic even to oxygen-dependent organisms. Organisms have developed extensive antioxidant defenses, and as awareness of the important roles of reactive oxygen species (ROS) in animal and plant pathology increases so does the interest of medical researchers, physiologists, and plant pathologists, in the antioxidant defense systems in cells and tissue.

Excessive production of ROS in mammals can affect cellular homeostasis and lead to oxidative stress, and is associated with inflammation,[1] hypercholesterolemia,[2] diabetes mellitus,[3] hypertension,[4] ischemic heart disease,[5] and chronic heart failure.[6] Figure 1 shows a schema of the process of oxidative stress. Table I shows the roles of ROS *in vivo*. Table II lists both oxygen radicals (superoxide anion radical, commonly called superoide: $O_2^{\cdot-}$, hydroxyl radical: $OH^{\cdot}$, etc.) and certain nonradicals (ozone: O_3, peroxynitrite: $ONOO^-$, singlet oxygen: $^1O_2$, hydrogen peroxide: H_2O_2) that are oxidant or are easily converted into other radicals and nonradicals. Some of the ROS of medical interest are known to have very short half-lives.[7]

The respiratory chain of enzyme activity in the mitochondria is the main intracellular source of $O_2^{\cdot-}$. Figure 2 shows the steps in the four-electron reduction of molecular oxygen (O_2) to water via $O_2^{\cdot-}$, H_2O_2, and $OH^{\cdot}$. $O_2^{\cdot-}$ is produced by the one-electron reduction of molecular O_2 as the first intermediate in this pathway. While $O_2^{\cdot-}$ is mainly produced by dihydronicotinamide adenine dinucleotide

*Corresponding author; E-mail: miyasaka@md.okayama-u.ac.jp

 1546-198X/2006/4/144/011 doi:10.1166/sl.2006.014

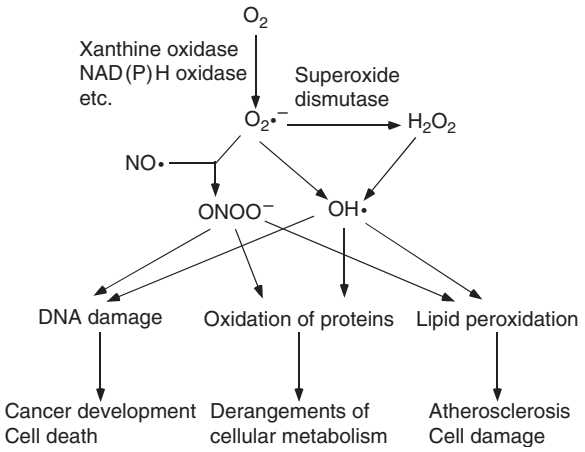

Fig. 1. Schematic illustration of mechanisms for the generation and elimination of ROS *in vivo*.

(NADH) dehydrogenase in mitochondria, other enzymes also produce $O_2^{\cdot -}$ such as reduced nicotinamide adenine dinucleotide phosphate (NADPH) oxidase in phagocytic cells, NADPH cytochrome P450 reductase in microsomes, and xanthine oxidase (XOD) and NAD(P)H oxidases in endothelial and vascular smooth muscle cells. For example, hypercholesterolemia increases endothelial production of $O_2^{\cdot -}$ by XOD activation.[8] Increased $O_2^{\cdot -}$ production may inactivate nitric oxide (NO) as endothelium-derived relaxing factor (EDRF) [9] contributing to the atherosclerotic process. In hypertension, oxidative stress is enhanced due to increased $O_2^{\cdot -}$ production by NAD(P)H oxidase and decreased scavenging of $O_2^{\cdot -}$ by extracellular superoxide dismutase (SOD).[10]

One family of highly-conserved enzymes has evolved to reduce $O_2^{\cdot -}$ is the SODs, which catalyze the reaction of $O_2^{\cdot -}$ with an electron and 2 protons to form H_2O_2.

$$2O_2^{\cdot -} + 2H^+ \xrightarrow{\text{SOD}} O_2 + H_2O_2 \qquad (1)$$

Three mammalian SODs have been identified: copper/zinc SOD (Cu/Zn SOD; SOD1), manganese SOD (Mn SOD; SOD2), and extracellular SOD (EC-SOD; SOD3). Cu/Zn SOD, the first member of the family discovered in mammals in 1969, is located in the cytosol and nucleus of all cell types.[10] Mn SOD, the second mammalian enzyme discovered from pig heart in 1973, is localized in the mitochondrial matrix.[11,12] The essential role of Mn

Table I. Roles of ROS *in vivo*.

Physiological condition (normal production)	Pathophysiological condition (overproduction)
By-product of ATP	Vascular dysfunction
Cytotoxicity against bacteria	Inflammation
Homeostatic regulation	DNA damage
Signal transfer of nerve system	Oxidation of proteins
	Lipid peroxidation

Table II. Reactive Oxygen Species.

Free radicals	
Superoxide	$O_2^{\cdot -}$
Hydroxyl	$OH^{\cdot}$
Hydroperoxyl	$HO_2^{\cdot}$
Peroxyl	$RO_2^{\cdot}$
Alkoxyl	$RO^{\cdot}$
Carbonate	$CO_3^{\cdot -}$
Carbon dioxide	$CO_2^{\cdot -}$
Nonradicals	
Hydrogen peroxide	H_2O_2
Hypobromous acid	HOBr
Hypochlorous acid	HOCl
Ozone	O_3
Singlet oxygen	$^1O_2$
Organic peroxides	ROOH
Peroxynitrite	ONOO$^-$
Peroxynitrous acid	ONOOH

SOD is maintaining mitochondrial function.[13] EC-SOD, the third and latest mammalian SOD discovered, was isolated from human lung by Marklund in 1982.[14] EC-SOD contains copper and zinc like Cu/Zn SOD but not manganese. Whereas the intracellular isoenzymes Cu/Zn SOD and Mn SOD are synthesized by virtually all mammalian cell types, important sources of EC-SOD are fibroblasts in peripheral tissues and glia cells in the central nervous system.[15] EC-SOD is secreted into the extracellular fluid (plasma, lymph, ascites, synovial fluid, and cerebrospinal fluid) [16] and reversibly binds to heparan sulphate proteoglycan ligands in the glycocalyx of the surface of most tissue cell types and in the interstitial matrix.[15] Table III lists these SODs.

$O_2^{\cdot -}$ also is eliminated by nonenzymatic antioxidant components such as tocopherol (vitamin E) and flavonoides.[17] Pietta et al. showed that ginkgoflavonol-glycosides and green tea (*Camellia sinensis*) catechins (types of tannin) metabolites have antioxidant capacity.[18] Of the many kinds of catechins in tea, such as (+)-catechin, (−)-epicatechin, (−)-epigallocatechin, (−)-epicatechin gallate, and (−)-epigallocatechin gallate, act as scavengers for $O_2^{\cdot -}$.[19] Catechins contained in green tea also directly scavenge NO, which is why green tea is reputed to be an excellent dietary source of antioxidant by virtue of its inhibitory effects on ROS metabolism.[20] Simonetti et al. showed that the levels of caffeic acid (hydroxycinnamic derivative) in human plasma increased linearly with dose of ingested of red wine, and that the caffeic acid concentrations correlated with the variation of plasma total antioxidant

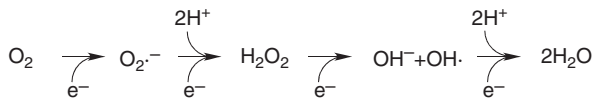

Fig. 2. Schematic illustration of one-electron reduction pathway of oxygen.

RESEARCH ARTICLE

Table III. Superoxide dismutase (SOD).

Type	Name	Metals	Subunit Size	Location
SOD1	Copper/zinc SOD	Cu/Zn	16 kDa	Cytosol and nucleus of all cell types
SOD2	Manganese SOD	Mn	16 kDa	Mitochondria
SOD3	Extracellular SOD	Cu/Zn	30 kDa	Fibroblasts, glial cells, and extracellular fluid

capacity.[21] Although such common foods may offer attractive targets for development of pharmaceutical products, they also are dietary sources of antioxidants that can act to confound *in vivo* investigations.

The high reactivity of $O_2^{\cdot-}$, abundant opportunities for auto-oxidation, and the scavenging system make the half-life of $O_2^{\cdot-}$ in biological systems extremely short. Real-time monitoring of $O_2^{\cdot-}$ production within the cell and in the extracellular matrix *in vivo* challenges current technological capacity. The reports about the sensors described in this article are of proof-of-concept studies of the production of $O_2^{\cdot-}$ in basic cellular processes. The methods include spectrophotometric assays, chemiluminescent detections, fluorescence-based assays, electron paramagnetic resonance (EPR) spectroscopy and spin trapping, electrochemical detection, and combinations of methods (Table IV). Table V lists the advantage and disadvantage of these ROS measurement systems. Published reviews on the measuring methods of vascular reactive species provide more detailed comparisons.[22–25]

Table IV. Methods of detecting superoxide.

Spectrophotometric assays	Cytochrome c
	Nitro blue tetrazolium (NBT)
Chemiluminescence assays	Luminol
	Coelenterazine
	2-methyl-6-phenyl-3,7-dihydroimidazo-[1,2-α]pyrazin-3-one (CLA)
	2-methyl-6-(4-methoxyphenyl)-3,7-dihydroimidazo[1,2-α]pyrazin-3-one (MCLA)
	Lucigenin
Fluorescence assays	Dihidroethidium (DHE)
	Dichlorofluorescein (DCF)
Electron spin resonance (ESR)	5,5-dimethylpyrroline-N-oxide (DMPO)
	5-dethoxyphosphoryl-5-methyl-1-pyrroline-N-oxide (DEPMPO)
Electrochemical detection = sensors	Catalase-based sensor
	Superoxide dismutase-based sensor

2. CONVENTIONAL METHODS FOR SUPEROXIDE DETECTION

2.1. Spectrophotometric Assays

Spectrophotometric assays measure the change of absorbance of reagents by reduction reaction with $O_2^{\cdot-}$, including cytochrome *c* (*cyt c*) reduction, and nitroblue tetrazolium (NBT) reduction, and aconitase reduction.

Cyt c reduction is a method widely used for measurement of $O_2^{\cdot-}$ production by various enzymes, tissue extracts, and cells. $O_2^{\cdot-}$ is measured as SOD-inhibitable reduction of *cyt c*, determined as an increase in absorbance of Fe(II)-*cyt c* at 550 nm.

$$Fe^{III}\,cyt\,c + O_2^{\cdot-} \rightarrow Fe^{II}\,cyt\,c + O_2 \qquad (2)$$

Several precautions to avoid overestimation are required in the use of this method, because *cyt c* is nonspecific for $O_2^{\cdot-}$, and reduced *cyt c* can be reoxidized by cytochrome oxidases, peroxidases and oxidants, including H_2O_2 and $ONOO^-$. The use of modified *cyt c* such as acetylated *cyt c* and succinoylated *cyt c* minimize these potentially misleading reactions.[26] However, modified *cyt c* cannot be used to measure $O_2^{\cdot-}$ released by uncoupled NO synthase (NOS) because neuronal NOS reduces native, acetylated and succinoylated *cyt c* by direct electron transfer.[27]

When *Cyt c* reduction is applied for the assay of SOD activity,[10,28] the reduction rate of *cyt c* by $O_2^{\cdot-}$ is monitored at 550 nm using the xanthine/XOD system as the source for $O_2^{\cdot-}$.

$$\text{Xanthine} + O_2 + H_2O \xrightarrow{\text{XOD}} \text{Uric acid} + 2H^+ + O_2^{\cdot-} \qquad (3)$$

SOD competes with *cyt c* for $O_2^{\cdot-}$ and decreases the reduction rate of *cyt c*. The rate of reduction of *cyt c*, inhibited by SOD, is plotted as reciprocal absorbance change per minute versus a standard concentration of SOD. One unit

Table V. Advantages and disadvantages of ROS measurement.

	Optical methods	Chemiluminescent methods	ESR(EPR)	Electrochemical methods
Object for detection	Spectrophotometry fluorescence	Chemiluminescence	Electron spin resonance spectrum	Electrode reaction
Easy and simple	yes	yes	no	yes/no
Quantitative	no	yes	yes	yes
Disadvantage	Qualitative	Probe selectivity Auto-oxidation	Complicated procedure	Hand-made
Real time monitoring	no	yes	no	yes
Real time *in vivo* monitoring	no	no	no	yes

of SOD is defined as that amount of enzyme, which inhibits the rate of *cyt c* reduction by 50%.

The formation of NBT reduced by $O_2^{\cdot-}$ to form monoformazan (NBT^+) can be monitored by spectrophotometer at 550 to 560 nm. NBT detects intracellular $O_2^{\cdot-}$; however, it is susceptible to reduction by several tissue reductases. The specificity for $O_2^{\cdot-}$ must be confirmed by inhibition of NBT staining by SOD. NBT has been shown to artificially generate $O_2^{\cdot-}$ by reacting with environmental O_2 under aerobic conditions. For these reasons, detection of $O_2^{\cdot-}$ in biological samples should not rely exclusively on NBT reduction.

2.2. Chemiluminescent Methods

Because chemiluminescent intensity is considered to be in proportion to $O_2^{\cdot-}$ concentration, it is an appropriate method of $O_2^{\cdot-}$ measurement.[29] And because they are more sensitive than other spectroscopic measurements, chemiluminescent methods frequently have been used for vascular tissue samples. Several chemiluminescent reagents have been used, including lucigenin (bis-*N*-methylacridinium), luminol (5-amino-2,3-dihydroxy-1,4-phthalayineione), coelenterazine [2-(4-hydroxybenzyl)-6-(4-hydroxyphenyl)-8-benzyl-3,7-dihydroimidazo [1,2-α]pyrazin-3-one],[30] and coelenterazine's analogs such as CLA (2-methyl-6-phenyl-3,7-dihydroimidazo[1,2-α]pyrazin-3-one) and MCLA [2-methyl-6-(4-methoxyphenyl)-3,7-dihydroimidazo[1,2-α] pyrazin-3-one].[31]

Among the chemiluminescent reagents, lucigenin has been used most widely to measure rapidly changing $O_2^{\cdot-}$ concentrations. The mechanism of $O_2^{\cdot-}$-dependent lucigenin chemiluminescence requires an initial one-electron reduction by which a lucigenin di-cation (Luc^{2+}) is transformed to a mono-cation radical ($Luc^{\cdot+}$). The mono-cation radical then reacts with $O_2^{\cdot-}$ to yield the unstable dioxetane ($LucO_2$), which spontaneously decomposes. This results in the formation of an electronically excited acridone, which emits light when it returns to a ground state (Fig. 3).

Guyllenhammar showed that lucigenin derived chemiluminescence possesses a high degree of specificity for $O_2^{\cdot-}$ produced from human neutrophils stimulated with a variety of soluble stimuli.[32] Auto-oxidation is negligible at low concentrations (<20 μmol/L[33] or 5 μM [34,35]). However, the concentrations of lucigenin must be controlled to avoid auto-oxidation at higher concentrations (up to 250 μmol/L), where redox cycling is favorable.[36]

$$Luc^{2+} \xrightarrow{\text{reduction}} Luc^{\cdot+} \quad (4)$$

$$Luc^{\cdot+} + O_2 \Leftrightarrow Luc^{2+} + O_2^{\cdot-} \quad (5)$$

Vásquez-Viar et al. demonstrated that lucigenin stimulates eNOS-dependent NADPH consumption and $O_2^{\cdot-}$ generation. In this reaction, lucigenin (Luc^{2+}) is reduced to the

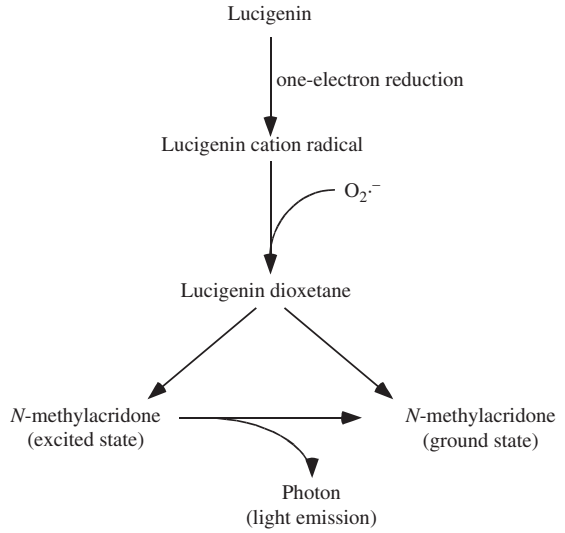

Fig. 3. Schematic illustration of the reaction pathway leading to lucigenin chemiluminescence.

$Luc^{\cdot+}$, which reacts with oxygen to regenerate lucigenin and $O_2^{\cdot-}$.[37]

$$NADPH/eNOS + Luc^{2+} \rightarrow Luc^{\cdot+} \quad (6)$$

$$Luc^{\cdot+} + O_2 \Leftrightarrow Luc^{2+} + O_2^{\cdot-} \quad (5)$$

Liochev and Fridovich showed that lucigenin (Luc^{2+}) is reduced to the $Luc^{\cdot+}$ by other enzymic reaction such as XOD + NADH, and glucose oxidase + glucose and then $Luc^{\cdot+}$ rapidly auto-oxidizes and produces $O_2^{\cdot-}$.[38] Because lucigenin undergoes a cycle of univalent reduction followed by auto-oxidation, the difficulties in controlling the possible enzymic reactions in cells and tissue limits its use in measuring $O_2^{\cdot-}$. Scheriber et al. performed real-time monitoring of $O_2^{\cdot-}$ production *in vitro* using lucigenin chemiluminescence[39] in brain slices during and after hypoxia, however the results were qualitative.

The mechanism of $O_2^{\cdot-}$-dependent luminol chemiluminescence requires an initial one-electron reduction by which a luminol is transformed to a luminol radical. The luminol radical reacts with $O_2^{\cdot-}$ to yield an unstable endoperoxide. The luminol endoperoxide decomposes to N_2 and aminophthallate. The aminophthallate, in an electronically exited state, relaxes into a ground state and emits a photon.

Luminol-derived chemiluminescence may be induced by a variety of ROS including $O_2^{\cdot-}$, $OH^{\cdot}$, and H_2O_2.[40] Thus, various scavengers such as uric acid for $ONOO^-$ and catalase for H_2O_2 are necessary to identify which ROS is responsible for the signal produced by luminol.

The above conventional chemiluminescent methods are useful for *in vitro* $O_2^{\cdot-}$ measurement in isolated tissues, isolated vessels or cultured cells. Recently, some of chemiluminescent methods have been applied *in vivo*, including the monitoring of $O_2^{\cdot-}$ production from the surface of rabbit

RESEARCH ARTICLE

heart and cat brain by the MCLA chemiluminescence;[41, 42] however, precise quantitation is problematic with the *in vivo* method.

2.3. Fluorescence-Based Assays

Fluorescence-based assays also have been widely used for detection of ROS in cultured cells and vascular tissues. Although these approaches are semi-quantitative, they provide important information on the localization of ROS in sample tissues and cells. Cells can be analyzed by a micro plate reader or by a fluorescence-activated cell sorter (FACS).[43] Fluorescent intensity provides quantitative information on ROS formation. Dihydrothidium (DHE) and dichlorofluorescein (DCF) are common fluorescent probes used to measure $O_2^{\cdot-}$. DHE is cell-membrane permeable and reacts with intracellular $O_2^{\cdot-}$ to form an intermediate product, which in turn interacts with DNA producing nuclear fluorescence at an excitation wavelength of 500–530 nm and an emission wavelength of 590–620 nm. Zhao et al. discovered another fluorescent product (excitation, 480 nm; emission, 567 nm) by the reaction of DHE and $O_2^{\cdot-}$.[44] DHE may react with $OH^{\cdot}$ and H_2O_2, it shows reasonable specificity to $O_2^{\cdot-}$. Oxidation transforms 2′,7′-dichlorodihydrofluorescein (DCFH) to the highly fluorescent 2′,7′-dichlorofluorescein (DCF). DCFH may also be auto-oxidized to form H_2O_2 and requires special precautions to avoid overestimation. DCF has been used to detect ROS in cultured cells, but the cell-membrane permeable type (DCF-diacetate: DCF-DA) must be used for tissue studies. Although DCF is not specific to $O_2^{\cdot-}$, and can fluoresce in response to a variety of ROS including H_2O_2, other peroxides, and $ONOO^-$, it is a useful marker of ROS.[45, 46]

2.4. Electron Spin Resonance Spectroscopy Methods

Electron spin resonance (ESR) spectroscopy, also known as electron paramagnetic resonance (EPR), detects molecules with unpaired electrons by means of spin-trap reagents, which incorporate radical molecules into their structure. Common spin trap reagents are nitrones such as 5,5-dimethylpyrroline-N-oxide (DMPO), which form –OH and –OOH adducts on reaction with the hydroxyl and $O_2^{\cdot-}$ radicals, respectively.[47] A more $O_2^{\cdot-}$-specific and stable spin trap reagent, 5-dethoxyphosphoryl-5-methyl-1-pyrroline-N-oxide (DEPMPO) has proven useful in measuring $O_2^{\cdot-}$ concentration in aqueous solution using liquid nitrogen freezing.[48] 5-ethoxycarbonyl-5-methyl-pyrroline-N-oxide (EMPO)-$O_2^{\cdot-}$ adduct (EMPO-OOH) is more stable than DEPMPO-$O_2^{\cdot-}$ adduct (DEPMPO-OOH). Zhang et al. showed that the signal-to-noise ratio of the ESR spectrum of EMPO-OOH is further enhanced by labeling the nitrone group in EMPO with a nitrogen-15 atom ([^{15}N]-EMPO).[49] However, some spin-trap reagents are more specific for $O_2^{\cdot-}$ than others. In the presence of reductants in tissues such as ascorbate, the spin active adducts are rapidly reduced to ESR silent species. Probe instability, tissue metabolism, lack of spin trap specificity and the high cost of ESR spectrometers make this technique more suitable for the *in vitro* detection of free radicals in small volume samples.

3. ELECTROCHEMICAL SENSORS FOR SUPEROXIDE MEASUREMENT

3.1. Cytochrome *c*-Based Sensors

In an early sensor design, McNeil et al. developed a monolayer gold disc electrode surface-modified with 4,4′-dithiobipyridine to monitor the reduction of *cyt c* by $O_2^{\cdot-}$.[50] The principle of this method is to measure the change in electric current by the reoxidation of reduced *cyt c* by $O_2^{\cdot-}$ at −25 mV. In this method, *cyt c* was not immobilized on the gold electrode but was only dissolved in sample solutions. They showed that the reduction of *cyt c* was specific to $O_2^{\cdot-}$, and the measured current was proportional to the spectrophotometric assay by *cyt c*. The measured current was proportional to the number of neutrophils that produce $O_2^{\cdot-}$, and then they concluded that this method is applicable to measurement of $O_2^{\cdot-}$ in biological samples.

Subsequently, McNeil et al. developed reagentless sensor system that is applicable to continuous direct monitoring $O_2^{\cdot-}$ concentration *in vitro*.[51] *Cyt c* was immobilized by passive adsorption to a monolayer, platinised activated carbon electrode (PACE). The rate of current production during reoxidation of *cyt c* reduced by $O_2^{\cdot-}$ was monitored using both xanthine/XOD and stimulated neutrophils as sources of $O_2^{\cdot-}$.

Fabian et al. showed that the PACE *cyt c* electrode is sensitive and responsive enough for real-time *in vivo* qualitative measurement of $O_2^{\cdot-}$ in brain tissue.[52, 53] To improve the measurement limit of enzymatic and cellular $O_2^{\cdot-}$ production, Tammeveski et al. adapted a 3,3′-dithiobis(sulfosuccinimidylpropionate) (DTSSP)-monolayer modified gold electrode and immobilized *cyt c* on the electrode.[54] Although the PACE electrode type sensor could not achieve real-time monitoring because of the small measurement area of the electrode, the DTSSP electrode had a larger area which enabled real-time monitoring of $O_2^{\cdot-}$. They applied this electrode to a quantitative *in vitro* analysis of $O_2^{\cdot-}$ released from lipopolysaccharide-activated human glioblastoma cells and demonstrated the relationship between $O_2^{\cdot-}$ and NO.[55]

Ge and Lisdat immobilized *cyt c* on a mercaptoundecanoic acid/mercaptoundecanol-modified gold wire electrode to improve electron transfer between *cyt c* and the electrode.[56] Büttemeyer et al. applied this *cyt c*-based sensor to real-time *in vivo* measurement in the gastrocnemius muscle tissue during reperfusion after ischemia, and demonstrated stable signals specific to $O_2^{\cdot-}$ during reperfusion injury.[57]

Lisdat et al. later designed a monolayer *cyt c* sensor for the measurement of antioxidant activity in analytical grade substances.[58] They used the $O_2^{\cdot-}$ produced by xanthine/XOD reaction, and the antioxidant activity quantified as a percentage of the signal decrease to determine the 50% inhibition value for flavonoids. The antioxidant activity was arranged in the order, flavanols > flavonols > flavones > flavonones > isoflavonones. Subsequent experiments using the same sensor design compared the *in vitro* $O_2^{\cdot-}$ scavenging activity and the *in vivo* antioxidant potential of methanolic extracts prepared from 10 Chinese tonifying herbs.[59] For the measurement of $O_2^{\cdot-}$ scavenging activity *in vitro*, they used hypoxanthine/XOD, and a *cyt c*-modified gold electrode $O_2^{\cdot-}$ sensor to measured the current changes caused by the addition of herbal extracts. They used CCl_4 hepatotoxicity model mice in experiments measuring the *in vivo* antioxidant potential of the herbal extracts. Plasma alanine aminotransferase activity and glutathione regeneration capacity were measured as the indices of antioxidant potential of the herbal extracts. They showed the $O_2^{\cdot-}$ scavenging activity *in vitro* and antioxidant activity of the herbal extracts fed to the mice, respectively, but the *in vitro* $O_2^{\cdot-}$ scavenging activity did not correlate well with the *in vivo* antioxidant activity in the mouse model.

3.2. The Basics of SOD-Based Sensors

Several SOD-immobilized sensors using the reaction of $O_2^{\cdot-}$ with SOD have been developed since 1989. McNeil et al. immobilized bovine Cu/Zn-SOD on a PACE monolayer sensor by passive adsorption.[51] The principle of $O_2^{\cdot-}$ measurement is as follows: SOD eliminates $O_2^{\cdot-}$ by the following reaction:

$$2O_2^{\cdot-} + 2H^+ \xrightarrow{\text{SOD}} O_2 + H_2O_2 \qquad (1)$$

These sensors determine $O_2^{\cdot-}$ concentration indirectly by measuring the amount of H_2O_2 produced by this enzymatic reaction.

$$H_2O_2 \xrightarrow{\text{electrode}} O_2 + 2H^+ + 2e^- \qquad (7)$$

Campanella et al. developed an SOD-immobilized biosensor.[54] SOD was physically entrapped in a kappa-carrageenan gel membrane, and then immobilized on the monolayer electrode. Figure 4 shows the structure and reaction mechanisms of SOD-immobilized $O_2^{\cdot-}$ sensor. They used the Clark electrode and an Ag/AgCl anode, between which −650 mV was applied. The Clark electrode and anode are covered with a polypropylene gas-permeable thin-film membrane. O_2 and H_2O_2 are produced by elimination reaction of $O_2^{\cdot-}$ by SOD [Eq. (1)]. The O_2 produced passes through the gas-permeable membrane and is measured by the electrode, so that the value of measurement indicates the amount of $O_2^{\cdot-}$. But O_2 also is consumed by $O_2^{\cdot-}$ product reactions such as the xthantine/XOD

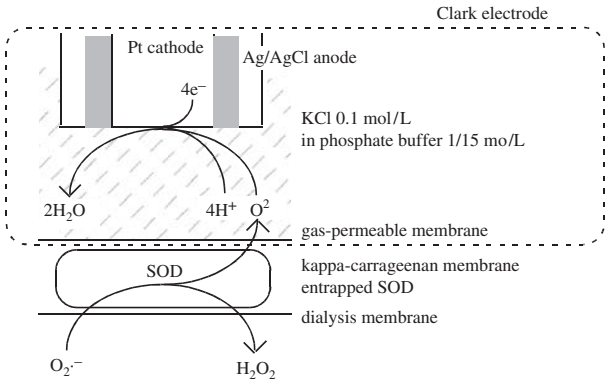

Fig. 4. Superoxide sensor with the Clark electrode by Campanella et al.

reaction [Eq. (3)], and accurate measurement of $O_2^{\cdot-}$ concentration with this type sensor is difficult.

An improved version of the sensor used a classical amperometric monolayer gold wire electrode for H_2O_2 as an indicator of $O_2^{\cdot-}$ production.[61] Figure 5 shows the structure and reaction mechanisms of this sensor. H_2O_2 produced by SOD [Eq. (1)] in the membrane surface diffuses through the membrane and reacts with the electrode. The SOD/H_2O_2 biosensor could measure $O_2^{\cdot-}$ concentration, and was used in a study of the activity of scavengers for $O_2^{\cdot-}$ (ascorbate, glutathione, and cysteine). The SOD/ H_2O_2 biosensor measured the $O_2^{\cdot-}$ released from homogenized healthy and cancerous kidney tissues, and showed that the amount of $O_2^{\cdot-}$ released from cancerous kidney tissues was greater than that from healthy tissue.[61]

Campanella et al. used the improved amperometric SOD biosensor *in vitro* to evaluate antioxidant properties of several fruits and vegetables obtained at a local market: garlic, shallot, onion, Japanese garlic, chilli, aloe, cauliflower, radish, carrot, tomato, kiwi fruit, mandarin, orange, lemon, grapefruit, and strawberry.[62] $O_2^{\cdot-}$ was produced by xanthine/XOD system in pH 7.5 PBS solution, and the calibration curve of the SOD sensor was recorded. The scavenging properties of these foods were evaluated from the percent ratio of slope values of the calibration curve

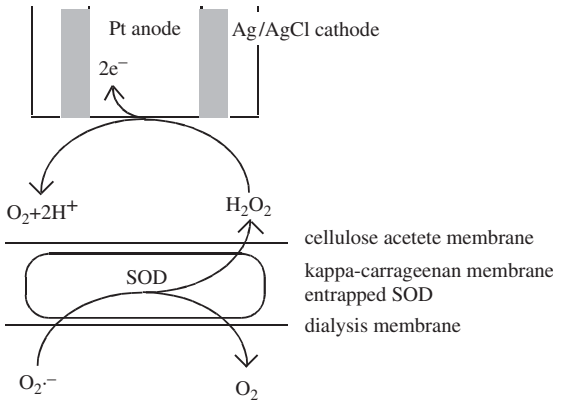

Fig. 5. Superoxide sensor with a classical amperometric electrode for H_2O_2 by Campanella et al.

RESEARCH ARTICLE

both in the absence and presence of each food. In the results, the slope values decreased from 18.7 to 78.1%. In related studies, Campanella et al. applied this amperometric SOD biosensor to determine the antioxidant capacity of different kinds of teas and herbal products such as decaffeinated (detheinated) tea, ordinary tea, green tea, and different fresh aromatic herbs, varieties of olives, and types of fresh fruits.[63,64] They concluded that the results obtained by the SOD biosensor were in good agreement with the results obtained by other methods such as the *cyt c* reduction method, and the spectrophotometric-NBT method.

Ge et al. used two types of SOD-immobilized sensors, CuZnSOD and FeSOD, in which each enzyme was immobilized on a 3-mercaptopropionic acid (MPA)-modified gold electrode, respectively.[65] $O_2^{\cdot-}$ was obtained via the hypoxanthine and XOD reaction, which had no catalytic current in the cyclic voltammogram, but had significant influence on the peak currents of oxidation and reduction of $O_2^{\cdot-}$.

3.3. Other Sensors

Campanella et al. developed a tyrosinase-immobilized biosensor for $O_2^{\cdot-}$ detection by applying a gaseous diffusion electrode for oxygen.[66] Phenol is converted to *o*-quinone through the reaction catalyzed by tyrosinase.

$$\text{phenol} + O_2 \xrightarrow{\text{tyrosinase}} \text{o} - \text{quinone} + H_2O \qquad (8)$$

The O_2 consumed in this reaction is immediately detected by the electrode.

$$O_2 + 4H^+ + 4e^- \xrightarrow{\text{electrode}} 2H_2O \qquad (9)$$

$O_2^{\cdot-}$ inhibits the tyrosinase reaction, and the percentage of inhibition is proportional to $O_2^{\cdot-}$ concentration.

Galactose oxidase (GAO) was used in a similar manner for $O_2^{\cdot-}$ detection.[66] GAO separately catalyses both the oxidation of primary alcohol to its aldehyde, and the reduction of O_2 to H_2O_2. This catalytic activity is inhibited in the presence of certain free radicals.

$$RCH_2OH + O_2 \xrightarrow{\text{GAO}} RCHO + H_2O_2 \qquad (10)$$

The percentage of inhibition of this oxidation reaction can be used to determine free radical concentration such as $O_2^{\cdot-}$ and NO. GAO is not specific enough for use under complex conditions.

4. PREPARATION OF AN SOD-IMMOBILIZED $O_2^{\cdot-}$ SENSOR

A sensitive and stable $O_2^{\cdot-}$ sensor[67] uses the specificity of the enzymatic reaction of SOD with $O_2^{\cdot-}$ without any effect from other oxidants and reductants. The electron mediator, ferrocene-carboxaldehyde was used for efficient electron transfer.[68–70] The SOD sensor directly measures the current produced by reoxidation of SOD instead of the current from electrode reaction with H_2O_2 (Fig. 6).

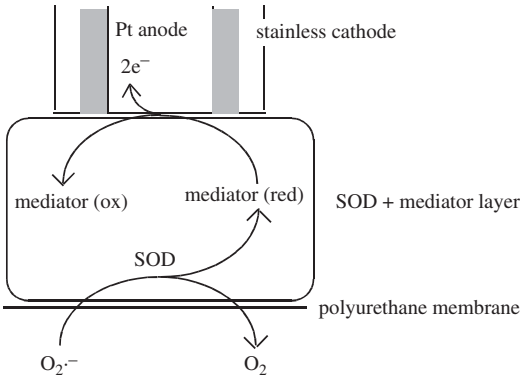

Fig. 6. SOD-immobilized superoxide sensor with a platinum wire electrode.

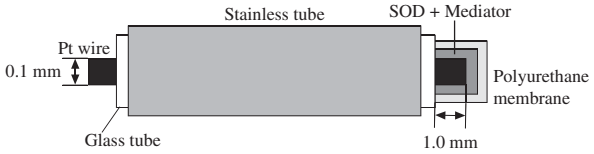

Fig. 7. Detailed schematic illustration of the SOD-immobilized superoxide sensor with a platinum wire electrode.

Figure 7 shows the structure of a simple SOD-immobilized $O_2^{\cdot-}$ sensor. The sensor consists of a polyurethane-coated platinum wire (diameter: 0.1 mm, and effective length: 1 mm) as the working electrode, a glass tube as the insulator, and a stainless tube (inner diameter: 0.94 mm) as the counter electrode. SOD (Mn-type) and the modulated ferrocene-carboxaldehyde mediator are immobilized on the electrode.

5. CALIBRATION OF THE SOD-IMMOBILIZED $O_2^{\cdot-}$ SENSOR

The SOD-immobilized $O_2^{\cdot-}$ sensor in Figure 7 is calibrated with $O_2^{\cdot-}$, which is enzymically produced in phosphate buffer saline (PBS) solution. The enzymatic reaction of xanthine and XOD synthesizes $O_2^{\cdot-}$ [Eq. (3)] as it does *in vivo*.[71] Figure 8 shows the experimental setup for calibration. The $O_2^{\cdot-}$ sensor is located in the detection chamber. Xanthine-PBS solution is perfused into the chamber at 2.8 ml/min. PBS solution with or without XOD is added at 0.2 ml/min to control $O_2^{\cdot-}$ production. Xanthine concentration in the detection chamber is 100 μM, and XOD concentration is controlled between 0 and 50 mU/ml by changing the flow rate. A charge of +0.5 V is applied to the working electrode, and the change in the current produced by the reoxidation reaction of SOD, which is reduced by dismutation of $O_2^{\cdot-}$, is measured by a potentiostat.

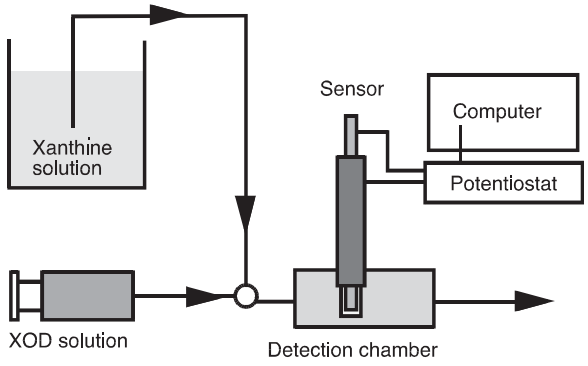

Fig. 8. Experimental setup for calibration of the SOD-immobilized superoxide sensor using superoxide produced by xanthine/XOD (see Fig. 7 for electrode detail).

Figure 9 shows typical traces of the measured current. When xanthine and XOD are mixed and injected into the chamber, the current gradually increases to the plateau level. When the XOD supply is stopped, the current decreases to baseline.

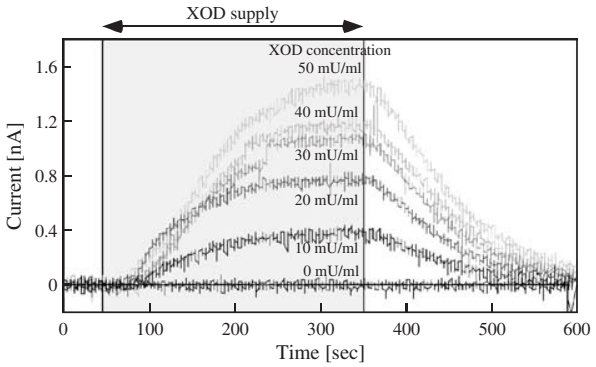

Fig. 9. Time courses of the current responses for superoxide produced by xanthine/XOD (0-50 mU/ml).

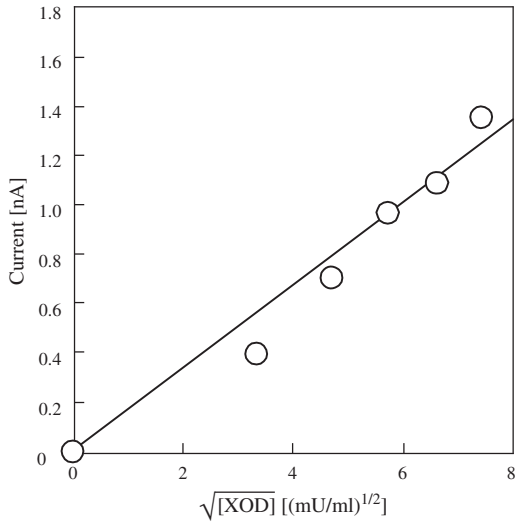

Fig. 10. Relationship of the peak current and XOD concentration (xthantine concentration: 100 μM, flow rate: 3 ml/min) measured by the SOD-immobilized superoxide sensor.

The plateau state level of $O_2^{\cdot-}$ $[O_2^{\cdot-}]$ plateau is expressed by equation 11:

$$[O_2^{\cdot-}]_{plateau} = \sqrt{\frac{k_1}{2k_2}}[XOD] \quad (11)$$

Where k_1 is the apparent rate constant of $O_2^{\cdot-}$ generation and k_2 is the non-enzymatic rate constant of dismutation reaction of $O_2^{\cdot-}$.[65] $[O_2^{\cdot-}]$ plateau is proportional to the square root of XOD concentration. Figure 10 shows the relationship between the plateau-level current and the square root of XOD concentration. A good linear relationship has been reported ($r^2 = 0.99$).[67]

6. MEASUREMENT OF $O_2^{\cdot-}$ RELEASED FROM ISOLATED ORGAN TISSUES

Oxidative stress is induced by a variety of factors such as toxic exposure to drugs, xenobiotics including endotoxin and carbon tetrachloride (CCl_4). It is known that XOD and NAD(P)H oxidase is activated by endotoxins, which increases $O_2^{\cdot-}$ production.[72,73] Miyasaka et al. used an endotoxin (lipopolysaccheide) in a rat model to measure increases in $O_2^{\cdot-}$ production by different organs.

Figure 11 shows the experimental setup for $O_2^{\cdot-}$ detection. The tissue samples heart, kidney, or liver of rat were put into a chamber located before the detection chamber. The working electrode was applied +0.5 V versus counter electrode, and the response current was monitored. After perfusion through the bypass and stabilization of the current, the flow channel was switched to the tissue-packed chamber. The $O_2^{\cdot-}$concentration in the perfusates was measured for 100 seconds, and then the flow channel was switched back to the bypass channel.

Figure 12 shows typical records of the measured current for isolated tissues (A: heart, B: liver, C: kidney). The large differences in the response currents were detected only in the endotoxin-shock group, indicating an increase in $O_2^{\cdot-}$ production by endotoxin in the kidney and liver.

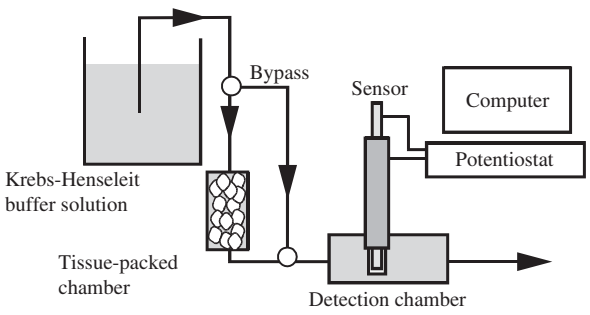

Fig. 11. Experimental setup for monitoring supeoxide released from isolated tissues.

RESEARCH ARTICLE

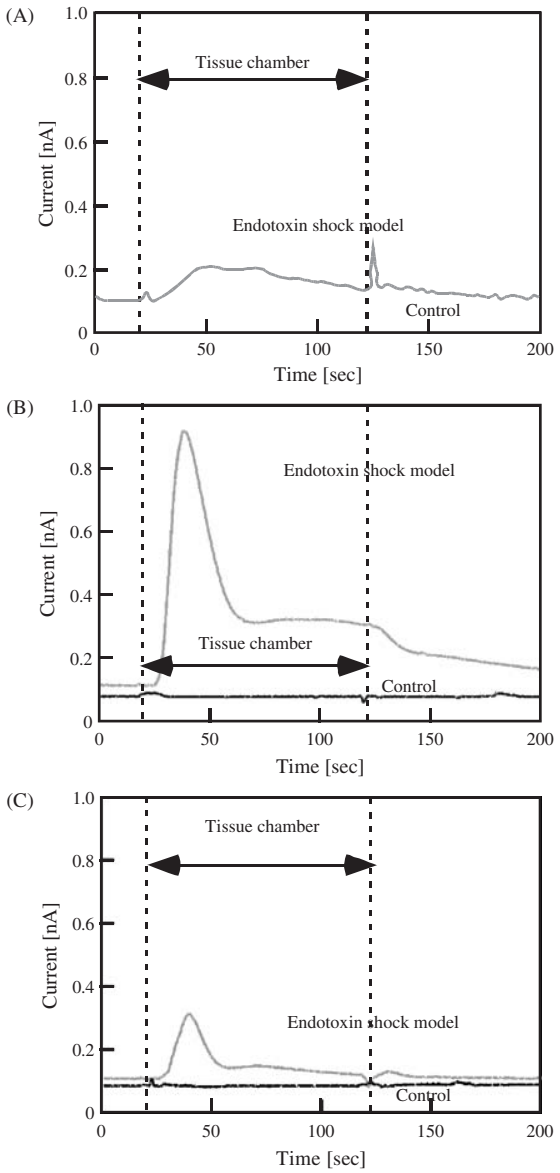

Fig. 12. Time courses of monitored superoxide released from isolated tissues: (A) heart, (B) liver, and (C) kidney.

7. THE FUTURE OF $O_2^{\cdot-}$ SENSORS

Krylow et al. miniaturized a disposable sensor that used a *cyt c*-modified thick-film electrode in the $O_2^{\cdot-}$ sensor, and measured H_2O_2 concentration by changing the applied potential.[74] They used a monolayer screen-printed gold-electrode on a ceramic substrate, which made the working electrode surface approximately three times larger than the geometrical area. Then they electroactively immobilized *cyt c* and measured re-oxidation current of *cyt c* reduced by $O_2^{\cdot-}$ like *cyt c*-based sensors. The sensitivity of this sensor was reported to be increased by a factor of about four compared with a metal-substrate sensor.

The monolayer *cyt c* electrodes are limited by the amount of *cyt c* immobilized on the electrode surface.[75] Beissenhirtz et al. immobilized 2–15 layers in an assembly of *cyt c* and a polyelectrolyte on a gold wire electrode.[75] This sensing mechanism was based on an electron transfer-modified gold electrode on which *cyt c* was immobilized.[56, 58] The best sensitivity for $O_2^{\cdot-}$ produced by hypoxanthine/XOD reaction was gained by a six-layer electrode in their series. Furthermore, thermal treatment at 45 °C for 30 min of the multilayer assembly offered sufficient electrode stability for serial sensor application and storage.

In a simplified approach to electrode preparation, Di et al. developed an SOD immobilized sensor based on a thin silica-PVA sol–gel film on a gold electrode.[76] The direct electron transfer between SOD and gold electrode occurred without any mediators or promoters, which enabled a fast response rate. The measurement mechanism of this sensor was based on the catalytic current of SOD immobilized on the electrode. These sensors would need to be biocompatible for *in vivo* use.

8. CONCLUSIONS

The key developments of $O_2^{\cdot-}$ sensors and the preliminary studies described in this review traces the progression of simple electrodes of coated wire, to carbon or ceramic substrates, micro arrays, and other chip designs. A number of design issues pertain to the next steps in moving beyond the proof-of-concept level if reliable, sensitive and specific simultaneous monitoring of intra- and extracellular $O_2^{\cdot-}$, production in real time *in vivo* is to be achieved. In practical terms, the sensitivity, and storage life of the electrodes must increase significantly. Electrode preparation time must be reduced through kits or mass production of complete electrodes. Further improvements in the self-assembly of multiple or mono-layers of electron-transfer promoters such as cysteine in thin film or thick-film designs could bring reproducible, quantitative applications within reach of researchers in small laboratories. $O_2^{\cdot-}$ sensors can be expected to be reported in basic and wider applications that include clarification of the oxygen-sensing pathway and regulatory relationships, identification of additional SOD family members, and characterization of effects of expression in various species in normal tissues, under disease conditions, and in response to drugs.

Lessons learned from development of the various $O_2^{\cdot-}$ sensors can be applied to other important molecules for other medical purposes such as subcutaneous monitoring. However, the long-term biocompatibility of the implant components remains an important hurdle to overcome.

References and Notes

1. C. A. Gunnett, D. D. Heistad, D. J. Berg, and F. M. Faraci, *Am. J. Physiol. Heart Circ. Physiol.* 279, H1555 (**2000**).
2. Y. Ohara, T. E. Peterson, H. S. Sayegh, R. R. Subramanian, J. N. Wilcox, and D. G. Harrison, *Circulation.* 92, 898 (**1995**).

3. N. N. Orie, W. Zidek, and M. Tepel, *Am. J. Hypertens.* 12, 1169 (**1999**).
4. J.-Z. Sun, X.-L. Tang, S.-W. Park, Y. Qiu, J. F. Turrens, and R. Bolli, *J. Ciln. Invest.* 97, 562 (**1996**).
5. K. Nakazono, N. Watanabe, K. Matsuno, J. Sasaki, T. Sato, and M. Inoue, *Proc. Natl. Acad. Sci.* 88, 10045 (**1991**).
6. Y. Taniyama and K. K. Griendling, *Hypertension* 42, 1075 (**2003**).
7. I. Fridovich, *Ann. NY Acid. Sci.* 893, 13 (**1999**).
8. Y. Ohara, T. E. Peterson, and D. G. Harrison, *J. Clin. Invest.* 91, 2546 (**1993**).
9. G. M. Rubanyi and P. M. Vanhoutte, *Am. J. Physiol. Heart Circ. Physiol.* 250, H822 (**1986**).
10. J. M. McCord and I. Fridovich, *J. Biol. Chem.* 241, 6049 (**1969**).
11. R. A. Weisiger and I. Fridovich, *J. Biol. Chem.* 248, 3582 (**1973**).
12. R. A. Weisiger and I. Fridovich, *J. Biol. Chem.* 248, 4793 (**1973**).
13. Y. Li, T.-T. Huang, E. J. Carlson, S. Melov, P. C. Ursell, J. L. Olson, L. J. Noble, M. P. Yoshimura, C. Berger, P. H. Chan, D. C. Wallace, and C. J. Epstein, *Nat Genet.* 11, 376 (**1995**).
14. S. L. Marklund, *Pro. Natl. Acad. Sci. USA* 79, 7634 (**1982**).
15. S. L. Marklund, *Biochem. J.* 266, 213 (**1990**).
16. S. L. Marklund, E. Hollme, and L. Hellner, *Clin. Chim. Acta.* 126, 41 (**1982**).
17. E. A. Ostrakhovitch and I. B. Afanas'ev, *Biochem. Pharmacol.* 62, 743 (**2001**).
18. P. Pietta, P. Simonetti, C. Gardana, and P. Mauri, *J. Pharm. Biomed. Anal.* 23, 223 (**2000**).
19. F. Nanjo, M. Mori, K. Goto, and Y. Hara, *Biosci. Biotechnol. Biochem.* 63, 1621 (**1999**).
20. T. Nakagawa and T. Yokozawa, *Food Chem. Toxicol.* 40, 1745 (**2002**).
21. P. Simonetti, C. Gardana, and P. Pietta, *J. Agric. Food Chem.* 49, 5964 (**2001**).
22. M. M. Tarpey and I. Fridovich, *Circ Res.* 89, 224 (**2001**).
23. T. Münzel, I. B. Afanas'ev, A. L. Kleschyov, and D. G. Harrison, *Arterioscler Thromb. Vasc. Biol.* 22, 1761 (**2002**).
24. M. M. Tarpey, D. A. Wink, and M. B. Grisham, *Am. J. Physiol. Regul. Integr. Comp. Physiol.* 286, R431 (**2004**).
25. B. Halliwell and M. Whiteman, *Br. J. Pharmacol.* 142, 231 (**2004**).
26. M. J. Green and H. A. O. Hill, *Methods in Enzymology* 105, 3 (**1984**).
27. J. Weaver, P. Tsai, G. L. Cao, L. J. Roman, and G. M. Rosen, *Anal. Biochem.* 320, 141 (**2003**).
28. L. Flohé and F. Ötting, *Methods in Enzymology.* 105, 93 (**1984**).
29. I. B. Afanas'ev, E. A. Ostrakhovitch, E. V. Mikhal'chik, and L. G. Korkina, *Luminescence.* 16, 305 (**2001**).
30. M. M. Tarpey, C. R. White, E. Suarez, G. Richardson, R. Radi, and B. A. Freeman, *Circ Res.* 84, 1203 (**1999**).
31. Y. Kambayashi and K. Ogino, *J. Toxicol. Sci.* 28, 139 (**2003**).
32. H. Gyllenhammar, *J. Immunol. Methods.* 97, 209 (**1987**).
33. Y. Li, H. Zhu, and M. A. Trush, *Biochim. Biophys. Acta.* 1428, 1 (**1999**).
34. Y. Li, H. Zhu, P. Kuppusamy, V. Roubaud, J. L. Zweier, and Michael A. Trush, *J. Biol. Chem.* 273, 2015 (**1998**).
35. M. P. Skatchkov, D. Sperling, U. Hink, A. Mülsch, D. G. Harrison, I. Sindermann, T. Meinertz, and T. Münzel, *Biochem. Biophys. Res. Commun.* 254, 319 (**1999**).
36. I. B. Afanas'ev, E. A. Ostrachovitch, and L. G. Korkina, *Arch. Biochem. Biophys.* 366, 267 (**1999**).
37. J. Vásquez-Vivar, N. Hogg, K. A. Pritchard, Jr., P. Martasek, and B. Kalyanaraman, *FEBS Letters* 403, 127 (**1997**).
38. S. I. Liochev and I. Fridovich, *Arch. Biochem. Biophys.* 337, 115 (**1997**).
39. S. J. Schreiber, D. Megow, A. Raupach, I. V. Victorov, and U. Dirnagl, *Brain Res.* 703, 227 (**1995**).
40. M. A. Trush, M. E. Wilson, and K. Van Dyke, *Methods Enzymol.* 57, 462 (**1978**).
41. S. Ushiroda, Y. Maruyama, and M. Nakano, *Jpn. Heart J.* 38, 91 (**1997**).
42. K. Yamaguchi, D. Uematsu, Y. Itoh, S. Watanabe, and Y. Fukuuchi, *Keio J. Med.* 51, 201 (**2002**).
43. G. Rothe and G. Valet, *J. Leukoc. Biol.* 47, 440 (**1990**).
44. H. Zhao, S. Kalivendi, H. Zhang, J. Joseph, K. Nithipatikom, J. Vásquez-Vivar, and B. Kalyanaraman, *Free Radic. Biol. Med.* 34, 1359 (**2003**).
45. O. Myhre, J. M. Andersen, H. Aarnes, and F. Fonnum, *Biochem. Pharmacol.* 65, 1575 (**2003**).
46. H. Possel, H. Noack, W. Augustin, G. Keilhoff, and G. Wolf, *FEBS Lett.* 416, 175 (**1997**).
47. P. Wang and J. L. Zweier, *J. Biol. Chem.* 271, 29223 (**1996**).
48. M. Dambrova, L. Baumane, I. Kalvinsh, and J. E. S. Wikberg, *Biochem. Biophys. Res. Commun.* 275, 895 (**2000**).
49. H. Zhang, J. Joseph, J. Vasquez-Vivar, H. Karoui, C. Nsanzumuhire, P. Martásek, P. Tordo, and B. Kalyanaraman, *FEBS Letters* 473, 58 (**2000**).
50. C. J. McNeil, K. A. Smith, P. Bellavite, and J. V. Bannister, *Free Rad. Res. Comms.* 7, 89 (**1989**).
51. C. J. McNeil, K. R. Greenough, P. A. Weeks, C. H. Self, and J. M. Cooper, *Free Rad. Res. Comms.* 17, 399 (**1992**).
52. R. H. Fabian, D. S. DeWitt, and T. A. Kent, *J. Cereb. Blood Flow Metab.* 15, 242 (**1995**).
53. R. H. Fabian, J. R. Perez-Polo, and T. A. Kent, *J. Neurosci. Res.* 60, 795 (**2000**).
54. K. Tammeveski, T. T. Tenno, A. A. Mashirin, E. W. Hillhouse, P. Manning, and C. J. McNeil, *Free Rad. Biol. Med.* 25, 973 (**1998**).
55. P. Manning, C. J. McNeil, J. M. Cooper, and E. W. Hillhouse, *Free Rad. Biol. Med.* 24, 1304 (**1998**).
56. B. Ge and F. Lisdat, *Anal. Chim. Acta* 454, 53 (**2002**).
57. R. Büttemeyer, A. W. Philipp, J. W. Mall, B. Ge, F. W. Scheller, and F. Lisdat, *Microsurgery* 22, 108 (**2002**).
58. S. Ignatov, D. Shishniashvili, B. Ge, F. W. Scheller, and F. Lisdat, *Biosens. Bioelectron.* 17, 191 (**2002**).
59. M. K. Beissenhitz, R. C. H. Kwan, K. M. Ko, R. Renneberg, F. W. Scheller, and F. Lisdat, *Phytother. Res.* 18, 149 (**2004**).
60. L. Campanella, G. Favero, and M. Tomassetti, *Anal. Lett.* 32, 2559 (**1999**).
61. L. Campanella, G. Favero, L. Persi, and M. Tomassetti, *J. Pharm. Biomed. Anal.* 23, 69 (**2000**).
62. L. Campanella, G. Favero, L. Persi, and M. Tomassetti, *J. Pharm. Biomed. Anal.* 24, 1055 (**2001**).
63. L. Campanella, A. Bonanni, and M. Tomassetti, *J. Pharm. Biomed. Anal.* 32, 725 (**2003**).
64. L. Campanella, A. Bonanni, G. Favero, and M. Tomassetti, *Anal. Bioanal. Chem.* 375, 1011 (**2003**).
65. B. Ge, F. W. Scheller, and F. Lisdat, *Biosens. Bioelectron.* 18, 295 (**2003**).
66. L. Campanella, L. Persi, and M. Tomassetti, *Sensors and Actuators B* 68, 351 (**2000**).
67. K. Endo, T. Miyasaka, S. Mochizuki, S. Aoyagi, N. Himi, H. Asahara, K. Tsujioka, and K. Sakai, *Sensor and Actuators B* 83, 30 (**2002**).
68. T. Miyasaka, Y. Taniyama, K. Sakai, and Y. Yoshimi, *ASAIO J.* 43, M505 (**1997**).
69. T. Miyasaka, Y. Yoshimi, and K. Sakai, *J. Chem. Eng. Jpn.* 31, 29 (**1998**).
70. S. Aoyagi, Y. Suzuki, K. Sakai, T. Miyasaka, and Y. Yoshimi, *Electrochem.* 69, 251 (**2001**).
71. I. Fridovich, *J. Biol. Chem.* 245, 4053 (**1970**).

72. P. M. Hassoun, F.-S. Yu, C. G. Cote, J. J. Zulueta, R. Sawhney, K. A. Skinner, H. B. Skinner, D. A. Parks, and J. J. Lanzillo, *Am. J. Respir. Crit. Care Med.* 158, 299 **(1998)**.
73. R. P. Brandes, G. Koddenberg, W. Gwinner, D.-Y. Kim, H.-J. Kruse, R. Busse, and A. Mügge, *Hypertension.* 33, 1243 **(1999)**.
74. A. V. Krylow, M. Beissenhirtz, H. Adamzig, F. W. Scheller, and F. Lisdat, *Anal. Bioanal. Chem.* 378, 1327 **(2004)**.
75. M. K. Beissenhitz, F. W. Scheller, and F. Lisdat, *Anal. Chem.* 76, 4665 **(2004)**.
76. J. Di, S. Bi, and M. Zhang, *Biosens. Bioelectron.* 19, 1479 **(2004)**.

SENSOR LETTERS
Vol. 4, 155–159, 2006

Efficient Taste Sensors Made of Bare Metal Electrodes

Carlos E. Borato[1,2], Fábio L. Leite[1,2], Osvaldo N. Oliveira, Jr.[1,*], and Luiz H. C. Mattoso[2]

[1] *Instituto de Física de São Carlos, Universidade de São Paulo, Caixa Postal 369, 13560-970 São Carlos, SP, Brazil*
[2] *EMBRAPA Instrumentação Agropecuária, CP 741, 13560-970, São Carlos, SP, Brazil*

(Received: 22 March 2006. Accepted: 13 April 2006)

In attempts to reduce cost and increase sensitivity of taste sensors we have found out that a novel, inexpensive set of chrome-deposited electrodes may be used in impedance spectroscopy measurements for sensing with great performance. High sensitivity is demonstrated by detecting, reproducibly, μM amounts of NaCl, HCl, sucrose, which represent basic tastes, and Cu^{2+} ions. This high sensitivity can also be used to distinguish complex liquids such as wines. Surprisingly, there was no need to cover the metal electrodes with nanostructured films of organic sensitive materials, which further reduces the cost of the sensing units. This sensitivity is attributed to interface effects between the metal electrodes and the liquid samples, which may be investigated with atomic force spectroscopy as illustrated in this paper.

Keywords: Chrome-Deposited Electrodes, Basic Taste, Heavy Metal, Taste Sensors.

RESEARCH ARTICLE

1. INTRODUCTION

The advent of taste sensors based on impedance spectroscopy with sensing units obtained with nanostructured films has brought considerable advances in terms of sensitivity to detect trace amounts of substances in a solution and the ability to distinguish among complex liquids such as different types of wine, coffee, juices, and milk.[1–4] Among the advantages of this type of taste sensor are no need of a reference electrode and the possibility to analyze non-electrolyte liquids.[5] The main challenge now is to evolve from prototypes to costly-effective industrial production, which is being pursued in our group. A number of steps may be taken in order to optimize the sensor performance and reduce costs, including the search for materials that bring higher performances at lower costs, tests of reproducibility and robustness of the sensing units, and cheaper systems for measuring the electrical response. In this communication we show that an inexpensive array of chrome-deposited electrodes can be used to detect low amounts (μM) of substances representing basic tastes and a heavy metal. This sensitivity also makes it possible to distinguish between different wines.

2. EXPERIMENTAL DETAILS

The electrodes were obtained by electrochemical deposition of chrome on a glass slide, according to a pre-printed pattern of 5 pairs of fingers with dimensions of $27.25 \times 2.40 \times 0.04$ mm, separated by 0.1 mm from each other. Five units of such electrodes—with no deposited film on top of the chrome—were assembled on a fiberglass slide to form an array. The electrodes were connected to the measuring apparatus through a Card edge connector. The array was placed onto a small trough in which the liquid sample is placed. Figure 1 shows the sensor array and the trough to hold the liquid samples. The solutions of NaCl, HCl, and sucrose were prepared from a stock solution of 50×10^{-3} mol/L in distilled water, from which dilutions were made to achieve concentrations of 20, 10, 5, 1×10^{-3} mol/L and 10^{-6} mol/L. Measurements were also performed with solutions of $CuSO_4 \cdot 5H_2O$ in Milli-Q water at various concentrations, as will be presented in the next Section. The red and white wines were provided by Brazilian producers Embrapa, Miolo, and Salton, and used as received. Impedance measurements were carried out with a Solartron 1260A impedance/gain phase analyzer at 200, 400, 600, 800, and 1 KHz, and bias voltage of 50 mV, with the electrodes being immersed into the liquid samples. The array remained immersed for 20 minutes in each of the solution before the measurements, carried out at 25 °C. After each measurement the units were washed with distilled water. Principal components analysis was employed to analyze the data obtained from the various sensing units for each liquid studied, using MATLAB version 6.1 (for a detailed description of PCA analysis see Ref. [6]).

*Corresponding author; E-mail: chu@if.sc.usp.br

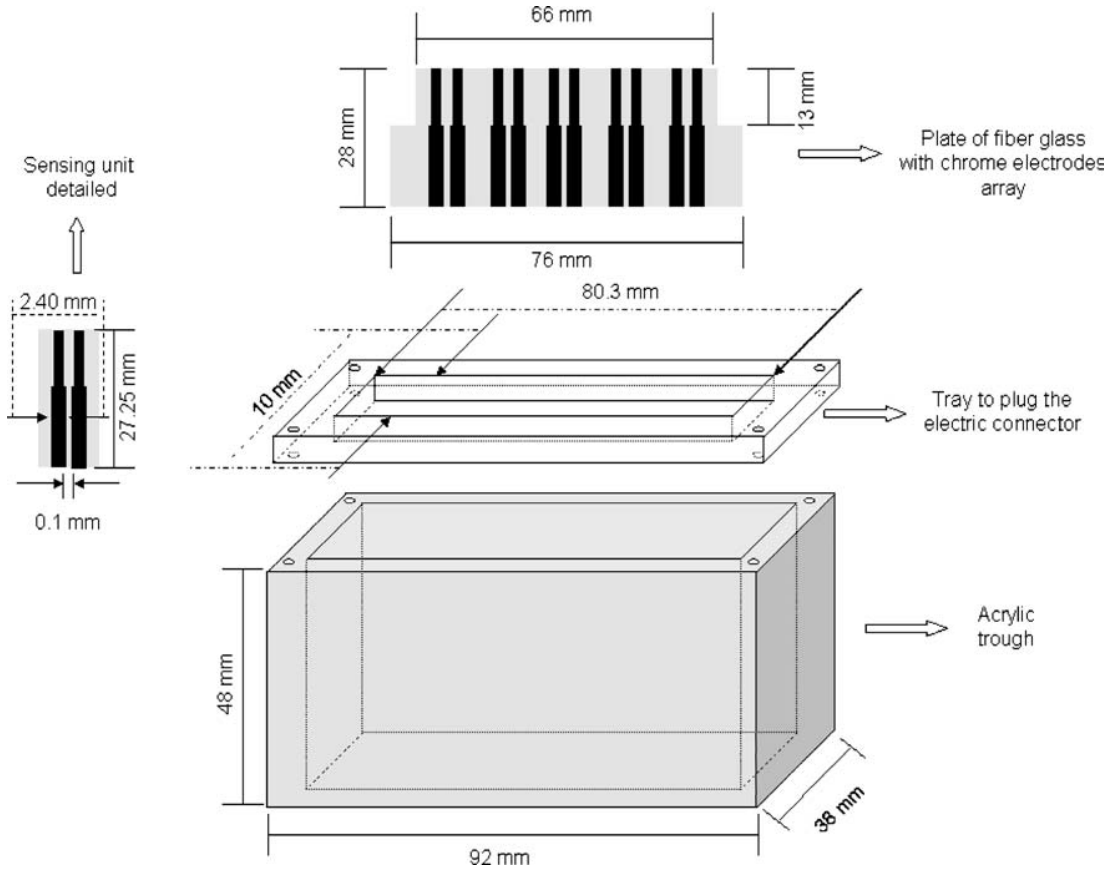

Fig. 1. Detailed diagram of the sensing units of electrodeposited chrome and the trough made to hold the liquid sample and insert the sensor array.

3. RESULTS AND DISCUSSION

The sensitivity to μM concentrations of the basic tastes, namely sweet, salty, and sour is illustrated in PCA plots of Figure 2. For these measurements, an array of 5 sensors was employed, none of which had a film adsorbed on them; they were made of bare metal. The data were extracted from impedance spectroscopy measurements, and refer to the capacitance of the system at 200 Hz. For all frequencies studied, viz. 200, 400, 600, 800, and 1000 Hz, it is possible to distinguish between the different tastes. However, only at low frequencies (see results for 200 Hz in Fig. 2) is it possible to distinguish solutions at the μM concentrations from pure water. The reason for the higher sensitivity at 200 Hz is associated with the physical phenomena governing the electrical response. Taylor and MacDonald[7] showed that at higher frequencies (>10 kHz), the response is dominated by the electrode capacitance. At 1 kHz, the response from the film dominates, whereas at 100–200 Hz the double-layer governs the response. Because the high sensitivity appears to be associated with surface phenomena, changes in the double layer are expected to be more prone to occur when the liquid is modified by trace amounts of substances.

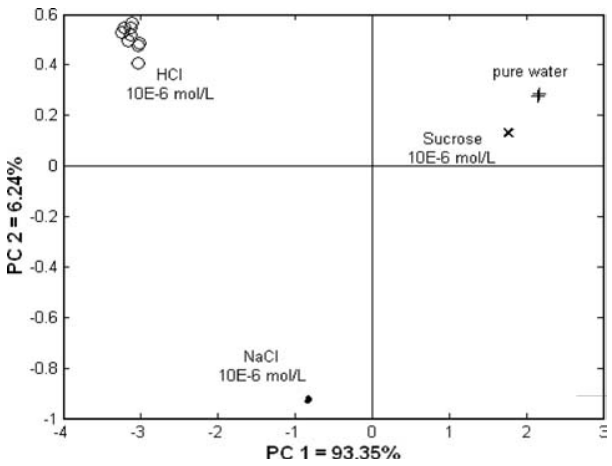

Fig. 2. PCA plots for sweet ($\times$), salt ($\bullet$), sour ($\circ$), and pure water ($+$) substances at $f = 200$ Hz.

It is surprising that the array could be made of sensing units that were nominally identical. (By "nominally identical" we mean that the chrome electrodes were produced with the same experimental procedure of electrodeposition. However, with this method the electrodes are not very homogeneous, varying particularly in morphology or oxide

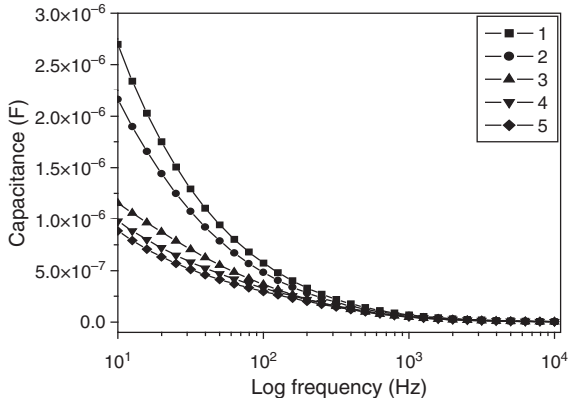

Fig. 3. Capacitance versus frequency plot showing that each of the sensing units has a characteristic electric curve. NaCl solution of $C = 5 \times 10^{-3}$ mol/L. The symbols corresponding to the sensing units 1 through 5 are given in the inset.

layer coating the metal). Therefore, because the electrical response depends on the interface effects, distinct responses were obtained for these nominally identical electrodes, as depicted in Figure 3. Cross-sensitivity can then be achieved with electrodes of the same metal, but with different morphologies. The capacitance decreases with increasing frequencies, as illustrated in Figure 3 for NaCl, and is higher for higher concentrations of NaCl, KCl, and HCl while for sucrose the capacitance decreases with increasing concentrations (results not shown). For each of the tastants, a pattern is observed regardless of the concentration. Also observed is a large difference in capacitance for sucrose in comparison to the other substances because sucrose solution contains almost no ions (it is not an electrolyte).

In order to prove that the cross-sensitivity obtained with bare metal electrodes could be useful in distinguishing samples with low detection limits, we performed a series of experiments (including control experiments) varying the substances. For instance, the distinguishing ability of the sensor array for concentrations at the μM level was tested for $CuSO_4$, with measurements taken on different days and with samples prepared in different days. The results shown in Figure 4 illustrate dispersion in the measurements for pure water if the time for equilibration differs, though it is clear that the samples containing $CuSO_4$ could be distinguished. We felt, however, that we had to check whether the differences in the pure water samples could not jeopardize the conclusions drawn so far, and decided to perform a number of control experiments. The results of these control experiments may be summarized as follows.

The mere manipulation of water in changing from one flask to the other may generate pure water samples that are distinguishable in the electrical measurements, probably because impurities are non-deliberately included. The electrical response may also vary with time due to ageing affects (e.g., from oxygen uptake). In fact, the electrical

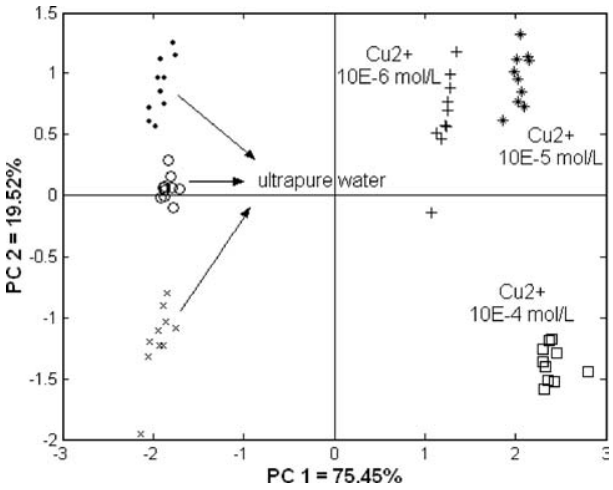

Fig. 4. PCA plot showing the addition of amounts of Cu^{2+} in ultrapure water: (•), (○), (×) pure water, (+) 10^{-6} mol/L of Cu^{2+}, (∗) 10^{-5} mol/L of Cu^{2+} and (□) 10^{-4} mol/L of Cu^{2+}.

measurements serve as excellent control tool for the water purity, similarly to what Taylor et al.[8] suggested for lateral conductance in Langmuir monolayers, which was found to be affected strongly by trace amounts of impurities in the water subphase. In order to be sure that we could detect small amounts of tastants or ions deliberately introduced in the liquid samples, we performed the experiments depicted in Figure 5. In one set, measurements were taken with a pure water sample within intervals of 30 min. For the 31st measurement, pure water was added to the sample (i.e., no impurity was deliberately introduced, but the sample suffered manipulation). A change in capacitance could be measured, but this was negligible if the scales used were chosen to accommodate the data for the incorporation of 1 μM of $CuSO_4$, which was done in the other set of experiments. The results of the latter are shown in the upper curve, indicating that the measured capacitance changed more appreciably when adding the Cu^{2+} ions. If a lower concentration of $CuSO_4$ was used in the measurement, then it was difficult to distinguish between this solution or a manipulated sample of pure water (with addition of

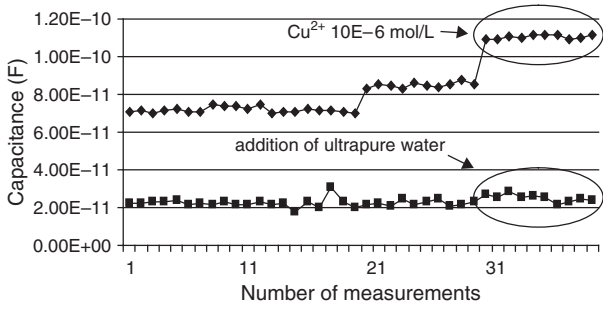

Fig. 5. Comparison among addition of 10^{-6} mol/L of Cu^{2+} (◆) and ultrapure water (■) in ultrapure water. Note in the circled regions that addition of 10^{-6} mol/L of Cu^{2+} can be distinguished from the control measurements, while the addition of pure water cannot.

RESEARCH ARTICLE

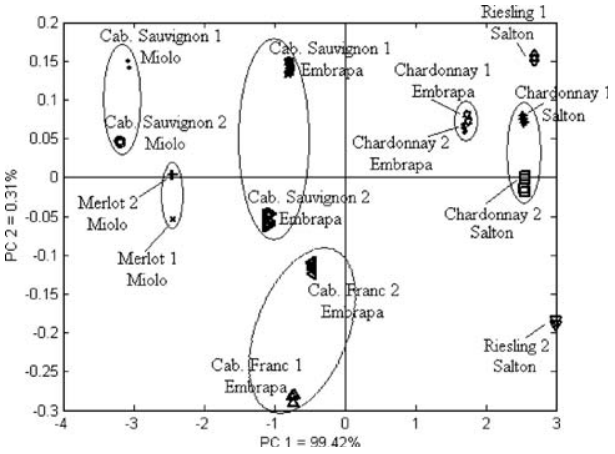

Fig. 6. PCA plots for capacitance data at 1 kHz for red wine samples of Cabernet Sauvignon Miolo 2000, Merlot Miolo 2000, Cabernet Sauvignon Embrapa 1999, Cabernet Franc Embrapa 1999, in addition to white wines Chardonnay Salton 1999, Chardonnay Embrapa 1999, Riesling Salton 1998. In each case measurements were made with 2 bottles, named 1 and 2. The results indicate that the sensor is capable of distinguishing wines of different grapes, and wines from the same grape but different producers (e.g., Embrapa and Miolo for Cabernet Sauvignon).

more pure water). From these results we infer that incorporation of $CuSO_4$ in concentrations below 1 μM could not be distinguished from the dispersion in the data due to mere manipulation of water samples, but the efficacy of the sensor array was demonstrated for concentrations equal to or above 1 μM.

Analogously to previous works,[2,9] we exploited the sensitivity of the taste sensors to distinguish among wines. The PCA plots in Figure 6 indicate that the sensor array is able to distinguish between wines of the same brand but different grapes, namely Cabernet Sauvignon and Merlot from the company Miolo (Brazil), and wines of the same grape but different produces (e.g., Cabernet Sauvignon from Miolo and Embrapa).

The explanation for the high sensitivity of the sensor arrays (electronic tongues) may lie on the strong dependence of electrical properties of interface systems on the liquid environment next to the interface. This is actually similar to the findings by Taylor et al.,[8] who pointed out that bulk measurements were not sufficient to detect the level of impurities in the water that surface measurements could do. Indeed, with force spectroscopy measurements carried out with an atomic force microscope (AFM) we show that water is aged upon exposure to air. Figure 7a is typical force curve obtained in water on mica surface (pH $\sim$ 7), which shows the presence of van der Waals interactions for short times (<1 h) (see more details on force spectroscopy in Ref. [10]). We employed a mica substrate in this experiment, rather than the chrome electrodes, because at the pH of water the appearance of the double-layer force is readily appreciated, being illustrative of the importance of interface effects.

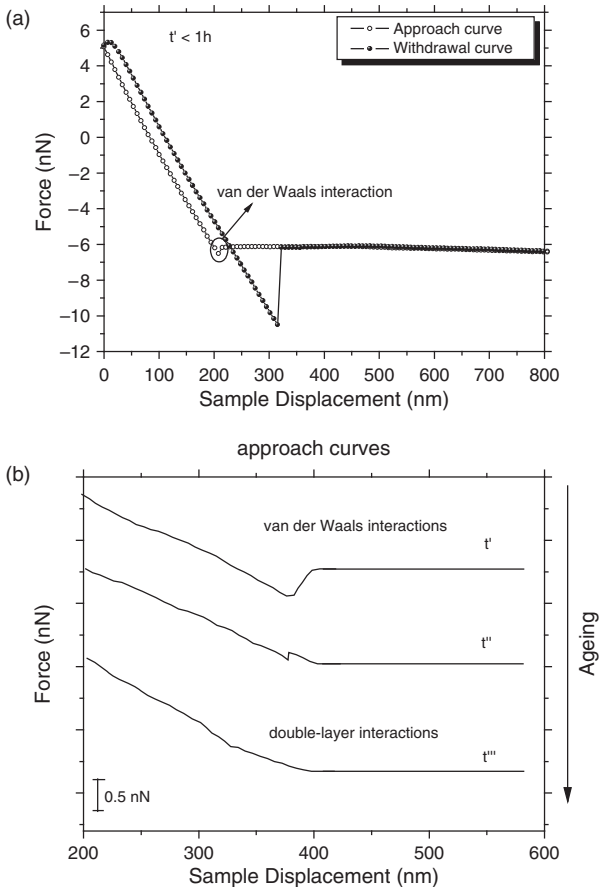

Fig. 7. (a) Typical force curve for a AFM tip and mica sample immersed in water and (b) schema (approach curves) showing water ageing for various periods of time (increasing in the direction $t' < t'' < t'''$). The difference between each of two times, $t' - t''$ or $t'' - t'''$ is 2 h.

The presence of impurities in the cell is found to affect the force curves. Here we employed pure water to investigate water ageing during several times, which are significantly altered as shown schematically in Figure 7b. For short periods, the curve displays a minimum with the distance between the tip of silicon nitrite ($\varepsilon_{\text{tip}} = 7.4$, $k_c = 0.03$ N m^{-1}) and a flat mica surface ($\varepsilon_{\text{mica}} = 5.4$),[11] which indicates the predominance of attractive van der Waals interactions. For longer times, repulsive double-layer forces dominate until the force curve is practically purely repulsive (for t'''). The double-layer contribution is repulsive for the following reason: It is energetically favorable for a surface charge to be surrounded by a medium with large dielectric constant like water. If the tip approaches the double layer region it replaces the water. Since the tip material has a lower dielectric constant than water, the situation is now energetically unfavorable and the tip is repelled by the double layer charge.[12] Ageing of the water is accompanied by a change to lower pH values, which then increases the charge of the silicon nitrite tip (whose isoelectric point is at pH 6.3[12]), whereas mica is negatively charged. The net result is an increase in the repulsive, double-layer force.

4. CONCLUSIONS

The results from atomic force spectroscopy indicate clearly that a very thin layer of water adjacent to the metallic substrates is affected when small changes occur in the liquid, as was the case of the ageing of water. This may be behind the high sensitivity of the sensing units, for interface phenomena—particularly those associated with double-layers—dominate the electrical response of the sensor at the frequency (200 Hz) where sensitivity was maximum. It is also consistent with the finding that sensitivity was decreased when nanostructured films deposited onto the electrodes were replaced by cast, thicker films.[13] The surprising feature of the sensing units used here was the absence of any sensitive organic material. It appears that, being a predominantly interface effect, the changes in morphology due to irregularities in the chrome deposition are sufficient to lead to distinct electrical responses that can be exploited to produce as a characteristic fingerprint of a given liquid in a sensor array. The sensitivity toward basic tastes of the sensor array presented here is similar to that obtained with interdigitated gold electrodes covered with nanostructured films,[13] while the distinguishing ability for different wines also compares with previous works.[2, 9, 14] The obvious advantage of the array made with bare metal electrodes is the simplicity and low cost. It should be stressed, nevertheless, that state-of-the-art sensors are expected to include coating materials that may also respond specifically to the analyte, as indicated by arrays containing immobilized enzymes.[15]

Acknowledgments: This work was supported by FAPESP, CNPq, Rede Nanobiotec256 and CT-Hidro/MCT (Brazil). The authors are grateful to Dr. Wilson T. Lopes for useful discussions.

References and Notes

1. B. Lawton and R. Pethig, *Measure. Sci. Technol.* 4, 38 (**1993**).
2. A. Riul, Jr., H. C. Souza, R. R. Malmegrim, D. S. Santos, Jr., A. C. P. L. F. Carvalho, F. J. Fonseca, O. N. Oliveira, Jr., and L. H. C. Mattoso, *Sens. Actuators B Chem* 98, 77 (**2004**).
3. C. E. Borato, A. Riul, Jr., M. Ferreira, O. N. Oliveira, Jr., and L. H. C. Mattoso, *Instrumentation Science and Technology* 32, 21 (**2004**).
4. A. Legin, A. Rudnitskaya, Y. Vlasov, C. Di Natale, F. Davide, and A. D'Amico, *Sens. Actuators B Chem.* 44, 291 (**1997**).
5. A. Riul, Jr., R. R. Malmegrim, F. J. Fonseca, and L. H. C. Mattoso, *Biosens. Bioelectron.* 18, 1365 (**2003**).
6. K. R. Beebe, R. J. Peel, and M. B. Seasholtz, Chemometrics: A Pratical Guide, John Wiley and Sons, New York (**1998**).
7. D. M. Taylor and A. G. MacDonald, *J. Phys. D.-Appl. Phys.* 20, 1277 (**1987**).
8. D. M. Taylor, O. N. Oliveira, Jr., and H. Morgan, *Thin Solid Films* 173, L141 (**1989**).
9. A. Riul, Jr., D. S. Dos Santos, Jr., K. Wohnrath, R. Di Thommazo, A. A. C. P. L. F. Carvalho, F. J. Fonseca, O. N. Oliveira, Jr., D. M. Taylor, and L. H. C. Mattoso, *Langmuir* 18, 239 (**2002**).
10. F. L. Leite and P. S. P. Herrmann, *J. Adhesion Sci. Technol.* 19, 365 (**2005**).
11. T. J. Senden and C. J. Drummnond, *Colloids Surf. A* 94, 29 (**1995**).
12. E. F. De Souza, G. Ceotto, and O. Teschke, *J. Mol. Catalysis A* 167, 235 (**2001**).
13. M. Ferreira, A. Riul, Jr., K. Wohnrath, F. J. Fonseca, O. N. Oliveira, Jr., and L. H. C. Mattoso, *Anal. Chem.* 75, 953 (**2003**).
14. A. Guadarrama, J. A. Fernández, M. Íñiguez, J. Souto, and J. A. de Saja, *Analytica Chimica Acta* 411, 193 (**2000**).
15. V. Zucolotto, A. P. A. Pinto, T. Tumolo, M. L. Moraes, M. S. Baptista, A. Riul, Jr., A. P. U. Araújo, and O. N. Oliveira, Jr., *Biosens. Bioelectron.* 21, 1320 (**2006**).

SENSOR LETTERS
Vol. 4, 160–164, 2006

RESEARCH ARTICLE

Kinetic Assay of Trypsin with a Wireless Magnetoelastic Sensor

Shihui Wu[1], Qingyun Cai[1,*], and Craig A. Grimes[2]

[1] *Department of Chemistry, State Key Laboratory of Chemo/Biosensing and Chemometrics, Hunan University, Changsha 410082, P. R. China*
[2] *Department of Electrical Engineering, and Department of Materials Science and Engineering, The Pennsylvania State University, University Park, Pennsylvania 16802, USA*

(Received: 2 February 2006. Accepted: 15 February 2006)

A wireless magnetoelastic trypsin sensor is fabricated by first coating a magnetoelastic ribbon-like sensor with a pH-sensitive polymer and then upon it a layer of trypsin. In response to an externally applied time-varying magnetic field, the magnetoelastic sensor mechanically vibrates at a characteristic frequency that is inversely dependent upon the mass of the attached film. As the magnetoelastic sensor is magnetostrictive, the mechanical vibrations of the sensor launch magnetic flux that can be detected remotely from the sensor using a pickup coil. The trypsin-catalyzed hydrolysis of N-α-benzoyl-L-arginine ethyl ester (BAEE) decreases the ambient pH, resulting in the pH-responsive polymer shrinking, and consequently the resonance frequency of the sensor increasing due to the decreased mass loading. The optimum pH and temperature are investigated. The kinetic parameters of both the immobilized and free trypsin are measured. Immobilization of trypsin resulted in the enzyme activity decreasing by about 50%. The magnetoelastic sensor demonstrates a linear shift in resonance frequency with trypsin concentration between 24 U/ml and 360 U/ml with a trypsin detection limit of 24 U/ml, and can be used to detect the substrate BAEE ranging from 0.4 mM to1.5 mM.

Keywords: Trypsin, Enzyme, Remote Sensor, Magnetoelastic Biosensor.

1. INTRODUCTION

Trypsin is a widely used pancreatic serine protease, commonly used for protein cleavage because of its high specificity and ability to digest insoluble or adsorbed protein. Trypsin cleaves peptide bonds at the carboxylate terminal side of lysine and arginine residues. Much attention has been paid to proteases in relation to bacterial identification.[1–3] Protease in serum or other body fluids provides important information on various pathological conditions, particularly in the diagnosis of human pancreatic diseases.[4] The detection and immobilization of trypsin are of great interests since trypsin can not be easily retrieved from the reaction systems.

Immobilized trypsin are widely employed in the field of food and clinical testing industries, such as the electrochemical trypsin sensors for the rapid and quantitative measurement of protein solution,[5,6] the analysis of enzyme inhibitors[7] and as microreactors for peptide mapping.[8] A variety approaches have been developed for trypsin immobilization: trypsin covalently immobilized on epoxy-modified silica monolithic support with a single reaction step,[9] poroszyme immobilized trypsin cartridges,[10] and trypsin-encapsulated sol–gel,[11,12] to cite but a few examples. Several methods have been proposed for the kinetic detection of trypsin, such as capillary electrophoresis (CE),[8] fluorimetry,[13] surface acoustic wave-impedance sensing analysis,[14] electrochemical assay of trypsin with protamine as substrate and polymer membrane as sensing layer[15,16] and immunoradiometric assay using two monoclonal antibodies directed to human trypsin 1 for the measuring of trypsin (ogen) in biological fluids.[17] These methods differ markedly in sensitivity.

In this work a low cost, easily fabricated, wireless magnetoelastic trypsin sensor was fabricated and used for the kinetic detection of trypsin. In a time-varying magnetic field, magnetoelastic materials efficiently translate magnetic to mechanical energies, so the magnetoelastic ribbon longitudinally vibrates at a fundamental characteristic resonance frequency f_r that inversely depends on the sensor

*Corresponding author; E-mail: qycai0001@hnu.cn

 1546-198X/2006/4/160/005 doi:10.1166/sl.2006.010

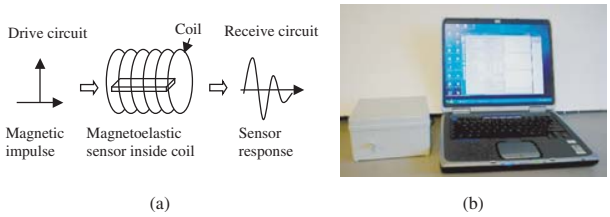

Fig. 1. Schematic showing operation of the wireless magnetoelastic sensor (a) and the magnetoelastic sensor-reader box (b, on left) connected to a portable computer via a RS232 port. The computer interface allows for user-control of measurement parameters, data display, and data storage.

length L. With sensor width and thickness given by: much smaller than length Young's modulus E, and density ρ[18] the resonance frequency is

$$f_r = \sqrt{\frac{E}{\rho}}\frac{1}{2L} \tag{1}$$

A small mass load Δm evenly deposited on a sensor of mass m_0 shifts the measured resonant frequency by:[18]

$$\Delta f = -f_r\frac{\Delta m}{2m_0} \tag{2}$$

The frequency shift is downward with increasing mass. Figure 1 illustrates the operating principle of the magnetoelastic sensor. A magnetic field is used to excite the sensor, causing it to mechanically vibrate at a resonance frequency which shifts in response to mass loading.[19, 20] The mechanical vibrations of the magnetostrictive material, in turn, generate a magnetic flux that can be remotely detected using a simple pick-up coil. A frequency counting technique, previously described,[21] implanted by use of micro-processor based electronics is employed to determine the resonance frequency of the magnetoelastic sensor. No physical connections between the sensor and the detection system are required for signal telemetry, nor is precise alignment necessary per optical telemetry systems The facile wireless capabilities of the magnetoelastic sensor platform makes it a powerful tool for *in situ* and *in vivo* analyses. Published applications include glucose, microbial biosensors[22, 23] and blood coagulation monitoring.[24]

The trypsin biosensor in this paper is fabricated by first coating the magnetoelastic sensor with a pH-sensitive polymer and then upon it a layer of trypsin. The trypsin catalyzed hydrolysis of BAEE results in the formation of H^+ which cause the pH responsive polymer to shrink and, in turn, consequently increase the resonance frequency due to the decreased sensor mass load. The sensor transduction signal is derived from the polymer mass difference between its relatively shrunken state in acidic solution and relatively swollen state in alkaline solution. In alkaline solution, the polymer is electrically charged due to acrylic acid dissociation and additional swelling arises from the osmotic pressure exerted by the charged carboxylic group and its mobile counterions.[25] Water molecules enter the polymer to lower the concentration of network ions until an equilibrium of osmotic pressure is achieved both inside and outside the polymer.

The effect of pH and temperature on the enzymatic activity of trypsin were investigated with kinetic parameters (the Michaelis-Menten constant, K_m, and the maximum initial rate V_{max}) estimated by using the Lineweaver-Burk plot.[26] As the immobilization process generally causes a decrease in enzyme activity that is a key factor while trypsin is used as microreactors for peptide mapping, the effect of immobilization on the trypsin activity was investigated. Using the proposed sensor the enzymatic hydrolysis process can be wirelessly monitored.

2. EXPERIMENTAL DETAILS

2.1. Materials

Trypsin (EC3.4.21.4, 1000∼1500 BAEE units/mg), bovine serum albumin (BSA) were obtained from Sigma Co., *N*-α-Benzoyl-L-arginine ethyl ester hydrochloride(BAEE), glutaric dialdehyde (25 wt% in water) were purchased form Sinopharm Chemical Reagent Co., Ltd. (China), Acrylic acid, poly (ethylene glycol) diacrylate (PEGD), and isooctyl acrylate were purchased from Aldrich (Milwaukee, WI) and the inhibitor, monomethyl ether hydroquinone was removed using an inhibitor remover disposable column (Aldrich) prior to use. 2,2′-Azobis(isobutyronitrile) (AIBN), dimethylaminopropyl-3-ethylcarbodiimide (EDC), and *N*-hydroxysuccinimide (NHS) were purchased from Aldrich and used as received. Bayhydrol 110, an anionic dispersion of an aliphatic polyester urethane resin in water/*N*-methyl-2-pyrrolidone solution (50% w/v) was purchased from Bayer Corp. (Pittsburgh, PA). Deionized and distilled water were used throughout the experiment. Trypsin and BAEE solution were freshly prepared before use. A 28-μm-thick ribbon of Metglas alloy 2826 MB, alloy composition $Fe_{40}Ni_{38}Mo_4B_{18}$, was used as received from Honeywell Corp. The sensors, 20 mm × 6 mm × 28 μm rectangles, were cut from the ribbon. The resonance frequency of an uncoated sensor in air is approximately 105 kHz.

2.2. Sensor Fabrication

The pH-sensitive polymer is a copolymer synthesized by free radical copolymerization of acrylic acid and isooctylacrylate in dimethylformamide, as described in Ref. [22]. The magnetoelastic sensors were ultrasonically cleaned in Micro-Cleaning solution, followed by a water and acetone rinse, and then dried in a stream of nitrogen. About 10 μl Bayhydrol 110 was applied to both sides of the cleaned sensors by dip-coating. The polyurethane-coated sensors were dried in air and then heated at 150 °C for 2 h to form a robust protective membrane, which offers a NH group for binding the pH-sensitive polymer and protects the iron-rich magnetoelastic substrate from corrosion.

RESEARCH ARTICLE

The polyurethane-protected sensor was then coated with 12 μl of 23 g/l pH-sensitive polymer in ethanol, which contains 0.46 g/l EDC and 0.38 g/l NHS. The polymer coated sensors were dried in air and then heated in a vacuum at 120 °C to form the amide bond between the pH-sensitive polymer and polyurethane. While the pH-sensitive polymer-coated sensor can be used to detect free trypsin activity, in this work it was further coated to achieve the working trypsin biosensor. The pH-polymer coated sensor was dipped in 0.02% EDC and NHS solution in water, rinsed with water, and upon it was applied 10 μl of pre-crosslinked trypsin solution, containing 19.2 g/l trypsin, 12.5 g/l BSA, and 0.1% glutaric dialdehyde in water, on both sides. The sensor was then placed in a refrigerator (4 °C) for over 20 h to allow the cross-linking reaction to proceed, as trypsin can undergo autolysis and lose its activity. Unreacted trypsin was removed by rinsing the sensor with PBS buffer. The as-prepared sensor was then dried in air at room temperature and stored at 4 °C.

2.3. Measurement

Prior to use the functionalized sensor was immersed in 0.05 M pH 7.0 PBS buffer for 20 min to wet the polymer, which resulted in a 100 Hz drop in resonance frequency. The wetted sensor was immersed in a small vial that fit into the magnetoelastic sensor reader box, containing 0.005 M phosphate buffer solution (containing 10 mM NaCl) and incubated at 25 °C for about 10 min to stabilize the reaction response. This step is necessary since increasing salt concentration results in the pH polymer shrinking due to osmotic pressure.[22] As an electrolyte, the substrate BAEE can cause a small response even in the absence of trypsin. Blank experiments without trypsin indicate that 1 mM BAEE can cause a frequency increase of about 80 Hz. Therefore in this work 10 mM NaCl was added as the supporting electrolyte to stabilize any osmotic effect. Finally 10 μl BAEE solution was added to the detection cell and the resonant frequency recorded as a function of time with a magnetoelastic sensor reader.[27]

3. RESULTS AND DISCUSSION

3.1. Sensor Response Profiles

The hydrolysis of BAEE produces H^+, resulting in shrinking of the pH responsive polymer and, in turn, increasing the resonance frequency due to the decrease in sensor mass loading. A linear shift in frequency was observed between pH 4.0 and 9.0 with a slope of 250 Hz/pH. Figure 2 shows the frequency shift when BAEE is hydrolyzed by the immobilized trypsin. The frequency shift rate, $\Delta F/\Delta t$ in Hz/min, over the first 4 min is used to express the enzymatic hydrolysis rate, since the trypsin-catalyzed hydrolysis rate was relatively constant over the first 4 min. It takes about 10 min to complete the hydrolysis reaction; the frequency shift within the first 10 min is also recorded to characterize the enzyme activity.

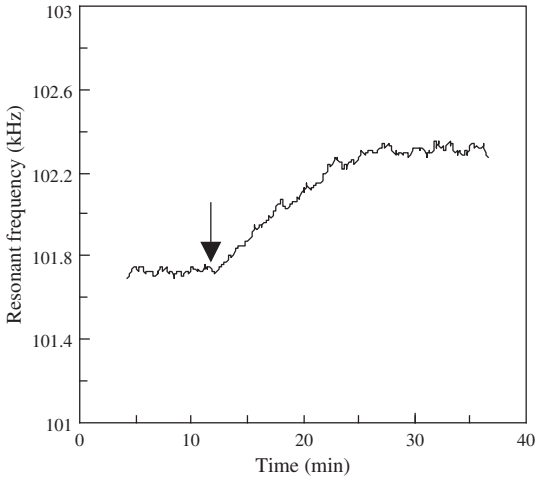

Fig. 2. Typical response curves of magnetoelastic sensor during the enzymatic hydrolysis of BAEE at a concentration of 1 mM. (the down arrow refers to addition of BAEE).

3.2. The Effect of Reaction Time on Sensor Sensitivity

In the sensor fabrication process trypsin was chemically bonded on BSA through glutaric dialdehyde, and BSA was then bonded to the pH polymer through amide bond. Trypsin, BSA, and glutaric dialdehyde were first mixed in water in a glass vial to start the cross-linking reaction. As trypsin can undergo autolysis and lose its activity, the cross-linking reaction was proceeded at 4 °C within a refrigerator. When the reaction time is less than half an hour, little responses were observed due to inadequate trypsin immobilization; when the reaction time is about an hour, the sensors exhibit good sensitivity, but are unstable, the sensitivity declined fast with usage times; when the reaction time is more than 20 h, stable and good sensitivity were obtained. In this work the reaction time for cross-linking was 20 h. However longer reaction periods could cause excess cross-linking reducing the enzyme activity.

3.3. The Effect of pH and Temperature

Figure 3 shows the pH-dependent trypsin activity, determined by the frequency shift during the first 10 min upon addition of one milliliter of 1 mM BAEE solution that was hydrolyzed by the immobilized trypsin on the magnetoelatic sensor. The tested pH value ranged from 6.5 to 8.8. The maximum response (ΔF) appears with a pH of approximately 7.7. The optimum temperature for trypsin was also investigated under the same experimental conditions. Figure 4 shows that trypsin has an activity maximum near 25 °C. So the succeeding experiments were carried out under pH 7.7 and 25 °C.

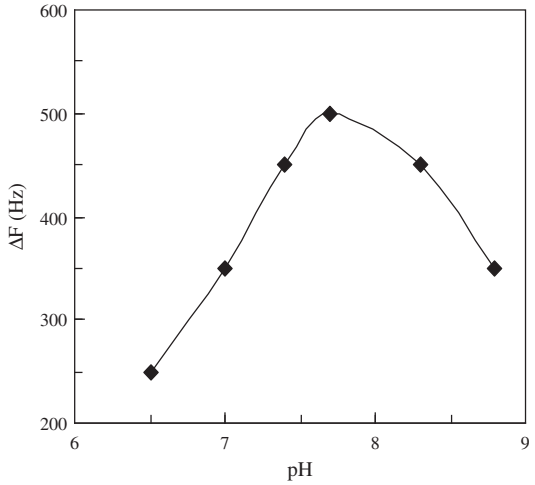

Fig. 3. Effect of pH on trypsin activity at 25 °C.

3.4. The Effect of Immobilization on the Trypsin Activity

The effect of the immobilization on the trypsin activity was investigated by measuring the kinetic parameters of both the immobilized and the free trypsin using the Lineweaver-Burk equation:[26]

$$\frac{1}{V} = \frac{K_m}{V_{\max}} \times \frac{1}{[S]} + \frac{1}{V_{\max}} \tag{3}$$

Where V and $V_{\max}$ are the initial hydrolysis rate and the maximum hydrolysis rate in Hz/min, respectively, K_m is the Michaelis-Menten constant and $[S]$ the BAEE concentration in mM.

The initial hydrolysis rate (V) was obtained by linear fitting the ΔF-t data within the first 4 min. As shown in Figure 5, $1/V$ is linear to $1/[S]$ for both the immobilized and free trypsin in the investigated BAEE concentrations of $0.4 \sim 1.5$ mM. The determined kinetic parameters are: $K_m = 9$ mM, $V_{\max} = -833.3$ Hz/min ($n = 6$, $r = 0.997$) for immobilized trypsin; and $K_m = 4.5$ mM, $V_{\max} = -270.3$ Hz/min ($n = 6$, $r = 0.996$), for free trypsin. The higher Michaelis-Menten constant value of the immobilized trypsin indicates that the immobilization reduces trypsin activity by about 50%.

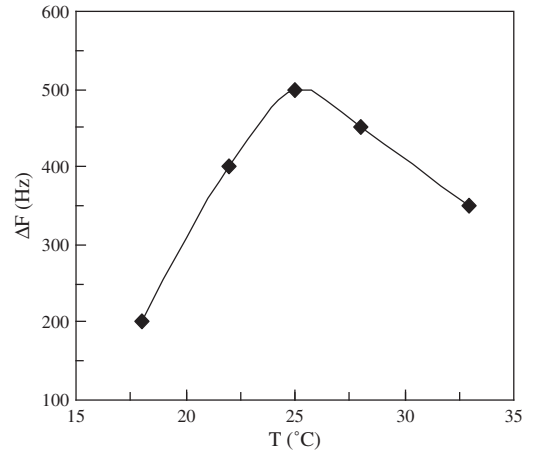

Fig. 4. Effect of temperature on trypsin activity at pH 7.7.

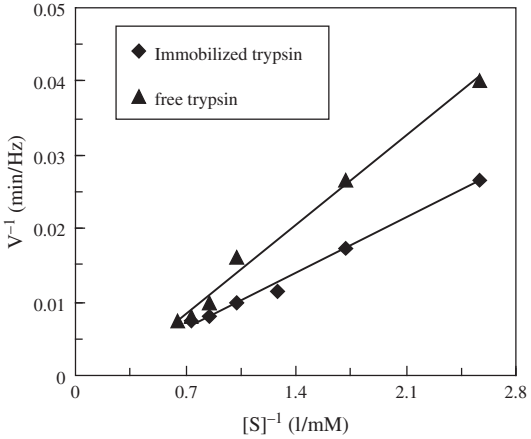

Fig. 5. The dependence of the reciprocal of enzymatic hydrolysis rate on the reciprocal of concentration of BAEE (25 °C, pH 7.7).

3.5. Detection of Trypsin and BAEE

The magnetoelastic sensor response to trypsin ranging from 24–720 U/ml was investigated in this work. Frequency shift rates, $\Delta F/\Delta t$ in Hz/min, over the first 4 min is linear to trypsin activity in solution over the range of 24–360 U/ml, as shown in Figure 6. The detection sensitivity for trypsin of the magnetoelatic sensor is more sensitive than the colorimetric titration method,[28] which is based on the measurement of *p*-nitrophenol released by the irreversible reaction of trypsin with specific active cite of the titrant *p*-nitrophenyl-*p*-guanidinobenzoate (500–25,000 U/ml); comparative to electrode methods (10–200 U/ml[15] and 5.4–108 U/ml[16]), but less sensitive than surface

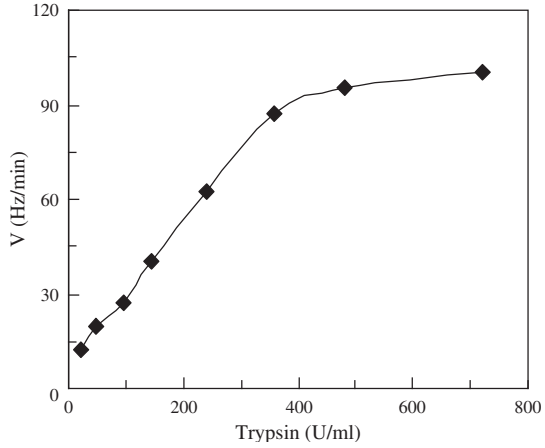

Fig. 6. A calibration curve for determination of trypsin activity. The hydrolysis rates (V) were estimated by measuring the frequency increase within the first 4 min caused from the hydrolysis of 1 mM BAEE under pH 7.7 and 25 °C.

RESEARCH ARTICLE

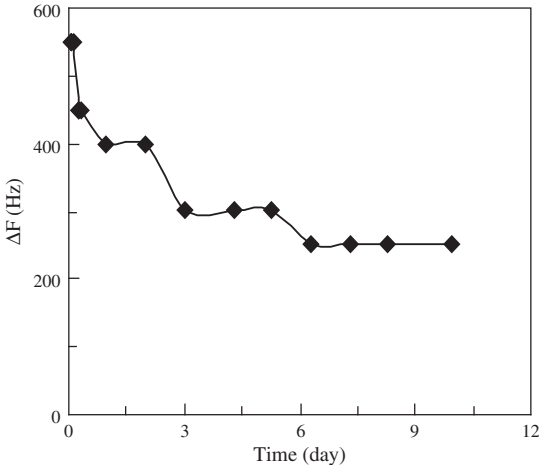

Fig. 7. The long-term stability by measuring the frequency shift (ΔF) within the first 10 min caused from the hydrolysis of 1 mM BAEE under pH 7.7 and 25 °C.

acoustic wave sensor[14] (0.3U/ml). The magnetoelastic sensor, however, can be used for wireless and remote detection, which is particularly useful for *in situ* clinical assay.

BAEE in solution was detected using the trypsin-immobilized magnetoelastic sensor. Linear response was observed in the concentration range of 0.4–1.5 mM.

The long-term stability of the trypsin sensor was tested by repeatedly measuring the frequency shift within the first 10 min (ΔF) resulted from the trypsin-catalyzed hydrolysis of 1 mM BAEE under pH 7.7 and 25 °C. As shown in Figure 7, the sensor response decreased rapidly in the first three days and then became stable. The sensor sensitivity was reduced by 33% in the first 3 days, and 50% over the first 5 days primarily due to the trypsin dissolving. sThe relative stability in the following days indicates that the immobilized trypsin is stable.

4. CONCLUSIONS

A wireless remote magnetoelastic trypsin biosensor is described based on the enzymatic hydrolysis of BAEE by the immobilized trypsin. The pH change of the solution caused the coated pH-sensitive polymer to shrink, and consequently resulted in aresonant frequency change. The optimum pH and temperature were investigated to be pH 7.7 and 25 °C, respectively. The magnetoelastic sensor can be used to detect trypsin at 24 U/ml to 360 U/ml and BAEE at 0.4 mM to 1.5 mM, which is more sensitive than the colorimetric titration method and comparative to electrode methods. The kinetic parameters of both the immobilized and free trypsin were determined. The immobilization of the enzyme reduced the activity by about 50%. The sensor sensitivity, however, was relatively stable after first uses.

Acknowledgments: We are grateful for the financial support from the National Science Foundation of China under the grant 20475016, the Specialized Research Fund for the Doctoral Program of Higher Education under grant 20050532024, and the Scientific Research Foundation of Hunan University. C. A. Grimes gratefully acknowledges partial support of this work by the National Science Foundation under grant BES-0426170.

References and Notes

1. J. P. Dworzanski, A. P. Snyder, R. Chen, H. Zhang, D. Wishart, and L. Li, *Anal. Chem.* 76, 2355 (**2004**).
2. L. M. Ben, B. van, A. G. Hulst, A. L. de Jong, and E. R. J. Wils, *J. Chromatogr. A* 970, 95 (**2002**).
3. T. Larsson, J. Bergström, C. Nilsson, and K. A. Karlsson, *FEBS Lett.* 469, 155 (**2000**).
4. D. M. Goldberg, *Clin. Chim. Acta* 291, 201 (**2000**).
5. S. J. Setford, S. F. White, and J. A. Bolbot, *Biosens. Bioelectron.* 17, 79 (**2002**).
6. P. Sarkar, *Microchem. J.* 64, 283 (**2000**).
7. J. Borch and P. Roepstorff, *Anal. Chem.* 76, 5243 (**2004**).
8. E. Bonneil, M. Mercier, and K. C. Waldron, *Anal. Chim. Acta* 404, 29 (**2000**).
9. E. Calleri, C. Temporini, E. Perani, C. Stella, S. Rudaz, D. Lubda, G. Mellerio, J. L. Veuthey, G. Caccialanza, and G. Massolini, *J. Chromatogr. A* 1045, 99 (**2004**).
10. S. Hara, V. Katta, and H. S. Lu, *J. Chromatogr A.* 867, 151 (**2000**).
11. K. Sakai-Kato, M. Kato, and T. Toyo'oka, *Anal. Chem.* 75, 388 (**2003**).
12. M. T. Dulay, Q. J. Baca, and R. N. Zare, *Anal. Chem.* 77, 4604 (**2005**).
13. E. W. Voss, C. J. Workman, and M. E. Mummert, *Biotechniques* 20, 286 (**1996**).
14. Q. Y. Cai, R. H. Wang, L. Y. Wu, L. H. Nie, and S. Z. Yao, *Microchem. J.* 55, 367 (**1997**).
15. J. H. Yun, M. E. Meyerhoff, and V. C. Yang, *Anal. Biochem.* 224, 212 (**1995**).
16. H. S. M. Abd-Rabboh, S. A. Nevins, N. Durust, and M. E. Meyerhoff, *Biosens. Bioelectron.* 18, 229 (**2003**).
17. P. Lafont, O. Guy-Crotte, C. Paulin, D. Galvain, S. Mertani, C. Frigarella, and Y. Barbier, *Clin. Chim. Acta.* 235, 197 (**1995**).
18. S. Schmidt and C. A. Grimes, *Sens. Actuators A* 94, 189 (**2001**).
19. Q. Y. Cai and C. A. Grimes, *Sens. Actuators B* 71, 112 (**2000**).
20. C. A. Grimes and D. Kouzoudis, *Sens. Actuators A* 84, 205 (**2000**).
21. K. F. Zeng, K. G. Ong, C. Mungle, and C. A. Grimes, *Rev. Sci. Instrum.* 73, 4375 (**2002**).
22. Q. Y. Cai, K. F. Zeng, C. M. Ruan, T. A. Desai, and C. A. Grimes, *Anal. Chem.* 76, 4038 (**2004**).
23. C. M. Ruan, K. F. Zeng, O. K. Varghese, and C. A. Grimes, *Anal. Chem.* 75, 6494 (**2003**).
24. L. G. Puckett, G. Barrett, D. Kouzoudis, C. Grimes, and L. G. Bachas, *Biosens. Bioelectron.* 18, 675 (**2003**).
25. A. R Khokhlov, S. G. Starodubtzev, and V. V. Vasilevskaya, *Adv. Polym. Sci.* 109, 123 (**1993**).
26. H. Lineweaver and D. J. Burk, *J. Am. Chem. Soc.* 56, 658 (**1934**).
27. K. Sankar, C. M. Ruan, K. F. Zeng, and C. A. Grimes, *Sens. Actuators B* 107, 640 (**2005**).
28. T. Chase and E. Shaw, *Biochem. Biophys. Res. Commun.* 29, 508 (**1967**).

SENSOR LETTERS
Vol. 4, 2006

Selected Peer-Reviewed Papers from International Conference of Thermal, Mechanical, and Multiphysics Simulation and Experiments in Microelectronics and Microsystems (EUROSIME'2005)

This special section includes selected papers presented at the *International Conference of Thermal, Mechanical, and MultiPhysics Simulation and Experiments in Microelectronics and Microsystems (EuroSimE)* held in Berlin, 18–20 April 2005. The annual EuroSimE conference was initiated in 2000, as the only international conference focusing on mechanical, thermal, and thermo-mechanical simulation and experiments in microelectronics and microsystems, in order to meet the growing needs and challenges of this rapidly progressing field. This edition features the addition of a parallel track in multiphysics simulation. In total, the conference had more than 100 technical papers divided in 22 sessions.

Selected papers were submitted to an independent peer-review process. They cover significant contributions concerning the use of advanced modeling and simulation techniques relevant for the computer aided design of microsystems.

The conference was possible, thanks to the kind sponsorhip of IEEE, FhG-IZM-Berlin, Philips, Nokia, and Robert Bosch GmbH, and the efforts of the organizing and local committees. I would like to thank specially G. Q. Zhang, L. J. Ernst, P. Rodgers, M. Meuwissen, and last but not least, O. de Saint Leger.

I would like to thank also the following reviewers for their valuable contribution: M. Salleras, S. Mijalkovic, E. Lemaire, D. Elata, A. Wymyslowski, J. P. Polizzi, G. Schrag, E. Rudnyi, N. Cordero, C. Tsamis, and E. Ferraris.

Dr. Santiago Marco,
Guest Editor
Sistemes d'Instrumentació i Communicacions
Departament d'Electrònica, Universitat de Barcelona
Martí i Franqués 1, 08028-Barcelona, Spain
E-mail: santi@el.ub.es

ABOUT THE GUEST EDITOR

Dr. Santiago Marco is Associate Professor (Profesor Titular) at the Departament d'Electronica of Universitat de Barcelona since 1995. He received the degree in Physics from the Universitat de Barcelona in 1988. From 1989 to 1990 he was working in the electro-optical characterization of deep levels in GaAs. From 1990 to 1993 he was regular visitor of the Centro Nacional de Microelectrònica, Bellaterra, Spain. In 1993, he received his Ph.D. (honor award) degree from the Departament de Física Aplicada i Electrònica, Universitat de Barcelona, for the development of a novel silicon sensor for *in-vivo* measurements of the blood pressure. In 1994, he was a post-doc researcher at the Department of Electronic Engineering, Universita di Roma 'Tor Vergata', working in Data Processing for Artificial Olfaction. He has published about 60 papers in scientific journals and books, as well as more than 100 conference papers. His current research interests are twofold: chemical instrumentation based on intelligent signal processing and microsystem modeling.

 1546-198X/2006/4 doi:10.1166/sl.2006.009

SENSOR LETTERS
Vol. 4, 165–173, 2006

Parametric Model Reduction for Fast Simulation of Cyclic Voltammograms

Lihong Feng[1,*], Darius Koziol[2], Evgenii B. Rudnyi[2], and Jan G. Korvink[2]

[1] *ASIC and System State-key Laboratory, Microelectronics Department, Zhangjang Campus, Fudan University, Pudong new District, Shanghai, China*
[2] *IMTEK-Institute for Microsystem Technology, University of Freiburg, Freiburg, Germany*

(Received: 4 January 2006. Accepted: 12 April 2006)

Model order reduction is a well-established technique for fast simulation of large-scale models based on ordinary differential equations, especially those in the field of integrated circuits and micro-electro-mechanical systems. In this paper, we propose the use of parametric model reduction for fast simulation of a cyclic voltammogram. Instead of being considered as a time varying system, the model for a cyclic voltammogram is treated as a system with a parameter (applied voltage) which is to be preserved during model reduction. Because voltage is preserved in the symbolic form during model reduction, we can simulate the cyclic voltammogram with a reduced system and therefore invest much less time and memory as compared with direct simulation based on the original large-scale model. We present our approach for a case study based on scanning electrochemical microscopy.

Keywords: Model Order Reduction, Compact Model, Simulation, Scanning Electrochemical Microscopy (SECM), Voltammogram.

RESEARCH ARTICLE

1. INTRODUCTION

During the last 15 years, Scanning Electrochemical Microscopy (SECM) has evolved from a basic feedback application to a powerful tool for analyzing local electrochemical properties or for modifying surfaces.[1] In recent years, the addition of submicron-scale spatial resolution has increased its capacity for interdisciplinary applications. For example, the technique has been used to measure local kinetics and study chemical reactivity and topology of samples or micro fabrications. In particular, SECM finds many applications in current problems in the biological field. For instance, procedures to characterize surfaces with high local resolution and chemical sensitivity are of great importance for biotechnology, biomedicine, and biosensors. With the combination of chemical specificity and spatial resolution, SECM offers a unique basis for studying surface properties in the sub-μm range.

Quantitative mathematical models have been developed for different operating modes of the SECM, for example, feedback and generator/collector modes, steady state and transient measurements, diffusion-controlled or kinetic-controlled processes.[2,3] However, except for some very specific problems, like the diffusion-controlled current on a circular electrode far away from the border, solutions can only be obtained by numerical simulation, which is based on discretization of the model in space by an appropriate method like finite differences,[4] finite elements,[5] or boundary elements.[6,7] After discretization, a high-dimensional system of ordinary differential equations is obtained. Its high dimensionality leads to high computational cost. This results in a situation where an accurate model is available in principle but is hard to use in practice.

In recent years, several model order reduction (MOR) methods[8–10] have been proposed in order to get a quick and accurate simulation of very large-scale integrated circuits and micro-electro-mechanical systems (for a quick overview see.[11]) They have proved to be very efficient but to our knowledge, they have not yet been applied to electrochemical simulation. One of the reasons is that there are at least two additional problems that should be solved before model reduction can be employed in electrochemistry.

In order to derive a mathematical model for electrochemistry, at least one reaction between two species should be considered. Therefore, it is impossible to set the initial state of all the species equal to zero. Hence, the initial condition of the ordinary differential equations is always nonzero. It happens that for such a system, the

*Corresponding author; E-mail: lhfeng@fudan.edu.cn

conventional model order reduction methods[8–11] cannot be applied immediately because they deal only with systems possessing the zero initial condition. In this paper, we propose a transformation technique, which avoids the nonzero initial condition so that the methods above can be successfully applied to obtain an accurate solution.

Another problem is that, during simulation of a voltammogram, the voltage that changes in time enters the system matrices. Formally speaking, this makes a dynamic system time varying and hence conventional model reduction methods[8–11] cannot be applied. There are special model reduction methods for time varying systems[12, 13] but, in our view, one can suggest much more efficient solution by exploring the special structure of the dynamic system in the case of electrochemistry by relying on parametric model reduction methods.[14, 15] In the present paper, we will show that, after proper modification, the time varying electrochemical model for voltammogram simulation can be successfully reduced by the parametric model reduction technique.

The paper is arranged as follows. In Section 2, we describe our case study and the derivation of the discretized ordinary differential equations (the starting point for model order reduction). It is worthy to note two points here. First, we use a model based on scanning electrochemical microscopy. In this case one can ignore convection and this simplifies modeling. However otherwise, our setup is common to many typical experiments in electrochemistry. Second, our goal is to perform research on model reduction. As a result, we make comparison between the original full scale and reduced models only. The validation of the original model is beyond the scope of the present paper.

In Section 3, we review conventional model order reduction methods based on a projection technique and show its limitations when dealing nonzero initial conditions and time varying systems. Then we propose a transformation technique, which solves the problem with nonzero initial conditions. Then we show how to apply parametric model reduction to solve the electrochemical model when system matrices depend on voltage changing in time. The efficiency of parametric model order reduction is presented in Section 4 with numerical simulation results. Finally, some conclusions are drawn.

2. CASE STUDY

We consider a cylindrical electrode as shown in Figure 1. The computation domain under the 2D-axisymmetrical approximation includes the electrolyte under the electrode. We assume that the concentration does not depend on the rotation angle. A single chemical reaction takes place on the electrode:

$$Ox + e^- \underset{k_b}{\overset{k_f}{\Leftrightarrow}} \mathrm{Red} \tag{1}$$

where k_f and k_b are reaction rates for the forward and backward reactions accordingly.

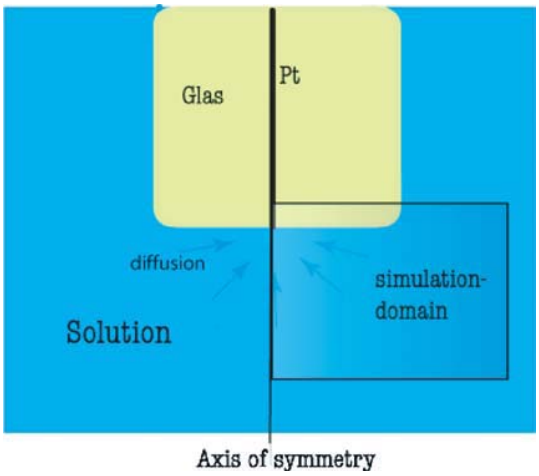

Fig. 1. The computational geometry.

According to the theory of SECM,[2] the species transport in the electrolyte is described by diffusion only. The diffusion partial differential equation is given by the second Fick law as follows

$$dc_1/dt = D_1 \cdot \nabla^2 c_1 \tag{2}$$

$$dc_2/dt = D_2 \cdot \nabla^2 c_2 \tag{3}$$

where $c_1(r, z, t)$ is the concentration field of species Ox and $c_2(r, z, t)$ is the concentration field of species Red, D_1 and D_2 are the respective species diffusion coefficients, t is the time. The initial conditions are

$$c_1(0) = c_{1,0}, \quad c_2(0) = c_{2,0} \tag{4}$$

Conditions at the glass and the bottom of the bath are described by the Neumann boundary conditions of zero flux

$$\nabla c_1 \cdot \vec{n} = 0 \qquad \text{and} \qquad \nabla c_2 \cdot \vec{n} = 0$$

Conditions at the border to the bulk are described by Dirichlet boundary conditions of constant concentration, equal to the initial conditions

$$c_1 = c_{1,0}, \quad c_2 = c_{2,0}$$

To describe the reaction rate on electrode surfaces for chemical reaction (1), the Buttler-Volmer equation has been used,

$$j = k_f \cdot c_{Ox} - k_b \cdot c_{\mathrm{Red}} \tag{5}$$

The reaction constants for the forward reaction and the backward reaction are given as follows

$$k_f = k^0 e^{(\alpha z F(U-U^0)/RT)} \tag{6}$$

$$k_b = k^0 e^{(-(1-\alpha) z F(U-U^0)/RT)} \tag{7}$$

where k^0 is the heterogeneous standard rate constant, and α is an empirical transmission factor for a heterogeneous reaction. F is the Faraday-constant, R is the gas constant, T is the temperature and z is the number of exchanged

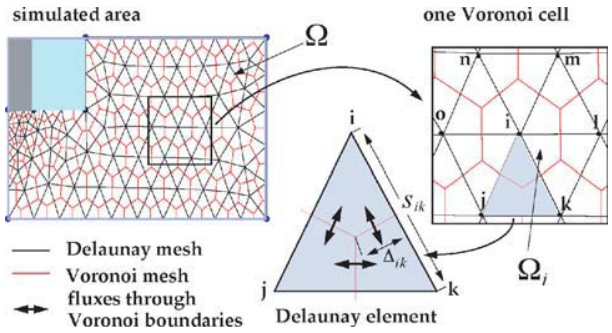

Fig. 2. The discretization scheme.

electrons per reaction. $u = U - U_0$ is the difference between the electrode potential and the reference potential. This difference, to which we refer below as voltage, is changed during the measurement of a voltammogram. This allows us to write the boundary conditions at the electrode as follows,

$$\nabla c_1 \cdot \vec{n} = j \qquad \text{and} \qquad \nabla c_2 \cdot \vec{n} = -j \tag{8}$$

The control volume method has been used for the spatial discretization of (2) and (3) (see Fig. 2). The considered domain Ω is covered by a grid consisting of N_n nodes with $x_i \in \Omega, i = 1, 2, \ldots, N_n$. These nodes are connected by edges as shown in Figure 2. The resulting triangular mesh, in which no angle is bigger than 90° is of type Delaunay, also known as the primary mesh.

Around each node i, we construct a box Ω_i whose edges are composed of the mid-perpendiculars of all the edges terminating in node i. These boxes form the secondary or Voronoi mesh. The resulting equations for the discretization are given as follows:

$$V_i \dot{c}_{1,i} = D_1 \sum_j \frac{S_{ij}}{\Delta_{ij}} (c_{1,j} - c_{1,i}) \tag{9}$$

$$V_i \dot{c}_{2,i} = D_2 \sum_j \frac{S_{ij}}{\Delta_{ij}} (c_{2,j} - c_{2,i}) \tag{10}$$

where i stands for the i-th node and the sum over j includes all neighboring nodes. S_{ij} is the distance between the nodes i and j. Δ_{ij} is the length of the part of Voronoi mesh which belongs to the Delaunay element and the nodes i and j. V_i is the volume (in 2D the area) of the Voronoi cell which belongs to node i.

Equations (9) and (10) are not yet coupled. The coupling arises from the discretization of the mixed boundary conditions at the electrode. The resulting system of ordinary differential equations is as follows

$$E\, d\vec{c}/dt + K(\mathrm{u}(t))\vec{c} = F, \vec{c}(0) = \vec{c}_0 \neq 0 \tag{11}$$

where E and $K(\mathrm{u}(t))$ are system matrices, $K(\mathrm{u}(t))$ is a function of voltage that in turn depends on time. The voltage appears in the system matrix due to the boundary conditions (8) where, in turn, the voltage comes from Eqs. (5) to Eq. (7). $\vec{c} \in R^n$ is the vector of unknown concentrations, R^n means that there are n elements in the real-valued vector $\vec{c}$, n is usually referred to as the dimension of the system (11). The vector $\vec{c}$ includes both the Ox and Red species. The vector F is the load vector, which arises as a consequence of the Dirichlet boundary conditions imposed at the bulk boundary of the electrolyte. The total current is computed as an integral (sum) over the electrode surface.

3. MODEL ORDER REDUCTION

3.1. General Idea of Model Order Reduction

The dimension n of system (11) is usually around 10^4–10^6. It is always time consuming if we use conventional numerical integration methods, for example backward Euler, to directly simulate (11) time step by time step over a typical time interval. The model order reduction technique replaces the original large dimensional system (11) with a compact model and at the same time, makes sure that the solution computed from the compact model is as accurate as that computed directly from the original large system.

Most often, model order reduction is based on a projection technique when the projection basis is found by implicit moment matching.[8–10] We refer below to these methods as conventional model reduction. It should be noted that there are other approaches for model reduction like balanced truncation approximation and proper orthogonal decomposition (see review[11] for details). However, the parametric model reduction introduced in Section III.D is the generalization of implicit moment matching and at present it is unclear how to preserve parameters in other model reduction approaches. As a result, we limited ourselves in the present paper to model reduction methods based on implicit moment matching.

It should be noted here that conventional model reduction can deal with models with constant system matrices only. In other words, in Eq. (11), it is required that the matrices E, K, F do not depend on time or some other parameters. For simplicity, we assume in this section that the matrix K is formed at a constant voltage value. The basic idea of model order reduction is to find a projection matrix V such that $V^T V = I$ and the unknown vector $\vec{c}$ can be sufficiently approximated by $\vec{c} \approx V\bar{z}$, with a rectangular matrix $V \in R^{n \times q}$ such that the number of columns much less than the number of rows, $q \ll n$. This gives us

$$EV\, d\bar{z}/dt + KV\bar{z} = F \tag{12}$$

After multiplying (12) by V^T from the left, we obtain the final reduced small system (compact model) with unknown vector $\bar{z} \in R^q$, which is of much smaller dimension q:

$$V^T EV\, d\bar{z}/dt + V^T KV\bar{z} = V^T F \tag{13}$$

RESEARCH ARTICLE

3.2. Conventional Projection Technique

In order to perform model order reduction described in subsection *A*, the projection matrix V needs to be computed. With the assumption that the initial condition of the system is zero ($\vec{c}_0 = 0$), the conventional method of constructing V is based on the transfer function of the original system (11). In the case of system (11), we are not interested in the complete concentration vector $\vec{c}$ but in a few outputs computed as linear combinations of concentrations, i.e.

$$\bar{y} = L\vec{c} \tag{14}$$

Natural choice for electrochemistry here is the current that is computed directly from the concentration vector as a linear combination.

Provided that the matrix K is constant, the Laplace transformation of (11) and (14) with initial condition $\vec{c}_0 = 0$ is as follows

$$\begin{aligned} sEC(s) + KC(s) &= F\mathrm{U}(s) \\ Y(s) &= LC(s) \end{aligned} \tag{15}$$

The transfer function is defined as

$$H(s) = Y(s)/U(s) = L(sE+K)^{-1}F \tag{16}$$

By choosing an expansion point, $s = s_0 + \sigma$, $H(s)$ can be expanded into series around s_0,

$$H(\sigma) = \sum_{i=0}^{\infty} LM^i r\sigma^i \tag{17}$$

where $M^i = -(s_0E+K)^{-1}E$, $r = (s_0E+K)^{-1}F$.

The projection matrix V is constructed as follows

$$spancolumn\{V\} = span\{(r, Mr, \ldots, M^j r\} \tag{18}$$

by satisfying $V^TV = I$. In Eq. (18), *spancolumn* means the subspace spanned by the columns in V; *span* means the subspace spanned by $r, Mr, \ldots M^j r$. The condition $V^TV = I$ means that the columns in V form a group of orthonormal vectors for the subspace spanned by $r, Mr, \ldots M^j r$. Usually, the reduced system (13) can approximate the original system (11) quite well even for small j. The reduced system will be more accurate if more terms are included in the right hand side of Eq. (18). Detailed theoretical proof is given elsewhere.[9]

The conventional method of computing V has an assumption that the initial condition of the system must be zero so that a transfer function in the form of Eq. (16) can be obtained. However, from the Laplace transformation of the system in Eq. (11), we have that

$$\int_0^\infty E\dot{\vec{c}}e^{-st}dt + \int_0^\infty K\vec{c}e^{-st}dt = \int_0^\infty Fe^{-st}dt$$

After integration, we actually obtain

$$\begin{aligned} sEC(s) + KC(s) &= FU(s) + E\vec{c}_0 \\ Y(s) &= LC(s) \end{aligned}$$

and

$$\begin{aligned} H(s) = Y(s)/U(s) &= L(sE+K)^{-1}F \\ &+ L(sE+K)^{-1}E\vec{c}_0/U(s) \end{aligned} \tag{19}$$

The expression in Eq. (19) contains $\vec{c}_0$. When $\vec{c}_0 = 0$, it is the same as Eq. (16). However when $\vec{c}_0$ is nonzero, only the first part in Eq. (19) would be considered to construct the projection matrix V as is done in Eq. (18) and the resulting reduced model might be inaccurate.

Another reason is that with the reduced model we cannot describe well all possible initial conditions. We mean that Eq. (11) can be considered as a family of initial value problems with different $\vec{c}_0 \neq 0$. A normal way to obtain the initial condition of the reduced system is by projection $\vec{z}_0 \approx V^T\vec{c}_0$. However, if we use such $\vec{z}_0$ to compute the initial condition of the original system we obtain $\vec{c}_0 \approx V\vec{z}_0 = VV^T\vec{c}_0$. It is clear that we can only obtain an approximation of the nonzero initial condition $\vec{c}_0^r = VV^T\vec{c}_0$. $\vec{c}_0^r$ is a projection of the original $\vec{c}_0$ to the low-dimensional subspace and it will be very inaccurate if $\vec{c}_0$ is far away from the subspace spanned by V. Such a situation is shown in Figure 3, where $\vec{c}_0^r = VV^T\vec{c}_0$ is in the subspace spanned by V, *span{V}* , while the original $\vec{c}_0$ is not. This happens to be also the case in our example.

From the above analysis, we can conclude that there are two important difficulties to overcome before conventional model reduction can be employed for the model described by Eq. (11). First, the initial condition of the system is always nonzero in our case, i.e., $\vec{c}_0 \neq 0$. Second, in Eq. (11), the matrix $K(\mathrm{u}(t))$ depends on the voltage that in turn depends on time in the simulation of a cyclic voltammogram. This feature must be preserved in the reduced model. In the following subsections, we will first propose a transformation technique to validate the conventional model reduction method for the nonzero initial condition. Then, we review the parametric model reduction technique to deal with the voltage dependent case. Finally, we combine the parametric model reduction technique with the transformation technique to obtain a reduced model for Eq. (11).

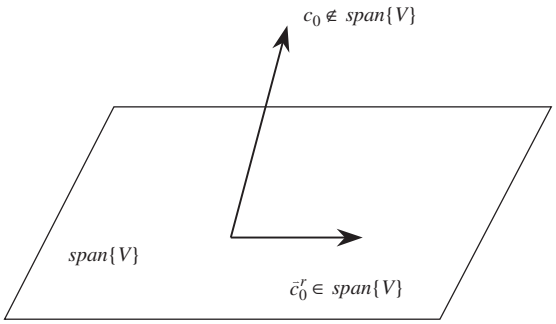

Fig. 3. Inaccuracy of initial condition caused by conventional projection technique.

3.3. Projection Technique with Transformation

The natural solution for a problem above is to transform system (11) to the standard state-space formulation. Let us define a new unknown vector $\tilde{\vec{c}} = \vec{c} - \vec{c}_0$ and then obtain a new system for $\tilde{\vec{c}}$

$$\begin{aligned} E\dot{\tilde{\vec{c}}} + K\tilde{\vec{c}} &= F - K\vec{c}_0, \tilde{\vec{c}}(0) = 0 \\ \tilde{Y}(t) &= L\tilde{\vec{c}} \end{aligned} \tag{20}$$

It is clear that the transformed system (20) possesses zero initial conditions by definition so that the conventional projection technique of subsection *B* can be employed to perform model reduction on this new system. One can prove that

$$H(s) = L(sE + K)^{-1}\tilde{F} = \sum_{i=0}^{\infty} M^i \tilde{r}\sigma^i$$

where $\tilde{F} = F - K\vec{c}_0$, $\tilde{r} = (s_0 E + K)^{-1}\tilde{F}$, M is defined as in Eq. (17). The projection matrix $\tilde{V}$ can be computed in a similar way as

$$spancolumn\{\tilde{V}\} = span\{(\tilde{r}, M\tilde{r}, \ldots, M^j\tilde{r}\} \tag{21}$$

The same way as in Eq. (12) and (13), we obtain a small dimensional reduced system as follows

$$\tilde{V}^T E\tilde{V}\dot{\tilde{z}} + \tilde{V}^T K\tilde{V}\tilde{z} = \tilde{V}^T F \tag{22}$$

The unknown vector $\vec{c}$ for the original system (11) can be restored by

$$\vec{c} = \tilde{\vec{c}} + \vec{c}_0 \approx \tilde{V}\vec{z} + \vec{c}_0 \tag{23}$$

In this way the nonzero initial condition is preserved exactly, because from $\vec{z}_0 = \tilde{V}^T\tilde{\vec{c}}_0 = 0$ we have that $\tilde{\vec{c}}_0^r = \tilde{V}\vec{z}_0 = 0$, then we obtain $\vec{c}_0^r = \tilde{\vec{c}}_0^r + \vec{c}_0 = c_0$, which means that the initial condition $\vec{c}_0^r$ computed from the reduced system (22) is identical to the exact initial condition $\vec{c}_0$. In the end, the accuracy of the reduced system (22) will only depend on the accuracy of projection matrix $\tilde{V}$, which is easily met by adding more terms into the right hand side of Eq. (21).

3.4. Parametric Model Reduction

In this subsection, we review recently developed model reduction methods which can preserve parameters during the model reduction process. We will show how they can be applied to the time varying electrochemical model in Eq. (11) in the next subsection.

The parametric model reduction method proposed in Ref. [13] deals with a two-parameter system in the following form

$$\begin{aligned} (s_1E_1 + s_2E_2 - E_0)x &= b\mathrm{w} \\ y &= cx \end{aligned} \tag{24}$$

where corresponding reduced model is

$$\begin{aligned} (s_1\hat{E}_1 + s_2\hat{E}_2 - \hat{E}_0) &= \hat{b}\mathrm{w} \\ \hat{y} &= \hat{c}x \end{aligned} \tag{25}$$

where

$$\begin{aligned} &\hat{E}_1 = V^T E_1 V, \hat{E}_2 = V^T E_2 V, \\ &\hat{E}_0 = V^T E_0 V, \hat{b} = V^T b, \hat{c} = cV \end{aligned}$$

The projection matrix V is computed from the transfer function of (24) where we explicitly write that it depends on both parameters

$$h(s_1, s_2) = c(s_1E_1 + s_2E_2 - E_0)^{-1}b \tag{26}$$

$h(s_1, s_2)$ can be expanded into series of both s_1 and s_2,

$$\begin{aligned} h(s_1, s_2) &= -c[I - (E_0^{-1}E_1s_1 + E_0^{-1}E_2s_2)]^{-1}E_0^{-1}b \\ &= -c\sum_{i=0}^{\infty}(E_0^{-1}E_1s_1 + E_0^{-1}E_1s_2)^iE_0^{-1}b \\ &= -c\sum_{j=0}^{\infty}\sum_{k=0}^{j}[F_k^j(E_0^{-1}E_1, E_0^{-1}E_2)s_1^{j-k}s_2^k]E_0^{-1}b \end{aligned}$$

where F_k^j is the matrix before $s_1^{j-k}s_2^k$. For example,

$$\begin{aligned} &F_0^1 = E_0^{-1}E_1, F_1^1 = E_0^{-1}E_2, F_0^2 = (E_0^{-1}E_1)^2 \\ &F_1^2 = (E_0^{-1}E_1)(E_0^{-1}E_2) + (E_0^{-1}E_2)(E_0^{-1}E_1) \\ &F_2^2 = (E_0^{-1}E_2)^2, \ldots \end{aligned} \tag{27}$$

The moments for both parameters are as follows

$$-cF_k^j(E_0^{-1}E_1, E_0^{-1}E_2)E_0^{-1}b \tag{28}$$

the projection matrix V is computed based on the moments in Eq. (28), that is

$$colspan\{V\} = span\left\{\bigcup_{m=0}^{j}\bigcup_{k=0}^{m}F_k^m(E_0^{-1}E_1, E_0^{-1}E_2)E_0^{-1}b\right\} \tag{29}$$

Theorem 4 in Ref. [14] guarantees the accuracy of the reduced model by proving that a certain number of the moments in the reduced model (25) will match the corresponding moments in the original model (24):

$$\begin{aligned} cF_k^m(P^{-1}E_1, P^{-1}E_2)P^{-1}b = \hat{c}F_k^m(\hat{P}^{-1}\hat{E}_1, \hat{P}^{-1}\hat{E}_2)\hat{P}^{-1}\hat{b} \\ 0 \le k \le m \le j+1 \end{aligned}$$

This method was extended to systems with any number of parameters in Ref. [15], where a linear system with p parameters is defined as

$$\begin{aligned} (s_1E_1 + s_2E_2 + \cdots + s_pE_p - E_0)x &= b\mathrm{w} \\ y &= cx \end{aligned} \tag{30}$$

Since c does not contribute the projection matrix V, the series expansion of x instead of the transfer function is considered in Ref. [15]. From (30) we have

$$\begin{aligned} x &= -[I - (s_1E_0^{-1}E_1 + \cdots + s_pE_0^{-1}E_p)]^{-1}E_0^{-1}b\mathrm{w} \\ &= -\sum_{m=0}^{\infty}[s_1E_0^{-1}E_1 + \cdots + s_pE_0^{-1}E_p]^mE_0^{-1}b\mathrm{w} \end{aligned}$$

RESEARCH ARTICLE

$$= \sum_{m=0}^{\infty} \sum_{k_2=0}^{m-(k_3+\cdots+k_p)} \cdots \sum_{k_{p-1}=0}^{m-k_p} \sum_{k_p=0}^{m} [F_{k_2,\cdots k_p^m}(E_0^{-1}E_1,\ldots,E_0^{-1}E_p)b\mathrm{w}]s_1^{m-(k_2+\cdots+k_p)}s_2^{k_2}\cdots s_p^{k_p}$$

where $F_{k_2,\ldots,k_p^m}$ is similarly defined as in Eq. (27).

The projection matrix V is constructed by the terms of the series above, that is

$$colspan(V) = span\left\{\bigcup_{m=0}^{m_q}\bigcup_{k_2=0}^{m-(k_p+\ldots+k_3)}\cdots\bigcup_{k_{p-1}=0}^{m-k_p}\bigcup_{k_p=0}^{m} F_{k_2,\ldots k_p}^{m}E_0^{-1}b\right\} \tag{31}$$

or alternatively,

$$\begin{aligned} colspan(V) = span\{&E_0^{-1}b,(E_0^{-1}E_1)E_0^{-1}b,(E_0^{-1}E_2)E_0^{-1}b\ldots,\\ &(E_0^{-1}E_p)E_0^{-1}b,(E_0^{-1}E_1)^2E_0^{-1}b,\\ &[(E_0^{-1}E_1)(E_0^{-1}E_2)+(E_0^{-1}E_2)(E_0^{-1}E_1)]E_0^{-1}b,\ldots,\\ &[(E_0^{-1}E_1)(E_0^{-1}E_p)+(E_0^{-1}E_p+E_0^{-1}E_1)]E_0^{-1}b,\\ &(E_0^{-1}E_2)^2E_0^{-1}b,[(E_0^{-1}E_2)(E_0^{-1}E_3)\\ &+(E_0^{-1}E_3)(E_0^{-1}E_2)]E_0^{-1}b,\ldots,[(E_0^{-1}E_2)(E_0^{-1}E_p)\\ &+(E_0^{-1}E_p)(E_0^{-1}E_2)]E_0^{-1}b,\ldots,(E_0^{-1}E_p)^mE_0^{-1}b\} \end{aligned}$$

In this way of computing V, there is another theorem in Ref. [15] which proves that the moments included in Eq. (31) are conserved by the reduced model. In the next subsection, we will show the applicability of this method to the model of Eq. (11).

3.5. Application to the Electrochemical Model

For the electrochemical model in Eq. (11), the system matrix K depends on the voltage which in turn plays the role of an input function that changes in time. According to the theory from Section 2, we can express this dependence as follows

$$K = G + s_1D_1 + s_2D_2$$

where G, D_1, D_2 are constant matrices and s_1 and s_2 are the functions of the voltage applied to the electrode

$$s_1(t) = e^{u(t)}, \quad s_2(t) = e^{-u(t)}$$

with $u(t) = v(t) - v_0$ and where v_0 is the reference voltage.

As result, the system (11) can be re-written as follows:

$$E\,d\vec{c}/dt + G\vec{c} + (s_1D_1 + s_2D_2)\vec{c} = \mathrm{F} \tag{32}$$

where the two scalar functions $s_1(t), s_2(t)$ are considered as parameters.

Taking into account that the initial condition of system (11) is a nonzero vector, $\vec{c}_0 \neq 0$, the Laplace transformation for Eq. (32) produces

$$(sE + s_1D_1 + s_2D_2 + G)x(s) = \mathrm{F}U(s) + E\vec{c}_0 \tag{33}$$

where $x(s)$ is the Laplace transformation of $\vec{c}$. By comparison, (33) is different from (30) when $p = 3$. This means that (31) cannot be used yet to construct the projection matrix for Eq. (32). However, as has been discussed in subsection C, we can first transform the vector in Eq. (32) as $\tilde{\vec{c}} = \vec{c} - \vec{c}_0$ without loss of accuracy and obtain a new system with respect to $\tilde{\vec{c}}$,

$$E\,d\tilde{\vec{c}}/dt + G\tilde{\vec{c}} + (s_1D_1 + s_2D_2)\tilde{\vec{c}} = \mathrm{F} + G\vec{c}_0 + s_1D_1\vec{c}_0 + s_2D_2\vec{c}_0 \tag{34}$$

For the new system, the initial condition is exactly zero, $\tilde{\vec{c}}_0 = \vec{c}_0 - \vec{c}_0 = 0$. After Laplace transformation, (34) becomes,

$$sEx(s) + Gx(s) + (s_1D_1 + s_2D_2)x(s) = \widetilde{F}U(s) \tag{35}$$

with $\widetilde{F} = F + G\vec{c}_0 + s_1D_1\vec{c}_0 + s_2D_2\vec{c}_0$.

Equation (35) is of almost the same form as Eq. (30), except that the vector b in Eq. (30) is not related with the parameters, whereas the vector $\widetilde{F}$ is dependent on two parameters. However, one can deal with this just after inspecting Eq. (31). In Eq. (31), the vector b is one of the base vectors to span the subspace for matrix V, in Eq. (35) the vector $\widetilde{F}$ is acting the same role as b. $\widetilde{F}$ is actually the linear combination of the three vectors, $(F + G\vec{c}_0)$, $D_1\vec{c}_0$, $D_2\vec{c}_0$. Therefore, when we construct the projection matrix V according to Eq. (31), we can replace the vector b in Eq. (30) by the three vectors above, that is, define a new matrix $B = (F + G\vec{c}_0, D_1\vec{c}_0, D_2\vec{c}_0)$ so that it is independent of the parameters. We construct the projection matrix V for Eq. (35) according to Eq. (31) as

$$\begin{aligned} colspan(V) = span\{&G^{-1}B,(G^{-1}E)G^{-1}B,(G^{-1}D_1)G^{-1}B,\ldots,\\ &(G^{-1}D_2)G^{-1}B,(G^{-1}E)^2G^{-1}B,\\ &[(G^{-1}E)(G^{-1}D_1)+(G^{-1}D_1)(G^{-1}E)]G^{-1}B,\ldots,\\ &[(G^{-1}E)(G^{-1}D_2)+G^{-1}D_2+G^{-1}E)]\\ &G^{-1}B,(G^{-1}D_1)^2G^{-1}B,\ldots,(G^{-1}D_2)^jG^{-1}B\} \end{aligned}$$

The final reduced model is

$$\widehat{E}\,dz/dt + \widehat{G}z + (s_1\widehat{D}_1 + s_2\widehat{D}_2)z = \widehat{F} \tag{36}$$

where

$$\widehat{E} = V^TEV, \quad \widehat{G} = V^TGV, \quad \widehat{D}_1 = V^TD_1V,$$
$$\widehat{D}_2 = V^TD_2V, \quad \widehat{F} = V^T\widetilde{F}$$

After obtaining the solution z in Eq. (36), we return back to the solution $\tilde{\vec{c}}$ in Eq. (34) via $\tilde{\vec{c}} \approx Vz$, the original solution $\vec{c}$ in Eq. (11) can be computed by $\vec{c} = \tilde{\vec{c}} + \vec{c}_0$.

In the next section, we will show the efficiency of parametric model reduction for the simulation of a voltammogram with numerical simulation results for the case study described in Section 2.

4. NUMERICAL EXPERIMENTS

In this section, we present simulation results to show both the accuracy of the proposed transformation technique to deal with nonzero initial conditions and the efficiency of the parametric model order reduction method combined with the transformation technique.

Figure 1 and Figure 2 show the layout of the scanning electrochemical microscope for which the partial differential equations in Eqs. (2) and (3) are derived (see Section 2). Figure 1 is the computational unit and Figure 2 is the discretization scheme of the control volume method. The resulted system in Eq. (11) is of dimension 16912, that is $\vec{c} \in R^{\mathrm{n}}$, and $n = 16912$. We have limited the dimension of the system on purpose, as our goal was to research on the method rather than to develop a scalable implementation. In the figures below, q represents the dimension of the reduced small system, that is, the unknown vector $\vec{z} \in R^{q}$.

In order to give clear and simple description for the transformation technique, we simulated the current after imposing voltage $E - E_0 = 0.1$ V, that is, we set the system matrix K in Eq. (11) as a constant matrix. The simulation results for the transformation technique are shown in Figures 4–9.

In Figure 4, we show the plot of the solution for the current. We compare the solution by conventional projection technique and the solution by the proposed transformation technique with the solution computed by direct simulation. One can see that for the conventional projection technique (dotted line), the reduced system of dimension 100 cannot reproduce the initial condition of the current. At the same time, the solution derived by the proposed transformation technique is indistinguishable from the solution computed by traditional direct simulation.

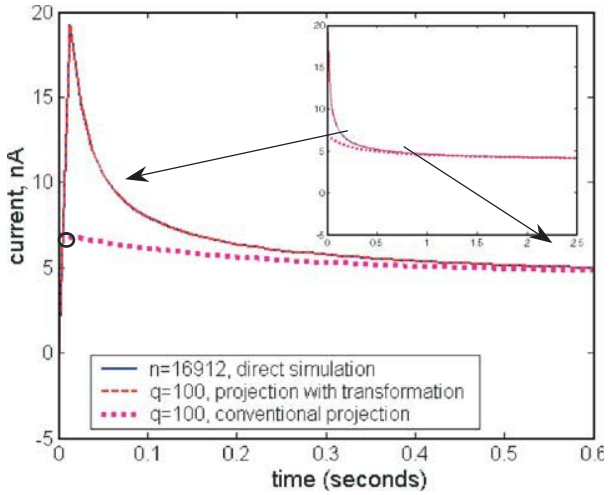

Fig. 4. Comparison between direct simulation and model reduction for the electrode current. The small circle on the vertical axis indicates the mismatch of the conventional projection method for initial condition.

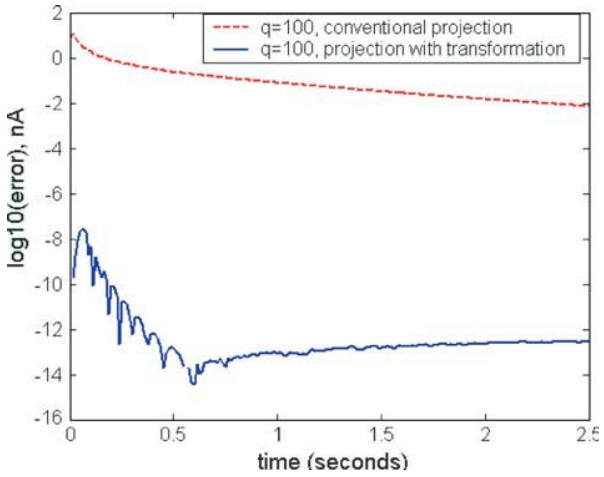

Fig. 5. Errors of model reduction with two different projection techniques for the solution of electrode current.

The simulation errors of the two model order reduction techniques are displayed in Figure 5. The error is defined as

$$error = |y(t) - \hat{y}(t)| \tag{37}$$

where $y(t)$ is the current computed by direct simulation for system (11), $\hat{y}(t)$ is the current computed by reduced system in Eqs. (13) or (22). In order to put the errors of the two different model order reduction techniques into one figure, we use a logarithmic plot. The dashed line is the error of the reduced system in Eq. (13) by the conventional projection technique. The solid line is the error of the reduced system in Eq. (22) by the proposed transformation technique. They again show that the results of the model reduction with transformation technique are very accurate.

In Figure 6 and Figure 7, we further show the accuracy of model order reduction with simulation results for the current obtained from several reduced models of different

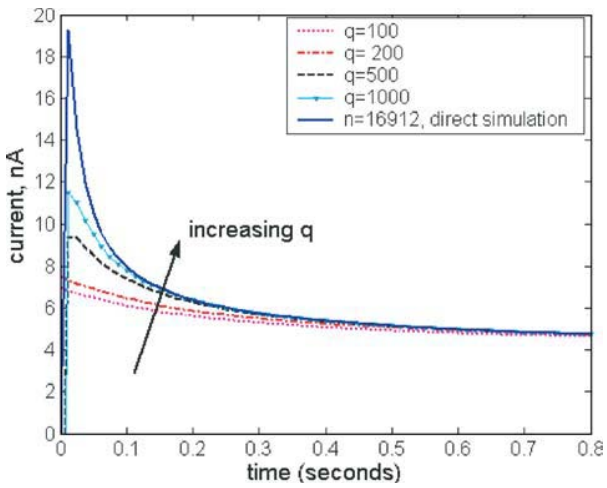

Fig. 6. Solution for electrode current by different dimensions of reduced models with conventional model reduction.

RESEARCH ARTICLE

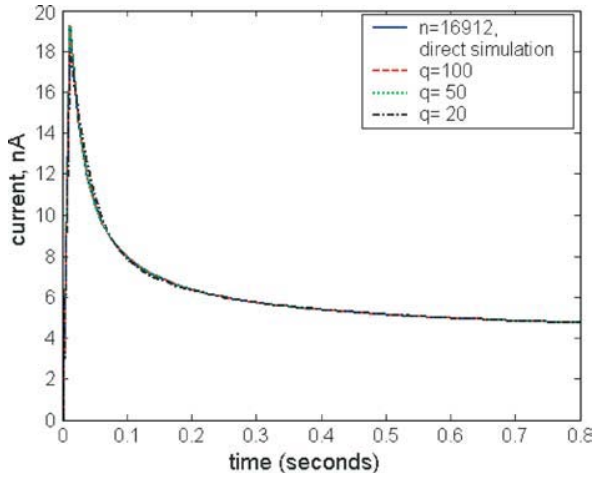

Fig. 7. Solution for electrode current by different dimensions of reduced models with proposed transformation technique.

dimensions. In Figure 6, the simulation results are from four different reduced models of dimension 100, 200, 500, and 1000, respectively by the conventional projection technique. In Figure 7 we plot simulation results, which are from three different reduced models of respective dimensions 20, 50, 100 by the proposed transformation projection technique. From Figure 6, we can see that the results of the reduced models by conventional projection technique are not accurate even if we increase the dimension of the reduced model to 1000. For the proposed transformation technique, it can be seen that the results of the reduced model are still very accurate even if the dimension of the reduced model is very small ($q = 20$). The errors of the reduced models by the proposed transformation technique are all below 10^{-6} for the three cases.

Figures 8–11 show the simulation results of the original full-scale model and the reduced model obtained by the parametric model reduction method combined with the proposed transformation technique for the cyclic

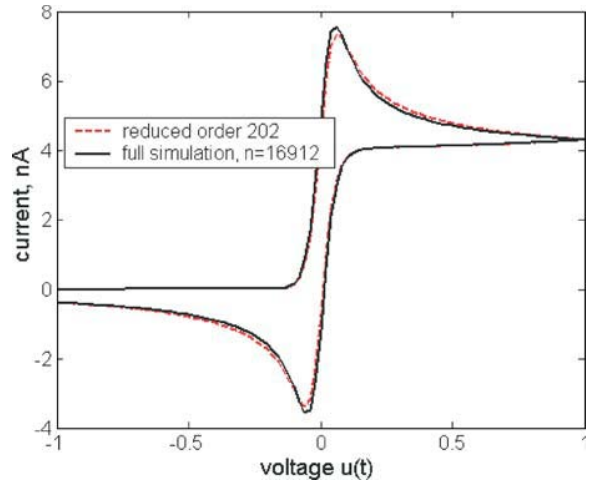

Fig. 8. Simulated cyclic voltammogram for $du/dt = \pm 0.5$.

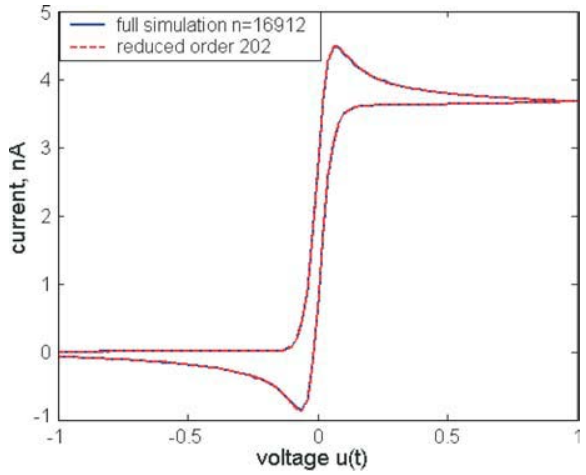

Fig. 9. Simulated cyclic voltammogram for $du/dt = \pm 0.05$.

voltammogram. The dimension of the reduced model is $q = 202$. The voltage follows a symmetric triangular waveform:

$$\begin{cases} u = u_0 + at, & 0 < t < t_{u_{\max}} \\ u = u_0 - at, & t_{u_{\max}} < t < 2t_{u_{\max}} \end{cases}$$

The figures display the current as a function of voltage (not in time) as this is the usual way to represent voltammograms. The solid line is the result computed by full simulation of the original large model, the dashed line is the result computed by the small reduced model. The results of the reduced model are accurate for a wide range of the dynamic behavior when the value of du/dt changes by three orders of magnitude (0.0005–0.5).

The major cost to integrate a system of ordinary differential Eq. (11) is the solution of a system of linear equations during time stepping. Let us compare the timing between a solution of a linear system of dimension $n = 16912$ for the original problem and dimension $q = 100$, 50, 20 for the reduced system. We use the sparse solver

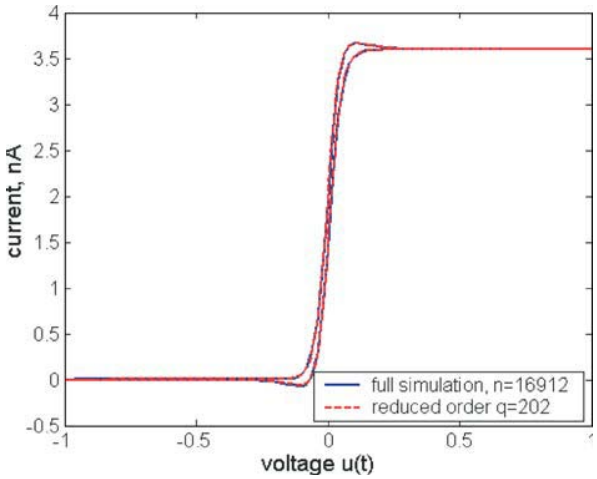

Fig. 10. Simulated cyclic voltammogram for $du/dt = \pm 0.005$.

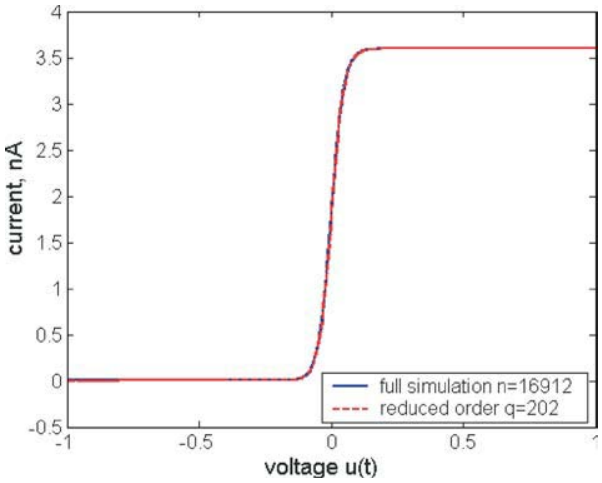

Fig. 11. Simulated cyclic voltammogram for $du/dt = \pm 0.0005$.

UMPACK[16] to solve a linear system for the original system, and LAPACK[17] to simulate the reduced system on the same workstation. The solution time on Sun Sparc Ultra-80 for the original system is 1.5 seconds, whereas solution of the reduced small model costs only 0.003, 0.0007, 0.0003 seconds respectively with respective speed factors 500, 2143, and 5000.

5. CONCLUSION

We have shown that it is feasible to apply model reduction in electrochemistry by addressing two major challenges: nonzero initial conditions and changes of the applied voltage in time. As was already mentioned, our case study is straightforward. However, it includes all features of a typical experiment in cyclic voltammetry and we believe that it is representative enough for this conclusion.

First, we have demonstrated that nonzero initial conditions are, mathematically speaking, far away from the low dimensional subspace that captures the system dynamics. The transformation technique presented in the paper allowed us to solve this problem and obtain a very accurate but low dimensional reduced system.

Second, we have introduced a parametric model order reduction technique in order to build a compact model to describe a voltammogram scan. Parametric model order reduction preserves the parameters in the original model in the reduced small model in the symbolic form so that the reduced small model can replace the original large model in simulation of a wide range of parameter values. At the same time, the reduced model produces solutions as accurate as the solution computed directly from the original large model.

Acknowledgments: This research is supported partly by NSFC research project 90307017, 60176017, 90207002, partly by the National Basic Research Program of China under the grant 2005CB321701, partly by Synopsys Inc., partly by Cross-Century Outstanding Schoolar's fund of Ministry of Education of China, partly by National 863 plan projects 2004AA1Z1050, Shanghai Science and Technology committee Key project 04JC14015 and Shanghai AM R&D fund 0418 and partly by a fund of the Alfried Krupp von Bohlen und Halbach-Stiftung of Germany.

References and Notes

1. A. J. Bard and M. V. Mirkin (Eds.), Scanning Electrochemical Microscopy, John Wiley and Sons, New York **(2001)**.
2. M. V. Mirkin, Theory in Scanning Electrochemical Microscopy, edited by A. J. Bard and M. V. Mirkin, John Wiley and Sons, New York **(2001)**, pp. 145–199.
3. A. L. Whitworth, D. Mandler, and P. R. Unwin, *Phys. Chem. Chem. Phys.* 7, 356 **(2005)**.
4. J. Heinze, M. Stoerzbach, Digital Simulation of Mass Transport to Ultramicroelectrodes. NATO ASI Series, Series E **(1991)**, Vol. 197, pp. 99–122.
5. T. Nann and J. Heinze, *Electrochem. Comm.* 1, 289 **(1999)**.
6. O. Sklyar and G. Wittstock, *J. Phys. Chem. B* 106, 7499 **(2002)**.
7. O. Sklyar, A. Kueng, C. Kranz, B. Mizaikoff, A. Lugstein, E. Bertagnolli, and G. Wittstock, *Analytical Chemistry* 77, 764 **(2005)**.
8. L. M. Silveira, M. Kamon, and J. White, Efficient Reduced-Order Modeling of Frequency-Dependent Coupling Inductances Associated with 3-D Interconnect Structures, *IEEE Transactions on Components Packaging and Manufacturing Technology Part B-Advanced Packaging*, **(1996)**, Vol. 19, pp. 283–288.
9. R. W. Freund, Reduced-Order Modeling Techniques Based on Krylov Subspaces and Their use in Circuit Simulation, in *Applied and Computational Control Signals and Circuits*, edited by B. N. Datta, Birkhauser, Boston **(1999)**, Vol. 1, pp. 435–498.
10. A. Odabasioglu, M. Celik, and L. T. Pileggi, PRIMA: Passive Reduced-Order Interconnect Macromodeling Algorithm, *IEEE Transactions On Computer-Aided Design of Integrated Circuits and Systems* **(1998)**, Vol. 17, pp. 645–654.
11. E. B. Rudnyi and J. G. Korvink, Review: Automatic Model Reduction for Transient Simulation of MEMS-Based Devices, Sensors Update **(2002)** Vol. 11, p. 3–33.
12. J. Roychowdhury, Reduced-Order Modeling of Time-Varying Systems, *IEEE Transactions On Circuits and Systems II-Analog and Digital Signal Processing* **(1999)**, Vol. 46, pp. 1273–1288.
13. J. R. Phillips, Projection-Based Approaches for Model Reduction of Weakly Nonlinear, Time-Varying Systems, *IEEE Transactions on Computer-Aided Design of Integrated Circuits and Systems* **(2003)**, Vol. 22, pp. 171–187.
14. D. S. Weile, E. Michielssen, E. Grimme, and K. Gallivan, *Appl. Math. Lett.* 12, 93 **(1999)**.
15. L. Daniel, O. C. Siong, L. S. Chay, K. H. Lee, and J. White, A Multiparameter Moment-Matching Model-Reduction Approach for Generating Geometrically Parameterized Interconnect Performance Models, *IEEE Trans. Computer-Aided Design of Integrated Circuits and Systems* **(2004)**, Vol. 23, pp. 678–693.
16. T. A. Davis. Algorithm 832: UMFPACK V4.3, an Unsymmetric-Pattern Multifrontal Method. ACM Transactions on Mathematical Software **(2004)**, Vol. 30, pp. 196–199.
17. E. Anderson, Z. Bai, C. Bischof, J. Demmel, J. Dongarra, J. Du Croz, A. Greenbaum, S. Hammarling, A. McKenney, S. Ostrouchov, and D. Sorensen. LAPACK Users' Guide. SIAM, Philadelphia, PA **(1995)**, 2nd edn.

SENSOR LETTERS
Vol. 4, 174–183, 2006

RESEARCH ARTICLE

Computer Assisted Design Study of a Non-Silicon Capacitive Pressure Sensor System

M. H. H. Meuwissen*, E. P. Veninga, M. W. W. J. Tijdink, and M. G. H. Meijerink

TNO Science and Industry, P. O. Box 6235, NL 5600 HE Eindhoven, The Netherlands

(Received: 11 September 2005. Accepted: 4 December 2005)

The application of numerical techniques for the design of a capacitive pressure sensor system in non-silicon materials is described. These techniques have been used to address issues related to the thermo-mechanical performance of the sensor system. This comprises the selection of the materials and dimensions used for the sensor itself and the substrate on which it is mounted. Moreover, simulations are applied to aid in the selection of suitable solder interconnect materials and dimensions. Where possible, the accuracy of the numerical predictions is assessed by comparing them to experiments on physical prototypes. The application of numerical simulations allowed for a reduction in the number of physical tests and thereby a reduction in design time and costs. A sensor system was specified based on the outcome of the design studies. It proved to meet the functional demands imposed by the targeted application on a laboratory scale.

Keywords: Non-Silicon Pressure Sensor System, Numerical Modelling, Soldering, Assembly and Packaging.

1. INTRODUCTION

Micromachined pressure sensors are already commercially available for many years.[1,2] However, they are typically fabricated in silicon which warrants their use only for applications in which they can be manufactured in large volumes because of the high costs for production facilities. In order to enable the production of low- and mid-volume series at reasonable unit prices, the materials and production costs have to be reduced considerably. This could possibly be achieved by the use of other materials and processes that are commonly applied and proven in micro-electronics.

The work presented in this paper is part of a project targeted at the development of a low-cost pressure sensor in non-silicon materials. The principle of this sensor is schematically shown in Figure 1.

The sensor basically consists of a thin circular membrane placed parallel to a rigid reference plane. The membrane and the rigid plane act as the two electrodes of a capacitor. Deflection of the membrane due to a pressure difference results in a change in capacity. The capacity changes are logged and used to calculate the pressure on the membrane.

The pressure sensor is to be applied for monitoring the ageing of a solid rocket propulsion material. For this particular material, ageing is accompanied by volumetric shrinkage. Since the material is stored in a rigid container, volumetric shrinkage causes a change of hydrostatic pressure which exerts a pulling load on the sensor membrane as shown in Figure 1.

Next to the low unit-price, other typical demands set for this application are: Ability to operate in a temperature domain ranging from −40 °C to +60 °C, ability to measure pressures of up to 5 bar, and ability to function over a time span of more than one year.

The pressure sensor is mounted on a Low-Temperature Co-fired Ceramic (LTCC) substrate. LTCC technology is readily available for the realisation of complex electronic circuits. In addition to the features of standard thick-film technology, LTCC allows for the integration of interconnect, actives, and passives inside the substrate, thereby creating a compact way of packaging and interconnecting electronic components. Apart from these benefits, it is characterised by other advantages such as hermeticity, bio-compatibility, close thermal matching with silicon, and advantages in high-frequency applications because of its low-loss tangent and high dielectric constant which is also stable over a broad range.[3]

For the current application, the substrate is used to accommodate the logging, interface, and transmission circuitry and the power supply. The LTCC substrate is placed as a lid on a box-shaped housing to protect the support electronics and power unit from environmental attacks. The set up is schematically shown in Figure 2.

*Corresponding author; E-mail: marcel.meuwissen@tno.nl

 1546-198X/2006/4/174/010 doi:10.1166/sl.2006.018

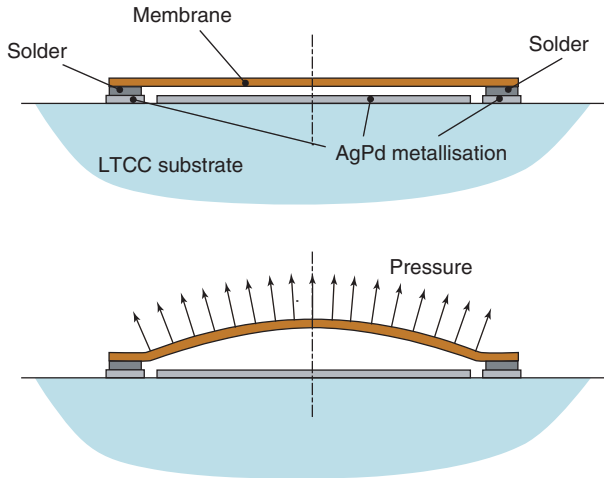

Fig. 1. Pressure sensor consisting of a thin circular membrane mounted onto a Low-Temperature Co-fired Ceramic (LTCC) substrate. In the intended application, a pulling load is exerted on the membrane resulting in an upward deflection.

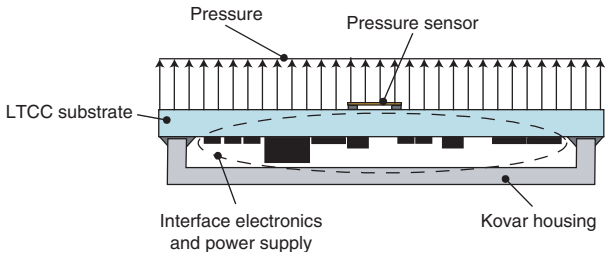

Fig. 2. Schematic layout of the pressure sensor, its supporting electronics, and power supply.

During the design phase of the autonomous pressure sensor, several aspects had to be addressed related to its thermo-mechanical behaviour. Finite element techniques were applied in addition to experiments on physical prototypes to arrive at a thermo-mechanically sound pressure sensor design. In particular, this concerns the following aspects:

- Sensor membrane: (i) response (deflection) to applied pressure, (ii) selection of suitable material and dimensions, (iii) selection of solder interconnect to the LTCC substrate (material and layout).
- LTCC substrate: estimation of its probability of failure under pressure load and selection of suitable dimensions.
- Interconnect between LTCC substrate and Kovar housing: feasibility study.

2. SENSOR MEMBRANE

Simulations of the mechanical response of the sensor membrane and its interconnect to the substrate are aimed at two aspects:
(i) determination of suitable membrane material and dimensions, and
(ii) selection of a suitable solder interconnect material and determination of a feasible interconnect layout.

2.1. Calculated Response of the Sensor Membrane to an Applied Pressure

Because of the simple shape of the sensor membrane, a straightforward analytical model can be derived to describe its mechanical and electrical response to pressure changes. As mentioned in the introduction, a change in pressure difference is detected electrically by a change in capacity. The capacity C for the current configuration is determined from:

$$C(p) = \int_{r=0}^{R_e} \frac{2\pi r \varepsilon}{h(r,p)}\, dr \qquad (1)$$

where, R_e is the radius of the rigid reference plane, ε the dielectric constant of the medium between the two electrodes, p is the pressure, and h is the distance between the upper and lower electrode (see Fig. 3).

The distance between the lower electrode and the membrane is the sum of the initial distance at zero pressure (h_0) and the deflection of the membrane due to the applied pressure. For a clamped circular plate loaded by a uniform pressure, the deflection w is given by[4]:

$$w(r) = \frac{p(R_m^2 - r^2)^2}{64D} \qquad (2)$$

with R_m the radius of the membrane and D the flexural rigidity:

$$D = \frac{Et^3}{12(1-\nu^2)} \qquad (3)$$

where E is the Young's modulus, t is the plate thickness, and ν the Poisson's ratio.

Using Eqs. (1) to (3), the membrane deflection and capacity changes can be calculated for different configurations. The results are summarised in Table I.

The lowest sensitivity is found for a thick Kovar membrane (250 μm) with a small radius (2.5 mm). In addition, the thick copper (200 μm) and LTCC (270 μm) membranes with the same diameter have a relatively low

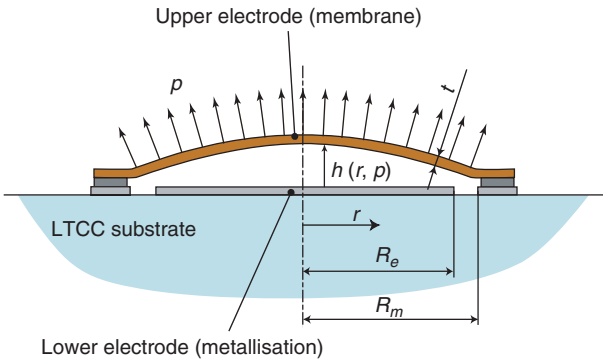

Fig. 3. Explanation of symbols.

RESEARCH ARTICLE

Table I. Maximal deflection and capacity change due to an applied pressure of 5 bar for several configurations (membrane dimensions and materials). Initial gap height h_0 is 40 μm and lower electrode radius $R_e = 1.5$ mm for all configurations.

Configuration			Capacity change [pF]	Maximal deflection of centre [μm]
Material	t [μm]	R_m [mm]		
Cu	200	2.5	0.10	3.5
Cu	100	2.5	1.57	27.7
Fe	100	2.5	0.64	16.6
LTCC	270	2.5	0.05	1.7
LTCC	270	3.5	0.24	6.5
LTCC	135	2.5	0.48	13.6
Kovar	250	2.5	0.04	1.5

sensitivity as well. The other configurations have significantly higher sensitivities.

2.2. Measured Response of the Sensor Membrane to an Applied Pressure

Figure 4 shows the results of an actual experiment using an LTCC membrane. In the experiment an LTCC membrane (thickness 270 μm, radius 2.5 mm) is subjected to a constant pressure for nearly 3 days. The sensor membrane is attached to the substrate by an SnAg3Cu0.5 solder alloy. The electrical capacity is measured with a 0.001 pF resolution.

For the unloaded membrane, the capacity is approximately 2.015 pF. From Eq. (1), the initial electrode distance h_0 is estimated at 31 μm. Using this estimate, the calculated capacity at 5 bar pressure is 2.09 pF, whereas the measured value is slightly less than 2.06 pF.

The sensor shows some capacity drift over the 3 day period (approximately 0.005 pF). This drift may possibly be attributed to time dependent behaviour of the solder material. After removal of the pressure, the membrane does not fully recover to its original deflection. This also indicates the presence of one or more irreversible mechanisms.

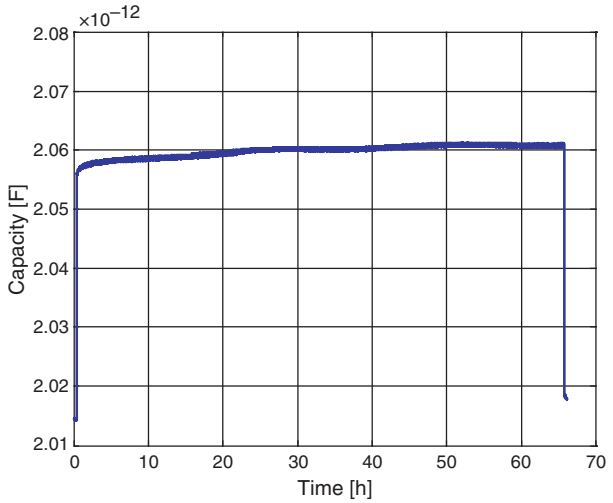

Fig. 4. Measured capacity of a 270 μm thick LTCC (membrane radius $R_m = 2.5$ mm) during testing. At $t = 0$ hours 5 bar pressure is applied, held constant for nearly 66 hours, and removed again.

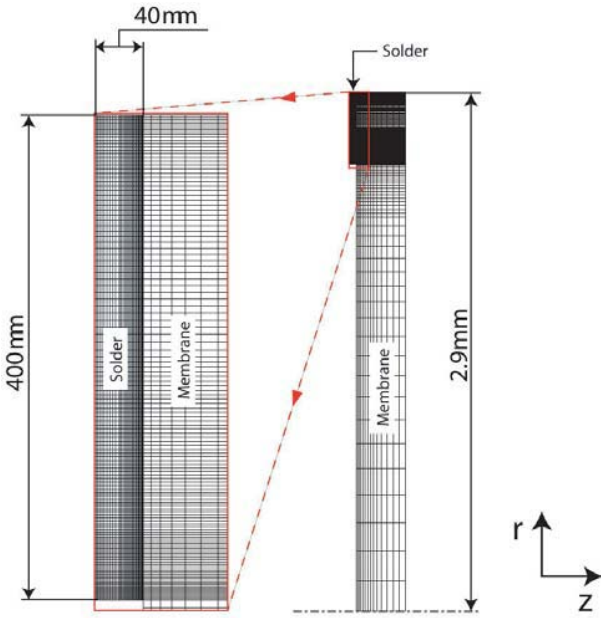

Fig. 5. Finite element mesh used for the axi-symmetric model consisting of the sensor membrane and a solder ring.

2.3. Finite Element Model

In order to gain some insight in the observed drift in the response of the sensor, an axi-symmetric model is implemented in a finite element package. This model comprises of the sensor membrane and a ring of solder material placed at the periphery of the membrane. Characteristics of the mesh of this model are shown in Figure 5. The width of the solder ring is 400 μm and its height is 40 μm. The radius of the membrane is 2.9 mm.

The membrane is assumed to behave linear elastistically whereas a creep law is adopted for the solder material. Simulations are carried out for both SnAgCu solder and eutectic SnPb solder. For the SnAgCu solder, the following creep law is used:[5]

$$\frac{d\varepsilon_{cr}}{dt} = C_1[\sin h(C_2\sigma)]^n \exp\left(\frac{E_{act}}{RT}\right) \qquad (4)$$

where R is the universal gas constant, ε_{cr} the creep strain, σ the stress, and T the temperature. The parameters in Eq. (4) are taken from literature[6] and summarised in Table II.

Table II. Parameters used in the creep Eq. (4) applied for the SnAgCu solder alloy.

Parameter	Value
C1	$7.925 \cdot 10^{+5}$
C2	0.0356 MPa^{-1}
E_{act}	$6.79 \cdot 10^{+4}$ J/mol
n	6

Table III. Parameters in the creep Eq. (5) applied for the eutectic SnPb solder.

Parameter	Value
C	16.534 K mm^2/N s
α	751
Q	$8.78 \cdot 10^{-20}$ J
n	3.3

For describing the creep behaviour of the eutectic SnPb solder the following creep law is applied:[7]

$$\frac{d\varepsilon_{cr}}{dt} = C\frac{G}{T}\left[\sin h\left(\alpha\frac{\sigma}{G}\right)\right]^n \exp\left(\frac{-Q}{kT}\right) \qquad (5)$$

where G is the shear modulus and k is Bolzmann's constant. The other parameters are taken from literature[5] and summarised in Table III. The plastic behaviour of the solder material is neglected in the current simulations. The other parameters required for the model are taken from literatur[8] and summarised in Table IV.

The top surface of the LTCC membrane is loaded by a uniform pressure which is increased linearly from 0 to 5 bar in 100 s and maintained at that level for 3 days.

Figure 6 shows the deflection of the centre of the membrane as a function of time for the two solder alloys. For the SnAgCu solder, the deflection increases by 0.11 μm over 3 days due to creep. From the experiments, the drift was estimated at 0.1 μm. Given the relatively large scatter on LTCC substrate thickness, the unknown thickness h_0, and the relatively crude approximation of the creep behaviour (only second level creep included), the numerical value compares well to the experimental one. For the eutectic SnPb solder alloy, the calculated creep over the 3 day period is much higher: about 0.88 μm.

The calculated stresses in the solder material remained well below the yield stress of the material, indicating that the inclusion of plastic behaviour in the model for the solder is unnecessary.

Figure 7 shows a part of the SnAgCu solder material in the region where the accumulated equivalent creep strain attains the highest values after 3 days. It can be seen that the maximal creep strain is concentrated in a corner-point (singular point). The peak values should thus be treated with care since they are mesh dependent. The strains somewhat further away are approximately 1%.

From the experimental and numerical investigations, it can be concluded that drift leads to an unacceptable

Table IV. Parameters used for the elastic part of the models. The parameters are taken from literature.

Material	Young's modulus [GPa]	Poisson's ratio [−]
Solder (SnAgCu)	38	0.40
Solder (SnPb)	30	0.37
LTCC (membrane)	100	0.30

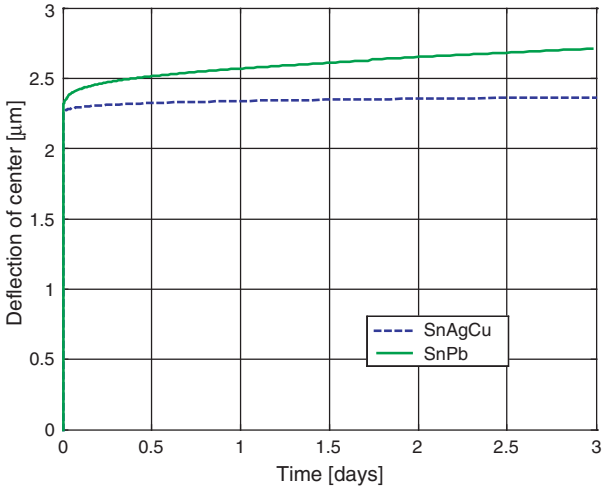

Fig. 6. Calculated deflection of the centre of the membrane during application of a uniform pressure (5 bar).

disturbance of the measurements. After 3 days, the drift on the out-of-plane displacement of the membrane is already 5% whereas a drift of less than 1% is acceptable for the intended application. The simulations support the hypothesis that the drift is caused by creep in the solder interconnect.

The sensor must be able to operate at temperatures up to 60 °C over time periods of up to one year. Higher temperatures generally lead to more pronounced creep behaviour

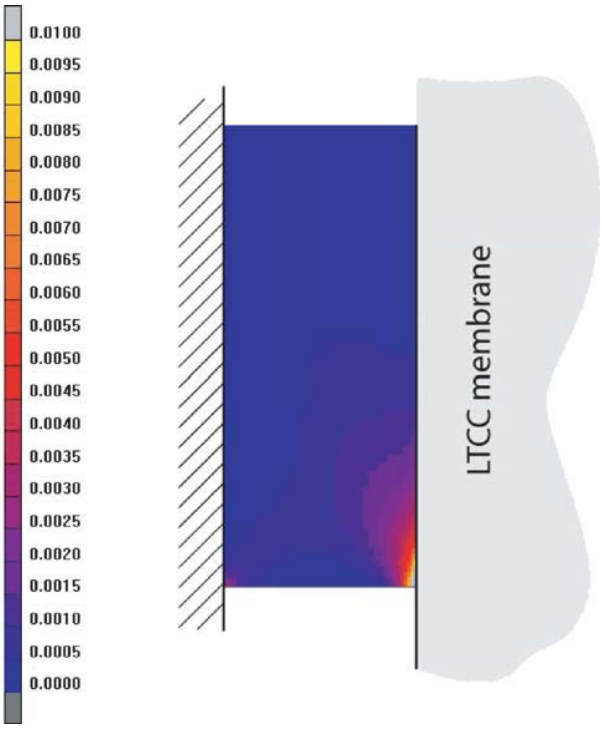

Fig. 7. Accumulated creep strain in the SnAgCu solder interconnect after 3 days under a constant pressure load of 5 bar on the membrane surface.

RESEARCH ARTICLE

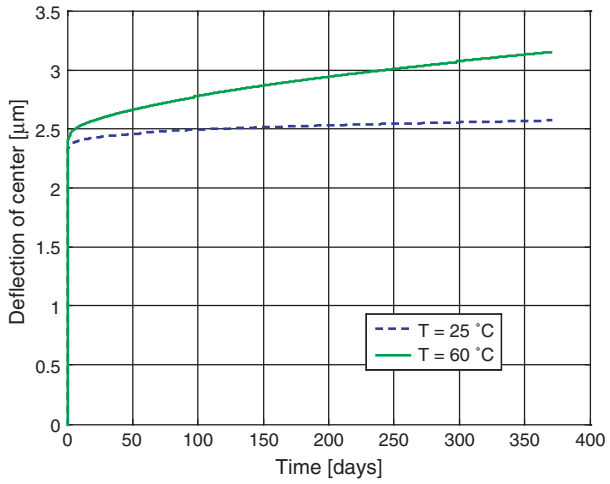

Fig. 8. Calculated displacement of the centre of the membrane as a function of time at a constant pressure on the surface (5 bar) at 25 °C and 60 °C.

in the solder material. The previous analysis is repeated for a time period of 1 year at 25 °C and 60 °C for the SnAgCu solder. It should be noted that 5 bar pressure over 1 year is a worst case scenario for the present application. In practice, it is loaded for much shorter time spans at this pressure level. Figure 8 shows the calculated displacement of the centre of the membrane as a function of time. At 25 °C the drift over a one year time span is 14% whereas the drift has increased to nearly 40% at 60 °C. These high drift values are not acceptable for the current application.

Even for the SnAgCu solder, the drift of the out-of-plane displacement of the membrane is quite high, especially at higher temperatures. The additional deflection is caused by creep deformation in a fairly localised domain in the interconnect. For reducing the creep strains in this region, it is investigated whether a geometrical change of the membrane as shown in Figure 9 can improve the situation.

It is expected that the addition of a reinforcement ring will reduce the localised stress levels in the solder ring and thereby the accumulated creep strain over time.

Initial simulations using this new configuration indeed showed a reduction of drift of the centre of the membrane. These simulations were carried out with relatively arbitrarily values selected for the different geometrical parameters.

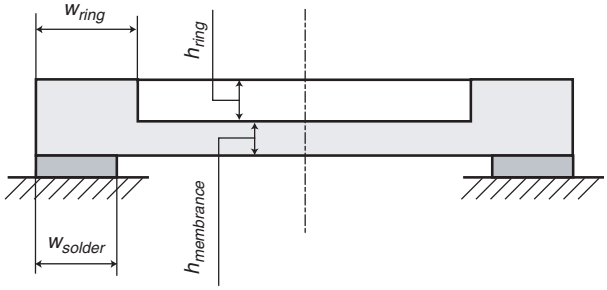

Fig. 9. Adjustments to the LTCC membrane (addition of a reinforcement ring) aimed at reducing the creep strains in the solder interconnect.

In order to determine the sensitivity of these parameters on the drift of the membrane deflection, a Design of Experiments (DoE) approach is utilised.[9] An L8 orthogonal scheme is used. The parameters to be varied are (see Figure 9):

(i) width of the solder ring w_{solder} (low/high: 0.4 mm/0.6 mm),

(ii) width of the reinforcement ring w_{ring} (low/high: 0.7 mm/1.1 mm),

(iii) height of the reinforcement ring h_{ring} (low/high: 405 μm/810 μm),

(iv) thickness of the membrane t_{membrane} (low/high: 135 μm/270 μm.

Within this scheme the following interactions are taken into account: i×ii, i×iii and i×iv.

The relative out-of-plane displacement drift of the membrane (displacement drift divided by initial displacement) over a one year period is used as output for the DoE. The main effects resulting from the DoE analysis are summarised in Figure 10. The optimal configuration is given by $w_{\text{solder}} = 0.6$ mm, $w_{\text{ring}} = 1.1$ mm, $h_{\text{ring}} = 810$ μm, and $t_{\text{membrane}} = 135$ μm.

In the next step, possible interactions with factor w_{solder} have been investigated and depicted in an interactions plot (Fig. 11). The nearly parallel lines for the interactions with the factors w_{ring} and t_{membrane} indicate that there is no significant interaction effect. A rather strong interaction effect can however be seen between the factors w_{solder} and h_{ring}. Since the combination of levels which yield the lowest drift is going to be included in the optimum configuration, no further measures have been taken.

The optimal configuration was not a setting used for the DoE runs. A simulation run with the optimal settings showed a displacement drift of 0.25% over a one year period. For a temperature increase to 60 °C this value increases to 0.5%. Both values are within the design limits.

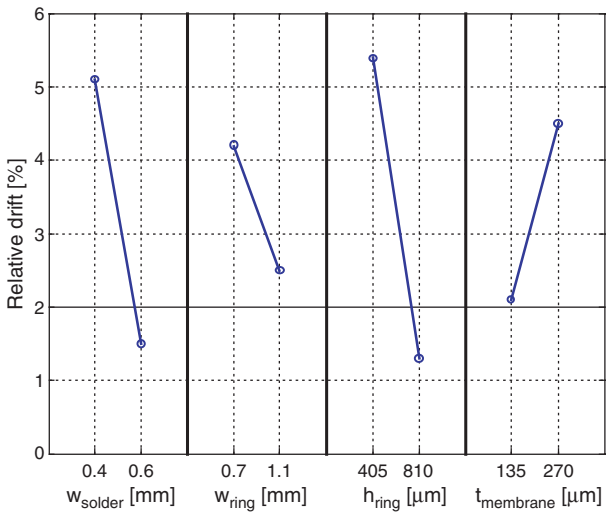

Fig. 10. Main effects of parameters on relative drift.

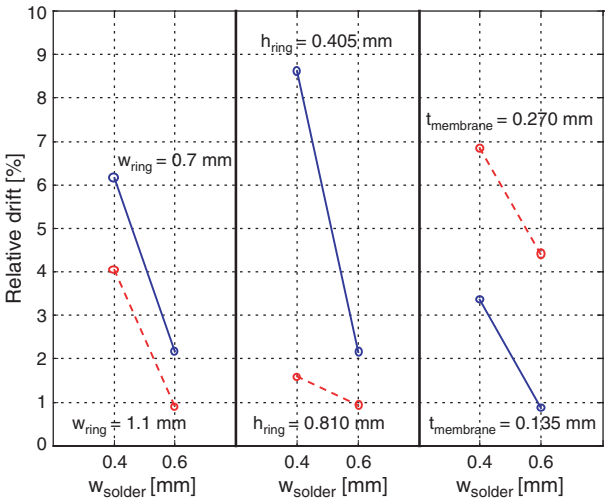

Fig. 11. Interactions between parameters on relative drift.

As a disadvantage of this solution, the additional cost required for fabricating membranes with reinforcement rings should be mentioned. An alternative is investigated in parallel in which use is made of another solder material with lower creep sensitivity: AuSn20. Unfortunately, the creep behaviour of this material has not been as thoroughly investigated as that for the more commonly used SnPb37 and SnAgCu alloys. Due to the lack of appropriate creep models for this material, it was not possible to assess its performance by numerical simulations and therefore physical prototypes incorporating this solder material were built and tested. An example of the response of a membrane attached to the surface with this solder material is shown in Figure 12. The drift in the measured capacity is significantly reduced compared to samples soldered with SnAgCu solder (see for example Fig. 4).

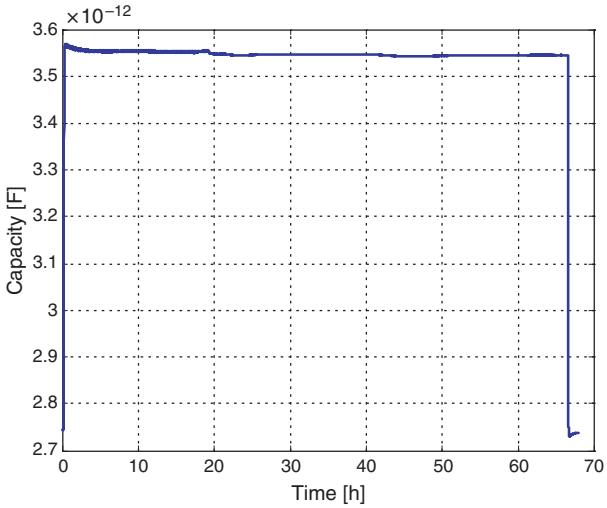

Fig. 12. Capacity measured on a membrane (stainless steel, $t = 200\ \mu$m, $R_m = 2.5$ mm) soldered to the LTCC substrate using AuSn20. At $t = 0$ hours, 5 bar pressure is applied, attained for nearly 70 hours and removed again. The slight drop in capacity is due to a slight reduction in applied pressure during the experiment.

3. LTCC SUBSTRATE

3.1. Probability of Failure

In order to accommodate all electronic components on the backside of the LTCC substrate, the width and length dimensions have to be set to at least 24×55 mm^2. The thickness is determined by the maximal load the substrate has to withstand (5 bar). In order to determine the minimal required thickness, finite element simulations were performed in combination with experiments on the LTCC material.

Among other factors, the critical tensile stress of the LTCC substrate is determined by the materials properties (homogeneity), processing conditions and the particular layout of the layers (orientation, presence of inclusions such as electrically conductive tracks, *et cetera*). Since there is some scatter on these parameters from sample to sample, it can be expected that there will be scatter in the critical strength of the samples as well. Here, the strength of the LTCC material is characterised by applying a Weibull approach.[10, 11] In this approach, the probability of failure is assumed to be a function of the applied stress and the volume under stress:

$$F = 1 - \exp\left[-\int_v \left(\frac{\sigma}{\sigma_0}\right)^m dV\right] \tag{6}$$

where F is the probability of failure, V is the volume, σ is the stress, and σ_0 and m are two parameters to be determined from measurements.

For determining the parameters σ_0 and m, three point bending experiments are carried out on samples with dimensions $10 \times 55 \times 1.6$ mm^3, which were supported on two rollers placed 27 mm apart. These samples were cut

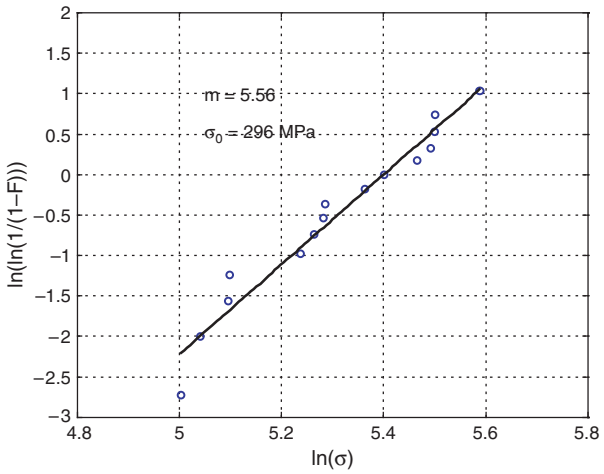

Fig. 13. Measurements and fitted Weibull curve.

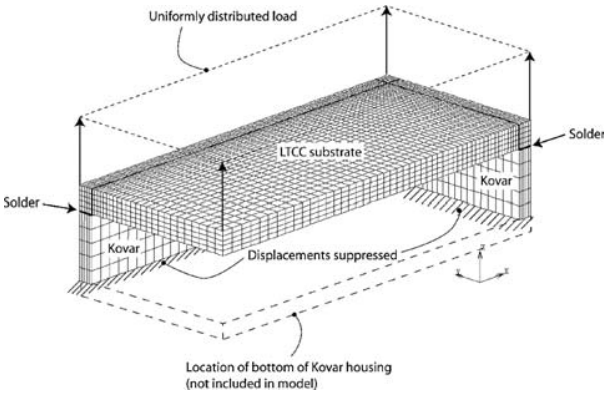

Fig. 14. 3D finite element mesh used for calculating the probability of failure of the LTCC substrate.

from larger LTCC substrates by laser. The characteristics of the sample material were similar to those of the final design (in terms of number of layers, presence of vias, and type of metallization materials).

The results of the bending tests are summarised in Figure 13. This figure also shows the fitted Weibull curve Eq. (6). The fit was determined by linear least squares regression.

The Weibull parameters are used in combination with finite element simulations to determine the probability of failure of a substrate with particular dimensions. For all design variants, the lateral dimensions of the LTCC substrate are set to 24×55 mm.[2] Several thickness values are evaluated in the range from 0.8 mm to 1.6 mm Eq. (6) is used to calculate the probability of failure for a design using for σ the maximal principal strain in a point as calculated with the finite element model. If the maximal principal strain in a point of the substrate is smaller than 0, σ at that location is set to 0 in order to accommodate for the fact that the LTCC material will be able to withstand compressive stresses much better than tensile stresses.

The finite element model for one of the configurations is shown in Figure 14. The model includes the LTCC substrate, a part of the (Kovar) housing and the solder interconnect between the housing and the substrate. The top surface of the substrate is assumed to be loaded by a uniform pressure (directed upward) which is increased from 0 to 5 bar. The displacements on the bottom face of the Kovar housing are suppressed. Due to symmetry in the assembly only one quarter is modelled. The bottom of the Kovar housing was not included in the model as this is

Table V. Parameters used for the elastic part of the constitutive models. The values are taken from literature.

Material	Young's modulus [GPa]	Poisson's ratio[−]
Solder (SnPb)	30	0.37
Kovar	137	0.31
LTCC	100	0.30

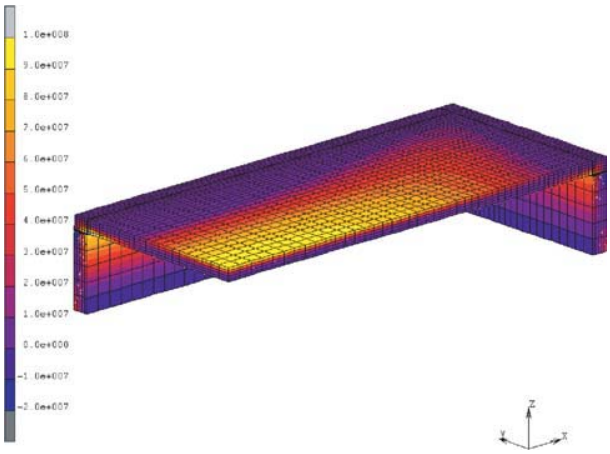

Fig. 15. Maximal principal stress in the assembly at a pressure load of 5 bar for an LTCC substrate thickness of 0.8 mm.

expected to have only a marginal influence on the deformations of the LTCC substrate.

The LTCC and Kovar materials are assumed to behave elastically whereas an elasto-plastic model with bi-linear kinematic hardening is taken for the SnPb solder material.[12] The parameter values are taken from literature and summarised in Table V.

Figure 15 shows the distribution of the maximal principal stresses in the assembly for an LTCC substrate thickness of 0.8 mm and a maximal load of 5 bar.

Using the calculated stresses and the Weibull equation fitted on the measurements, the probability of failure for different configurations can be calculated. The probability of failure is shown in Figure 16 for several values for the LTCC substrate thickness. It can be seen that for the 0.8 mm LTCC thickness, the probability of failure of the substrate at 5 bar pressure is approximately 12.5% whereas this value has dropped to less than 0.04% for the 1.6 mm thickness.

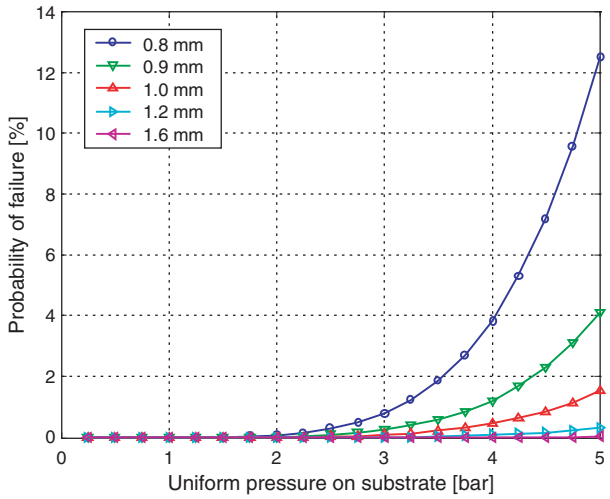

Fig. 16. Probability of failure of the LTCC substrate versus applied pressure for different substrate thicknesses.

4. INTERCONNECT BETWEEN LTCC SUBSTRATE AND KOVAR HOUSING

The second critical solder interconnect in the assembly is that of the LTCC substrate to the Kovar housing (see Fig. 2). In order to investigate the stress levels that develop in this interconnect during pressure load, a finite element model is created of the assembly.

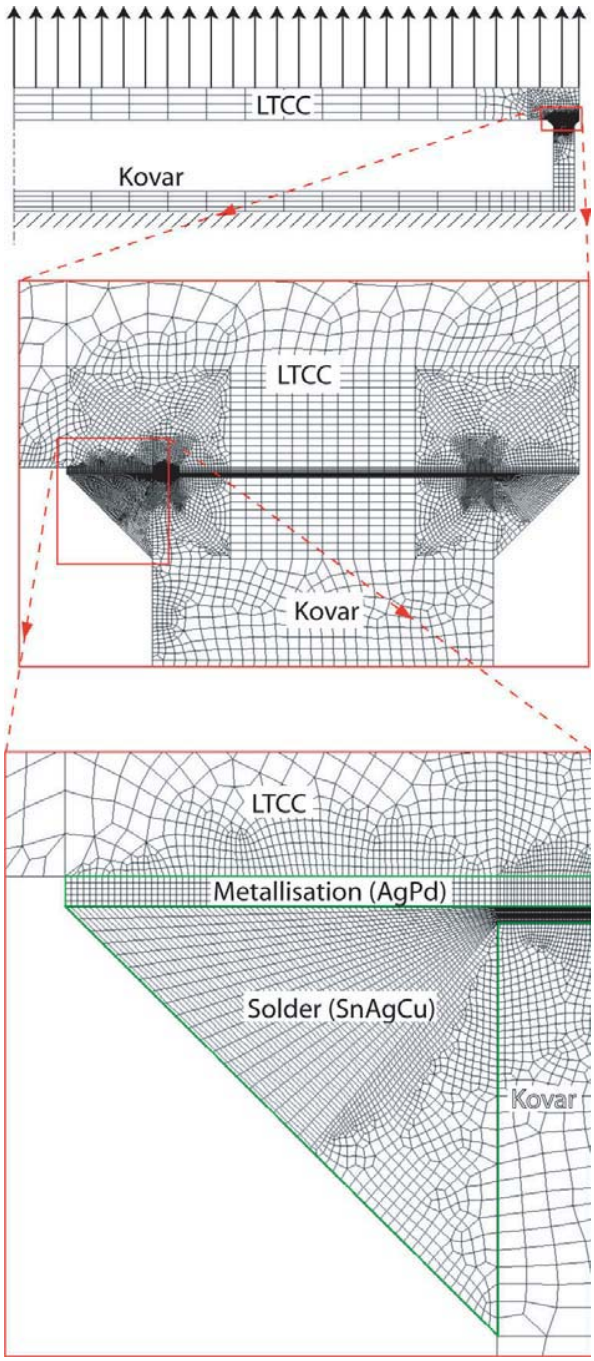

Fig. 17. Finite element model of the LTCC substrate and Kovar housing.

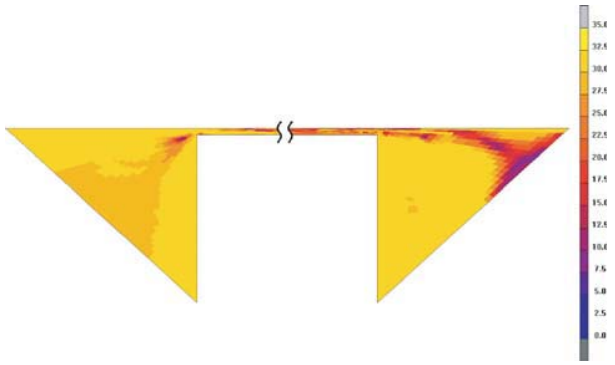

Fig. 18. Equivalent Von Mises stress in the solder interconnect at maximal pressure on substrate surface.

For time efficiency reasons, an axi-symmetric model is used although the assembly actually has a rectangular shape. Given the intended use of this initial model, this simplification is deemed acceptable. Figure 17 shows some details of the finite element mesh.

The LTCC substrate is loaded by a maximal pressure of 5 bar. The bottom (right side in Fig. 17) of the Kovar housing is fixed.

Figure 18 shows the equivalent Von Mises stress in the solder interconnect. The maximal stress is approximately 35 MPa which is well above the initial yield strength of the material (approximately 23 MPa).

As a measure for reducing the stresses on the solder interconnect, the interior of the Kovar housing is filled with an epoxy resin. Repeating the analysis for this new configuration, the maximal stresses in the solder interconnect reduce to an acceptable level of 2 MPa.

A new problem introduced by filling the cavity with epoxy is the thermal mismatch between this material and the other components. This is studied using the same model for a thermo-mechanical analysis. For this analysis, the materials in the assembly are assumed to behave linear elastically except for the solder material which is assumed to behave elasto-plastically.[12] The parameters for the elastic domain were taken from literature except for the epoxy material and AgPd metallisation. For the latter two materials, estimates were made. All parameters used in the simulations are given in Table VI.

Table VI. Parameters in elastic domain. The parameters for the epoxy and metallization materials are estimates. The other parameters are taken from literature.

Component	Young's modulus [GPa]	Poisson's ratio [−]	Coefficient of thermal expansion [ppm/°C]
Solder	38	0.40	23.0
LTCC	100	0.30	6.5
Kovar	138	0.31	3.5
Epoxy	5	0.35	30.0
Metallization	76	0.37	19.6

RESEARCH ARTICLE

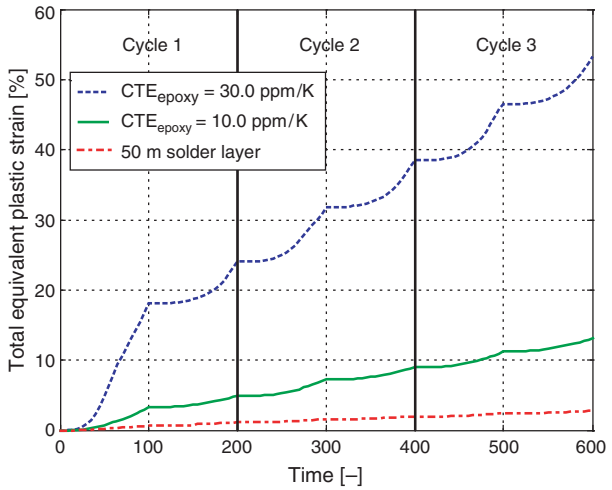

Fig. 19. Equivalent plastic strain in the solder interconnect for two values of the coefficient of thermal expansion (CTE) of the epoxy material.

A uniform temperature is assumed over the whole domain. This temperature is varied in time between −40 °C and 60 °C. A total of 3 cycles is simulated.

Figure 19 shows the development of the equivalent plastic strain during the three temperature cycles. Using the initial value for the coefficient of thermal expansion (30.0 ppm/°C) for the epoxy material, the accumulated strains in one cycle are unacceptably high (around 14%). Choosing the coefficient of thermal expansion of the epoxy material closer to that of the other materials in the assembly (10 ppm/°C), leads to a significant reduction of accumulated plastic strain. It should be mentioned however, that this value is extremely low as the coefficient of thermal expansion of commercially available filled epoxies is typically in the range of 20 to 25 ppm/°C below the glass transition temperature. Nevertheless the strain accumulation is still about 4% per cycle. This strain accumulation is mainly caused by the local thermal mismatch between the solder material and the other materials.

By increasing the solder layer thickness, this strain accumulation can be reduced even further. As an example, Figure 19 also shows the accumulated strain for a solder layer thickness of 50 μm instead of 10 μm. In this situation the accumulated plastic strain is reduced to 0.8% per cycle.

5. PHYSICAL PROTOTYPE

Figure 20 shows a functional prototype of the autonomous system with on top of the LTCC substrate the pressure sensor membrane and the antenna. The LTCC substrate is fabricated in panel form by Via Electronic. The membranes are mounted using a flip chip bonder. This enables both accurate alignment in x- and y-direction and the possibility to maintain the required assembly height of the membrane during soldering. The solder material is AuSn20 which is

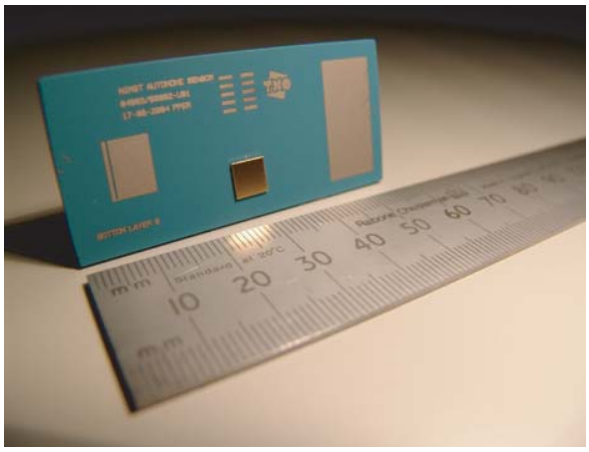

Fig. 20. Complete autonomous system including the sensor membrane, LTCC substrate, and Kovar.

applied as preform. Before further assembly, the pressure sensors are tested by a specially designed tool which can load the sensors in panel form by air pressure. The SMT-components on the secondary substrate side are mounted using a standard refow-soldering process. During this operation the interconnection of the sensor membrane will not re-melt due to the 280 °C melting temperature of AuSn20. After SMT-assembly the systems are cut out by laser and functionally tested. To finally close the systems, a ring of solder paste is printed on the edges of the LTCC substrate, a Kovar housing is placed and subsequently reflow soldered to seal the package. In case a filling is needed, the Kovar housings are provided with laser cut holes. The prototypes proved to meet the functional requirement to measure pressures of up to 5 bar with sufficient sensitivity. Figure 21 shows the results of a step-stress test.

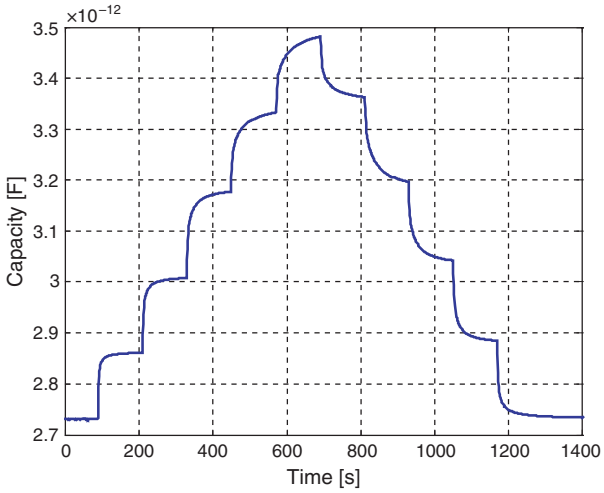

Fig. 21. Response of a pressure sensor to a step-stress test. The relaxation-like variation of the capacity versus time is caused by the testing equipment and the way in which the pressure is applied onto and removed from the sensor membrane.

6. CONCLUSIONS

Numerical simulations have been applied in combination with experiments in the thermo-mechanical design of a pressure sensor. The simulations were applied for the selection of suitable dimensions for the sensor-membrane and LTCC substrate onto which the sensor is mounted. Furthermore, they were applied for determining suitable solder interconnect materials and dimensions.

Initial experiments on a sensor prototype showed an unacceptably high drift of the out-of-plane displacement of the sensor membrane over time. Simulations were conducted to assess several geometrical design changes to reduce this drift. From these simulations it was concluded that the suggested changes did indeed lead to an improved design. However, the design change (addition of reinforcement ring) would also increase the cost of the sensor membrane fabrication. The application of a more creep resistant solder (AuSn20) was investigated as an alternative. Tests on physical prototypes with this solder alloy showed the drift to be reduced within acceptable limits.

The dimensions of the LTCC substrate was partly (width and length) determined by the number and size of the components (logging, interface, and transmission electronics, power supply) that had to be accommodated on it. The thickness of the substrate has been selected based on Weibull statistics.

Finally, the interconnect between the LTCC substrate and the Kovar housing was investigated. It was found that special precautions had to be taken in order to reduce the stresses in the solder interconnect.

The application of simulation techniques led to a significant reduction of the effort required for building and testing of physical prototypes, which in turn reduced design time and costs.

Future work will include life testing of prototypes to assess their long term stability and (thermo-mechanical) reliability.

Acknowledgments: The authors would like to thank Via Electronic GmbH in Germany for their technical support and for producing the LTCC test structures.

References and Notes

1. S. M. Sze, Semiconductor Sensors, John Wiley and Sons Inc. (**1994**).
2. S. A. Campbell and H. J. Lewerenz, Semiconductor Machining, Fundamentals and Technology (**1998**).
3. P. K. Khanna, B. Hornbostel, T. Jäger, and W. Schäfer, *MST News* 4/04, 40 (**2004**).
4. S. P. Timoshenko and S. Woinowsky-Krieger, Theory of Plates and Shells, McGraw-Hill (**1959**).
5. J. H. Lau, Ball Grid Array Technology, McGraw-Hill Inc., New York (**1995**), Chap. 13.
6. J. P. Clech, Review and Analysis of Lead-Free Solder Material Properties (**2004**).
7. R. Darveaux and K. Banerji, *IEEE Trans. Components, Hybrids, Manufact. Technol.* 15, 1013 (**1992**).
8. T. Siewert, S. Liu, D. R. Smith, and J. C. Madeni, Database for Solder Properties with Emphasis on New Lead-Free Solders (**2002**).
9. R. Roy, A Primer on the Taguchi Method, Van Nostrand Reinhold (**1990**).
10. W. Weibull, *J. Appl. Mech.* 18, 293 (**1951**).
11. D. W. Richerson, Modern Ceramic Engineering: Properties, Processing, and Use in Design, Marcel Dekker, Basel (**1992**).
12. S. Wiese, S. Rzepka, and E. Meusel, EuroSimE 2002, Paris (**2002**), p. 79.

SENSOR LETTERS
Vol. 4, 184–190, 2006

RESEARCH ARTICLE

Out of Plane Flexural Behaviour of Thin Polysilicon Films: Mechanical Characterization and Application of the Weibull Approach

Fabrizio Cacchione[1], Alberto Corigliano[1,*], Biagio De Masi[2], and Marco Ferrera[2]

[1] *Department of Structural Engineering, Politecnico di Milano, Piazza L. da Vinci 32, 20133 Milano, Italy*
[2] *MEMS Business Unit. STMicroelectronics, via Tolomeo 1, 20010 Cornaredo, Milano, Italy*

(Received: 6 December 2005. Accepted: 12 April 2006)

A new MEMS for on-chip mechanical testing of 0.7 μm thick polysilicon film has been designed, modelled, and fabricated. The polysilicon film is electrostatically loaded under bending until rupture in the out of plane direction, by means of electrostatic attraction in the direction orthogonal to the substrate. This is at difference with previous works of the same Authors, in which results relevant to in plane loading conditions have been presented. 3D Finite Element (FE) and Boundary Element (BE) models of the structure were used during the design and data reduction phases. Tests were carried out at room temperature and at atmospheric humidity. The measured Young's modulus obtained on 20 tested polysilicon specimens was 174 ± 9 GPa. Rupture stress computed after 21 tests, treated with the Weibull statistical theory, gave Weibull material parameters $\sigma_0 = 2237$ MPa, with a Weibull modulus $m = 5.1$.

Keywords: MEMS, Polysilicon, Mechanical Characterization, Bending Tests, Weibull Approach.

1. INTRODUCTION

The development of polysilicon MEMS technology and the large and fast diffusion of relevant applications, have forced researchers in the direction of a complete and correct characterization of polysilicon at the scale of micron.[1,2] In particular, the issue of MEMS reliability and mechanical characterization of polysilicon has become very important in the recent scientific literature.[3–14] Many approaches have been proposed in order to obtain parameters characterizing the mechanical response of polysilicon: Elastic parameters, rupture strength, and fracture properties under monotonic and cyclic loading.

The Authors have recently proposed a fully on-chip procedure for the characterization of polysilicon, based on *ad hoc* designed MEMS for mechanical testing.[13–16,20] The main advantage of on-chip approaches with respect to out of chip ones is related to the possibility of precisely characterising the same material which is used to produce MEMS without any disturbance induced by the manipulation of small specimens in the laboratory. Another advantage consists in the possibility of avoiding complicate gripping systems and data acquisition methods. In spite of the above mentioned advantages, a series of disadvantages still affect the on-chip methodologies, mainly related to the technological limitations associated to the MEMS production and to the limited possibility to load the specimens in various conditions.

The purpose of the present paper is to present recent results which aim at partially overcoming the limitations on loading conditions related to on-chip approaches. A MEMS has been designed with a parallel plate electrostatic actuator which loads (up to rupture) under out-of plane bending a couple of beam-shaped specimens. By means of a data reduction procedure based on the measurement of the capacitance variation, it is possible to obtain the value of the Young's modulus of the polysilicon specimen and that of the maximum stress at rupture.

The particular loading conditions chosen in the present study have been motivated by two main reasons: The necessity to precisely control an electrostatically actuated movement in the direction orthogonal to the substrate and the need to verify the existence of differences in the elastic and rupture properties of polysilicon for in plane and out of plane bending, possibly related to the anisotropy of the particular structure of the material originated by the production process.

*Corresponding author; E-mail: alberto.corigliano@polimi.it

 1546-198X/2006/4/184/007 doi:10.1166/sl.2006.016

An outline of the paper is as follows. In Section 2 the layout and the main properties of the out-of-plane electrostatic actuator are briefly described. Section 3 is devoted to the description of the data reduction procedure and of numerical simulations. The obtained experimental results and the adopted Weibull approach are discussed in Section 4. Section 5 contains some closing remarks.

2. OUT OF PLANE ELECTROSTATIC ACTUATOR

The purpose of the present work has been the mechanical characterization of thin polysilicon films produced by means of the surface micromachining process called Thelma™ developed and used by the MEMS Business Unit of ST-Microelectronics.[14]

A set of test structures for on-chip fracture characterization of 0.7 μm thick polysilicon film have been designed, modelled, and fabricated. Figure 1 shows the whole device, while Figure 2 is a zoom of the central part where the beam specimens are placed. An holed plate of 15 μm thick polysilicon is suspended on the substrate by means of four elastic springs placed at the four corners. The holed plate is also connected to the thin polysilicon film specimens placed at the centre, as shown in Figure 2. The two symmetric specimens are in turn connected on one side to the holed plate, while on the other are rigidly connected to the substrate. The two specimens are therefore equivalent to a couple of doubly clamped beams. The holes in the plate are due to the etching process for the elimination of the sacrificial layer, thus allowing for movement of the holed plate with respect to the substrate.

The movement in the direction orthogonal to the substrate is obtained by electrostatic attraction of the holed plate towards the substrate. The whole plate and the

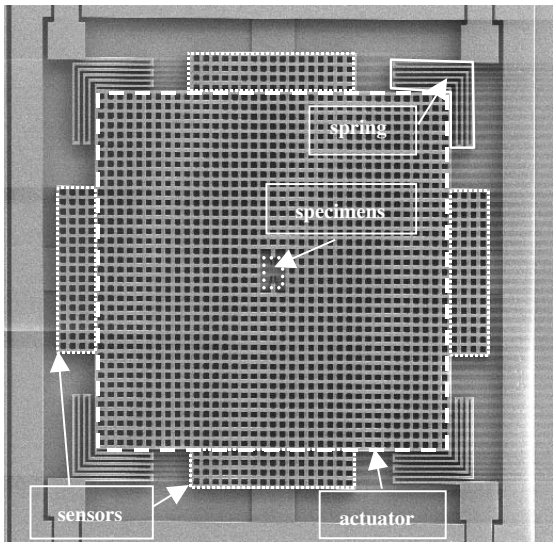

Fig. 1. Parallel plate actuator for out of plane bending tests: general view.

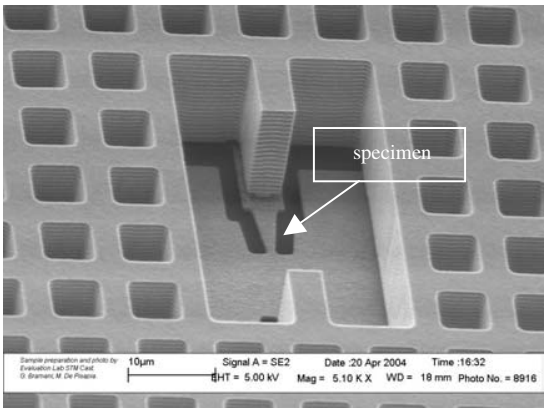

Fig. 2. Parallel plate actuator for out of plane bending tests: detail of one of the specimens.

substrate thus act as a parallel plate electrostatic actuator. When the plate moves towards the substrate, the couple of specimens bend, as schematically depicted in Figure 3.

It is important to remark that only the squared part of the holed plate acts as an actuator (see Fig. 1), while the holed rectangular parts added to each side of the plate act as sensors; these in turn allow for the experimental determination of the capacitance variation and of the vertical movement, as discussed in Section 3.

The choice of on-chip electrostatic actuation was driven by the advantage of great precision and absence of misalignment due to external manipulation.

The length of each specimen is 7 μm; in order to force the rupture in an *a priori* chosen section, their cross section changes with a linearly varying width which decreases from 3 μm to 1 μm (see Fig. 2).

Due to the end constraint of the specimens, the internal stresses were not released. The length of the specimen was kept short enough to avoid Eulerian buckling due to the internal stresses. An estimation of the residual stress gradient was done measuring with a profilometer the deformed shape of released cantilevers fabricated on the same die of the test structure. In order to measure the residual stress, an array of doubly clamped beams with different length was used. The residual stress was then extracted from the buckling load of the shorter beam of the array which undergoes buckling.

A linear elastic 3D FE model of a quarter of the central part of the structure was used during the design phase, in order to optimize the shape of the specimen with the goal to obtain rupture; Figure 4 shows some details of the FE mesh.

Fig. 3. Specimens loaded in bending.

RESEARCH ARTICLE

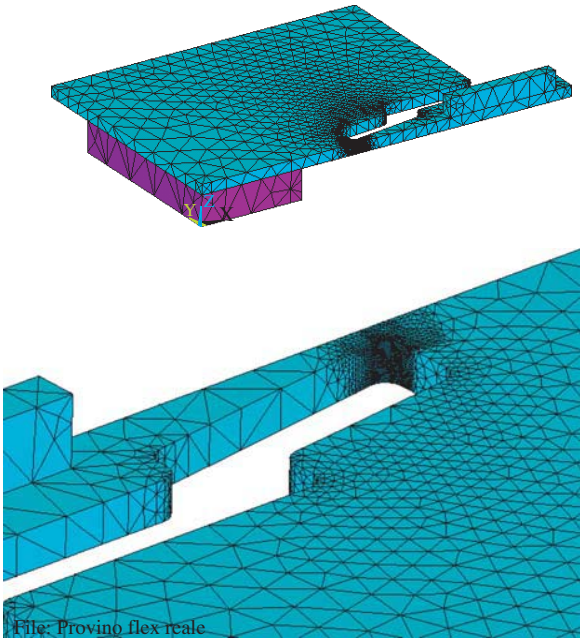

Fig. 4. Details of the Finite Element Mesh.

3. DATA REDUCTION SCHEME AND NUMERICAL SIMULATIONS

Tests were carried out at room temperature and at atmospheric humidity, with a probe station mounted on an optical microscope (see also[14, 20] for further details on the experimental setup). A slowly increasing voltage was applied in order to induce quasi-static loading conditions in the specimen. The input voltage given to the structure and the variation of the capacitance induced by the displacement of the rotor was measured connecting an Agilent Precision LCR Meter between two pads. The LCR resolution, in the range of measures of interest in this work, is ± 1 fF.

The experimentally determined capacitance versus voltage plots were transformed in force versus displacement plots by making use of relationships between capacitance and displacement and between voltage and electrostatic force, respectively. These relations were obtained by means of accurate electrostatic BE and FE simulations given the complex geometry of the actuator and of the sensing system and the subsequent difficulty in applying analytical formulae.

A series of electrostatic BE simulations on one of the lateral sensors allowed for the determination of a capacitance variation versus vertical gap plot, which was directly used in order to transform experimental capacitance variation data in vertical displacements. The analyses were carried out decreasing the gap between the rotor and the stator part of the sensing electrodes from the value 1.8 μm until 0.2 μm, with a step equal to 0.1 μm. Figure 5 shows the BE discretization of one of the sensors, while in Figure 6

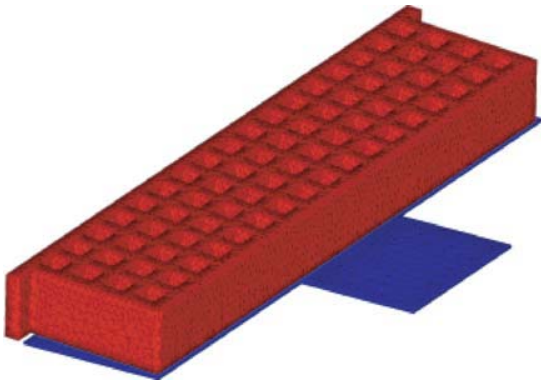

Fig. 5. BE discretization for one of the sensors.

it is shown the obtained sensing capacitance versus gap plot. The BE results were fitted with the expression below, also plotted in Figure 6:

$$g = \frac{0.2598}{C^2 + 1.3112\,C - 0.0315} \tag{1}$$

where g is the gap and C the measured capacitance. Notice that Eq. (1) can be used for values of C greater than 0.0236 pF, which is one of the zeros of the denominator.

FE electrostatic simulations were used in order to obtain the vertical force of attraction on the square holed plate acting as a rotor. In Figure 7 it is shown the 3D model used to this purpose: A quarter of a representative volume containing 100 holes was modelled, surrounded by a large volume of air. The electrostatic field was then found in the air surrounding the polysilicon plate, applying an imposed voltage as boundary conditions.

The analyses were carried out varying the gap between the plate and the substrate, in order to get the force versus gap relationship. The direct result of the analysis was the electrostatic energy of the system. The numerical results were fitted by means of a 6th order polynomial; computing the derivative of the energy with respect to the displacement, it was possible to obtain the force.

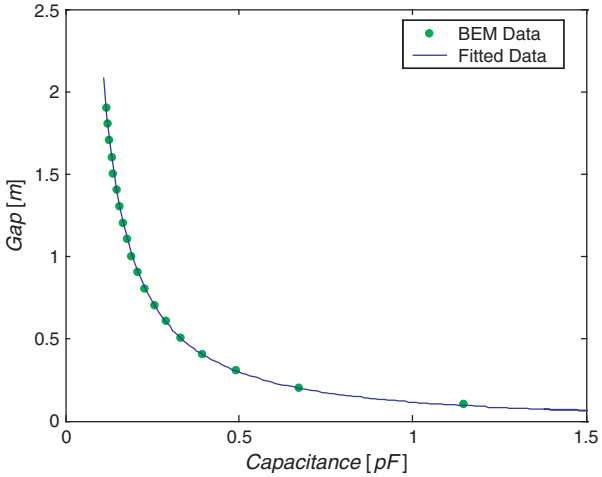

Fig. 6. Sensing capacitance versus gap plot.

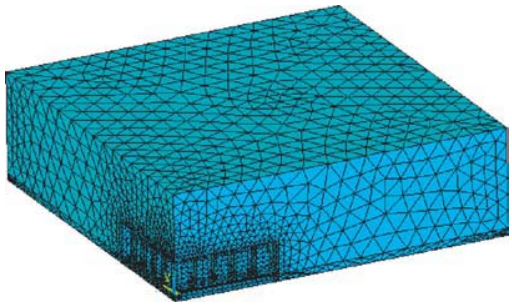

Fig. 7. FE discretization of the air surrounding a part of the actuator.

These results were compared (see Fig. 8) with the analytical formula for the electrostatic force developed by an infinitely thin square plate, without holes, with the same lateral dimensions, taking into account perimetrical fringing effects:

$$F_{\text{act}} = \frac{1}{2}\varepsilon_0\left[\frac{l^2}{(g_0-x)^2} + \frac{P}{2\pi}\frac{1}{(g_0-x)}\right]V^2 \qquad (2)$$

where ε_0 is the permittivity of vacuum, l the side of the plate, V the applied voltage, P the perimeter of the plate, g_0 the gap at rest and x the displacement.

As it is possible to see in Figure 8, in the gap range available for the actuation ($2.8 \div 4.2$ μm), the two curves are almost superposed. From the results of FE electrostatic simulations it was therefore deduced that the attractive vertical force can be computed by making use, with negligible error, of the analytical relation (2).

By means of the above briefly described procedure, the experimental capacitance versus voltage plot was transformed for each test in a force versus displacement one, as in the example shown in Figure 9.

Starting from the force-displacement plot, the force acting on the specimens was obtained by subtracting the part equilibrated by the elastic suspension springs in the four corners of the holed plate (see Fig. 1). An elastic 3D FE solution of the specimen under bending in the vertical plane (Fig. 10) was then used to relate the global stiffness of the specimen to the Young's modulus and the force at rupture to the maximum tensile stress in the specimen. Experimental values of Young's modulus and rupture stress were therefore finally obtained.

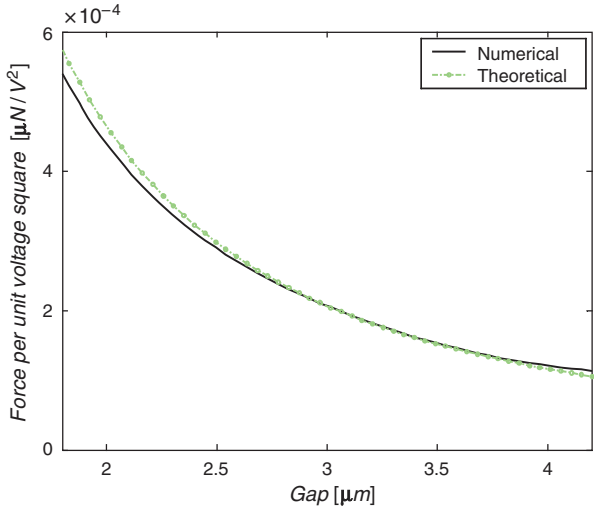

Fig. 8. Actuation force versus gap plots.

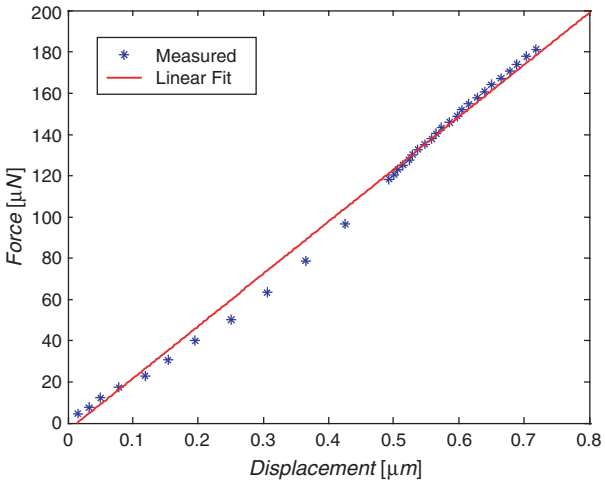

Fig. 9. Force-displacement plots obtained after the data reduction procedure.

The above briefly described data reduction procedure is analogous to that adopted in the previous paper[16] where it is described with more details.

A key point in the data reduction procedure, is the high sensitivity of the results to the value of the vertical gap between the holed plate and the substrate. In order to have an idea of this sensitivity, in Figure 11 a plot of the relative variation of the obtained Young's modulus $\Delta E/E$ versus the relative variation of the gap $\Delta g/g$ is shown. The results of Figure 11 have been obtained by considering the reference values $E = 175$ GPa, $g = 1.6$ μm with g variable in the range $1.5 \div 1.7$ μm. As it can be appreciated from Figure 11, the relative variation of the Young's modulus

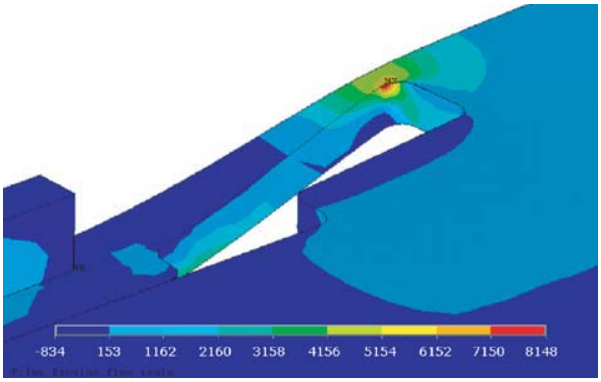

Fig. 10. Example of finite element results: deformed mesh and maximum principal stress (in MPa) obtained with an imposed vertical displacement = 1.4 μm.

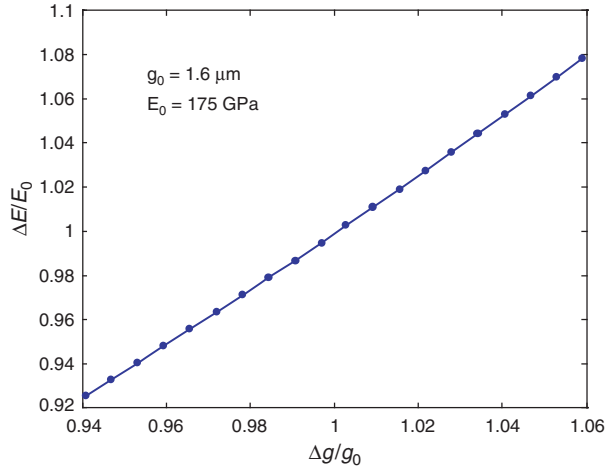

Fig. 11. Relative variation of the Young's modulus with respect to relative variation of the vertical gap.

with respecte to the relative variation of g is of the order of 100%. This fact must be carefully considered in the whole data reduction procedure also because the vertical gap cannot be easily measured on the real device and it can strongly depend on the quality of the etching process. In the results here presented a mean value of $g = 1.65\ \mu$m was used.

4. EXPERIMENTAL RESULTS AND APPLICATION OF WEIBULL APPROACH

The value of Young's modulus obtained from 20 tests was 174 ± 9 GPa, as shown in Figure 12.

The data concerning rupture of the specimens were interpreted in the framework of the Weibull approach for brittle materials,[18, 19] extending what already done in[14] (see also the parallel work.[20]) The application of the Weibull approach allows for a satisfying interpretation of stress gradient and size effects in the experimental rupture data.

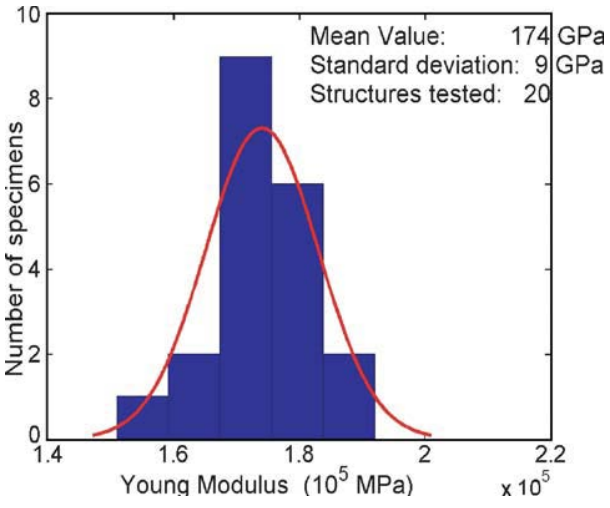

Fig. 12. Distribution of experimental results for the Young modulus.

In the case of a multi-axial, non uniform stress state it is usually assumed that cracks form in the planes normal to the principal stresses $\sigma_1(\mathbf{x})\sigma_2(\mathbf{x})$, $\sigma_3(\mathbf{x})$; the probability of failure is then given by:

$$P_f = 1 - \exp\left[-\frac{1}{\Omega_r}\int_\Omega \sum_{i=1}^{3}\left\langle\frac{\sigma_i(\mathbf{x}) - \sigma_u}{\sigma_0}\right\rangle_+^m d\Omega\right] \quad (3)$$

where Ω is the volume of the solid, Ω_r is a statistically uniform representative volume, σ_u, σ_0, and m are material parameters, $\langle\bullet\rangle_+$ denotes the positive part of $\bullet$ ($\langle\bullet\rangle_+ = \bullet$ if $\bullet > 0$; $\langle\bullet\rangle_+ = 0$, if $\bullet \leq 0$). Equation (3) is obtained from the one usually considered for a uniformly stressed uniaxial bar iterating the hypothesis of statistical uniformity of every volume and computing the joint probability of survival for every infinitesimal volume; a recent discussion can be found in Refs. [19, 20].

The general expression (3) is here applied under the assumption that $\sigma_u = 0$, which means that all level of stresses have an influence on the probability of failure. Equation (3) is then re-written in a more compact way as:

$$P_f = 1 - \exp\left[-\frac{1}{\Omega_r}\int_\Omega \left(\frac{\tilde{\sigma}(\mathbf{x})}{\sigma_0}\right)^m d\Omega\right] \quad (4)$$

once the equivalent stress $\tilde{\sigma}(\mathbf{x})$ is defined by:

$$\tilde{\sigma}(\mathbf{x}) \equiv \left(\sum_{i=1}^{3}\langle\sigma_i(\mathbf{x})\rangle_+^m\right)^{1/m} \quad (5)$$

The above relations can be used in order to estimate the probability of failure P_f of a given structure or solid once the *Weibull parameters* m and σ_0 are known and the elastic distribution of stresses has been computed via analytical formula or numerical solutions, e.g., the FE method.

Parameters m and σ_0 are usually experimentally determined starting from a series of uniaxially tensile tests on cylindrical specimens of volume Ω and surface area A; in this simple case Eq. (3) reduces to:

$$P_f = 1 - \exp\left[-\frac{\Omega}{\Omega_r}\left(\frac{\sigma}{\sigma_0}\right)^m\right] \quad (6)$$

Weibull parameters can be identified also from a specimen or structure loaded in a multiaxial situation with a non-uniform stress distribution, like the one here considered. Let us re-write Eq. (3) in a form similar to (6):

$$\begin{aligned} P_f &= 1 - \exp\left[-\frac{1}{\Omega_r}\int_\Omega \left(\frac{\tilde{\sigma}(\mathbf{x})}{\sigma_0}\right)^m d\Omega\right] \\ &\equiv 1 - \exp\left[-\frac{\Omega}{\Omega_r}\left(\frac{\sigma_{\text{nom}}}{\sigma_0}\right)^m \beta^m\right] \end{aligned} \quad (7)$$

where β is defined by

$$\beta^m \equiv \frac{1}{\sigma_{\text{nom}}^m \Omega}\int_\Omega \sum_{i=1}^{3}\langle\sigma_i(\mathbf{x})\rangle_+^m d\Omega \equiv \frac{1}{\Omega}\int_\Omega (h(\mathbf{x}))^m d\Omega \quad (8)$$

and σ_{nom} represents a nominal stress in the non uniformly stressed specimen or structure, which acts as a scaling parameter for the elastic response. Notice that function $h(\mathbf{x})$ defined by Eq. (8b) depends only on the normalized stress distribution in the linear elastic response and is therefore independent of the load level.

In order to compare the behaviour of different structures, it is possible to define a critical stress level as the nominal stress level $\sigma_{\text{nom}\,0}$ evaluated in the structure when the probability of failure is equal to 63.2%, in full equivalence to the interpretation of σ_0 for a uniaxially, uniformly loaded specimen. From Eq. (6b) it thus follows

$$\sigma_{\text{nom}\,0} = \frac{\sigma_0}{\beta}\left(\frac{\Omega_r}{\Omega}\right)^{1/m} \tag{9}$$

Given two structures (1) and (2), it is therefore possible to write

$$(\sigma_{\text{nom}\,0})_1 = \frac{\sigma_0}{\beta_1}\left(\frac{\Omega_r}{\Omega_1}\right)^{1/m}; \quad (\sigma_{\text{nom}\,0})_2 = \frac{\sigma_0}{\beta_2}\left(\frac{\Omega_r}{\Omega_2}\right)^{1/m};$$
$$\frac{(\sigma_{\text{nom}\,0})_1}{(\sigma_{\text{nom}\,0})_2} = \frac{\beta_2}{\beta_1}\left(\frac{\Omega_2}{\Omega_1}\right)^{1/m} \tag{10}$$

Relations (10) allow us for a direct comparison of the behaviour of structures with different volumes and stress distributions. The variation of parameter $\sigma_{\text{nom}\,0}$ with the volume clarifies the kind of size effect related to the statistical uniform distribution of defects described by a Weibull approach. $\sigma_{\text{nom}\,0}$ is inversely proportional to the volume and this dependence increases with decreasing m; at the limit, by letting m to infinite, the statistical size effect disappears. Noteworthy is also the dependence of $\sigma_{\text{nom}\,0}$ on the parameter β, which in turn depends on the stress non-uniformity.

Further details on the particular application of Weibull theory can be found in the parallel paper.[20] Starting from the experimental values of rupture stress, the statistical treatment implied in the Weibull approach was applied

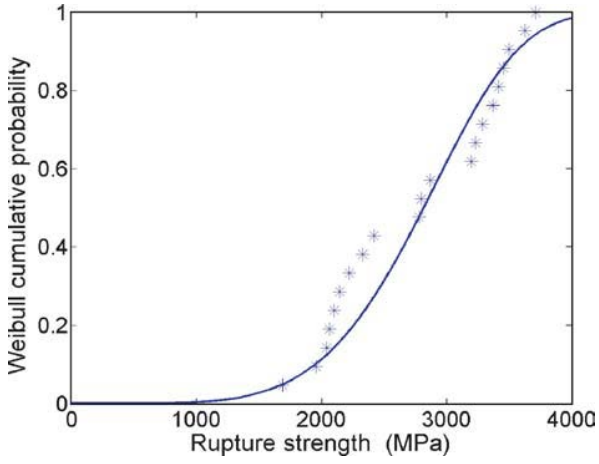

Fig. 13. Weibull cumulative probability of rupture strength.

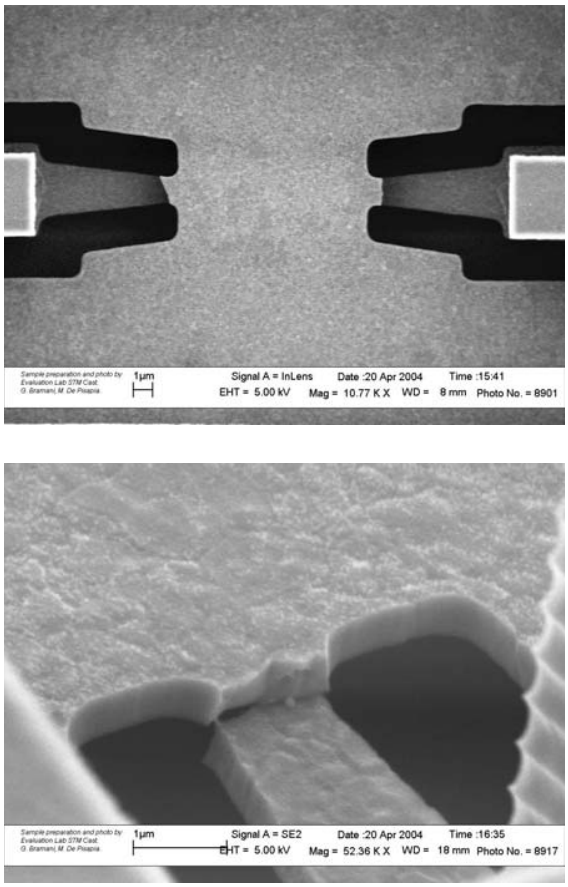

Fig. 14. Specimens after rupture.

taking into account the non-uniformity of the stress field in the specimens; this in turn implies the computation of volume integrals in Eq. (8) on the whole specimen volumes. The whole procedure was based on the 3D FE model already used during the design phase and for the evaluation of rupture stress. Volume integrals were computed by means of a numerical Gaussian integration on each tethraedral FE with quadratic displacement field.

21 specimens have been brought to rupture; the obtained Weibull parameters are $\sigma_0 = 2237$ MPa; $m = 5.1$, while the nominal stress value of Eq. (8) is $\sigma_{\text{nom}\,0} = 3026$ MPa. The experimental results and the cumulated Weibull plot are shown in Figure 13. An example of specimens after rupture is shown in Figure 14 where it can be clearly observed a specimen broken in the thinner cross section, as expected during the design phase.

5. DISCUSSION AND CONCLUSIONS

The results presented in the paper concern an ongoing research activity based on the use of on-chip tests for the mechanical characterization of thin polysilicon films.

A set of test structures was designed and fabricated to characterize the flexural behaviour of polysilicon films in a plane orthogonal to the substrate and to evaluate the

possible influence of grain morphology on the mechanical response. The device has been based on a holed parallel plate actuator which is attracted by the substrate in the direction orthogonal to it. A system of elastic springs keeps the holed plate suspended over the substrate. A couple of bending specimens is placed at the centre of the device.

The electrostatic actuation in the vertical direction developed loads large enough to break the specimen, as expected during the design phase.

In parallel works,[16, 20] results concerning the rupture properties of polysilicon captured by means of in-plane loading have been recently published. In particular, results concerning 0.7 μm thick polysilicon film with have been discussed.[20] The Weibull parameters there obtained are $\sigma_0 = 1840$ MPa; $m = 6.2$, which are different from those obtained in the present work for out of plane loading: $\sigma_0 = 2237$ MPa; $m = 5.1$. A possible explanation for the remarkable difference obtained in the two sets of Weibull parameters can be the influence of different loading conditions which could locally initiate different rupture mechanisms. As already discussed at the end of Section 3, an additional reason for possible discrepances in the results can be found in the influence of geometrical parameters like the gap between the holed plate and the stator.

Careful consideration and possible improvements in the whole data reduction procedure seem to be necessary before judging the present preliminary results as representative of the possibly remarkable difference between in plane and out of plane behaviour of polysilicon films.

Acknowledgment: The contribution of EU NoE Design for Micro and Nano Manufacture (PATENT-DfMM), contract n°: 507255 is gratefully acknowledged.

References and Notes

1. J. W. Gardner, V. K. Varadan, and O. O. Awadelkarim, Microsensors MEMS and Smart Devices, Wiley, Chichester **(2001)**.
2. S. E. Lyshevski, MEMS and NEMS, Systems Devices and Structures, CRC Press, Boca Raton **(2002)**.
3. S. Greek, F. Ericson, S. Johansson, and J. A. Schweitz, *Thin Solid Films* 292, 247 **(1997)**.
4. P. M. Oostemberg and S. D. Senturia, *J. Microelectromech. Syst.* 6, 107 **(1997)**.
5. W. N. Sharpe, K. T. Turner, and R. L. Edwards, *J. Exp. Mech.* 39, 162 **(1999)**.
6. H. Kahn, R. Ballarini, R. L. Mullen, and A. H. Heuer, *Proc. R. Soc. Lond. A* 455, 3807 **(1999)**.
7. H. Kahn, N. Tayebi, R. Ballarini, R. L. Mullen, and A. H. Heuer, *Sens. Actuators A* 82, 274 **(2000)**.
8. T. Ando, M. Shikida, and K. Sato, *Sens. Actuators A* 93, 70 **(2001)**.
9. I. Chasiotis and W. G. Knauss, *Exp. Mech.* 42, 51 **(2002)**.
10. J. Bagdahn and W. N. Sharpe, Jr., *J. Microelectromech. Syst.* 12, 302 **(2003)**.
11. D. Gao, C. Carraro, V. Radmilovic, and R. T. Howe, *J. Microelectromech. Syst.* 13, 972 **(2004)**.
12. C. S. Oh, H. J. Lee, S. G. Ko, S. W. Kim, and H. G. Ahn, *Sens. Actuators* 117, 151 **(2005)**.
13. A. Villa, B. De Masi, A. Corigliano, A. Frangi, and C. Comi, *Proceedings Second MIT Conference on Computational Fluid and Solid Mechanics*, Boston, Elsevier **(2003)**, Vol. 1, P. 722.
14. Corigliano, B. De Masi, A. Frangi, C. Comi, A. Villa, and M. Marchi, *J. Microelectromech. Syst.* 13, 200 **(2004)**.
15. B. De Masi, A. Villa, A. Corigliano, A. Frangi, C. Comi, and M. Marchi, *Proceedings MEMS04*, Maastricht **(2004)**.
16. F. Cacchione, B. De Masi, A. Corigliano, and M. Ferrera, *Sens. Lett.* 4, 38 **(2006)**.
17. W. Weibull, *J. Appl. Mech.* 18, 293 **(1951)**.
18. P. Stanley and E. Y. Inanc, Probabilistic Methods in the Mechanics of Solids and Structures. in *Proceedings Symposium to the memory of W. Weibull*, Stockholm, Springer-Verlag, Berlin **(1984)**.
19. Z. Bažant, Y. Xi, and S. Reid, *J. Eng. Mech. ASCE* 117, 2609 **(1991)**.
20. A. Corigliano, F. Cacchione, B. De Masi, and C. Riva, *Meccanica.* 40, 485 **(2005)**.

SENSOR LETTERS
Vol. 4, 191–199, 2006

Multiphysics for Structural Topology Optimization

Zhenyu Liu[1,*], Jan G. Korvink[1], and Michael L. Reed[2]

[1] Department of Microsystems Engineering, University of Freiburg-IMTEK, Freiburg D-79110, Germany
[2] Department of Electrical and Computer Engineering, University of Virginia, Charlottesville, VA, USA

(Received: 28 November 2005. Accepted: 12 April 2006)

Coupled simulation environment for MEMS devices are already available in a variety of commercial and freeware software packages. However, structural optimization for the multiphysics case has not been fully discussed yet. In most published cases, the optimization algorithm merely follows the traditional single-field problem case, in which design variable and sensitivity are updated sequentially. This paper presents a promising method to implement structural topology optimization via a fully coupled partial differential equation (PDE) expression. The multiphysical structural optimization is integrated via derivation of a suitable Lagrangian-Euler equation. The update of the structural topology is implemented through evolving material boundaries with the level set method. The accuracy of the boundary position is preserved with the h-adaptive mesh refinement method. A benchmark example of structural topology optimization which includes coupled effects is presented in order to demonstrate the feasibility of this method.

Keywords: Topology Optimization, Level Set Method, Moving Mesh Method, Finite Element Method, FEMLAB.

RESEARCH ARTICLE

1. INTRODUCTION

Microelectromechanical systems (MEMS) are miniaturized devices that consist of both mechanical and electrical parts. These systems can sense and actuate on a micro scale and can function individually or be arrayed on a macro scale.[1–3] A realistic physical model for a MEMS device can compose all areas of continuum physics, such as the mechanical, thermal, and electromagnetic energy domains. On accurate numerical simulation for MEMS device should include a single mathematical expression for each energy domain and possible interactive coupling among all the energy domains (Fig. 1).[4] Because of the complexity of coupling effects, an efficient numerical algorithm to solve the coupled PDE is a key point in order to obtain a reasonable numerical solution. Generally, there are two methods to discretize the coupled PDEs. The first is the sequentially de-coupled method by which the coupled PDEs are de-coupled and then all the PDEs are solved sequentially. The second is the direct method in which the coupled PDEs are discretized together and all the unknowns are solved simultaneously. For the sequentially de-coupled method, it is easy to find a suitable algorithm for each PDE. However, the solving sequence of the de-coupled PDEs will influence the convergence and accuracy of the numerical solution. In the case of direct discretization, the coupling effect is directly included in the discretized equations. However, this procedure will result in a large scale nonlinear equation system which needs an efficient numerical algorithm to obtain a converged solution. Nonlinear algorithms have experienced major progress and the direct discretization method is becoming more popular in MEMS simulation.

To date, fully coupled simulation environments have been implemented in several commercial and freeware software packages.[5–7] However, structural optimization for multiphysics has not been discussed adequately. The optimization algorithm merely follows the traditional single-field problem case, in which the optimization procedure is implemented by iterations of sequentially coupled solvers for direct physical problems and sensitivity analysis. Because of the multiphysical interaction, the sensitivity of coupled problem is really complicated in most cases.[8–12] An integrated and efficient simulation and optimization methodology for multiphysics is needed for MEMS devices. In this paper, we discuss a coupled optimization method for a single objective function, a single constraint and multiple fields in MEMS. All the numerical examples in this paper are implemented in the software environment FEMLAB.[6]

*Corresponding author; E-mail: zhenyu@imtek.de

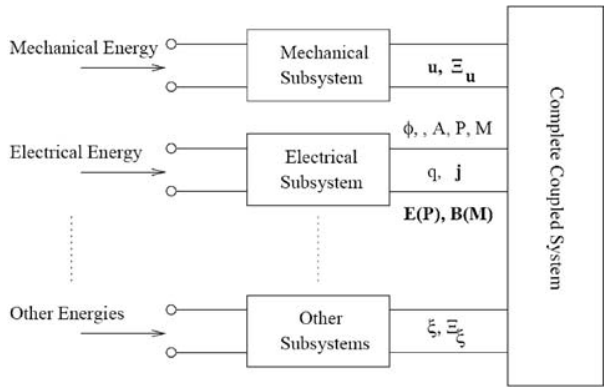

Fig. 1. Coupled physical domains in MEMS device.

2. FULLY COUPLED PDE FORMULATION FOR SINGLE-FIELD STRUCTURAL TOPOLOGY OPTIMIZATION

Structural optimization has great potential to improve the performance of MEMS device. Generally, one has to follow the optimization procedure as shown in Figure 2. Because of the complexity of coupled effects in MEMS devices, the sensitivity analysis is very complicated in most cases. Typically, the element density type method, such as the SIMP (solid isotropic microstructures with penalization) method is used to implement structural topology optimization.[13] However, the expression of the structural layout is non-smooth because of piece-wise constant density value is used to express the material domain. Even though this will not cause serious numerical problems for the structural optimization of pure mechanical problems, a material non-smooth expression will lead to unexpected results for other types of structural optimization, such as thermal problems.[14] One of the simplest remedies to overcome the problem of a material non-smooth expression is the nodal density type method, where material density is interpolated smoothly with nodal density values.[15] In MEMS simulation, the actuation force is normally either a body force or a surface force. During structural topology optimization, these two kinds of forces are referred to as design-dependent loads, which mean that the load vector changes with the evolution of the structural layout.[16] With either the element or nodal density type method, there is no explicitly defined material boundary. So the implementation of the design-dependent load is not straightforward. Basically, the level set method belongs to the shape optimization method. Because of its ability to merge holes during the optimization, it has recently become popular in structural topology optimization. When compared with the density type method, one of the distinguishing advantages of the level set method is that the material boundary is expressed with the zero level set contour, therefore the design dependent load is easily implemented during the optimization procedure.[17, 18] Here we introduce the use of the level set method to transform a typical optimization procedure to a coupled PDEs expression, so that the structural optimization procedure can be solved as a pseudo-time dependent coupled PDE problem.

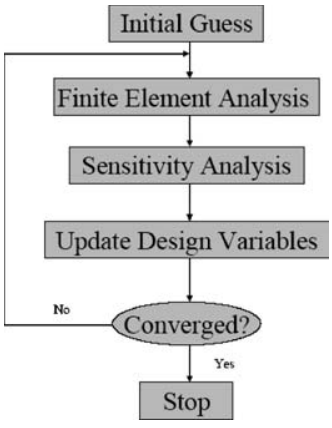

Fig. 2. The procedure of structural optimization.

2.1. Mechanical Problem

A typical structural topology optimization problem for 2D compliance minimization can be written as

$$\left.\begin{aligned} \min: \quad & C(\phi,\varepsilon)=\int_\Omega \frac{1}{2}E(\phi)\varepsilon^T D\varepsilon d\Omega \\ \text{s.t.} \quad & \nabla\cdot(E(\phi)\sigma)=f \\ & \int_\Omega H(\phi)d\Omega=\mathrm{Vol}^* \end{aligned}\right\} \tag{1}$$

where the design domain is represented by Ω, the linear elastic equilibrium equation is used to calculate the displacement field u, strain tensor is ε and stress tensor is σ, E is the design variable which is defined by the level set surface Φ as $E(\phi)=H(\phi)+(1-H(\phi))E_{\min}$, where $E_{\min}$ is a small number, such as 0.001, to avoid singularity of the stiffness matrix, D is the elasticity matrix in which the material Young's modulus is E_0, and Vol^* is the material volume constraint in the design domain. The Heaviside function $H(\phi)$ is defined as

$$H(\phi(x))=\begin{cases} 0 & \phi\le 0 \\ 1 & \phi>0 \end{cases} \tag{2}$$

and the derivative of the Heaviside function, $\delta(\phi)$ is defined as

$$\delta(\phi(x))=\frac{dH(\phi(x))}{d\phi} \tag{3}$$

The level set function $\phi(x)$ is an implicit function for a given domain Ω with smooth boundary which satisfies

$$\left.\begin{aligned} &\phi(x)>0 \quad x\in\Omega^+ \text{ (material)} \\ &\phi(x)=0 \quad x\in\partial\Omega \text{ (boundary)} \\ &\phi(x)<0 \quad x\in\Omega^- \text{ (hole)} \end{aligned}\right\} \tag{4}$$

The area constraint condition which is typically used in compliance minimization design is presented. The

optimization problem (1) can be solved by the level set method.[19, 20] To derive the level set equation which moves the material boundaries, we combine the objective function and constraints together by using a Lagrangian formulation, and then derive a corresponding Euler-Lagrangian equation.

Using the Lagrangian multiplier λ, we can rewrite problem (1) as

$$J(\varepsilon, \phi, \lambda) = \int_\Omega \left[\frac{1}{2} E(\phi) \varepsilon^T D \varepsilon + \lambda \left(H(\phi) - \frac{\text{Vol}^*}{\text{Vol}^\Omega} \right) \right] d\Omega \tag{5}$$

where Vol^Ω is the area of the entire design domain. From classical calculus, we know that the extrema of functional (5) is attained at the position where $J' = 0$. To obtain the level set equation which uses a level set surface to express the structural topology implicitly, we need to calculate the variation of the level set surface. For the variation of a material domain which is expressed by the Heaviside function of the level set surface ϕ, we have

$$\delta H(\phi) = \frac{\partial H(\phi)}{\partial \phi} \delta\phi = \delta(\phi)\delta\phi = \delta\phi|_{\phi=0} \tag{6}$$

Where $\delta\phi$ is the variation of ϕ, and $\delta(\phi)$ is the Dirac delta function. Based on knowledge of structural shape optimization, only the normal velocity on the material boundary will influence the change of the shape, the tangential velocity will not influence the deformation of the geometry, merely its parameterization. We assume that the zero level set contour ($\phi = 0$) moves only in the normal direction. For an infinitesimal variation δl which is along the normal direction $\bar{n}$, a new zero level set is ϕ' and we have

$$\begin{aligned} \delta\phi|_{\phi=0} &= \phi'(x) - \phi(x) = \phi(x + \delta l \cdot \bar{n}) - \phi(x) \\ &= \nabla\phi \cdot (\delta l \cdot \bar{n}) = |\nabla\phi| \delta l \end{aligned} \tag{7}$$

where the normal vector $\bar{n} = \nabla\phi / |\nabla\phi|$. For problem (5), the variation of the level set surface on the material boundary can be expressed as

$$\delta_\phi J = \int_\Omega \left[\frac{1}{2}(1 - E_{\min}) \varepsilon^T D \varepsilon + \lambda \right] \delta(\phi) |\nabla\phi| \delta l \, d\Omega \tag{8}$$

The corresponding Euler-Lagrangian equation at the extreme value point is

$$\left[\frac{1}{2}(1 - E_{\min}) \varepsilon^T D \varepsilon + \lambda \right] \delta(\phi) |\nabla\phi| = 0 \tag{9}$$

In most cases, it is impossible to solve Eq. (9) directly. One general technique is to solve the level set equation numerically

$$\frac{\partial \phi}{\partial t} - \left[\frac{1}{2}(1 - E_{\min}) \varepsilon^T D \varepsilon + \lambda \right] \delta(\phi) |\nabla\phi| = 0 \tag{10}$$

The auxiliary variable t is used as pseudo time. The method is also called gradient descent flow. In the case of a well-posed optimization problem, the solution can hopefully converge to a local minimum based on different initial values. As a result, we can solve the coupled PDEs. So the 2D compliance minimization topology optimization problem can be transformed into the following coupled plane stress equation and time-dependent reaction-diffusion equation

$$\left.\begin{aligned} &\nabla \cdot (E(\phi)\sigma) = f \\ &\frac{\partial \phi}{\partial t} - \left[\frac{1}{2}(1 - E_{\min}) \varepsilon^T D \varepsilon + \lambda \right] \delta(\phi) |\nabla\phi| = \alpha \Delta\phi \end{aligned}\right\} \tag{11}$$

with a suitable initial condition for ϕ_0. Here an artificial diffusion term $\alpha\Delta\phi$ is added to overcome numerical oscillations during the evolution of level set surface. The coefficient α is proportional to the mesh size and reaction term. The Lagrangian multiplier is expressed as

$$\lambda = -\frac{\int_\Omega [1/2(1 - E_{\min}) \varepsilon^T D \varepsilon] \delta^2(\phi) |\nabla\phi| d\Omega}{\int_\Omega \delta^2(\phi) |\nabla\phi| d\Omega} \tag{12}$$

Here we call the first equation in Eq. (11) the state equation for the direct problem and the second equation the optimization equation for the structural optimization problem. Figure 3 is a typical example of a compliance minimization structural topology optimization problem. The short cantilever beam is clamped on the left side and a vertical force acts on the midpoint of the right side. The area constraint condition is 0.3 Vol^Ω. The design domain is discretized with 2466 triangular linear elements.

2.2. Electrostatic Problem

In topology optimization, one of the most commonly used objective functions is the stored potential energy inside a

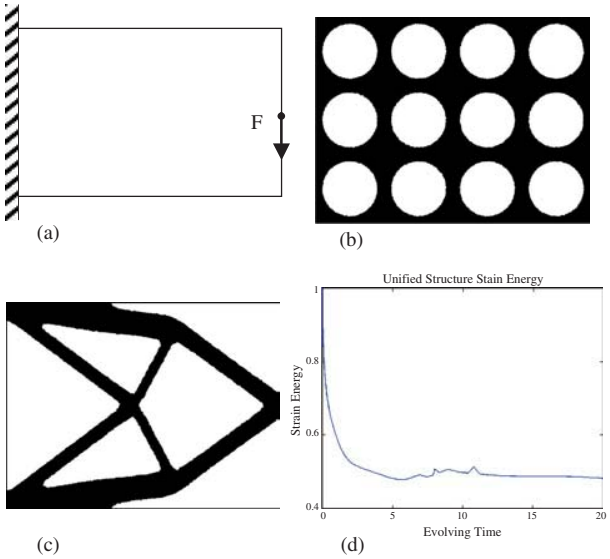

Fig. 3. Structural topology optimization of a purely mechanical problem. (a) design domain (b) initial structural topology (c) optimized structural topology (d) optimization procedure of the structural strain energy.

design domain. For the electrostatic problem, the electric energy can be expressed as $\mu(\phi)\nabla V^T \nabla V/2$, where V is the electric potential, ∇V is the electric field vector, μ is dielectric permittivity which is defined by a level set surface Φ as $\mu(\phi) = \mu_{\text{mat}} H(\phi) + (1 - H(\phi))\mu_{\text{air}}$ where μ_{air} is the dielectric permittivity of the air and μ_{mat} is the dielectric permittivity of the design material. The equilibrium equation which controls the electrostatic problem is the Poisson equation. Following a similar procedure as for the mechanical problem, a maximization of the electrostatic energy problem can be expressed as

$$\left.\begin{aligned} \max: \quad & C(\phi, \nabla V) = \int_\Omega \frac{1}{2}\mu(\phi)\nabla V^T \nabla V d\Omega \\ \text{s.t.} \quad & \nabla \cdot (\mu(\phi)\nabla V) = 0 \\ & \int_\Omega H(\phi) d\Omega = \text{Vol}^* \end{aligned}\right\} \tag{13}$$

A fully coupled PDE expression of topology optimization for the electric potential energy problem with area constraint can be similarly expressed as

$$\left.\begin{aligned} & \nabla \cdot (\mu(\phi)\nabla V) = 0 \\ & \frac{\partial \phi}{\partial t} - \left[\frac{1}{2}(\mu_{\text{mat}} - \mu_{\text{air}})\nabla V^T \nabla V + \lambda\right]\delta(\phi)|\nabla \phi| = \alpha \Delta \phi \end{aligned}\right\} \tag{14}$$

where

$$\lambda = -\frac{\int_\Omega [1/2(\mu_{\text{mat}} - \mu_{\text{air}})\nabla V^T \nabla V]\delta^2(\phi)|\nabla \phi| d\Omega}{\int_\Omega \delta^2(\phi)|\nabla \phi| d\Omega} \tag{15}$$

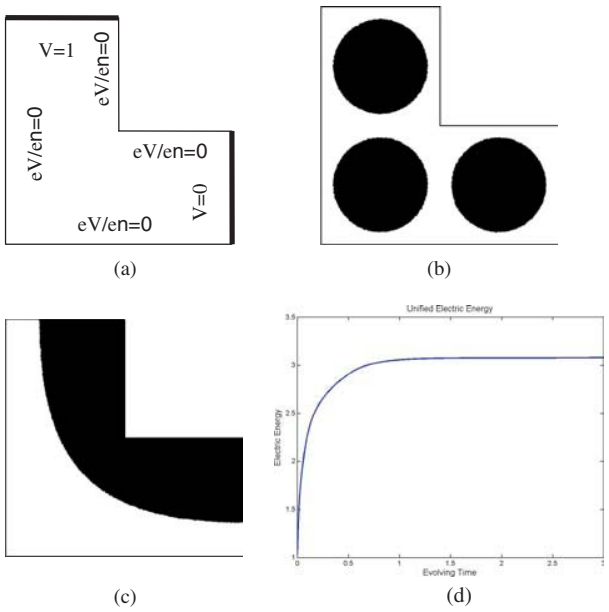

Fig. 4. Structural topology optimization of a purely electrostatic problem for maximum stored energy. (a) design domain (b) initial structural topology (c) optimized structural topology (d) optimization procedure of the electric energy.

For the same reason as for the mechanical problem, an artificial diffusion term is added in the right hand of the second equation in Eq. (14). Figure 4 is a typical example of an energy maximization structural topology optimization problem. The L-shape domain is chosen as design domain with given potential and insulation boundary conditions. The area constraint condition is 0.5 Vol^Ω. The design domain is discretized with 2561 triangular linear elements. Since we know that the electrical field is concentrated at the inner bend of the L-shaped domain, we see that the optimized structure is correct, since the optimization procedure places the material with higher dielectric constant here.

3. H-ADAPTIVE MESH REFINEMENT FOR STRUCTURAL TOPOLOGY OPTIMIZATION

The application of the level set method to structural topology optimization has provided a new level of flexibility in expressing the change of topology when compared with the element density method. Usually, a design domain with regularly distributed mesh is discretized and the whole iterative procedure is based on this fixed mesh. The accuracy of the finite element solution and the position of the boundaries are largely dependent on the mesh density. Thus one has to discretize the design domain with a reasonable number of elements in order to balance the computational cost and the accuracy of boundary position. Mesh adaptation has become an indispensable tool in the numerical solution of partial differential equation in order to improve the computational accuracy and efficiency. This is especially useful in domain in which time-dependent gradient concentration or large solution variations occur within the physical solutions.

There are three methods in which the dynamic mesh adaptation can be implemented, p-adaptation, h-adaptive mesh refinement (H-AMR) and the r-adaptive moving mesh (R-AMM) method. In the H-AMR the mesh is remeshed locally or globally based on error estimates in order to capture the significant part of the solution.[21, 22] In R-AMM the moving mesh is based on the solution of a moving mesh equation.[23, 24] The mesh topology is kept unchanged but the mesh grids are shifted throughout the region to best approximate the solution globally. In Ref. [25], we discussed how to implement R-AMM structural topology optimization. In this paper, we will focus on the H-AMR structural topology optimization within the framework of fully coupled PDE formulation.

The key point when combining structural topology optimization and the H-AMR method is to define a remeshing strategy. This will guarantee the quality of the finite element solution and smooth the expression of the material domain, while keeping a reasonable number of design variables. Generally, the error estimator is used to determine the adaptation strategy, since the exact solution of the

direct problem is unknown in general. For a linear elastic equation the error estimator by Zienkiewicz and Zhu[26] can be expressed as

$$\|e\|_{\text{energy}} \approx \int_{\Omega} (\sigma^* - \sigma^h)^T C^{-1} (\sigma^* - \sigma^h) d\Omega \qquad (16)$$

where σ^* is the smoothed stress in the Gaussian points, σ^h is the approximated nodal stress and C is the material tensor. Equation (16) measures the strain energy error in an average sense over all elements. However, for structural topology optimization with the level set method, the accuracy of the Heaviside and Dirac delta function of the level set surface, which are used to capture the material domain and boundary, cannot be improved by the strain energy error estimator. A specified error estimator which is based on the property of the level set surface can be defined as

$$\|e\|_{\text{ls}} \approx \int_{\Omega} (\nabla H(\phi)^* - \nabla H(\phi)^h)^T (\nabla H(\phi)^* - \nabla H(\phi)^h) d\Omega \qquad (17)$$

where $\|e\|_{\text{ls}}$ is the error estimator for the material domain which is expressed by a level set surface. Figure (5) shows the different effects of two different error estimators of the short cantilever beam example. The beam is clamped on the left side and a fixed force acts on the right-down corner. Both cases are remeshed to use a similar number of elements. The final optimal topologies are quite similar to each other in that the convergence of structural optimization with mesh adaptation is not affected by the error estimators we used. Meanwhile, the overall computational cost for structural optimization is reduced when compared with using a global refined mesh. One can choose one of the error estimators to mesh the design domain for different purposes. In the next section, the error estimator in Eq. (17) is used.

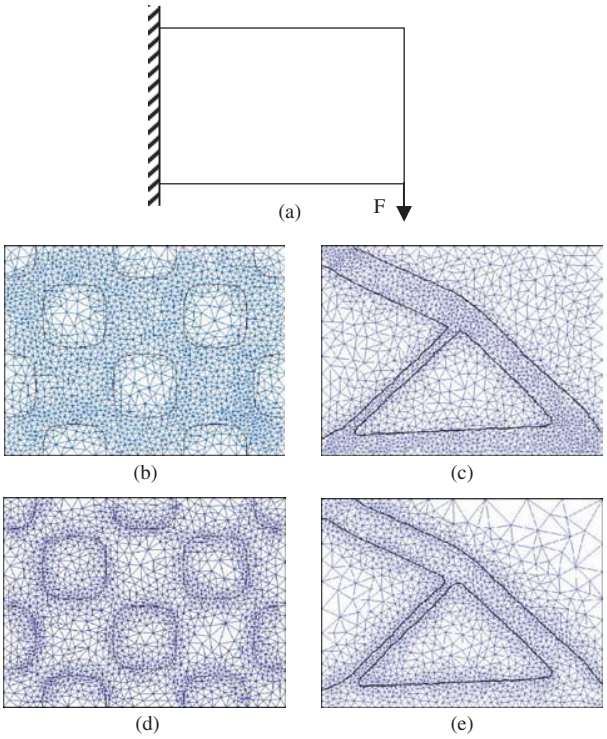

Fig. 5. Structural topology optimization with H-AMR method of a classical benchmark problem. (a) design domain, (b) and (c) Initial and optimized structure topology and meshing (3384 and 3374 triangular elements) using the strain energy error estimator, (d) and (e) Initial and optimized topology and meshing (3085 and 3275 triangular elements) use the level set surface error estimator.

4. FULLY COUPLED PDE FORMULATION FOR ELECTRO-MECHANICAL STRUCTURAL TOPOLOGY OPTIMIZATION

Typically, the compliance minimized topology optimization problem is presented with a constant load force. In MEMS, the electrostatic force is often used to actuate devices. In this case, the amplitude and direction of the electrostatic force will change with the update of a structure's topology and its deformation. Hence we have a coupled optimization problem. Here we present two examples for compliance minimized topology optimization with an electrostatic actuation force.

The design domain and mechanical boundary conditions of the first example are shown in Figure 6a and the electrostatic boundary conditions in Figure 6b. In this example, we assume that the deformation of the structure is small enough so that the electrostatic force will not be changed by the deformation of the structure. The coupling effect between the mechanical and electrostatic problem merely comes from the electrostatic force which will be controlled by the structural topology inside the design domain. So the electrostatic force is a design-dependent load. This is completely different from the fixed load vector case.

For the finite element analysis, the two coupled equations, mechanical and electrostatic, are given by

$$\left.\begin{aligned} \nabla \cdot (\mu \nabla V) &= 0 \\ \nabla \cdot \sigma &= F_{\text{fixed}} + F_{\text{ele}} \end{aligned}\right\} \qquad (18)$$

where F_{fixed} is a fixed load vector and the F_{ele} is the electrostatic force which is dependent on the distribution of the material. The material inside the design domain is SiO_2. The optimization objective is to minimize the deformation of the whole structure with area constraint. The electrostatic force is used to decrease the deformation of the structure. For this kind of weakly coupled optimization problem, the sequential analysis and optimization method has been discussed in Ref. [27]. To make a clear comparison of the traditional sequential method and the fully coupled PDE formulation method we proposed in this paper, we derive the sensitivity expression with the traditional method first.

When using the typical element density design variable method to implement the structural topology optimization,

RESEARCH ARTICLE

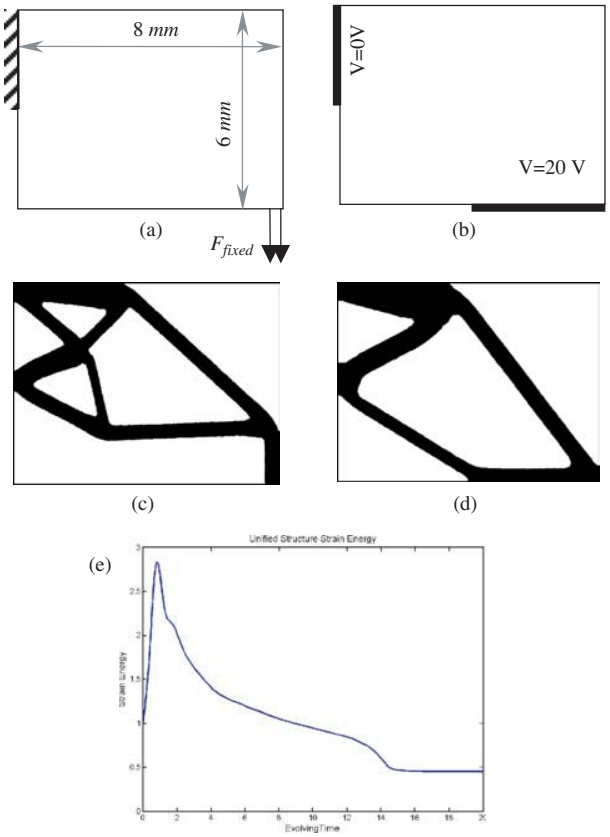

Fig. 6. Compliance minimized topology optimization of a cantilever beam. (a) mechanical design domain and boundary conditions, (b) electrostatic design domain and boundary conditions, (c) optimized material distribution when only the fixed load vector F acts upon the structure, (d) optimized material distribution when both the load vector F and the electrostatic forces act upon the structure, (e) optimization procedure of the structural strain energy of Figure 6d.

both equations in Eq. (18) depend on element design variable ρ_i^p

$$\left.\begin{aligned}\nabla\cdot(\mu(\rho)\nabla V)=0\\ \nabla\cdot(E(\rho)\sigma)=F_{\text{fixed}}+F_{\text{ele}}(\rho,\nabla V)\end{aligned}\right\} \tag{19}$$

One can add Eq. (19) into the original objective function via the finite element discretized expression

$$U_{\text{out}}=U^T K^{\text{ME}}U+\lambda_1 K^{\text{PO}}V+\lambda_2(K^{\text{ME}}U-F_{\text{fixed}}-F_{\text{ele}}) \tag{20}$$

where λ_1 and λ_2 are Lagrangian vectors, K^{PO} and K^{ME} are the stiffness matrices of the electrostatic equation and the linear elastic equation, U is mechanical displacement vector and V is scalar electrical potential. Using the adjoint method, the sensitivity is:

$$\begin{aligned}\frac{\partial U_{\text{out}}}{\partial\rho_i^p}&=2^*U^T K^{\text{ME}}\frac{\partial U}{\partial\rho_i^p}+U^T\frac{\partial K^{\text{ME}}}{\partial\rho_i^p}U+\lambda_1\frac{\partial K^{\text{PO}}}{\partial\rho_i^p}V\\&\quad+\lambda_2\left[\frac{\partial K^{\text{ME}}}{\partial\rho_i^p}U-\frac{\partial F_{\text{ele}}}{\partial\rho_i^p}\right]+\lambda_1 k^{\text{PO}}\frac{\partial V}{\partial\rho_i^p}+\lambda_2 K^{\text{ME}}\frac{\partial U}{\partial\rho_i^p}\end{aligned} \tag{21}$$

To remove the terms $\partial U/\partial\rho_i^p$ and $\partial V/\partial\rho_i^p$ in the sensitivity, the following expressions should be set to zero

$$\begin{aligned}(2*U^T K^{\text{Me}}+\lambda_2 K^{\text{ME}})=0\\ \lambda_1 K^{\text{PO}}=0\end{aligned} \tag{22}$$

With the solution for λ_1 in terms of λ_2, the sensitivity can be simplified as

$$\begin{aligned}\frac{\partial U_{\text{out}}}{\partial\rho_i^p}&=U^T\frac{\partial K^{\text{ME}}}{\partial\rho_i^p}U+\lambda_1\frac{\partial K^{\text{PO}}}{\partial\rho_i^p}V\\&\quad+\lambda_2\frac{\partial K^{\text{ME}}}{\partial\rho_i^p}U-\lambda_2\frac{\partial F_{\text{ele}}}{\partial\rho_i^p}\end{aligned} \tag{23}$$

To obtain the sensitivity in Eq. (23), one has to solve the displacement and electric potential solution first with Eq. (19) and then calculate two adjoint vectors with Eq. (22). The expression of the sensitivity is relatively complicated even for this weakly coupled problem. Because the traditional optimization method solves the direct physical problem first and then derives sensitivity sequentially, the state variables (displacement and electric potential) are treated as implicit functions of the design variables. Then sensitivity analysis should include the derivative terms of the state variables and the design variables. Several papers and books discuss the derivation of sensitivity in the case where displacement is treated as an implicit function of the design variables.[9, 10, 27]. In this paper, we set the displacement and electric potential as independent of the design variables, that is, the state and design variables are defined in a composite vector. This method is called the simultaneous analysis and design (SAND) method.[28] One of the distinguished advantages of the SAND method is that the derivation of the sensitivity is relatively straightforward, especially when one wants to implement structural optimization in which the state variables are controlled by multi-physical problems. For example, equilibrium equations could include mechanics, electrostatics, and thermo-electric effects. The state variables include displacement, electrostatic field, thermal stress, etc. The coupling effects include surface coupling of mechanism and electrostatics, domain coupling of mechanics and thermo-electric effects. In this case, the sensitivity analysis of the traditional method is extremely complicated. However, the expression of the SAND method is much simpler for coupled problems, especially in which the load vector is design-dependent. One remaining question is how to establish the relationship between the de-coupled state and design variables. One of the possibilities is to derive a corresponding optimization equation based on the specified objective function and to solve the fully coupled equilibrium equation and optimization equation simultaneously.

When using the fully coupled PDE formulation, we do not need to calculate the Lagrangian vectors (Eq. 22)

explicitly. The structural topology optimization problem can be expressed with the level set method as

$$\left.\begin{aligned} \text{min:} \quad & C(\phi, \varepsilon, \nabla V) = \int_\Omega \frac{1}{2} E(\phi)\varepsilon^T D\varepsilon d\Omega \\ \text{s.t.} \quad & \nabla \cdot (E(\phi)\sigma) = F_{\text{fixed}} + F_{\text{ele}} \\ & \nabla \cdot (\mu(\phi)\nabla V) = 0 \\ & \int_\Omega H(\phi)\, d\Omega = \text{Vol}^* \end{aligned}\right\} \quad (24)$$

In the optimization equation, the level set surface which expresses the evolving of the structural layout is not influenced by the design-dependent electrostatic force. The evolving of the level set surface still can be expressed by the coupling effect of the first two equations in Eq. (25). To sum up, the coupled PDE formulation to express structural topology optimization is:

$$\left.\begin{aligned} & \nabla \cdot (\mu(\phi)\nabla V) = 0 \\ & \nabla \cdot (E(\phi)\sigma) = F_{\text{fixed}} + F_{\text{ele}} \\ & \frac{\partial \phi}{\partial t} - \left[\frac{1}{2}(1 - E_{\min})\varepsilon^T D\varepsilon + \lambda\right]\delta(\phi)|\nabla\phi| = \alpha\Delta\phi \end{aligned}\right\} \quad (25)$$

Figure 6c shows the optimized structural topology when only F_{fixed} acts and Figure 6d is the optimized topology when both F_{fixed} and F_{ele} act on the structure. Figure 6e is the optimization procedure of the structural strain energy.

In MEMS, the electrostatic force is commonly used to actuate the slender structures. This is a typical self-consistent electromechanical analysis which involves determining mechanical displacement to balance the electrostatic force on the surface. There are two different methods to solve this surface coupling problem, the sequentially coupled solver and the directly coupled solver. To implement structural optimization with the coupled method, the directly coupled solver is used to calculate the structural deformation. The design domain is shown in Figure 7. There are two subdomains, subdomain 1 has fixed material property and subdomain 2 is the optimization domain. Here we discuss three different load cases. In the first case, a fixed load vector ($F_{\text{fixed}} = 1\mu N$) is added on the middle point of the upper surface of the whole domain. In the second case, the electrostatic force acts on the structure. In the last case, both the fixed load and electrostatic force act on the structure. The objective of structural optimization is still compliance minimization with area constraint. The material inside both subdomains is Aluminium with Young's modulus of 70 GPa and Poisson ration of 0.33.

For the first case, we still can use the compliance minimization model in Eq. (1). In addition, we consider the geometrically large deformation for the elastic equilibrium equation. So the strain tensor ε has a nonlinear relationship

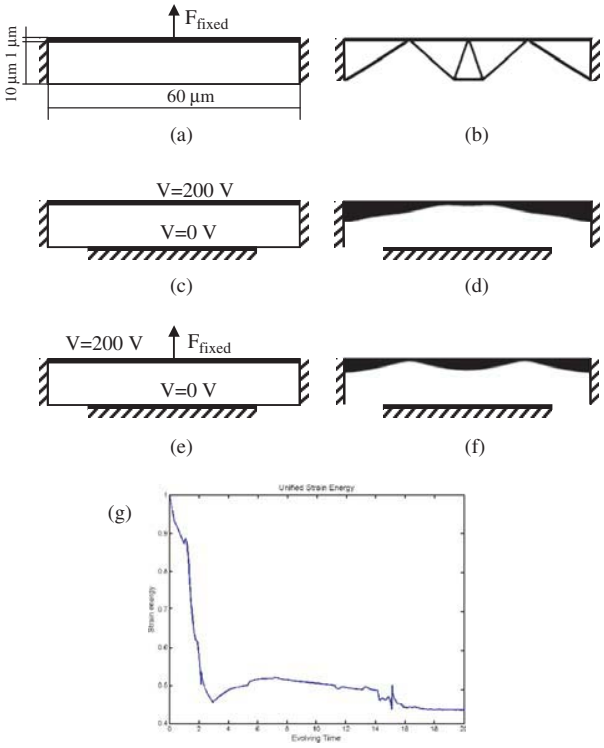

Fig. 7. Compliance minimized topology optimization of a fixed-fixed end beam. (a) and (b) initial design domain and optimized topology with fixed load vector, (c) and (d) initial design domain and optimized topology with electrostatic force, (e) and (f) initial design domain and optimized topology with both the fixed load vector and electrostatic force, (g) optimization procedure of the structural strain energy of Figure 7f.

with the displacement vector

$$\left.\begin{aligned} \varepsilon_x &= \frac{\partial u}{\partial x} + \left(\left(\frac{\partial u}{\partial x}\right)^2 + \left(\frac{\partial v}{\partial x}\right)^2\right) \\ \varepsilon_y &= \frac{\partial v}{\partial y} + \left(\left(\frac{\partial u}{\partial y}\right)^2 + \left(\frac{\partial v}{\partial y}\right)^2\right) \\ \varepsilon_{xy} &= \left(\frac{\partial u}{\partial y} + \frac{\partial v}{\partial x}\right) + \left(\frac{\partial^2 u}{\partial x \partial y} + \frac{\partial^2 v}{\partial x \partial y}\right) \end{aligned}\right\} \quad (26)$$

Since we use the SAND method in which the design variable ϕ and the displacement vector are independent of each other, the optimization equation is still same as the second equation in Eq. (11). The first equation in Eq. (11) is solved with a nonlinear iterative solver for large deformation analysis. The optimized structural topology is shown in Figure 7b.

For the second load case, a consistent solution for the electromechanical problem is needed. To coincide with the fully coupled optimization method we propose in this paper, we choose a direct coupled solver where the deformed mesh caused by the structural deformation is simulated by the ALE method.[4, 32] In FEMLAB, the

RESEARCH ARTICLE

coupled ALE method can be implemented with following coupled Eqs. [6]

$$\left.\begin{aligned}\nabla\cdot(\mu(\phi)\nabla V_X)&=0\\ \nabla\cdot(E(\phi)\sigma)&=F_{ele}\\ \nabla\cdot(G\nabla X)&=0\end{aligned}\right\} \tag{27}$$

where $\boldsymbol{X}$ expresses the deformed nodal position because of structural deformation, G is the mesh monitor function which controls the local property of the deformed mesh, V_X means that the value of the electrical potential is calculated for the deformed mesh and $\mu(\phi)=\mu_{\max}H(\phi)+(1-H(\phi))\mu_{\text{air}}$ where $\mu_{\max}$ is a large number to approximate the distribution of the electrical potential. In this example $\mu_{\max}=100$. Using the moving mesh equation (the third equation in Eq. (27)), all of the displacement, force and electrical potential boundary conditions can be implemented in the original coordinates. This method can deal with the electromechanical coupling directly before pull-in occurs. For the optimization examples we presented here, the fixed-fixed end beam in subdomain 1 is used to avoid the pull-in occurring during the optimization procedure with reasonable electrical potential conditions. The coupled optimization equations are

$$\begin{aligned}\nabla\cdot(\mu(\phi)\nabla V_X)&=0\\ \nabla\cdot(E(\phi)\sigma)&=F_{\text{ele}}\\ \nabla\cdot(\nabla X)&=0\\ \frac{\partial\phi}{\partial t}-\left[\frac{1}{2}(1-E_{\min})\varepsilon^T D\varepsilon+\lambda\right]\delta(\phi)|\nabla\phi|&=\alpha\Delta\phi\end{aligned} \tag{28}$$

Here the mesh monitor function is the unit function so that the mesh is smoothly modified on the whole design domain. On each mesh node, there are 6 degrees of freedom (dofs), two displacement dofs, one electrical potential dof, two moving mesh position dofs, and one level set surface dof. However, the optimization equation remains unchanged despite the complicated coupled forward problems. The optimized result is shown in Figure 7d.

In the last case, both the fixed load vector and electrostatic force act on the structure. So this is a multiple load optimization problem. Based on the analysis of the first two cases, the optimization equation for these two loads is

$$\begin{aligned}\nabla\cdot(E(\phi)\sigma_1)&=F_{\text{fixed}}\\ \nabla\cdot(\mu(\phi)\nabla V_X)&=0\\ \nabla\cdot(E(\phi)\sigma_2)&=F_{\text{ele}}\\ \nabla\cdot(\nabla X)&=0\\ \frac{\partial\phi}{\partial t}-\left[\frac{1}{2}(1-E_{\min})(\varepsilon_1^T D\varepsilon_1+\varepsilon_2^T D\varepsilon_2)+\lambda\right]&\\ \delta(\phi)|\nabla\phi|=\alpha\Delta\phi&\end{aligned} \tag{29}$$

where ε_1 and ε_2 are the strain vectors corresponding to two load cases. The optimized result is shown in Figure 7f.

5. CONCLUSION

This paper presents a procedure to implement single objective function, single constraint, and multiphysics structural topology optimization by a fully integrated PDE expression via the level set method. The optimization procedure is implemented through a pseudo-time dependent optimization equation. Expressing the sensitivity with the SAND method is much simpler than using the traditional sequential coupled algorithm. Several examples demonstrate the use of the method we proposed. The efficiency and accuracy of this optimization method strongly depends on the power of the nonlinear algorithm for large scale problems. Practical optimization of MEMS requires multi-objectives, multi-constraints, together with multiphysical problems. Our work will now focus on these issues.

Acknowledgments: This work is supported by Deutsche Forschungsgemeinschaft (DFG) 1883/5-3.

References and Notes

1. B. F. Romanowicz, Methodology for the Modeling and Simulation of Microsystems, Kluwer Academic Publishers **(1998)**.
2. S. D. Senturia, Microsystem Design, Kluwer Academic Publishers **(2000)**.
3. A. Nathan and H. Baltes, Microtransducer CAD, Physical and Computational Aspects, Springler-Verlag **(1999)**.
4. K. Zeng, Z. Liu, and J. G. Korvink, *Microsystem Technologies* 10, 387 **(2004)**.
5. http://www.ansys.com/.
6. http://www.femlab.com.
7. http://www.bsac.eecs.berkeley.edu/cadtools/sugar.
8. L. Yin and G. K. Ananthasuresh, *Sens. Actuators, A* 97, 599 **(2002)**.
9. O. Sigmund, *Comput. Methods Appl. Mech. Engrg.* 190, 6577 **(2001)**.
10. O. Sigmund, *Comput. Methods Appl. Mech. Engrg.* 190, 6605 **(2001)**.
11. E. C. N. Silva, J. S. O. Fonseca, and N. Kikuchi, *Computational Mechanics* 19, 397 **(1997)**.
12. S. Nishiwaki, M. I. Frecker, S. Min, and N. Kikuchi, *Int. J. Numer. Meth. Engrg.* 42, 535 **(1998)**.
13. G. I. N. Rozvany, *Struct. Multidisc Optim.* 21, 90 **(2001)**.
14. G. H. Yoon and Y. Y. Kim, *Int. J. Numer. Meth. Engrg.* **(2006)**, in press.
15. S. F. Rahmatalla and C. C. Swan, *Struct. Multidisc. Optim.* 27, 130 **(2004)**.
16. V. B. Hammer and N. Olhoff, *Struct. Multidisc. Optim.* 19, 85 **(2000)**.
17. T. Belytschko, S. P. Xiao, and C. Parimi, *Int. J. Numer. Meth. Engrg.* 57, 1177 **(2003)**.
18. M. Y. Wang, X. Wang, and D. Guo, *Comput. Methods Appl. Mech. Engrg.* 192, 227 **(2003)**.
19. J. A. Sethian and A. Wiegmann, *J. Comp. Phys.* 163, 489 **(1999)**.
20. G. Allaire, F. Jouv, and A. Toader, *J. Comp. Phys.* 194, 363 **(2004)**.
21. J. Costa and M. K. Alves, *Int. J. Numer. Meth. Engrg.* 58, 83 **(2003)**.
22. A. Schleupen, K. Maute, and E. Ramm, *Struct. Multidisc. Optim.* 19, 282 **(2000)**.
23. W. Cao, W. Huang, and R. D. Russell, *Appl. Numer. Math.* 47, 121 **(2003)**.
24. G. Beckett, J. A. Mackenzie, and M. L. Robertson, *J. Comp. Phys.* 182, 478 **(2001)**.

25. Z. Liu and J. G. Korvink, Adaptive Moving Mesh Level Set Method for Structure Topology Optimization (Research Report) **(2004)**.
26. O. C. Zienkiewicz and J. Z. Zhu, *Int. J. Numer. Meth. Engrg.* 24, 337 **(1987)**.
27. M. P. Bendsoe and O. Sigmund, Topology Optimization Theory, Methods and Applications, Springer **(2003)**.
28. J. S. Arora and Q. Wang, *Struct. Multidisc. Optim.* 30, 251 **(2005)**.
29. O. Sigmund, *Struct. Multidisc. Optim.* 21, 120 **(2001)**.
30. Z. Liu, J. G. Korvink, and R. Huang, *Struct. Multidisc. Optim.* 29, 407 **(2005)**.
31. S. Osher and R. Fedkiw, Level Set Methods and Dynamic Implicit Surfaces, Springer **(2002)**.
32. L. A. Jakobsen, E. Lund, and H. Møller, Shape Sensitivity Analysis of Time Dependent Fluid-Structure Interaction Problems Using the ALE Method, *Proc. 4th World Congress on Structural and Multidisciplinary Optimization* **(2001)**.

SENSOR LETTERS
Vol. 4, 200–205, 2006

RESEARCH ARTICLE

Spring Constant Models for Analysis and Design of MEMS Plates on Straight or Meander Tethers

Maryna Lishchynska*, Nicolas Cordero, Orla Slattery, and Conor O'Mahony

Tyndall National Institute, Lee Maltings, Prospect Row, Cork, Ireland

(Received: 28 November 2005. Accepted: 12 April 2006)

Comprehensive spring constant models are developed to analyse the electromechanical behaviour of elastically suspended MEMS plates. These models account for residual (post-fabrication) stress, finite stiffness of real anchors, and non-rigidity of the plate. Based on the models developed, the pull-in voltage of microfabricated switches is determined for a wide range of device geometries. Experimental measurements verify the accuracy of the models developed, which is within 11%. The results also show that significant errors (over 100%) in predicting the device pull-in behaviour may result if conventional models are applied to the plate-tethers system.

Keywords: Spring Constant, Elastically Suspended Plate, RF Switch, Pull-in Voltage, MEMS.

1. INTRODUCTION

Suspended plates find a wide range of applications as key elements in various microdevices such as MEMS varactors for wireless communication systems[1–6] and RF switches.[7–10] These plates are usually supported by spring-like suspensions such as cantilever (straight) or meander type tethers (Fig. 1). Although these types of structures have been previously modelled with conventional equations, the assumptions and simplifications inherent to those models make them unsuitable (or inaccurate) for use where a high degree of design accuracy is desired.

The primary goal of this paper is to develop models for accurate evaluation of the spring constant of suspended plates on straight or meander tethers. Such models incorporate fabrication non-idealities such as residual stress, real anchors, and also account for the plate compliance. This is achieved by extracting spring constant values from Finite Element Method (FEM) simulation data and experimental validation.

2. PREVIOUS/CONVENTIONAL MODELS

MEMS varactors and RF switches usually consist of a movable plate suspended above the ground on elastic elements or tethers (Fig. 2). Altering the vertical position of the plate using externally applied forces (e.g., thermal, electrostatic, piezoelectric, etc.) changes the capacitance of the structure and influences the electrical characteristics of the device. Removal of the applied forces allows the plate to return to its original undeflected position because of the mechanical restoring forces exerted by the tethers. Plates suspended by four tethers of two geometries, straight or meander (Fig. 3), are considered in this paper.

For small displacements the restoring force F from a spring displaced a distance δ is given by Hooke's law:[11]

$$F = -K\delta \tag{1}$$

where K is the spring constant.

The mechanical spring constant of micromachined structures controls the response of the devices to external influences such as pressure or voltage. Knowing the spring constant, such important behavioural characteristics as the pull-in voltage $V_{\text{pull-in}}$, the resonance frequency f_{res} and the deflection δ of the structure due to an externally applied force can be easily found using the following well-known expressions:[1, 12–13]

$$V_{\text{pull-in}} = \sqrt{\frac{8K^{\text{total}}h^3}{27\varepsilon A}} \tag{2}$$

$$f_{\text{res}} = \frac{1}{2\pi}\sqrt{\frac{K^{\text{total}}}{m}} \tag{3}$$

$$\delta = -\frac{F}{K^{\text{total}}} \tag{4}$$

where K^{total} is the spring constant of the entire structure, ε is the electrical permittivity, A is the common plate-electrode area, m is the mass, F is the applied force, and

*Corresponding author; E-mail: marynal@tyndall.ie

1546-198X/2006/4/200/006 doi:10.1166/sl.2006.011

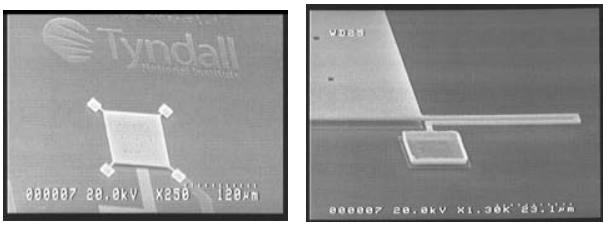

(a) (b)

Fig. 1. Micromachined plates suspended by (a) straight tethers and (b) meander tethers.

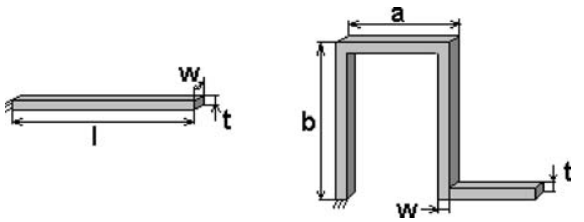

(a) (b)

Fig. 3. (a) Straight and (b) meander tethers typically used as micro-spring suspensions.

h is the electrical gap. Therefore, accurate evaluation of the spring constant is the key to accurate modelling and design of the structure.

Conventional models assume that the total spring constant of the structure, K^{total}, is the sum of the spring constants of the individual tethers,[1, 2, 7]

$$K^{\text{total}} = \sum k_0^s \tag{5}$$

where k_0^s are calculated using known expressions:

$$k_0^s = \begin{cases} \dfrac{Ewt^3}{l^3}, \quad \text{for a straight tether}^{7} & \text{(6a)} \\ \left(\dfrac{8a^3+2b^3}{3EI_x} + \dfrac{ab(3b+15a)}{3GJ} - \dfrac{a^2\left(\frac{2a}{EI_x}+\frac{3b}{GJ}\right)^2}{2\left(\frac{a}{EI_x}+\frac{b}{GJ}\right)} - \dfrac{b^2}{2}\left(\dfrac{a}{GJ}+\dfrac{b}{EI_x}\right)\right)^{-1}, \\ \quad \text{for a meander tether}^{13} & \text{(6b)} \end{cases}$$

Such models assume the plate to be rigid and do not account for the residual stresses and anchor compliance that are inevitable with most micromachining technologies.[7, 14, 15] As a result, large errors may occur when calculating the spring constant of the structure. This is clearly illustrated in Table I. Experimental studies also report a significant discrepancy.[7]

There are a number of factors causing this inconsistency, residual stress and non-rigidity of the plate being the most significant ones. Non-ideal anchors, typical in MEMS, also influence the spring constant.[14, 15] The following sections of this paper discuss the development of comprehensive spring constant models which take account of these factors.

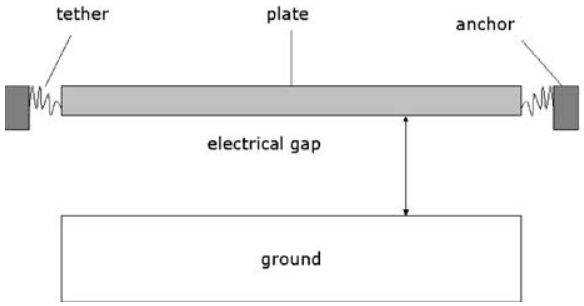

Fig. 2. Cross-section of the plate suspended on elastic elements.

3. STRESS ANALYSIS IN SUSPENDED PLATES

Residual stress is induced during the fabrication of most microstructures. Under this stress, deformations and changes in the mechanical behaviour of the structure occur. For instance, in-plane residual stress results in the stiffening of most microstructures,[16] an effect that is undesirable in many RF applications. Therefore, any residual stress present must be taken into account when modelling.

The generation of residual stress in micromachined structures is complicated and depends heavily on the specifics of the fabrication process. Furthermore, simulations undertaken in this work show that the stress in suspended structures redistributes after release. Consequently most of the post-release stress is concentrated in the tethers and the plate itself is nearly stress-free.

A more detailed look at the behaviour of straight tethers in a stressed device reveals not only stiffening of the cantilever-like suspensions (Fig. 4a), resulting in an increase of the spring constant, but also an extra bending of the anchor, implying a decrease in the spring constant (Fig. 4b). These two phenomena superpose in a complex way. Meander tethers, on the other hand, absorb much more stress through deformation (Fig. 5). All these effects should be taken into account when modelling the spring constant.

Table I. Comparison of FEM simulated and analytical (1), (2) values of spring constant (MPa · μm) for straight and meander suspended plates.

	Straight tethers; plate size, μm^2			Meander tethers; plate size, μm^2				
	100×100	200×200	300×300	10×10	50×50	100×100	200×200	300×300
Analytical	28.28	28.28	28.28	9.26	9.26	9.26	9.26	9.26
Simulated	14.7	13	11	7.75	6.58	5.68	4.18	3.27

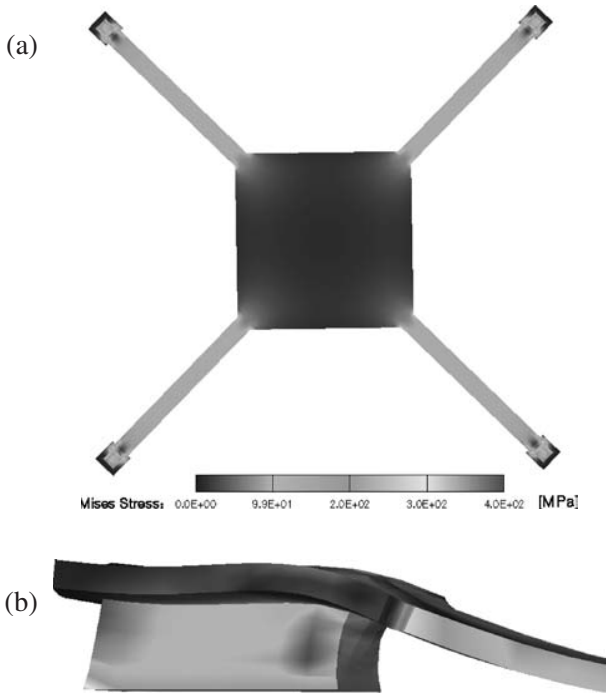

Fig. 4. Simulated stress redistribution in plate suspended by straight tethers (a) and local deformation (exaggerated) of the anchor of the pillar-supported guided-end cantilever due to the stress, no external load applied (b). Initial biaxial stress is 100 MPa. Lighter areas indicate higher residual stress, darker areas represent lower stress.

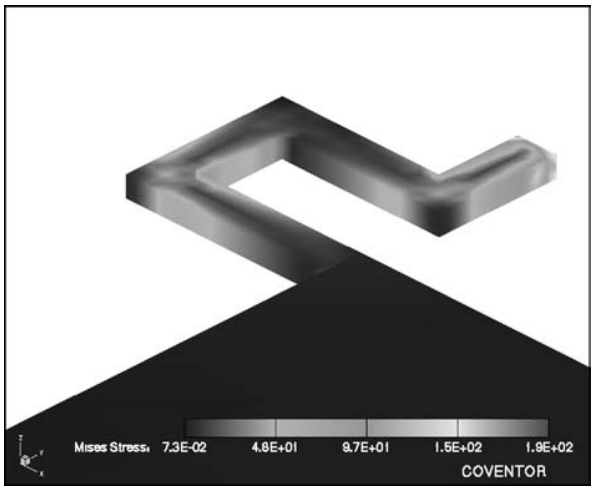

Fig. 5. Simulated stress redistribution (MPa) in plate suspended by meander tethers.

4. MODELLING THE SPRING CONSTANT

A previously described technique of extracting analytical models from FEM simulation data[17] was applied here. It can be roughly described in the following set of steps.

(1) A dimensional analysis is firstly undertaken. The purpose of this exercise is to establish a basic relationship between the dimensional parameters that have a significant role in the device performance. In the case when an exact solution exists for the ideal structure the dimensional part of a relation can be easily found. However, when there is no predefined equation for the ideal case, more investigation is needed. Dimensional analysis reduces the number of variables in the formula since the contribution of the main parameters is already found. The remaining variables are transformed into dimensionless ones, hence reducing their number further.
(2) FE simulation data relating the behaviour of structures of a given geometry to dimensionless parameters is generated. Parametric studies on all contributing parameters should be carried out as well.
(3) The final closed-form formula (function representation) is obtained by manipulation of the output data from FE simulation followed by accurate curve fitting.
(4) Experimental validation of the models is conducted where possible.

The following two subsections present the development of the spring constant model for straight tethers system in greater detail and provides the final model for meanders-plate system.

4.1. Plate on Straight Tethers

Expression (6a) assumes an ideally fixed guided-end cantilever (Fig. 3a) and does not account for the non-ideal anchors that are typical of MEMS structures. Nevertheless, according to our simulation study and experimental works of other authors,[14, 15] real anchors significantly affect the spring constant of the structure and need to be taken into account when modelling.

Consider an anchored guided-end cantilever (Fig. 6). This structure was modelled and its deflection under a concentrated load was simulated in Coventor.[18] As no experimental work on stress relaxation has been done in this study an elastic material model was used for simulations. Then, applying Hooke's law, the spring constant was calculated as

$$k_s = -\frac{F}{\delta} \tag{7}$$

A parametric study of the cantilever spring constant with varying dimensional parameters was carried out and the numerical data were interpolated by least square method (Microsoft Excel). Results revealed a linear dependence of the normalised spring constant (k_s/k_s^0) on h/l as $(k_s/k_s^0)^{-1} = 1 + 4h/l$. This yields the following equation for the spring constant of the guided-end cantilever with non-ideal anchor:

$$k^s = \frac{k_0^s}{1+4h/l} \tag{8}$$

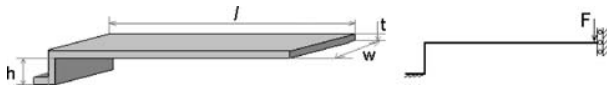

Fig. 6. Schematic of the anchored guided-end cantilever.

Micromachined beams that are prevented from stretching/shrinking by mounting conditions (e.g., doubly fixed beam, guided-end cantilever) are very sensitive to residual stress σ.[1,7] At the same time, non-ideal anchors allow more compliance and stress absorption than ideal ones, thus reducing the overall stiffness of the structure.[15] These two phenomena superpose but do not cancel each other. In fact, they significantly affect the spring constant of the structure. Since the classical model of the spring constant of the guided-end cantilever incorporating axial stress[13] does not account for non-ideal anchors, the following model allowing for the coupled effects of residual stress and non-ideal anchor was established in this work:

$$k^s = \frac{k_0^s}{\left(1+0.65\frac{\sigma}{E}\left(\frac{l}{t}\right)^2\right)^{-1} + \frac{4h}{l}\left(1+1.96e5\sqrt{\frac{\sigma}{E}}\frac{h^{0.22}w^{1.28}t}{l^{2.5}}\right)} \tag{9}$$

Here, the first term in the denominator is due to the stress stiffening of the cantilever. The second term represents the support post and its increased compliance due to biaxial residual stress σ. The value of k_0^s is calculated using (6a).

Applications of the conventional formula (5) are usually based on the assumption that the movable plate is rigid and that there is no localised deformation in connection (joint) areas. However, our simulation study shows that the movable plate does actually deform (Fig. 7), thus affecting the total spring constant of the device K^{total}. In this work, the spring constant of plates suspended on straight tethers was determined by loading the plate with a low pressure and converting the deflection into K^{total} via Hooke's law (7). Then the formula for the total spring constant of the structure (Fig. 1a) was established:

$$K^{\text{total}} = \frac{4k^s}{1+0.15wL^2/l^3} \tag{10}$$

where L is the plate side length. Together, Eqs. (9) and (10) comprise a closed-form model for the spring constant of a plate on straight suspensions (Fig. 1a).

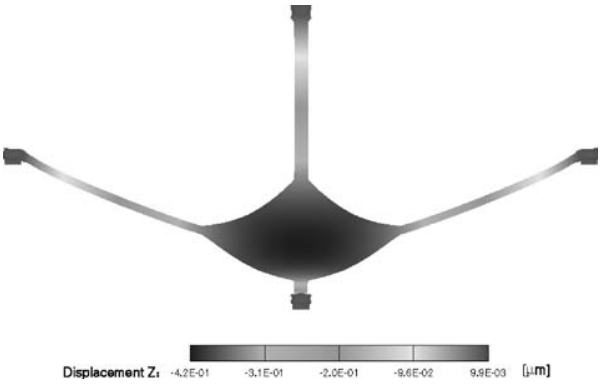

Fig. 7. Deformation of the plate suspended on straight tethers under uniform pressure; the dark area in the middle of the plate indicates its local deformation (exaggerated 100 times).

4.2. Plate on Meander Tethers

Because of an inherent complex cross-axis coupling in meander springs (Fig. 3b) and complex tethers-plate coupling, accurate modelling of plates with such tethers is a challenging task. The presence of biaxial residual stress affects the spring constant even more. FEM simulations revealed no tangible effect of residual stress on the spring constant of stand-alone meanders (less than 1%); it is only when meanders are in a plate-tethers system that the effect of residual stress becomes pronounced and substantial. This is because of the high compliance of the meanders and in-plane deformation of the device. In order to account for all these effects, the technique described in the beginning of this section was applied and the following formula for calculation of the spring constant of plates with meander tethers has been developed:

$$K^{\text{total}} = 4 * k_s^0 \frac{1+2.4(\sigma/E)(a/b)^{1.4}((w-1.5)^{0.8}L^{0.7})/(t^{1.5})}{1+58(a\sqrt{b}L\sqrt{w-1.95})/((3a+b)^3)} \tag{11}$$

where k_s^0 is calculated via (6b). As with any non-empirical equations, the models developed here require validation which is the aim of the next section.

5. EXPERIMENT/VERIFICATION AND SENSITIVITY ANALYSIS

RF switches microfabricated in the Tyndall National Institute (Fig. 1) were used to experimentally validate the models. The switches consisted of a 1 μm thick aluminium plate (100×100 μm^2 or 200×200 μm^2) suspended on either 50 μm $\times$ 5 μm cantilever or 10 μm $\times$ 8 μm $\times$ 2 μm meander tethers. Mechanical material properties assumed in calculations are presented in Table II. Using blanket film tests and the Stoney formula,[19] it was experimentally found that biaxial tensile stress induced during the fabrication process was of the order of 35 MPa. The pull-in voltage of the structures was measured using a capacitance-voltage test system. This voltage represents an electromechanical instability point at which time the switch collapses or "pulls-in" onto an underlying electrode.[15]

This voltage is predicted by the following expression

$$V_{\text{pull-in}} = \sqrt{\frac{8K^{\text{total}}h^3}{27\varepsilon A}} + V_{\text{offset}} \tag{12}$$

where the spring constant values were estimated via Eqs. (9), (10), (11). The zero-voltage airgap h was measured using white-light interferometry.[21] Note that formula (12) incorporates one extra term V_{offset}, not present in the conventional Eq. (2), which is a measured value of the

Table II. Material properties of Al thin film.

Young's modulus, GPa	Poisson's ratio	Ref.
74	0.34	[20]

RESEARCH ARTICLE

voltage offset ($V_{offset} = 0.55$ V) due to dielectric charging.[22] Measured and modelled results were found in very good agreement, with a maximum discrepancy of 11% (Fig. 8). It is also clear that significant errors (over 100%) may result in predicting pull-in voltage when the spring constant is calculated via the conventional model (5), (6). These models assume the plate to be rigid and neglect the effects of residual stress and non-ideal anchors.

In order to investigate combined effects of residual stress and non-ideal anchors (anchor compliance) on the spring constant a parameter sensitivity study was undertaken. Thus, the spring constant was calculated for variable values of residual stress and anchor height with all other parameters held constant. Analysis of the results, presented in Figure 9, shows a strong interaction between the two parameters that is reasonably anticipated. On the other hand, for zero stress K^{total} converges to the value predicted by the conventional model. Anchor height is found to be the most critical design parameter controlling low spring constant of a device incorporating residual stresses.

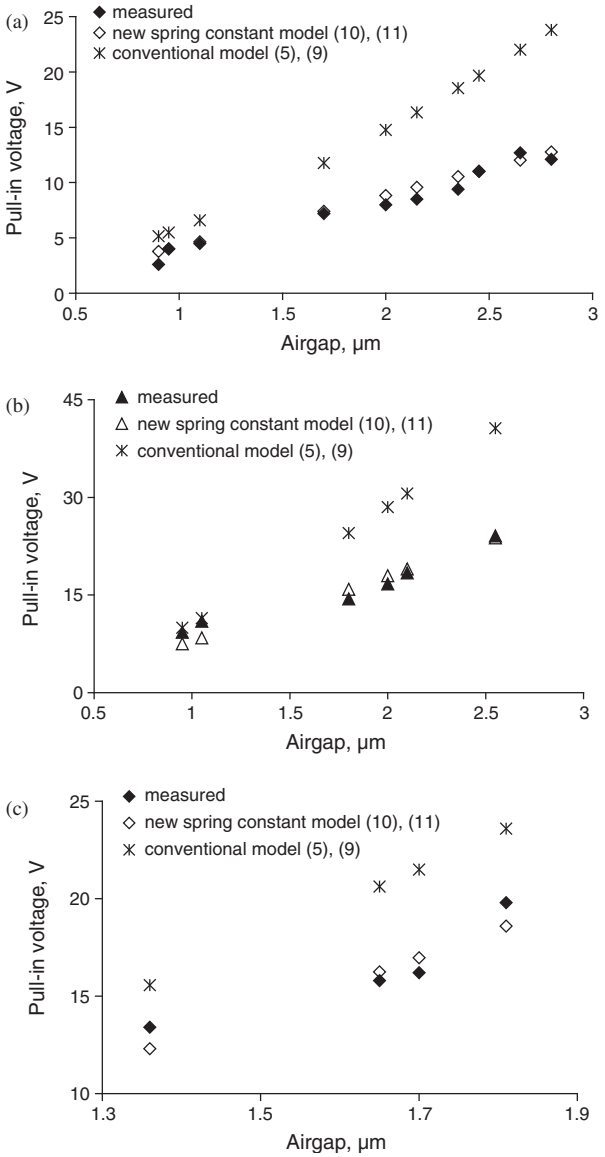

Fig. 8. Modelled and measured pull-in voltage for 100×100 μm^2 (a) and 200×200 μm^2 (b) plates suspended on straight tethers and 100×100 μm^2 plate on meander (10 $\mu m \times 8$ $\mu m \times 2$ μm) tethers (c).

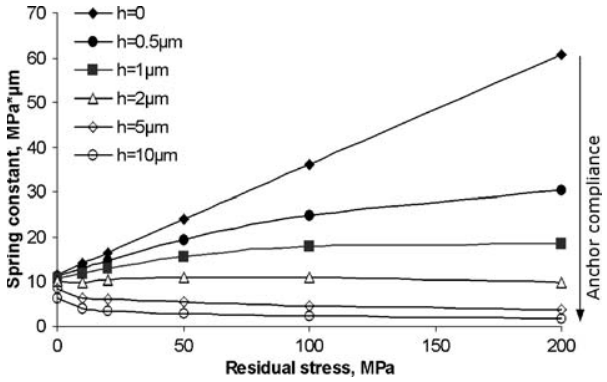

Fig. 9. Results of sensitivity study: Effect of coupling of residual stress and anchor compliance.

6. CONCLUSIONS

Comprehensive models for calculating the spring constant of a plate suspended by four straight or meander tethers, common to MEMS tunable capacitors and RF switches, have been developed. These models account for residual stress and non-ideal anchors typical of microfabricated structures, and were validated by comparison with experimentally measured values. Correlation to within 11% was achieved. The results also indicate that significant errors may result in predicting the spring constant when the combined effects of residual stress, non-ideal anchors, and non-rigidity of the plate are neglected or underestimated. The findings can be used for evaluation of the spring constant and consequently the pull-in voltage, the resonant frequency or the deflection of microstructures based on the suspended plate.

Acknowledgments: This work has been funded by Irish Research Council in Science, Engineering, and Technology. The RF switch fabrication has been carried out with the support of Enterprise Ireland under the ATRP program.

NOMENCLATURE AND ABBREVIATIONS

E—Young's modulus
L—plate side length
w—width of the cantilever suspension
t—thickness of the device
l—length of cantilever suspension
K^{total}—total spring constant of the suspended structure

k_s—spring constant of a pillar-supported guided-end cantilever
k_0^s—spring constant of an ideally fixed guided-end cantilever
h—anchor height/electrical gap
F—force
σ—fabrication residual stress
MEMS—microelectromechanical systems
RF—radio frequency
FEM—finite elements method

References and Notes

1. G. M. Rebeiz, *RF MEMS, Theory, Design, and Technology* Wiley, Hoboken **(2003)**.
2. A. Dec and K. Suyama, *IEEE Transactions on Microwave Theory and Techniques* 46, 12 **(1998)**.
3. Jun Zou, Chang Liu, Jose Shutt-Aine, Jinghong Chen, and Sung-Mo Kang, *International Electron Device Meeting*, San Francisco **(2000)**.
4. C. T.-C. Nguyen, *Proc. IEEE International Micro Electro Mechanical Systems Workshop*, Heidelberg, Germany **(1998)**.
5. H. Nieminen, V. Ermolov, K. Nybergh, S. Silanto, and T. Ryhänen, *J. Micromech. Microeng.* 12 **(2002)**.
6. Z. Olszewski, M. Hill, C. O'Mahony, R. Duanne, and R. Houlihan, *J. Micromech. Microeng.* 15, S122 **(2005)**.
7. D. Peroulis, S. P. Pacheco, K. Sarabandi, and L. P. B. Katehi, *IEEE Transactions on Microwave Theory and Techniques* 51, 1 **(2003)**.
8. C. O'Mahony, R. Duane, M. Hill, and A. Mathewson, *Proc. Design, Test, Integration and Packaging of MEMS/MOEMS Conference*, Montreux, Switzerland **(2004)**.
9. S. P. Pacheco, L. P. B. Katehi, and C. T.-C. Nguyen, *IEEE MTT-S Int. Microwave Symp. Dig.* 1 **(2000)**.
10. C. O'Mahony, R. Duane, M. Hill, and A. Mathewson, *Proc. 15th Micromechanics Europe*, Leuven, Belgium **(2004)**.
11. P. P. Benham, R. J. Crawford, and C. G. Armstrong, *Mechanics of Engineering Materials*, Pearson, Essex **(1996)**.
12. J. A. Pelesko and D. H. Bernstein, *Modeling MEMS and NEMS*, Chapman and Hall/CRC, Florida **(2002)**.
13. R. J. Roark and W. Young, *Formulas for Stress and Strain*, McGraw-Hill, New York **(2000)**.
14. B. D. Jensen, F. Bitsie, and M. de Boer, *Proc. SPIE Micromachining and Microfabrication*, Santa Clara, USA **(1999)**.
15. C. O'Mahony, M. Hill, R. Duane, and A. Mathewson, *J. Micromech. Microeng.* 13, S75 **(2003)**.
16. M. Gere and S. Timoshenko, *Mechanics of Materials*, Boston, PWS-Kent **(1990)**.
17. M. Lishchynska, N. Cordero, and O. Slattery, *Analog Integrated Circuits and Signal Processing* 44, 109 **(2005)**.
18. CoventorWare version 2005. *Reference Guides and Tutorials*, www.coventor.com
19. D. Campbell, Handbook of Thin Film Technology, edited by Maissel, Glang, McGraw-Hill, New York **(1970)**, Chap. 12.
20. M. Chilmungund, R. B. Inturi, and J. A. Barnard, *Thin Solid Films* 270, 260 **(1995)**.
21. C. O'Mahony, M. Hill, M. Brunet, R. Duane, and A. Mathewson, *Meas. Sci. Technol.* 14, 1807 **(2003)**.
22. C. O'Mahony, R. Duane, M. Hill, and A. Mathewson, *Electron. Lett.* 41 **(2005)**.

SENSOR LETTERS
Vol. 4, 206–213, 2006

RESEARCH ARTICLE

Coupled Electro-Mechanics Simulation Methodology of the Dynamic Pull-in in Micro-Systems

V. Rochus[1,*], D. J. Rixen[2], and J. C. Golinval[1]

[1] *University of Liège, Département d'Aérospatiale, Mécanique et Matériaux, LTAS-Vibrations et Identification des Structures, Chemin des chevreuils, 1, B52/3, B-4000 Liège, Belgium*
[2] *T. U. Delft, Faculty of Design, Engineering and Production Engineering Dynamics Mekelweg 2, 2628 CD Delft, The Netherlands*

(Received: 12 May 2005. Accepted: 4 December 2005)

The aim of this paper is to deal with multi-physics simulation of micro-electro-mechanical systems (MEMS) based on an advanced numerical methodology. MEMS are very small devices in which electric as well as mechanical and fluid phenomena appear and interact. Because of their microscopic scale, strong coupling effects arise between the different physical fields, and some forces, which were negligible at macroscopic scale, have to be taken into account. In order to accurately design such micro-electro-mechanical systems, it is of primary importance to be able to handle the strong coupling between the electric and the mechanical fields. In this paper, the finite element method (FEM) is used to model the electro-mechanical interactions and to perform static and transient analyses. The application example considered here is a micro-bridge consisting of a clamped-clamped beam suspended over a substrate (the lower electrode). When a voltage is applied between the beam and the substrate, electrostatic forces appear which force the beam to bend. When the applied voltage increases, the electrostatic forces become dominant and the plates stick together. The corresponding critical voltage is called the pull-in voltage. When the dynamic behaviour of the system is taken into account, it is shown that two new parameters have to be defined: the dynamic pull-in displacement and the dynamic pull-in time.

Keywords: Electro-Mechanical Coupling, Nonlinear, Finite Element Method, Micro-Electro-Mechanical Systems.

1. INTRODUCTION

To analyse the static and dynamic behaviour of electrostatically actuated Micro-Electro-Mechanical Systems (MEMS), the electromechanical coupling has to be accounted for. Since the electrostatic domain is influenced by the deformation of the structural components, the Finite Element discretisation of the electrostatic domain needs to be properly updated. The common approach is based on a staggered procedure, which consists on iterating between the mechanical domain and the electrostatic domain using separate software.[1] Boundary elements are also currently used in order to avoid moving mesh problems. Another approach consists in using predefined capacitance between structural nodes or applying structural reduction techniques together with finite difference evaluation of electrostatic coupling. However, such techniques cannot easily handle strong coupling effects in an accurate manner. In the present work, a fully coupled electro-mechanical formulation is proposed. The method provides fully consistent tangent stiffness matrices and allows static equilibrium positions to be found, to evaluate natural frequencies and to compute transient dynamic responses in a non-staggered way. An interesting application of the proposed method is the analysis of the dynamic behaviour of electrostatically actuated micro-bridges when a sudden voltage step is applied on the electrodes. The dynamic behaviour of this type of micro-systems is also studied by Nayfeh in Ref. [2] where an AC voltage is applied and by Dequesnes[3] for carbon nanotube based switches. In this paper it is shown that dynamic transients may lead to pull-in instabilities even though the applied voltage is smaller than the static pull-in voltage usually defined as design criterion and a characterisation of the dynamic pull-in voltage and the dynamic pull-in time is performed.

*Corresponding author; E-mail: V.Rochus@ulg.ac.be

 1546-198X/2006/4/206/008 doi:10.1166/sl.2006.017

2. ELECTRO-MECHANICAL COUPLING

In order to understand the physical phenomena of electro-mechanical coupling, the reference problem shown in Figure 1 is considered. It consists in a capacitor made of two parallel plates between which a voltage is applied. The upper plate is supported by a spring and the lower plate is grounded. This mass-spring model is representative of the mode of operation of electrostatically actuated MEMS devices.

For the sake of simplicity, the electrodes of the capacitor are considered as infinite planes and the electric charges are supposed to be evenly distributed on the surfaces. This approximation allows fringing fields to be neglected and to reduce the system to a one-dimensional problem. The capacitor is also considered to be in vacuum and no damping is considered in the model. The dynamic equilibrium equation of the system is:[4]

$$m\ddot{d} = -k(d - d_0) - \frac{1}{2}\varepsilon_0 \frac{V^2}{d^2} \tag{1}$$

where d is the distance between the two plates; m is the mass of the upper electrode; k is the spring stiffness and ε_0 is the permittivity of free space. It can be noted from the equation that the dynamic behaviour of the structure depends on the applied voltage V and on the initial gap between the plates d_0.

2.1. Static Pull-in Voltage

The static equilibrium equation of the system is the following:

$$k(d - d_0) + \frac{1}{2}\varepsilon_0 \frac{V^2}{d^2} = 0 \tag{2}$$

When the applied voltage increases, it creates an attraction force between the electrodes and the upper plate moves closer to the grounded plate. When the electrostatic forces in $1/d^2$ become dominant with respect to the mechanical force so that the plates stick together, a critical voltage is reached. This critical voltage is called the static pull-in voltage. The analytical expressions of the static pull-in voltage and of the corresponding pull-in distance are given in Ref. [4]:

$$V_{pi} = \sqrt{\frac{8}{27}\frac{kd_0^3}{\varepsilon_0}} \quad \text{and} \quad d_{pi} = \frac{2}{3}d_0 \tag{3}$$

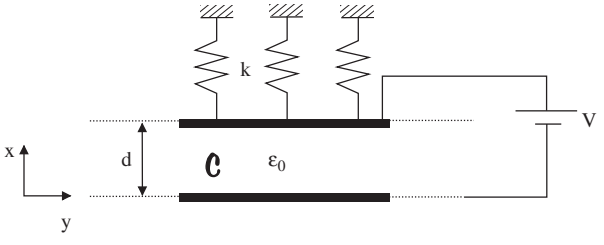

Fig. 1. Definition of the reference problem.

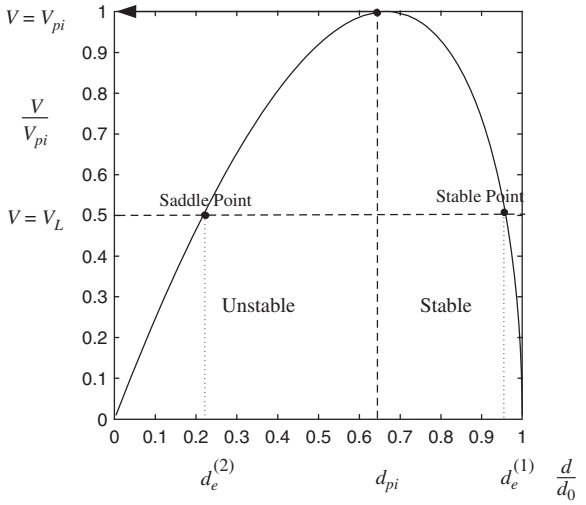

Fig. 2. Evolution of the normalized displacement with the normalized voltage.

When the applied voltage V is smaller than the pull-in voltage, two equilibrium positions exist: $d_e^{(1)}$ and $d_e^{(2)}$ as shown in Figure 2. When $V = Vpi$, the two equilibrium positions merge into one point (d_{pi}, V_{pi}). Beyond V_{pi}, no equilibrium position exists.

2.2. Dynamic Pull-in

The dynamic equilibrium equation may also be written in a non-dimensional form defining the following variables:

$$V^* = \frac{V}{V_{pi}} \quad d^* = \frac{d}{d_0}, \quad \omega_0^2 = \frac{k}{m} \tag{4}$$

The dynamic behaviour of the coupled system corresponding to different initial conditions are shown in the phase diagrams of Figures 3(a) to 3(d) (assuming $\omega_0 = 1$).

- (a): Phase diagram of the pure mechanical model. No voltage is applied, the system is stable.
- (b) and (c): a voltage $V < V_{pi}$ is applied. The system is stable near the equilibrium position and oscillates in a non-linear way. If the initial displacement is large enough, the moving plate can reach a position close to the fixed electrode so that the electrostatic forces become higher than the spring restoring force: the plates collapse on one another and stick together.
- (d): $V \geq V_{pi}$: For any initial condition, the system is unstable and the phase diagram diverges to two solutions: $d = 0$, $\dot{d} = \pm\infty$.

A second critical voltage is now defined. As stated in Ref. [4], when $V < V_{pi}$, a stable area may be observed in the phase diagram corresponding to the ellipsoid area in Figure 3(b). If we refer to the static pull-in definition, the system is stable. But if the dynamic behaviour is considered, the problem may become unstable. Indeed, if the system has enough energy to pass over a second characteristic point called the dynamic pull-in position, the

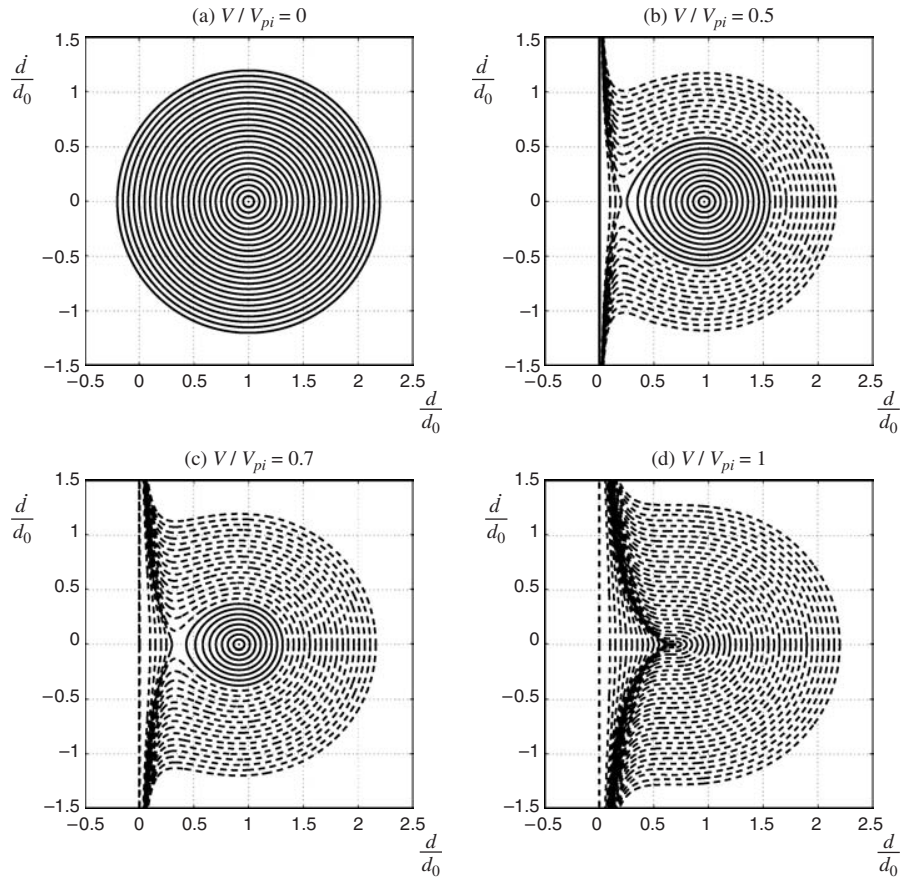

Fig. 3. Phase diagrams for different values of voltage.

system becomes unstable. The dynamic pull-in voltage is defined as the voltage for which the system becomes unstable when it is suddenly applied to the system at rest.

3. FINITE ELEMENT FORMULATION

To simulate electro-mechanically coupled systems, common software use weak coupling procedures in the sense that the electrostatic and the mechanical domains are discretised and treated iteratively in separate solvers. This basic iterative method is commonly presented in the literature (see e.g., Lee et al.[1]) In this paper, we propose a finite element formulation to solve the electrostatic and mechanical domains simultaneously in a strong coupled form. One of the advantages of this formulation is that the tangent stiffness matrix of the electro-mechanical problem can be explicitly constructed. Thus the natural frequency of the electro-mechanical system can be directly evaluated around a given equilibrium configuration and the transient dynamic response can be more easily computed.

The consistent way of deriving a finite element discretisation to model electro-mechanical coupling is using variational calculus. Starting from the energy of the coupled problem, nodal forces are obtained for an element by derivation of the energy. The tangent stiffness matrix of the coupled problem is then obtained by linearisation of the equilibrium equations in the vicinity of an equilibrium position (see in Ref. [4]):

$$\begin{pmatrix} \mathbf{K}_{uu}(\phi) & \mathbf{K}_{u\phi}(\phi) \\ \mathbf{K}_{\phi u}(\phi) & \mathbf{K}_{\phi\phi} \end{pmatrix} \begin{pmatrix} \Delta\mathbf{U} \\ \Delta\Phi \end{pmatrix} = \begin{pmatrix} \Delta\mathbf{f}_m \\ \Delta\mathbf{f}_e \end{pmatrix} \tag{5}$$

where subscripts u and ϕ refer respectively to the mechanical and electrostatic domains; $\Delta\mathbf{U}$ is the displacement vector and $\Delta\mathbf{f}_m$ is the vector of mechanical forces; $\Delta\Phi$ is the electric potential vector and $\Delta\mathbf{f}_e$ is the vector of electrostatic forces. It can be observed that the tangent stiffness matrix is symmetric and that coupling terms such as $\mathbf{K}_{u\phi}$ and $\mathbf{K}_{\phi u}$ appear between mechanical and electric degrees of freedom. It should be noted that the tangent stiffness matrix, unlike in the common approach, is not obtained by finite difference, but derives naturally from the variational approach and can be easily assembled using the finite element model. More details about the expression of the coupling matrix may be found in Ref. [4].

4. APPLICATION TO A MICRO-BRIDGE

The application of the proposed method is illustrated on the example of a beam-type micro-resonator composed of two electrodes: a clamped-clamped beam and a substrate

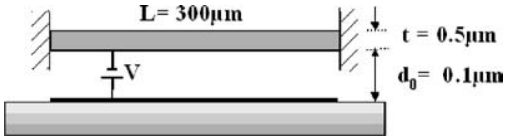

Fig. 4. Micro-Bridge.

as shown in Figure 4. The beam is made of silicon with a density of 2648.38 kg/m^3 and a Young's modulus of 77 GPa. Its length is 300 μm, its thickness is 0.5 μm and its width is about 10 μm. The initial gap d_0 between the electrodes is set to 0.1 μm. In that case, the displacements remain small so that linear structural deformation can be assumed. The only nonlinear effect comes from the electrostatic coupling. If d_0 is equal or bigger than 6 μm, geometrical nonlinear effect would be important as shown in Ref. [5]. In that case, the geometric nonlinearity induced by the mechanical displacement of the structure has to be taken into account in the formulation. For the sake of clarity, the small displacement assumption is considered in the following.

4.1. Finite Element Modelling

The system of Figure 4 is modelled using mechanical and electrostatic finite elements. The mechanical domain is discretised by non-compatible elements, which permits to take into account the bending of the beam.[6] The electrostatic domain is modelled using two types of elements: pure electrostatic elements for the surrounding environment of the beam and electro-mechanical coupling elements at the border with the beam. These coupling elements allow the mechanical structure to be loaded by the electrostatic forces. When the mechanical structure is displaced the mesh of the electrostatic domain is deformed. The method used to displace the nodes is to consider the electrostatic domain as a virtual structure which deforms under the action of the interface displacement.

4.2. Static Equilibrium

The static pull-in voltage is first computed by evaluating the static equilibrium position of the system when V is incremented. To this purpose, the classical Riks-Crisfields continuation technique is used to reach equilibrium positions in the unstable region.[4] The typical pull-in curve is plotted in Figure 5 where the voltage is given in function of the displacement at the middle of the beam. It is observed that the static pull-in voltage appears at 0.0397 Volt. For this particular example, the large displacement assumption would provide the same results.

4.3. Dynamic Behaviour

In this section, the transient dynamic response of the system is computed when the voltage is suddenly applied between

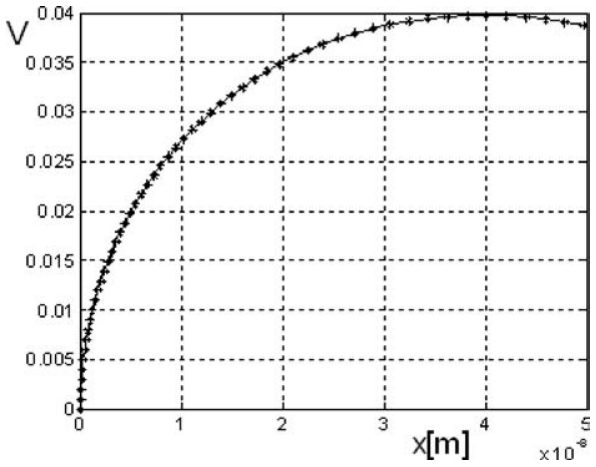

Fig. 5. Static Pull-in Voltage.

the two electrodes i.e., when the time-history of the voltage corresponds to a step function as illustrated in Figure 6.

The Newmark time-integration scheme has been used to calculate the time response of the system with a small numerical damping ($\alpha = 0.05$). The results obtained are depicted in the phase plot of Figure 7. Instability is observed for voltages higher than or equal to 0.0363 V. Thus the dynamic pull-in voltage may be defined as the voltage amplitude such that, when applied suddenly, it leads to the dynamical instability of the system. Another characteristic parameter of the system is the pull-in time, which is defined as the time needed for the plates to stick together when the pull-in voltage is applied. In this example, the difference between the static and the dynamic pull-in voltage is around 8.7% and the pull-in time is estimated to 20.7 μs.

4.4. Parametric Study

Approximate expressions are given in the literature for the static pull-in voltage of simple systems such as a clamped-clamped beam. They are very useful for the preliminary design of simple micro-systems. In the paper by Osterberg and Senturia,[7] an analytical formula is proposed to better match the experiment results:

$$V_{pi} = \sqrt{\frac{4\gamma_1 B}{\varepsilon_L^4 \gamma_2^2 [1 + \gamma_3 \frac{d_0}{b}]}} \tag{6}$$

with $\gamma_1 = 2.79$, $\gamma_2 = 0.97$, $\gamma_3 = 0.42$, and $B = Et^3 d_0^3$. The parameters γ_1, γ_2, and γ_3 were introduced in the formula

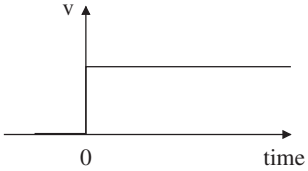

Fig. 6. Step of voltage.

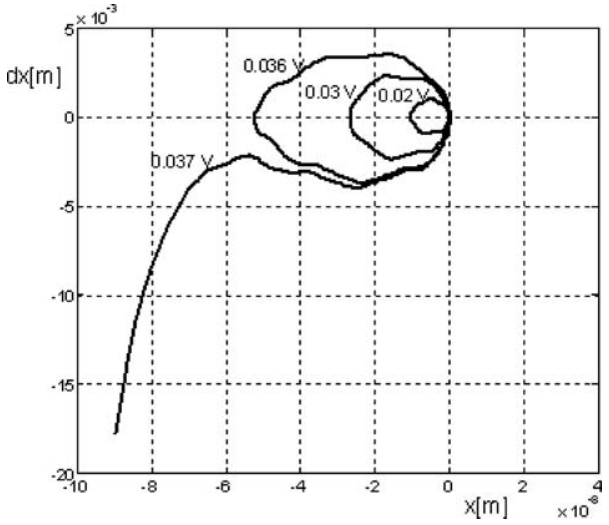

Fig. 7. Evolution of pull-in voltage with the thickness of the beam.

to fit the experiments. In the particular example considered here, the term $\gamma_3(d_0/b)$ is negligible.

The static pull-in voltage given by this semi-empirical formula is estimated to 0.0398 Volt, which is in very good agreement with our finite element simulation result. Regarding to the dynamic pull-in voltage, no analytical expression exists even for the one-dimensional problem. To build such relations for the dynamic pull-in voltage and the pull-in time, all the dimensions and structural parameters of the system have been modified independently in the following. The objective is to identify the dependency of the dynamic pull-in voltage and the pull-in time with the length L, the thickness t, the initial gap d_0, the Young's modulus E and the mass density ρ of the beam.

4.4.1. Variation of the Length of the Beam

Figure 8 shows the evolution of the static pull-in voltage (black points) and of the dynamic pull-in voltage (white

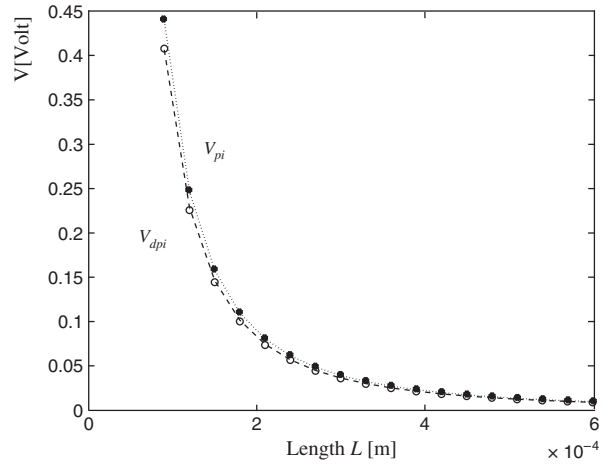

Fig. 8. Evolution of pull-in voltage with the length of the beam.

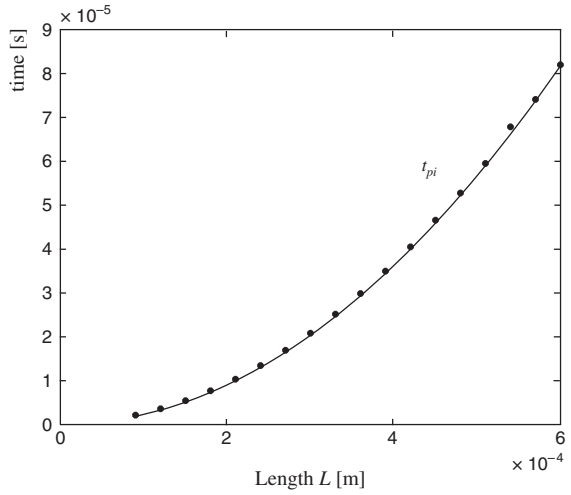

Fig. 9. Evolution of pull-in time with the length of the beam.

circles) with respect to the length of the beam. These results were obtained by finite element simulations. In the two cases, the pull-in voltages decrease when the length of the beam increases. The fitting of the results by the relation A_1/L^2 for the static pull-in voltage and by A_2/L^2 for the dynamic pull-in voltage gives the results: $A_1 = 3.57\ 10^{-9}$ V.m^2 and $A_2 = 3.3\ 10^{-9}$ V.m^2. Parameters A_1 and A_2 are very close and their difference does not provide any important information on the behaviour of the system. For this reason, they will not be considered in the following. The difference between the two pull-in voltages is about 8%.

The second dynamic parameter to fit is the pull-in time. The pull-in time is given in Figure 9 for different lengths of the beam. The black points are the Finite Element results. It is found to increase with the squared-length of the beam. The function used to fit the finite element results is BL^2 with $B = 228.37$ s/m^2.

4.4.2. Variation of the Thickness of the Beam

When the thickness t of the beam is varied from 0.1 μm to 1 μm, the pull-in voltage increases as shown in Figure 10. Indeed the increase of the thickness increases the stiffness of the structure so that it needs more voltage to bend it. It is found that both the static and the dynamic pull-in voltage are proportional to $t^{3/2}$. This relation is used to plot the dashed line and the dotted line which follows very well the finite element results in Figure 10. The evolution of the pull-in time with the thickness of the beam is plotted in Figure 11. It decreases when the thickness increases. The function used to fit the numerical results is inversely proportional to the thickness: $B\,(1/t)$.

4.4.3. Variation of the Initial Gap

In this subsection, the distance between the two electrodes is changed. That means that the structural behaviour of

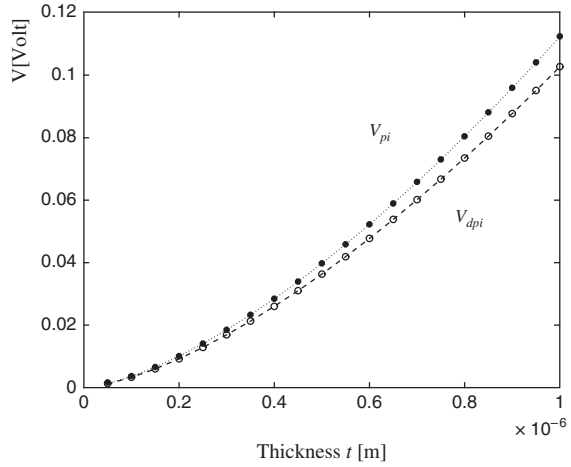

Fig. 10. Evolution of pull-in voltage with the thickness of the beam.

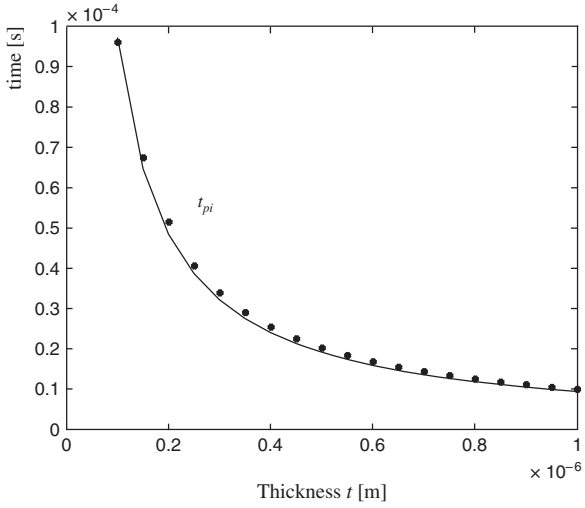

Fig. 11. Evolution of pull-in time with the thickness of the beam.

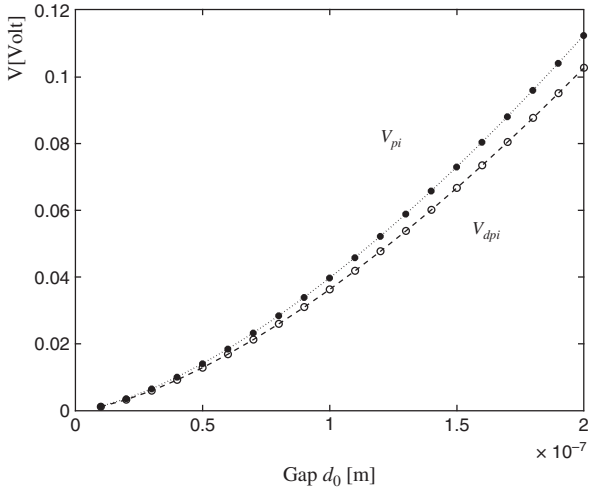

Fig. 12. Evolution of pull-in voltage with the gap between the electrodes.

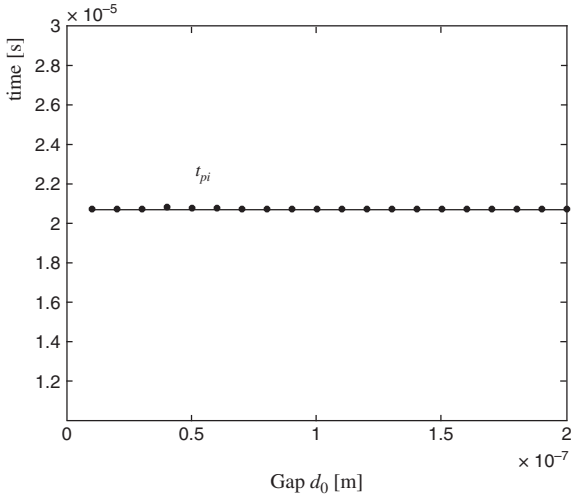

Fig. 13. Evolution of pull-in time with the gap between the electrodes.

the beam is not modified. Only the electrostatic forces are increased when the gap is reduced. The variations of the static and dynamic pull-in voltages with respect to the initial gap d_0 are shown in Figure 12. Both the static and the dynamic pull-in voltages are found to be proportional to $d_0^{3/2}$. When the gap is reduced the electrostatic forces are more important for the same structural stiffness. It needs then less voltage to achieve the pull-in voltage as shown in Figure 12. The plot in Figure 13 shows an important result: the pull-in time does not depend on the distance between the electrodes. Only the mechanical behaviour of the beam determines the value of the pull-in time.

4.4.4. Variation of Young's Modulus

In the two next subsections, the material characteristics of the beam are studied. The first one is the Young's modulus. It can be found easily that the static and dynamic pull-in voltages are proportional to $\sqrt{E}$ as shown in Figure 14 as already found in the one-dimensional analysis. When the Young's modulus increases, the stiffness of the structure increases and the pull-in voltages increases. Figure 15 shows that the pull-in time is proportional to $1/\sqrt{E}$.

4.4.5. Variation of the Mass Density

In Figure 16, it is observed that the static pull-in voltage as well as the dynamic pull-in voltage do not depend on the mass density of the beam. On one hand, in the case of the static pull-in voltage, it is understandable since this voltage is obtained from the static equilibrium equation. On the other hand, the dynamic pull-in voltage is obtained by a time-integration of the dynamic equilibrium equation for different values of voltage. Its independence with respect to the mass density is not expected. Figure 17 shows that the dynamic pull-in time increases when the mass density increases. It is proportional to $\sqrt{\rho}$.

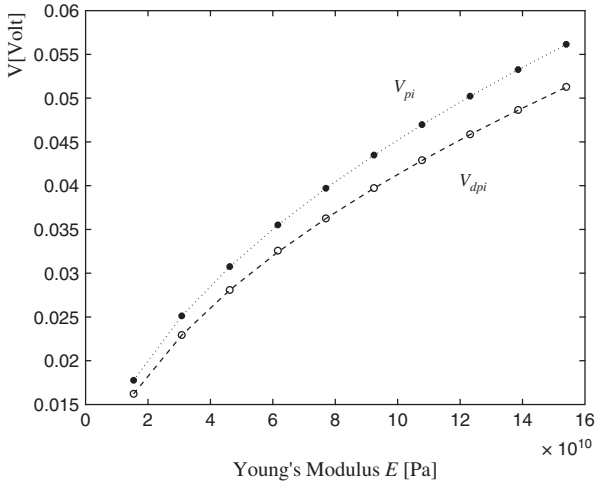

Fig. 14. Evolution of pull-in voltage with the Young's Modulus.

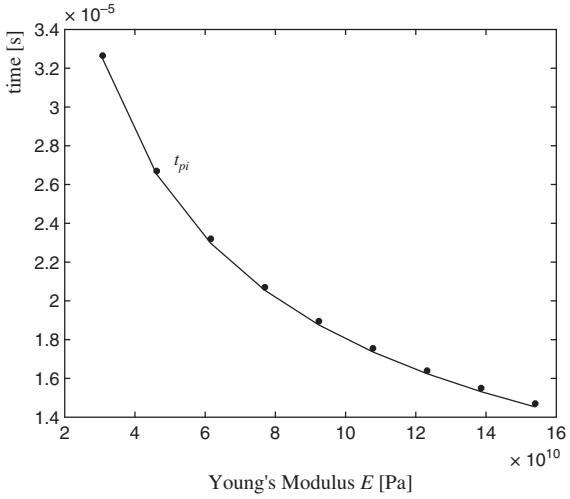

Fig. 15. Evolution of pull-in time with the Young's Modulus.

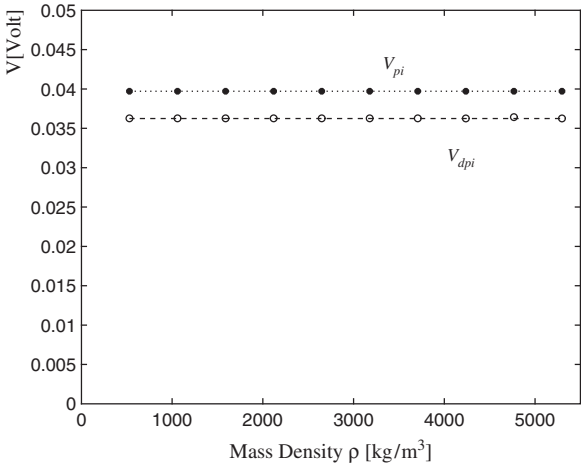

Fig. 16. Evolution of pull-in voltage with the mass density of the beam.

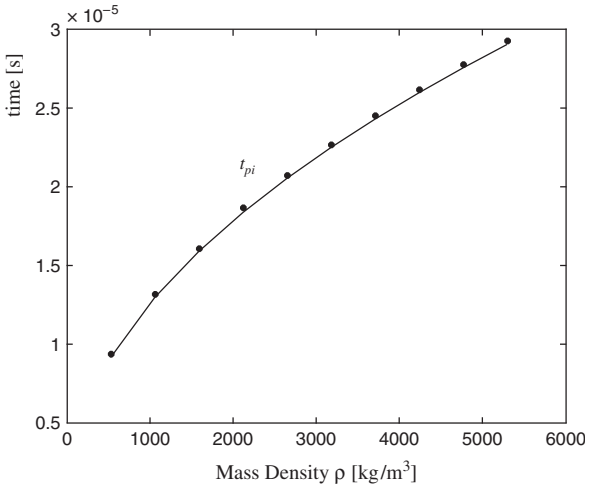

Fig. 17. Evolution of pull-in time with the mass density of the beam.

4.4.6. Variation of the Void Permittivity

On the graph of the evolution of the pull-in voltage with the permittivity presented in Figure 18 the pull-in voltages change as $1/\sqrt{\varepsilon}$. The pull-in time is totally independent of the permittivity as shown in Figure 19.

4.4.7. Discussions

The sensitivity of the static and dynamic pull-in voltages and of the pull-in time to all the parameters defining the micro-bridge was studied. By collecting all the results, expressions may be written for the pull-in voltages and pull-in time in the case of deep beams.

Static Pull-in Voltage:

$$V_{spi} = A_1\sqrt{\frac{Et^3d_0^3}{\varepsilon L^4}} \quad \text{with} \quad A_1 = 3.4196\ ([-]) \qquad (7)$$

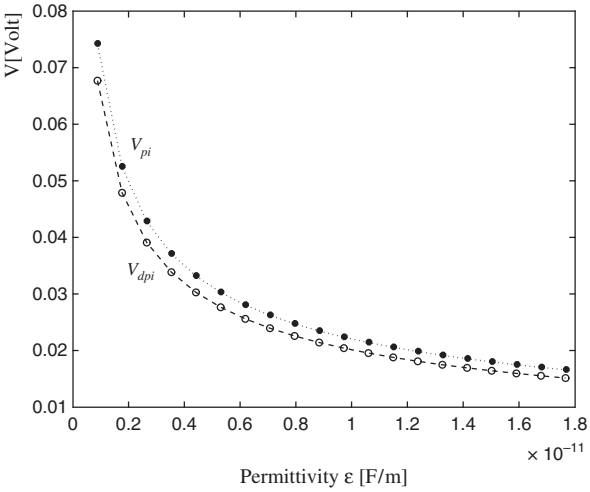

Fig. 18. Evolution of pull-in voltage with the permittivity.

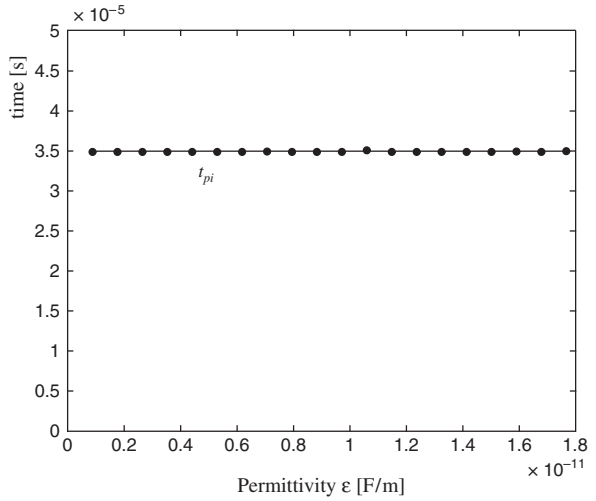

Fig. 19. Evolution of pull-in time with the permittivity.

Dynamic Pull-in Voltage:

$$V_{dpi} = A_2\sqrt{\frac{Et^3d_0^3}{\varepsilon L^4}} \quad \text{with} \quad A_2 = 3.152\ ([-]) \qquad (8)$$

Pull-in time:

$$t_{pi} = B\frac{L^2}{t}\sqrt{\frac{\rho}{E}} \quad \text{with} \quad B = 0.615\ ([\sqrt{m}]) \qquad (9)$$

The relation given here for the static pull-in voltage obtained here is very similar to the expression proposed in the first section. One remarkable result is the independence of the dynamic pull-in voltages with respect to the mass density and the independence of the pull-in time with respect to the distance between the electrodes.

5. CONCLUSIONS

The advantage of the methodology used in this paper compared to the common staggered approach found in commercial software is that the tangent stiffness matrix of the coupled problem is directly available. It permits to compute easily the static pull-in voltage with a good accuracy. It also allows the dynamic behaviour of the system to be simulated using time-integration algorithms. In a previous paper,[5] we have shown that there is a non-negligible difference between the static and the dynamic pull-in voltages. Here, some analytical expressions for the dynamic pull-in voltage and the pull-in time have been proposed. These expressions may be used for the design of electrostatically actuated micro-bridges.

Acknowledgments: The first author acknowledges the financial support of the Belgian National Fund for Scientific Research. Part of the work presented in this text is supported by the Communauté Française de Belgique—Direction Générale de la Recherche Scientifique in the framework Actions de Recherche Concertées (convention ARC 03/08-298). The second author acknowledges the financial support of the Koiter Institute form the Delft University of Technology, The Netherlands.

References and Notes

1. W. S. Lee, K. C. Kwon, B. K. Kim, J. H. Cho, and S. K. Young, *Journal of Modeling and Simulation of Micro-systems* 2, 83 **(2001)**.
2. A. H. Nayfeh and M. I. Younis, *Journal of Micromechanics and Microengineering*, 15, 1840 **(2005)**.
3. M. Dequesnes, Z. Tang, and N. R. Aluru, *Journal of Engineering Materials and Technology—Transactions of the ASME* 126, 230 **(2004)**.
4. V. Rochus, D. J. Rixen, and J. C. Golinval, *International Journal for Numerical Methods in Engineering*, (submitted to).
5. V. Rochus, D. J. Rixen, and J. C. Golinval, Electrostatic Coupling of MEMs Structures: Transient Simulations and Dynamic Pull-in. *The 2004 Workshop on Coupled Problems, Processes, and Phenomena: Modelling, Control, and Analysis*, Orlando **(2004)**.
6. O. C. Zienkiewicz, The Finite Element Method. *IE* **(1977)**, pp. 272–276.
7. P. M. Osterberg and Stephen D. Senturia, M-Test: A test Chip for Mems Material Property Measurement Using Electrostatically Actuated Test Structures. *IEEE*, **(1997)**, Vol. 6, pp. 107–118.